

ANKA

User Reports 2012/2013

SYNCHROTRON RADIATION FACILITY ANKA



User Reports 2012 and 2013

This annex lists all reports which have been submitted by users until September 2014. ANKA expects reports to be released for publication within two years after accomplishment of the experiment. The reports are organized according to science fields and beamlines.

**ANKA User Office
Karlsruhe Institute of Technology (KIT)**

Research Areas (in alphabetic order)

1. Actinide Science [ANS]
2. Catalysis [CAT]
3. Condensed Matter [CM]
4. Environment [ENV]
5. Life Science (Biology, Biointerfaces) [LSC]
6. Materials [MAT]
7. Nano and Micro Technologies [NMT]
8. X-Ray and THz/IR Technology [TIR]
9. Other Topics

ANKA Beamlines (in alphabetic order)

1. Beamline for actinide research [INE]
2. Infrared/THz microspectroscopy beamline [IR2]
3. Infrared/THz spectroscopy and ellipsometry beamline [IR1]
4. Soft X-ray spectroscopy, microscopy and spectromicroscopy beamline [WERA]
5. Single crystal X-ray diffraction beamline [SCD]
6. Vacuum UV beamline for synchrotron circular dichroism spectroscopy [UV-CD12]
7. X-ray absorption spectroscopy beamline [XAS]
8. X-ray beamline for environmental research [SUL-X]
9. X-ray fluorescence spectroscopy beamline [FLUO]
10. X-ray topography & tomography beamline [TOPO-TOMO]

Table of Contents

User Reports 2012

1. Actinide Science [ANS]

Project Leader	First Author	Report Title	Beamline	Page
F. Lebreton	F. Lebreton	Local structure and charge distribution in $U_{1-x}Am_xO_{2\pm\delta}$ ($0.15 \leq x \leq 0.50$)	INE	10
P. Panak	N. Bauer	EXAFS investigation on actinide and lanthanide transferrin complexes	INE	12
D.R. Fröhlich	D.R. Fröhlich	EXAFS investigation on the formation of Am(III) chloro complexes in saline solutions at temperatures up to 200 °C	INE	14
A. Godelitsas	A. Godelitsas	The nature of uranium in sedimentary rocks of Epirus region (NW Greece)	INE, SUL-X	16
S. Kozimor	A. C. Olson	Identifying the Role of Covalency in Transuranic Extractants	INE	18
M. Philippe	P.M. Martin	In-situ high temperature XAS experiments on oxide nuclear fuels and precursors	INE	20
E. Curti	E. Curti	XANES and EXAFS measurements on Se-doped UO_2 and on simulated nuclear waste glass	INE	22
N. Banik	N. Banik	XAFS studies of NpO_2^+ behavior on Illite	INE	24
D. Fellhauer	D. Fellhauer	Solubility and speciation of Np(V) in alkaline $CaCl_2$ solutions	INE	26
X. Gaona	X. Gaona	Solubility and aqueous speciation of An(VI) in NaCl solutions	INE	28
B. Kienzler	C. Bube	μ -XAFS/XRF/XRD investigation of U(VI) phases in cement alteration products	INE	30
H. Curtius	H. Curtius	Fe, Co, Ni K edge XAFS investigation on transition metal (M=Fe,Co,Ni) doped hydrotalcite $[Mg_{3-y}M_yAl(OH)_8Cl] \cdot xH_2O$	INE	32
V. Petrov	V. Petrov	Solubility limiting Np(V) solid phases in NaCl solutions	INE	35

2. Catalysis [CAT]

No reports

3. Condensed Matter [CM]

Project Leader	First Author	Report Title	Beamline	Page
H. Peisert	F. Latteyer	Chloroaluminum phthalocyanine thin films: chemical reaction and molecular orientation	WERA	37
M.A. Uribe-Laverde	M.A. Uribe-Laverde	XMCD study of the Magnetic Proximity Effect in over-doped of $YBa_2Cu_3O_{7-x}/LaMnO_{3+x}$ Superlattices	WERA	40
K. Medjanik	A. Chernenkaya	Charge carrier localization in $(DOEO)_4[HgBr]_4 \bullet TCE$ and Peierls transition in TTF-TCNQ single crystals by temperature-dependent NEXAFS	WERA	42
J. Klanke	J. Klanke	Intra-Molecular Charge Transfer in Cu:Tetraazaporphyrin investigated by X-ray Magnetic Circular Dichroism	WERA	44

Table of Contents

4. Environment [ENV]

Project Leader	First Author	Report Title	Beamline	Page
A.Voegelin	A.Voegelin	Structure of fresh and aged Fe(III)-precipitates	SUL-X, XAS	46
J. Majzlan	J. Majzlan	Arsenic speciation in synthetic and natural Fe oxide matrices	SUL-X	48
U. Fittschen	U. Fittschen	Confocal XRF Imaging of elemental deposition of Mn, Ni and Cu on the graphite anode in cycled $\text{LiNi}_{0.5}\text{Mn}_{1.5}\text{O}_4$ /graphite full cells	FLUO	50
A.Voegelin	A.Voegelin	Iron oxidation products: Structural changes induced by precipitate drying and in-situ time-resolved oxidation experiment	SUL-X, XAS	52
K.-H. Knorr	K.-H. Knorr	Experimental report: Speciation of organic sulphur in humic acids and natural organic matter after reaction with hydrogen sulfide	SUL-X, XAS	54
J. Majzlan	J. Majzlan	Speciation of Zn and As in mining waste near Olkusz in Poland	SUL-X	56
K. Garbev	K. Garbev	Synchrotron-based XRD in situ Hydrothermal Investigation of Novel Hydraulic Binding Materials	SUL-X	58
K. Garbev	K. Garbev	Synchrotron-based XRD in situ Investigation of Novel Hydraulic Binding Materials: Formation of $\alpha\text{-C}_2\text{SH}$ from Ca(OH)_2 and Quartz Sand	SUL-X	60
J. Osan	J. Osan	Micro-XRF and micro-XRD study of the uptake of radionuclides by argillaceous rocks	FLUO	63

5. Life Science (Biology, Biointerfaces) [LSC]

Project Leader	First Author	Report Title	Beamline	Page
P.Kursula	H. Han	Conformational changes in vertebrate myelin proteins in membrane-mimetic conditions followed by SRCD spectroscopy	UV-CD12	65
P.Wadhvani	P. Wadhvani	Structure and aggregation tendency of membrane active peptides	UV-CD12	66
D. Windisch	D. Windisch	Investigation of the PDGF receptor Beta and the onco-protein E5 from bovine papillomavirus in lipid bilayers by SR-CD	UV-CD12	68
S. Afonin	V. Kubyskhin	Conformational analysis of novel cell-penetrating peptide SAP analogues in membrane-mimetic systems	UV-CD12	70
C.Streli	B. Pemmer	Differential accumulation of trace elements in human osteoblastic and chondroblastic osteosarcoma tissue	FLUO	72
J. L. Lopes	J. L. Lopes	Study of the insertion and membrane orientation of the antimicrobial peptide Plantaricin149 and analogs by SRCD and O-SRCD	UV-CD12	75

Table of Contents

6. Materials [MAT]

Project Leader	First Author	Report Title	Beamline	Page
H.Klein	H.Klein	Complete Texture Analysis with Pole Figure Measurements close to the Absorption Edge	PDIFF	76
H.Peisert	U. Aygül	New low band gap polymers: orientation and self-organization properties	XAS	78
Y. Cheng	Y. Cheng	Report on the flexible compatible SRCL instrument at TopoTomo	TOPO-TOMO	81
A. Jianu	A. Jianu	Characterization of oxide layers thermally grown on FeCrAl- based model alloys during exposure to heavy liquid metals	PDIFF	83
K. Horn	A. L. Walter	Luminescence, patterned metallic regions and photon mediated structural changes in half fluorinated graphene sheets.	PDIFF	85
T. Farago	T. Farago	In-situ Radiography of an Emulsification Process	TOPO-TOMO	87
H. Bracht	S. Eon	Structural investigation of isotopically enriched silicon multilayers	SCD	88
P. Gruber	J. Lohmiller	In situ tensile testing of nanoscale Cu/Nb multilayers	PDIFF	90
R. Kügler	R. Kügler	In-situ synchrotron radiation XRD study of particle formation during precipitation of barium sulphate	PDIFF	92
H.Behrens	A. Fiege	Sulphur speciation in basaltic glasses upon decompression	SUL-X	94
H. Peisert	U. Aygül	Molecular orientation of donor/acceptor blends - Influence of PCBM on the orientation of polymers	XAS	96

7. Nano and Micro Technologies [NMT]

Project Leader	First Author	Report Title	Beamline	Page
A.Powell	C. E. Anson	Crystallographic Characterisation of Large Paramagnetic Aggregates of Transition-Metal Cations	SCD	98
S.Indris	S.Indris	In Situ XAS Investigations on Fe/Mn Phosphates and Silicates During Operation in a Battery	XAS	100
S.Indris	S.Indris	In Situ XRD Investigations on Fe/Mn Phosphates and Silicates During Operation in a Battery	PDIFF	102
A. Pohl	A. Pohl	A XAFS study of the conversion reaction mechanism in FeF ₃ cathode materials for Li-ion batteries	INE, XAS	104
B. Khanbabaee	B. Khanbabaee	Near-surface density profiling of Fe ion irradiated Si (100) using extremely asymmetric diffraction by variation of the wavelength	PDIFF	107
A.Powell	C. E. Anson	Crystallographic Characterisation of Large Paramagnetic Aggregates of Transition-Metal Cations	SCD	109

8. Others [MR]

Project Leader	First Author	Report Title	Beamline	Page
H.Behrens	A. Fiege	Sulphur speciation in basaltic melts	SUL-X [MR]	111

Table of Contents

User Reports 2013

1. Actinide Science [ANS]

Project Leader	First Author	Report Title	Beamline	Page
C. Gaillard	C. Gaillard	Mecanism of extraction of Uranium(VI) in an ionic liquid with a neutral extractant (TBP, DMDBMA): determination of the extracted complexes stoichiometry by EXAFS	INE	113
D. Prieur	D. Prieur	Structural investigation of self-irradiation damaged AmO ₂	INE	115
K. Dardenne	K. Dardenne	XAFS investigation of a genuine HAWC glass fragment sampled from the Karlsruhe Vitrification Plant (VEK)	INE	117
F. Lebreton	F. Lebreton	In-situ XAS measurements at high temperature on transuranium-bearing oxide fuels and precursors	INE	119
D. Prieur	D. Prieur	Structural investigation of uranium-neptunium mixed dioxides	INE	120
D.R. Fröhlich	D.R. Fröhlich	EXAFS study of Am(III) complexation with oxalate as a function of pH	INE	122
F. Heberling	F. Heberling	Eu ³⁺ and Gd ³⁺ sorption at Aragonite and Calcite	INE	124
N. Finck	N. Finck	Fate of Lu(III) during 2-line ferrihydrite transformation	INE	126
M. Herm	M. Herm	Speciation of Nd(III) in MgCl ₂ -Mg(NO ₃) ₂ systems	INE	128
I. Pidchenko	I. Pidchenko	Plutonium oxidation states speciation in perchloric acid by high-energy resolution XANES technique	INE	132
T. Fernandes	T. Fernandes	Characterisation of the environment of U and Th in the effluent of a uranium treatment plant	INE	134
A. Kutzer	S. Bahl	Investigation of Ca, Ba and Cs molybdates in a Mo bearing borosilicate glass	INE	137
N. Bauer	N. Bauer	EXAFS investigation on actinide and lanthanide transferrin complexes	INE	139
N. Finck	N. Finck	Zr(IV) co-precipitation with clay minerals	INE	141
T. Prübmann	T. Prübmann	Pu L ₃ edge high energy-resolution X-ray absorption near edge structure investigations of actinide partitioning complexes	INE	143
T. Prübmann	T. Prübmann	A multi-analyser crystal spectrometer at the INE-Beamline	INE	145
M. Wiedemann	M. Wiedemann	EXAFS investigations on incorporated Eu(III) in brucite at high ionic strength	INE	147
J.-Y. Lee	J.-Y. Lee	Formation behavior of ternary Me-UO ₂ -CO ₃ species in weakly alkaline condition (Me = Ca ²⁺ and Mg ²⁺)	INE	149

2. Catalysis [CAT]

No reports

Table of Contents

3. Condensed Matter [CM]

Project Leader	First Author	Report Title	Beamline	Page
H. Peisert	M. Glaser	Charge transfer at the interface between cobalt phthalocyanine and epitaxially grown MnO	WERA	152
J. Geck	J. Geck	XMCD study of the intrinsic magnetic properties of $\text{Co}_2\text{Cr}_{1-x}\text{Fe}_x\text{Al}$	WERA	154
S. Lazarev	S. Lazarev	Semi-polar GaN grown on prepatterned sapphire substrate X-ray investigation	SCD	155
H. Peisert	H. Peisert	Interfacial electronic structure of iron phthalocyanine on epitaxial grown manganese oxide films	WERA	158

4. Environment [ENV]

Project Leader	First Author	Report Title	Beamline	Page
J. Majzlan	J. Majzlan	Environmental conditions of formation of low-temperature pyrite in sediments near Jenikov, Czech Republic	SUL-X	160
A. Vögelin	A. Vögelin	Structure of (Ca-)Fe(III)-phosphate and mode of As(V) incorporation into Fe oxidation products	SUL-X, XAS	161
Ch.Streli	C. Vanhoof	Speciation of Arsenic in aerosol samples with K-edge XANES in fluorescence mode continuation	SUL-X	163
H. Pöllmann	K.Pöhler	Synchrotron based X-ray diffraction study of the hydrothermal behavior of (Al, Na, K, Sr, Ba)-stabilized Ca_2SiO_4 polymorphic modifications	SUL-X	165
J. Osan	J. Osan	Micro-XRF and micro-XRD study of radionuclide uptake by argillaceous rocks	FLUO	168
J. Osan	J. Osan	Micro-EXAFS study of radionuclide uptake by argillaceous rocks	SUL-X	170
J. Osan	J. Osan	Micro-EXAFS study of radionuclide uptake by argillaceous rocks	SUL-X	172
S. Kaufhold	S. Kaufhold	About the relation between tetrahedral charge and Fe-content of dioctahedral smectites and the role of tetrahedral iron	INE, SUL-X, XAS	173
K.-H. Knorr	Z.-G. Yu	Redox-speciation of organic sulphur in natural organic matter – stability of organic sulfur compounds and implications for anaerobic electron transfer	SUL-X	174

5. Life Science (Biology, Biointerfaces) [LSC]

Project Leader	First Author	Report Title	Beamline	Page
A. Geyer	U. Meyberg	Conformational analysis of synthetic minicollagens	UV-CD12	178
S. L. Grage	S. L. Grage	Influence of antimicrobial peptides on the morphology of phospholipid bilayers	PDIF	180
S. Keller	M. Textor	SRCD Measurements of Mistic in Membrane-Mimetic Environments	UV-CD12	182

Table of Contents

5. Life Science (Biology, Biointerfaces) [LSC]

Project Leader	First Author	Report Title	Beamline	Page
M. Farquharson	E. Dao	Determining Levels and Distributions of Various Trace Metals in Human Skin: An investigation involving paraffin embedded and freeze-dried samples	FLUO	184
M. Kazanci	M. Kazanci	The Effect of Processing Conditions on the Secondary Structures of Synthetic Collagen Nanofibers	UV-CD12	186
C. Strelci	M. Rauwolf	Comparison of Manganese Concentration and Distribution in Human Osteoporotic and Non-Osteoporotic Bone using Synchrotron Micro X-Ray Fluorescence Imaging	FLUO	188
J. Czapl-Masztafiak	J. Czapl-Masztafiak	The chemical forms of sulfur in prostate cancer tissue analysed by means of XAS	SUL-X	190
J.C. Damalio	J.C. Damalio	Interaction of putative amyloidogenic peptides from human Septin 2 with membrane models	UV-CD12	192

6. Materials [MAT]

Project Leader	First Author	Report Title	Beamline	Page
T. Brezesinski	C. Weidmann	Rechargeable Li-Batteries: Mechanistic Insights by In Operando X-ray Diffraction	PDFIFF	194
N. Pashniak	A. Abboud	Investigation of plastic deformations in Si, Steel and Cu samples with a new 384x384 EROSITA pnCCD and a white X-ray synchrotron source.	TOPO- TOMO	196
H. Peisert	U. Aygöl	Influence of annealing on the molecular orientation of polymer/fullerene blends	XAS	199
F. Pforr	F. Pforr	X-ray absorption spectroscopy on $(1-x)\text{Bi}_{1/2}\text{Na}_{1/2}\text{TiO}_3-x\text{BaTiO}_3$ of different composition	SUL-X, XAS	201
T. Tuomi	S. Sintonen	Threading dislocations in GaN studied by synchrotron radiation x-ray topography	TOPO- TOMO	203
A. Jianu	A. Jianu	Stability domain of alumina thermally grown on Fe-Cr-Al- based alloys exposed to molten Pb		205
A. Zimina	A. Zimina	NEXAFS, EXAFS and XRD study of KI one-dimensional crystals within CNTs	PDFIFF	207
A. Danilewsky	A. Danilewsky	Small Angle Grain Boundaries in Multi-Crystalline Silicon for Photovoltaics	TOPO-TOMO	209
E. Wieland	E. Wieland	Identification of Fe-bearing phases in cements	XAS	211
H. Peisert	M. Ivanovic	Relationship between the chemical structure of low band gap polymers and self-organization properties	XAS	213
P. Walter	P. Walter	Real time investigation of thin lms growth in sputter deposition processes	PDFIFF	215
S. Djaziri	S. Djaziri	Mechanical behavior and microstructural analyses of ultra-high strength pearlitic steel wires: new insights on the strengthening mechanism and the cementite dissolution during cold drawing of the pearlitic steel wires.	PDFIFF	217
T. Farago	T. Farago	In-situ Radiography of an Emulsification Process	TOPO-TOMO	219

Table of Contents

7. Nano and Micro Technologies [NMT]

Project Leader	First Author	Report Title	Beamline	Page
A. Powell	C. E. Anson	Crystallographic Characterisation of Large Paramagnetic Aggregates of Transition-Metal Cations	SCD	220
S. Stankov	S. Stankov	Electronic structure investigations of ultrathin EuxSi1-x films, nano-islands, and nanowires by XANES and EXAFS on the Eu L ₃ edge	SUL-X	222
A. Powell	C. E. Anson	Crystallographic Characterisation of Large Paramagnetic Aggregates of Transition-Metal Cations	SCD	224
H. Vogt	H. Vogt	Characterization of X-ray rolled prism lenses within MiQA project	TOPO-TOMO	226
S. Permien	S. Permien	MFe ₂ O ₄ (M = Co, Mg, Mn, Ni, Zn) nanoparticles as anode materials in Li-ion batteries: An in-situ study of the reaction pathway	PDIFF	228

8. X-Ray and THz/IR Technology [TIR]

Project Leader	First Author	Report Title	Beamline	Page
M. Schuh	J. Schwarzkopf	Investigating polarisation and shape of beam microwave	IR1	230
M. Schuh	P. Schönfeldt	Fluctuation of bunch length in bursting CSR: Measurement and simulation	IR1	233

Local structure and charge distribution in $U_{1-x}Am_xO_{2\pm\delta}$ ($0.15 \leq x \leq 0.50$)

F. Lebreton^{1,2)}, P.M. Martin³⁾, D. Horlait¹⁾, P. Coste¹⁾, T. Delahaye¹⁾

¹⁾ CEA, DEN, DTEC/SDTC/LEMA – 30207 Bagnols-sur-Cèze, France

²⁾ GEMH/ENSCI – 87065 Limoges, France

³⁾ CEA, DEN, DEC/SESC/LLC – 13108 Saint-Paul-lez-Durance, France

Introduction

Am is a minor actinide generated in nuclear fuels during irradiation. This long-lived element is responsible for a large part of the radiotoxicity of ultimate nuclear waste. In the GEN-IV International Forum context, closed fuel cycles are being proposed including the recycling of americium isotopes by transmutation in fast neutron reactors. Among the several fuel types proposed for transmutation, interest has risen over the recent years for mixed U-Am oxides, known as MABB (minor actinide-bearing blanket) fuels as they are destined for the core periphery. This project is dedicated to the study by XAS of several MABB with high and innovative Am contents.

Samples studied and experimental conditions

Nine samples were studied in this project (Table 1). Four of them are U-Am mixed oxides with different Am/(U+Am) ratios prepared according to the UMACS process [1]. The four other samples are single uranium or americium oxides, used as precursors for sample preparation and/or references for the XANES spectra. All samples were first characterized by XRD and exhibit a single phase, exception made of sample 6, which is composed of a mixture of A and C-type Am_2O_3 , presenting respectively a hexagonal and a cubic structure. Each sample was double-sealed in a polyethylene container adapted for measurements with the INE beamline N_2 cryostat, ensuring a sample temperature around 77 K.

XANES and EXAFS spectra were recorded at U and Am L_{III} edges in transmission and fluorescence modes. Because of ^{237}Np presence in the sample (as a result of ^{241}Am α -decay), EXAFS spectra were limited to 11.5 \AA^{-1} at the U L_{III} edge, whereas those at the Am L_{III} edges were collected up to 15 \AA^{-1} .

XANES results

The XANES spectra obtained for the samples 1 to 4 are presented in Figure 1 (left) for the U L_{III} edge (compared to those of samples 7 and 8) and in Figure 1 (right) for the Am L_{III} (compared to those of samples 5 and 6). At the U L_{III} edge, the sample spectra are shifted towards higher energies compared to that of UO_2 . This shift progressively increases with the Am content, so that the 40 and 50%-Am sample spectra are found between those of U_4O_9 and U_3O_8 . At the Am L_{III} edge, no significant deviations between the samples are observed. Based on these results, Am appears to remain trivalent whatever the composition, whereas U is present at an oxidized state compared to U^{+IV} . For the 15 and 30%-Am samples, U oxidation state is presumably attained through the insertion of U^{+V} in the lattice. For the higher Am contents however, the presence of U^{+VI} can be envisaged, considering that the corresponding spectra are between those of $U^{+IV/+V}_4O_9$ and $U^{+V/+VI}_3O_8$.

EXAFS results

EXAFS spectra and the corresponding Fourier transforms obtained for the samples 1 to 4 at Am L_{III} edge are presented in Figure 2. On the latter, only Fourier transforms consistent with the XRD results are obtained, i.e., corresponding to a standard fluorite structure with two main peaks associated to the first Am-O and Am-U/Am shells. Similar results were obtained at the U L_{III} edge. The refinement of the EXAFS spectra is currently begin performed, and will bring information about the evolution of the structure at local range in these materials and notably on the influence of the Am content on the interatomic distances.

Table 1: Samples studied in this project.

#	Formula	Synthesis method
1	$U_{0.85}Am_{0.15}O_{2\pm\delta}$	UMACS
2	$U_{0.70}Am_{0.30}O_{2\pm\delta}$	UMACS
3	$U_{0.60}Am_{0.40}O_{2\pm\delta}$	UMACS
4	$U_{0.50}Am_{0.50}O_{2\pm\delta}$	UMACS
5	$AmO_{2-\delta}$	Precursor powder
6	$Am_2O_{3+\delta}$	Heat treatment of $AmO_{2-\delta}$
7	U_3O_8	Precursor powder
8	U_4O_9	Furnished by ILL

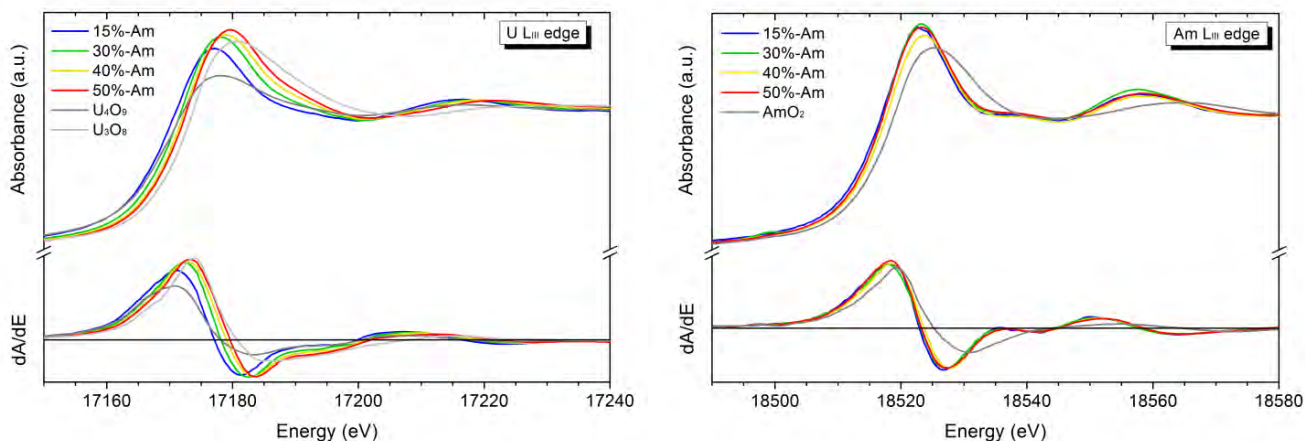


Figure 1. XANES spectra obtained for samples 1 to 4 at (left) U L_{III} and (right) Am L_{III} edge.

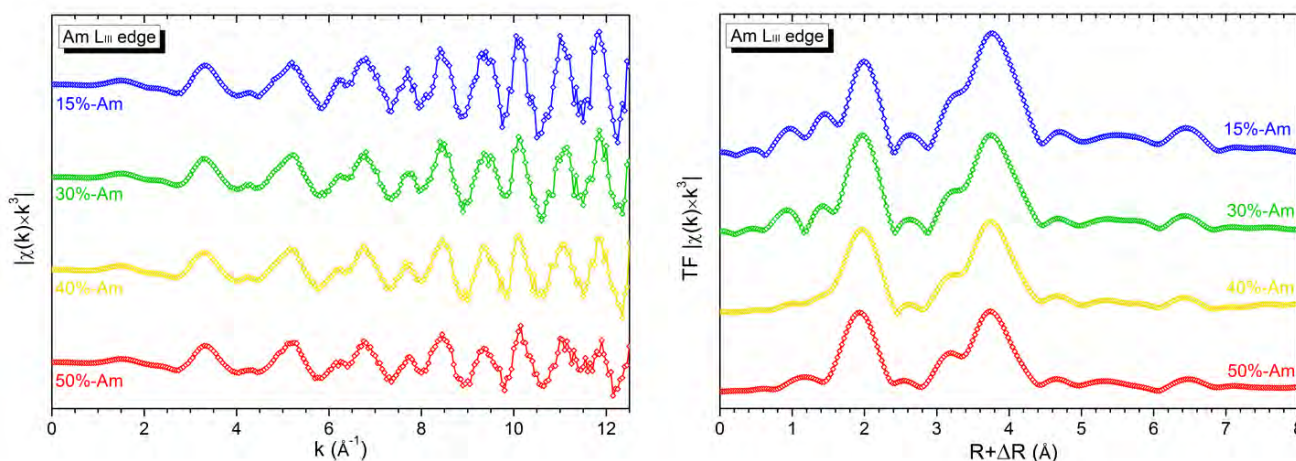


Figure 2. EXAFS spectra (left) and associated Fourier transforms (right) obtained for samples 1 to 4 at the Am L_{III} edge.

Conclusion

The results obtained in this project show the high stability of Am at the trivalent state in U-Am mixed oxides, compensated for by the oxidation of U to U^{+V} (or even U^{+VI}). O/M (oxygen-to-metal) ratio variations thus occur only through U oxidation state. These results are thus consistent with previously reported data on compounds with lower Am contents [2-4].

These results were presented during the E-MRS 2013 Spring Meeting in Strasbourg [5].

Acknowledgements

This project was carried out in the frame of the European Actinet-I3 program, which is acknowledged for his support. D. Horlait and F. Lebreton are thankful the CEA PACFA program for post-doc and Ph.D. funding, respectively. The authors also want to thank C. Marquardt, C. Guihard and M. Bataille for sample preparation and transport to ANKA.

References

- [1] T. Delahaye, F. Lebreton, *et al.*, *J. Nucl. Mater.* 432 (2013) 305-12.
- [2] D. Prieur, P.M. Martin, *et al.*, *Inorg. Chem.* 50 (2011) 12437-45.
- [3] T. Nishi, M. Nakada, *et al.*, *J. Nucl. Mater.* 418 (2011) 311-2.
- [4] D. Prieur, P.M. Martin, *et al.*, *J. Nucl. Mater.* 434 (2013) 7-16.
- [5] F. Lebreton, P.M. Martin, *et al.*, “ $U_{1-x}Am_xO_{2\pm\delta}$ solid solution study”, E-MRS 213 Spring Meeting, Strasbourg, France.

EXAFS investigation on actinide and lanthanide transferrin complexes

N. Bauer^{1),2)}, D. R. Fröhlich^{1),2)}, K. Dardenne¹⁾, J. Rothe¹⁾, P. J. Panak^{1),2)}

¹⁾ Karlsruhe Institute of Technology (KIT), Campus Nord, Institute for Nuclear Waste Disposal (INE),
P.O. Box 3640, 76021 Karlsruhe (D)

²⁾ University of Heidelberg, Department of Physical Chemistry, Im Neuenheimer Feld 253, 69120 Heidelberg (D)

In case of accidental release of radionuclides into the environment, actinides represent a severe health risk to human beings after being incorporated by e.g. inhalation, ingestion or wounds. Contrary to other metals, actinides have no known essential function in biochemical reactions. For a better understanding of the actinide behavior and their toxic effects in man a fundamental knowledge on the mechanisms of relevant biochemical reactions in the body is needed which can be an important prerequisite for the design and success of potential decontamination therapies.^[1]



Figure 1: 3D structure of human serum transferrin with N-lobe (green) and C-lobe (red). Each lobe houses one Fe(III) metal binding site.^{[2] [3]}

Transferrin is an iron carrier protein in the blood. Since about 30 % of the protein is complexed to iron in normal blood serum, non-saturated transferrin is available for the complexation of other metal ions. Literature data on the structure of actinide transferrin complexes are rare. Most complexation studies have been performed with indirect speciation methods (filtration, centrifugation etc.). Our fluorescence spectroscopic results on Cm(III) transferrin show for the first time the formation of two different actinide transferrin species depending on experimental conditions (pH, protein concentration). In order to obtain detailed structural information on the complexes, EXAFS investigations were performed.

Experimental

Am(III), Eu(III) and Np(V) transferrin solutions (Eu(III)-Tf: $c(\text{Eu(III)}) = c(\text{Tf}) = 6 \cdot 10^{-4} \text{ M}$; Np(V)-Tf: $c(\text{Np(V)}) = c(\text{Tf}) = 5 \cdot 10^{-4} \text{ M}$; Am(III)-Tf: $c(\text{Am(III)}) = c(\text{Tf}) = 1 \cdot 10^{-3} \text{ M}$; Am(III)-Tf (70 K): $c(\text{Am(III)}) = 5 \cdot 10^{-4} \text{ M}$, $c(\text{Tf}) = 2.4 \cdot 10^{-3} \text{ M}$) at pH 7.2 and 8.5 were prepared in the radiochemical laboratories at the INE (KIT, Karlsruhe).

Am/Eu/Np L_{III}-edge EXAFS spectra were collected in fluorescence mode in standard detection geometry at the INE-Beamline. The measurements were either performed at room temperature or at ~77 K (Am(III) only) using a liquid N₂ cryostat (OI OptistatDN). The data evaluation was performed using the software packages Athena 0.8.061^[4] and EXAFSPAK.^[5] Theoretical scattering phases and amplitudes were calculated with FEFF8.40^[6] using the crystal structure of Fe-Transferrin (RCSB-PDB entry: 3QYT) and replacing Fe by Am, Np, or Eu. The best theoretical model was fit to the k³-weighted raw Am/Np/Eu L_{III}-edge EXAFS data.

Discussion

The k³-weighted Am L_{III}-edge EXAFS spectra and the related Fourier Transforms of the Am(III) transferrin samples at pH 7.2 and 8.5 recorded at low temperature are shown in fig. 2. Both show clearly visible differences in the whole k-range. While the spectrum at pH 7.2 can be described

with one coordination sphere ($N = 8.7$, $R = 2.47 \text{ \AA}$) in good agreement with data for the Am(III) aquo ion^[7], the sample at pH 8.5 shows a more complicated coordination structure. This spectrum has been fitted with one, two or three coordination spheres (table 1). Again about 9 neighbors are present in the first shell but the distance is significantly shorter ($R = 2.38 \text{ \AA}$) as expected in case of strong multidentate coordination of Am(III) at the transferrin binding cleft. Unspecific binding to functional groups at the protein would result in longer distances and can be excluded. The consideration of two additional coordination shells ($N \approx 3$ at $3.72\text{-}3.73 \text{ \AA}$, $N \approx 7$ at 5.19 \AA) is followed by a slight but visible improvement of the fit (see reduced errors in table 1). The presence of these coordination spheres points to the formation of a complex but well-defined bonding environment in the Am(III) transferrin complex. However, EXAFS does not allow to distinguish between coordinating N- or O-atoms.

In contrast to Am(III), Np(V) spectra did not show any complexation by transferrin, probably due to the less pronounced complexation properties of Np(V). In the case of Eu(III), the sample at pH 7.2 shows the presence of several coordination spheres at higher distances. The corresponding spectra were recorded at room temperature, hence the low signal/noise ratio resulted in a high reduced error (2.04).

In conclusion, the present study confirms the formation of an Am(III) transferrin species at pH 8.5 which is in good agreement with previous TRLEFS studies on the interaction of Cm(III) with transferrin. Furthermore, the related structural parameters were determined for the first time and confirm that Am(III) is incorporated into the transferrin structure at the Fe(III) binding site.

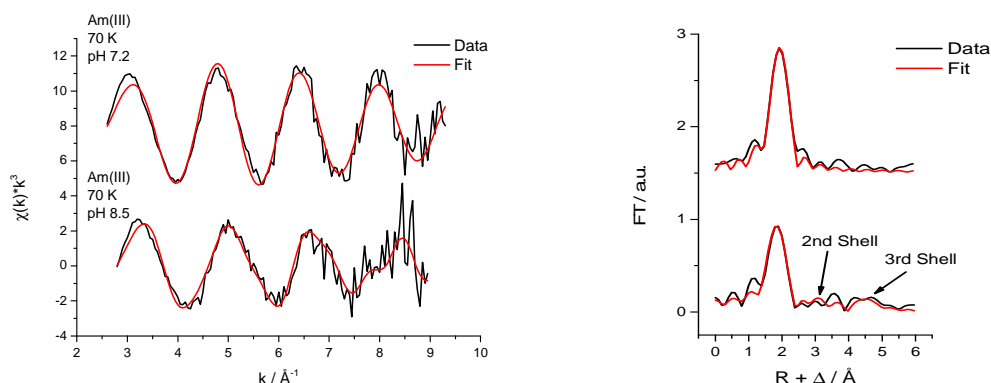


Figure 2: Left: Experimentally measured (black) and fitted (red) EXAFS spectra at the Am L_{III} -edge of the Am(III) transferrin complex at pH 7.2 and 8.5 (both recorded at 70 K); Right: Corresponding experimentally measured (black) and fitted (red) Fourier Transforms.

Table 1: Summary of the best-fit parameters of the EXAFS spectra of the Am(III) transferrin samples ($\sim 77 \text{ K}$).

M	T [K]	pH	1 st Shell			2 nd Shell*		3 rd Shell*		ΔE_0	Red. Er.
			N	R / \AA	$\sigma^2 / \text{\AA}^2$	N	R / \AA	N	R / \AA		
Am	70	7.2	8.7 (0.5)	2.47 (1)	0.007 (1)	-	-	-	-	-6.2 (0.6)	0.41
			8.8 (1.0)	2.38 (1)	0.013 (2)	-	-	-	-	-3.8 (1.0)	0.67
Am	70	8.5	8.6 (1.0)	2.38 (1)	0.012 (2)	3.0 (1.0)	3.73 (3)	-	-	-3.8 (0.9)	0.63
			8.8 (1.0)	2.38 (1)	0.013 (2)	2.8 (1.0)	3.72 (3)	6.8 (2.3)	5.19 (3)	-4.0 (0.9)	0.59

* $\sigma^2 / \text{\AA}^2$ was set to 0.003 and fixed during the fit

- [1] A. E. V. Gorden, J. D. Xu, K. N. Raymond, P. Durbin, *Chem. Rev.* **2003**, 103, 4207-4282.
 [2] J. Wally, P. J. Halbrooks, C. Vornrhein, M. A. Rould, S. J. Everse, A. B. Mason, S. K. Buchanan, *J. Biol. Chem.* **2006**, 281, 24934-24944.
 [3] H. Z. Sun, H. Y. Li, P. J. Sadler, *Chem. Rev.* **1999**, 99, 2817-2842.
 [4] B. Ravel, M. Newville, *J. Synchrotron Radiat.* **2005**, 12, 537-541.
 [5] G. N. George, Pickering, I.J., Stanford/USA, **2000**.
 [6] A. L. Ankudinov, C. E. Bouldin, J. J. Rehr, J. Sims, H. Hung, *Physical Review B* **2002**, 65.
 [7] P. G. Allen, J. J. Bucher, D. K. Shuh, N. M. Edelstein, I. Craig, *Inorg. Chem.* **2000**, 39, 595-601.

EXAFS investigation on the formation of Am(III) chloro complexes in saline solutions at temperatures up to 200 °C

D.R. Fröhlich¹⁾, A. Skerencak²⁾, J. Rothe²⁾, P.J. Panak¹⁾²⁾

¹⁾ Ruprecht-Karls-Universität Heidelberg, Physikalisch-Chemisches Institut, D-69120 Heidelberg

²⁾ Karlsruher Institut für Technologie, Institut für Nukleare Entsorgung, D-76344 Eggenstein-Leopoldshafen

Introduction

The temperature in the near-field of a repository for high-level nuclear waste will reach temperatures of up to 200 °C in the case of rock salt [1]. As a result of the increased temperature, the aqueous chemistry of the stored radionuclides will change significantly [2]. Due to the long half-lives and high radiotoxicities, the transuranium elements are of particular interest with respect to the long-term safety assessment. In case of access of water to a repository in a rock salt formation, chloride will be present at very high concentrations. It is known that chloride is a weak ligand at room temperature [3]. But temperature dependent TRLFS studies showed that the complex formation of chloride with Cm(III) increases significantly when the temperature is raised up to 200 °C [4]. In the present work, Am(III) was selected as a representative to study the effect of high temperatures on the complexation behaviour of trivalent actinides in chloride solutions. The molecular structure of Am(III) chloro complexes in the temperature range up to 200 °C was investigated by EXAFS spectroscopy for the first time.

Experimental procedure

An acidic solution (pH \approx 1) of 1 mM Am(III) in 3 M NaCl solution was prepared in the radiochemical laboratories at the INE (KIT, Karlsruhe). To study the temperature dependence of the interaction between Am(III) and chloride, a newly designed high-temperature EXAFS cell was used. This set-up has already been used for previous EXAFS studies (ANS-88).

Am L_{III}-edge EXAFS spectra were collected in fluorescence mode at an angle of 90 ° using the 5 pixel Ge detector (Canberra Ultra-LEGe). Measurements were performed at temperatures of 25, 90, and 200 °C. For data evaluation the software packages EXAFSPAK, Athena 0.8.061, and Artemis 0.8.012 were used. Theoretical scattering phases and amplitudes were calculated with FEFF8.40 using the crystal structures of AmO₂ and AmCl₃. In all cases, the models were fit to the k³-weighted raw EXAFS spectra.

Results

Figure 1 shows the measured k³-weighted Am L_{III}-edge EXAFS spectra and the related Fourier Transforms. While the spectra at 25 and 90 °C look similar, the EXAFS spectrum at 200 °C shows some differences (e.g., the position of the second oscillation around k = 5 Å⁻¹). In the related Fourier Transforms, this difference is more pronounced as the peak in the pseudo-radial distribution at 200 °C is broadened visibly. This can be attributed to the presence of chloride in the coordination sphere of americium. The results of the fitting are summarized in Table 1. The spectra at 25 and 90 °C can be described without contribution of chloride resulting in 9-10 oxygen neighbours at a distance of 2.45-2.48 Å which is in good agreement with literature data (e.g., [3]). At 200 °C, about 2.5 chloride ligands have to be included in the fit to describe the experimental data. Furthermore, the debye-waller factor of the Am-O shell increases continuously with increasing temperature from 0.007 at room temperature to 0.015 at 200 °C. On the other hand, the obtained Am-O and Am-Cl distances are significantly shorter compared to literature values (see Table 1) as well as our data at 25, and 90 °C. This phenomenon can be attributed to an asymmetric (non-Gaussian) distribution of distances which is known to occur at high temperatures [5]. To account for this effect a third cumulant has to be included in the theoretical model. The inclusion of a third cumulant in the fit (see Table 1) resulted in Am-O and Am-Cl distances of 2.44 and 2.78 Å, respectively. These values are in agreement to the literature data [3].

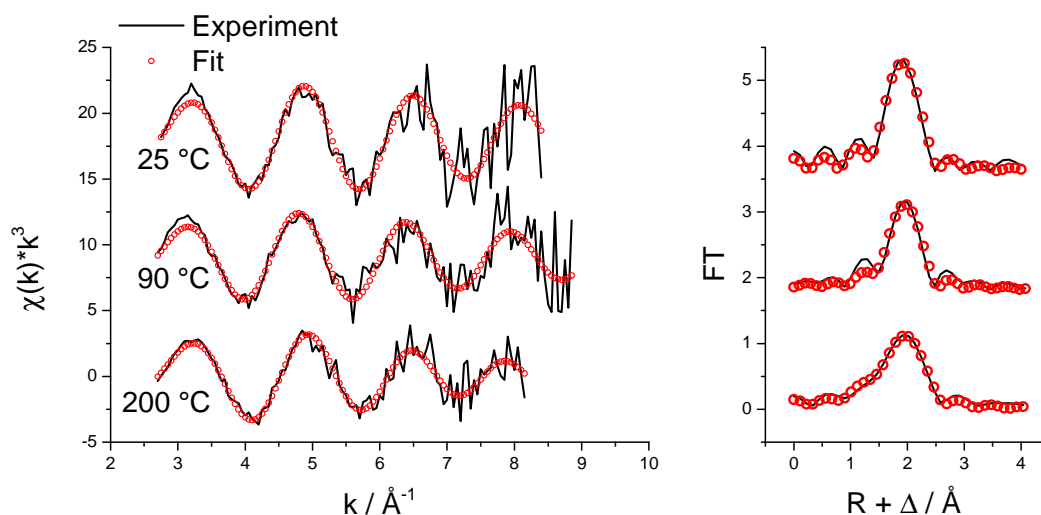


Figure 1: k^3 -weighted Am L_{III} -edge EXAFS spectra and related Fourier transforms as a function of temperature. Fit without consideration of a third cumulant.

Table 1: Structural parameters determined for Am(III) in the presence of chloride (3 M NaCl solution) as a function of temperature (Errors given in brackets).

Temperature / °C	Am-O			Am-Cl			ΔE_0 / eV	k-range
	N	R / Å	σ^2 / Å ²	N	R / Å	σ^2 / Å ²		
25	9.6 (1.3)	2.45 (1)	0.007 (2)	-	-	-	-4.9 (1.3)	2.75-8.40
90	9.0 (1.2)	2.48 (1)	0.009 (2)	-	-	-	-5.0 (1.3)	2.65-8.85
200**	7.4 (2.9)	2.34 (5)	0.015 (6)	2.4 (0.7)	2.66 (2)	0.005*	-9.5 (2.5)	2.70-8.15
200***	7.6 (1.3)	2.44 (5)	0.015*	2.8 (0.2)	2.78 (4)	0.005*	-5.8 (2.0)	2.70-8.15
25 (10 M LiCl) [3]	7.6 (0.3)	2.48	0.009*	1.2 (0.1)	2.80 (1)	0.005*	-7.3	1-11
25 (12.5 M LiCl) [3]	6.4 (0.3)	2.51	0.009*	1.8 (0.1)	2.81 (1)	0.005*	-6.1	1-11

$S_0^2 = 0.9$, *fixed during fit, **without considering a third cumulant, ***third cumulant set to 0.003 (Am-O), 0.003 (Am-Cl)

Whereas room temperature EXAFS measurements showed no complexation of trivalent actinides (Pu(III), Am(III), Cm(III)) with chloride at chloride concentrations < 8 M [3], a clearly visible interaction between Am(III) and chloride was observed at 200 °C at a relatively low chloride concentration of 3 M in the present study. These results emphasize the importance of thermodynamic data at elevated temperatures to accurately describe the complexation behaviour of actinides with inorganic and organic ligands in the near field of a potential repository for high-level nuclear waste.

Acknowledgements

This work has been supported by the German Federal Ministry of Economics and Technology (BMWi) under contract number 02E11031.

References

- [1] T. Brasser et al., GRS report GRS-247, 2008.
- [2] L. Rao, *Chem. Soc. Rev.*, 2007, **36**, 881-892.
- [3] P.G. Allen et al., *Inorg. Chem.*, 2000, **39**, 595-601.
- [4] A. Skerencak, Dissertation, Universität Heidelberg, 2010.
- [5] G. Dalba et al., *J. Synchrotron Rad.*, 1997, **4**, 243-255.

The nature of uranium in sedimentary rocks of Epirus region (NW Greece)

A. Godelitsas¹⁾, T.J. Mertzimekis¹⁾, P. Gamaletsos¹⁾²⁾, J. Göttlicher²⁾, R. Steininger²⁾

¹⁾ School of Sciences, University of Athens, 15784 Panepistimioupoli Zographou, Greece

²⁾ Karlsruhe Institute of Technology, Institute for Synchrotron Radiation, Hermann-von-Helmholtz-Platz 1, 76344 Eggenstein-Leopoldshafen, Germany

Uranium in the ocean waters (typical concentration: 3.2 ppb) follows anoxic pathways and it is mainly removed from the solution by chemical processes taking place at the interface of organic-rich sediments. It is therefore correlated to organic carbon whereas the diagenetic cycle of the element may include reduction of U^{6+} to U^{4+} related to sulphate bio-reduction. However, further tectonic and weathering processes may modify the primary distribution and speciation of U in marine sediments. The average abundance of U in carbonate sedimentary rocks is 2.2 ppm while the concentration of U in relevant Tethyan rocks from SE Europe and the Middle East is reported to be in the range 1–10 ppm. There are also limestones and dolomitic limestones from Mt. Kithaeron (central Greece), containing unusually elevated U concentrations up to ca. 56 ppm. [e.g. 1-3].

Epirus region (NW Greece) is generally composed of Mesozoic (250 - 65 million years old) sedimentary and ophiolitic rocks derived from the Tethys paleo-Ocean. The sedimentary rocks are mostly limestones and shales while the ophiolitic rocks represent old oceanic crust (a sequence of ultrabasic and basic rocks originating in Earth's mantle). Ophiolites, limestones and shales are fundamentally poor in actinide elements (typical concentrations: <0.1, 2.2 and 3.5 ppm respectively) and therefore no elevated actinide concentrations would be expected in Epirus region. However, in some areas the natural radioactivity is high due to the presence of phosphate-bearing sedimentary rocks, i.e. phosphorites [4].

Phosphorites are marine sediments containing an average of 120 ppm U, and may significantly contribute in U geochemical anomalies. Additionally, they are rich in light rare-earth elements/LREE, but not in Th (6.5 ppm) and other HFSE. However, the studied samples from Epirus region concerned tectonized/re-processed phosphatized limestone. Detailed gamma-ray measurements using HPGe showed that the geological material exhibits significant radioactivity mainly due to ^{238}U -series ($^{234\text{m}}\text{Pa}$: 8182 Bq/Kg, ^{226}Ra : 6852 Bq/Kg, ^{214}Pb : 7260 Bq/Kg, ^{214}Bi : 6232.18 Bq/Kg). Bulk geochemical analyses using ICP-OES/MS showed variable U concentrations with a notable value of 648 ppm in the case of the dark organic-rich part of the rock (Fig. 1). Relatively high concentrations of Cd, probably related to apatite, were also revealed [4]. On the other hand, the rock is geochemically depleted in LILE (e.g. Cs, Rb, K), as well as in As, Sb and Se in contrast to red soils ("Terra Rossa") of the region [5].

The SR μ -XRF study (Fig. 2) revealed that U is accumulated (together with P, Sr, Y, and most likely S) in certain areas of the dark organic-rich part of the rock which includes, according to supplementary XRD, SEM-EDS and FT-IR data, abundant apatite and organic matter. The areas with very low U and high Ca concentrations consist of calcite, whereas V and La are related to metallic Fe-oxide phases. The corresponding UL_3 -edge μ -XANES spectra indicated the presence of U^{4+} which could be associated to apatite-group minerals and/or organic matter. The occurrence of U^{4+} in calcite [3, 6], formed in low-T, is considered to be less possible.

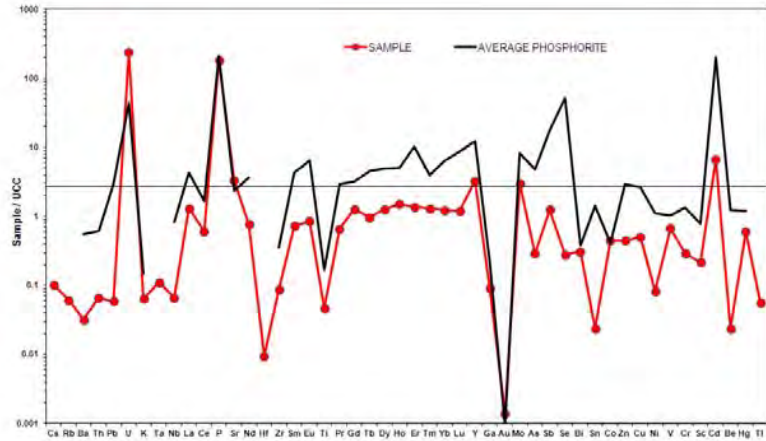


Fig. 1: U-bearing phosphatised limestone sample from Epirus region (NW Greece) and Upper Continental Crust-normalized multielement spidergrams indicating an exceptional U geochemical anomaly [4]

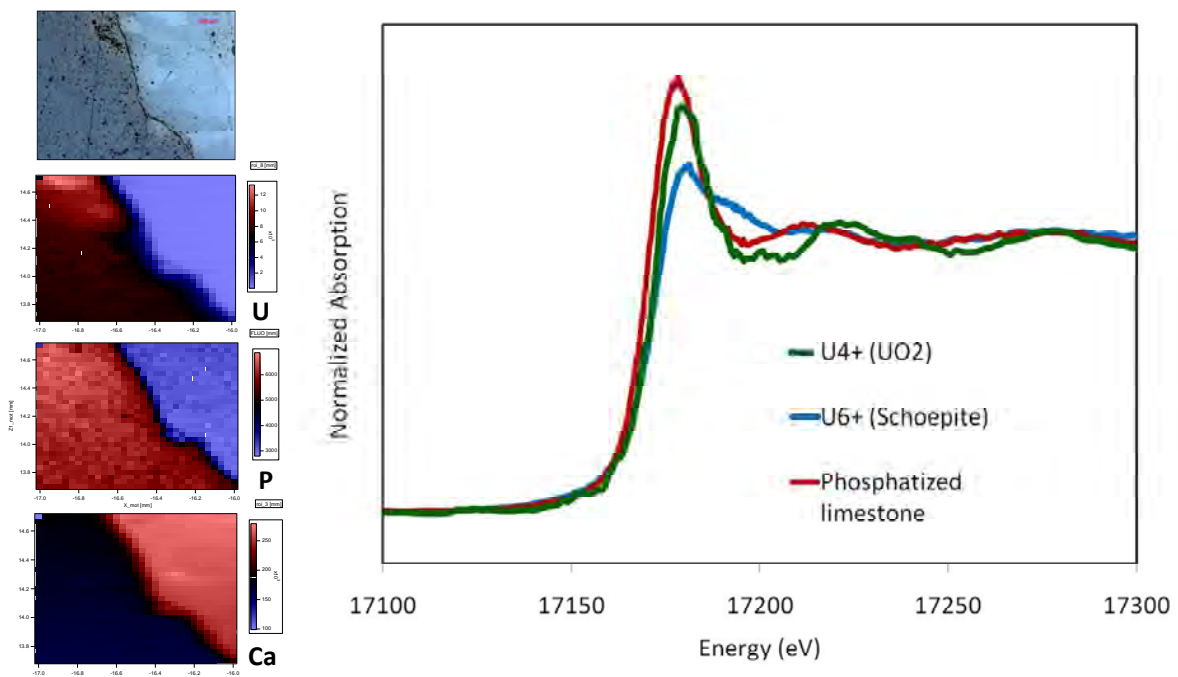


Fig. 2: SR μ -XRF elemental maps and representative preliminary UL_3 -edge μ -XANES spectra of Epirus U-bearing phosphatised limestone together with U^{4+} and U^{6+} reference materials

References

- [1] G.P. Klinkhammer & Palmer M.R. (1991), *Geochim. Cosmochim. Acta*, **55**, 1799-1806.
- [2] S.N. Ehrenberg et al. (2008), *AAPG Bull.*, **92**, 691-707.
- [3] J. Göttlicher et al. (2009), *Geochim. Cosmochim. Acta*, **73**, A457.
- [4] I. Tzifas et al. (2014), *J. Geochem. Explor.* **143**, 62-73.
- [5] A. Godelitsas et al., *to be submitted*.
- [6] N. Sturchio et al. (1998), *Science*, **281**, 971-973.

Identifying the Role of Covalency in Transuranic Extractants

A. C. Olson¹, S. A. Kozimor¹, T. Vitova², M. W. Loeble¹

¹ Los Alamos National Laboratory, PO Box 1663, Los Alamos, New Mexico, 87501, USA

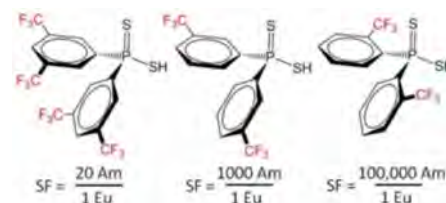
² Karlsruhe Institute of Technology, Institute for Nuclear Waste Disposal, Hermann-von-Helmholtz-Platz 1, D-76344 Eggenstein-Leopoldshafen, Germany

Introduction

Nuclear energy is the most viable alternative to fossil fuel combustion until large-scale renewable energy technologies can be implemented. However, use of nuclear energy is limited by the difficulties associated with remediation, management, and disposal of nuclear waste. A significant hazard is associated with the minor actinides present in spent fuel, creating environmental and safety concerns. Advanced nuclear fuel cycles proposed for future waste mitigation rely on separation of trivalent actinides from trivalent lanthanides, which could decrease the time required to store nuclear waste by ~1000-fold.

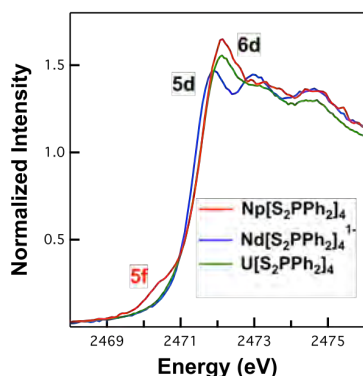
Currently, the extraction of actinides from lanthanides represents the most daunting chemical challenge facing advanced fuel cycle development, as 4*f*- and 5*f*-elements share similar chemical properties and are difficult to separate [1]. Some soft-donor ligands, i.e. dithiophosphinic acids (HS₂PR₂), are known to selectively extract actinides from lanthanides, Figure 1. While record separation factors on the order of 100,000 can be achieved, the preference for binding actinides is not well understood, and surprisingly subtle changes associated with the arene group drastically affect the separation (e.g. CF₃ group position) [2,3]. However, recent S K-edge X-ray absorption spectroscopy and time-dependent density functional theory (TDDFT) studies revealed unique electronic structure properties for the S₂P(*o*-CF₃C₆H₄)₂¹⁻ anion, whose conjugate acid exhibits exceptionally high extraction selectivity for actinides over lanthanides [4]. Accordingly, a number of actinide- and lanthanide-dithiophosphinate complexes were synthesized and evaluated.

Fig. 1: Dithiophosphinate extractants.



S K-edge XAS Analysis of *f*-element–Dithiophosphinate Complexes

Fig. 2: S K-edge XAS for M(S₂PPh₂)₄^{x-}.



In an effort to quantify covalent interactions and determine the relative contributions of 6*d* vs. 5*f* orbitals in actinides, a series of *f*-element M(S₂PPh₂)₄^{x-} (M = Nd, x = 1; M = U, Np, x = 0) complexes were analyzed using S K-edge XAS at the INE beam line for actinide research at ANKA, Figure 2. Peak assignments in these spectra were made based on a systematic study of transition metal–dithiophosphinate complexes by S K-edge XAS and TDDFT. As expected based on previous analyses, the prominent feature near 2472 eV – associated with d-orbital mixing – moved to higher energy as the principle quantum number increased for each metal (i.e. moving from Nd to U or Np). In addition, the feature showed increased intensity for Np and U vs. Nd, suggesting increased d-orbital participation in M–S bonding for the actinides. For Np(S₂PPh₂)₄, a small pre-edge feature near 2470 eV was partially resolved from the

rising edge. Based on previously established d- and f-orbital energy trends [5], this lower-energy feature is likely associated with f-orbital mixing, providing the first unambiguous experimental evidence for covalent bonding between actinide 5*f* and S 3*p* orbitals.

P K-edge XAS of Dithiophosphinate Actinide Extractants

A series of P K-edge XAS experiments were also conducted to quantify the relative orbital mixing electronic structure of P-ancillary groups for the diverse family of dithiophosphinates studied previously [4]. By systematically changing the identity of the arene substituents from Me to Ph, *p*-CF₃C₆H₄, *m*-CF₃C₆H₄, and *o*-CF₃C₆H₄. The resulting spectra were quite complicate, and efforts to correlate the ancillary effects of the Me, Ph, CF₃C₆H₄ groups on orbital mixing with the PS₂ core are underway. Specifically, TDDFT calculations are being conducted to help guide spectral interpretation.

Cl K-edge XAS of Related Actinide and Lanthanide Complexes

Developing a general understanding of carefully selected actinide and lanthanide complexes can lead to improved understanding of their bonding capabilities for separations. For example, the electronic properties of the octahedral hexachloro complexes ThCl_6^{2-} , UCl_6^{2-} and PuCl_6^{2-} are well established and understood. Therefore, those compounds are ideal to study and determine the relative contributions of valence 6d and 5f orbitals in M–Cl bonding. Chlorine K edge data provides new evidence of both 5f and 6d orbitals in actinide–ligand bonding in UCl_6^{2-} and PuCl_6^{2-} . For all three MCl_6^{2-} complexes studied, transitions into linear combinations of Cl 3p orbitals with metal d orbitals of t_{2g} symmetry are spectroscopically resolved (2824.0 eV for ThCl_6^{2-} ; 2823.9 eV for UCl_6^{2-} and 2824.2 eV for PuCl_6^{2-}), as curve fits of Cl K edge spectra show in Figure 4. However, in case of the f^0 system ThCl_6^{2-} it is assumed that those transitions overlap with transitions into metal-based antibonding orbitals with f character, which cannot be spectroscopically resolved. In contrast, spectra of the f^2 system UCl_6^{2-} and the f^4 system PuCl_6^{2-} show less intense pre edge features at lower energies (UCl_6^{2-} : 2822.4 eV; PuCl_6^{2-} : 2822.7 eV and 2821.3 eV), which we attribute to transitions into antibonding orbitals resulting from linear combinations of Cl 3p orbitals with metal based f orbitals of t_{1u} and t_{2u} symmetry. The seventh f orbital of a_{2u} symmetry does not overlap with Cl 3p orbitals and is therefore nonbonding. The increase in f intensity we attribute to the evolution of actinide 5f orbital energy as one progresses across the row from Th to Pu. As one moves toward the later actinides, the 5f orbitals decrease in energy and for PuCl_6^{2-} there is a better energy match the An 5f orbital energies and the Cl 3p orbitals, which results in better orbital mixing.

Future Efforts

The results provided will likely result in publication of three manuscripts that will be send to high impact chemistry journals. Specifically, we plan to submit this work to the *J. Am. Chem. Soc.*, *Chem. Sci.* and *Nature Chemistry*. While the Cl K-edge XAS data for the AnCl_6^{2-} series has been reproduced multiple times at two different synchrotrons (ANKA and SSRL), the S K-edge XAS data for $\text{M}(\text{S}_2\text{PPh}_2)_4^{1-}$ and P K-edge XAS data on the $\text{S}_2\text{PR}_2^{1-}$ results needs to be reproduced. Hence, before the later two papers can be submitted for publication, additional experiments at ANKA have been requested.

Acknowledgements

We are grateful to help from Melissa Denecke, Kathy Dardenne, and Joerge Rothe for their intellectual contributions, technical support, and stimulating discussion.

[1] Choppin *J. Lett-Common Met.* **1983**, 93, 323.

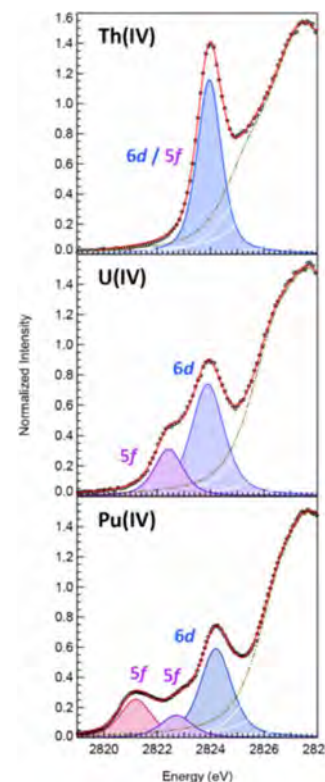
[2] (a) Zhu, Y. *et al. Solvent Extr. Ion. Exch.* **1996**, 14, 543. (b) Klaehn *et al. Inorg. Chim. Acta* **2008**, 361, 2522.

[3] (a) Zhu *et al. Solvent Extr. Ion. Exch.* **1996**, 14, 61. (b) Peterman *et al. Separation Sci. Tech.* **2010**, 45, 1711.

[4] Daly, S. R. *et al. J. Am. Chem. Soc.* **2012**, 134, 14408.

[5] Pepper *et al. Chem. Rev.* **1991**, 91, 719.

Fig. 4: Cl K-edge spectra (circles) and curve fits (best fit in red) for AnCl_6^{2-} compounds (An = Th, U, Pu).



In-situ high temperature XAS experiments on oxide nuclear fuels and precursors

P.M. Martin¹⁾, F. Lebreton^{2),3)}, D. Neuville⁴⁾, R Bès¹⁾, M. Bataille²⁾, E. Welcomme⁵⁾, T. Delahaye²⁾

¹⁾ CEA, DEN, DEC/SESC/LLC – 13018 Saint-Paul-lez-Durance, France

²⁾ CEA, DEN, DTEC/SDTC/LEMA – 30207 Bagnols-sur-Cèze, France

³⁾ GEMH/ENSCI – 87065 Limoges, France

⁴⁾ Géochimie & Cosmochimie, CNRS-IPGP, Paris Sorbonne Cité – 75005 Paris, France

⁵⁾ CEA, DEN, DRCP/SERA/LCAR – 30207 Bagnols-sur-Cèze, France

Introduction

The present experiment was dedicated to perform the first in-situ XAS (X-ray absorption spectroscopy) at high temperature on radioactive samples, more precisely U-based samples. Its main purposes were, on the first hand, to performed measurements on U- and U/Ln-based compounds, notably microspheres obtained from the WAR (wet-acid resin) process [1], and, on the other, to validate the experimental set-up for future experiments on more hazardous/radioactive compounds such as Am- or Pu-bearing samples.

Experimental conditions

A dedicated experimental setup was designed, based on a setup previously developed for in-situ measurements at high temperatures whether under air or a controlled atmosphere [2,3]. The furnace consists of a Pt/Ir wire presenting a 0.5 mm-diameter hole in its centre. The sample can be either crushed and mixed with ethanol to form a paste that can be deposited on the hole or, in the case of a microsphere, directly inserted in the hole, as shown in Fig. 1. To perform measurements with U-bearing materials, the furnace was placed inside a Plexiglas box sealed during the experiments. Both the furnace and the box are equipped with Kapton windows to let incident, transmitted and fluorescence signals going through, as well as a silica window allowing temperature measurements using a pyrometer. Fig. 2 shows the experimental set-up with a U-bearing sample around 1670 K. For this experiment, measurements were performed up to 1770 K under air, Ar or Ar-H₂(4%). The samples studied were single or mixed U/Ln compounds, whether oxide or microsphere oxide precursors synthesized using the CRMP process [1]. A list of the samples and measurement conditions is given in Table 1. Considering the low mass of sample per analysis, measurements were all performed in fluorescence mode, focused on the XANES region.



Fig. 1: Microsphere placed in the hole of the wire before measurements.

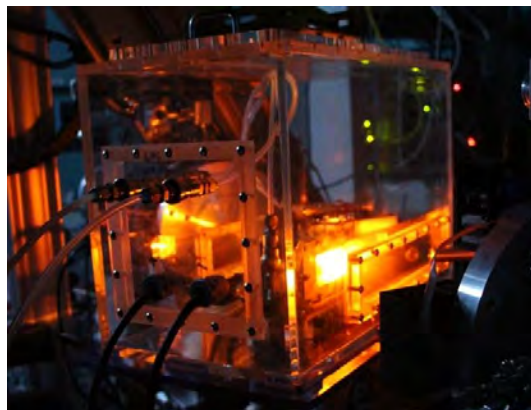


Fig. 2: Experimental set-up for in-situ XAS measurements (sample temperature is 1670 K).

Table 1: Samples studied during the experiment and conditions of measurements.

Sample	Studied edges and maximal temperatures
(Ce _{0.8} Gd _{0.2}) microspheres	Ce L _{III} (1670 K under air)
Ce oxide	Ce L _{III} (1440 K under air and 1670 K under Ar)
(U _{0.9} Ce _{0.1}) oxide	Ce L _{III} (1070 K under Ar) and U L _{III} (1270 K under Ar and 1470 K under Ar-H ₂)
(U _{0.8} Gd _{0.2}) microspheres	Gd L _{III} (1470 K under air and 1770 K under Ar-H ₂) and U L _{III} (1070 K under air)
U microspheres	U L_{III} (1070 K under air and 1670 K under Ar-H₂)
(U _{0.79} Ce _{0.21}) microspheres	Ce L _{III} (1270 K under air and Ar-H ₂)

Results

The experiments were notably focused on the phenomena occurring during the conversion of microsphere oxide precursors. In this report, a focus on the study of the conversion of a U-loaded microsphere is given. The microsphere was first heated under air at 450 K (1 h), 620 K (4 h), 770 K (2 h) and 1070 K (1 h), which corresponds, in the CRMP process, to the heat treatment of oxide conversion. The atmosphere was then changed to Ar-H₂ (4%) for three 1 h-plateaus at 1070 K, 1270 K and 1770 K, conditions close to those used during the heat treatments of reduction and sintering of the CRMP process. XANES spectra at the U L_{III} edge recorded during these isothermal plateaus are presented in Fig. 3 together with those of three U-based reference compounds: U^{+IV}O₂, U^{+IV/V}₄O₉ and U^{+V/+VI}₃O₈.

During the heating under air, the XANES spectra progressively shift towards higher energies, indicating the oxidation of U. At 450 K, sample spectrum is close to that of U^{+IV}, but from 770 K a clear shift appears and the sample spectra is almost aligned with that of U₃O₈ at 1070 K. The spectrum shapes also evolve with temperature. At 450 K, the flat signal indicates the presence of the cations loaded in the polymer resin. A first oscillation progressively appears when the temperature increases and is even similar to that of U₃O₈ at 1070 K. These observations are thus consistent with a progressive formation of an oxide, U₃O₈, through the oxidation of the U cations loaded in the resin. When the atmosphere is changed to the reducing one, the XANES spectrum correspond to that of UO₂, indicating the reduction of U in the sample, which occurs almost immediately (i.e., in less than the 5 min required to change the atmosphere).

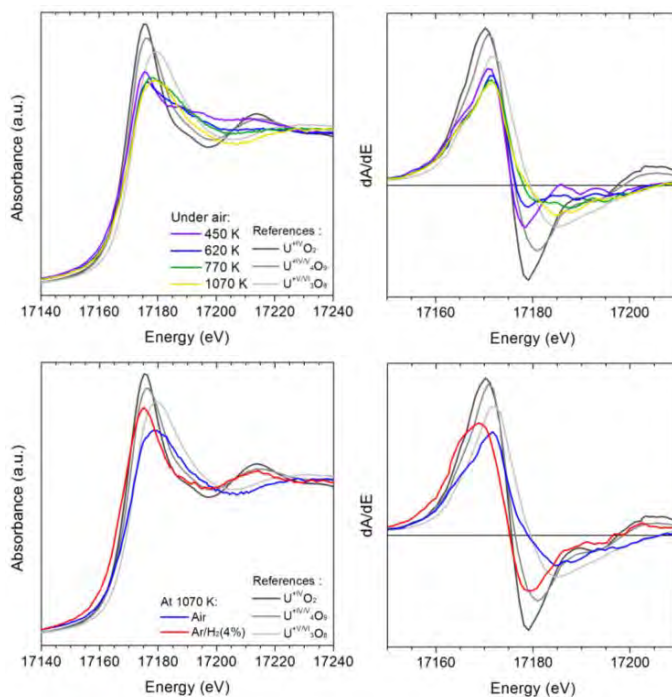


Fig. 3: XANES spectra at the U L_{III} edge of the U microsphere: (up) heating under air and (down) change from air to Ar-H₂ (4%).

Conclusion

The first in-situ high temperature measurements on U-bearing samples were performed during this experiment. They were focused on U/Ln oxide behaviours and on the conversion into oxides of several U/Ln precursors for nuclear fuel fabrications. The results obtained notably showed, through XANES spectra, the successive variations of oxidation states of the cations occurring during these conversions, as well as some changes in local symmetry and crystallinity. These results will also be further detailed in publications and presentations in international conferences. Concerning the experimental setup, the experiment confirmed the feasibility of the measurements in a double-sealed environment under controlled conditions. It thus represents the first step of a bigger project, which aims at performing in-situ XAS measurements on transuranium (i.e., Pu, Am, Np)-bearing samples.

Acknowledgements

Thanks have to be addressed to M. Sichert for the set-up development and organization of the experiment as well as to M. Caisso, C. Braut, V. Brethenoux and P. Coste for sample preparation. The CEA PACFA program is acknowledged for his support through F. Lebreton Ph.D funding.

References

- [1] E. Remy, S. Picart, S. Grandjean, T. Delahaye *et al.*, J. Eur. Ceram. Soc. 32 (2012) 3199-3209.
- [2] V. Magniena, D.R. Neuville, L. Cormier, J. Roux *et al.*, Geochim. Cosmochim. Acta., 72 (2008) 2157-2168.
- [3] D.R. Neuville, L. Cormier, D. de Ligny, J. Roux *et al.*, Amer. Min. 93 (2008) 228-234.

XANES and EXAFS measurements on Se-doped UO₂ and on simulated nuclear waste glass

E. Curti¹⁾, A. Froideval²⁾, I. Guenther-Leopold³⁾

¹⁾ Laboratory for Waste Management, Paul Scherrer Institute, Villigen, Switzerland

²⁾ Laboratory for Nuclear Materials, Paul Scherrer Institute, Villigen, Switzerland

³⁾ Hot Laboratory Division, Paul Scherrer Institute, Villigen, Switzerland

Background and objectives

In the framework of the EU-project “FIRST-Nuclides” (grant agreement no. 295722) it was proposed to carry out X-ray absorption spectroscopy (XAS) measurements in order to study oxidation state and coordination environment of safety-relevant, supposedly mobile radionuclides (¹²⁹I, ⁹⁹Tc, ¹³⁵Cs and ⁷⁹Se) in spent nuclear fuel. To this aim, a beamtime proposal for the INE beamline was submitted (ANKA proposal Nr. 1593). The determination of the oxidation state via XANES would allow predicting the mobility (solubility) of such nuclides during aqueous corrosion in an underground repository for radioactive waste. For instance, selenium may occur as sparingly insoluble Se(-II), Se(0) species or soluble Se(IV), Se(VI), which would increase the short-term release of ⁷⁹Se from the spent fuel upon aqueous corrosion.

Here, we report on preliminary XAS measurements performed between November 15th and 18th 2012 at the INE beamline. During this measurement campaign, we tested the feasibility of the proposed experiments with highly radioactive nuclear waste material. To this aim, Se K-edge absorption spectra were collected for inactive or slightly radioactive simulants, specifically UO₂ and borosilicate glass, both doped with Se concentrations similar to those expected in nuclear waste materials. All the measurements described in this report were carried out using in-house beamtime kindly granted to us by INE.

Sample preparation and XAS measurements

The simulated spent fuel samples were prepared by mixing and homogenizing depleted UO₂ powder with pre-defined concentrations of SeO₂ of 10, 100 and 2000 ppm. The so-prepared powders were pressed manually in a conventional XAS sample holder and sealed with Kapton tape. Samples of Magnox Waste (MW) borosilicate glass (SeO₂ ~ 3000 ppm), produced at the Sellafield reprocessing facility to simulate one of two reference compositions for Swiss vitrified nuclear waste, were prepared as polished monolithic chip (pristine, untreated glass) or as thin sections. The latter samples consisted of glass powder that had been previously leached with deionized water during 12 years [1]. All spectra were collected in fluorescence mode with a beam size of about 500 μm × 200 μm.

Results

The Se-K edge XANES spectra recorded for the UO₂ samples showed, as expected, signal/noise ratios improving with increasing SeO₂ concentration (Fig. 1). An edge jump was visible even for the sample with only 10 ppm SeO₂, in spite of the heavy U-bearing matrix. In addition, Se K-edge EXAFS spectra were successfully recorded for the 100 ppm sample up to $k \sim 8 \text{ \AA}^{-1}$. The analysis of the average spectrum yielded interatomic distances and coordination numbers roughly consistent with the crystal structure of the SeO₂ compound used as dopant (Fig. 2 and Table 1). These results indicate that XANES allows the identification of the Se oxidation state and that even EXAFS could be successfully measured in real spent fuel samples, in which expected Se concentrations are in the 100 ppm range.

XANES spectra were successfully recorded also for both pristine and leached MW glass samples, revealing that the aqueous corrosion process caused partial oxidation of Se(IV) to Se(VI) (Fig. 3).

Conclusions

The test measurements carried out on simulated nuclear waste materials show that - at the INE beamline - it is possible to measure Se-K XANES spectra in a matrix as heavy as UO₂ down to a concentration of 10 ppm Se, demonstrating that analogous measurements in real nuclear waste are likely to be successful. Moreover, the

present results suggest that Cs L, I L and Tc K-edges XAS spectra should also be measurable, since the concentrations of Cs, I and Tc in spent fuel are considerably higher than for Se.

Fig. 1: Comparison of the XANES spectra recorded at the Se K-edge for three UO_2 samples doped with different SeO_2 concentrations with the metallic Se reference spectrum.

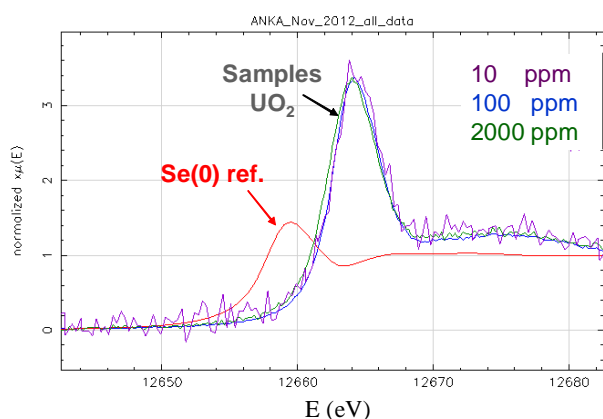


Fig. 2: EXAFS signal extracted from the Se K-edge XAS spectrum of the UO_2 sample doped with 100 ppm SeO_2 (in blue) compared to the fit of the experimental data (in red). The results of the fit of the experimental data are given in Table 1.

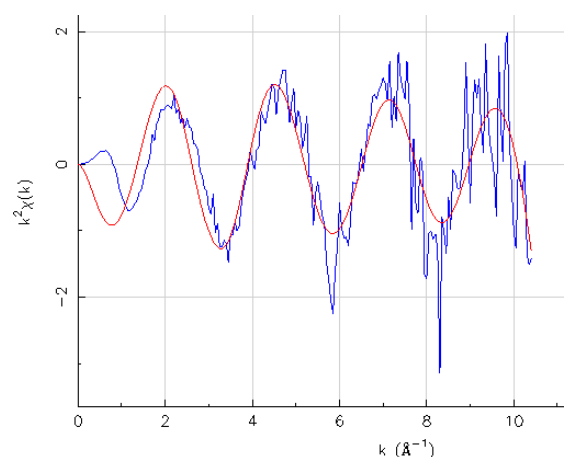
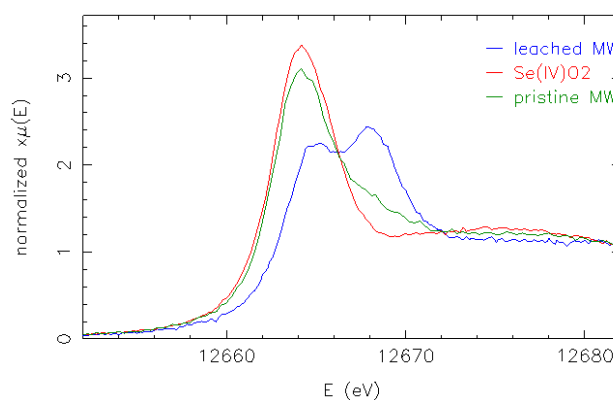


Table 1: Results of the EXAFS fit for the UO_2 sample doped with 100 ppm Se.

	Fit Se-O	SeO_2 model
R[Å]	1.66 ± 0.02	1.62
CN	4.0 ± 1.1	4
σ^2	0.002 (fixed)	
S_0	0.91 (fixed)	
E_0	0.00 (fixed)	

Fig. 3 Comparison of the Se K-edge XANES spectra of pristine and leached MW glass compared to Se(IV)O_2 reference.



References

[1] Curti E., Grolimund D. and Borca C.N. (2012) A micro-XAS/XRF and thermodynamic study of $\text{Ce}^{\text{III/IV}}$ speciation after long-term aqueous alteration of simulated nuclear waste glass: Relevance for predicting Pu behavior? *Appl. Geochem.* **27**, 56-63.

Acknowledgements

Drs. J. Rothe and K. Dardenne from the INE beamline are gratefully acknowledged for invaluable assistance during and before the measurements. Many thanks are due to Dr. B. Kienzler for offering us INE in-house beamtime. A. Lagotzki (PSI) is also thanked for his help in the organization of the sample transport from PSI to ANKA. This project was supported by the European Union's European Atomic Energy Community's (Euratom) Seventh Framework Programme FP7/2007-2011.

XAFS studies of NpO_2^+ behavior on Illite

N.L. Banik, R. Marsac, C. M. Marquardt, J. Rothe

Karlsruhe Institute of Technology (KIT), Institute for Nuclear Waste Disposal (INE),
D-76344 Eggenstein-Leopoldshafen, Germany

Motivation

Understanding radionuclide sorption onto purified clays is an important prerequisite with respect to long term predictive simulations of heterogeneous natural clays. [1] Neptunium (Np) is of relevance in the context of high level radioactive waste disposal because of its high radiotoxicity, the long half-life of the ^{237}Np isotope and the high mobility of Np(V) under oxidizing conditions. Under these conditions, Np exists as the NpO_2^+ ion, is highly soluble and reveals only weak sorption to clay mineral surfaces [1]. Solubility and mobility of Np are thus strongly influenced by various chemical parameters such as Eh, pH, ionic strength and complexation with various ligands. The present study focuses on the sorption behavior of NpO_2^+ to Illite, where batch experiments are combined with spectroscopy techniques. The aim of this study is to characterize Np sorption and speciation on Illite samples at varying chemical conditions by X-ray absorption near edge structure (XANES) and X-ray photoelectron spectroscopy (XPS). The structure of sorbed Np species is investigated by EXAFS.

Experimental

Materials: For all batch experiments, stock solutions of neptunium in the pentavalent oxidation state are used and their purity verified by UV-Vis/NIR spectroscopy. The Np concentration is determined by liquid scintillation counting (LSC) and ICP-MS. The Na-Illite used in this work was provided through the EC project CP CatClay (www.catclay.org). The source material is derived from lacustrine continental sediments deposited at the Upper Eocene (~ -35 Ma) in the basin of Le Puy en Velay (Massif Central, France).

Batch experiments: Sorption experiments are carried out at initial Np concentrations in the range of $3.0 \cdot 10^{-4}$ M at room temperature with varying ionic strengths. The Illite is preconditioned with 0.1 and 3.0 M NaCl by continuously shaking the suspension for 1 to 6 weeks to achieve equilibrium pH. After mixing Np(V) solution with the preconditioned Illite suspensions, the pH values are readjusted by adding 0.1 M HCl or 0.1 M NaOH. For characterisation of the suspensions the solid and liquid phases are separated by ultracentrifugation (90,000 rpm for 1 h). The supernatants are analysed in order to determine the content of free Np remaining in the liquid phase.

XAFS measurements: Np L3- XAFS measurements are performed at the INE-Beamline for actinide research. Np-Illite suspensions are filled into 200 μl capped PE vials and mounted in an air tight sample holder, which is connected to an Ar supply line at the experimental station to keep the samples under oxygen-free conditions. The Np L3-XAFS spectra are calibrated against the first derivative XANES spectrum of a Zr foil ($E(\text{Zr } 1s) = 17998.0 \text{ eV}$). All Np L3-XAFS spectra are measured in fluorescence yield detection mode at room temperature, using a 5 Pixel LEGe solid state detector and Ar filled ionization chamber as intensity monitor.

Batch Results

NpO_2^+ sorption to Illite is investigated at pH 7-10, $[\text{Np(V)}]_{\text{tot}} = 3.10^{-4}$ M, in 0.1-3.0 M NaCl and at a solid to liquid ratio of 20 g/L in an argon glove box. Earlier sorption results show that NpO_2^+ surface speciation is dominated by cation exchange reactions until pH ~6. NpO_2^+ surface complexation to silanol or aluminol groups located on the edges of Illite particles is very weak and becomes relevant only for pH >6. Surface complexation modeling suggests the formation of 3 types of Np(V) surface species depending on the pH: (i) NpO_2^+ sorbed via cation exchange sites, (ii) NpO_2^+ surface complexation to unprotonated silanol/aluminol groups located at the edges of clay particles and (iii) surface complexation of NpO_2OH via the latter mechanism. The Np-Illite samples are prepared at pH 7 and 10, where the maximum surface complexation is expected for NpO_2^+ and NpO_2OH , respectively. As batch results indicate an increase of the Np(V) sorption with increasing ionic strength (where a decrease would have been expected), XAFS was applied to reveal a possible change of Np speciation upon variation of ionic strength and contact time.

XANES Results

The XANES results for Np-Illite samples are summarized in Table 1. The Np L3-XANES spectra measured after 1 week and 6 weeks contact time for the Np(V) sorption samples are shown in Fig. 1. The white line (WL) positions and those of the first inflection point (cf. Table 1) indicate that the +5 oxidation state is retained for all four samples. Reduction to the tetravalent state of Np with time is not observed. There are slight but significant differences in signal between the 0.1 M and 3.0 M NaCl samples, especially in the WL peak heights.

Figure 1: Normalized Np L3-XANES spectra of NpO_2^+ sorption samples after 1 week and 6 weeks equilibration time.

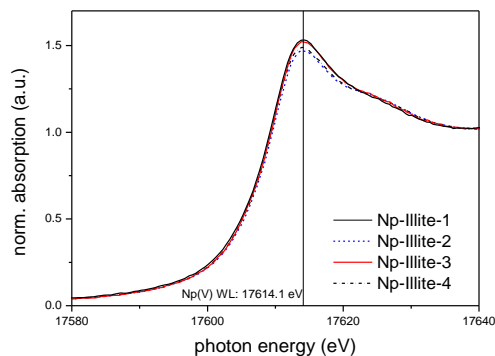


Table 1: Energy positions of the Np L3-XANES first inflection point and white line maximum positions for Np(V) sorption samples. All values are given in eV (estimated calibration error $\Delta E \pm 0.5$ eV).

Sample number	NaCl/pHc	Contact time	First inflection point	White line maximum
1	0.1 M/7.0	6 weeks	17610.5	17614.2
2	0.1 M/10	6 weeks	17609.6	17614.1
3	3.0 M/7.0	1 week	17610.5	17614.1
4	3.0 M/10	1 week	17609.6	17614.1

EXAFS results

The conformational change of the neptunyl moiety derived from this observation is confirmed by EXAFS analysis. Corresponding R-space fit parameters are summarized in Table 2.

Table 2: EXAFS fit parameter

Np(V)-Illite sample	k-range (\AA^{-1}) fit-range (\AA)	Shell	N	R (\AA)	ΔE_0 (eV)	σ^2 (\AA^2)	r-factor
1	3.40-12.05	O1	2.0 ^f	1.90(1)	1.18	0.0040	0.011
	0.70-2.45	O2	2.6	2.46(2)	1.37	0.0085	
2	3.40-13.50	O1	2.0 ^f	1.86(1)	2.16	0.0016	0.002
	0.77-3.13	O2	3.5	2.41(2)	-3.25	0.0101	
		Si	0.6	3.20(3)	-0.23	0.0002	
3	3.45-11.55	O1	2.0 ^f	1.87(1)	-4.34	0.0051	0.003
	0.70-2.27	O2	3.1	2.41(2)	-1.29	0.0045	
4	3.40-13.95	O1	2.0 ^f	1.86(1)	-0.94	0.0010	0.021
	1.23-4.11	O2	3.5	2.44(2)	3.08	0.0091	
		Np	0.6	3.97(2)	-1.05	0.0002	

EXAFS fit parameters: O1 axial oxygen backscatterer, O2 equatorial oxygen backscatterer, ^f indicates fixed parameter, S_0^2 fixed at 1

Several conclusions can be drawn from visual inspection of the four data sets: (i) in agreement with XANES spectral features, all samples exhibit EXAFS signals dominated by a first oxygen coordination shell split for short Np-O distances in the neptunyl moiety (O1) and longer Np-O bonds to equatorial oxygen atoms (O2); (ii) FT peaks beyond O1/O2 are questionable for pH 7 samples, no clear indication of distant backscatterers can be found; (iii) FT peaks representing higher distant shells (2,4) are only significant for the pH 10 samples. EXAFS spectra also indicate surface complexation of Np(V) on Illite at 0.1 M NaCl (i.e., Si at 3.20 \AA), and Np(V) surface precipitation 3.0 M NaCl (i.e., Np at 3.97 \AA).

Reference

[1] Geckeis, H., Lützenkirchen, J., Polly, R., Rabung, T., and Schmidt, M. (2013) Mineral–Water Interface Reactions of Actinides, Chem. Rev., 13 (2), pp 1016–1062

Solubility and speciation of Np(V) in alkaline CaCl₂ solutions

D. Fellhauer^{1,2)}, M. Altmaier¹⁾, V. Neck(†)¹⁾, J. Rothe¹⁾, J. Runke¹⁾, Th. Fanghänel²⁾³⁾

¹⁾ Karlsruhe Institute of Technology, Institut für Nukleare Entsorgung, P.O. Box 3640, 76021 Karlsruhe, Germany

²⁾ Heidelberg University, Institute of Physical Chemistry, Im Neuenheimer Feld 253, 69120 Heidelberg, Germany

³⁾ European Commission, JRC, Institute for Transuranium Elements, P.O. Box 2340, 76125 Karlsruhe, Germany

Introduction

For the reliable long-term performance assessment of nuclear waste in a salt based repository a robust understanding of the aquatic chemistry and thermodynamics of actinides in concentrated chloride systems is required. In the case of water intrusion into a repository actinides might come in contact with alkaline CaCl₂ solutions. CaCl₂ brines can form due to corrosion processes of cementitious waste in concentrated MgCl₂ solutions, given that certain stoichiometric requirements are fulfilled.

In recent studies at KIT-INE the solubility of tri-, tetra- and hexavalent actinides was investigated in alkaline CaCl₂ solutions [1-5]. For An(IV) (An = Th, Np, Pu) and Cm(III) the formation of hitherto unknown ternary Ca-An-OH complexes was observed leading to an enhanced An solubility in the alkaline pH range. In the case of Th(IV) Ca₄[Th(OH)₈]⁴⁺ could be identified by EXAFS as predominant species. For U(VI) in alkaline CaCl₂ solutions Altmaier *et al.* [5] observed the transformation of initial metaschoepite phase UO₃·2H₂O(cr) into more stable calcium diuranate CaU₂O₇·3H₂O(cr). These examples show that Ca²⁺ strongly affects both aqueous speciation and solid phase composition of actinides. In this contribution our latest investigations are discussed: the systematic study on the solubility, speciation and solid phase formation of pentavalent Np in dilute to concentrated (0.25-5.5 M) alkaline CaCl₂ solutions.

Experimental

Solubility experiments were conducted at room temperature (22 ± 2°C) under Ar atmosphere. Appropriate amounts of the corresponding Np(V) hydroxide phases (Ca_{0.5}NpO₂(OH)₂·1.3H₂O(s) or CaNpO₂(OH)_{2.6}Cl_{0.4}(s)·2.0H₂O(s)) were suspended in 10-30 ml 0.25 to 5.5 M CaCl₂ solutions and investigated as independent batch samples. The aqueous phase of the samples were analysed for pH_m = -log [H⁺], redox potential E_h (combination electrodes) and Np concentration (LSC after 10kD ultrafiltration) as function of time. Aqueous Np(V) speciation was determined by Vis-NIR, XANES and EXAFS). Solid phases were characterized by different methods e.g. XRD, quantitative chemical analysis, DTA, SEM-EDS. Experimental solubility data were evaluated by the specific ion interaction theory SIT or Pitzer approach.

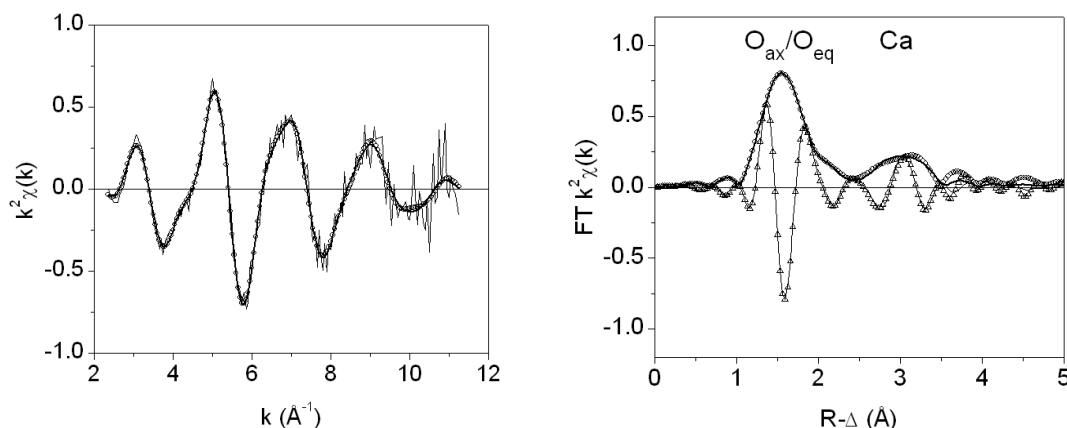


Fig. 1: k²-weighted Np L3-EXAFS $\chi(k)$ -function (left) and Fourier transform (right) of aqueous 6 mM Np(V) in 4.5 M CaCl₂ at pH_m 12.2.

Results

About 250 mg of freshly precipitated greenish $\text{NpO}_2\text{OH}(\text{am})$ were equilibrated in alkaline CaCl_2 solution. Under the experimental conditions the initial solid phase was not stable: in the course of the experiments, metastable $\text{CaNpO}_2(\text{OH})_{2.6}\text{Cl}_{0.4}(\text{s}) \cdot 2.0\text{H}_2\text{O}(\text{s})$ and stable $\text{Ca}_{0.5}\text{NpO}_2(\text{OH})_2 \cdot 1.3\text{H}_2\text{O}(\text{s})$ were identified as solubility controlling solid phases. Slope analysis of the corresponding solubility curves and Vis-NIR-spectroscopy confirmed that unhydrolysed Np(V) is predominant aqueous Np species between $\text{pH}_m = 8$ and 10. For $[\text{CaCl}_2] \geq 1.0 \text{ M}$ and $\text{pH}_m > 11$ a steep increase of the solubility curve with slope $\approx +3$ was observed pointing to the formation of a so far not described ternary Ca-Np(V)-OH complex with five hydroxo ligands. For further characterization of this species the aqueous phase of one of the samples was analyzed by L3-Np EXAFS at ANKA (sample characteristics: 6 mM Np(V) in 4.5 M CaCl_2 at $\text{pH}_m = 12.2$).

Figure 1 displays the L3-Np EXAFS $k^2\chi(k)$ -function and the Fourier transformed spectrum. The structural parameters obtained from least-squares fitting are summarized in table 1. The results confirm that a Np(V) hydroxo complex with Ca in the inner-sphere is predominant in highly alkaline, concentrated CaCl_2 solutions. Based on the outcome of the EXAFS analysis and additional thermodynamic evaluation of the solubility data, the corresponding species is best described by assuming three coordinating Ca^{2+} ions: $\text{Ca}_3[\text{NpO}_2(\text{OH})_5]^{2+}$. With this information a consistent thermodynamic model was derived which additionally includes the ternary complex $\text{Ca}[\text{NpO}_2(\text{OH})_2]^+$, prevailing in the mid-alkaline region $\text{pH}_m = 10.5$ to 11. The SIT and Pitzer approach were used to determine the equilibrium constants at ionic strength $I = 0$, $\log *K^\circ$ and $\log *\beta^\circ$, and the corresponding ion interaction parameters.

Table 1: Structural parameters of the predominant aqueous Np(V) species in 4.5 M CaCl_2 at pH_m 12.2 obtained from EXAFS least-squares fitting.

Sample	k-range (\AA^{-1}) fit-range (\AA)	shell	N	R (\AA)	ΔE_0 (eV)	σ^2 (\AA^2)	r-factor (%)
Np(V)(aq) in 4.5 M CaCl_2 $\text{pH}_m = 12.2$	2.35-11.27 0-3.53	O_{ax} O_{eq} Ca	0.9 3.5 2.4	1.86 2.29 3.38	1.13 -1.37 -7.23	0.0013 0.0122 0.0136	0.2

References

1. M. ALTMAIER et al., "Solubility of Zr(IV), Th(IV) and Pu(IV) hydrous oxides in CaCl_2 solutions and the formation of ternary Ca-M(IV)-OH complexes" *Radiochim. Acta*, **96**, 541-550 (2008).
2. B. BRENDEBACH et al., "EXAFS Study of Aqueous Zr^{IV} and Th^{IV} Complexes in Alkaline CaCl_2 Solutions: $\text{Ca}_3[\text{Zr}(\text{OH})_6]^{4+}$ and $\text{Ca}_4[\text{Th}(\text{OH})_8]^{4+}$ " *Inorg. Chem.*, **46**, 6804-6810 (2007).
3. T. RABUNG et al., "A TRLFS study of Cm(III) hydroxide complexes in alkaline CaCl_2 solutions" *Radiochim. Acta*, **96**, 551-559 (2008).
4. D. FELLHAUER et al., "Solubility of tetravalent actinides in alkaline CaCl_2 solutions and formation of $\text{Ca}_4[\text{An}(\text{OH})_8]^{4+}$ complexes: A study of Np(IV) and Pu(IV) under reducing conditions and the systematic trend in the An(IV) series" *Radiochim. Acta*, **98**, 541-548 (2010).
5. M. Altmaier et. al, "Solubility of U(VI) and formation of $\text{CaU}_2\text{O}_7 \cdot 3\text{H}_2\text{O}(\text{cr})$ in alkaline CaCl_2 solutions", Migration 2005, book of abstracts.

Solubility and aqueous speciation of An(VI) in NaCl solutions

X. Gaona, D. Fellhauer, J. Rothe, M. Altmaier

Karlsruhe Institute of Technology, Institut für Nukleare Entsorgung, Karlsruhe, Germany

The redox chemistry of the Np(V/VI) couple under alkaline conditions remains largely unknown. In the aqueous phase, the formation of hexavalent anionic species (e.g. $\text{NpO}_2(\text{OH})_3^-$ and $\text{NpO}_2(\text{OH})_4^{2-}$) has been proposed [1], although no thermodynamic data are currently selected in the NEA reviews [2]. The same thermodynamic data gap applies to Pu(VI), for which only first and second hydrolysis products ($\log^*\beta_{1,1}$ and $\log^*\beta_{1,2}$) are currently selected by the NEA. In analogy to U(VI) [3], the precipitation of Na- and Ca-neptunates and plutonates is also expected. The formation of these aqueous species and solid compounds may significantly limit the stability field of Np(V) and Pu(IV) in cementitious and saline environments, and therefore deserves further attention.

Solubility experiments were performed to determine the thermodynamic properties of Np(VI) aqueous species and solid compounds forming in dilute to concentrated alkaline NaCl solutions. A Np(VI) stock solution (with ~200 mg of ^{237}Np) was prepared by electrolysis of Np(V) in HCl, and precipitated at $-\log[\text{H}^+] = 12$ in NaCl 2.5 M. After two months of equilibration, the resulting solid phase was distributed in 5 experimental series of increasing I (0.1 M, 0.5 M, 1.0 M, 2.5 M and 5.0 M NaCl), with $7 \leq -\log[\text{H}^+] \leq 14$. Oxidizing conditions ensuring the stability of Np(VI) were achieved with 5×10^{-3} M NaClO in each sample. The aqueous concentration of Np was measured after 10 kD ultrafiltration by liquid scintillation counting (LSC). Solid phase was characterized by XRD, chemical analysis, SEM-EDS and XANES/EXAFS.

A Pu(VI) stock solution (with ~100 mg of ^{242}Pu) was prepared by electrolysis of Pu(IV) in HClO_4 . Analogously to Np(VI) solubility experiments, the Pu(VI) stock solution was neutralized with an alkaline solution aiming at $-\log[\text{H}^+] = 12$ in NaCl 2.5 M. Despite the expected large oversaturation with respect to $\text{PuO}_2(\text{OH})_2 \cdot \text{H}_2\text{O}(\text{cr})$, and eventually a Na-plutonate, no solid phase was precipitated (even after 9 months of equilibration time). Supernatant solution (~5 mM Pu(VI)) was characterized by UV-vis and XANES/EXAFS.

XRD, chemical analysis, SEM-EDS and EXAFS characterization of the solid phases considered for the Np(VI) solubility experiments indicated the prevalence in all systems ($0.1 \text{ M} \leq I \leq 5.0 \text{ M}$) of a neptunate-like structure with a Na:Np ratio 1:1, likely $\text{Na}_2\text{Np}_2\text{O}_7 \cdot x\text{H}_2\text{O}$. EXAFS further indicated the predominance of a distorted structure, where Np-O_{ax} and Np-O_{eq} distances were longer and shorter, respectively, than in usual neptunyl moieties. In all cases, solubility curves obtained showed three different regions (see Fig. 1): region a. $6 \leq -\log[\text{H}^+] \leq 8-9$, showing a steep decrease in the solubility with a slope ~ 3; region b. $8-9 \leq -\log[\text{H}^+] \leq 10-11$, with a nearly pH-independent [Np], and region c. $10-11 \leq -\log[\text{H}^+] \leq 13-14$, showing an increase in the solubility with a well-defined slope of 1. Regions b and c agree very well with observations previously reported for U(VI) under similar experimental conditions. Given the stoichiometry of the solid phase and considering the analogies with U(VI), the following equilibrium reactions can be proposed for regions b and c, respectively: $\text{NaNpO}_2\text{O}(\text{OH})(\text{cr}) + \text{H}_2\text{O} \Leftrightarrow \text{Na}^+ + \text{NpO}_2(\text{OH})_3^-$ and $\text{NaNpO}_2\text{O}(\text{OH})(\text{cr}) + 2\text{H}_2\text{O} \Leftrightarrow \text{Na}^+ + \text{NpO}_2(\text{OH})_4^{2-} + \text{H}^+$.

Despite the large oversaturation expected with respect to $\text{PuO}_2(\text{OH})_2 \cdot \text{H}_2\text{O}(\text{cr})$ (and eventually $\text{Na}_2\text{Pu}_2\text{O}_7 \cdot x\text{H}_2\text{O}$), no Pu(VI) solid phase formation occurred in the alkaline 2.5 M NaCl solutions after 9 months (see Fig. 1). Evaluation of the XANES data collected for the aqueous sample confirmed the predominance of Pu(VI) aqueous species, according with reference spectra published elsewhere [4]. Furthermore, Pu-O_{ax} and Pu-O_{eq} distances consistent with Pu(VI) resulted from the fitting of EXAFS data ($1.78 \pm 0.02 \text{ \AA}$ and $2.29 \pm 0.03 \text{ \AA}$, respectively). A more distant shell fitted at $3.77 \pm 0.05 \text{ \AA}$ was assigned to a Pu-backscattering atom. This hypothesis was confirmed by back-transforming the corresponding FT feature to the k^3 -weighted EXAFS function (Fig. 2).

3. Altmaier, M. et al., "Solubility of U(VI) in NaCl and MgCl₂ solution" Proceedings of the Migration Conference (2003).
4. Brendebach, B. et al., "X-ray absorption spectroscopic study of trivalent and tetravalent actinides in solution at varying pH values" *Radiochimica Acta*, 97, 701–708 (2009).
5. Neck, V. et al., "Solubility and redox reactions of Pu(IV) hydrous oxide: Evidence for the formation of PuO_{2+x}(s, hyd)" *Radiochimica Acta*, 95, 193–207 (2007)

μ -XAFS/XRF/XRD investigation of U(VI) phases in cement alteration products

C. Bube, K. Dardenne, M.A. Denecke, B. Kienzler, V. Metz, T. Prüßmann, J. Rothe, D. Schild, E. Soballa, T. Vitova

Karlsruhe Institute of Technology, Institute for Nuclear Waste Disposal, P.O. Box 3640, 76021 Karlsruhe, Germany

Cementation is a common conditioning method to fix and solidify low and intermediate level radioactive waste (LLW/ILW) prior to disposal in a future nuclear waste repository. To assist prognosis of the long-term safety of solidified cementitious waste, alteration of radionuclide bearing cement products in dilute aqueous solutions has been studied quite extensively. Yet, in chloride-rich solutions relevant for final LLW/ILW disposal in rock salt, thermodynamic data and thorough understanding of cement corrosion and radionuclide leaching behaviour are lacking. To alleviate this deficit, full-scale corrosion experiments with simulated waste products were performed.

U(VI) doped cement blocks were exposed to NaCl (monolith 'F31') and MgCl₂ (monolith 'F33') brines at the Asse II salt mine (Northern Germany) for almost two decades. Previous bulk powder U L3-XANES, laser spectroscopy and XRD measurements suggest the presence of a Ca-U(VI)-silicate phase, e.g., uranophane, in the corroded waste products [1]. U L3-XANES white lines (WL) and multiple scattering (MS) features obtained for the corroded cement samples appeared significantly broadened compared to corresponding features in crystalline reference compound spectra. Coexistence of different U(VI) coordination environments associated with high structural disorder or highly distorted U(VI) coordination environments in the corroded cement were assumed to explain the difference between the corroded cement sample and reference XANES. Recent μ -Raman spectroscopy data indicate that U-rich hot spots found in the corroded cement matrix with dimensions up to several tens of μ m are likely diuranate phases [2].

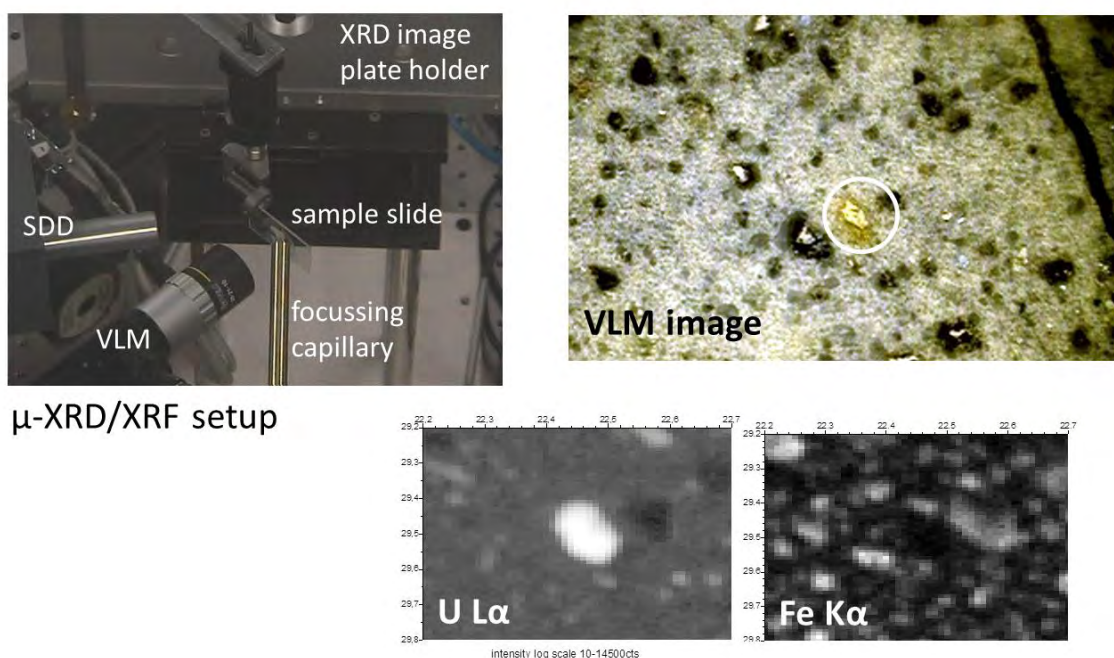


Fig. 1: top left - μ -XRD/XRF setup at INE-Beamline; top right - visible light microscopy (VLM) image of U-rich hot spot in sample F33-B1-50 (marked by circle); bottom - U L α and Fe K α fluorescence maps (scale in mm) recorded with a silicon drift detector (SDD) showing U-Fe anti-correlation (cf. [1] for sample nomenclature).

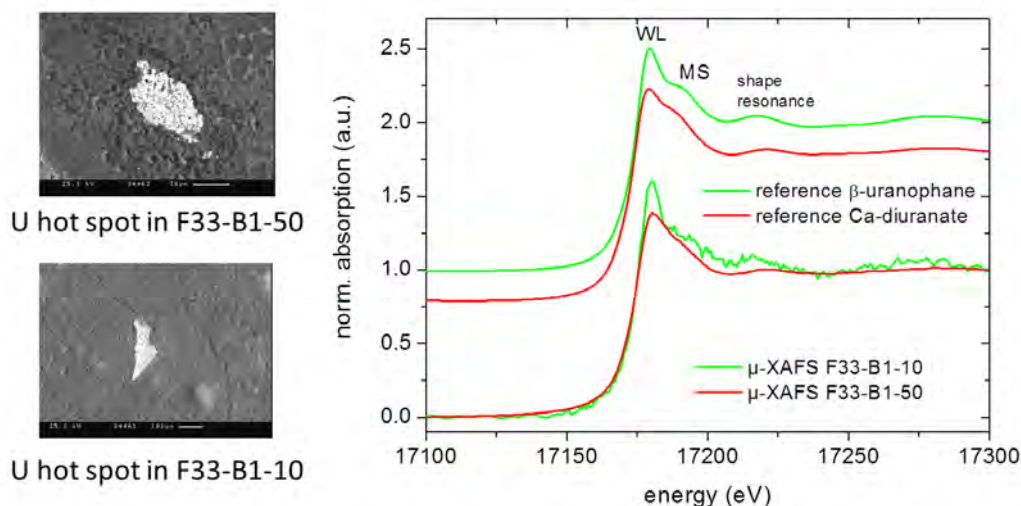


Fig. 2: left – SEM images of U-rich hot spots in sample F33-B1-50 (MgCl_2 system, top) and in sample F33-B1-10 (bottom); right – U L3 μ -XANES spectra recorded at these spots compared to XANES of crystalline U(VI) reference compounds calcium-diuranate and uranophane.

Spacially resolved XRD, XRF and U L3-XAFS spectra are recorded at the INE-Beamline for actinide science, employing the modular microfocus setup providing lateral resolution better than $30\ \mu\text{m}$. Monoliths F31 and F33 are examined as thin sections cut from bore cores and mounted on glass slides. μ -XRF element distribution maps and μ -XAFS (EXAFS/XANES) spectra are recorded by detecting U $L\alpha$ and cement matrix fluorescence lines with a silicon drift (Vortex) detector. XANES spectra are normalized against the energy dependent flux delivered by the polycapillary focusing optic with a pin diode recorded at the sample position. Laue type XRD patterns are registered in transmission mode by using image plates mounted perpendicular to the beam at about $150\ \text{mm}$ distance from the sample (Fig. 1). Sample areas of interest are selected from previously recorded SEM backscattering electron images (high contrast for U hot spots) and placed in the beam path using a three-axis positioning sample stage mount and the VLM. The y and z stage axes (right angles to the beam direction; the x-axis determines the focus) are used to subsequently scan the selected areas and precisely position the U hot spots in the beam path for μ -XANES and μ -XRD measurements. Uranium-rich aggregates identified in μ -XRF element distribution maps were found to generally exhibit XANES energy positions and spectral features characteristic for U(VI) dioxo-moieties, thus clearly confirming the presence of hexavalent U in the cement matrix after long time exposure to NaCl and MgCl_2 brines. XANES features for most U hot spots and for areas recorded in more diffuse U distributions located nearby are nearly indistinguishable. Both resemble the XANES for diuranate ($\text{CaU}_2\text{O}_7/\text{Na}_2\text{U}_2\text{O}_7 \cdot x\text{H}_2\text{O}$), indicating a similar type phase was formed throughout the probed F31 and F33 sample volumes (Fig. 2, red curves). Nevertheless, at least one U hot spot found in sample F33-10 (corroded in MgCl_2 brine, thin section taken close to the F33 monolith surface) exhibits distinct XANES features in agreement with that for uranophane ($\text{Ca}(\text{UO}_2)_2(\text{SiO}_3\text{OH})_2 \cdot 5\text{H}_2\text{O}$; Fig. 2, green curves). This finding is in accordance with thermodynamic solubility calculations, which postulate both diuranates and uranophane as possible solubility limiting phases in the cement/ MgCl_2 system, whereas diuranate is solely identified as solubility limiting phase in the cement/NaCl system. μ -XRD measurements of numerous U enriched sample spots show these to be X-ray amorphous; no clear evidence is obtained for the presence of any crystalline uranium phase. All diffraction patterns identified in these experiments can be attributed to cement corrosion phases.

References

1. B. Kienzler, V. Metz, B. Brendebach, N. Finck, M. Plaschke, Th. Rabung, J. Rothe, D. Schild, *Radiochim. Acta* 98, 675–684 (2010)
2. Bube, C., Metz, V., Schild, D., Lagos, M., Bohnert, E., Garbev, K., Altmaier, M., Kienzler, B., 1st Internat. Symp. on Cement-based Materials for Nuclear Wastes (NUWCEM 2011), Avignon, October 11-14, 2011, Proc. on CD-ROM O319

Fe, Co, Ni K edge XAFS investigation on transition metal (M=Fe,Co,Ni) doted hydrotalcite $[\text{Mg}_{3-y}\text{M}_y\text{Al}(\text{OH})_8\text{Cl}]\cdot x\text{H}_2\text{O}$

H. Curtius¹, K. Dardenne²

¹ Forschungszentrum Jülich GmbH (FZJ), Institut für Energie- und Klimaforschung - Nukleare Entsorgung und Reaktorsicherheit (IEK-6) IEK-6, 52425 Jülich, Germany

² Karlsruher Institut für Technologie (KIT), Institut für Nukleare Entsorgung (INE), Hermann-von-Helmholtz-Platz 1, 76344 Eggenstein-Leopoldshafen, Germany

Three transition metal doped Cl-hydrotalcites are investigated: $\text{Mg}_{2.90}\text{Fe}_{0.097}\text{Al}_{1.00}(\text{OH})_{7.95}\text{Cl}_{1.04} \cdot 2.46 \text{H}_2\text{O}$ (light orange), $\text{Mg}_{2.92}\text{Co}_{0.10} \text{Al}_{1.015}(\text{OH})_8\text{Cl}_{1.03} \cdot 2.07 \text{H}_2\text{O}$ (light pink) and $\text{Mg}_{2.92}\text{Ni}_{0.09} \text{Al}_{0.95}(\text{OH})_8\text{Cl}_{1.09} \cdot 2.27 \text{H}_2\text{O}$ (light green).

The samples are investigated as powder pressed without dilutant into 7mm diameter pellets. Samples synthesis, pellets preparation and measurements are done under inert gas. X-ray diffraction patterns are recorded for all three samples and matched with the hydrotalcite crystal structure [1]. This structure belongs to the double layered hydroxides (LDH) material. The cations are located at the center of octahedrons forming a sheet while the anions and / or water molecules are arranged in interlayers between two octahedron sheets (Fig.1). The interatomic distances for the nearest coordination shells are listed in Table 1. For comparison, the distances of the nearest coordination shells are given for the fougierite structure $(\text{Fe}(\text{OH})_2)(\text{OH})_{0.25} (\text{H}_2\text{O})_{0.5}$ [2], a hydrotalcite analogue compound where Mg/Al are completely replaced by Fe with a ratio Fe(II)/Fe(III)=3.

Fe/Co/Ni K edge x-ray absorption fine structure

Back-scatterer	N	R(Å)
O	6	2.01
Mg/Al	6	3.05
O	6	3.65
Cl*	1	3.79/4.18/4.86/5.17/6.00
O	12	4.76
Mg/Al	6	5.28
Mg/Al	6	6.09
O	12	6.42

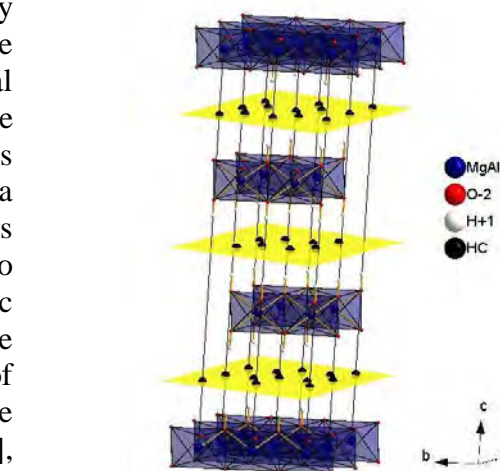


Fig. 1: Perspective view of hydrotalcite crystal structure. Yellow planes denote the interlayers where CO_3^- or Cl^- are located.

Back-scatterer	N	R(Å)
O	6	2.09
Fe	6	3.19
O	6	3.82
Cl*	1	4.15-4.70/5.65-6.38
O	12	4.97
Fe	6	5.53
Fe	6	6.38
O	12	6.71

Table 1: Metric parameters (R =distances, N =coordination numbers), of hydrotalcite with metal cation as center. Distances are given for undoped hydrotalcite [1] (left) and for the fougierite [2] (right). *possible positions for $\text{Cl}^-/\text{CO}_3^-$ in the interlayer, the positions represented in Fig. 2 are marked in yellow

(XAFS) spectra are recorded at the INE-Beamline at ANKA. Spectra are energy calibrated to the first inflection point in the XANES of a Fe/Co/Ni foil (7.112 / 7.709 / 8.333 keV respectively), measured simultaneously. The XAFS signal is recorded at room temperature in transmission

mode using N₂-filled ionization chambers at ambient pressure. Si<111> crystals are used in the double crystals monochromator, operating in fixed-exit mode. The parallel alignment of the crystal faces is detuned to ~70% of the maximum beam intensity at the beginning of each scan. The incident intensity is then held constant by means of a piezo-driven feedback system to the second crystal.

EXAFS fits are performed with Artemis, a program of the IFEFFIT package [3], using phase and amplitude data calculated for a 128 atom cluster (~8Å diameter sized centred on the individual metal cations) [1], where the carbonate groups are simply replaced by chloride. Among the possible occupation sites for Cl⁻ in the interlayer four are represented. For Cl atoms, single path scattering files for phase and amplitude are used. For Ni and Co doped compounds, the multiple scattering paths (MS) for the first oxygen shell is taken into account in the fit. The k-range used in modelling is [4.2 – 14.7Å⁻¹] for Ni doped Cl-hydroxalcite, [4.2 – 14.2Å⁻¹] for Co doped Cl-hydroxalcite and [3.4 – 11.4Å⁻¹] for Fe doped Cl-hydroxalcite. All fits are performed in the R-space simultaneously on the k²- and k³-weighted data.

Results and discussion

Ni and Co have very similar environments as showed in Fig. 2. The compounds seem to have an organized structure as neighbours contributions can still be seen at around 6Å (5.6Å in the FT not phase shift corrected). On the contrary, the EXAFS signal for the Fe-doped hydroxalcite and its FT differ significantly compared with the spectra of the two other cations Ni and Co.

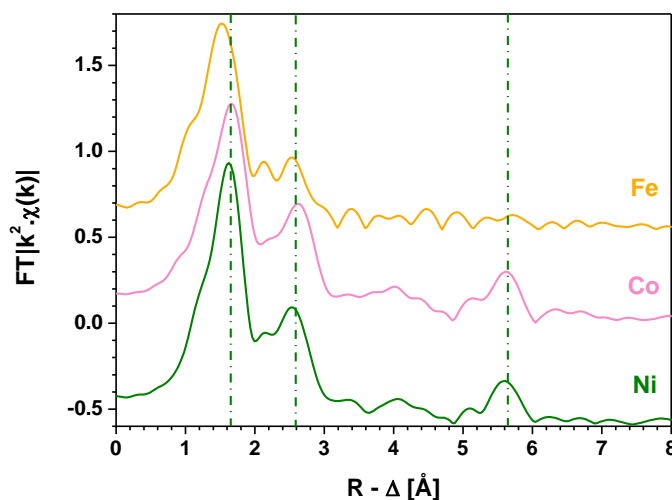


Fig. 2: FT magnitude taken in the range 3.2-13.5 Å⁻¹ for all samples.

First the FT peak around 6Å is not visible anymore; the useful information seems to end at around 3.0Å. k²-weighted EXAFS of the samples and back Fourier transform signal in the range 0.8-3.1Å for all three samples were recorded and fitted to obtain structural parameters. The results were compared with bond distances expected according to the bond valence theory predictions (Table 2).

The first shell distance is slightly longer for Co (2.08Å) compared to Ni (2.04Å). These distances are matching very well the expected distance predicted by the valence bond theory for a metal cation at oxidation state +II in a six-fold coordination. The complete predictions for oxidation state +II and +III in coordination 4 and 6 are given in Table 2. Concerning the Fe sample, we obtained a first coordination sphere with 6 oxygen atoms at 2.00 Å with a Debye-Waller factor (σ^2) of 7.40Å². This bond distance is far from the one expected for Fe(II) in octahedral coordination as shown in Table 2 or as found for six-fold coordinated Fe(II) in the literature (2.16Å in FeO [4]). Even in the case of fougérite (Iron LDH), where the crystal structure

Cation - O	CN	R (Å)	Ro (Å)
Ni(II)	4	1.91	1.654
	6	2.06	
Co(II)	4	1.95	1.692
	6	2.10	
Fe(II)	4	1.99	1.734
	6	2.14	
Ni(III)	4	1.74	1.74
	6	1.89	
Co(III)	4	1.79	1.70
	6	1.94	
Fe(III)	4	1.87	1.759
	6	2.01	

Table 2: Bond distances expected according to the bond valence theory predictions. The relationship between bond length (R) and bond valence (s) is: $s = \exp((R_o - R)/B)$ where R_o and B are bond valence parameters that depend on the two atoms forming the bond [5]. B is 0.37. CN: coordination number

confirmed by XANES analysis. It shows unambiguously that the major part of Fe is in oxidation state +3, as no evidence for Fe(II) is found as given by analytic methods.

Conclusion

These results match the XRD structure data within the errors inherent to EXAFS. We conclude that the Ni and Co cations are incorporated as divalent cations in the hydrotalcite structure at the crystallographic position of Al/Mg, i.e., in the octahedral sheet. They are likely replacing the Mg^{2+} as it is expected from the stoichiometry and the matching charge.

For Fe, EXAFS results are compatible with Fe incorporation in the hydrotalcite structure in the octahedral sheet, but as trivalent cation with formation of Fe-Fe pairs.

Acknowledgments

We would like to thank Nicolas Finck for providing the Fe reference data. We thank the ANKA synchrotron source for providing the beamtime.

References

- [1] ICSD: 81963.
Bellotto, M.; Rebours, B.; Clause, O.; Lynch, J.; Bazin, D.; Elkaim, E. (1996) *J. Phys. Chem.*, 100(20) 8527
- [2] ICSD: 159700
Trolard, F., Bourrie, G., Abdelmoula, M., Refait, P., Feder, F. (2007) *Clay Clay Miner* 55, 323
- [3] Newville, M.; Livins, P.; Yacoby, Y.; Rehr, J.J.; Stern, E.A. (2003) *Phys. Rev. B*, 47, 14126
- [4] ICSD: 82233
Fjellvag, H.; Gronvold, F.; Stolen, S.; Hauback, B.C. (1996) *J. Solid State Chem.*, 124, 52
- [5] Brown and Altermatt (1985) *Acta Cryst.* B41, 244

parameters account for both Fe(II) and Fe(III) (ratio 3:1) in octahedral positions, the mean value is found to be 2.09Å (crystal structure data [2]).

Such a short bond distance can be achieved either by Fe(II) in tetrahedral or Fe(III) in octahedral coordination. The hydrotalcite or fougérite structure does not supply tetrahedral sites. X-ray diffraction study of the present samples does not give any evidence for the presence of other crystalline phase besides hydrotalcite. Furthermore, the Fe K EXAFS intensity cannot be matched with fourfold oxygen coordination. Presence of Fe(III) in the octahedra is very likely as it occurs in fougérite and in the hydrotalcite at the position of trivalent cations (Al^{3+}), too. Furthermore, trivalent iron is suggested by the light orange color of the sample (fougérite has blue-green to bluish-gray colour) and is additionally

Solubility limiting Np(V) solid phases in NaCl solutions

V.G. Petrov¹⁾, K. Dardenne²⁾, X. Gaona²⁾, D. Fellhauer³⁾, S.N. Kalmykov¹⁾, M. Altmaier²⁾

¹⁾ Lomonosov Moscow State University, Department of Chemistry, Leninskie gory, 1/3, 119991 Moscow, Russia

²⁾ Karlsruhe Institute of Technology, Institute for Nuclear Waste Disposal (KIT-INE), Hermann-von-Helmholtz-Platz 1, D-76344 Eggenstein-Leopoldshafen, Germany

³⁾ Institute for Transuranium Elements, Joint Research Center, EC, Hermann-von-Helmholtz-Platz 1, D-76344 Eggenstein-Leopoldshafen, Germany

Introduction

Among the actinides relevant for the long-term safety assessment of nuclear waste repositories, Np is one of the most relevant due to its potentially high mobility and the high stability of its pentavalent oxidation state over a wide range of pH under non-reducing Eh conditions. Solubility limitations of the actinides are the key processes influencing mobility and retention. It has been reported by different authors that in carbonate-free aqueous solutions of different ionic strengths, Np(V) solubility is limited by oxyhydroxide phases, either by $\text{NpO}_2(\text{OH})(\text{am})$ or $\text{NpO}_2(\text{OH})(\text{cr})$, but only very limited information on the composition of these solids is available so far. Thus in the present study we have analyzed the characteristics of neptunium solubility-limiting Np(V) solid phases in equilibrium with supernatant in dilute to concentrated NaCl solutions.

Experimental

Solubility experiments and sampling were carried out under inert gas (Ar) atmosphere for more than 18 months. Solutions of NaOH/NaCl and HCl/NaCl were used for adjusting the pH_c , keeping the respective ionic strength conditions constant. X-ray absorption spectroscopy was used to characterize the neptunium solubility limiting solid phases. XRD, SEM-EDS and quantitative chemical analysis were used as well.

Results

Several solid phases have been analyzed from solubility studies under different pH and ionic strength conditions in NaCl media showing distinctly different features. It is known from both experimental data and thermodynamic calculations, that Np(V) solubility in carbonate-free media follows the following trends: decrease of Np concentration with slope “-1” at pH_c values < 11, constant values of [Np] (slope “0”) at $11 < \text{pH}_c < 12$, and increase of [Np] with slope “+1” at $\text{pH}_c > 12$. In our studies, the reported behavior has been confirmed in solutions with relatively low ionic strength (0.1 M NaCl). However, increasing ionic strength conditions resulted in significant changes of Np solubility: in the pH_c region 11.5 – 12.0 a pronounced drop in the solubility is observed,

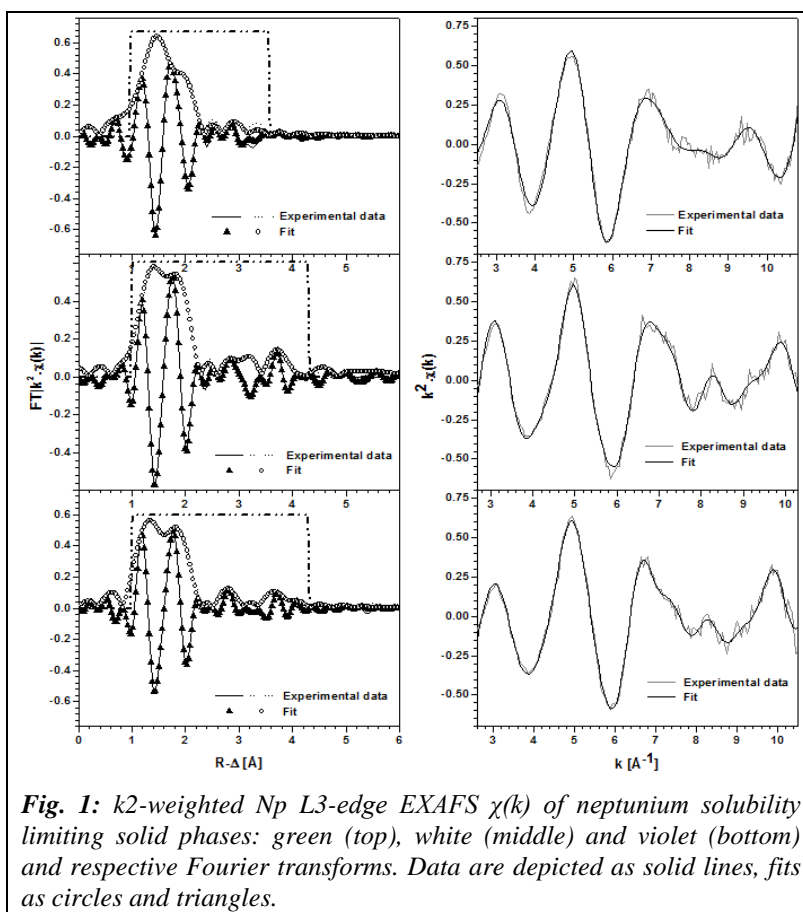


Fig. 1: k^2 -weighted Np L3-edge EXAFS $\chi(k)$ of neptunium solubility limiting solid phases: green (top), white (middle) and violet (bottom) and respective Fourier transforms. Data are depicted as solid lines, fits as circles and triangles.

accompanied by a change of solid phase color from green to white clearly indicating solid phase transformation. Further increase of pH_c to strongly alkaline conditions results in increased neptunium solubility and another change of solid phase color from white to light violet.

XANES analysis confirms the Np(V) redox state in all of the samples regardless of color. The k^2 -weighted Np L3-edge EXAFS $\chi(k)$ of neptunium solubility limiting solid phases and respective Fourier transforms are shown in Fig. 1. For all **green** solids EXAFS evaluation showed no visible Np-Np interaction and fitted only with the two first oxygen shells. For **white** solids the data is well reproduced using four shells and structure matches the $(\text{Na}_2\text{U}_2\text{O}_7)_{0.5}$ structure with a few rearrangement due to the substitution of U through Np. The fit results are given in Table 1. The “yl” oxygen distance is shorter compared to U (1.81 Å for 1.91 Å) and as a result equatorial distances are longer (2.37 Å for 2.31 Å) to match the mean valence. Np-Np distance is equal to U-U distances, whereas Np-Na slightly longer (3.90 instead of 3.84 Å). EXAFS data evaluation for **violet** solid phases did not match sodium uranate structure. The obtained structural parameters fitted to $\text{NaNpO}_2(\text{OH})_2(\text{s.})$ reported by Almond et al. [1]. The data is reproduced using five shells. The coordination numbers of atoms were fixed to match $\text{NaNpO}_2(\text{OH})_2(\text{s.})$ structure. The fit results are given in Table 1.

From chemical analysis, SEM-EDS and XRD studies it was observed, that all **green** solids in contact have the same amorphous structure and low content of sodium (0.1-0.3 Na/Np ratio). In contrast, the less soluble **white** solids have well-defined crystalline structure with platelets crystallites and a Na/Np ratio of about 1, pointing to the formation of Na-Neptunates. **Violet** solids observed in highly alkaline solutions ($\text{pH}_c > 13.0$) in spite of similar shape of crystallites (needles) and sodium abundance (Na/Np ratio ~ 1) have different well-defined crystalline structures depending on the ionic strength. The very low content of Cl observed by SEM-EDS in the samples indicate that no chloride is present in the solids and the reported Na/Np ratios are not affected by analytical artifacts due to NaCl impurities in the solids.

Our investigations show, that with increasing pH_c and NaCl concentration, neptunium(V) hydroxide undergoes significant phase transformations towards Na-neptunate phases presently not accounted for in thermodynamic models.

Table 1: Structural parameters of Np solubility limiting phases obtained from EXAFS evaluation.

Sample	Backscatterer	R (Å), (± 0.01 Å)	N (± 20 %)	$\sigma^2(\text{Å}^2)*10^{-3}$	ΔE_0 (eV)	goodness of fit (%)
green solid	O	1.81	1.3	0.73	-0.2	0.8
	O	2.40	4.7	10.7	-0.2	
	MS	3.62	1.4	2.9	-0.4	
white solid	O	1.83	2*	0.64	5.0	0.4
	O	2.38	6*	3.58	5.0	
	Na	3.84	6*	14.1	-3.8	
	Np	3.91	6*	11.06	4.78	
violet solid	O	1.82	2*	1.0	3.3	0.2
	O	2.39	5*	3.1	3.3	
	Na	3.27	2*	3.9	-5.0	
	Na	3.74	3*	24	-5.0	
	Np	3.89	2*	4.0	0.8	

*R = distances, N = coordination numbers, σ^2 = EXAFS Debye-Waller factors, ΔE_0 = relative energy shifts held as global parameters for like atoms, MS – multiscattering, * fixed*

Acknowledgements

The research leading to these results has received funding from the European Union's European Atomic Energy Community's (Euratom) Seventh Framework Programme FP7/2007–2011 under grant agreement n° 212287 (RECOZY project). We also acknowledge Ministry of Education and Science of Russian Federation (Contracts 02.740.11.0853 and 11.519.11.5011) and ACTINET-i3 Integrated Infrastructure Initiative for financial support.

Chloroaluminum phthalocyanine thin films: chemical reaction and molecular orientation

F. Latteyer¹⁾, H. Peisert¹⁾, J. Uihlein¹⁾, P. Nagel²⁾, M. Merz²⁾, S. Schuppler²⁾, T. Chasse¹⁾

¹⁾ Institut für Physikalische und Theoretische Chemie, Universität Tübingen, Auf der Morgenstelle 18, 72076 Tübingen, Germany

²⁾ Karlsruher Institut für Technologie, Institut für Festkörperphysik, 76021 Karlsruhe, Germany

Introduction:

Polar phthalocyanines have been investigated intensively in the recent past. In contrast to the more familiar CuPc or ZnPc, the polar metal phthalocyanines are not planar but umbrella like and tilted by 7° leading to a symmetry lowering from D_{4h} to C_{4v} . It can be expected that the presence of a molecular dipole moment offers a route to control the growth of the molecules in thin films by external factors. Indeed, it was shown for TiOPc, AlClPc or VOPc, that electric and magnetic fields can influence the molecular orientation, the polymorphism, and the surface morphology [1-4]. On the other hand, it can be shown, that for devices containing Pcs as active layers the efficiency is affected by the growth, interface properties, the molecular orientation and electronic properties are essential factors. In this context, possible chemical reactions in air become important.

The aim of the present study is a detailed investigation of the chemical reaction of monomer AlClPc to the μ -(oxo)dimers $(PcAl)_2O$ in thin films deposited on indium-tin oxide (ITO), we focus on the influence of environmental conditions as well as on the molecular orientation. The molecular orientation of AlClPc and $(PcAl)_2O$ on ITO was investigated by methods with different surface sensitivities: Raman and NEXAFS in TEY and PEY mode as schematically illustrated in Fig. 1. The surface sensitivity of NEXAFS depends on the chosen detection mode. In the case of total electron yield (TEY) all electrons that emerge from the surface are (indirectly) detected and slow secondary electrons of about 5 eV dominate the signal. Since these electrons can escape from the sample after several inelastic scattering processes they originate to a large extent from layers deeper as the mean free path of the electrons. On the other hand, for partial electron yield (PEY) detection, the retarding voltage of the detector determines the kinetic energy of the electrons (in our case higher than 350 eV) and essentially specific Auger electrons are detected. This results in a sampling depth of about 1-2 nm for PEY NEXAFS and about 10 nm for TEY NEXAFS.[48]

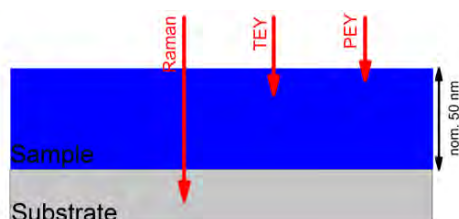


Figure 1. Illustration of the probing depth for the different methods (Raman, TEY, PEY).

Experimental details:

The NEXAFS and XPS measurements were carried out at the soft x-ray beamline WERA. The energy resolution at the N-K edge was set to approx. 200 meV, the degree of linear polarization was 95%. The NEXAFS spectra have been measured in total electron yield (TEY) (sample current) and partial electron yield (PEY) (channeltron) mode. The TEY and PEY spectra were recorded parallel at the same spot and at the same time. The spectra have been normalized to equal step heights. To evaluate the intensity of π^* -resonances, the areas have been estimated by numerical integration of the region from 397.5 eV to 402 eV assuming that the edge structure is at higher photon energies.

The thin films of AlClPc with nominal film thicknesses of 50 nm have been prepared by physical vapor deposition from a temperature controlled cell on ITO substrates in ultra-high vacuum (UHV). It was

verified by XPS that air exposure at room temperature leads not to a chemical reaction. The subsequent annealing to 300°C for 1 – 1.5 h initiates the reaction to the μ -(oxo)dimer. The annealing of the films was performed at ambient conditions (exposure to air). Before and after the reaction the films were characterized again by NEXAFS, XPS, Raman and UV/vis spectroscopy.

Results:

For phthalocyanines, the molecular orientation can be probed by NEXAFS monitoring the relative intensities of N 1s- π^* excitations.[5] Spectral features at photon energies < 402 eV correspond essentially to N 1s - π^* transitions and at > 402 eV they are described mainly by N 1s - σ^* transitions. N K-edge absorption spectra were taken from AICIPc films before and after the reaction in both TEY and PEY mode as a function of the incidence angle of the p-polarized synchrotron radiation and selected spectra (for $\theta = 10^\circ$, grazing incidence) and $\theta = 90^\circ$, normal incidence) are displayed in Fig. 2. Difference spectra ($90^\circ - 10^\circ$) have been drawn to make the changes of the linear dichroism clearly visible. The spectra in of the as deposited film show a similar tendency for both modes (TEY, PEY): The maximum of the N1s- π^* excitations are observed at grazing incidence ($\theta = 10^\circ$) in Fig. 2(a) pointing to a preferential orientation of the molecular plane perpendicular relative to the substrate surface (preferred lying absorption geometry). The decreasing and increasing intensity of the π^* and σ^* resonances from grazing to normal incidence are clearly visible in the TEY and PEY difference spectra ($90^\circ - 10^\circ$), respectively. After the reaction, the dichroism appears weaker (Fig. 2(b)) in particular for spectra taken in TEY mode. The angle-dependence of the N1s- π^* resonance intensity is summarized for all measured angles quantitatively in Fig 2(c). The expected functional behavior for perfectly lying and standing molecules assuming a polarization degree of 100% are plotted as broken lines in Fig. 2(c). A tendency for lying molecules is observed for the film before and after the deposition since the angular dependence follows the dotted line for lying molecules, indicating that there is a preferential orientation within the upper 10 nm of the film (with a lower degree of ordering). It is clearly visible that TEY and PEY intensities show a similar behavior for the as deposited film.

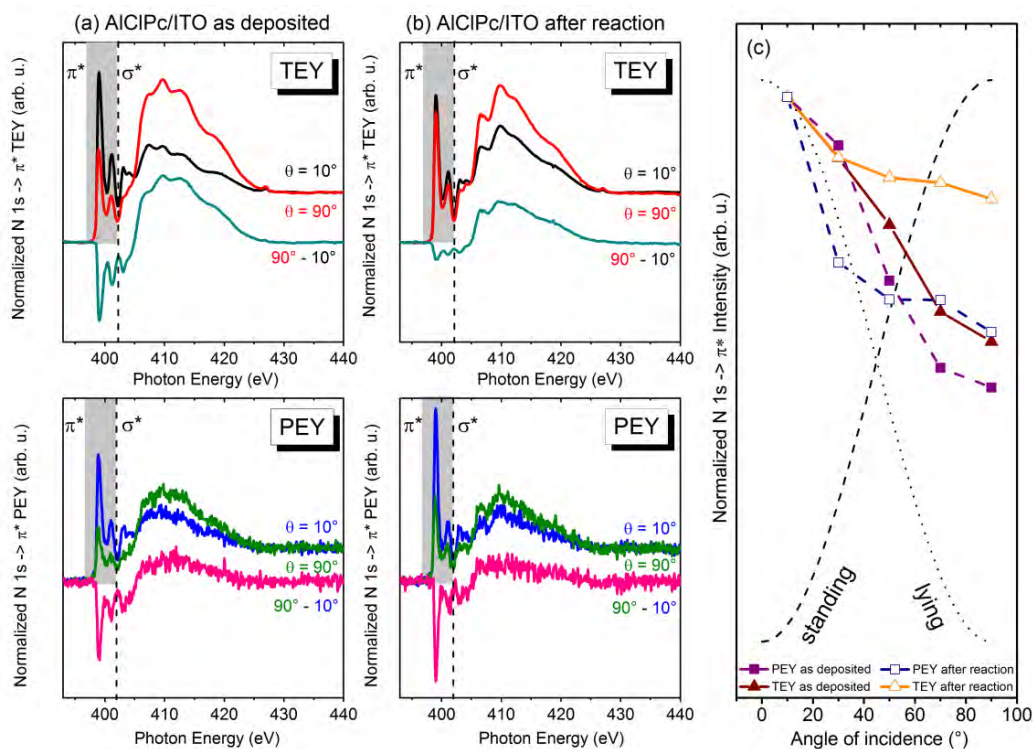


Figure 2. (a), (b) NEXAFS spectra with included difference spectra of AICIPc for the as deposited film (a) and after annealing (b). The upper panels show spectra measured in TEY mode, the lower panels PEY mode. The angles given denote the incidence angle of the incoming p-polarized light relative to the substrate. (c) Angle-dependence of the intensity of the π^* resonances for the as deposited and annealed film. The expected intensity profiles for lying and standing molecules are indicated by dotted and dashed lines, respectively. The different behavior of the intensities from spectra measured in TEY and PEY mode point to a different orientation of the uppermost layer with respect to the bulk.

In contrast, after the reaction, the angular dependencies of the TEY and PEY show a different evolution; the angle dependence of the resonances of the TEY (more sensitive to the bulk) is less pronounced and indicates less ordered structures similar to the observation using Raman spectroscopy (not shown). The angle dependence of the PEY resonances on the other hand (sensitive for the layers close to the surface) is nearly similar to the as deposited film. The different information depth of PEY, TEY and Raman offer a route to distinguish between the molecular orientation at the surface and in the bulk. The differences of the molecular orientations in dependence of the film thickness might be related to the ability for reorganization of the Pc molecules. Due to a bigger steric hindrance the molecules in the bulk appear to be less able to rearrange during the reaction whereas molecules at the surface arrange in a favored geometry comparable to the situation before the reaction. Thus, the molecular orientation seems to be “maintained” especially close to the surface even after a chemical reaction.

For a possible application of AICIPc in devices, it would be very important to protect the materials from water in combination with high temperatures. On the other hand, ultrathin films of oriented $(\text{PcAl})_2\text{O}$ might be prepared on substrate surfaces by a reaction of annealed AICIPc in a humid environment.

Acknowledgement

We thank W. Neu for technical assistance and T.V. Basova as well as V. Kiselev for fruitful discussions. Financial support by the German Research Council (PE 546/5-1 and CH 132/23-1) is gratefully acknowledged. ANKA Angströmquelle Karlsruhe is acknowledged for the provision of beamtime.

References

- [1] V. Kolotovska, M. Friedrich, D.R.T. Zahn, G. Salvan, J Cryst Growth **291** (2006) 166-174.
- [2] B.E. Schuster, T.V. Basova, H. Peisert, T. Chassé, ChemPhysChem **10** (2009) 1874-1881.
- [3] T.V. Basova, V.G. Kiselev, V.A. Plyashkevich, P.B. Cheblakov, F. Latteyer, H. Peisert, T. Chassé Chem Phys **380** (2011) 40-47.
- [4] T.V. Basova, V. Plyashkevich, F. Petraki, H. Peisert, T. Chassé J Chem Phys **134** (2011) 124703-8.
- [5] H. Peisert, I. Biswas, M. Knupfer, T. Chassé Phys Status Solidi B **246** (2009) 1529-1545.

XMCD study of the Magnetic Proximity Effect in overdoped of $\text{YBa}_2\text{Cu}_3\text{O}_7/\text{LaMnO}_{3+x}$ Superlattices

M.A. Uribe-Laverde, S. Das, K. Sen, D.K. Satapathy, I. Marozau, C. Bernhard

University of Fribourg, Department of Physics and Fribourg Centre for Nanomaterials, Chemin du Musée 3, CH-1700 Fribourg, Switzerland

Introduction

Based on a combined polarized neutron reflectometry (PNR) and x-ray magnetic circular dichroism (XMCD) study, we have recently reported a magnetic proximity effect (MPE) in superconductor/ferromagnet (SC/FM) superlattices (SLs) of $\text{YBa}_2\text{Cu}_3\text{O}_7$ (YBCO)/ $\text{La}_{2/3}\text{Ca}_{1/3}\text{MnO}_3$ (LCMO) and YBCO/ LaMnO_{3+d} (LMO) [1]. This MPE involves a strong suppression of the FM moment on the LCMO side of the interface and, at the same time, the induction of a Cu FM moment on the YBCO side. Surprisingly, the MPE is very pronounced for the SL with metallic LCMO layers whereas it is almost absent for the one with insulating LMO. This suggests that the MPI is an intrinsic effect that is controlled by the electronic properties of the FM manganite layers. To support this hypothesis, we grew a new YBCO/LMO SL under different conditions to obtain a higher concentration of excess oxygen where the LMO layers are weakly conducting [2].

Experimental

During our last beamtime, we performed therefore XMCD measurements on the YBCO/LMO SL grown using the pulsed laser deposition technique [3]. We scanned the regions around the Mn and Cu edges measuring for Mn in saturation, with and applied field of 3T, and for Cu in low-field, with an applied field of 0.5T after saturating with 3T, and in saturation. To obtain the dichroism we inverted both the incident beam polarization and the direction of the applied magnetic field, the results shown are the average over all measurements. All measurements were performed in a grazing incidence setup with the beam forming an angle of $\sim 75^\circ$ with the sample normal. We lost one day of the assigned beamtime due to an unexpected shut down of the synchrotron. For another 1 ½ days the synchrotron beam was very unstable, this results in data that are very difficult to normalize.

Results

The XMCD data together with the resistivity and PNR data for this new YBCO/LMO SL are shown in Fig. 1 on the right hand side. The comparison with the SLs with highly conducting LCMO and nearly insulating LMO layers are shown in the panels on the left and the middle of Fig. 1. It confirms that in the new SL with weakly conducting LMO layers the intensities of the 2nd order Bragg peak in the PNR data and of the Cu-XMCD signal are indeed intermediate between the ones of the strongly conducting LCMO and the insulating LMO. This confirms our hypothesis that the MPE is intrinsic and depends strongly on the electronic properties of the FM manganite layers.

Conclusions

We could detect an enhanced Cu XMCD signal in a YBCO/LMO SL with weakly conducting LMO layers as compared to a previously investigated SL with insulating LMO layers. We have thus established a correlation between the electronic properties of the FM manganite layers and the occurrence of the MPE in this kind of system. Whether the strong suppression of the magnetic moment on the FM side of the interface and the induced antiparallel Cu-moment are correlated to each other or are independent consequences of the electronic reconstruction at the interface is still to be determined.

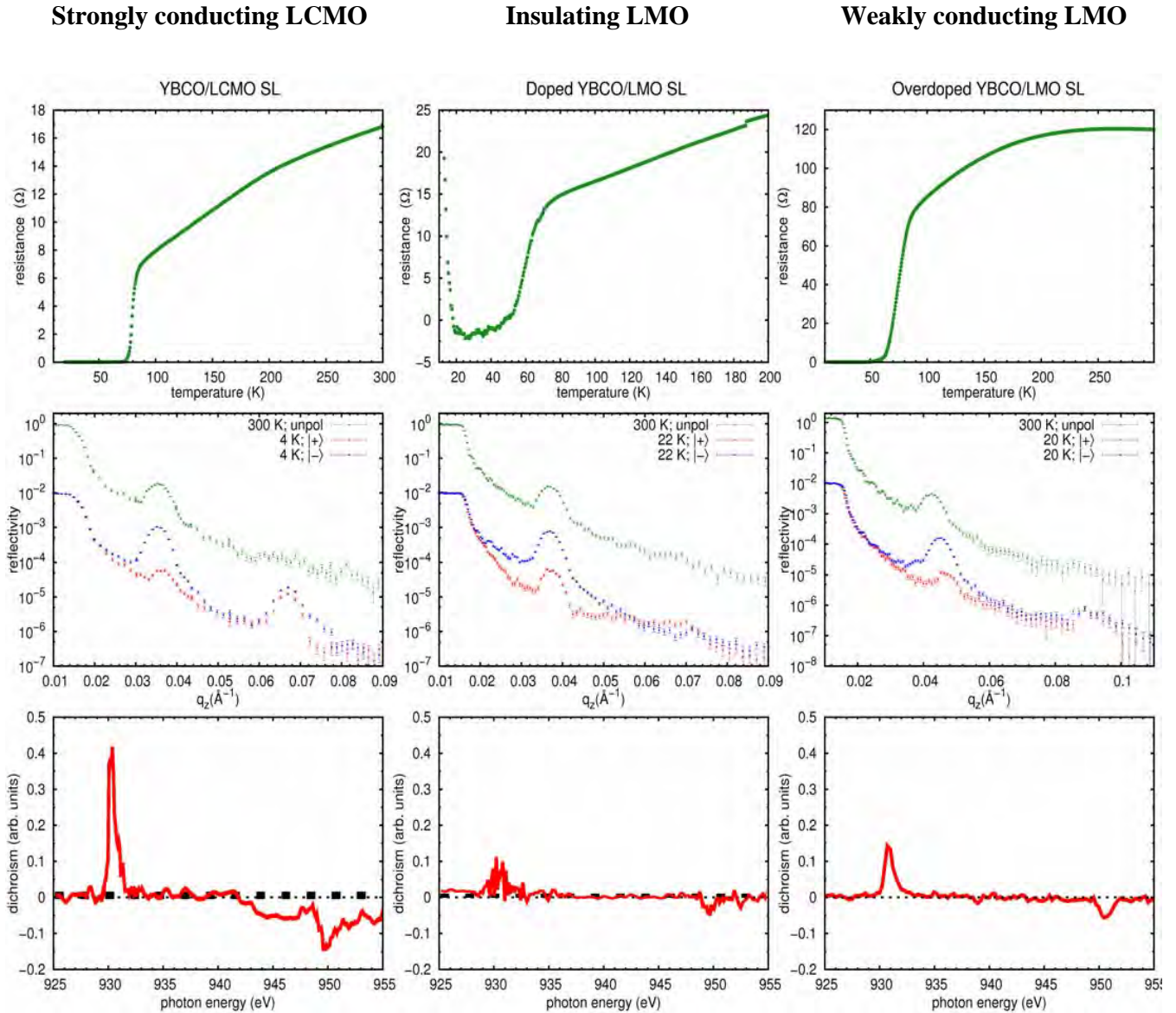


Fig. 1: Resistivity, polarized neutron reflectometry (PNR) and Cu-edge XMCD data for superlattices with different conducting properties of the FM manganite layers. For the SLs with the conducting LCMO and LMO layers the FM transition at $T^{\text{Curie}}=220\text{K}$ gives rise to an anomaly in the resistivity data. This anomaly is absent for the SL with insulating LMO where the resistivity is governed by the YBCO layers. The development of the 2nd order Bragg peak in the PNR curves at $T < T^{\text{Curie}}$ signifies the suppression of the FM moment in the interfacial region of the manganite layers, the more intense this peak the stronger the suppression. This effect is strongest for the strongly conducting LCMO, intermediate for the weakly conducting LMO and almost absent for the insulating LMO. The XMCD data show a similar trend, the Cu-edge dichroism is largest for LCMO, intermediate for weakly conducting LMO and almost absent for insulating LMO.

References

- [1] D.K. Satapathy et al., Phys. Rev. Lett. 108, 197201 (2012).
- [2] J. Töpfer and J. B. Goodenough, J. Solid State Chem. 130, 117 (1997).
- [3] V. K. Malik et al., Phys. Rev. B 85, 054514 (2012).

Charge carrier localization in $(\text{DOEO})_4[\text{HgBr}]_4 \cdot \text{TCE}$ and Peierls transition in TTF-TCNQ single crystals by temperature-dependent NEXAFS

A. Chernenkaya^{1),2)}, K. Medjanik²⁾, A. Kotov³⁾, P. Nagel⁴⁾, M. Merz⁴⁾, S. Schuppler⁴⁾, E. Yagubskii³⁾, Enric Canadell⁵⁾, Jean-Paul Pouget⁶⁾, G. Schönhense²⁾

¹⁾ Graduate School Materials Science in Mainz, Staudingerweg 9, 55128, Mainz, Germany;

²⁾ Institut für Physik, Johannes Gutenberg-Universität, Staudinger Weg 7, 55128, Mainz;

³⁾ Institute of Problems of Chemical Physics, Russian Academy of Science, 142432 Chernogolovka, Russia;

⁴⁾ Karlsruhe Institute of Technology, Institut für Festkörperphysik, Hermann-v.-Helmholtz-Platz 1, 76344 Eggenstein-Leopoldshafen, Germany;

⁵⁾ Institut de Ciència de Materials de Barcelona (ICMAB-CSIC), Campus de la UAB, 08193 Bellaterra, Spain;

⁶⁾ Laboratoire de Physique des Solides, Université Paris-Sud, CNRS UMR 8502, 91405 Orsay, France.

Introduction

Low-dimensional organic conductors are very interesting objects for investigation by near-edge absorption fine structure (NEXAFS) spectroscopy. It provides a direct access for the electronic structure of unoccupied states and the radiation damage of organic crystals is tolerable. The information about the electron density in specific states additionally to resistivity or magnetic properties provides important information about phase transitions and charge carriers localization. The aim of the present work was to gain information of the unoccupied electronic states using NEXAFS in order to discuss the origin of phase transitions in organic charge transfer single crystals $(\text{DOEO})_4[\text{HgBr}]_4 \cdot \text{TCE}$ and TTF-TCNQ. These experiments were done at the WERA beamline at ANKA using the liquid He-cooling facility.

Charge carrier localization in $(\text{DOEO})_4[\text{HgBr}]_4 \cdot \text{TCE}$ single crystals

The new asymmetrical molecule DOEO (1,4-(dioxandiil-2,3-dithio) ethylenedithiotetrathia-fulvalene) and its cation-radical salt $(\text{DOEO})_4[\text{HgBr}]_4 \cdot \text{TCE}$ (where TCE is 1,1,2-trichloroethane) were recently synthesized in the Institute of Problems of Chemical Physics in Chernogolovka, Russia^[1]. The transport properties^[1], electron spin resonance study^[2] and magnetic measurements suggest the existence of phase transitions at $T=70$ and 120 K. The sulfur L-edge NEXAFS and the temperature dependence of the relative peak intensity of the first line of it (Fig. 1) show the electron density redistribution with further localization below 60 K. Taking into account the antiferromagnetic ordering below 40 K that is visible from the temperature dependence of magnetic susceptibility, we can observe this rearrangement.

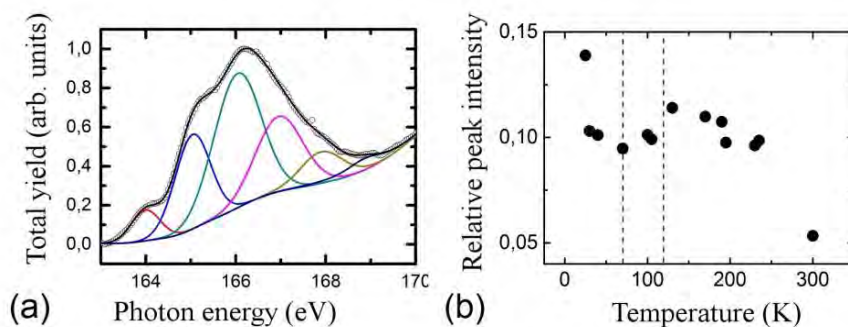


Fig. 1: Sulfur L-edge NEXAFS spectra of the $(\text{DOEO})_4[\text{HgBr}]_4 \cdot \text{TCE}$ crystal at $T = 300$ K. Circles denote the experimental data, thin curves mark the partial spectra obtained by a multipeak deconvolution of the experimental spectra. (b) Temperature dependence of the NEXAFS resonance peak intensities in the sulfur L-edge spectra of $(\text{DOEO})_4[\text{HgBr}]_4 \cdot \text{TCE}$. Peak intensities are taken from the fits in Fig. 1 (a) and are normalized to the area of peak 1 at each temperature.

Peierls transition in TTF-TCNQ single crystals

The TTF-TCNQ is a well-known one-dimensional charge transfer salt with a rich phase diagram consisting in the establishment of successive $2k_F$ Peierls transitions at critical temperatures of 54, 49 and 38 K. In several previous NEXAFS studies^[3,4] it was found that the theoretically-expected $\sigma^*(\pi(a_g, b_{3u}))$ -transition was absent. In the present work, we performed a temperature-dependent investigation. The spectra consist of all theoretically predicted peaks, including the “missing” transition, and show a clear temperature dependence.

When cooling TTF-TCNQ from 100 K down to 80 K (see fig. 2) there are significant changes in intensities of all three orbitals of the cyano groups: $\sigma^*(\pi(a_g, b_{3u}))$, $\pi^*(\pi(b_{3g}, a_u))$ and $\sigma^*(\pi(b_{1g}, b_{2u}))$. This is a clear signature

of changes in the electronic structure that could be caused by local and fluctuating pre-transitional structural distortions on the TCNQ stacks, which, in particular, involve an out-of-plane intramolecular deformation of TCNQ. Upon further cooling of the crystals below 60 K one observes an increase of the $\pi^*(\pi(b_{3g}, a_u))$ intensity value of the cyano groups. This is a fingerprint of the onset of the upper Peierls transition which develops a true Peierls gap on the TCNQ stacks. At this transition the electronic and structural CDW modulations of the TCNQ stack are frozen and different unoccupied states should appear above the Peierls gap. Such a redistribution of the unoccupied electronic states could be caused by the substantial displacement of the quinoid ring with respect to the cyano groups in a direction perpendicular to the TCNQ plane, which leads to a “boat-like” deformation of the acceptors.

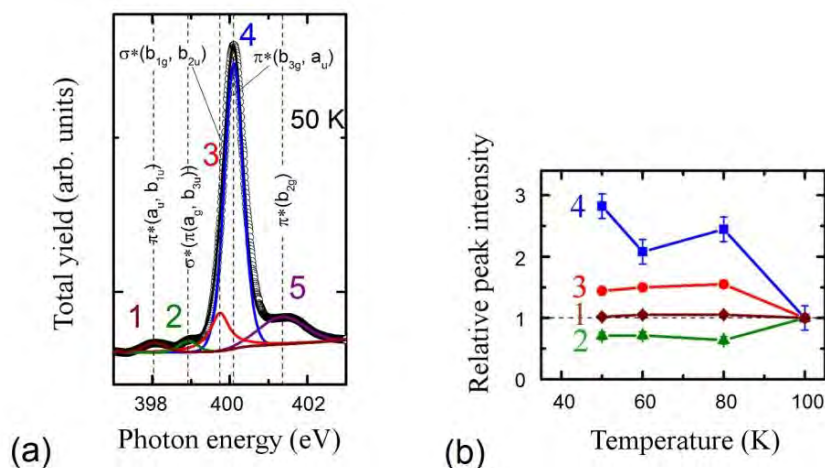


Fig. 2: (a) Nitrogen K-edge NEXAFS spectra of the TTF-TCNQ crystal at $T = 50$ K. Circles denote the experimental data, thin curves mark the partial spectra obtained by a multiplex deconvolution of the experimental spectra. Vertical lines give the signal positions according to the DFT calculation. (b) Temperature dependence of the NEXAFS resonance peak intensities in the nitrogen K-edge spectra of TTF-TCNQ. Peak intensities are taken from the fits in Fig. 2 (a) and are normalized to the area of peak 5 at 100 K.

Summary

In the present work we have experimentally determined the electronic structure of unoccupied states of two types of single crystals - $(\text{DOEO})_4[\text{HgBr}_4]\cdot\text{TCE}$ and TTF-TCNQ. In $(\text{DOEO})_4[\text{HgBr}_4]\cdot\text{TCE}$ we have found fingerprints of charge carriers redistribution with further localization at $T < 60$ K. Based on temperature dependences of magnetic susceptibility, transport properties^[1], electron spin resonance study^[2] and electron density distribution we propose a mechanism of localization with appearance of antiferromagnetic islands in $(\text{DOEO})_4[\text{HgBr}_4]\cdot\text{TCE}$.

In TTF-TCNQ we have performed temperature-dependent NEXAFS investigation. Our study shows an evidence of a Peierls transition on the TCNQ stacks. Furthermore, the data provides the first experimental evidence of a modification of intra-molecular orbitals due to a CDW (charge density wave) instability in a molecular conductor. In addition, we clearly resolve the experimental data, consisting of all theoretically predicted peaks, including the “missing” transition $\sigma^*(\pi(a_g, b_{3u}))$ in the cyano groups of TCNQ, and therefore we discussed the real electronic structure and its evolution with variable temperature.

Acknowledgements

The project is funded through Transregio SFB TR 49 (Frankfurt, Mainz, Kaiserslautern) and Graduate School of Excellence MAINZ. Work in Bellaterra was supported by MINECO (Grants FIS2012-37549-C05-05 and CSD2007-00041) and Generalitat de Catalunya (2014SGR301).

References

- [1] A. Bardin et. al., *Coord. Chem.*, **2006**, 32, 88 ; [2] A. Chernenkaya, et. al., *Phys. Sol. St.*, **2012**, 54, 2391.
 [3] J. Fraxedas, et. al., *Phys. Rev. B* **2003**, 68, 195115; [4] M. Sing, et. al., *Phys. Rev. B* **2007**, 76, 245119.

Intra-Molecular Charge Transfer in Cu:Tetraazaporphyrin investigated by X-ray Magnetic Circular Dichroism

J. Klanke¹⁾, S. Diehl²⁾, T. Methfessel²⁾, D. Bayer²⁾, S. Schuppler³⁾, P. Nagel³⁾, M. Merz³⁾, E. Rentschler¹⁾, and H.J. Elmers²⁾

¹⁾ Institut für Anorganische und Analytische Chemie, Universität Mainz, D-55099 Mainz, Germany

²⁾ Institut für Physik, Universität Mainz, D-55099 Mainz, Germany

³⁾ Forschungszentrum Karlsruhe GmbH, Institute for Synchrotron Radiation, Hermann-von-Helmholtz-Platz 1, D-76344 Eggenstein-Leopoldshafen, Germany

Phthalocyanines (Pc) have emerged as a promising molecular component for artificial photosynthetic systems, since they exhibit large absorption in the visible region, contain large, conjugated π -systems suitable for efficient electron-transfer processes, and possess strongly reducing or oxidizing characteristics determined by the nature of the central metals and the peripheral substituents. The magnetic properties of phthalocyanine-based conjugates have recently attracted large scientific interest [1], revealing large orbital anisotropies and an anisotropic spin dipole moment up to twice the isotropic spin in a metal-organic layer. The main characteristics of phthalocyanines are their unique electronic, optical and redox properties associated with the planarity of the π -conjugated ring that imparts interesting physical and chemical properties, including the facility of stacking and yielding molecular films on solid surfaces or in the bulk. While tetrapyrridyl porphyrins have been modified with transition metal complexes in order to generate convenient building-blocks and connectors for assembling supramolecular systems and nanostructured materials, much less work has been done for the phthalocyanine system.

The stoichiometric template reaction of pyrizino[2,3-f][1,10]phenanthroline-2,3-dicarbonitril (Dicnq), bis(4-tert-butylphenyl)-fumarodinitril (Dinit) and X(II)-acetat (X=Cu or Zn) provides a coordination site for a Ru(II)-ion at the tetraazaporphyrin molecule forming the macrocycles X3Dinit1Dicnq. Addition of Ru(III)-chloride to X3Dinit1Dicnq thus binds a Ru(II)-ion at the macrocycle, forming X3Dinit1Dicnq-1Ru. In order to study the influence of four coordinated Ru(II)-ions we synthesized Cu(II)phenanthralocyanin (Cu4Dicnq) from four Dicnq ligands and Cu(II)-acetat. Because of the limited solubility of Cu4Dicnq and thus hindrance to coordinate Ru ions we used [Ru(bipy)₂Dicnq](PF₆)₂ as a precursor for synthesizing the macrocycle in a template reaction with Cu(II)-ions. This synthesis route thus enables the investigation of Cu4Dicnq-4Ru. Using X-ray absorption spectroscopy at the Cu L-edge and Ru M-edges we investigated the electron-transfer process within the ruthenated metallo(II)-phthalocyanine complexes.

X-ray absorption spectra were measured at the WERA beamline at the synchrotron ANKA using the XMCD end station. All spectra were measured at 20 K.

Fig. 1(a,b) shows the X-ray absorption spectra measured at the Ru M-edges for Cu3Dinit1Dicnq-1Ru and Zn3Dinit1Dicnq-1Ru. The central peak is tentatively attributed to the 3p-5s transition although it appears rather large. A shift of 0.5(1) eV of the M₃ peak to larger photon energy is observed if the Zn(II)-ion is replaced by the Cu(II)-ion. This indicates that in the latter case a fractional charge is shifted from the Ru(II)-ion to the Cu(II)-ion, thus partly filling the empty Cu states. Further evidence for this charge transfer is gained from the comparison of Cu L-edge absorption spectra for Cu3Dinit1Dicnq-1Ru and Cu3Dinit1Dicnq shown in Fig. 1(d,e). Here, we observe a shift of 0.6(1) eV of the Cu L₃ edge to lower photon energies if the Ru ion is added, again indicating increased charge localized at the Cu ion. The observed shifts correspond to a sizable charge transfer of 0.4 e from Ru and 0.2 e to Cu according to calculations using CTM4XAS.

In contrast to Cu₃Dinit1Dicnq, Cu₄Dicnq reveals a shift of 0.1(1) eV of the Cu L₃ edge to larger photon energies if the Ru ion is added. Here, charge transfer does not occur. The result is attributed to the 2,2' bipyridin ligand coordinated to the Ru(II) ion in the case of Cu₄Dicnq-4Ru that has a strong electron attraction effect and thus outmatches the 4d-3d electron transfer observed for Cu₃Dinit1Dicnq-1Ru where chloride is coordinated to Ru.

The XMCD results at the Ru M edges reveal zero magnetic moment. The comparatively large error is of the order of 0.1 μ_B per Ru ion because of the small Ru signal. The Cu moment can be measured more precisely and comprises values of the order of 0.1 μ_B per Cu ion. At a temperature of 20 K the measured moments increase linearly with the applied field at least up to 4 T. The magnetic moments measured by XMCD correspond to a saturation value of roughly 1 μ_B per Cu ion. This is compatible with SQUID susceptibility measurements revealing a local moment of 1 μ_B per molecule for Cu₃Dinit1Dicnq and 2 μ_B per molecule for Cu₃Dinit1Dicnq-1Ru, indicating a finite Ru moment of 1 μ_B which was not be detectable by our XMCD measurements. Similar magnetic Cu moments were also measured for Cu₄Dicnq and Cu₄Dicnq-4Ru.

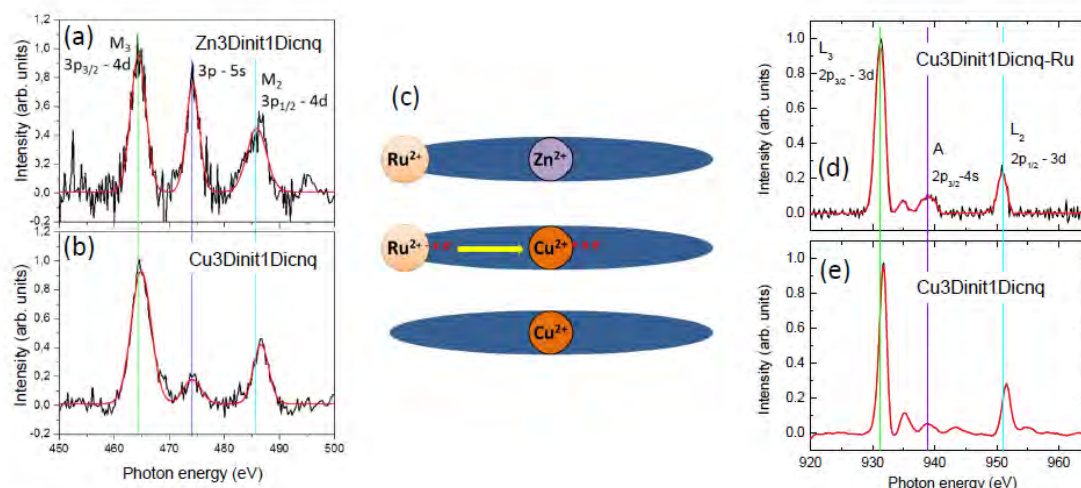


Fig. 1: X-ray absorption spectra measured at the Ru M-edges for Zn₃Dinit1Dicnq-1Ru (a) and Cu₃Dinit1Dicnq-1Ru (b). (c) Sketch of the intra-molecular charge transfer. X-ray absorption spectra measured at the Cu L-edges for Cu₃Dinit1Dicnq-1Ru (d) and Cu₃Dinit1Dicnq (e).

Table 1: Summary of magnetic moments determined by XMCD and SQUID.

	$\mu_0 H$ (T)	$\mu_{\text{spin}} (\mu_B)$	$\mu_{\text{orb}} (\mu_B)$	$\mu_{\text{sum}} (\mu_B)$	$\mu_{\text{sum}} (\mu_B) / \mu_0 H (\mu_B/T)$	$\chi_{\text{SQUID}} T (\text{cm}^3 \text{K mol}^{-1})$
Cu ₃ Dinit1Dicnq	4.5	0.11(2)	0.01(2)	0.12(2)	0.027(5)	0.40(1)
Cu ₃ Dinit1Dicnq-1Ru	4.5	0.10(5)	0.00(5)	0.10(5)	0.022(10)	0.69(1)
Cu ₄ Dicnq	7	0.15(2)	0.01(2)	0.16(2)	0.023(3)	0.52(1)
Cu ₄ Dicnq-4Ru	7	0.12(1)	0.02(1)	0.14(1)	0.020(2)	0.90(1)
Cu ₄ Dinit	4.5	0.14(1)	0.01(1)	0.15(1)	0.033(2)	0.37(2)

Acknowledgements

Financial support from the graduate school of excellence MAINZ is gratefully acknowledged.

- [1] J. Klanke, E. Rentschler, K. Medjanik, D. Kutnyakhov, G. Schönhense, S. Krasnikov, I. V. Shvets, S. Schuppler, P. Nagel, M. Merz, and H. J. Elmers, Phys. Rev. Lett. **110**, 137202 (2013).

Structure of fresh and aged Fe(III)-precipitates

A. Voegelin¹, A-C. Senn¹, S. Mangold², S. J. Hug¹, R. Kaegi¹

¹ Eawag, Swiss Federal Institute of Aquatic Science and Technology, Überlandstrasse 133, CH-8600 Dübendorf, Switzerland

² Forschungszentrum Karlsruhe GmbH, Institute for Synchrotron Radiation, D-76344 Eggenstein-Leopoldshafen, Germany

Introduction

The oxidation of dissolved Fe(II) at oxic/anoxic boundaries leads to nanoparticulate Fe(III)-precipitates that profoundly impact the cycling of Fe and other major and trace elements in natural and engineered aquatic systems. In earlier work, we showed that dissolved phosphate (P) and silicate (Si) interfere with Fe(III)-polymerization and thereby determine the structure and composition of fresh Fe(III)-precipitates [1,2]. More recently, we showed that Fe(III) precipitation in the presence of P is highly dynamic, and that amorphous Fe(III)-phosphate formed until complete P removal from solution may undergo rapid transformation due to continuing Fe(III) polymerization and concomitant P release back into solution [3]. In on-going work, we explore the interdependent effects of dissolved P, Si and Ca on (i) the structure and composition of fresh and aged Fe(III)-precipitates, (ii) concomitant variations in precipitate reactivity, and (iii) implications for co-transformed As. To characterize Fe(III)-precipitates from laboratory experiments, we use X-ray absorption spectroscopy (XAS) and other techniques (TEM, XRD, FTIR). In our last experiment at ANKA, we analysed the structure of fresh Fe(III)-precipitates formed at initial dissolved P/Fe ratios of 0-2 in the absence or presence of Ca and/or Si and of analogous precipitates aged for 30 days at 40°C using Fe K-edge XAS.

Materials and Methods

Experiments were performed in 8 mM NaHCO₃ or 4 mM CaCO₃ background electrolyte adjusted to pH 7.0 using CO₂ gas. After adding 0.25 mM Si (Na₂SiO₃), 6.7 μM As(V) and P (NaH₂PO₄×H₂O) as required, 0.5 mM Fe(II) (FeSO₄×7H₂O) were spiked to the aerated solutions to initiate Fe(II) oxidation. From each treatment, one duplicate was sampled after 4 h (fresh) and the other after aging for 30 days at 40°C (aged). Unfiltered and filtered (0.2-μm) solutions were collected for analysis by ICP-MS. The Fe(III)-precipitates retained on filter membranes were air-dried and prepared as pellets for Fe K-edge XAS. The experimental spectra were analysed by linear combination fitting (LCF) using reference spectra (Fig. 1B, from ref. [1]) of amorphous to poorly crystalline Fe(III) precipitates with increasing degree of Fe(III) polymerization (Fe-P = amorphous Fe(III)-phosphate; HFO = hydrous ferric oxide; 2L-Fh = 2-line ferrihydrite) and of crystalline Fe(III)-oxyhydroxides (Goe = goethite; Lp = lepidocrocite).

Results and Discussion

For selected treatments, molar precipitate P/Fe ratios as a function of initial dissolved P/Fe ratios are shown in Fig. 1A, and LCF results for selected precipitates from these treatments are given in Fig. 1C. In general, trends in precipitate P/Fe ratio nicely correlated with spectroscopic results. Differences in precipitate P/Fe ratio between fresh precipitates formed in Na- and Ca-bicarbonate solutions indicated enhanced co-precipitation of P in the presence of Ca. The LCF results (Fig. 1C) indicated dominant formation of lepidocrocite in the absence of P, and nearly exclusive formation of Fe(III)-phosphate under conditions of incomplete P removal from solution (i.e., above ~0.5 and ~0.8 in Na- and Ca-bicarbonate electrolyte). Thus, in the presence of Ca, direct bonding between Ca and P likely enhanced P co-precipitation and resulted in higher degree of Fe polymerization by decreasing the P interference. At initial dissolved P/Fe ratios less than ~1.0, precipitates aged in NaHCO₃ electrolyte exhibited much lower P/Fe ratios than the respective fresh precipitates (Fig. 1A) reflecting the re-solubilisation of a major fraction of total P. Accordingly, the respective LCF indicated a substantial increase in Fe(III)-polymerization with aging. In the Ca-bicarbonate system, these aging effects were much less pronounced (not shown in Fig. 1). This suggested that Ca became co-precipitated into mixed Ca-Fe(III)-phosphates and thereby substantially slowed down further Fe(III)-polymerization and P release back into solution. In treatments including Si (results not shown), Si did not reduce P uptake into fresh precipitates but prevented the formation of crystalline Fe(III)-precipitates at low P/Fe and slowed precipitate polymerization and P release during aging.

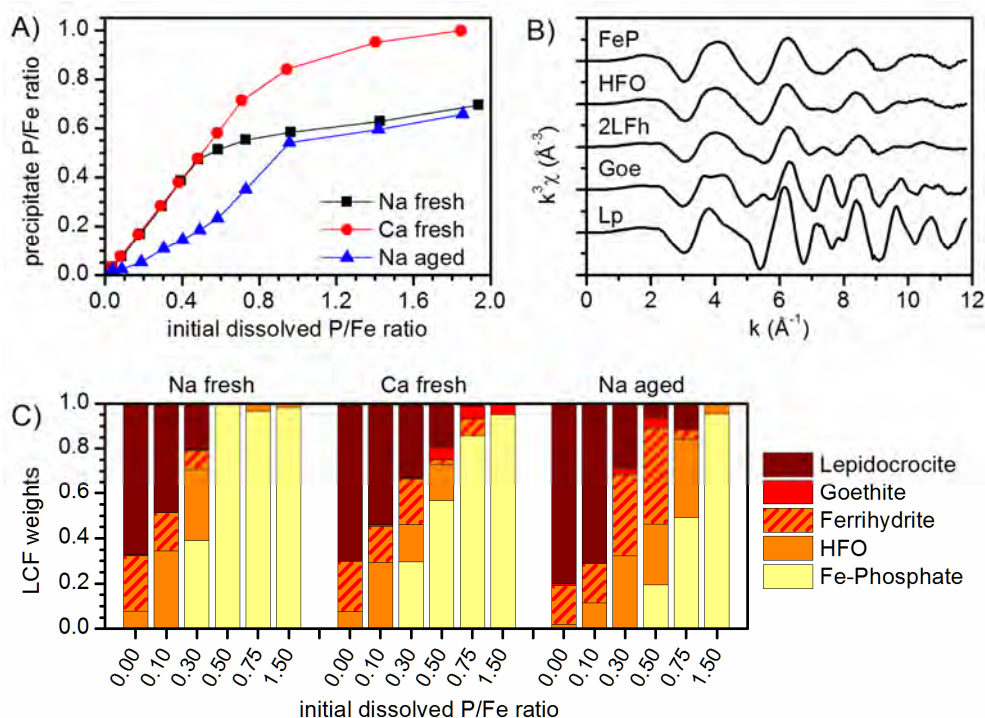


Figure 1. (A) Molar precipitate P/Fe ratio as a function of initial dissolved P/Fe ratio for fresh (4 h) precipitates formed in Na- and Ca-bicarbonate electrolyte (“Na fresh” and “Ca fresh”) and aged in Na-bicarbonate electrolyte (“Na aged”). (B) Fe K-edge EXAFS reference spectra used for LCF analysis. (C) LCF results for selected precipitates.

Conclusions and Outlook

This study provides detailed insight into the interdependent effects of Ca, P and Si on Fe(III) polymerization and precipitate structure after Fe(II) oxidation and subsequent aging. Information on the molecular-level structure of the amorphous to poorly crystalline precipitates obtained by XAS is key to rationalize variations in precipitate composition and solubility. The morphological characterization of the same set of precipitates by TEM is currently underway and will allow to further expand our system understanding.

The precipitates studied here were formed in the presence of trace amounts of As(V) (As/Fe=0.013). Preliminary data suggest that the mode and extent of As incorporation systematically varies with precipitate structure, i.e., with P/Fe ratio and absence/presence of Ca during synthesis. In addition, our current results reveal small but systematic variations in local Fe coordination in Fe(III)-phosphates that point towards formation of short-range-ordered Ca-Fe(III)-phosphate in the presence of Ca and amorphous Fe(III)-phosphate in the absence of Ca. In continuing work, we aim to combine XAS at the K-edges of As, Ca, and Fe to constrain the mode of As(V) uptake in different fresh and aged precipitates (in relation to the extent of As removal/solubility) and to better characterize the structural order of mixed Ca-Fe(III)-phosphate clusters. Ultimately, these studies will significantly advance the mechanistic understanding of Fe oxidation products and their impact on nutrient and contaminant dynamics in natural and engineered environmental systems.

Acknowledgements

We thank Thomas Rüttimann for help in the laboratory and Stefan Mangold for support at the XAS beamline at ANKA. ANKA is acknowledged for the provision of synchrotron beamtime.

References

- [1] Voegelin, A.; Kaegi, R.; Frommer, J.; Vantelon, D.; Hug, S. J. (2010) Effect of phosphate, silicate, and Ca on Fe(III)-precipitates formed in aerated Fe(II)- and As(III)-containing water studied by X-ray absorption spectroscopy. *Geochim. Cosmochim. Acta* 74, 164-186.
- [2] Kaegi, R.; Voegelin, A.; Folini, D.; Hug, S. J. (2010) Effect of phosphate, silicate, and Ca on the morphology, structure and elemental composition of Fe(III)-precipitates formed in aerated Fe(II) and As(III) containing water. *Geochim. Cosmochim. Acta* 74, 5798-5816.
- [3] Voegelin, A.; Senn, A.-C.; Kaegi, R.; Hug, S. J.; Mangold, S. (2013) Dynamic Fe-precipitate formation induced by Fe(II) oxidation in aerated phosphate-containing water. *Geochim. Cosmochim. Acta* 117, 216-231.

Report for the beamtime ENV-226 (SUL-X beamline)

Arsenic speciation in synthetic and natural Fe oxide matrices

Juraj Majzlan and Ralph M. Bolanz

Friedrich-Schiller-University Jena, Institute of Geosciences, 07745 Jena, Germany

Hematite ($\alpha\text{-Fe}_2\text{O}_3$) is one of the most common iron oxides and a sink for the toxic metalloid arsenic. Arsenic can be immobilized by adsorption to the surface of hematite or other iron oxides. The possibility of incorporation into the structure, on the other hand, was never really seriously entertained. In our study we present evidence that, besides adsorption, the incorporation of As into the hematite crystals can be of great relevance for As immobilization.

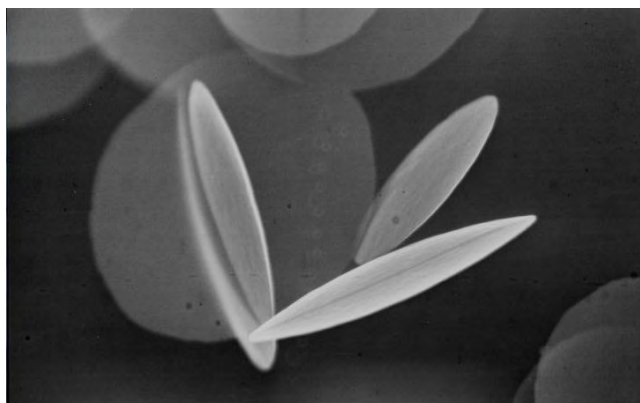


Fig. 1. Disc-like particles of As-doped hematite synthesized at 200 °C. Particle size ~ 1 μm .

Arsenic-doped hematite (Fig. 1) was synthesized by transformation of As-doped ferrihydrite at 70 or 200 °C. X-ray absorption spectra were collected for a series of As-hematite samples as well as a suite of reference compounds angelellite ($\text{Fe}_4\text{O}_3(\text{AsO}_4)_2$), scorodite ($\text{FeAsO}_4 \cdot 2\text{H}_2\text{O}$), kaňkite ($\text{FeAsO}_4 \cdot 3.5\text{H}_2\text{O}$), parasymplectite ($\text{Fe}_3(\text{AsO}_4) \cdot 8\text{H}_2\text{O}$), bukovskýite ($\text{Fe}_2(\text{SO}_4)(\text{AsO}_4) \cdot 9\text{H}_2\text{O}$), and adamite ($\text{Zn}_2(\text{OH})\text{AsO}_4$). Angelellite, a triclinic iron arsenate with structural relations to hematite, can epitaxially intergrow along the (210) plane with the (0001) plane of hematite.

Investigation of electron-transparent slices in a transmission electron microscope showed that arsenic is homogeneously distributed inside the hematite crystals, with a maximum concentration of 1.9 wt% As in one of the samples. Using selected-area electron diffraction, we identified these particles as hematite, hence, it is not an As-rich impurity within the hematite sample.

The EXAFS spectra of the samples and reference materials (Fig. 2) show a general similarity of the ferric and zinc arsenates in the first and second shell, mostly because the As-O and As-Fe(Zn) distances scatter in these compounds within a relatively narrow range. The EXAFS spectra of the As-hematite were fitted with a number of models of which angelellite was found to perform the best, although a better fit was desired.

To address this problem, we have constructed a model of angelellite-like cluster in the structure of hematite (Fig. 3), making use of the fact that the structures can be epitaxially intergrown. This model performs even better than the pure angelellite model. The immediate local environment of As^{5+} is found to be angelellite-like but the further surrounding ($> 3.5 \text{ \AA}$) can be fit better with hematite structure. These results suggest that As can be incorporated into hematite in the form of angelellite-like clusters.

Arsenic incorporation by a simple insertion of As into a tetrahedral interstitial site in hematite was previously proposed by Violante et al. (2007), based on a work on the phosphate incorporation in hematite by Galvez et al. (1999). The geometric similarity of the arsenate and phosphate tetrahedra led to the assumption that they would behave similarly. Such simple incorporation mechanism is problematic because it requires that a number of iron

cations will be removed and the remaining positive charge cannot be easily compensated, for example by hydrogen atoms. There are simply not enough oxygen atoms which could be protonated to charge-balance this substitution.

The mechanism proposed in this study explains the possibility of As incorporation into the hematite structure better and is in a very good agreement with the experimental data, supported especially by the EXAFS measurements.

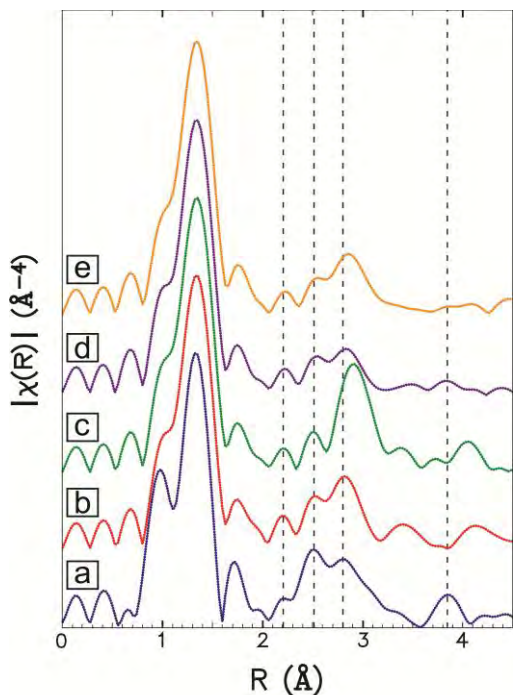


Fig. 2. FT EXAFS spectra of a) As-hematite, b) angelellite, c) scorodite, d) kaňkite, e) parasymplectite.

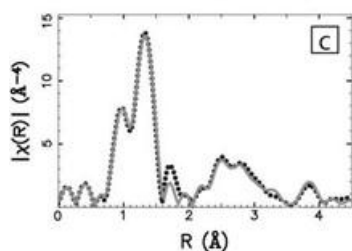


Fig. 4. Fit (grey) to the EXAFS data (black) using the angelellite-like cluster in the hematite structure (see Fig. 3).

The fit (Fig. 4) achieved with the angelellite-in-hematite model reproduces all features of the measured data and confirms the validity of this model. The results of our study show that hematite is capable of storing substantial amounts of arsenic over long (geological) periods of time.

Gálvez, N.; Barrón, V.; Torrent, J. Preparation and properties of hematite with structural phosphorus. *Clay. Clay. Miner.* **1999**, 47, 375-385.

Violante, A.; Gaudio, S.D.; Pigna, M.; Ricciardella, M.; Banerjee, D. Coprecipitation of arsenate with metal oxides. 2. Nature, mineralogy, and reactivity of iron(III) precipitates. *Environ. Sci. Technol.* **2007**, 41, 8275-8280.

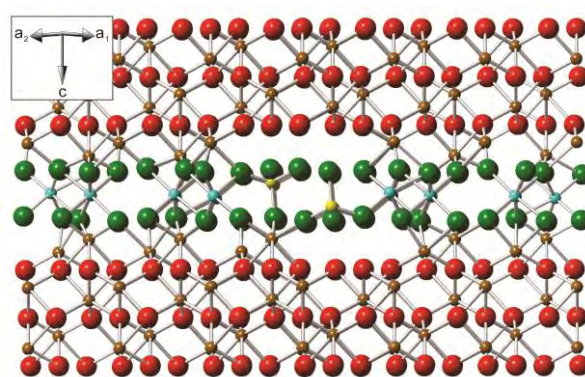


Fig. 3. A structural model used to fit the EXAFS data. The model represents an angelellite-like cluster within the structure of hematite. Red and green spheres represent oxygen from the structure of hematite and angelellite, respectively. The brown and blue spheres are iron atoms from the structure of hematite and angelellite, respectively. Yellow spheres are arsenic atoms.

Confocal XRF Imaging of elemental deposition of Mn, Ni and Cu on the graphite anode in cycled LiNi_{0.5}Mn_{1.5}O₄ /graphite full cells

U. Fittschen^{1,5)}, U. Bösenberg²⁾, M. Falk⁴⁾, M. Menzel¹⁾, B. Jache⁴⁾, J. Janek⁴⁾, R. Simon³⁾

¹⁾ University of Hamburg, Institute of Inorg. Applied. Chemistry, Martin-Luther King Plz. 6, 20146 Hamburg, Germany

²⁾ DESY Deutsches Elektronen Synchrotron; Notkestr. 85, D-22607 Hamburg, Germany

³⁾ Forschungszentrum Karlsruhe GmbH, Institute for Synchrotron Radiation, Hermann-von-Helmholtz-Platz 1, D-76344 Eggenstein-Leopoldshafen, Germany

⁴⁾ Chemistry Department University of Giessen; Giessen, Germany

⁵⁾ Washington State University, Pullman, WA, USA

Li-ion battery cell capacity fade caused by 3d metal leaching from the cathode and their subsequent deposition on the graphite anode is one key factor in cell degradation. Solvation of 3d metals for different cathode materials into the electrolyte has been studied including e.g. LiCoO₂, LiMn₂O₄, LiNi_{0.5}Mn_{1.5}O₄. According to Choi and Manthiram [1] about 0.7% Mn and 2% Ni (55°C) from LiNi_{0.5}Mn_{1.5}O₄ are solved in the electrolyte and increase during cycling (50cycles) at elevated temperatures (60°C) to several percent estimated from the weight loss of the electrode. Amine et al. [2] concluded from impedance measurements that cathode material is deposited on the Anode and Yang et. al [3] found Cu from the current collector and Mn from the cathode in SEM/EDX images of graphite anodes. Takahara [4] found Fe on the surface of graphite anodes cycled against LiFePO₄ cathodes using Glow Discharge Optical Emission Spectroscopy (Gd-OES) sputtering material starting from the surface „electrode/separator interface (E/S)“ and processing into the bulk material. These analyses indicate an accumulation of metal ions at the E/S interface. Accumulation has been studied as deep as a few μm in depth of the anode. Until now, to the best of our knowledge, nobody has studied the penetration of these metal ions into the pores of the graphite anode and their fate if the eventually deposit on the surface of the graphite particles. In this study deposition of 3d metal ions from LNMO/graphite full cells was studied using confocal μ-XRF.

We aim to show the full impact of deposition such as Mn and Ni species on the anode over the complete depth of the graphite cathode. A spatial resolution of 10x10x20μm³ was reached using 3D confocal micro-XRF imaging (CMXRF) at the ANKA Fluo beam line. The setup includes a polycapillary half lens on the detector side and compound refractive lenses to focus the primary beam. An energy dispersive SDD-detector (Vortex, SII NanoTechnology USA Inc., Northridge, CA, USA), having an energy resolution of 133 eV@MnK_α, was used to record fluorescence spectra at each voxel. The spatial resolution in depth was given by the polycapillary half lens and determined to be 19 μm for 9.7keV (AuL_α). The resolution is energy dependent and increases with energy. The resolution in X and Y direction was 10 μm and is given by the compound refractive lenses (CRLs). The excitation energy of beam was set to 17.4 keV using a double multilayer monochromator (W-Si multilayers in 2.7 nm period). Details of the beamline are described elsewhere [5]. An integration time of 3 s per voxel was used for the anodes and 1 s per voxel for the cathode. All data was normalized to a beam current of 100 mA. The K_α-lines were used for the determination of all elements investigated besides Ba, where the L_α-line was used. PyMCA was used for deconvolution of the spectra. To obtain a 3D image of the elemental distribution several 2D profiles in steps of 10 μm were recorded and compiled using the software package Avizo standard (FEI, Berlin, Germany).

XRF allows for a high information depth, in this case we could cover the complete depth of the graphite cathode (ca 200μm). The results, see figure 1, show that Mn and Ni from the cathode do not only deposit at the E/S interface penetrate to the same extend into the pores, we show that other metal ions like Cu deposit predominantly at the E/S interface indicating different reactivity and chemical processes. From complementary bulk determination of Ni and Mn concentrations from the cycled anode using micro-wave assisted digestion and TXRF we estimated concentration of Mn ca. 10pg/pixel (LOD ca. 0.150pg/pixel) and Ni ca. 4pg/pixel (LOD ca. 0.060 pg/Pixel).

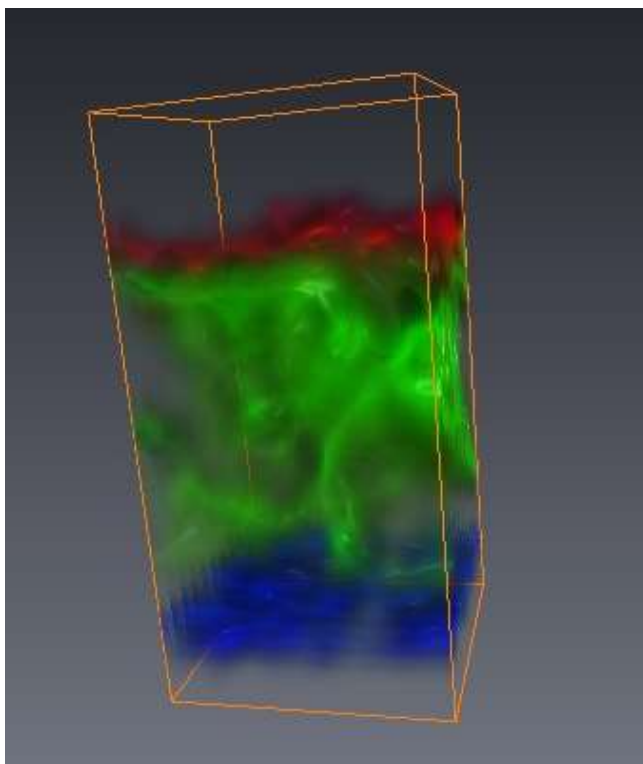


Fig. 1 Ni (gr), Ga (bl) Cu (r): 3D fluorescence images over an area of $100 \times 100 \times 200 \mu\text{m}^3$ with the current collector at the bottom, Ni in the bulk material and Cu on top at the E/S interface

Acknowledgements

We acknowledge the Synchrotron Light Source ANKA for provision of beamtime at the FLUO beamline.

References

- [1] Choi W, Manthiram A, Comparison of Metal Ion Dissolutions from Lithium Ion Battery Cathodes, *J. Electrochem. Soc.* (2006) 153(9):A1760-A1764.
- [2] Amine, K.; Lui J.; Kang, I.; Hyung, Y.; Vissers, D.; Henriksen, G.; Improved lithium manganese oxide spinel/graphite Li-ion cells for high-power applications, *J. Power Sources* (2004), 129:14-19.
- [3] L. Yang, M. Takahashi, B. Wang, A study on capacity fading of lithium-ion battery with manganese spinel positive electrode during cycling, *Electrochim. Acta* (2006), 51, 3228–3234
- [4] H. Takahara, H. Miyauchi, M. Tabuchi, T. Nakamura, Elemental Distribution Analysis of LiFePO₄/Graphite Cells Studied with Glow Discharge Optical Emission Spectroscopy (GD-OES), *J. Electrochem. Soc.*, (2013) 160 (2) A272-A278
- [5] Simon, R., Buth, G., & Hagelstein, M. *Nucl. Instrum. Methods Phys. Res. Sect. B* 2003; 199, 554.

Iron oxidation products: Structural changes induced by precipitate drying and in-situ time-resolved oxidation experiment

A. Voegelin¹, A-C. Senn¹, S. J. Hug¹, R. Kaegi¹, S. Mangold²

¹Eawag, Swiss Federal Institute of Aquatic Science and Technology, Überlandstrasse 133, CH-8600 Dübendorf, Switzerland

²Forschungszentrum Karlsruhe GmbH, Institute for Synchrotron Radiation, D-76344 Eggenstein-Leopoldshafen, Germany

Introduction

The oxidation of dissolved Fe(II) at oxic/anoxic boundaries leads to nanoparticulate Fe(III)-precipitates that profoundly impact the cycling of Fe and other major and trace elements in natural and engineered aquatic and terrestrial systems. In earlier work, we showed that dissolved phosphate (P) and silicate (Si) interfere with Fe(III)-polymerization and thereby determine the structure and composition of fresh Fe(III)-precipitates [1, 2]. More recently, we showed that Fe(III) precipitation in the presence of P is highly dynamic, and that amorphous Fe(III)-phosphate forming exclusively until complete P removal from solution may subsequently undergo rapid transformation due to continuing Fe(III) polymerization [3]. In natural as well as technical systems, freshly formed Fe(III)-precipitates may periodically dry out. Drying may alter precipitate structure and reactivity, leading for example to reduced ion sorption capacity or reduced dissolution and transformation rates [4, 5]. In continuing experiments, we therefore evaluated different types of fresh Fe precipitates with respect to structural changes induced by precipitate drying. Furthermore, we performed an in-situ time-resolved experiment to monitor Fe precipitate formation during Fe(II) oxidation an initial molar dissolved phosphate/Fe(II) ratio of 0.3 to obtain direct XAS-based evidence for initial Fe(III)-phosphate formation.

Materials and Methods

Different Fe(III)-precipitates were synthesized in 8 mM NaHCO₃ or 4 mM CaCO₃ electrolyte adjusted to pH 7.0 using CO₂ gas. After addition of Si (Na₂SiO₃) or P (NaH₂PO₄×H₂O) as required (no Si and P; Si/Fe 2, Si/Fe 0.5, P/Fe 0.65, P/Fe 0.3, P/Fe 0.15), 0.5 mM Fe(II) (FeSO₄×7H₂O) were spiked to the aerated solutions to initiate Fe(II) oxidation. The precipitates were stored for 10 days in their synthesis solution prior to XAS analysis. After filtration, the wet precipitates were mixed with water and cellulose and measured as pastes in transmission mode at room temperature. The remaining precipitate was dried overnight under N₂-gas, mixed with cellulose and pressed into 13-mm pellets for XAS analysis.

An in-situ experiment was performed in 1 L of 8 mM NaHCO₃ adjusted to pH 6.3 using CO₂ gas. Phosphate was adjusted to 0.3 mM. Using a piezo pump, this solution/suspension was continuously pumped through the wet-cell available at the XAS beamline, which is equipped with Kapton windows. Immediately after adding 1 mM Fe(II) to the aerated solution, continuous Fe K-edge EXAFS data acquisition was started (3 min per scan from 7.0 to 7.5 keV, i.e., up to ~10 Å⁻¹ in k-space).

Results and Discussion

The Fe K-edge EXAFS spectra of different precipitates formed in NaHCO₃ background electrolyte before and after drying are shown in Figure 1A. As expected from own previous work [1-3], the precipitate formed in the absence of P and Si was dominantly lepidocrocite, the precipitates formed at Si/Fe of 0.5 and 2 ferrihydrite-like hydrous ferric oxides, the precipitate at P/Fe 0.65 an amorphous Fe(III)-phosphate and at P/Fe of 0.3 a mixture of Fe(III)-phosphate and lepidocrocite/ferrihydrite. Visually, the spectra of the dried samples (red lines) closely resembled the corresponding wet samples (black lines), suggesting that structural changes were not drastic during drying. However, small differences were observed that we interpreted on the basis of linear combination fitting using reference spectra for lepidocrocite and amorphous to poorly-crystalline Fe(III)-precipitates exhibiting varying degrees of octahedral Fe(III) linkage and polymerization. These results indicated two systematic trends: (i) Drying led to a decrease of the lepidocrocite fraction (where present) in favour of an increased ferrihydrite-like fraction. We interpreted this trend as indicative for an increase in the structural disorder at the surface of nanoparticulate lepidocrocite during drying. (ii) Drying increased the extent of corner-sharing Fe-Fe linkage of the hydrous ferric oxide-ferrihydrite precipitate fraction. These changes may affect the reactivity of the Fe precipitates and also need to be considered when studying dry precipitates to infer their formation during Fe(II) oxidation in aqueous solution.

The EXAFS spectra from the time-resolved in-situ experiment are shown in Figure 1B. For analysis by linear combination fitting, always 5 spectra covering 15 min reaction time were averaged. The results showed that exclusively amorphous Fe-phosphate (initially containing also a minor fraction of Fe(II)) formed until dissolved phosphate became depleted (~75 min), in line with our conclusion from earlier studies [1-3]. After that time, continuing Fe(II) oxidation led to lepidocrocite formation. During the experiment, however, increasing amounts of precipitate accumulated on the Kapton® windows of the flow-through cell. Although this resulted in spectra with higher signal-to-noise ratio dominated by the solid-phase rather than dissolved Fe(II), this accumulation also induced some uncertainty because the accumulated precipitate may not exactly represent the precipitate in the suspension.

Conclusions and Outlook

The analysis of wet and dried Fe(III)-precipitates revealed structural changes that may strongly affect their chemical reactivity, an aspect that we plan to investigate in future work. In addition, the results suggest that structural changes induced by sample drying need to be considered when using structural information gained on dry precipitates to elucidate precipitate formation in aqueous solution. Time-resolved experiments provide a means to get direct insight into precipitate formation during Fe(II) oxidation in solution without need for sample separation and preparation. For future work on Fe precipitate formation, transformation and its impact on trace elements, however, the in-situ setup needs to be optimized to ensure that the bulk precipitate is representatively probed.

Acknowledgements

We thank Thomas Rüttimann and Irene Brunner for help in the laboratory. ANKA is acknowledged for the provision of synchrotron beamtime.

References

- Voegelin, A.; Kaegi, R.; Frommer, J.; Vantelon, D.; Hug, S. J., *Effect of phosphate, silicate, and Ca on Fe(III)-precipitates formed in aerated Fe(II)- and As(III)-containing water studied by X-ray absorption spectroscopy*. *Geochim. Cosmochim. Acta* 2010, 74, 164-186.
- Kaegi, R.; Voegelin, A.; Folini, D.; Hug, S. J., *Effect of phosphate, silicate, and Ca on the morphology, structure and elemental composition of Fe(III)-precipitates formed in aerated Fe(II) and As(III) containing water*. *Geochim. Cosmochim. Acta* 2010, 74, 5798-5816.
- Voegelin, A.; Senn, A.-C.; Kaegi, R.; Hug, S. J.; Mangold, S., *Dynamic Fe-precipitate formation induced by Fe(II) oxidation in aerated phosphate-containing water*. *Geochim. Cosmochim. Acta* 2013, 117, 216-231.
- Jones, A. M.; Collins, R. N.; Rose, J.; Waite, T. D., *The effect of silica and natural organic matter on the Fe(II)-catalysed transformation and reactivity of Fe(III) minerals*. *Geochim. Cosmochim. Acta* 2009, 73, 4409-4422.
- Raiswell, R.; Vu, H. P.; Brinza, L.; Benning, L. G., *The determination of labile Fe in ferrihydrite by ascorbic acid extraction: Methodology, dissolution kinetics and loss of solubility with age and de-watering*. *Chem. Geol.* 2010, 278, 70-79.

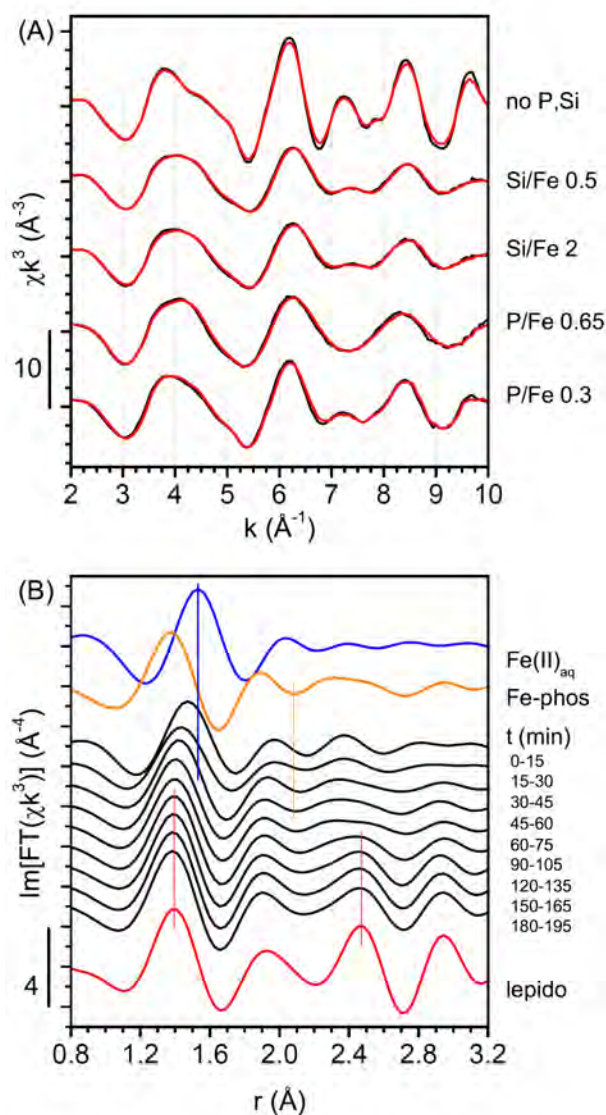


Figure 1. (A) Fe K-edge EXAFS spectra of Fe precipitates formed in NaHCO₃ electrolyte at different molar Si/Fe and P/Fe ratios before (black lines) and after (red lines) drying. (B) Imaginary part of Fourier-transformed EXAFS spectra collected in-situ during dissolved Fe(II) oxidation (black lines; time after Fe(II) spike in min) compared to reference spectra of aq. Fe(II), amorphous Fe(III)-phosphate, and lepidocrocite.

Experimental report: Speciation of organic sulphur in humic acids and natural organic matter after reaction with hydrogen sulfide

Klaus-Holger Knorr¹⁾, Jörg Göttlicher²⁾

¹⁾ University Münster, Institute of Landscape Ecology, Hydrology Group, Heisenbergstr. 2, 48149 Münster, Germany

²⁾ Karlsruhe Institute of Technology, ANKA Synchrotron Radiation Facility, Hermann-von-Helmholtz-Platz 1, D-76344 Eggenstein-Leopoldshafen, Germany

Introduction

Although it has been hypothesized that electron transfer upon reaction of hydrogen sulphide and organic matter is an important process in anaerobic environmental systems [1], there is little known about the actual electron budgets between organic matter and the numerous sulphur species being formed upon reaction. This is especially true for the formation of organic sulphur species, which cannot be assessed by conventional analytical techniques. In few recent studies, XANES has been successfully applied to identify the speciation of sulphur in organic mixtures [2] and within natural organic matter [3, 4]. The aim of his project was to investigate the redox speciation of sulphur in organic matter upon reaction with hydrogen sulphide, to trace the organic sulphur species preferentially formed during this reaction, and to compare the results with natural samples from the anaerobic profile of various peatlands.

Experiments and Methods

For calibration to quantify the contribution of individual organic sulphur functional groups, standard compounds for organic sulphur species were used according to available studies (Table 1) [5, 6]. All samples were measured in the fluorescence mode.

Table 1: Reference compounds used in this experiment, comment about suitability based on obtained results, and location of peak maximum in eV. Values in brackets indicate secondary, lower peaks; n.m.: not measured

Compound	CAS No.	Comment	Peak max. (eV)
1 Sulfuric acid mono(2-aminoethyl)ester	926-39-6	Probably impurities of sulfonates (S ^{+V})	2481.76, (2480.22)
2 Sodium methanesulfonate	2386-57-4	Suitable	2480.24
3 Dimethylsulfone	67-71-0	Too high vapour pressure, not suitable for vacuum	2479.02
4 DL Methionine sulfoxide	62697-73-8	Suitable	2475.29
5 L-Cysteine	52-90-0	Suitable	2472.34
6 4,4'-Dithiodibutyric acid	2906-60-7	Suitable	2471.63, (2473.17)
7 5,5'-Dithiobis(2-nitrobenzoic acid)	69-78-3	Suitable	2471.71, (2473.64)
8 Sodium Sulfate	7757-82-6	Suitable	2481.71
9 Dibenzothiophene	132-65-0	Too high vapour pressure, not suitable for vacuum	2472.79
10 Dibenzylsulfide	538-74-9	Too high vapour pressure, not suitable for vacuum	n.m.
11 Pyrite	-	Suitable	2471.70
12 Zinc sulphide	1314-98-3	Suitable, but peak max. shifted to higher eV despite oxidation state of -II (due to ionic binding)	2472.77
13 Elemental sulphur	7704-34-9	Suitable, but losses in vacuum	2471.66
14 Sigma Aldrich Humic Acid	1415-93-6	To be analyzed	2481.31, (2480.0 shoulder, 2475.00, 2473.26)

Higher vapour pressure of certain compounds (see Table 1) limited their measurements in vacuum, as applied at the SUL-X beamline. Due to effects of self-absorption for measurements in the fluorescence mode, all references and samples had to be tested in different dilutions to determine the optimum sulphur content for accurate determination of the species distribution [2, 4]. Best results were obtained with final sulphur contents in the powdered sampled of 2 or 4 %. Dilutions of reference compounds were done with microcrystalline cellulose. Natural samples of humic and fulvic acid, and peat samples were found to contain 2-4 % of sulphur and were therefore measured without dilution.

Results for references and Linear Combination Fitting of mixtures and natural samples

The used organic and inorganic model compounds could sufficiently be distinguished in terms of the sulphur redox state by the location of the maximum of the absorption peak (Table 1, Fig. 1A). This yielded satisfying results for LCF of defined mixtures (Fig. 1B) However, sulphur species with an oxidation state of 0 or lower showed considerable overlap and could not clearly been distinguished (Fig. 1A). Most suitable for fitting of

spectra of natural samples were sulphate ester, sulfonate, sulfone, dithiobutyric acid, cysteine, and partly also sulfoxide (compare Fig. 1A and C, D). Analysis of humic acids before and after reaction with H_2S revealed clear differences in terms of increased reduced sulphur functional groups and partly a decrease in oxidized groups (Fig. 1C), while there were little differences in humic acids before and after chemical reduction with H_2/Pd . The measurement of natural samples clearly showed a decrease of oxidized sulphur species and increase of reduced species with depth and increasing decomposition of the peat as previously described for sediments [7]. LCF of contributing sulphur species were so far mostly within an error of $\pm 10\%$, but may be improved in future measurements, using an extended set of reference in an LCF fit that is constrained to non-negative contributions as described in Manceau & Nagy 2012 [5].

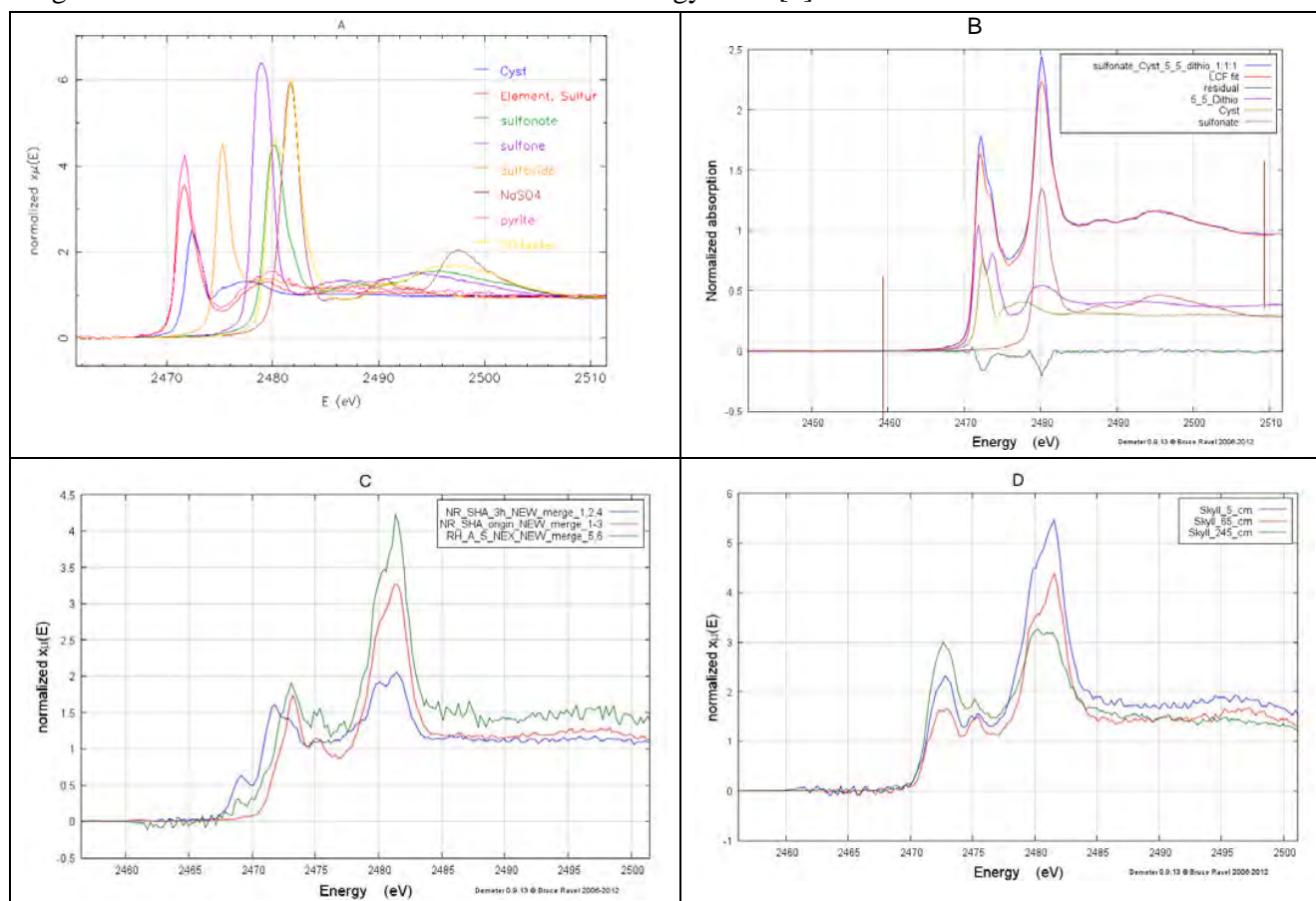


Figure 1: Examples of reference spectra (upper left, A), linear combination fitting (LCF) of a defined mixture (upper right, B), humic acid sample before and after reaction with H_2S (bottom left, C), and natural peat samples with a depth gradient (bottom right, D). See table 1 for full component names (Cyst: 5, Element. Sulfur: 13, sulfonate: 2, sulfone: 3, sulfoxide: 4, $NaSO_4$: 8, pyrite: 11, SO_4 -ester: 1)

Acknowledgements

The help of Ralph Steininger during measurements and interpretation is greatly acknowledged. Moreover, Zhiguo Yu and the laboratory staff at the Dept. of Hydrology (Univ. of Bayreuth) helped in sample preparation and measurements. Funding was provided also through the DFG grant KN 929/2-1.

References

1. Heitmann, T.; Blodau, C., Oxidation and incorporation of hydrogen sulfide by dissolved organic matter. *Chem. Geol.* **2006**, *235*, (1-2), 12-20.
2. Almkvist, G.; Boye, K.; Persson, I., K-edge XANES analysis of sulfur compounds: an investigation of the relative intensities using internal calibration. *Journal of synchrotron radiation* **2010**, *17*, (5), 683-688.
3. Einsiedl, F.; Mayer, B.; Schafer, T., Evidence for incorporation of H_2S in groundwater fulvic acids from stable isotope ratios and sulfur K-edge X-ray absorption near edge structure spectroscopy. *Environ. Sci. Technol.* **2008**, *42*, (7), 2439-2444.
4. Prietzel, J. r.; Botzaki, A.; Tyufekchieva, N.; Brettholle, M.; Thieme, J. r.; Klysubun, W., Sulfur Speciation in Soil by S K-Edge XANES Spectroscopy: Comparison of Spectral Deconvolution and Linear Combination Fitting. *Environ. Sci. Technol.* **2011**, *45*, (7), 2878-2886.
5. Manceau, A.; Nagy, K. L., Quantitative analysis of sulfur functional groups in natural organic matter by XANES spectroscopy. *Geochim. Cosmochim. Acta* **2012**, *99*, (0), 206-223.
6. Jokic, A.; Cutler, J. N.; Ponomarenko, E.; van der Kamp, G.; Anderson, D. W., Organic carbon and sulphur compounds in wetland soils: insights on structure and transformation processes using K-edge XANES and NMR spectroscopy. *Geochim. Cosmochim. Acta* **2003**, *67*, (14), 2585-2597.
7. Brüchert, V., Early diagenesis of sulfur in estuarine sediments: the role of sedimentary humic and fulvic acids. *Geochim. Cosmochim. Acta* **1998**, *62*, (9), 1567-1586.

Speciation of Zn and As in mining waste near Olkusz in Poland

Final report for the proposal ENV-242

Users: Prof. Juraj Majzlan, University Jena (DE); Irena Jerzykowska, Jagellonian University (PL)

Oxidation zones of ore deposits offer valuable insights into the long-term fate of many metals and metalloids. In this work (Majzlan et al. 2014), we have studied a paleo-acid rock drainage (ARD) system – the oxidation zone of Mississippi-valley type Zn-Pb deposits near Olkusz in southern Poland. The ARD systems exhausted their acid-generating capacity and have come almost to the conclusion of the mineral and geochemical transformations. Primary pyrite, marcasite, galena and sphalerite have been decomposed but the acidity was neutralized by the abundant carbonate host rocks. Iron oxides (Fig. 1a, 1b) are represented mostly by goethite, either well-crystalline or nanocrystalline, as determined by a combination of powder X-ray diffraction, micro-X-ray diffraction at the SUL-X beamline, and Mössbauer spectroscopy. Iron oxides bind a substantial amount of arsenic, to a lesser extent also zinc, lead, and cadmium, as shown by electron microprobe analyses (Fig. 1c) and sequential extractions. The X-ray absorption spectroscopy data from the SUL-X beamline (Fig. 1e, 1f) of the local environment of arsenic in goethite suggest the existence of bidentate mononuclear complex, in addition to the more common bidentate binuclear complex. These results suggest that arsenic is incorporated in the crystal structure of goethite, in addition to adsorbed to the surface of the particles or occluded in the voids and pores. Zinc is stored in smithsonite, hemimorphite, and as octahedral cations in the Zn-rich sheet aluminosilicates (Fig. 1d). Zinc is bound in goethite as a mixture of tetrahedrally and octahedrally coordinated cations. This study shows that the mature system binds the metals from the primary sulfides relatively strongly. Yet, some release of the metals was observed in this study, either in the laboratory (by sequential extractions) and in nature (e.g., neoformed Zn phyllosilicates). The physical conditions in the oxidation zone and on the surface are largely similar but the metals, to a certain extent, are still mobile in the soils. We may speculate that their mobility near the surface, in the mining waste, may be enhanced by a higher water/rock ratio than in the oxidation zone. This result implies that although the studied material is relatively benign, it still has a potential to cause local environmental problems.

Majzlan, J., Jerzykowska, I., Michalik, M., Göttlicher, J., Steininger, R., Błachowski, A., Ruebenbauer, K., 2014: Mineralogy of and speciation of Zn and As in Fe-oxide-clay aggregates in the mining waste at the MVT Zn-Pb deposits near Olkusz, Poland. *Chemie der Erde - Geochemistry* (in press)

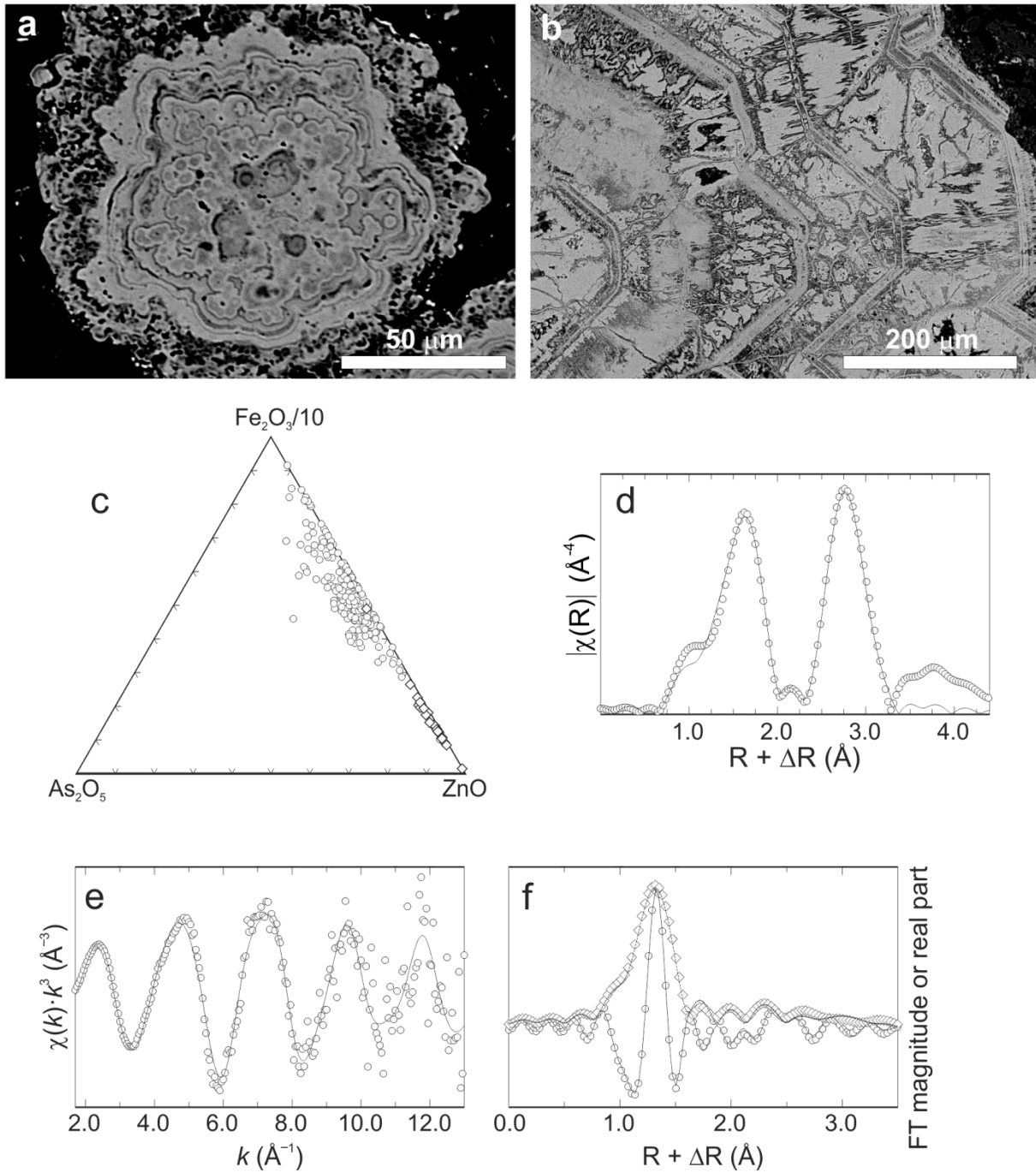


Fig. 1. Results and data from the study of the paleo-ARD system in Olkusz, Poland. Details in text.

Synchrotron-based XRD in situ Hydrothermal Investigation of Novel Hydraulic Binding Materials

K. Garbev¹⁾, P. Ullrich¹⁾, B. Gasharova²⁾, Jörg Göttlicher²⁾, Ralph Steininger²⁾

¹⁾ KIT, Institute for Technical Chemistry, Hermann-von-Helmholtz-Platz 1, D-76344 Eggenstein-Leopoldshafen, Germany

²⁾ KIT, Institute for Synchrotron Radiation, Hermann-von-Helmholtz-Platz 1, D-76344 Eggenstein-Leopoldshafen, Germany

Introduction

A novel cementitious material named Celitement has been developed at Karlsruhe Institute of Technology (KIT). Celitement consists of nanocrystalline calcium-hydrosilicates, which harden upon reaction with H₂O in a very similar way like the ordinary Portland cement does. Celitement is produced in a two stage process: 1. Hydrothermal synthesis of crystalline and nanocrystalline Calcium-Silicate-Hydrates (C-S-H phases, C = CaO, S = SiO₂, H = H₂O). 2. Tribochemical treatment of the hydrothermal product. A quintessential point of the production of Celitement is the hydrothermal synthesis. The formation of C-S-H phases is a complicated process, which is dominated by nucleation and extreme disequilibrium. The long term purpose of the study is to investigate the kinetics and mechanisms of formation of crystalline and nanocrystalline C-S-H phases during the hydrothermal process. Method of choice for this investigation is *in-situ* X-ray diffraction.

Experimental

A reaction cell meeting both, the synthesis conditions (200°C, 16 bar saturated steam pressure, high alkalinity of the media, pH=13) and ANKA instrumental requirements was developed (Figure 1). The reaction volume of the cell is 30 µl and is confined between two sapphire windows and a sapphire spacer. The path length is 1mm (+ 2 x 0.4 mm windows). The heating is realised by four heating cartridges controlled by two thermo elements connected to a Eurotherm controller 3508. The measurements took place on the SUL-X beamline in transmission at E=16 keV. The exact determinations of the wavelengths of the single experiments were performed by measuring LaB₆ in a capillary positioned in the plane of the reaction cell. The diffraction rings were detected by CCD positioned at 136 mm from the cell. The 2θ range detected by the CCD was in the most experiments between 3-30° 2θ which corresponds to d = 14 Å - 1.5 Å at a wavelength of 0.77744 Å. A verification of the temperature calibration was performed with standard materials BN and KNO₃ (NIST). The cell was filled in a Glovebox at ITC under N₂ flux in order to avoid carbonation. The starting materials Ca(OH)₂ (produced by heating CaCO₃ at 1000°C for 24 hours and quenching in deionised boiled water) and highly dispersed SiO₂ (Aerosil, Evonik) were mixed in ratio CaO/SiO₂ (C/S) = 2 and pressed as pellet (4 mm diameter). Mixture of H₂O and 1M NaOH was added (water/solid ratio (W/S) = 2 and 5) and the cell was closed tightly. After transfer to the beamline the cell position was determined. The temperature program included: 1) heating from room temperature to 200°C within 10 min. 2) Iso-temperature step at 200°C for 480 min. 3) Cooling to room temperature. During all steps XRD measurements were performed at a rate of 1-2 min. In addition some short runs with the starting materials (Ca(OH)₂, C-S-H phase) alone were performed. All together five runs of the *in-situ* hydrothermal syntheses were done.

Results

Figure 2 presents the X-ray diffraction patterns taken during the hydrothermal reaction of the sample with W/S=5 as a function of time. Formation of C-S-H begins obviously already upon mixing of the starting materials at room temperature, which is shown by the broad “hump” at 14.75° 2θ corresponding to the (110) reflection of C-S-H (d=3.03Å). After reaching 200°C a very quick dissolution of Ca(OH)₂ is observed (rapid diminishing of the intensities of all reflections) accompanied by an accelerated formation of C-S-H-phase. Short after that (20min after reaching 200°C) a formation of α-Ca₂[HSiO₄](OH) (α-C₂SH) is seen. This is confirmed by the appearance of its strongest reflection (122) at 13.94° 2θ (3.24 Å). Its intensity increases over time. The intensity of the broad reflection (110) of the C-S-H reaches its maximum after 50 minutes at 200°C and begins slowly to decrease. Comparing the development of the reflection intensities of both C-S-H phase and α-C₂SH implicates that the latter grows at the expense of the former. Very interesting observation is the recrystallization of Ca(OH)₂ during the cooling from 200°C to room temperature. It is unlikely that this

is due to supersaturation of some dissolved $\text{Ca}(\text{OH})_2$ in the fluid phase which was simply in excess during the reaction at 200°C . Furthermore the solubility of $\text{Ca}(\text{OH})_2$ is higher at lower temperature. One explanation for this behavior could be that one of the solid phases available might be unstable upon cooling and undergoes partial dissolution which in turn increases the concentration of Ca^{2+} ions in the solution leading to precipitation of $\text{Ca}(\text{OH})_2$. Indeed a closer observation of the (110) reflection of the C-S-H phase indicates rapid drop of its intensity after beginning of the cooling cycle.

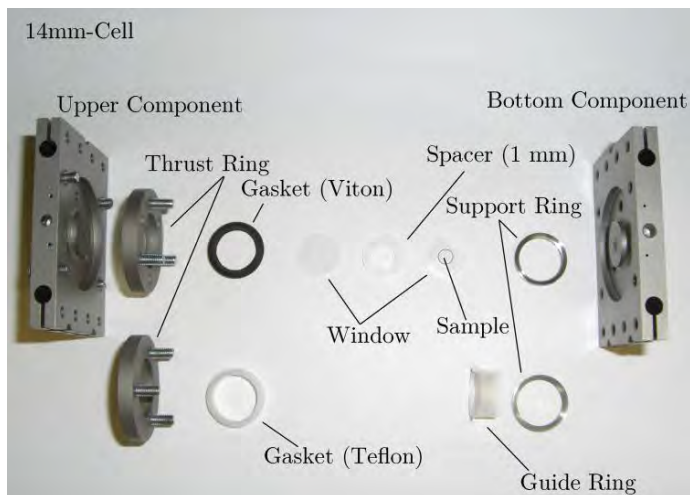


Fig. 1: A) Exploded view of the hydrothermal cell.



B) The cell on the SULX Beamline at ANKA

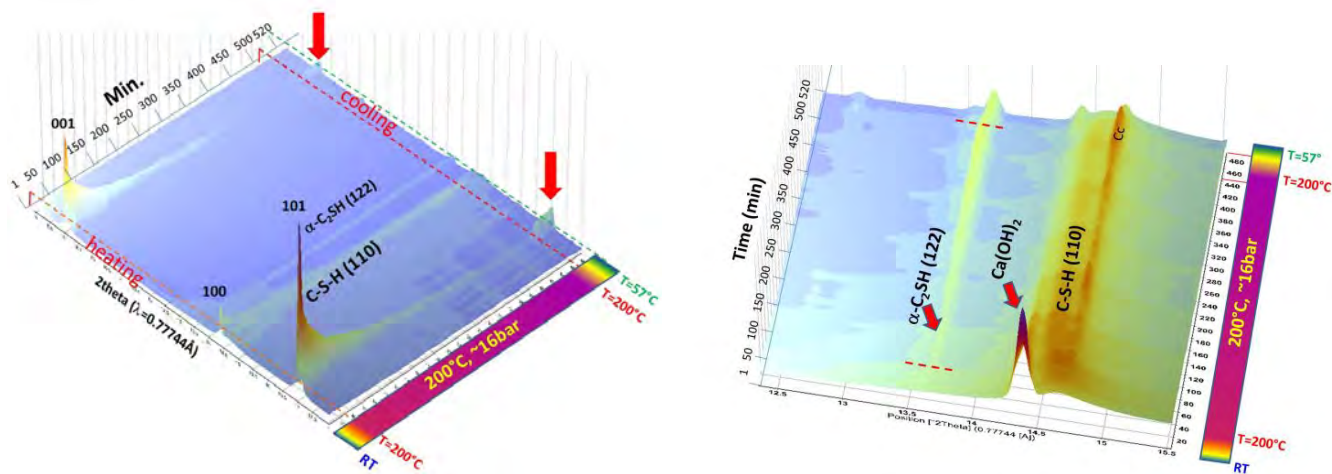


Fig. 2: In situ XRD patterns showing the development of a hydrothermal reaction (200°C , 16 bar) with starting materials $\text{Ca}(\text{OH})_2$ and SiO_2 ($C/S=2$, $W/S=5$) as a function of time. Left: larger view in 2θ range $8-18^\circ$. Arrows show recrystallization of $\text{Ca}(\text{OH})_2$ upon cooling. Right: detail view in the 2θ range $12.5-15.5^\circ$.

Conclusions

The hydrothermal cell dedicated for investigations of the reaction kinetics and mechanisms of formation of calcium silicate hydrates on the SUL-X beamline delivers deep insight in this process. The first results give essential information about the importance of the nanocrystalline C-S-H phase as a precursor for the formation of $\alpha\text{-C}_2\text{SH}$ as well as about the dissolution-precipitation behaviour of the components in the system $\text{CaO-SiO}_2\text{-H}_2\text{O}$ as a function of temperature under hydrothermal conditions.

Acknowledgements

The authors would like to thank Ralf Weigel for his excellent work on the design and development of the reaction cell.

Synchrotron-based XRD *in situ* Investigation of Novel Hydraulic Binding Materials: Formation of α -C₂SH from Ca(OH)₂ and Quartz Sand

K. Garbev¹⁾, P. Ullrich¹⁾, B. Gasharova²⁾, J. Göttlicher³⁾, R. Steininger³⁾, P. Stemmermann¹⁾

¹⁾ KIT, Institute for Technical Chemistry (ITC), Hermann-von-Helmholtz-Platz 1, D-76344 Eggenstein-Leopoldshafen, Germany

²⁾ KIT, Institute for Photon Science and Synchrotron Radiation (IPS), Hermann-von-Helmholtz-Platz 1, D-76344 Eggenstein-Leopoldshafen, Germany

³⁾ KIT, ANKA, Hermann-von-Helmholtz-Platz 1, D-76344 Eggenstein-Leopoldshafen, Germany

Introduction

Calcium-Silicate-Hydrates (C-S-H phases, C=CaO, S=SiO₂, H=H₂O) are the essential product of the cement hydration and therefore responsible for its chemical and mechanical properties. Furthermore hydrothermally synthesized C-S-H phases are the main constituents of aerated concrete, borehole cementing products and precursors of novel cementitious materials like Celitement. The large family of the C-S-H phases includes both: nanocrystalline products known as the general term C-S-H(I) with variable CaO/SiO₂ (C/S) ratio and various crystalline compounds. The later include more than 20 known structures with C/S=0.5-3.0. The hydrothermal synthesis of C-S-H phases is a rather complicated process, dominated by nucleation, extreme disequilibrium and strong dependence upon starting materials (source of CaO and SiO₂ and water/solid-ratio, w/s) and temperature and pressure profile. In the literature there are only scarce data on *in situ* observation of the formation of certain crystalline C-S-H phases mostly of interest for the aerated concrete chemistry (11Å tobermorite: Ca_{4.5}[Si₆O₁₆](OH)·5H₂O, xonotlite: Ca₆[Si₆O₁₆](OH)₂, gyrolite: Ca₁₆Si₂₄O₆₀ (OH)₈·14(H₂O)). On the other hand there are no data available for kinetics and mechanisms of formation of compounds like α -Ca₂[HSiO₄](OH) (α -C₂SH) or C-S-H(I), which are promising precursors for development of novel energetically and CO₂ efficient cements. Key issue for the establishing of these materials as suitable replacement of ordinary Portland cement (OPC) is that the starting materials needed for their production are available on a large scale in nature. In contrast to the production of OPC, where limestone and clay are used as raw materials, the formation of Celitement needs compounds with lower C/S ratio. One material meeting these requirements is quartz sand. Therefore this study focuses on the investigation of the kinetics and mechanisms of formation of α -C₂SH during the hydrothermal process with starting materials quartz sand and Ca(OH)₂ by means of *in situ* XRD.

Experimental

The hydrothermal reaction was followed in a dedicated reaction cell with reaction volume of 30 μ L confined between two sapphire windows and a sapphire spacer. The path length is 1mm (+ 2 x 0.4 mm windows). The heating is realised by four heating cartridges controlled by four thermocouples connected to a Eurotherm controller 3508. The XRD measurements were performed on the SUL-X beamline in transmission at E=16 keV with a spot size of 300 μ m x 150 μ m. The detection was carried out by the CCD detector positioned at a distance of 136 mm from the cell. The 2 θ range covered by the CCD detector was 3-30° 2 θ which corresponds to d = 14 Å - 1.5 Å at 0.77621 Å wavelength. The cell was filled in a glovebox under N₂ flux in order to avoid carbonation. The starting materials Ca(OH)₂ (produced by heating CaCO₃ p.a. at 1000°C for 4 hours and quenching in deionised boiled water) and quartz sand (94% SiO₂, Friedrich GmbH Quarzsandwerke) were mixed in ratio CaO/SiO₂ (C/S) = 2 and pressed as pellet (4 mm diameter). Mixture of H₂O and 1M NaOH was added (water/solid ratio (W/S) = 2). After transfer to the beamline the cell position was determined. The temperature program included: 1) heating from room temperature to 200°C within 15min.; 2) iso-temperature step at 200°C for 402min.; 3) Cooling to 60°C (60min.) with iso-temperature step at 60°C for additional 30min.; 4) Cooling to room temperature. During all steps XRD measurements were performed at a rate of 3min.

Results

Figure 1 presents the XRD patterns taken during the hydrothermal reaction of the sample as a function of time and at particular temperature. Formation of α -C₂SH is first observed by appearing of reflections (122) and (002) after 20min. At the same time formation of a new C-S-H phase (recognizable at its (110) reflection)[1] also takes place but at a very slow rate. Very quick dissolution of both Ca(OH)₂ and quartz is

observed. Figure 2A presents the development of the FWHM, net area and intensity of reflection (001) for $\text{Ca}(\text{OH})_2$ (CH). Upon raising the T° to 200°C ordering along [001] takes place shown by the decrease of the FWHM. The strong decrease of the area and intensity in the following 20 min. shows rapid dissolution followed by moderate dissolution in the range 30 min. - 240min. The FWHM does not show significant change. The region between 240-280min. shows once again very rapid dissolution followed by its slowing down in the range 280-420min. The latter is accompanied by an increase of the FWHM. Lowering of the T° from 200°C to 60°C leads to further decrease of the area and intensity of the (001) reflection and increase of the FWHM. The reflection (101) of quartz (Fig 2C) shows complex behavior with increasing its area and intensity upon heating to 200°C (probably due to crystal enlargement) followed by rapid decrease in the range 20-60min. A moderate dissolution follows (60-200min.) with subsequent increased dissolution rate (200-240min.). After 4 hours no quartz reflections are detectable. Figures 2B and 2D show the development of reflections (122) and (223) of $\alpha\text{-C}_2\text{SH}$ during the experiment. A rapid formation is observed within 20-30min. after beginning (Fig. 2D) followed by a slow increase of the peak area in the range 30-70min. Quick further formation of $\alpha\text{-C}_2\text{SH}$ takes place between 70-200min. followed by an even more accelerated area and intensity increase in the range 200-270min. Between 270-420min a plateau regarding peak area, intensity and FWHM of the $\alpha\text{-C}_2\text{SH}$ reflections is observed. In the same range a maximum of formation of additional nanocrystalline C-S-H phase is reached (Fig. 1, Fig. 2D). The presence of C-S-H phase is due to the higher dissolution rate of quartz compared to that of $\text{Ca}(\text{OH})_2$ which leads to enrichment of SiO_2 . Upon cooling from 200° to 60°C , an increase of area and intensity and decrease of the FWHM of the $\alpha\text{-C}_2\text{SH}$ reflections is seen. One explanation for this behavior is possibly the increased stability of $\alpha\text{-C}_2\text{SH}$ at temperatures lower than 200°C under hydrothermal conditions. In this case the role of the Debye-Waller factor must be also taken upon consideration.

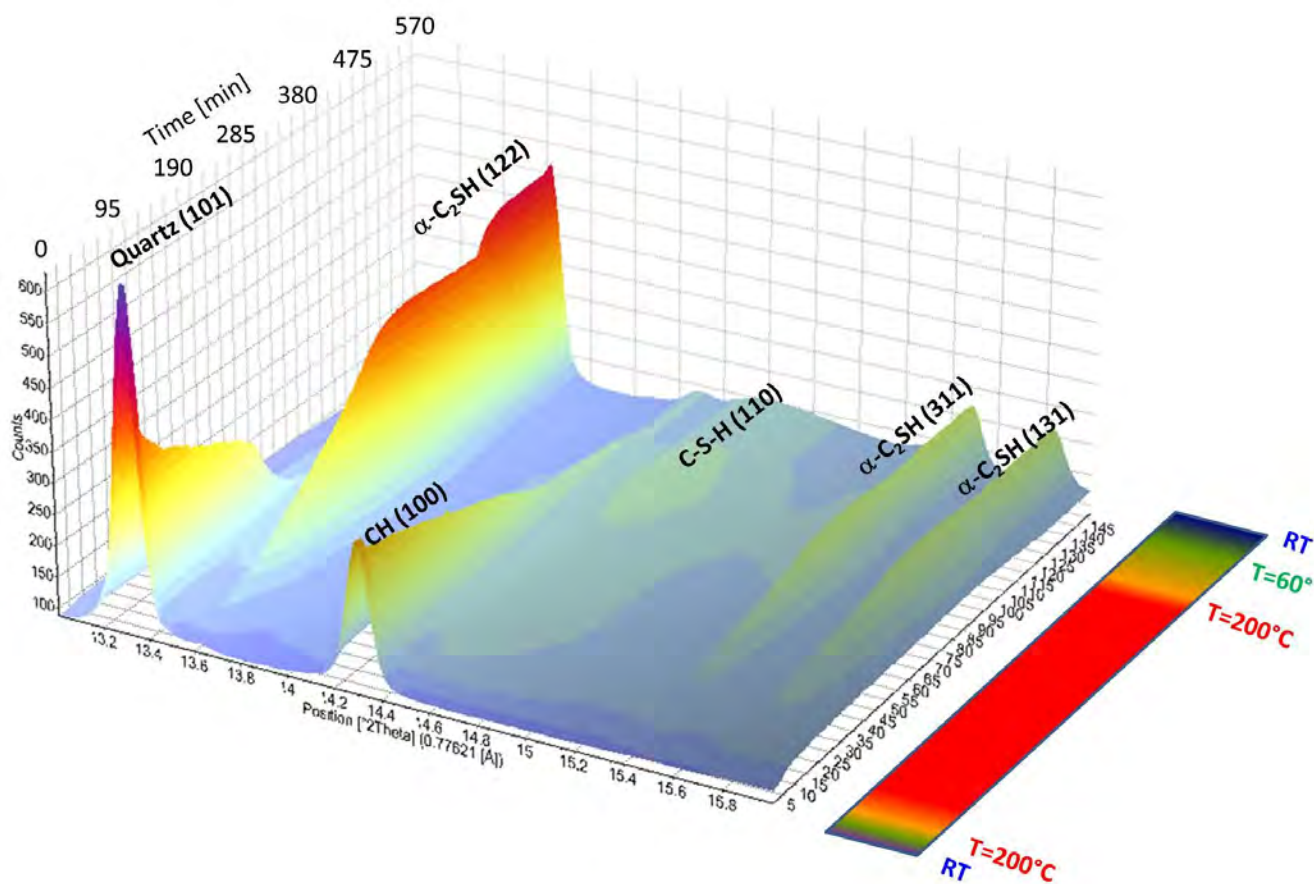


Fig. 1: In situ XRD patterns showing the kinetics of the hydrothermal reaction (200°C , 16 bar) of the starting materials $\text{Ca}(\text{OH})_2$ and SiO_2 (quartz sand) ($\text{C/S}=2$, $\text{W/S}=2$) as a function of time.

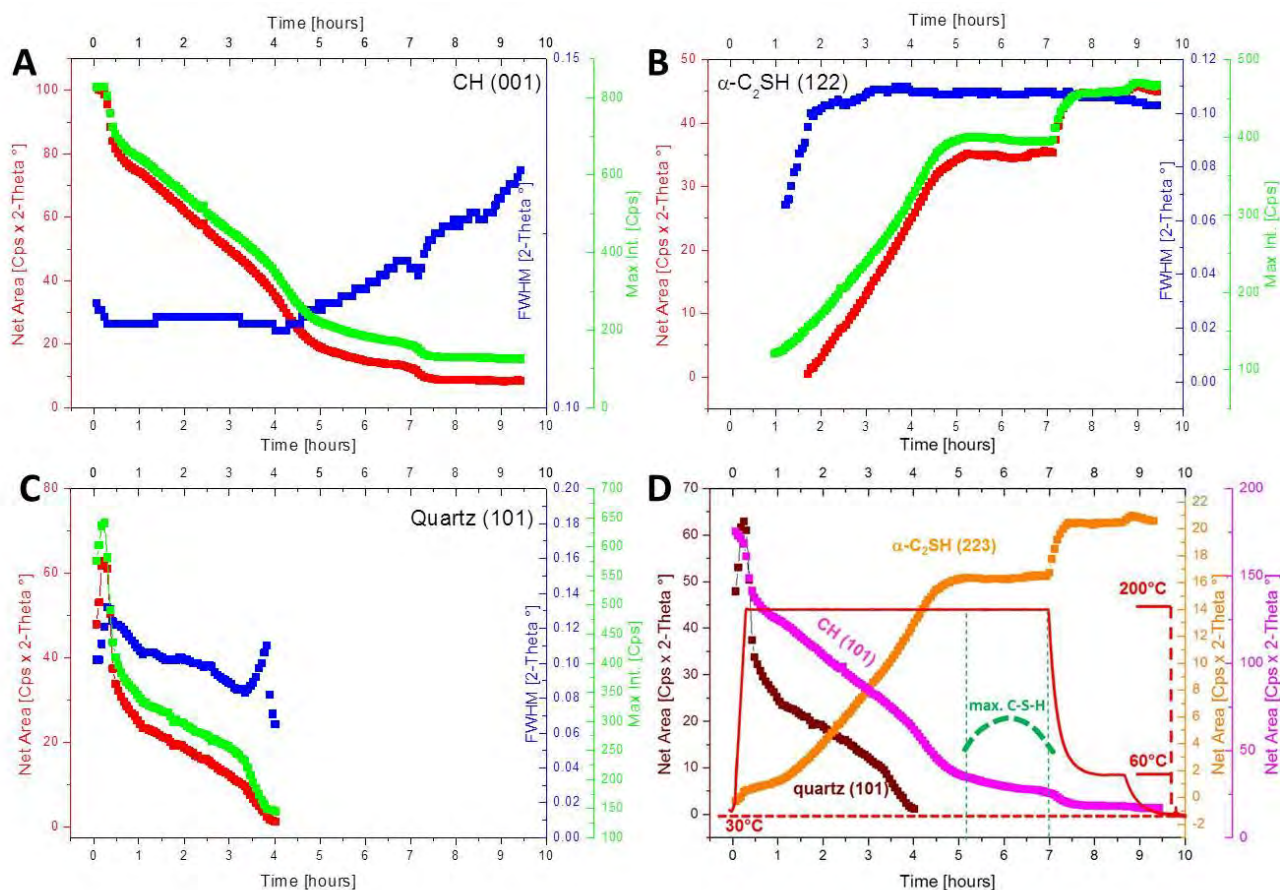


Fig. 2: Development of the reflection characteristics (FWHM, net area and intensity) of (001) of $\text{Ca}(\text{OH})_2$ (CH)(A); (122) of $\alpha\text{-C}_2\text{SH}$ (B); (101) of quartz (C) as function of the reaction time and temperature. The net areas of the reflections (223) $\alpha\text{-C}_2\text{SH}$, (101) $\text{Ca}(\text{OH})_2$ and (101) quartz are compared in (D). The temperature profile of the experiment is shown in (D). Dashed line in D indicates the maximum formation of C-S-H (not scaled)

Conclusions

The in situ XRD experiments at the SUL-X beamline on the hydrothermal formation of $\alpha\text{-C}_2\text{SH}$ from $\text{Ca}(\text{OH})_2$ and SiO_2 (quartz) provide essential details about the dissolution-precipitation behaviour of the components in the system $\text{CaO-SiO}_2\text{-H}_2\text{O}$ as a function of time and temperature under hydrothermal conditions. The observations point to a multi-stage process starting with quick nucleation within the first minutes after reaching 200°C followed by slow crystallization up to 60min. The consequent accelerated formation of $\alpha\text{-C}_2\text{SH}$ reaches its apex between 200-270min followed by a plateau. Differences in the dissolution rate of $\text{Ca}(\text{OH})_2$ and SiO_2 (quartz) lead to local disequilibrium and to formation of nanocrystalline C-S-H phase. The XRD data taken during the cooling process deliver valuable information about the stability fields of the phases involved.

Acknowledgements

The authors would like to thank Ralf Weigel for his excellent work on the design and development of the reaction cell and Nigel Smale for his commitment during this beam time period.

References

[1] K. Garbev, G. Beuchle, M. Bornefeld, L. Black, P. Stemmermann, Cell dimensions and composition of nanocrystalline calcium silicate hydrate solid solutions. Part 1: Synchrotron-based X-ray diffraction. *J. Am. Ceram. Soc.*, 91 [9] 3005-3014 (2008).

Micro-XRF and micro-XRD study of the uptake of radionuclides by argillaceous rocks

J. Osán¹), D. Breitner¹), M. Fábrián¹), F. Gergely¹), R. Dähn²), M. Marques²), R. Simon³)

¹) Centre for Energy Research, Hungarian Academy of Sciences, P.O. Box 49, H-1525 Budapest, Hungary

²) Laboratory for Waste Management (LES), Paul Scherrer Institute, 5232 Villigen PSI, Switzerland

³) Karlsruhe Institute of Technology, Institute for Synchrotron Radiation, Hermann-von-Helmholtz-Platz 1, D-76344 Eggenstein-Leopoldshafen, Germany

Introduction

Argillaceous rocks are being considered in many radioactive waste management programmes as suitable host rock formations for the deep geological disposal of radioactive waste. Clay minerals which are important components in such rock types have generally strong radionuclide retention properties. Transport in natural barriers depends strongly on retardation like chemical sorption or other physical processes. Consequently, an understanding of sorption processes, and of the physico-chemical parameters, which influences them, is becoming increasingly important. The present study focuses on the interaction of escaped radionuclides with the host-rock surrounding the planned high-level radioactive waste (HLW) repositories in Hungary (Boda Claystone Formation – BCF) and in Switzerland (Opalinus Clay – OPA). The aim is to identify the mineral phases responsible for the uptake of key radionuclides representing transuranium elements, fission and corrosion products by the host rock on the microscale. For this reason, combined synchrotron-radiation micro-XRF mapping and micro-XRD measurements were performed on thin sections subjected to sorption experiments, using inactive Cs(I), Ni(II), Nd(III) and natural U(VI).

Materials and methods

The rocks investigated were prepared from geochemically characterized cores from drillings in BCF and OPA. Thin sections were prepared on 350- μm thick high-purity silicon wafers from BCF and on 1-mm thick quartz glass from OPA. The average thicknesses of the sections are 30–60 μm . Samples were subjected to 24–72 hour sorption experiments with one ion of interest added, using synthetic porewater for Cs and Ni, and a 0.1 M NaCl solution for Nd, Th and U as background electrolyte. The NaCl solution was employed due to solubility constraints to ensure a sufficient loading of the element of interest for micro-XRF while avoiding precipitation in the solution itself. The experiments were performed at the FLUO beamline of ANKA. The white beam of a bending magnet was monochromatized by a W/Si multilayer double monochromator. A silicon-drift detector was used to collect fluorescence spectra. Because of the high iron content of the rock sections, micro-XRF elemental mapping of samples treated with Cs(I) or Nd(III) was performed first at an energy of 7.1 keV below the Fe-K absorption edge. A Fresnel zone plate was used as a focusing element, providing a $3 \times 8 \mu\text{m}^2$ spot size. The combined micro-XRF/micro-XRD measurements were performed at a primary beam energy of 17.5 keV, using a compound refractive lens for focusing a beam down to a spot size of $2 \times 5 \mu\text{m}^2$. Elemental maps were recorded for the adsorbed element (Cs, Ni, Nd, Th, U) as well as for the major and minor elements of the rock (e.g. K, Ca, Fe, Pb), using a 5 μm step size and 4–10 s counting time per pixel. The elemental maps served as a basis for selection of positions of interest for μ -XRD analyses, and for investigating correlation between the element of interest and elements representative for distinct minerals. Diffraction images were collected from selected positions of the samples employing a 130 mm diameter CCD detector, using a 60–120 s counting time. Corrections for detector tilt and azimuthal integration were performed using the *XRDUA* software [1].

Results

For samples treated with Cs and Nd, a small portion of the area scanned at 7.1 keV was remapped at 17.5 keV. The small portions were selected in such a way that they contain characteristic features in the K, Ca and Mn maps. Based on the overlaying of the two maps, horizontal and vertical drift values could be calculated in a spatial resolution of 5 μm . This way the rescan of the whole areas was not necessary, the original maps collected at 7.1 keV could be successfully used for selection of points of interest for micro-XRD measurements, based on the drift-corrected coordinates.

Elemental mapping at 7.1 keV confirmed that clay minerals play an important role in the uptake processes for Cs, but enrichment of Nd was observed around Ca and Mn-rich phases. Cs was found to be highly correlated with K ($r > 0.9$), as the element representing clay minerals (illite). Micro-XRD results of selected positions revealed that Cs and Ni are associated to illite and smectite phases [2].

For Th, only weak correlation was observed due to the lower coverage than expected from calculations. For U, secondary mineralisation around carbonate veinlets and vugs infillings was also observed on a different thin section treated with U(VI)-containing NaCl solution at identical conditions, showing that the U-rich rings were not sample preparation artefacts. The secondary mineralization was found to be a result of dissolution of ankerite and the formation of iron oxyhydroxide phase which can effectively bind U(VI) [3]. This behaviour was observed at slightly acidic conditions (pH 6.8) using a 0.1 M NaCl background electrolyte and 72 h reaction time. These conditions were applied in order to avoid precipitation in the solution and to reach a sufficiently high U load on the thin sections (around 50 $\mu\text{g/g}$) for the micro-XRF measurements. Calculations using the 2 Site Protolysis Non Electrostatic Surface Complexation and Cation Exchange (2SPNE SC/CE) sorption model [4] predicted that under porewater conditions (pH 8.0) the maximum equilibrium concentrations were limited because of solubility constraints resulting in the estimated amounts of sorbed U too low for the micro-XRF investigations. Since the observed local enrichments of U and Nd are in the 5–10 μm range, it would be essential to investigate in the future if they occur also at neutral or slightly basic conditions, and to gain information on the kinetics of the secondary mineralization and dissolution.

Acknowledgements

The research leading to these results has received funding from the Swiss-Hungarian Cooperation Programme through Project n° SH/7/2/11

References

- [1] De Nolf W, Janssens K. Surf. Interface Anal. 2010, 42, 411-418
- [2] Breitner D, Osán J, Török S, Sajó I, Dähn R, Máthé Z, Szabó C. X-ray microspectroscopic investigations of Ni(II) uptake by argillaceous rocks of the Boda Siltstone Formation in Hungary. NEA Clay Club Proceedings 2011
- [3] Breitner D, Osán J, Fábrián M, Szabó C, Dähn R, Marques M, Sajó IE, Máthé Z, Török S. Retention mechanisms of U(VI) in Boda Claystone Formation as the candidate host rock of high activity and long lived nuclear waste repository in Hungary. Submitted to Applied Geochemistry.
- [4] Bradbury MH, Baeyens B. Sorption modelling on illite. Part II: Actinide sorption and linear free energy relationships. Geochimica et Cosmochimica Acta 73 (2009) 1004-1013

Conformational changes in vertebrate myelin proteins in membrane-mimetic conditions followed by SRCD spectroscopy

H. Han^{1,2)}, S. Laulumaa^{1,2)}, P. Kursula^{1,2,3)}

¹⁾ University of Oulu, Department of Biochemistry & Biocenter Oulu, Linnanmaa H4, FIN-90570 Oulu, Finland

²⁾ Centre for Structural Systems Biology (CSSB-HZI), German Electron Synchrotron (DESY), Notkestraße 85, D-22607 Hamburg, Germany

³⁾ University of Hamburg, Department of Chemistry, Hamburg, Germany

Background

We are mainly interested in the structure and function of proteins specifically expressed in the vertebrate myelin sheath, a target of a number of disabling neurological diseases. Myelin proteins, in general, have little homology to other proteins, and are intimately associated with the multilayered lipid membranes of myelin. Our aim is to obtain detailed information on the structure-function-dynamics relationships in myelin proteins, using for example, high-resolution X-ray and neutron crystallography, synchrotron SAXS, (SR)CD, neutron scattering, fluorescence spectroscopy, calorimetry, and surface plasmon resonance.

Methods

During our beamtime on UV-CD12 in 2012, we collected SRCD data for a number of samples, which mainly represented different myelin peripheral membrane proteins in a number of membrane-mimetic conditions. In addition, we continued measuring data from myelin protein peptides in detergent micelles to complement earlier work on the folding of these peptides.

Results & Discussion

We obtained a significant insight into the membrane interactions of two myelin peripheral membrane proteins during our recent experiments, and the data, together with complementary experiments, are currently being written up for publication. Also the peptide experiments are being prepared for publication.

In many cases, we saw significant conformational changes in the protein, when SRCD was measured in the presence of vesicles, bicelles, micelles, or organic solvents. Some of these clear effects were completely unexpected and hence, very interesting.

For our neutron experiments, we have been producing perdeuterated protein samples. The measured SRCD spectra indicated that the folding of these labeled samples is indistinguishable from the non-labeled proteins.

Further work will include, for example, more detailed studies using oriented CD spectroscopy (OCD) setups, hopefully at the UV-CD12 beamline of ANKA.

Acknowledgements

We wish to thank the staff at the UV-CD12 beamline for excellent support. Our work has been funded by the Academy of Finland, the Sigrid Jusélius Foundation (Finland), and the European Spallation Source (Sweden).

Structure and aggregation tendency of membrane active peptides

P. Wadhvani¹⁾ and Jochen Bürck¹⁾

¹⁾ Karlsruhe Institute of Technology, Institute of Biological Interfaces (IBG-2),
Hermann-von-Helmholtz-Platz 1, D-76344 Eggenstein-Leopoldshafen, Germany

Introduction:

As a continuation of our previous proposal (A2011-018-002901) in this proposal (A2012-019-002860) we continue to focus on the structure-function analysis of membrane active peptides which are prone to aggregation. Aggregation of protein and peptides is often related either to their toxicity or to the disease caused by the mal-functioning of the protein in question. Most often, this aggregation of peptides is induced in the membrane plane or can be initiated by the lipids themselves. Therefore, our specific aims here were to understand the secondary structure of two membrane active peptides that have shown strong aggregation in presence of lipids. Furthermore, we test the reversibility of these aggregates and to see what drives the aggregation, if it can be possibly reversed.

Systems studied:

The two systems that were tested in the above mentioned proposal include:

- (1) an α -helical cell penetrating peptide TP10 and
- (2) β -sheeted antimicrobial peptide KIGAKI

TP10 is a cell penetrating peptides and shows enhanced aggregation tendency which we believe is the cause of the associated toxicity. We have recently reported a detailed NMR study on TP10 and have found that N-terminal of TP10 tends to remain unfolded where as the C-terminal is able to fold into an α -helix.¹ To understand the detailed secondary structure of the peptide, we used site specific ¹⁹F- labelled peptides to determine the importance of residues which prevent or promote the aggregation of TP10 in the membrane. Furthermore we test the role of temperature and concentration on the aggregation tendency of TP10 wild type peptide.

KIGAKI is an antimicrobial peptide which is also known to aggregate and we believe that this aggregation is the prime cause of the associated toxicity. We have previously shown that KIGAKI is able to form fibrils in absence of lipids and since the aggregation is intrinsic property of the peptide, lipid bilayer just promotes the process of aggregation.^{2,3} By using site selective D-amino acids we have previously shown that it is possible to maintain the antimicrobial activity and decrease the toxic side effects in KIGAKI.² Since the activity(or toxicity) of the peptides is closely related to the structure of the peptide, here we investigate the secondary structure of the peptides by varying conditions such as membranes, temperature, or concentration.

Results and Discussion:

Our results for TP10-WT show that the peptide has much less tendency to aggregate under the conditions tested in the limited time available. We observe that TP10 WT peptide does not aggregate in aqueous buffers and Figure 1(A) shows that an helical structure is indeed preserved under these conditions. Furthermore, Figure 1(B) shows that in presence of small unilamellar vesicles TP10 also remains helical even up to a very high peptide to lipid ratio (P/L) of 1:1. At a moderately high P/L = 1:50, we also do not observe any signature spectrum of β -sheets. It remains to be tested if TP10 would also remain helical in oriented samples which are usually devoid of excess water and this may promote aggregation of the peptide as previously reported. Our investigations on the aggregating tendency of KIGAKI show that it can aggregate in absence or in presence of the lipid membrane. We have measured TEM of KIGAKI aqueous solution at 2mM and have previously evidenced distinct amyloid like fibrils for this peptide.³ By suitably substituting a D-amino acid it is possible

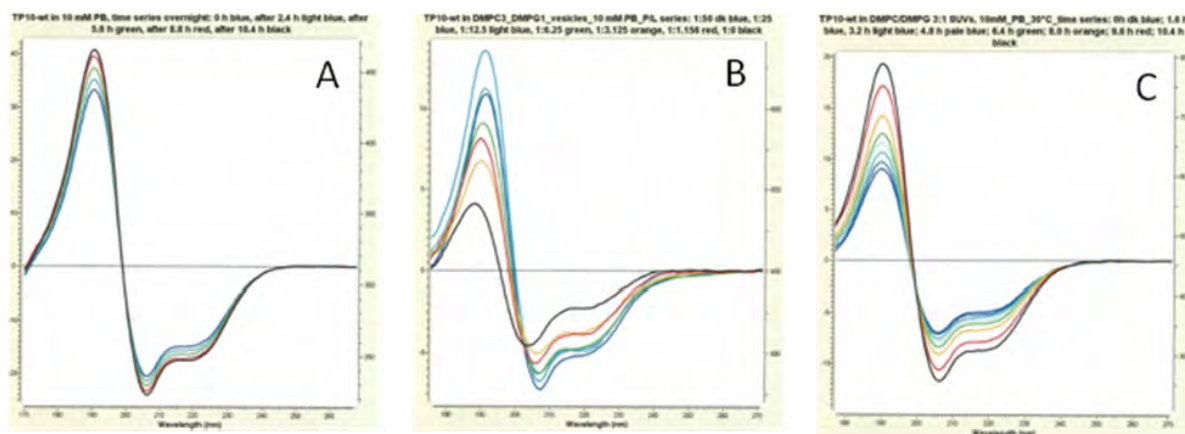


Figure 1: Influence of concentration, lipid and time on aggregation of TP10: (A) TP10 in 10mM phosphate buffer time course, (B) TP10 in DMPC/PG(3:1) as a function of peptide concentration (P/L =1:0, 1:1, 1:3,1:6,1:12, 1:25, 1:50), (C) TP10 in DMPC/PG(3:1) time course at P/L= 1:50.

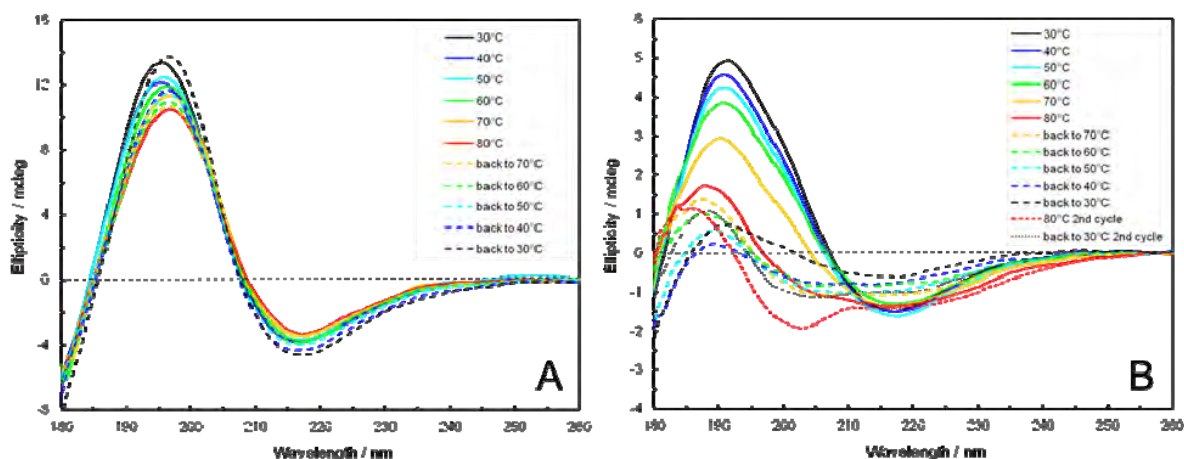


Figure 2: SRCD spectra of KIGAKI measured as a function of temperature: (A) wild type KIGAKI in DMPC/PG(3:1) show stable fibrils (B) KIGAKI-8D in DMPC/PG(3:1) show that thermal denaturation of fibrillar structure.

to delay the aggregation process or to increase the threshold of aggregation. Here, we studied if this aggregated peptide is irreversibly aggregated into β -sheets or can this be reversed by incorporating a D-amino acid. Our results show that KIGAKI-wild type forms stable aggregates which cannot be thermally unfolded as shown in Figure 2(A) where as by replacing a single L-amino acid by a D-amino acid, it is possible to break these aggregated sheets by application of heat.

These results would appear in respective publications authored by Parvesh Wadhvani, Jochen Bürck and Anne. S. Ulrich.

References:

- (1) Fanghanel, S.; Wadhvani, P.; Strandberg, E.; Verdurmen, W. P.; Burck, J.; Ehni, S.; Mykhailiuk, P. K.; Afonin, S.; Gerthsen, D.; Komarov, I. V.; Brock, R.; Ulrich, A. S. *PLoS One* **2014**, *9*, e99653.
- (2) Wadhvani, P.; Reichert, J.; Strandberg, E.; Burck, J.; Misiewicz, J.; Afonin, S.; Heidenreich, N.; Fanghanel, S.; Mykhailiuk, P. K.; Komarov, I. V.; Ulrich, A. S. *Phys Chem Chem Phys* **2013**, *15*, 8962.
- (3) Wadhvani, P.; Strandberg, E.; Heidenreich, N.; Burck, J.; Fanghanel, S.; Ulrich, A. S. *J Am Chem Soc* **2012**, *134*, 6512.

Acknowledgements: We thank Bianca Posselt and Siegmur Roth for their valuable help and technical assistance.

Investigation of the PDGF receptor Beta and the oncoprotein E5 from bovine papillomavirus in lipid bilayers by SR-CD

Dirk Windisch¹⁾, Marcel Zeitler²⁾, Colin Ziegler²⁾, Christian Weber²⁾

¹⁾ Karlsruhe Institute of Technology, Institute for Biological Interfaces, P. O. Box 3640, 76021 Karlsruhe, Germany

²⁾ Karlsruhe Institute of Technology, Institute of Organic Chemistry, Fritz-Haber-Weg 6, 76131 Karlsruhe, Germany

Introduction

The activity of many membrane proteins depends on direct molecular interactions, in which two or more molecules (of the same kind or of different kinds) assemble together to form a functional complex for example in signal transduction. To understand these protein-protein interactions it is necessary to investigate and characterize the biochemistry and biophysics of membrane proteins, especially how they integrate into the membrane, how they fold, and how they find and interact with their corresponding interaction partner(s).

The E5 oncoprotein from bovine papillomavirus is a small membrane protein that manipulates the function of the platelet-derived growth factor receptor β (PDGFR) in a ligand-independent way via highly specific helix-helix interactions causing host cell transformation and cancer formation [1]. Structural investigations done in our lab revealed that hydrophobic matching controls the tilt and the stability of PDGFR transmembrane domain [2]. We found that the isolated transmembrane segment of the receptor has a high propensity to dimerize as a left-handed coiled-coil dimer on its own. When reconstituted into thick phospholipid bilayers, this dimer is inserted essentially upright so that the crossing angle of the monomers is small enough to allow a close packing along the dimer-interface. Notably, increasing tilt in thin membranes destabilizes the dimer-interface resulting in protein aggregation due to hydrophobic mismatch. These findings suggest that the stably inserted dimer in thick membranes represents the biological active form of PDGFR.

In a complementary circular dichroism and solid state NMR analysis we wanted to investigate if the structure and membrane alignment of the E5 oncoprotein also depends on the membrane thickness. Therefore we investigated the structure of the E5 protein reconstituted in lipid bilayers of different thicknesses by synchrotron circular dichroism (SR-CD). In parallel, solid state NMR measurements were done to investigate how the protein is oriented in these lipid bilayers. The results of the structural investigation of the E5 protein reported here complement our previous findings about PDGFR. Taken together we got further insights in how E5 and PDGFR assemble to form a functional signal transduction complex [3].

We used SR-CD because the high background absorption of phospholipids, especially of unsaturated ones, restricted our conventional CD analysis of E5 and the PDGFR transmembrane domain to detergents and to the short, saturated lipids in the past. Due to the higher sensitivity and less background absorption in SR-CD it was possible to extend the spectrum of lipids which can be used for protein reconstitution to more natural-like unsaturated and longer lipids.

Experimental details

To investigate if the structure and function of E5 is also connected to bilayer thickness, we reconstituted recombinantly expressed and purified E5 protein in lipid vesicles made of DOPC (di-C18:1), DEiPC (di-C20:1), DErPC (di-C22:1) and DNPC (di-C24:1) in a protein-to-lipid ratio of 1:50 and a protein concentration of 2 mg/ml. Due to the increasing hydrocarbon chain length the lipid bilayer thickness increases from thin DOPC lipid bilayers to more thick DNPC membranes. The SR-CD measurements were carried out at the UV-CD12 beamline (ANKA, KIT) and spectra were recorded between 170 and 270 nm. For the first time it was possible to get high quality CD spectra of lipidic samples even down to 175 nm, which in the same way is not possible using conventional CD spectroscopy. Secondary structure estimation was performed using the CONTIN algorithm at the DICHROWEB server [4-6]. The quality of the fit between the experimental and back-calculated spectra corresponding to the derived secondary structure was assessed from the normalized-rootmean-square deviation (NRMSD), with a value of <0.1 considered a good fit.

Results

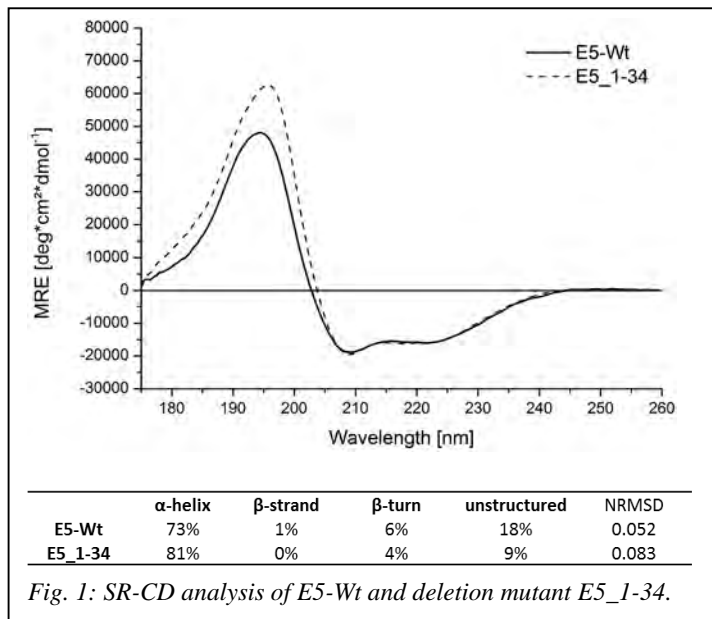


Fig. 1: SR-CD analysis of E5-Wt and deletion mutant E5_1-34.

more to the complementary solid state NMR spectra and thereby overlapping with the signals of the membrane-spanning part of E5.

When reconstituted in the more natural environment of lipid vesicles (which form lipid bilayers as cells do) the deletion mutant E5_1-34 showed a mostly helical secondary structure (Figure 2). Notably, we found an increase of the helical content from 71% in thin DOPC bilayers to 91% in thick DNPC bilayers while at the same time the unstructured parts decreased (Table 2). In thick membranes the helical transmembrane domain showed its maximal extension while in thin membranes the helical part is restricted to the hydrophobic core of the protein which is in agreement with the hydrophobic mismatch theory. The findings reported here showed that the E5 protein prefers thicker membranes where it probably interacts with the PDGF receptor which is known to be active in specific microdomains, so called caveolae, which are due to their sphingolipid/cholesterol-rich lipid composition thicker than the phospholipid-rich surrounding [7].

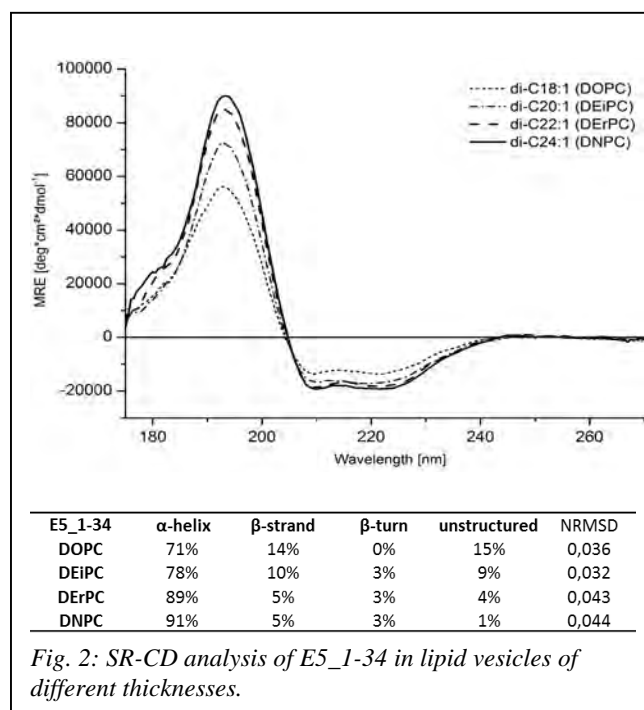


Fig. 2: SR-CD analysis of E5_1-34 in lipid vesicles of different thicknesses.

References:

- [1] Petti, L.; DiMaio, D.: 1992, Proc. Natl. Acad. Sci. U.S.A.: 89, 6736-6740
- [2] Muhle-Goll, C.; Hoffmann, S.; Afonin, S.; Grage, S.L.; Polyansky, A.A.; Windisch, D.; Zeitler, M.; Bürck, J.; Ulrich, A.S.: 2012, J. Biol. Chem.: 287, 26178-26186
- [3] Windisch, D.; Ziegler, C.; Grage, S.L., Weber, C.; Zeitler, M.; Bürck, J., Ulrich, A.S.: in preparation for publication
- [4] van Stokkum, I.H.; Spoelder, H.J.; Bloemendal, M.; van Grondelle, R.; Groen, F.C.: 1990, Anal. Biochem.: 191, 110-118
- [5] Whitmore, L.; Wallace, B.A.: 2004, Nucleic Acids Res.:32(Web Server issue), W668–W673
- [6] Lobley, A.; Whitmore, L.; Wallace, B. A.: 2002, Bioinformatics: 18, 211-212
- [7] Liu, P.; Ying, Y.; Ko, Y.G.; Anderson, R.G.: 1996, J. Biol. Chem.: 271, 10299-10303

Conformational analysis of novel cell-penetrating peptide SAP analogues in membrane-mimetic systems

V. Kubyshkin¹⁾, S. Afonin²⁾

¹⁾ Karlsruhe Institute of Technology, Institute of Organic Chemistry, Karlsruhe, Germany

²⁾ Karlsruhe Institute of Technology, Institute of Biological Interfaces IBG-2, Karlsruhe, Germany

Background

Cell-penetrating peptides (CPP) are a potent class of bio-compatible tools for non-toxic manipulation of living cells.[1] They act by co-translocating various cargoes (dyes, toxins, enzymes, nucleic acids) across plasma membrane without temporal compromise on membrane integrity. Structural requirements for the vehicle activity of these peptides are unclear and may improve design. SAP is a prototype CPP with unprecedentedly low toxicity in the cell culture studies. Structure of SAP in membranes was unknown, but the sequence and behaviour in solutions suggested equilibrium between amphiphilic polyproline-*L*-helix (PPII) and an unfolded state (random coil, RC). We have performed detailed structural study employing solid state ¹⁹F-NMR and suggested PPII in lipid bilayers. However, ssNMR interpretation depends on the structural assumption and was ambiguous as multiple conformational states were co-present. CD is among very few methods potentially able to detect PPII and distinguish it from other conformational states, in particular from RC. Goal of the SRCD study was to get insight into ensemble conformational behavior of SAP by an independent structural method. To this aim, a series of chemically modified SAP analogues were prepared aiming systematic stabilization or destabilization of the PPII and evaluated in aqueous buffers and artificial membranes as a function of temperature. CD-observed conformational equilibria thereafter were established. This way, our experiments at ANKA complemented the solid state NMR structural study and laid basis for resolving the ambiguities of the latter analysis.

Experimental

SRCD spectra of SAP analogues were measured on the UV-CD12 beamline at the synchrotron facility of the Karlsruhe Institute of Technology (ANKA). The spectra were collected between 270 and 175 nm at 0.1 nm intervals. Measurements at 10 mg/ml concentration and for the lipid-containing samples were done in circular demountable 13 μm CaF₂ cell, while for lower concentrations (e.g. 0.5 mg/ml) circular suprasil® cuvettes with a 0.1 mm pathlength were used. Each spectrum was acquired in three successive scans, at a scan rate of 10 nm/min, which were averaged prior to baseline correction. Background spectra were measured analogously and material content of the cuvettes differed only in the absence of peptide. For the temperature-dependent measurements hard- and software developed by S. Roth at the UV-CD12 beamline were used. Parameters of the temperature control were taken as close as possible to the conventional CD measurements performed in parallel. Data processing was carried out using CDtool software from B. A. Wallace group.[2] The spectral deconvolutions were performed with DICHROWEB.[3]

Results

SRCD in addition to a much better signal-to-noise in the concentrated or potentially crowded samples allowed collecting UVCD data down to 178 nm for quantitative spectral analysis. At concentrations as high as 50 mM, SAP and its analogues were soluble in water and the CD signal did increase compared to lower concentrations. We did not observe precipitation or scattering increase as usually seen when the peptides aggregate in solution, which allowed us to challenge the literature statement of SAP forming fibrils in water as main prerequisite for its CPP function.[4]

The general temperature behaviour of the Pro-substituted samples in solution followed the common trend, normally interpreted in the systems with a RC/PPII equilibrium as an increase of the RC content in the cost of PPII reduction. Upon heating (5-55°C) the aqueous samples, all three peptides display coherent lowering of the intensities at 227 and 204 nm. In the solid state NMR experiments, however, we did observe the opposite trend – higher temperatures were needed to achieve detectable non-random coil contributions from fluorine-labeled SAP analogues. Therefore SAP peptides were measured in the lipid-bound state.

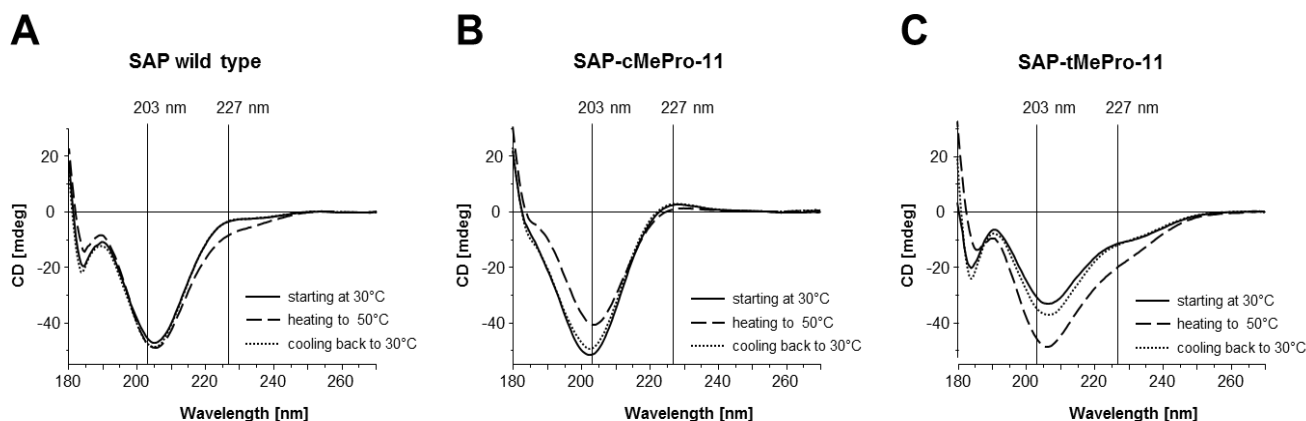


Fig. 1. UVCD of SAP and MePro-substituted analogues (containing *cis*- and *trans*-4,5-methanoprolines). Selected SRCD spectra from the temperature series (30°C, 35°C, 40°C, 45°C, 50°C; the series are collected in three consecutive heating/cooling cycles) of the peptides reconstituted in DMPC at a P/L 1/100 with 15 mg/ml total material concentration. (A) SAP wild type; (B) PPII-stabilized SAP-cMePro-11; (C) PPII-destabilized SAP-tMePro-11. Characteristic wavelengths of RC and PPII spectral contributions are marked for clarity.

The characteristic SRCD spectra in presence of a membrane are shown in Fig 1. Though general appearance of the CD spectra in all three peptides continued resembling RC/PPII mixtures, the equilibrium was shifted towards reduction of the PPII content. Furthermore, in all cases, heating to 50°C did reduce spectral features, associated with PPII and the initial equilibrium was possible to restore when the samples were set back to initial temperatures.

However, having collected UVCD signal in the 178-260 nm range we were able to deconvolute the spectra and estimate SAP conformational behaviour quantitatively. The analysis reveals non-neglectable contribution (in particular, β -structuring gave 27-35%, depending on the evaluation algorithm) from the non-RC/PPII conformations. Presence of other than PPII and RC conformations is very intriguing as at least for the β -strand and PPII mutual transformation is highly likely – both conformations are close to each other in the conformational space, and comparatively minor variation in structure (change in the single torsion angle φ , while PPII-to-RC needs asynchronous rotation around both backbone angles) is required for the transition.[5]

The data collected on CD12 beamline allowed us for the first time to suggest conformational plasticity being significantly pronounced in SAP, to disprove fibrilization of SAP in solution, to support structural analysis of membrane-bound SAP by solid-state NMR and to finally suggest a novel mechanism by which SAP interacts with lipid bilayers when realizing its CPP function.

Acknowledgements

We gratefully acknowledge Dr. J. Bürck, S. Roth and B. Posselt for the patronage at the beamline. CFN Project E1.2 and Land Baden-Württemberg (Landesgraduiertenförderung) are acknowledged for financial support.

References:

- [1] K.M. Wagstaff, D.A. Jans. (2006) *Curr. Med. Chem.* 13:1371-1387
- [2] J.G. Lees, B.R. Smith, F. Wien, A.J. Miles, B.A. Wallace. (2004) *Anal. Biochem.* 332:285-289
- [3] L. Whitmore, B.A. Wallace. (2008) *Biopolymers* 89:392-400
- [4] S. Pujals, J. Fernández-Carneado, C. López-Iglesias, M.J. Kogan, E. Giralt. (2006) *Biochim. Biophys. Acta* 1758:264-279
- [5] C.D. Syme, E.W. Blanch, C. Holt, R. Jakes, M. Goedert, L. Hecht, L.D.A. Barron. (2002) *Eur. J. Biochem.* 269:148-156

Differential accumulation of trace elements in human osteoblastic and chondroblastic osteosarcoma tissue

B. Pemmer⁽¹⁾, S. Smolek⁽¹⁾, M. Rauwolf⁽¹⁾, A. Maderitsch⁽¹⁾, C. Weixelbaumer⁽¹⁾, M. Foelser⁽¹⁾, A. Roschger⁽²⁾, C. Strelj⁽¹⁾, P. Wobrauschek⁽¹⁾, R. Windhager⁽³⁾, S. Lang⁽⁵⁾, R. Simon⁽⁴⁾, P. Roschger⁽²⁾, K. Klaushofer⁽²⁾, J.G. Hofstaetter^{(2), (3)}

(1) Atominstytut, Technische Universitaet Wien, Stationaltee 2, 1020 Vienna, Austria

(2) Ludwig Boltzmann Institute of Osteology at the Hanusch Hospital of WGKK and AUVA Trauma Centre Meidling, 1st Med. Dept., Hanusch Hospital, 1140 Vienna, Austria

(3) Department of Orthopaedic Surgery, Vienna General Hospital, Medical Univ. of Vienna, Austria

(4) Karlsruhe Institute of Technology, Institute for Synchrotron Radiation, Hermann-von-Helmholtz-Platz 1, D-76344 Eggenstein-Leopoldshafen, German

(5) Department of Pathology, Vienna General Hospital, Medical Univ. of Vienna, Austria

Introduction

Osteosarcoma is the most common primary bone malignancy and typically occurs during the adolescent growth spurt around the knee joint[1]. It is characterized by the production of tumor osteoid and immature bone matrix by malignant cells [2]. The current multidisciplinary approach in the treatment of osteosarcoma patients has significantly improved therapeutic outcome. With today's combination of chemotherapy and surgery long-term survival rates of more than 70% have been reported. However, very little is still known about the etiology of the tumor. In order to further improve treatment and to develop new treatment strategies it is pivotal to get more insight into the fundamental biology of the disease.

In recent years, the role of different minor and trace elements in various cancer types - e.g. breast cancer, prostatic carcinoma, has been studied by various groups [3-9]. These studies reported significant changes in the levels of certain trace elements, e.g. Zn, Cu and Fe, in cancer tissue. These metals bind to proteins - so called metalloproteins - that perform different biological and physiological functions [4]. In prostatic carcinoma for instance zinc (Zn) is decreased by 83% as compared to normal tissue [6]. In cancerous breast tissue a dramatic increase of median Zn, Cu and Fe values along with specific accumulation of these elements in the cancer tissue has been reported [5, 10].

However, very little is known about trace element levels and accumulations in osteosarcoma. Available data on blood serum levels of copper (Cu) and zinc (Zn) from patients with bone cancer show increased values for both elements (Cu: 1.5-fold, Zn: 1.2-fold) compared to healthy controls [11]. A study from 2001, using synchrotron radiation collimated by slits to 60x60 μm^2 , reported increased Cu and Zn values in the bone tumor tissue, with Zn values about 1.7-fold higher in the tumor than in normal tissue [12].

The concept of the experiment is to identify the lateral distribution of Zn, Fe and Ca in human osteosarcoma and to investigate if trace element levels and distributions are altered in the mineralized matrix of human osteosarcoma. Trace element levels will be compared to normal healthy bone adjacent to the tumor that was also removed during the surgical procedure

Experimental

Nine bone samples of human patients have been obtained following neoadjuvant chemotherapy and wide surgical resection at Dept. of Orthopaedics at Medical University of Vienna. The age range was 10 to 66 years and the tumor was always either in the proximal tibia or distal femur. Four samples have been identified as osteoblastic osteosarcomas and three as chondroblastic sarcomas and two as anaplastic osteosarcomas. The study was approved by the ethics committee at the Medical University.

A confocal SR μ -XRF setup, made up of two polycapillary half lenses with overlapping focal spots, has been installed at the Fluo beamline at ANKA. The beam size was $17 \times 10 \mu\text{m}^2$ and the depth resolution was $20 \mu\text{m}$ at 9.71 keV (Au-La). The excitation energy was set to 17 keV by a W/Si multilayer monochromator. The measuring time was set 2 sec./pixel for each map.

The areas of interest - malignant as well as healthy control bone tissue - were selected from the qBEI with respect to bone histomorphology. At these positions area scans in the sample surface were performed. The correct measurement plane for each sample area was determined by evaluation of depth scans in the area of interest. Elemental maps were obtained using the micro-XRF software package (spectrum fitting performed by AXIL) installed at the beamline. The element maps of Fe, Zn and Ca have then been clustered applying principal component analysis (PCA) and k-means clustering. The quantitative backscattered electron imaging (qBEI) data was used to correlate the obtained clusters with the healthy control tissue and the malignant tissue.

Results

Figure 1 shows the qBEI image and the element maps of an osteoblastic osteosarcom containing both, healthy control tissue (indicated as 1) and mineralized malignant tissue (2) respectively.

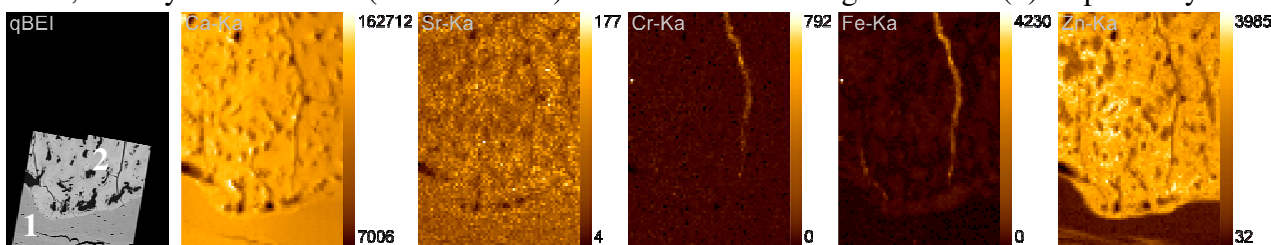


Figure 1: Sample TU1 - qBEI image and element maps of calcium (Ca), strontium (Sr), chromium (Cr), iron (Fe) and zinc (Zn) of a sample containing both, healthy (1) and malignant osteoblastic osteosarcoma tissue (2). Resolution: $17 \mu\text{m} \times 10 \mu\text{m}$ per pixel; Scan area: $1088 \mu\text{m} \times 950 \mu\text{m}$; Acquisition time: 2 sec. per pixel ; Normalized to cps and 100 mA ring current.

As it was already possible to identify increased intensities of Zn in the malignant calcified tissue compared to the healthy control bone matrix from the element maps (e.g. Figure 1) the detailed data evaluation confirmed this finding. The magnitude of Zn intensity increase shows a large variation between the different samples, with an average 6-fold increase of Zn in malignant calcified tissue. A correlation between Zn accumulation and the histological identified tumor type was not apparent (see Figure 2a).

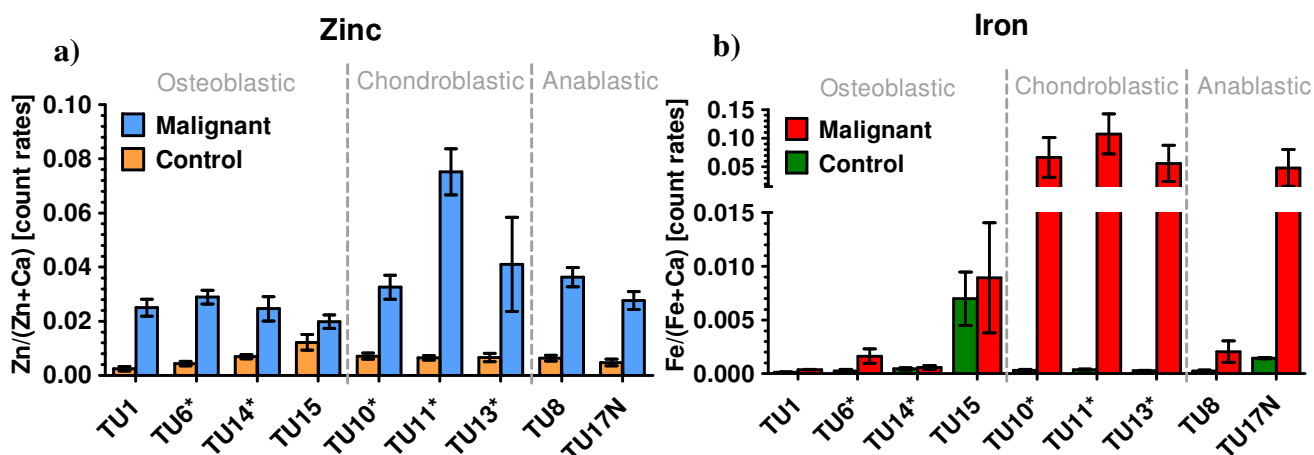


Figure 2: Values of Zn and Fe intensities normalized to calcium intensities in healthy bone tissue and mineralized malignant tissue. The results are categorised according to the histological diagnosis: high-grade (G3) osteoblastic osteosarcomas (osteoblastic), chondroblastic sarcomas (chondroblastic) and anaplastic osteosarcomas (anaplastic).

*) Samples have been measured during the previous beam time (BIO16). Data are shown for the sake of completeness.

As for Zn elevated levels of Fe have been found in the malignant calcified matrix compared to the control, with an average 70-fold increase of Fe in malignant calcified tissue.

Further more a strong correlation between cancer type and Fe accumulation was observed. The Fe increase in chondroblastic sarcoma is about 185-fold and 3-fold in osteoblastic osteosarcoma (data of the anaplastic osteosarcomas have been excluded).

The Fe accumulation may be further used to characterise the anaplastic osteosarcoma samples (TU8 & TU17N). Considering the Fe levels TU8 seems to be an osteoblastic osteosarcoma and TU17N a chondroblastic sarcoma.

Contaminations with Fe were inevitable since the use of steel tools in the sample preparation process is necessary. Typically the steel contamination are found in holes and cracks in the PMMA and can be identified through the coincidence of high Cr, Ni and Fe intensities, as can be seen in Figure 1 - the vertical crack in the right third. With help of these markers the contaminations could be easily excluded in the further data evaluation process.

These findings of differential accumulation of trace elements in normal and malignant bone samples may lead to new insights into basic tumor biology of osteosarcomas. However the cellular and molecular mechanisms leading to these accumulations are still unknown.

Acknowledgements

The ANKA Ångströmquelle Karlsruhe is acknowledged for the provision of beam time, and we would like to thank Dr. Rolf Simon for assistance using FLUO beamline.

The research leading to these results has received funding from Austrian Science Fund (FWF): P21905-N20.

References

1. Savage SA, Mirabello L. Using epidemiology and genomics to understand osteosarcoma etiology. *Sarcoma*. 2011;2011:548151. Epub 2011 Mar 8.
2. Kotz R, Salzer-Kuntschnik M., Lechner G et al: Knochentumoren. Stuttgart, Georg Thieme Verlag, 1984
3. Schwartz MK. Role of Trace Elements in Cancer. *Cancer Research* 1975;35(11 Part 2):3481-3487.
4. Al-Ebraheem, A., Goettlicher, J., Geraki, K., Ralph, S. and Farquharson, M. J. (2010), The determination of zinc, copper and iron oxidation state in invasive ductal carcinoma of breast tissue and normal surrounding tissue using XANES. *X-Ray Spectrometry*, 39: 332–337. doi: 10.1002/xrs.1272
5. Gupta SK, Shukla VK, Vaidya MP, Roy SK, Gupta S. Serum trace elements and Cu/Zn ratio in breast cancer patients. *Journal of Surgical Oncology* 1991;46(3):178-181.
6. Christudoss P, Selvakumar R, Fleming JJ, Gopalakrishnan G. Zinc status of patients with benign prostatic hyperplasia and prostate carcinoma. *Indian J Urol* 2011;27:14-8
7. Cortesi M, Fridman E, Volkov A et al. Clinical assessment of the cancer diagnostic value of prostatic zinc: A comprehensive needle-biopsy study. *The Prostate* 2008;68(9):994-1006.
8. Cortesi M, et al. Evaluating the cancer detection and grading potential of prostatic-zinc imaging: a simulation study. *Physics in Medicine and Biology* 2009;54(3):781.
9. Geraki K, et al. X-ray fluorescence and energy dispersive x-ray diffraction for the quantification of elemental concentrations in breast tissue. *Physics in Medicine and Biology* 2004;49(1):99.
10. Fisher GL, Byers VS, Shifrine M, Levin AS. Copper and zinc levels in serum from human patients with sarcomas. *Cancer* 1976;37(1):356-363.
11. Huang YY, Lu JX, He RG et al. Study of human bone tumor slice by SRXRF microprobe. *Nuclear Instruments and Methods in Physics Research Section A: Accelerators, Spectrometers, Detectors and Associated Equipment* 2001;467-468(Part 2):1301-1304.
12. Janssens K, Proost K, Falkenberg G, Confocal microscopic X-ray fluorescence at the HASYLAB microfocuss beamline: characteristics and possibilities. *Spectrochimica Acta Part B* 2004; 59(10-11):1637-1645.
13. Roschger P, Plenk H, Jr., Klaushofer K, Eschberger J 1995 A new scanning electron microscopy approach to the quantification of bone mineral distribution: backscattered electron image grey-levels correlated to calcium K alpha-line intensities. *Scanning Microsc* 9(1):75-86; discussion 86-78.

Study of the insertion and membrane orientation of the antimicrobial peptide Plantaricin149 and analogs by SRCD and O-SRCD

Jose Luiz Lopes, Leila M. Beltramini

University of Sao Paulo, Institute of Physics of Sao Carlos, Sao Paulo, Brazil

Introduction

Plantaricin149 (Pln149) is a linear cationic antimicrobial peptide, isolated from *Lactobacillus plantarum* NRIC149 [1-3] whose spectrum of inhibitory activity includes lactic acid bacteria, *Staphylococcus aureus*, *Pseudomonas aeruginosa*, *Saccharomyces cerevisiae*. The main purpose of our research with Pln149 is investigating its mechanism of action using model membranes in order to correlate with its bactericidal activity. Different inhibition assays were conducted with Pln149a showing its major ability to inhibit bacteria that contain high content of negatively charged phospholipid on cell membrane, which seems to be a feature shared with many other cationic antimicrobial peptides that present higher MIC values against Gram-positive bacteria. However, the activity of Pln149 against yeast suggests that different mechanism could be adopted by this peptide in front of zwitterionic lipids. O-SRCD and SRCD experiments were conducted with the intent of analyzing the secondary structure of the peptide in the presence of different anionic and zwitterionic lipids.

Short description of the main results

Oriented Synchrotron Radiation Circular Dichroism (O-SRCD) spectroscopy was employed with Plantaricin149 in different lipid films (zwitterionic and negatively charged phospholipids) composed of POPC, POPA, POPE, POPG were obtained in order to describe the orientation of the peptide on each film. The o-SRCD assays show that the antimicrobial peptide Pln149 is able to change from unordered to a helix conformation even on the presence of zwitterionic phospholipids (like POPC). This was a different behavior obtained for the peptide in solution, in which no conformational changes were observed on Pln149 in the presence of zwitterionic vesicles. Moreover, in the presence of the film, the peptide showed a surface orientation, facing the phospholipid head groups. This helix could perturb the integrity of cell membranes, by forcing a new packing of the lipids, and could be correlated with the disruption of the yeast cells.

In addition, analysis of the SRCD spectra of the peptide in the presence of membrane models composed of micelles of SDS, HPS and CTAB shows a strong dependence of the peptide to interact with negatively charged lipids.

Acknowledgements

We are grateful to Dr. Jochen Burck and Bianca Posset for assistance and help with the O-SRCD assays. This research was supported by FAPESP grants to JLSL and LMB.

References

- [1] Müller, DM; Carrasco, MS; Simonetta, AC; Beltramini, LM; Tonarelli, GG. A synthetic analog of plantaricin 149 inhibiting food-borne pathogenic bacteria: evidence for α -helical conformation involved in bacteria-membrane interaction. *J. Peptide Sci.* 13 (3), 171–178. 2007.
- [2] Lopes, JLS; Nobre, TM; Siano, S; Humpola, VM; Bossolan, NRS; Zaniquelli, MED; Tonarelli, G; Beltramini, LM. Disruption of *Saccharomyces cerevisiae* by plantaricin 149 and investigation of its mechanism of action with biomembrane model systems. *Biochim biophys acta biomembr*; 1788 (10): 2252-2258, 2009.
- [3] Lopes, JLS; Hissa, DC; Melo, VMM; Beltramini, LM. Interaction of antimicrobial peptide Plantaricin149a and four analogs with lipid bilayers and bacterial membranes. *Brazilian Journal of Microbiology*. 2014.

Complete Texture Analysis with Pole Figure Measurements close to the Absorption Edge

H. Klein, H. Sowa, L. Raue

Univ. Göttingen, GZG, Dept. of Crystallography, D-37077 Göttingen, Goldschmidtstr. 1

Theoretical background

The orientation distribution function $f(g)$ can be expressed as a series expansion using symmetrized spherical harmonic functions [1]. It can be split in an even and an odd part:

$$f(g) = f^e(g) + f^o(g) \geq 0 \quad (1)$$

Experimentally determined pole figures are the basis of this calculation (pole figure inversion). However, when measuring such pole figures it is not possible to distinguish between $[hkl]$ and $[-h-k-l]$ directions, either because of a centre of symmetry or as a consequence of Friedel's law. This involves that the calculation of texture $f(g)$ does not contain series terms of odd order.

From pole figures only coefficients of the series expansion of even order can be determined, although the odd ones are in general not zero. This leads to a falsification of the orientation distribution function known as the "ghost" phenomenon [2]. To solve the "ghost" problem many methods were suggested [3].

In the case of noncentrosymmetric materials Friedel's law may be broken by anomalous scattering in the vicinity of an absorption edge [4]. Therefore, it should be possible to determine the contribution of the odd-order terms $f^o(g)$ from polycrystal diffraction experiments [5].

The series expansion of the pole figures is similarly split into even and odd parts respectively, as the orientation distribution function $f(g)$ is in eq.1:

$$P_{hkl}^e(\alpha\beta) = \frac{1}{2}(P_{hkl}(\alpha\beta) + P_{hkl}(\pi - \alpha, \pi + \beta)) \quad (2)$$

$$r \cdot P_{hkl}^o(\alpha\beta) = \frac{1}{2}(P_{hkl}(\alpha\beta) - P_{hkl}(\pi - \alpha, \pi + \beta)) \quad (3)$$

Where α, β are the pole figure angles and

$$r = (\varphi_{hkl} - \varphi_{-h-k-l}) \quad (4)$$

φ_{hkl} is the Bijvoet ratio [6]. Hence, the pole figure corresponding to the true texture is then obtained by

$$P_{hkl}(\alpha\beta) = P_{hkl}^e(\alpha\beta) + P_{hkl}^o(\alpha\beta) \quad (5)$$

It is, however, necessary that only such pole figures are used for the determination of the odd part of the texture function for which $F_{hkl} \neq F_{-h-k-l}$ (Bijvoet pairs) – the direction $[hkl]$ must not run perpendicular to a mirror plane or a twofold axis of the crystal symmetry.

Experiment at ANKA

We used the Kappa-goniometer at beam line PDIFF equipped with a Princeton Instruments area detector, the beam-size was 0.5 mm x 0.5 mm. In order to perform measurements using wavelength close to the absorption edge of the investigated material, the first step was to adjust the energy for the samples. This was done using a LaB₆-standard. We intended to examine three different textured samples: ZnO, InAs and NiS. These samples show acentric symmetry and the absorption edges are in the energy range of this beam-line: Zn: 9.68 eV, As: 11.9 eV, Ni: 8.36

eV. Due to the strong crystallographic orientation of the samples, it was very time-consuming to determine the exposure time for each diffraction image. The pole figure measurement was first done using the φ -rotation of the diffractometer in 0.3° steps in the range $0^\circ \leq \varphi \leq 360^\circ$ [6]. It has been shown that it was necessary to use a smaller step size to receive the maxima of the poles. For our experiments we get 48 hours and we found that 24 hours were not sufficient to measure a set of pole figures even of one sample. Additionally, we had to deal with a large beam loss, so we could measure only the ZnO-sample. Further measurements could not be performed because of the breakdown of the storage ring.

It has shown at the data evaluation, that a lot of detector images could not be used, because of a very small background to peak relationship. Fortunately, we got beam-time at DESY Hamburg. There we successfully measured some pole figures close to the absorption edge. Fig.1 shows exemplarily some of these pole figures, they show clearly differences in intensities of the poles referring to the Bijvoet pairs.

Summarizing it is to say: the beam-line PDIFF could be very well suited for our experiments given that there is a longer measurement time and a more sophisticated detector. The support given by the beam-line scientist (Dr. Stephen Doyle) was extremely excellent.

References

- [1] Bunge, H.J. (2003). Texture Analysis in Materials Science, 2. Ed.. Cuvillier Verlag Göttingen.
- [2] Matthies, S. (1979). Phys. Stat. Sol. B **92**, K135-K138.
- [3] Hirsch, J. & Lücke, K. (1987). In: Theoretical Methods of Texture Analysis, Ed.: H.J. Bunge. DGM-Informationsgesellschaft Verlag Oberursel.
- [4] Bijvoet, A.J. (1951). Nature **168**, 271-272.
- [5] Bunge, H.J. & Esling, C. (1981). J. Appl. Cryst. **14**, 253-255.
- [6] H. Klein (2009). Adv. Eng. Mat. **11**, 6, 452-458.

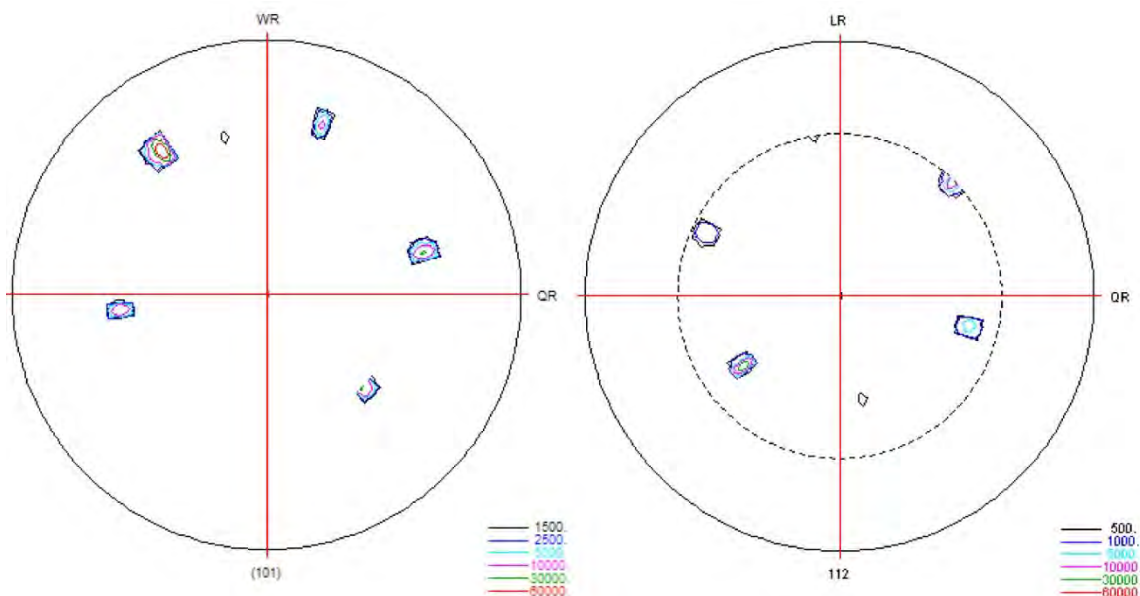


Fig.1. Pole figures of ZnO measured at the absorption edge. a) (101)-Pole figure, b) (112)-Pole figure

New low band gap polymers: orientation and self-organization properties

U. Aygül¹⁾, U. Dettinger¹⁾, D. Batchelor²⁾, S. Mangold²⁾, H. Peisert¹⁾, T. Chasse¹⁾

¹⁾ Institut für Physikalische und Theoretische Chemie, Universität Tübingen, Auf der Morgenstelle 18, 72076 Tübingen, Germany

²⁾ Karlsruher Institut für Technologie, Institut für Synchrotron Strahlung, 76021 Karlsruhe, Germany

Introduction:

Due to threats of rising energy costs and global warming Organic Photo Voltaics (OPVs) is a very attractive market for the next decade. Their flexibility, potential to tailor chemistry and structure, to different needs is desirable compared to their more efficient but environment unfriendly inorganic counterparts. The chief disadvantages of plastic solar cells are their short lifetime together with efficiency. In polymer-based “bulk heterojunction”-type (BHJ) solar cells, so-called “low bandgap” (LBG) materials, with alternating electron-deficient and electron-rich subunits, are promising donor components in the active layers [1]. Such materials may be able to improve the efficiency of OPV devices by increased absorption of the visible solar spectrum and also through optimization of the offset of the LUMO (lowest unoccupied molecular orbital) energy levels of the donor and acceptor. Use of these new materials requires in addition to a detailed understanding of the electronic properties knowledge of the orientation of the film. This is naturally important to thin film technology as orientation (tilt and azimuth) and film texture controls parameters such as mobility and so on, which are important for device efficiency and operation.

In our recent beamtime at ANKA we have demonstrated that NEXAFS (Near Edge X-Ray Absorption Fine Structure) is an ideal technique well-suited to investigate the bulk orientation of moderately thin films. The method provides additional and complementary information to that which has already been obtained with X-Ray diffraction studies [2]. Even applying doctor blade casting (Fig. 1), a relatively simple film preparation route from solution (which is essential for the cost efficiency of OSCs), a high degree of ordering was observed by NEXAFS for the state-of-the-art polymer P3HT and the LBG polymer PCBDTBT, whereas another LBG polymer (PCPDTQ) is mainly disordered [3].

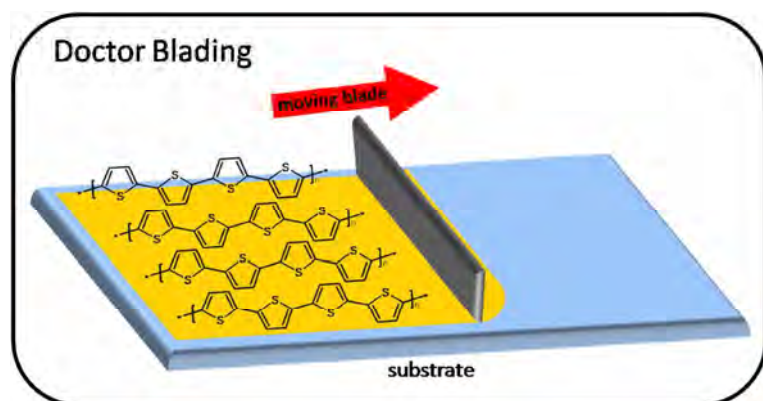


Fig.1: Schematic setup of doctor blade casting, applied for the preparation of the thin polymer films.

Obviously both the chemical and geometrical structure of the polymers determines the ability for their self-organization. Therefore we extend the studies to another model LBG polymer (PCPDTBBT, Fig. 2) available via cooperation with the synthesis group of Prof. Scherf (Wuppertal) and Konarka GmbH, supported by DFG (CH 132/24-1). Further, first measurements were carried out on blends of the active organic donor materials and the acceptor PCBM, as applied in BHJ solar cells. Chemical structures of all compounds are shown in Fig. 2. The effect of annealing on the orientation of such blends is investigated.

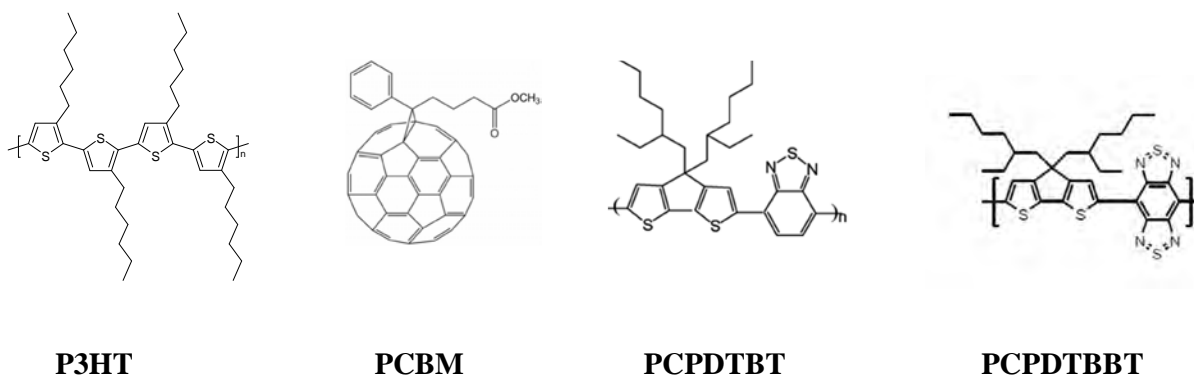


Fig. 2: Chemical structures of investigated compounds: the state of the art donor polymer P3HT, the acceptor molecule PCBM and the new low bandgap polymers PCPDTBT and PCPDTBBT

Experimental details:

Polymer films were prepared ex-situ by doctor blade casting and stored under well-defined ambient conditions. Annealing was carried out in dark and under N_2 -atmosphere. NEXAFS experiments were carried out at the XAS beamline. The beamline was usually set to an energy resolution of 300 meV and a polarization degree of > 0.95 . X-ray absorption spectra were measured in fluorescence yield mode.

Results:

PCPDTBBT:

In Fig. 3 S 1s XAS spectra of thin films of the new low bandgap polymer PCPDTBBT on ITO are displayed as a function of the angle θ between the sample surface and the electric field vector of the p-polarized synchrotron light (see inset). In a planar π conjugated carbon system the excitation from S 1s to a π^* orbital is allowed for E vertical to the molecular plane (parallel to $2p_z$), whereas the transition to σ^* is allowed for E parallel to the molecular plane and to the chemical in plane bond. The intense lower energy features *in Fig. 3* ($E < 2478$ eV) represent the π^* resonances, which are analyzed to determine the geometry. For clarity not all angles are shown. The observed intensity changes indicate the tendency for self-organization of PCPDTBBT and the presence of a preferred molecular orientation. However, the relatively small intensity variation compared to P3HT and PCPDTBT [3] point to a lower degree of ordering. The annealing of the sample causes apparently only minor changes.

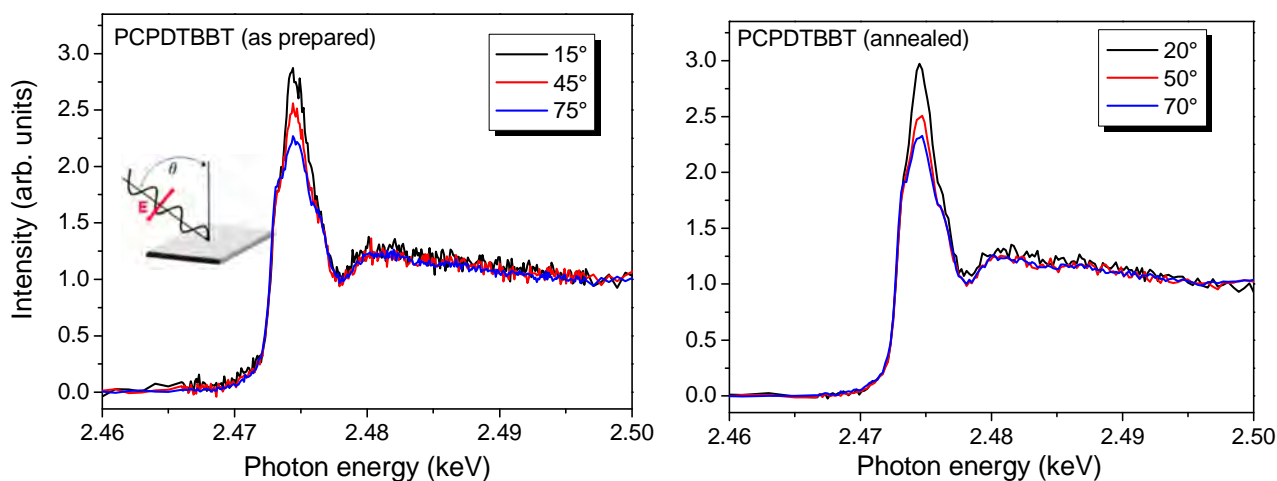


Fig. 3: Series of S1s excitation spectra of an “as prepared” PCPDTBBT film at room temperature (left) and after annealing (right) as a function of θ . An angle dependence is visible for PCPDTBBT.

On the other hand, as discussed in particular for PCPDTBT [3] the polarization of the transitions between 2470 and 2477 eV may contain beside the expected out of plane character also in plane contributions, and thus detailed calculations of the electronic structure seem to be necessary for an exact prediction of the molecular orientation and a detailed peak fit is necessary to distinguish between the two sulfur species.

P3HT/PCBM:

Angle dependent S 1s XAS spectra of the P3HT/PCBM blend film before and after annealing are shown in Fig.4 (not all measured angles shown). The angular dependence of the S 1s absorption edge is clearly visible in both cases.

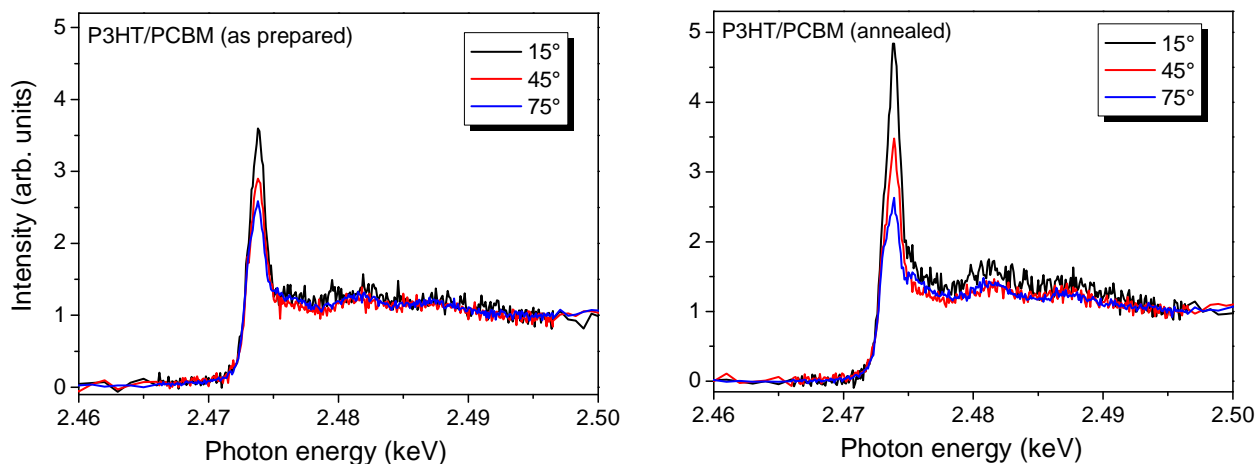


Fig. 2: Series of S1s excitation spectra of a pristine (left) and an annealed (right) P3HT/PCBM blend films on ITO as a function of the angle θ between the sample surface and the electric field vector of the p-polarized synchrotron light (see inset). The lower energy features ($E < 2478$ eV) represent the π^* resonances, which are analyzed to determine the geometry.

The maximum intensity for the S 1s $\rightarrow \pi^*$ excitation peak (circa 2473 eV) is observed at normal incidence and decreases with increasing angle θ (see inset of Fig 3) revealing an edge-on orientation of the thiophene-subunits. Compared to pristine P3HT [3] the angular dependency of the as prepared P3HT/PCBM blend is less pronounced. This means that the orientation of the thiophene units is disturbed by adding the acceptor molecule PCBM. However after the annealing the intensity range increases and the angular dependency of the S 1s $\rightarrow \pi^*$ excitation peak is now comparable to pristine P3HT.

Thus, annealing is an essential step in the sample preparation of “bulk heterojunction”-type solar cells, as the orientation of the polymer is improved. NEXAFS is an ideal technique for the study of the orientation and self-organization properties in particular for blends since the domain size of BHJ solar cells is usually less than a few 10 nm.

Acknowledgement

Technical support by W. Neu is gratefully acknowledged. For financial support we thank the German Research Council (CH 132/24-1). ANKA Angströmquelle Karlsruhe is acknowledged for the provision of beamtime. We thank Konarka GmbH for supplying us with P3HT and U. Scherf (University of Wuppertal) for supplying us with PCPDTBBT.

References

- [1] a) M. Morana, M. Wegscheider, A. Bonanni, N. Kopidakis, S. Shaheen, M. Scharber, Z. Zhu, D. Waller, R. Gaudiana, C. Brabec, *Adv. Funct. Mater.* **18** (2008) 1757; b) C. Soci, I.-W. Hwang, D. Moses, Z. Zhu, D. Waller, R. Gaudiana, C. J. Brabec, A. J. Heeger, *Adv. Funct. Mater.* **17** (2007) 632.
- [2] a) H. Sirringhaus, P. J. Brown, R. H. Friend, M. M. Nielsen, K. Bechgaard, B. M. W. Langeveld-Voss, A. J. H. Spiering, R. A. J. Janssen, E. W. Meijer, P. Herwig, D. M. de Leeuw, *Nature* 1999, 401, 685. b) J. F. Chang, B. Q. Sun, D. W. Breiby, M. M. Nielsen, T. I. Solling, M. Giles, I. McCulloch, H. Sirringhaus, *Chem. Mater.* 2004, 16, 4772.
- [3] U. Aygül, D. Batchelor, U. Dettinger, H. Peisert, T. Chassé, *J. Phys. Chem. C* **116** (2012) 4870–4874.

Report on the flexible compatible SRCL instrument at TopoTomo

Y. Cheng^{1),2)}

¹⁾ANKA, Institute for Synchrotron Radiation, Karlsruhe Institute of Technology (KIT),
Hermann-von-Helmholtz-Platz 1, D-76344 Eggenstein-Leopoldshafen, Germany

01-12-2011

The Aim

The motivation of this experiment was to build up the laminography instrument at TopoTomo. With the help of the first testing experiment at July, see report [1], this time we are on the purpose of searching for a new way to realize laminography which will be more flexible and easier built-up.

Experimental Description

Set-up was constructed as Figure 1. A rotation stage vertically sits on a large z-translation tower. The sample rotation then sits on an arm which is fixed to the vertical rotary stage.

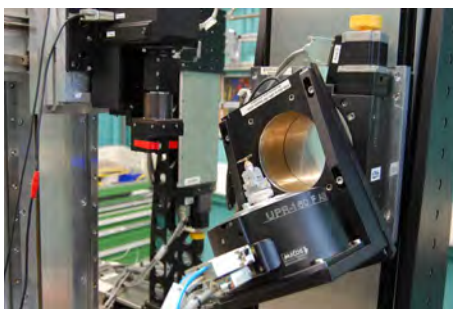


Figure 1: *New design of SRCL at TopoTomo.*

The advantages of this design are:

1. It is flexible to switch between tomography and laminography. (Original it has been used for tomography at topotable).
2. A large range of the inclined angle can be reached. The accessible tilted angle is only limited by the sample height upon the sample rotation stage.
3. Much more less components are needed to build it up. Easy to mount/unmount, easy to align, and easy to reach the height of the beam.

However, there are also things that need to be solved/improved for this design:

1. The limited space upon the sample rotation stage enormously restricts the acceptance for very large samples.
2. There is lack of a big rotation axis which is necessary to align the tilting axis perpendicular to the beam.
3. Automatic sample Regions of interest positioning should be foreseen. (Currently the sample positioning is done by manually adjusting the goniometer head).

Results

A micro-chip has been scanned and reconstructed (Figure 2) to prove the design. Nickel ball has been used for caculating the laminographic angle.

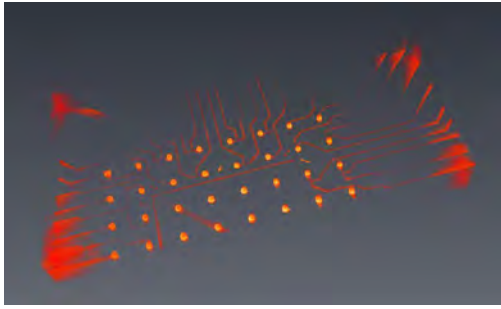


Figure 2: 3D rendering of a SRCL scan of micro solder bumps on flip chip at TopoTomo. Resolution $6.71\mu\text{m}$.

Conclusion and Outlook

Such multifunctional, quick build-up solution is very welcome at TopoTomo. It fulfills combination of tomography and laminography and easy alignment procedures. Most of the motor and axes precisions still need to be measured/tested.

Acknowledgements

The ANKA Ångströmquelle Karlsruhe is acknowledged for the provision of beamtime, and we would like to thank P. Vagovic for assistance using beamline, H. Schade for mechanics support, S. U. for electronics supports.

References

- [1] Y. Cheng. Technical report.

Characterization of oxide layers thermally grown on FeCrAl- based model alloys during exposure to heavy liquid metals

A. Jianu¹, A. Weisenburger¹, R. Fetzner¹, A. Heinzl¹, G. Müller¹, S. Doyle²

¹Karlsruhe Institute of Technology, Institute for Pulsed Power and Microwave Technology, Hermann-von-Helmholtz-Platz 1, D-76344 Eggenstein-Leopoldshafen, Germany

²Karlsruhe Institute of Technology, Institute for Synchrotron Radiation, Hermann-von-Helmholtz-Platz 1, D-76344 Eggenstein-Leopoldshafen, Germany

The use of heavy liquid metals (HLM), namely lead or lead-based alloys, in energy-related applications is currently under consideration because of their beneficial thermal and neutronic properties. However, HLM compatibility with structural steels, in terms of corrosion and mechanical resistance, causes considerable concern.

FeCrAlY coatings, deposited by plasma spraying and subsequently re-melted using pulsed electron beam (GESA process), are proposed for protecting steels against corrosion attack, when exposed to HLM containing small amounts of oxygen. The protection is provided by a thin, continuous alumina surface layer, grown during the exposure. The development of such layer requires a certain minimal Al content since selective Al oxidation occurs.

The first results of a systematic study concerning the corrosion behaviour of Fe-Cr-Al model alloys during their exposure to oxygen-containing (10^{-6} wt.%) lead in the temperature range 400–600 °C were published this year in Journal of Nuclear Materials [1]. In addition, communications related to this study were submitted and accepted at two major European conferences, which will be held in September 2013: EUROCORR and EUROMAT [2, 3].

The results of the evaluation of the Fe-Cr-Al specimens using characterization techniques (X-ray diffraction using conventional and synchrotron radiation at PDIFF beam line, scanning electron microscopy and X-ray photoelectron spectroscopy) were summarised in an oxide map, illustrating the stability domain of alumina, grown on Fe-Cr-Al-based alloys when exposed to molten, oxygen-containing lead (Fig.1).

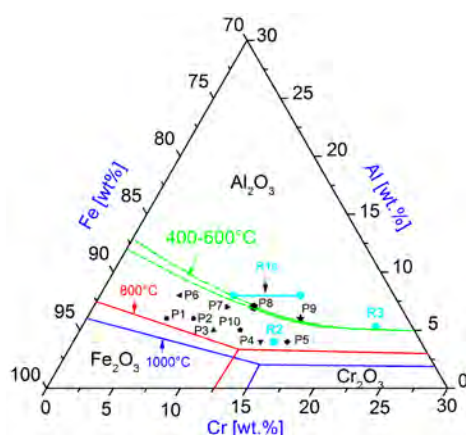


Fig. 1: Oxide map for the oxidation of Fe-Cr-Al-base model alloys exposed to oxygen containing molten lead in the temperature range 400 – 600 °C

The map includes also additional points (R1, R2 and R3) extracted from literature, corresponding to alumina forming alloys when exposed to HLMs, which fit very well with our findings. Chromium and aluminium contents of 12.5–17 wt.% and 6–7.5 wt.%, respectively, are high enough to obtain thin, stable and protective alumina scales on Fe-Cr-Al alloys, exposed to oxygen-containing lead at 400, 500 and 600 °C. Two alumina polymorphs were found to form

the protective scale: κ - Al_2O_3 at 400°C and 500°C and θ - Al_2O_3 at 600°C. No area with detached scale was observed and no trace of α - Al_2O_3 was detected.

It is known that the addition of some reactive elements (RE), such as Y, Zr and Hf, is responsible for the improvement of the stability and of the adherence of alumina scale formed on Fe-Cr-Al – based alloys, during the exposure in oxygen-containing atmosphere. However, the behaviour of Fe-Cr-Al-RE alloys during the exposure to HLMs, containing very small amounts of dissolved oxygen, is scarcely documented.

Based on the conclusions of the first part of our research activities (Fig. 1), eight new alloys containing Y were prepared and exposed to molten lead up to 5700 hours: $\text{Fe}_{78,5}\text{Cr}_{16}\text{Al}_6\text{Y}_{1,5}$; $\text{Fe}_{74,5}\text{Cr}_{16}\text{Al}_8\text{Y}_{1,5}$; $\text{Fe}_{76,5}\text{Cr}_{16}\text{Al}_6\text{Y}_{1,5}$; $\text{Fe}_{78,5}\text{Cr}_{12}\text{Al}_8\text{Y}_{1,5}$; $\text{Fe}_{82,5}\text{Cr}_9\text{Al}_7\text{Y}_{1,5}$; $\text{Fe}_{77,5}\text{Cr}_{14}\text{Al}_7\text{Y}_{1,5}$; $\text{Fe}_{76}\text{Cr}_{16}\text{Al}_8$; $\text{Fe}_{80}\text{Cr}_{12}\text{Al}_8$.

The surface morphology of all specimens was evaluated using SEM (Fig.2a). Selected specimens were also evaluated in June 2013 at PDIFF beamline (Fig. 2b).

XPS evaluation of the specimens is under way and will be corroborated with the results obtained from GI-XRD and SEM.

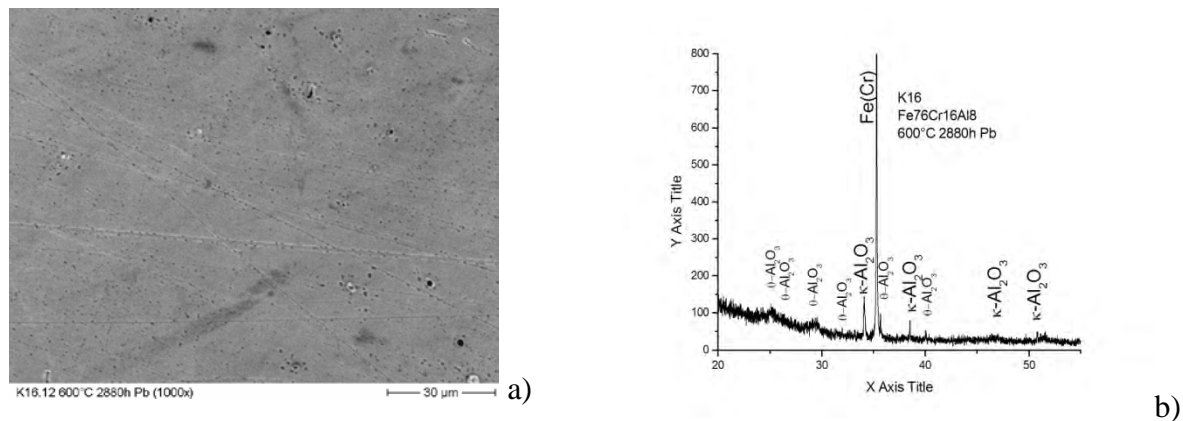


Fig. 2: Surface morphology (SEM - a) and XRD pattern (GI-XRD - b) of a multilayered Al_2O_3 scale grown during 2880h exposure to molten Pb, at 600 °C.

Acknowledgments

Financial support by GETMAT (FP7-212175) and LEADER (FP7-249668) within the EU-7th Framework program is gratefully acknowledged.

- [1] Oxide scales formed on Fe-Cr-Al - based model alloys exposed to oxygen containing molten lead, A. Weisenburger, A. Jianu, S. Doyle, M. Bruns, R. Fetzer, A. Heinzl, M. DelGiaco, W. An, G. Müller, J. of Nuclear Materials, 437 (2013) 282–292
- [2] FeCrAl-based coatings for improving corrosion resistance of steels exposed to molten Pb, A. Jianu, A. Weisenburger, R. Fetzer, M. Bruns, S. Doyle, A. Heinzl, G. Müller, oral presentation at EUROCORR2013.
- [3] Critical Al content required to form a protective alumina layer on Fe-Cr-Al alloys exposed to oxygen-containing molten lead, Adrian Jianu, Georg Mueller, Renate Fetzer, Annette Heinzl, Alfons Weisenburger, Ionelia Voiculescu, Victor Geanta, poster presentation at EUROMAT2013

Luminescence, patterned metallic regions and photon mediated structural changes in half fluorinated graphene sheets.

Andrew L. Walter^{1,2,3}, Hasan Sahin⁴, Ki-Joon Jeon⁵, Aaron Bostwick¹, Seyda Horzum⁴, Roland Koch⁶, Florian Speck⁶, Markus Ostler⁶, Peter Nagel⁷, Stefan Schuppler⁷, Michael Merz⁷, Luca Moreschini¹, Young Jun Chang⁸, Thomas Seyller⁹, Francois M. Peeters⁴, Karsten Horn², Eli Rotenberg¹

¹ Advanced Light Source (ALS), Lawrence Berkeley National Laboratory, Berkeley, California 94720, USA.

² Dept of Physical Chemistry, Fritz-Haber-Institut der Max-Planck-Gesellschaft, 14195 Berlin, Germany.

³ Donostia International Physics Centre, 20018 Donostia, San Sebastian, Spain.

⁴ Department of Physics, University of Antwerp, Groenenborgerlaan 171, B-2020 - Antwerpen, Belgium.

⁵ Department of Environmental Engineering, INHA University, Incheon, 402-751, Korea

⁶ Lehrstuhl für Technische Physik, Universität Erlangen-Nürnberg, 91058 Erlangen, Germany.

⁷ Karlsruhe Institute of Technology (KIT), 76344 Eggenstein-Leopoldshafen, Germany.

⁸ Department of Physics, University of Seoul, Seoul, 130-743, Korea.

⁹ Institut für Physik, Technische Universität Chemnitz, Reichenhainer Strasse 70, 09126 Chemnitz, Germany

Single-sided fluorination has been predicted to open an electronic band gap in graphene and to exhibit unique electronic and magnetic properties; however, this has not been substantiated by experimental reports. Our comprehensive experimental and theoretical study of this material on a SiC(0001) substrate shows that single-sided fluorographene (S-FG) exhibits two phases, a stable one with a band gap of ~ 6 eV and a metastable one, induced by UV irradiation, with a band gap of ~ 2.5 eV. The metastable structure, which reverts to the stable “ground-state” phase upon annealing under emission of blue light, is in our view induced by defect states, based on the observation of a nondispersive electronic state at the top of the valence band, not unlike that found in organic molecular layers. Our structural data show that the stable C_2F ground state has a “boat” structure, in agreement with our X-ray magnetic circular dichroism data, which show the absence of an ordered magnetic phase.

The single-sided fluorinated graphene studied here is prepared from epitaxial graphene grown on SiC(0001) and converted into quasi-freestanding graphene by hydrogen intercalation. Samples are then exposed to XeF_2 in a reaction chamber at elevated temperatures. The fluorine 1s core level photoemission line has only a single component, signalling a single adsorption site, while the carbon 1s line has several contributions, from the SiC substrate and the carbon atoms in the graphene layer. Fluorination gives rise to long-range ordered structures on the surface, as shown in the STM image in Figure 1; it displays a ridge-like structure, formed by adjacent fluorine atoms separated through valleys formed by fluorine-free carbon atoms in the “boat” phase, schematically shown in Figure 1.

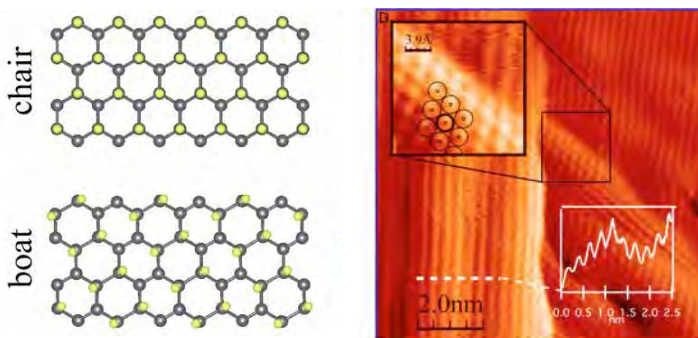


Figure 1: Model of the chair and boat conformations of S-FG (left). STM image ($U_{bias} = 2.5$ V, $I_{tip} = 1$ nA) from S-FG on H/SiC. The white inset shows a line profile taken from the thick white line, indicating the 2.5 Å height oscillations.

Conversion of pristine graphene into S-FG induces massive changes in the valence level electronic structure, as shown by the angle-resolved photoemission data in Figure 2. The linearly dispersing π states that cross at the K point, distinctive of pristine graphene, are removed and a set of strongly dispersing bands extends from about 3.5 eV down to around 12 eV. The uppermost band (~ 2 eV) is quite dispersionless across the entire Brillouin zone. The lower, strongly dispersing, bands are due to the in-plane bonds, and our DFT calculations demonstrate that the bands are quite different for the chair and boat conformation; the band gap of the boat phase is considerably larger. The -2eV dispersionless band is a result of photon mediated defect states as described in Ref 1.

Hydrogenated and fluorinated graphene have been intensely studied with a view to magnetic properties in metal-free compounds, and the question of whether half-fluorinated graphene exhibits a magnetically ordered phase has been debated. We have investigated the possible magnetic properties of half-fluorinated graphene using X-ray magnetic circular dichroism (XMCD) measurements of the C 1s and F 1s edges (Figure 3). These data show no appreciable dichroism signal at temperatures of 10 K and magnetic fields up to 3 T, which indicates a very small orbital long-range ferromagnetic moment; an analysis of the dichroism signals gives an upper limit to the magnitude of the orbital magnetic moment of 0.04 and 0.05 μ_B for C and F atoms, respectively. While a large spin magnetic moment cannot be excluded from these measurements, we conclude from the ARPES measurements and the XMCD experiments that the boat conformation of S-FG is a nonmagnetic semiconductor.

1. A.L.Walter et al., ACS Nano, in press.

Acknowledgments. The Advanced Light Source is supported by the Director, Office of Science, Office of Basic Energy Sciences, of the U.S. Department of Energy under Contract No. DE-AC02-05CH11231. This work was supported by the ESF and the DFG through the EUROCORES program EuroGRAPHENE. We gratefully acknowledge the Max-Planck Institute for Intelligent Systems Stuttgart for use of their XMCD end station at WERA, and the ANKA Ångströmquelle Karlsruhe for the provision of beamtime. K.J.J. acknowledges support from an INHA University Research Grant (INHA-47292). H.S. and F.M.P. were supported by the Flemish Science Foundation (FWO-VI), and the Methusalem Foundation of the Flemish government. H.S. is supported by an FWO Pegasus Marie Curie Fellowship.

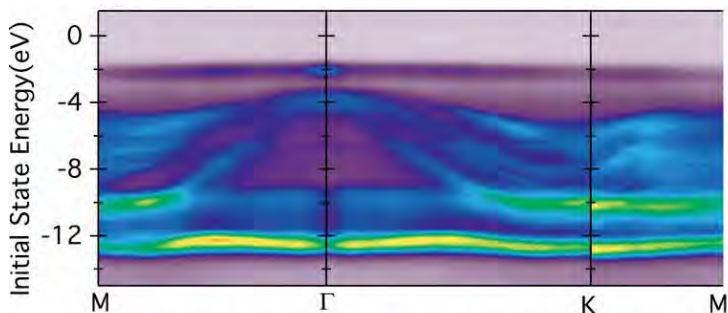


Figure 2: Valence band photoemission images from S-FG, showing the nondispersing states at ~ 2 eV binding energy, and the dispersing bands due to in-plane bonding.

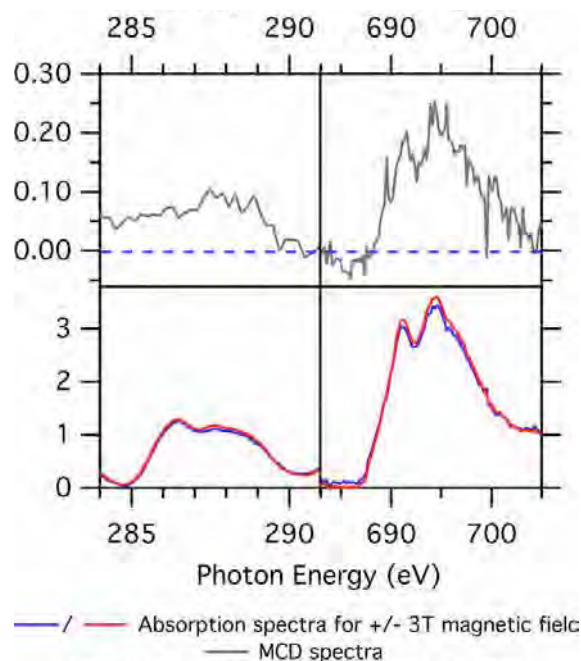


Figure 3: XMCD data obtained at the carbon 1s and fluorine 1s edges on a S-FG sample. Bottom: absorption spectra for a magnetic field parallel (red) and anti-parallel (blue). Top: circular dichroism plots.

In-situ Radiography of an Emulsification Process

T. Farago¹⁾, T. Dos Santos Rolo¹⁾, A. Hensel²⁾, M. Kraut²⁾

¹⁾ Karlsruhe Institute of Technology, Institute for Photon Science and Synchrotron Radiation, Hermann-von-Helmholtz-Platz 1, D-76344 Eggenstein-Leopoldshafen, Germany

²⁾ Karlsruhe Institute of Technology, Institute for Micro Process Engineering, Hermann-von-Helmholtz-Platz 1, D-76344 Eggenstein-Leopoldshafen, Germany

Experimental results

The aim of the experiment was to determine the imaging possibilities for studying an emulsification process at a synchrotron light source. Then, if possible, we were interested in the properties of the emulsification process in terms of droplet break up and formation.

We found that the diodomethane and water solution yields very good contrast for high-speed absorption radiography. However, the emulsification device was not optimized for X-ray radiation in terms of absorption so we were unable to record images at more than 5000 frames per second (FPS) with reasonable signal to noise ratio and pixel size 3.7 μm . We could have used larger pixels but then the spatial resolution would not suffice for process observation.

The speed of the stream recorded at 5000 FPS was too fast for image analysis (displacement in the order tens of pixels per frame). However, we were able to observe the jet elongation along its way in the. Thus, after using a device optimized for X-ray imaging we expect to be able to observe the process with imaging quality sufficient for data analysis.

Future plan

Our plan is to develop a device with as small projected thickness as possible in order for it not to absorb too much X-ray radiation, but strong enough to sustain the pressure of the liquid inside and to resist the radiation damage. After such a device is designed and manufactured, we would like to continue with this experiment. Namely, we will verify the imaging quality in terms of temporal and spatial resolution and that it suffices to observe the process. We also want to continue in improving the sample setup in terms of controlling the environment in an automated and reliable way, i.e. we need to be able to set the flow rate with high precision and keep it constant in order to match the measured and imaged results. After this step we can employ optical flow algorithms in order to track the droplets during their formation and break up processes.

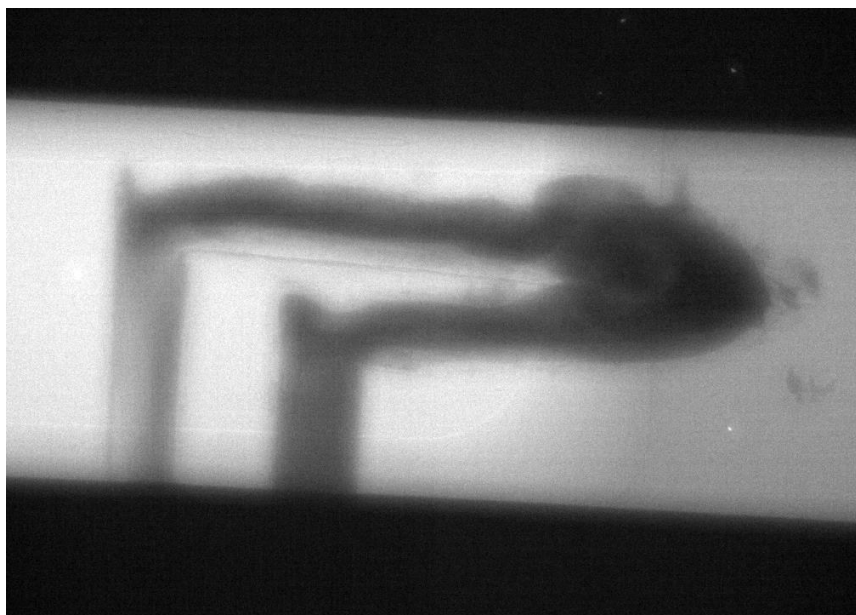


Figure 1: The emulsifier with oil flow

Structural investigation of isotopically enriched silicon multilayers

S. Eon¹⁾, H. Bracht¹⁾, D. Isenmann²⁾ and A. Plech²⁾

¹⁾ University of Münster, Institute of Materials Physics, Wilhelm-Klemm-str. 10, D-48149 Münster, Germany

²⁾ KIT, Institute for Photon Science and Synchrotron Radiation, Hermann-von-Helmholtz-Platz 1, D-76344 Eggenstein-Leopoldshafen, Germany

Purpose of the experiment

A manipulation of the thermoelectric properties of materials can be done by introducing interfaces, which change the thermal transport behavior [1]. For instance, in order to generate electrical power from existing heat gradients a material with high Seebeck coefficient, but low thermal conductivity is required. Thus the thermoelectric figure-of-merit can be maximized.

In spite of complicated materials it is also envisaged to use silicon as thermoelectric material. Unfortunately its thermal conductivity is very high at room temperature, which makes it a good thermoelectric material only at elevated temperature. It is desirable to modify independently the thermal conductivity from other material parameters, such as electrical conductivity. We explore the usage of silicon multilayer structures, which are characterized by alternating layers of different isotopes of silicon [2]. Electronically these layers can be regarded as bulk material, as the band structure is hardly affected by the isotope effect. At the same time the thermal transport will be affected by the presence of interfaces with acoustic impedance (coming from the different phonon energies of the sublayers). This opens up possibilities to decouple both conductivities. A recent approach to measure thermal conductivity is to follow laser-induced temperature decays as function of time. The so-called time-domain thermoreflectance [3] uses the temperature-related refractive-index change of a thin aluminum film on top of the nanostructure in question, while recently also time-resolved X-ray scattering became an appropriate tool for sensing of heating kinetics.

Heat conduction is in such an approach not only governed by the material beneath a thin metal film transducer, but also by the efficiency of heat crossing the film-substrate interface (thermal interface resistance TIR). It has been found that different coating techniques produce a strongly differing TIR, which can bias the evaluation of thermal conductivity strongly. In the present experiment we tried to elucidate the origin of these discrepancies. For that reason several films of gold were grown on top of a silicon wafer. These films were analysed at the SCD beamline with X-ray reflectivity (XRR) and diffraction. Furthermore experiments were conducted to measure the laser-induced heating and cooling of these films as function of time with 100ps time resolution (ESRF, beamline ID9b).

Technical setup

Gold films are grown either by thermal evaporation or sputtering with several thicknesses. Importantly a chromium layer was used optionally to enhance adhesion to the substrate (1-3 nm). Then the density profile perpendicularly to the substrate was measured by XRR and correlated to the cooling kinetics.

XRR was performed with a focused beam at SCD at 9 or 10 keV. A linear direct-converting pixel array (Mythen, Dectris) was used to record the reflection of the wafer, both specularly and diffuse scattering. Diffuse background is subtracted prior to fitting the XRR by matrix-transfer methods (Parratt algorithm).

Results

Heat conduction of these gold films changes by almost a factor of 10 depending on film thickness and chromium interlayer. In particular, the presence of a chromium film increases heat flow to the substrate by a factor of 2-3 [4]. XRR (Fig. 1a) shows high-quality layers in both cases (surface roughness 0.8-1.5 nm, depending on gold thickness) but a distinct difference of the density profile close to the substrate between the two cases (Fig. 1b).

It can be seen that a density step, probably related to the chromium film, is found in the one case. When a chromium film is missing, a density depression is seen between silicon and gold. This gives the clear evidence that a chromium film enhances adhesion (probably by wetting the silicon oxide and removing residual impurities or water). At the same time the enhanced contact at the interface also reduces the TIR.

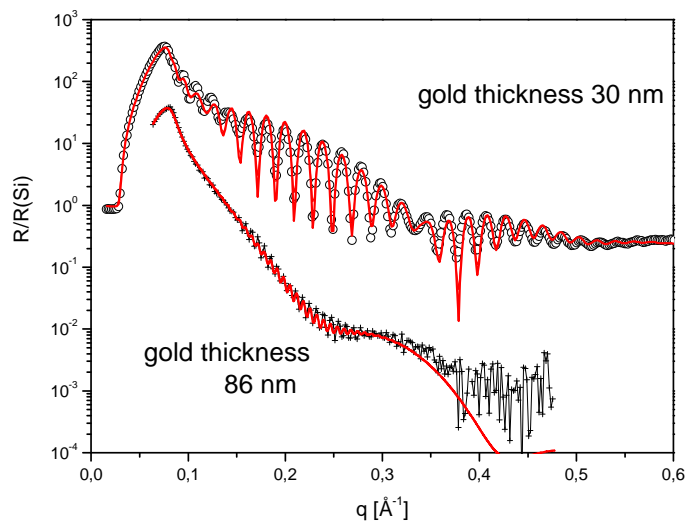


Fig. 1a: XRR of two representative thin films of gold on top of silicon. The 30 nm film has a nominally 2 nm chromium film as interlayer. Fits (red lines) are done with a 4-layer model.

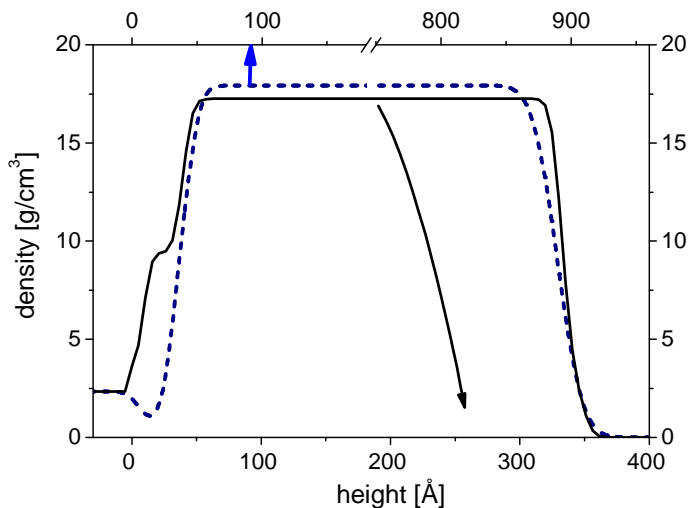


Fig. 1b: Density profiles as deduced from the fitting procedure. The largest difference is seen close to the interface, where a density gap is visible for the pure film, while a density step with 8 g/cm³ appears for the chromium interlayer.

The thickness dependence of the cooling times can be rationalized by the acting of the gold film as heat reservoir [5]. Thus a thicker film takes longer to cool down. The findings have an important impact on different kind of time-dependent investigations of heat transfer close to a surface. For best sensitivity to the surface-near region, a metal film should be used as transducer with smallest thickness possible (with preserved sensitivity on temperature) and best adhesion. The adhesion is found to be strongly enhanced, both mechanically and thermally, by using a chromium layer between silicon substrate and gold film. More details can be found at [6].

[1] A. Siems, S Weber, J Boneberg and A. Plech, *New. J. Phys.* 13 (2011) 043018.

[2] E. E. Haller, *Solid State Communications*, 133 (2005) 693-707.

[3] D.G. Cahill, W.K. Ford, K.E. Goodson, G.D. Mahan, A. Majumdar, H.J. Maris, R. Merlin, S.R. Phillpot, *J. Appl. Phys.* 93 (2003) 793.

[4] H. Bracht, N. Wehmeier, S. Eon, A. Plech, D. Issenmann, J. Lundsgaard Hansen, A. Nylandsted Larsen, J.W. Ager III, E.E. Haller, *Appl. Phys. Lett.* 101 (2012) 064103.

[5] B. Krenzer, A. Hanisch, A. Duvenbeck, B. Rethfeld, M. Horn von Hoegen, *J. Nanomater.* 2008 (2008) 590609.

[6] D. Issenmann, S. Eon, N. Wehmeier, H. Bracht, G. Buth, S. Ibrahimkuty, A. Plech, *Thin Solid Films* (2013) DOI: 10.1016/j.tsf.2012.10.132.

Acknowledgements

We acknowledge the DFG for funding under the Heisenberg program and within priority program SPP 1386. Help by G. Buth and V. Heger is greatly appreciated. We thank ANKA and ESRF for provision of beamtime.

In situ tensile testing of nanoscale Cu/Nb multilayers

J. Lohmiller¹⁾, M.N. Polyakov²⁾, A.M. Hodge²⁾, S. Doyle³⁾, P.A. Gruber¹⁾

¹⁾ Karlsruhe Institute of Technology, Institute for Applied Materials, Herrmann-von-Helmholtz-Platz 1, D-76344 Eggenstein-Leopoldshafen, Germany

²⁾ University of Southern California, Department of Aerospace and Mechanical Engineering, 90089 Los Angeles, California, USA

³⁾ Karlsruhe Institute of Technology, Synchrotronstrahlungsquelle ANKA, Herrmann-von-Helmholtz-Platz 1, D-76344 Eggenstein-Leopoldshafen, Germany

Nanoscale metallic multilayers (NMMs) consist of alternating nanoscale layers of two or more metals and have been shown to possess many desirable properties, such as high strength, corrosion resistance, and radiation resistance. Their behavior is generally attributed either to layer size effects or to the interfaces, which, as the layer thicknesses approach the order of a few nanometers, contribute to a substantial portion of the sample volume.^{5–8} However, some of the properties in NMMs could stem from changes in the layers' crystallographic structures, which have been reported to occur in layer sizes in the range of 1–300 nm.^{9–14} Although an alternate crystallographic phase would affect the microstructure of the entire multilayer, such changes have not been well studied. In this work, we studied the immiscible Cu/Nb NMM system. We specifically focused on the effect of Cu layer thickness on the microstructure and the mechanical properties of the NMM system. The Cu layer thickness was varied between 2, 5, 10 and 20 nm. The Nb layers were maintained at a constant thickness of 10 nm. The samples were deposited onto 50 μm polyimide substrates via magnetron sputtering. Figure 1 shows a schematic and an exemplary TEM micrograph of the cross section of the alternating Cu and Nb layers.

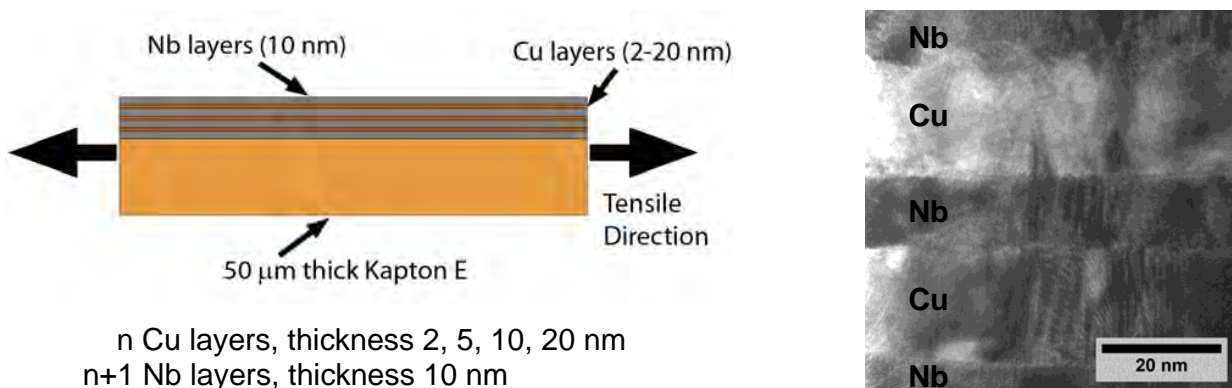


Fig. 1: Schematic (left) and exemplary TEM micrograph (right) of the Cu/Nb NMM system.

The NMM samples have been tested using a *in situ* Synchrotron tensile testing technique originally developed at the ANKA MPI-MF beamline [1]. This technique has been successfully transferred to the PDIFF beamline [2] and has been further developed during the current beamtime. The multilayer structure of the samples enable to investigate very thin film thicknesses as the diffraction volume is increased compared to an individual layer. Thereby size and interface effects on the mechanical properties of ultra thin films can be investigated. Using the transmission technique developed by the PI's group the evolution of the biaxial stress-state within the different film materials can be monitored during deformation. Sophisticated peak shape analysis [3-5] allows to follow the evolution of peak width and asymmetry during deformation and to determine reversible and irreversible shares of both parameters. This yields further insight into the different deformation mechanisms in addition to the characterization of the stress evolution. Figure 2 shows exemplary results of the *in situ* diffraction experiments. Special focus is given to the lattice strains in Cu and Nb layers and the failure strain of the NMM system. This gives insight in the mechanical interplay of the Cu and Nb layers in the NMM system and the corresponding size effects.

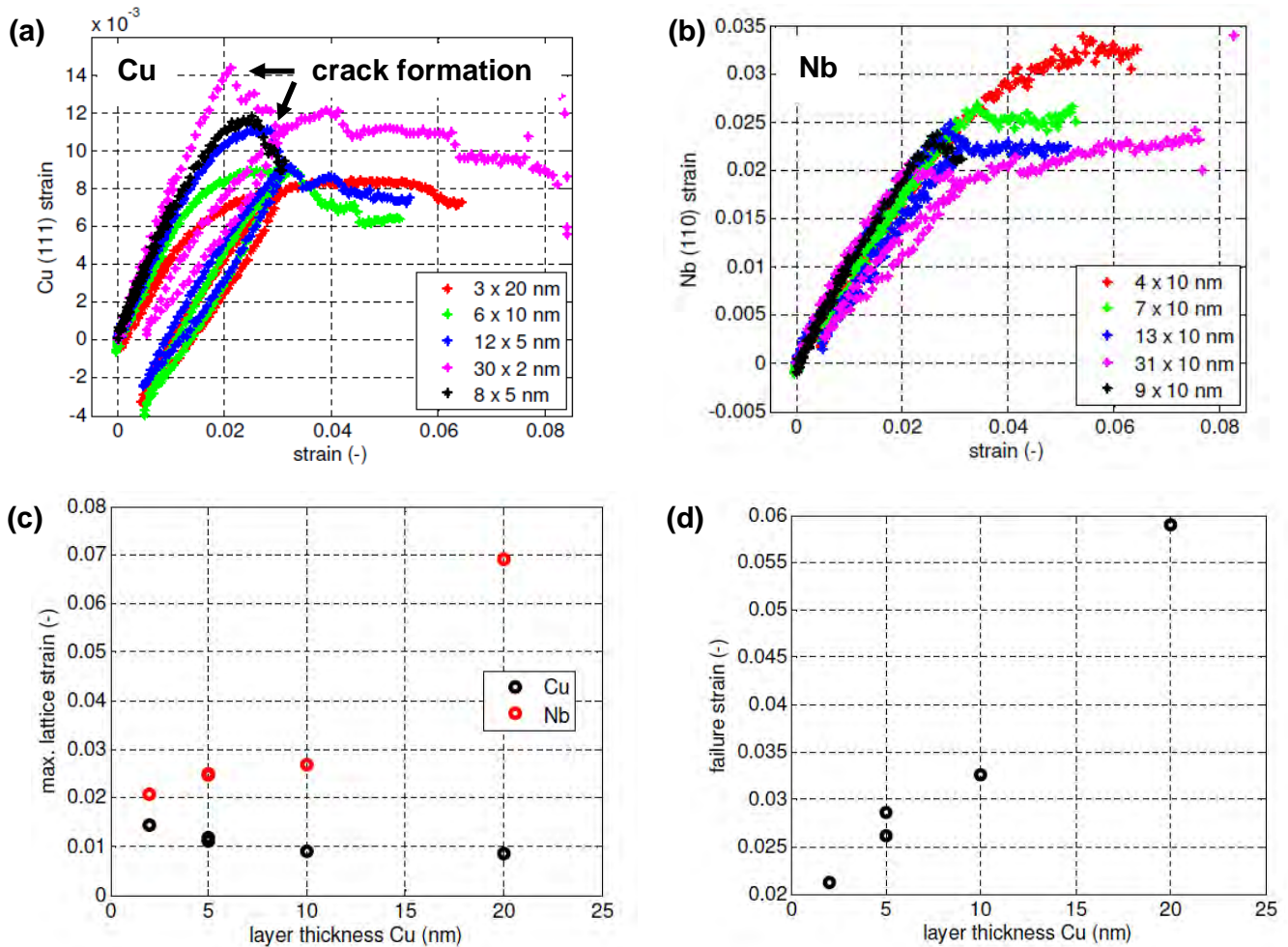


Fig. 2: Exemplary results of the in situ diffraction testing. (a), (b) Lattice strain as function of the total strain determined from the (111) fcc Cu and (110) bcc Nb reflection, respectively. (c) Maximum Cu and Nb lattice strain and (d) failure strain of the Cu layer as function of the Cu layer thickness.

Compared to a recent microstructural investigation on a similar Cu/Nb NMM system using Crystal Orientation and Phase mapping inside the TEM [6] it could be shown that even for the smallest layer thickness of 2 nm, the Cu layer is still crystalline and is entirely of fcc crystal structure. This was not clear from the TEM study. With respect to the mechanical properties, distinct size effects of strength and ductility down to 2 nm layer thickness could be observed. Surprisingly, opposite size effects could be observed for the Cu and Nb layers. For the Cu layers the maximum lattice strain which can be sustained increases with decreasing layer thickness resulting from an increase in strength. Concomitantly the ductility decreases indicated by the decreasing failure strain. This is attributed to the commonly observed mechanical size effect for fcc metals [1] but even smaller length scales could be investigated using the NMM system. However, for the Nb layers the opposite tendency was observed. The maximum lattice strain in the Nb layers increases with increasing Cu layer thickness although the Nb layer thickness is constant. This probably results from a size effect of the mechanical load sharing between the Cu and Nb layers. The origin of this size effect and the extraordinary high lattice strains in the Nb layers is not clear at the moment. Further data and microstructural analysis is on the way to better understand this behavior.

References

1. Gruber PA et al, *Acta Materialia* **56** (10), 2318-35 (2008).
2. Ulyanenkova T et al, *Physica Status Solidi A* **206** (8), 1795-1798 (2009).
3. Lohmiller J et al, *Physical Review Letters* **110**, 066101 (2013).
4. Lohmiller J et al, *Applied Physics Letters* **102**, 241916 (2013).
5. Lohmiller J et al, *Mechanics of Materials* **67**, 65–73 (2013).
6. M.N. Polyakov et al., *Applied Physics Letters* **102**, 241911 (2013).

In-situ synchrotron radiation XRD study of particle formation during precipitation of barium sulphate

R. Kügler¹⁾, D. Nazareus¹⁾, N. Klasen¹⁾, M. Kind¹⁾

¹⁾ Karlsruhe Institute of Technology (KIT), Institute of Thermal Process Engineering, Engelbert-Arnold-Strasse 4, 76131 Karlsruhe, Germany

Introduction

Precipitation or reaction crystallization is a very important industrial process. Many substances such as fine chemicals, pharmaceuticals, catalysts, pigments or ceramics are produced by precipitation. The mechanical, optical, electrical or catalytic properties of precipitated products can be influenced dramatically by adjusting precipitation conditions. Desired product properties are a defined particle size and a narrow particle size distribution, but also a specific particle morphology or product crystalline grade. In cases of very low solubility of the precipitated substances and for economic reasons, high supersaturation has to be used for the precipitation process. Due to these high supersaturation levels the associated primary processes, nucleation and crystal growth, proceed very quickly, often on timescales below one second. To influence particle formation processes and for tailoring the product properties, detailed knowledge of the fundamental mechanisms nucleation and crystal growth is of great importance. Especially in situ information on the development of crystalline phases during fast precipitation processes is not available in the open literature. To observe such fast solid formation processes, a fast measuring method is required, capable of measuring in very short time scales down to a few milliseconds.

Experimental method

A new measuring cell with a free jet of suspension inside was applied for the observation of the particle formation process of barium sulphate. Advantage of the new cell to the former used “flow-through-reaction-tube”-concept is that there is no contact between the supersaturated suspension and cell windows. No more corrective measurements were needed and peak information are available [1, 2]. The model substance barium sulphate was precipitated from aqueous sodium sulphate and barium chloride solutions. The aqueous reactants are continuously mixed in a Y-mixer connected with a pipe reactor of variable length. By changing the length of the pipe reactor, defined residence times, can be adjusted. After the pipe reactor, the suspension flows through an in situ measuring cell. Openings of the cell were closed with two parallel Kapton windows of 25 μm thickness each. An X-ray beam can penetrate the free suspension inside the measuring cell. Mass fraction and particle size of the crystalline precipitate were followed time-resolved using wide-angle (WAXS).

Results

To ensure that mixing of the educts has no influence on particle formation and to find convenient experimental conditions for the in situ experiments, the precipitation of barium sulphate was already studied offline by the authors.

All experiments described here were performed for different initial supersaturation S_a with a constant educt ratio R of one, which means the concentration ratio of barium to sulphate ions was equal before and during the precipitation. The time-resolved evolution of the X-ray diffraction diagram of barium sulphate was recorded beginning with a time of 35 ms up to 6 s. The mass of crystalline barium sulphate at every point in time is proportional to the integral intensity of the

peaks. Figure 1 shows a comparison of experimental data with an empiric simulation of the crystalline mass during precipitation.

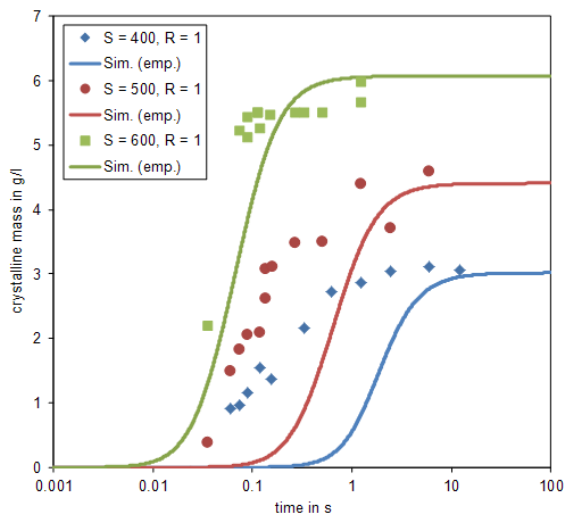


Fig. 1: Comparison of experimental data with an empiric simulation of the crystalline mass during precipitation

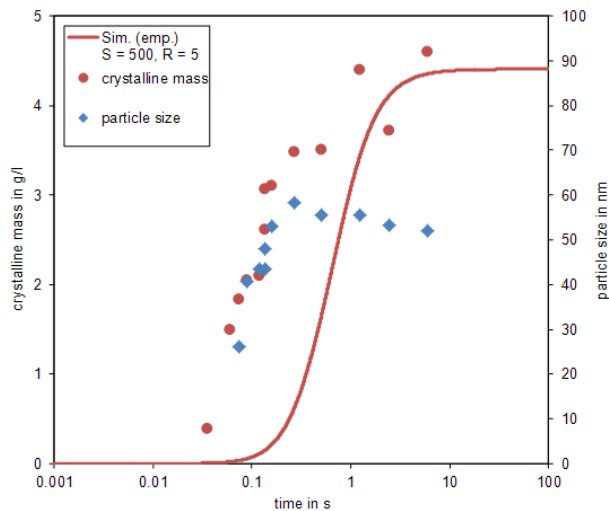


Fig. 2: Estimation of particle size during precipitation for $S_a = 500$ and $R = 1$

The particle or rather crystallite size of barium sulphate could be estimated with the width of the peaks by a Williamson-Hall plot. In figure 2 the evolution of the particle size is shown for $S_a = 500$. The size increased up to 60 nm during the precipitation process and seems to be limited by the measurement setup.

It was possible to directly observe a precipitation process on very short time scales without any correction measurements. Solubility equilibrium is reached below one second, which explains the lack of reliable kinetic data for precipitation processes at such high supersaturation in the open literature. The simulation results demonstrate a high degree of correspondence with experimental results at $S_a = 600$ but not at lower supersaturation. Here the primary processes of the precipitation reaction are not very well described by the used kinetics, consisting of nucleation and crystal growth. In the simulation a heterogeneous nucleation term was added in this region of supersaturation ($S_a < 600$) valid to the literature. It seems that below $S_a = 600$ no heterogeneous nucleation mechanism happens.

As an overall result it can be said that the experimental concept as it was successfully applied here, is a powerful tool for direct monitoring fast precipitation processes.

References

- [1] Haselhuhn, F., Doyle, S., Kind, M., J. Cryst. Growth, 289, (2006)
- [2] Kucher, M., Beierlein, T., Kind, M., AIChE J., 54, (2008)

Acknowledgements

We acknowledge the Synchrotron Light Source ANKA for provision of instruments at their beam lines and we would like to thank Dr. Stephen Doyle for assistance in using lab PDiff.

Sulphur speciation in basaltic glasses upon decompression

A. Fiege¹⁾, H. Behrens¹⁾

¹⁾ Leibniz Universität Hannover, Institut für Mineralogie, Callinstraße 3, D-30167 Hannover, Germany

Scientific Background

Sulphur (S) is the third most abundant volatile in magmatic systems and because of its polyvalent properties (S^{2-} to S^{6+}) it participates in various bio-/geo-/chemical processes. Large amounts of S can be released to a fluid phase upon magma ascent (\rightarrow decompression) and can be injected into the atmosphere during volcanic eruptions, considering that S strongly partitions into the (aqueous) fluid phase [e.g., 1]. Here, sulphur species – especially SO_2 – can impact global climate [2, 3]. In addition, degassing of S results in a significant fluid-melt S-isotope fractionation [4, 5]. Hence, a good knowledge of S degassing is central to understand Earth's S cycle and, thus, to improve our understanding of magmatic processes at depth; e.g., of the redox-transfer from the subducted oceanic slab to the overlying continental crust. Notably, S and S-isotope fluid-melt distribution strongly depends on, e.g., sulphur speciation/oxygen fugacity (fO_2), pressure, temperature and melt composition [6 to 11]. However, the available experimental dataset on S and S-isotope fluid-melt distribution is still limited, especially for basaltic systems.

In the current project we investigate the fluid-melt distribution of S and S-isotopes in basaltic system upon decompression under various conditions (e.g., temperature, oxygen fugacity (fO_2) and water content). An accurate determination of the S speciation in the glasses experimental samples is a prerequisite to allow an interpretation of obtained S and S-isotope partitioning data. To date, XANES spectroscopy is the only reliable technique to analyse sulphur speciation in silicate glasses with low sulphur contents (< 300 ppm).

Research projects

The *main objective* of this session was to complete the dataset for basaltic glasses which was obtained during our previous session (MR-??). These measurements are part of a current research project at our institute funded by the Deutsche Forschungsgemeinschaft (DFG; BE1720/25-1). At ANKA's SUL-X beamline we wanted to analyze the S speciation in basaltic glasses. The melt compositions of the analysed glasses correspond to a alkali-rich basalt glass (~46.8 wt% SiO_2 , ~10.5 wt% MgO) and a Mg-poor basaltic glass (~52.5 wt% SiO_2 , ~0.9 wt% MgO). The experimental approach of the isothermal decompression experiments comprises a three step procedure: *i) Basaltic starting glass:* Synthetic anhydrous basaltic glass were prepared by melting a mixture of oxide (Si, Al, Ti, Fe, Mg, Mn) and carbonate (Na, Ca, K) powders in a PtRh crucible at 1600°C for 2 hours and quenching the melt in a water bath. *ii) S-bearing starting glass:* Hydrous sulphur-bearing glasses were synthesized in internally heated pressure vessels (IHPV) at ~1030°C, 400 and variable fO_2 ($\log(fO_2) = QFM$ to $QFM + 4.2$; QFM: quartz-fayalite-magnetite buffer), using a mixture of the anhydrous basalt (Mg-poor or alkali-rich), de-ionized H_2O (3 to 7 wt%) and $CaSO_4 \times 2H_2O$ as a S source (300 to 1200 ppm S). *iii) Isothermal decompression experiments:* The volatile-bearing glasses were crushed and re-melted in IHPVs at high pressure (~400 MPa) and 1030, 1150, 1200 or 1250°C for ~5 min. Subsequently, the pressure was released continuously at constant T and at a rate of 0.1 MPa/s (\approx fast explosive Plinian eruption style) to final pressure of 70 MPa. The samples were either directly isobarically quenched to preserve strongly non-equilibrium conditions or annealed for various times (0 to 6 h) at final p - T conditions before quenching to approach near-equilibrium between melt and fluid. The resulting experimental products consist of a chemically homogeneous glass matrix and S-rich quenched fluid inclusions (bubbles).

Analytical methods

The quenched glasses were pre-characterized using various analytical techniques (electron microprobe: major element and S, Cl content; IR spectroscopy: H_2O contents; secondary ion mass spectrometry: S-isotope composition). The S concentration in the starting glasses and partially degassed glasses ranges from 300 to 1200 ppm. XANES spectroscopy at sulphur K edge (2472 eV) was conducted at ANKA's SUL-X beamline to investigate the speciation in the glasses. A beam size of $200 \times 100 \mu m$ was applied to measure bulk sulphur speciation on bubble free areas in the experimental basaltic glasses. Doubly polished thin sections were used for all XANES measurements to allow

identifying adequate spots for each analysis at the microscope (e.g., areas without bubbles and areas with high volume fractions of bubbles below the surface). The spectra were collected in the fluorescence mode and mainly quick XAFS scans (bragg axis is continuously running; ~330 energy points; energy increments: 0.3 eV in the edge region (~2.46 to ~2.50 keV) and 1 eV in the pre- and post-edge region) were performed to avoid irradiation damages [11].

Results and Discussion

The XANES analyses of oxidized glasses (~QFM+3) show a sharp sulphate peak (S^{6+}) at an energy of ~2481.4 eV. XANES spectra of experiments performed at intermediate redox conditions (QFM+1 < $\log(fO_2)$ < QFM+3) show an additional sulphide signal at 2468.4 to 2472.8 eV and/or a broad sulphide peak at ~2476.8 eV. In addition, at $\log(fO_2)$ < QFM+1 most S is present as sulphide in the quenched glasses. The peak positions are consistent with our previous XANES data gained at ANKAs SUL-X beamline and recent studies; e.g., [12].

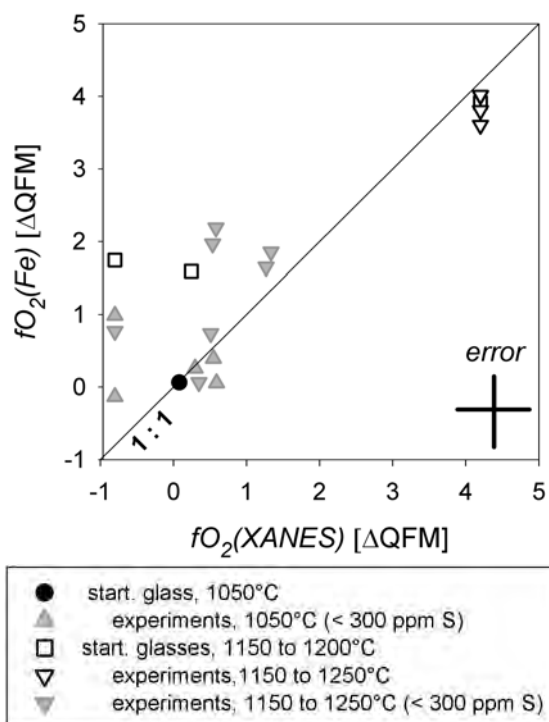


Figure 1: Results of S $K\alpha$ XANES analyses on S-bearing basaltic glasses conducted during our last beamtime at ANKA SUL-X.

The S-XANES spectra were used to estimate the fO_2 of our experiments [$fO_2(XANES)$] following the approach of Jugo et al. [12]. The results are compared to fO_2 values determined based on wet chemical (bulk) analyses of the Fe speciation in our sample [13] as well as on the model of Kress and Carmichael [14] [$fO_2(Fe)$]. A significant deviation between $fO_2(XANES)$ and $fO_2(Fe)$ was observed for reducing redox conditions (Fig. 1). It is suggested that $fO_2(XANES)$ often overestimates the redox conditions within the capsule if sulphide is the dominant S species because the distinct S^{2-} feature at ~2472 eV is not considered in the Jugo et al. [12] model. In addition, spectra at lower fO_2 are often noisy because of the lower S content in the melt, leading to a less accurate evaluation of the S speciation in the glasses when compared to oxidized systems.

The S-XANES data obtained at ANKA from 2009 to 2013 contributed significantly to 2 recently publications [4, 14] and to various abstracts (8). In addition, another manuscript is currently under review for publication in *Chemical Geology* and Dr. Jörg Göttlicher at KIT is a Co-Author of this paper.

Acknowledgements

Dr. Jörg Göttlicher and Dr. Ralph Steininger are greatly acknowledged for their support and patience during the beamtime. This work is funded by the DFG.

References

- [1] Keppler H. (1999), *Science* 284, 1652-1654; [2] Bluth G.J.S., Doiron S.D., Schnetzler C.C., Krueger A.J., Walter L.S., *Geophys. Res. Lett.* 19 (1992), 151-154; [3] Mandeville C.W., Webster J.D., Tappen C., Taylor B.E., Timbal A., Sasaki A., Hauri E., Bacon C.R. (2009), *Geochimica Et Cosmochimica Acta* 73, 2978-3012; [4] A., Holtz F., Shimizu N., Mandeville C.W., Behrens H., Knipping J.L. (2014), *Geoch. Cosmoch. Acta.*, *in press*; [5] Taylor B.E. (1986) *Rev. Mineral.* 16, 185-225; [6] Nagashima, S., Katsura T., *Bul. Chem. Soc. Jpn* 46 (1973), 3099-103; [7] Ooura M., Hanada T. (1998), *Glass Techn.* 39-2, 68-73; [8] Botcharnikov, R., Behrens H., Holtz F., Koepke J., Sato, H., (2004), *Chem. Geol.* 213, 207-225; [9] Lesne, P., Kohn, S.C., Blundy, J., Witham, F., Botcharnikov, R.E., Behrens, H. (2011), *J. Petrology* 52, 1737-1762; [10] Webster J.D., Botcharnikov R.E. (2011), *Rev. Mineral. Geochem.* 73, 247-283; [11] Backnäs L., Stelling J., Behrens H., Göttlicher J., Mangold S., Verheijen O., Beerkens R.G.C., Deubener J. (2008), *J. Am. Ceram. Soc.* 91, 721-727; [12] Jugo P.J., Wilke M., Botcharnikov E.B. (2010), *Geoch. Cosmoch. Acta* 74, 5926-5938; [13] Schuessler J.A., Botcharnikov R.E., Behrens H., Misti V., Freda C. (2008); [14] Kress V.C., Carmichael I.S.E. (1991), *Contrib. Mineral. Petrol.* 108, 82-92; [15] Fiege A., Behrens H., Holtz F., Adams F. (2014), *Geoch. Cosmoch. Acta.* 125, 241-264;

Molecular orientation of donor/acceptor blends - Influence of PCBM on the orientation of polymers

U. Aygül¹⁾, F. Latteyer¹⁾, M. Ivanovic¹⁾, D. Batchelor²⁾, S. Mangold²⁾, H. Peisert¹⁾, T. Chassé¹⁾

¹⁾ Institut für Physikalische und Theoretische Chemie, Universität Tübingen, Auf der Morgenstelle 18, 72076 Tübingen, Germany

²⁾ Karlsruhe Institute of Technology, ANKA, Hermann-von-Helmholtz-Platz 1, D-76344 Eggenstein-Leopoldshafen, Germany

Introduction

Low band gap materials remain an issue for the improvement of active layers in organic solar cells. Based on results of the previous investigations we put further emphasis on the investigation of new low band gap donor materials with potential for application in “bulk heterojunction”-type solar cells. The lowering of the band gap in these material can be achieved by a hybridization of the HOMO and LUMO levels of electron-rich and electron-deficient sub-units of the polymer which results also in a reduction of the bond-length alternation.[1] These materials show a better efficiency due to an improved absorption in the visible and near infrared regions of the solar spectrum and an optimization of the offset of the frontier energy levels of the donor and acceptor. On the other hand little is known about the self-organization properties of the polymer in the blend material (i.e. the material which is finally applied in OSCs). It can be shown, that the phase separation and the ordering of P3HT domains in P3HT/PCBM blends is correlated with improved photovoltaic efficiency [2]. Since the optimal domain size of BHJ solar cells is less than a few 10 nm [3,4], NEXAFS is in particular suited for such investigations and alternative methods, such as conventional diffraction studies become more complicated.

Experimental details

Polymer films were prepared ex-situ by doctor blade casting and stored under well-defined ambient conditions. Annealing was carried out in dark and under N₂-atmosphere. NEXAFS experiments were carried out at the XAS beamline. The beamline energy resolution at the sulfur edge is circa 300 meV and displays a polarization degree of > 0.95. X-ray absorption spectra were measured in fluorescence yield mode.

Results

First measurements were carried out on blends of the state of the art organic donor material P3HT and the acceptor PCBM. Sulfur K edge NEXAFS revealed a high degree of orientation for P3HT only after annealing of the sample.[5] Thus, annealing is an essential step in the sample preparation of “bulk heterojunction”-type solar cells. In the present beamtime we extended these studies to blends of other model LBG polymers, the chemical structure is shown in Fig. 1.

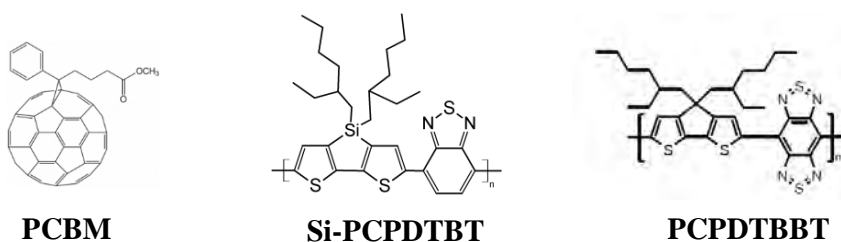


Fig. 1: Chemical structures of studied low band gap polymers as well as of the acceptor PCBM

First, we varied the content of the electron acceptor PCBM. The S-K edge NEXAFS spectra of Si-PCPDTBT/PCBM blends with the ratios 3:1, 1:1 and 1:3 as a function of the excitation angle are shown in Figure 2. These excitations are governed by selection rules. Depending on the direction of the electric field vector *E* of the linear polarized synchrotron light for planar molecules either transitions into π^* or σ^* orbitals are allowed, enabling the determination of the molecular orientation. Generally, an increased ordering of the polymers can be correlated with an increased angular dependence of the features in the XAS spectra in Fig 2; we focus on the most intense structure at about 2.474 keV. For the blend film with the polymer/fullerene ratio of 3:1 the intensity variation (i.e. the polarization dependence) of the sulfur K absorption peak is similar to the pure polymer. Therefore the self-organization of the polymer is not strongly disturbed in a blend film with a 3:1 ratio and the polymer shows the same molecular orientation. However if the amount of the

fullerene PCBM increases in the blend film, the intensity range of the sulfur NEXAFS peak diminishes and the PCBM seems to disturb the self-organization of Si-PCPDTBT. This suggests that with increasing amount of PCBM less domains with a crystalline polymer phase are present in the film. Instead more domains with pure PCBM are formed and prevent the self-organization of the polymer which is then disordered (amorphous polymer/PCBM phase).

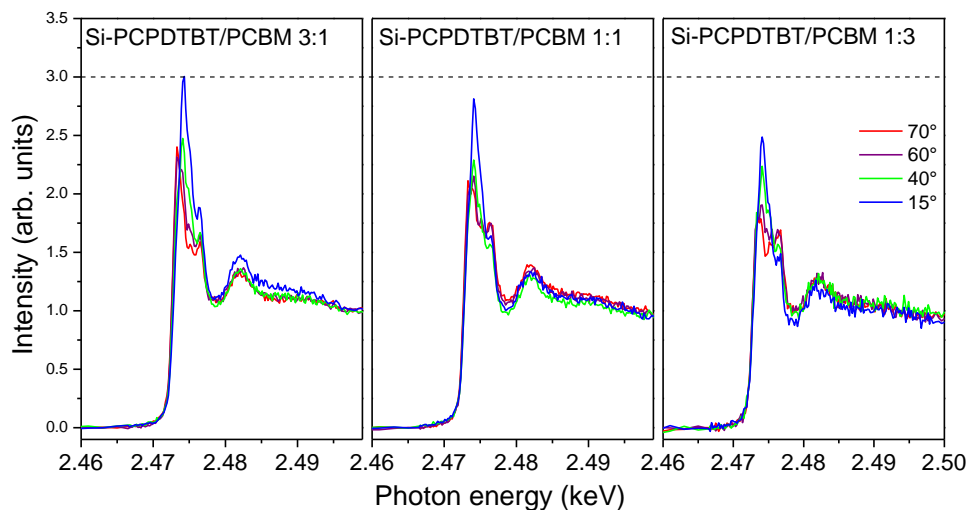


Fig. 2: Angle dependent S-K edge NEXAFS spectra of Si-PCPDTBT blends with different PCBM ratios.

Another focus of the beamtime was the study of the influence of the annealing on the self-organization. The NEXAFS spectra for a pristine and an annealed (393K) SI-PCPDTBT/PCBM blend film are shown in Figure 3. Surprisingly in the case of the Si-PCPDTBT blend thermal annealing at 393 K has almost no effect. The absorption spectra of the blend before and after annealing are very similar and almost no improvement of the ordering occurs. The same results were also obtained for a PCPDTBBT/PCBM blend film (not shown here). We assume therefore that for an improvement of the orientation and phase separation higher annealing temperatures are necessary which allow the thermal (re-)organization of the polymer subunits.

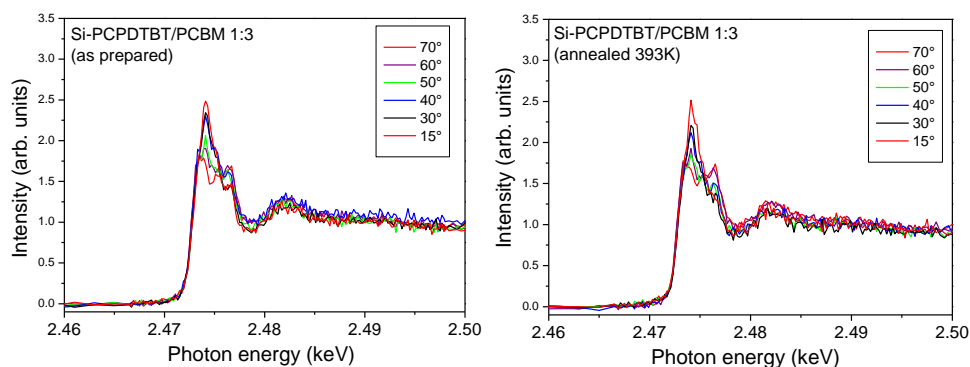


Fig. 3: Angle dependent S-K edge NEXAFS spectra of a Si-PCPDTBT:PCBM blend before and after annealing to 393 K.

Acknowledgements

For financial support we thank the German Research Council (CH 132/24-1). ANKA Angströmquelle Karlsruhe is acknowledged for the provision of beamtime. We thank H.-J. Egelhaaf (Belectric OPV) for helpful discussions and U. Scherf (University of Wuppertal) for supplying PCPDTBBT.

References

- [1] Brédas, J.L. *J.Chem.Phys.* **1985**, 82, 3808-3811.
- [2] R. Alex Marsh, Justin M. Hodgkiss, Sebastian Albert-Seifried, Richard H. Friend, *Nano Lett.* **10** (2010) 923–930
- [3] Mao-Yuan Chiu, U-Ser Jeng, Ming-Shin Su, Kung-Hwa Wie, *Macromolecules* **43** (2010) 428–432.
- [4] Ma, W. L.; Yang, C. Y.; Heeger, A. J. *Adv. Mater.* **19** (2007) 1387.
- [5] U. Aygül, D. Batchelor, U. Dettinger, H. Peisert, T. Chassé, *J. Phys. Chem. C* **116** (2012) 4870–4874.

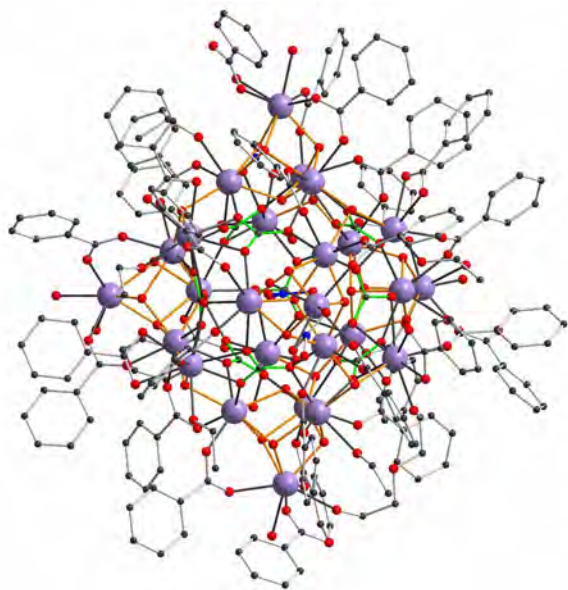
Crystallographic Characterisation of Large Paramagnetic Aggregates of Transition-Metal Cations

Christopher E. Anson¹⁾, Gernot Buth²⁾, Annie K. Powell¹⁾

¹⁾ Karlsruhe Institute of Technology, Institut für Anorganische Chemie, Engesserstr. 15, D-76131 Karlsruhe

²⁾ Karlsruhe Institute of Technology, Institut für Synchrotronstrahlung, Hermann-von-Helmholtz-Platz 1, D-76344 Eggenstein-Leopoldshafen

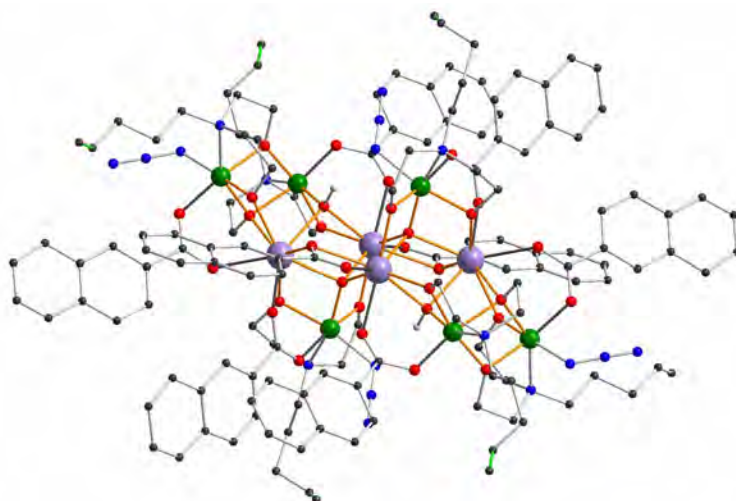
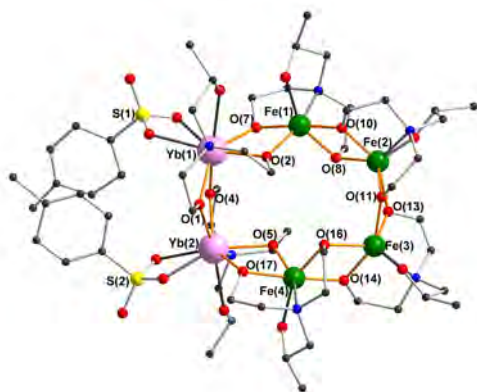
Recently, we and others have found that hydrothermal synthetic methods can be a useful route to very high nuclearity (up to Ln₇₉) coordination clusters of lanthanide cations. We have now found that similar compounds can be obtained via reactions carried out at ambient pressure; this should allow rather more control over the products obtained. We have determined the structure of [Dy₂₆(μ₃-OH)₂₆(μ₅-CO₃)₉(O₂CPh)₃₁(NO₃)₂(diethyleneglycol)(EtOH)₅(OH₂)₆](NO₃)_n(EtOH) on SCD. The approximately trigonal-bipyramidal core is composed of 26 Dy^{III} centres bridged by triply-bridging hydroxo and carbonato ligands; a nitrate anion in the centre of the cage may have acted as a template. The large amount of disordered solvent molecules in the lattice between the molecules results in very weak diffraction to higher 2θ angles, and synchrotron radiation was necessary to obtain a dataset with good resolution.



Molecular structure of [Dy₂₆(μ₃-OH)₂₆(μ₅-CO₃)₉(O₂CPh)₃₁(NO₃)₂(deg)(EtOH)₅(OH₂)₆](NO₃)

Dy violet, O red, C black, H atoms omitted for clarity.

Dy-OH bonds highlighted in orange, C-O bonds of the carbonato ligands shown as green

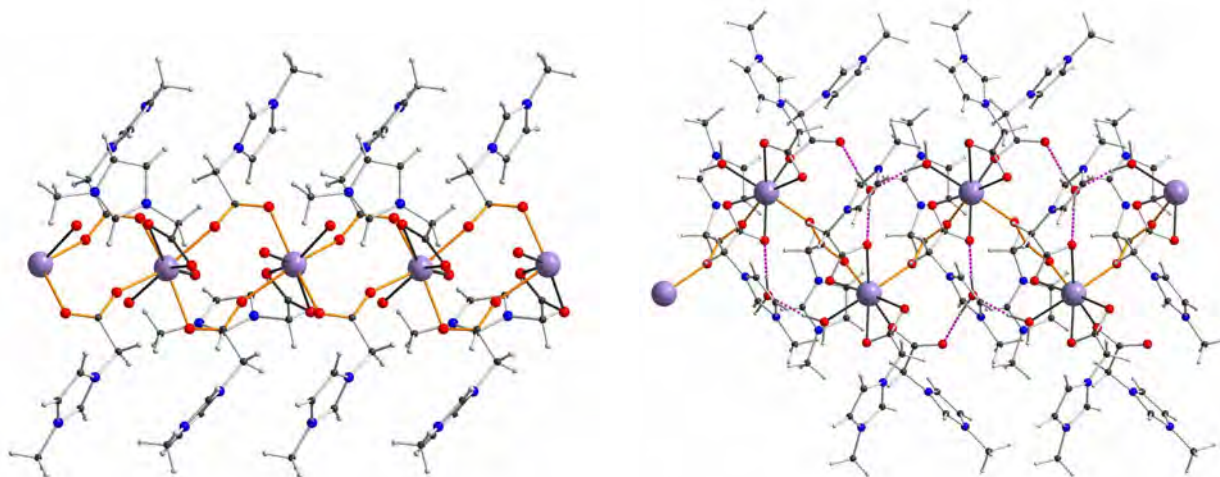


Molecular Structures of [Fe^{III}₄Yb^{III}₂(Me-tea)₄(Me-teaH)₂(tosylate)₂] (left) and [Fe^{III}₆Dy^{III}₄(O)₂(OH)₂(4-pentenyl-dea)₆(2-naph-CO₂)₈(N₃)₄] (right). The terminal C=C bonds in the pentenyl chains of the Fe₆Dy₄ are highlighted in green.

We have been studying the magnetic properties of the Single-Molecule Magnets $[\text{Fe}^{\text{III}}_6\text{Dy}^{\text{III}}_4(\text{O})_2(\text{OH})_2(\text{R-dea})_6(2\text{-naph-CO}_2)_8(\text{N}_3)_4]$, where R-deaH₂ is an *N*-substituted diethanolamine. There is a correlation between the SMM properties and the length of the chain R, resulting from changes in intermolecular interactions. We have measured the structure of the analogues with R = n-pentyl and 4-pentenyl, the vinylic group at the end of the latter chain will allow us to tether the clusters to silicon nanoparticles.

In our two previous reports, we described the structures of symmetrical ring-like Fe_8Ln_8 and $\text{Fe}_{10}\text{Ln}_{10}$ complexes with diethanolamine or triethanolamine ligands, in which the alkoxo-bridged iron and lanthanide ions alternate around the ring. By changing the lanthanide salt and/or using methyl-substituted triethanolamine ligands, it has proved possible to obtain smaller (5-, 6- or 8-membered) rings with less symmetrical structures. With lanthanide tosylates we obtained small crystals of a Fe_4Yb_2 complex, in which the Yb centres are adjacent in the ring, making a useful comparison to another Fe_4Yb_2 ring in which the two Yb are opposite each other.

There has been increasing interest recently in ionic liquids; salts with a melting point below 100 °C, as novel solvents, often with catalytic properties. We have used the zwitterionic ligand *N*-(1-methylimidazolium)-acetate (Me-imac), which combines a carboxylate group and a cationic organic ring, to obtain Fe_3 complexes with high positive charge that are ionic liquids. With dysprosium and this ligand, two complexes were obtained, a trifluorosulfonamide salt melting at 72 °C and a $(\text{PF}_6)^-$ salt melting at 103 °C. Both salts can be repeatedly melted and crystallised, but both form fine needle-like crystals, and the structures could only be determined at ANKA. Both compounds were found to be carboxylate-bridged coordination polymers of Dy, but with different bridging modes within the chains. The zig-zag chain in the $(\text{PF}_6)^-$ salt is stabilised by hydrogen-bonding from waters in the lattice, explaining its higher melting point (which is narrowly over the limit of 100 °C for true ionic liquids). By contrast, the crystal structure of the sulphonamide salt is largely stabilised by a range of weak C-H \cdots O and C-H \cdots F interactions. It is extremely rare for coordination polymers such as these to act as ionic liquids. The sulphonamide salt is also a Single-Chain Magnet, although this behaviour is of course only observed in a temperature regime (below 5 K) far below its melting point.



Structures of the Dy Polymers in $[\text{Dy}(\text{Me-imac})_3(\text{OH}_2)_2]\{(\text{CF}_3\text{SO}_2)_2\text{N}\}_3$ (left) and $[\text{Dy}(\text{Me-imac})_3(\text{OH}_2)](\text{PF}_6)_3 \cdot 2\text{H}_2\text{O}$ (right). Dy violet, O red, N blue, C black, carboxylate bridges highlighted in orange, hydrogen bonds as pink dashes.

Acknowledgements

We thank the DFG (Center for Functional Nanostructures) for financial support.

***In Situ* XAS Investigations on Fe/Mn Phosphates and Silicates During Operation in a Battery**

S. Indris¹⁾, H. Hain¹⁾, M. Kaus¹⁾, R. Chen¹⁾

¹⁾ Institute of Nanotechnology, Karlsruhe Institute of Technology, P.O. Box 3640, 76021 Karlsruhe, Germany

We investigated nanocrystalline $\text{Li}_2\text{Fe}_{1-y}\text{Mn}_y\text{SiO}_4$ ($y = 0, 0.5$) and LiCoPO_4 as electrode materials for Li-ion batteries by *in situ* XAS measurements on complete battery cells.

The series of Fe and Mn *K*-edge absorption spectra during first charge/discharge cycles for $\text{Li}_2\text{FeSiO}_4$ and $\text{Li}_2\text{Fe}_{0.5}\text{Mn}_{0.5}\text{SiO}_4$ are shown in Figure 1 and 2, respectively. A background subtraction and normalisation of the measured spectra has to be done with extremely high reproducibility. Changes in the average valence states and local site symmetries of both cations can be deduced from the curvature and the energy shift in the absorption edges. The corrected spectra are a linear combination of individual spectra of cation sites with different local structure and oxidation states. Therefore, it is possible to use principle component analysis (PCA) on the charging-discharging-cycle of each battery system to extract information about the number of independent changes in the system without prior in-depth knowledge about needed references and to gain information about the reversibility of the cycle. The normalized virtual components of the PCA are fitted to the set of spectra to extract their respective loadings. Component 0 is one spectrum of the data set and the fluctuation of the loading ($\sim 5/1000$) indicates the reliability of the normalisation. Component 1 of these data sets typically implies the change of the oxidation state, whereas the next one or two important components indicate smaller spectral changes, which are not linearly connected to the oxidation state change. Two obvious differences can be seen during charging of both battery systems. The edge position shifts to higher energies indicating the oxidation of the Mn and Fe cations from 2+ to 3+ (Figure 1b, Figure 2b,d). The disappearance of the shoulder of the absorption edge indicates a significant change in the symmetry of the binding orbitals. Dominko et al. [1] could identify in a similar battery system a change in the tetrahedral coordination of the central atoms (Mn and Fe). Manceau has shown lately [2] that spectra with the central atom in the same oxidation state can show a limited but significant shift in the absorption edge. As a consequence, the error of the quantification of cations in different oxidation states (without exact knowledge of each Mn or Fe species in the system) is at least $\pm 10\%$. The efficiency of Fe^{2+} - Fe^{3+} oxidation in $\text{Li}_2\text{FeSiO}_4$ is between 70-90%. The results of PCA and the plotted spectra prove both (Figure 1a and c) that this reaction is nearly perfectly reversible. For the $\text{Li}_2\text{Fe}_{0.5}\text{Mn}_{0.5}\text{SiO}_4$ system the oxidation rate is slightly higher for the Fe cations, but lower for the Mn cations. The comparison of the spectra of the discharged battery and the as-prepared battery shows no significant changes of the oxidation state on both edges. The oxidation starts first with Fe ions and at 4.2 V with Mn. The reduction during discharge starts immediately for Mn and at 3.4 V for Fe. In contrast to $\text{Li}_2\text{FeSiO}_4$, there are two remarkable differences for the $\text{Li}_2\text{Fe}_{0.5}\text{Mn}_{0.5}\text{SiO}_4$ system. After discharging of the latter battery, the shoulder in the absorption edge is missing, which indicates a change in the symmetry of the binding around the Fe and Mn atoms. In contrast to the data on the Fe edge, the results on the Mn edge indicate a larger irreversible change. The much higher first maximum in the spectrum (called “white line”) points to a production of a Mn^{2+} compound with a lower electron density around the Mn atom.

Similar results were obtained on the Co *K* edge for LiCoPO_4 cycled against Li metal in the voltage range from 2.5 V to 5.2 V (Fig. 3). These results reveal the very high reversibility of the oxidation/reduction process of $\text{Co}^{2+/3+}$ during Li removal/reinsertion.

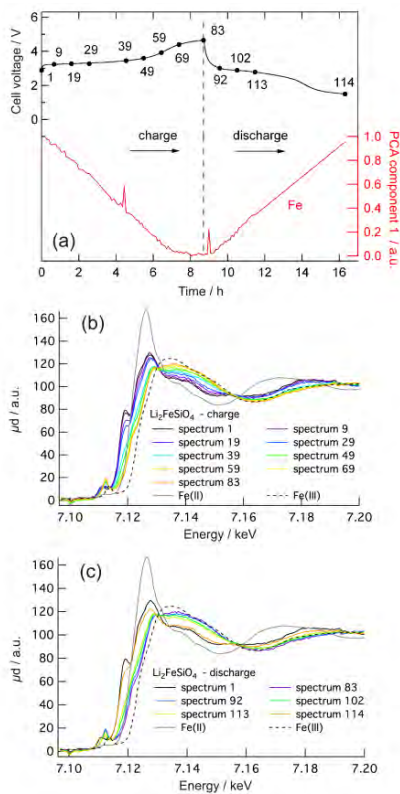


Figure 1. (a) Voltage profile during *in situ* XAS experiment for the first charge/discharge cycle of $\text{Li}_2\text{FeSiO}_4$ against Li metal in the voltage range 1.5–4.7 V at a current density of 20.6 mA g^{-1} (i.e., C/16) together with component 1 of the PCA. The corresponding Fe K-edge absorption spectra during (b) charge and (c) discharge.

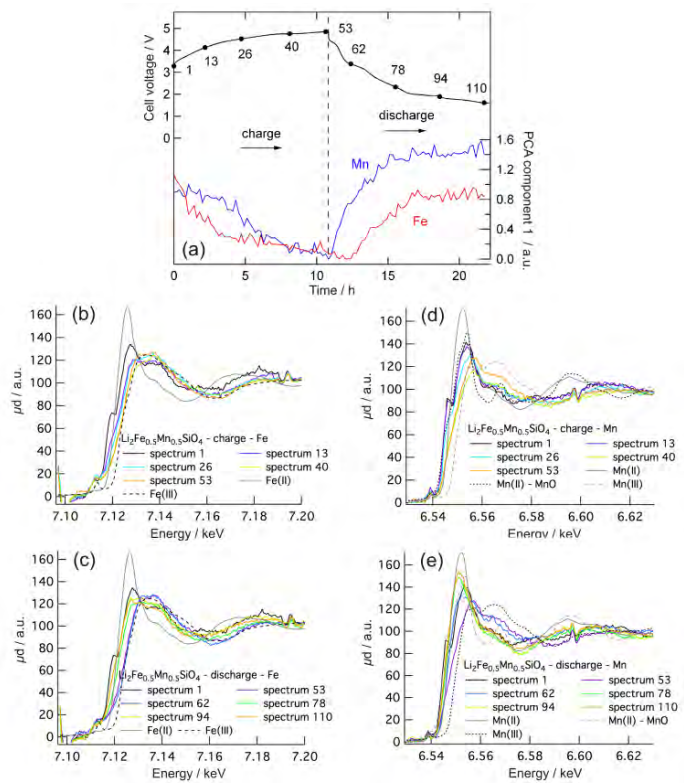


Figure 2. (a) Voltage profile during *in situ* XAS experiment for the first charge/discharge cycle of $\text{Li}_2\text{Fe}_{0.5}\text{Mn}_{0.5}\text{SiO}_4$ against Li metal in the voltage range 1.6–4.8 V at a current density of 16.5 mA g^{-1} (i.e., C/20) together with component 1 of the PCA of both edges. The corresponding Fe K-edge absorption spectra during (b) charge, (c) discharge and Mn K-edge absorption spectra during (d) charge, (e) discharge.

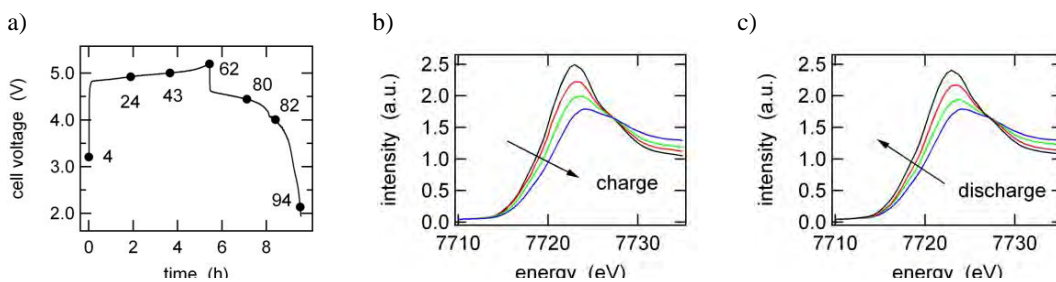


Figure 3. (a) Voltage profile during *in situ* XAS experiment for the first charge/discharge cycle of LiCoPO_4 against Li metal in the voltage range 2.5–5.2 V. The corresponding Co K-edge absorption spectra during (b) charge and (c) discharge.

- [1] Dominko, R.; Sirisopanaporn, C.; Masquelier, C.; Hanzel, D.; Arcon, I.; Gaberscek, M. *J. Electrochem. Soc.* **2010**, *157*, A1309.
 [2] Manceau, A.; Marcus, M. A.; Grangeon, S., *Am. Mineral.* **2012**, *97*, 816.

In Situ XRD Investigations on Fe/Mn Phosphates and Silicates During Operation in a Battery

S. Indris¹⁾, H. Hain¹⁾, M. Kaus¹⁾, R. Chen¹⁾

¹⁾ Institute of Nanotechnology, Karlsruhe Institute of Technology, P.O. Box 3640, 76021 Karlsruhe, Germany

We investigated nanocrystalline LiCoPO_4 as electrode materials for Li-ion batteries by *in situ* XRD measurements on complete battery cells. In comparison to LiFePO_4 , which is already extensively used in commercial Li-ion batteries, LiCoPO_4 has a higher oxidation/reduction potential and thus enables higher energy densities.

The first measurement was performed on LiCoPO_4 with an olivine structure (Fig. 1). These measurements show that the initial phase LiCoPO_4 (labeled with 'A' in Fig. 1) is transformed into the final product CoPO_4 ('C') via an intermediate phase with a composition of about $\text{Li}_{0.7}\text{CoPO}_4$ ('B'). This is in contrast to the mechanism established for LiFePO_4 where only two phases occur.

After a complete electrochemical cycle the XRD pattern is very similar to that of the starting material revealing that the electrochemical reaction in the active electrode material has a high reversibility. Therefore, the asymmetry in the voltage profile has to be ascribed to side reactions probably causing degradation of the electrolyte at highly oxidizing conditions. These electrolyte reactions are therefore also responsible for the degradation of the complete battery.

For the second material, non-olivine LiCoPO_4 (orthorhombic structure, space group Pn21 (no. 23)) the observed changes in the XRD pattern were less obvious (Fig. 2). The peaks of the initial structure show only a slight broadening and a reduction in intensity during charging against Li metal. This hints to an amorphization of the structure during Li removal and might explain the much lower reversibility of the Li insertion process for this material in comparison to the olivine phase.

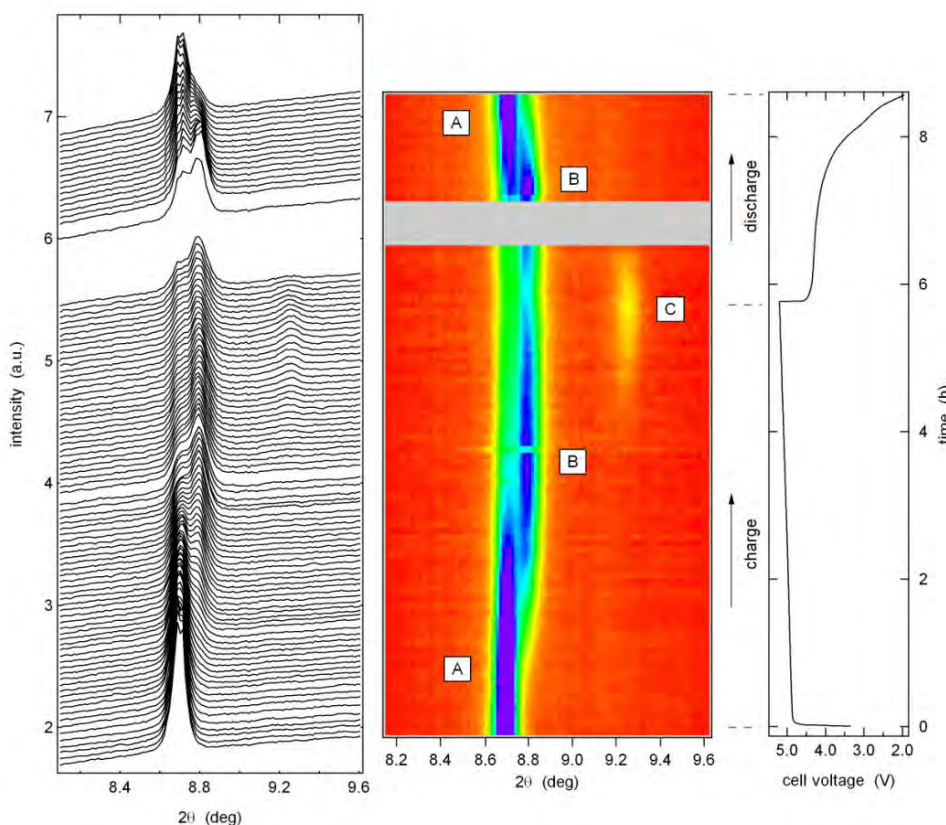


Fig. 1: In situ XRD measurements on olivine LiCoPO_4 during galvanostatic cycling against Li metal in a battery cell. The voltage profile as a function of time is shown on the right side.

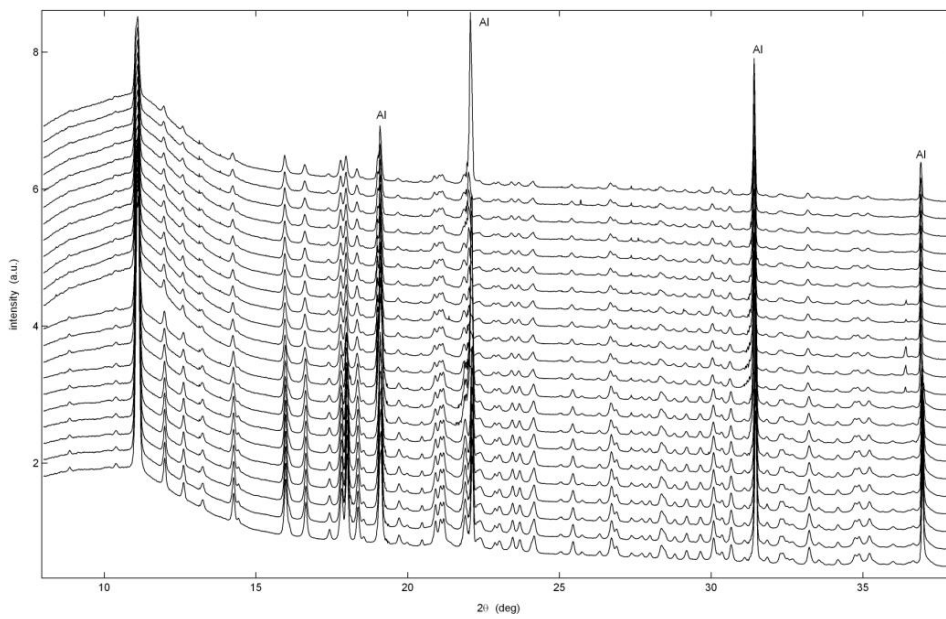


Fig. 2: In situ XRD measurements on non-olivine LiCoPO_4 during galvanostatic charging (top to bottom) against Li metal in a battery cell.

A XAFS study of the conversion reaction mechanism in FeF₃ cathode materials for Li-ion batteries

A. Pohl¹⁾, B. Das²⁾, F. Scheiba¹⁾, J. Rothe¹⁾, H. Ehrenberg¹⁾ and M. Fichtner^{1,2)}

¹⁾ Karlsruhe Institute of Technology, Hermann-von-Helmholtz-Platz 1, 76344 Eggenstein-Leopoldshafen, Germany

²⁾ Helmholtz Institute Ulm, Albert-Einstein Allee 11, 89081 Ulm, Germany

Introduction

The battery systems in use today are typically based on Li intercalation chemistry with a total capacity of 140-220 mAh/g [1]. Increase of the capacity can be achieved by using materials based on the conversion principle which are able to utilise all available oxidation states of the material, and capacities up to 600 mAh/g have been demonstrated [2]. Metal fluorides are ideal because they have a high operating voltage due to the strong M-F bond. However, fluorides are insulators making it difficult to apply directly as cathode materials. A number of methods have been found to overcome this problem: a) ball milling with conductive carbon and b) embedding the fluoride into a matrix of a mixed ionic/electronic conductor. We recently prepared LiF/Fe(V₂O₅) nanocomposites with varying V₂O₅ content of 0, 10, 15 and 20 wt. % by high energy

ball milling and obtained a stable specific capacity of 450 mAh/g (total weight) for a period of 20 cycles without noticeable capacity fading. Surprisingly, the XRD patterns of the composite show no reflections from the additive V₂O₅ or any new phases, but only reflections from the Fe and LiF starting materials. As the vanadium containing phases are amorphous, we collected *in situ* XAS data at the INE beamline during 1st charge (Fe K-edge) and 1st discharge (V K-edge) of the battery cell. We were interested to determine the oxidation state and local structure of the vanadium and iron containing species in these composites.

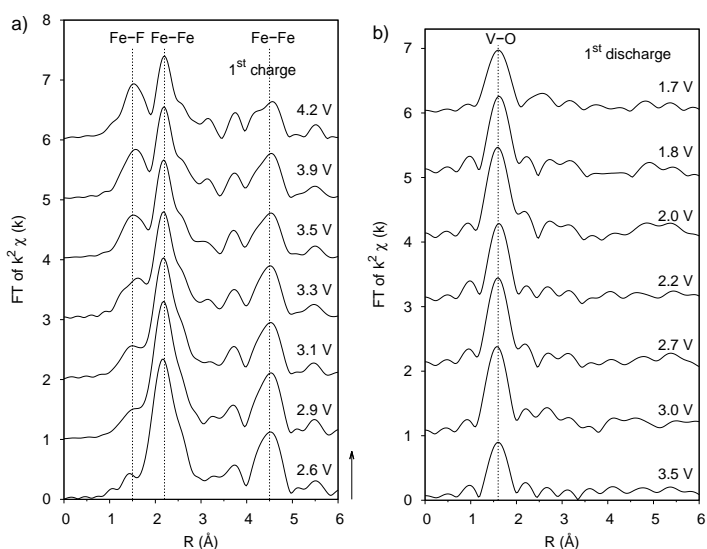


Fig. 1: Fourier transforms (FT) of $k^2\chi(k)$ collected a) during 1st charge at the Fe K-edge and b) during 1st discharge at the V K-edge of the *in situ* battery cell. The plots are offset by 1 and the R -scale was not corrected for the phase shift of the absorber atom.

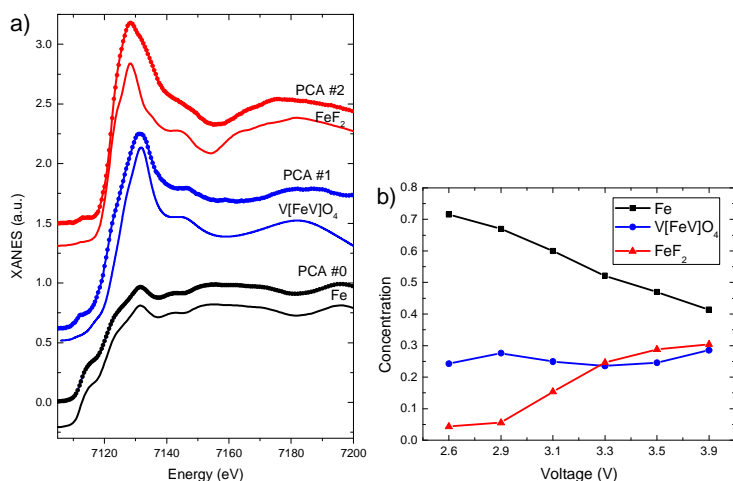


Fig. 2: Principal component analysis for the series of Fe K-edge XANES spectra showing a) obtained components and corresponding models and b) concentrations of the components during 1st charge.

Experimental

A nanocomposite with 15 wt. % V₂O₅ and a fixed Fe:LiF ratio of 1:3 was prepared by high energy ball milling. Electrodes for *in situ* characterisation were prepared by mixing the active material with PVDF-HFP and carbon black in a 70:15:15 wt.% ratio and adding a few drops N-methyl-2-pyrrolidone. The slurry was cast onto glassy carbon films and a home-built battery cell was assembled in an argon-filled glove-box. XAS data at the Fe K-edge and V K-edge were collected during the 1st cycle of the cell in transmission mode for ~30 min. per run with an energy range of 13-14 keV. The cell was cycled with at constant current of 0.1 mA.

Results and discussion

Fourier transforms of $k^2\chi(k)$ of selected Fe K-edge spectra (Fig 1a) show a peak at 1.5 Å between 2.0 V and 4.2 V, which

corresponds to Fe-F distances in rutile FeF_2 . At the same time, peaks at 2.20 Å and 4.50 Å, which are attributed to 1st and 3rd Fe-Fe coordination shells in metallic Fe, are reduced. In the V K-edge FT $k^2\chi(k)$ (Fig 1b), there is only one coordination shell at 1.6 Å corresponding to the 1st V-O distances, which changes very little in intensity and position as the battery is charged. A 2nd and 3rd coordination shell at higher r is completely absent highlighting the amorphous nature of the phases formed during ball milling. A fit to the 1st peak gave a scattered range of V-O distances of 2.02-2.08 Å during cycling. The V oxidation state, which was determined from the change of the pre-edge position, changed from $\text{V}^{3.9+}$ at 4 V to $\text{V}^{3.5+}$ at 1.7 V after 22 hours of discharge.

We have used principle component analysis (PCA) [3] to mathematically decompose the series of Fe K edge spectra at different voltages into sub-spectra. We found that the spectra can be reproduced by three components. We assumed the main component to be pure iron, which is also confirmed by Mössbauer spectroscopy. The shapes of the other two spectra were determined by the PCA tool and match FeF_2 and a new component (Fig 2a). At 3.9V, the concentration of FeF_2 was approx. 35 wt.%, which was formed electrochemically by the reaction of LiF with Fe during charge (Fig. 2b). Surprisingly, we found that ca. 25 wt.% of the new component was already present in the as prepared cell at open circuit potential, although no current was applied to the cell yet. Therefore the new phase could not have formed electrochemically and must have formed during ball milling. Since there are no new phases in the XRD pattern, this phase is amorphous.

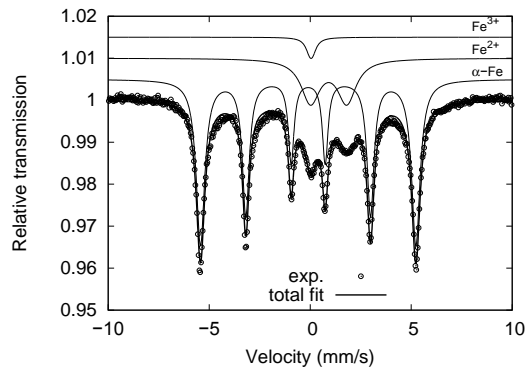


Fig. 3: Mössbauer spectrum of the as prepared LiF/Fe(V_2O_5) composite. The isomer shift is given relative to α -Fe.

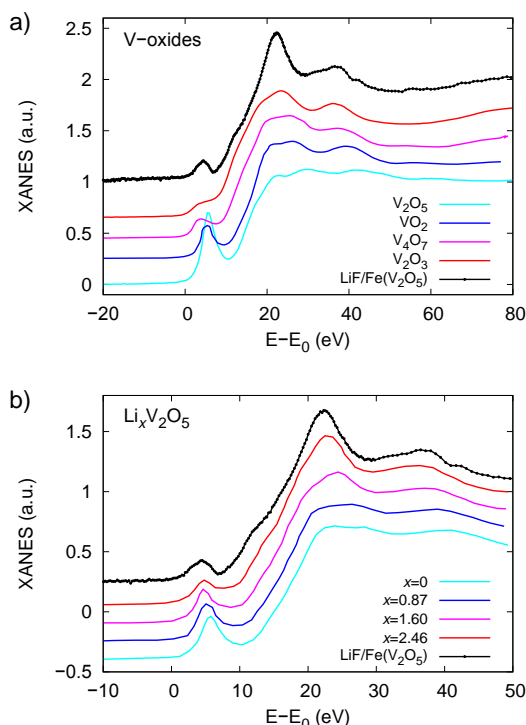


Fig. 4: Comparison of the XANES spectrum of the as prepared LiF/Fe (V_2O_5) nanocomposite (black dots) with spectra of a) vanadium oxides (data for VO_2 and V_4O_7 taken from ref. [6] and b) chemically lithiated $\text{Li}_x\text{V}_2\text{O}_5$ (data taken from ref. [7]). The energy is plotted relative to the V K-edge energy of 5.465 keV.

The Mössbauer spectrum of the LiF/Fe(V_2O_5) composite shows a large sextet from metallic Fe, a smaller Fe^{2+} doublet and a very small Fe^{3+} singlet (Fig. 3). The Fe^{2+} doublet has an isomer shift (IS) of 1.02 mm/s and a large quadrupole splitting (QS) of 1.79 mm/s, which are both too small for FeF_2 (IS 1.33 mm/s and QS 1.79 mm/s [4]). This precludes a simple reaction of Li with V_2O_5 with concomitant formation of FeF_2 . Instead, the Mössbauer parameters indicate that the Fe^{2+} is in an oxide spinel structure [5] and for $\text{Fe}[\text{V}_2]\text{O}_4$, isomer shifts of 1.13 mm/s, 1.07 mm/s and 0.91 mm/s have been reported. To obtain a quadrupole splitting, Fe must be located on the octahedral site and therefore the new component could be the inverse spinel $\text{V}[\text{FeV}]\text{O}_4$.

The experimental XANES spectrum of the cell at open circuit voltage shows a much smaller pre-edge than V_2O_5 indicating that a new compound has formed (Fig. 4). Vanadium oxide spectra with distorted octahedral VO_6 coordination such as VO_2 , V_4O_7 and V_2O_3 [6] seems to have the right intensity of the pre-edge, but our experimental spectrum shows a much higher intensity of the main absorption edge. A good match is found with $\text{Li}_x\text{V}_2\text{O}_5$ with $x = 2.46$ [7], but Li intercalation was found to be irreversible when $x > 1$. However, the mixed conducting matrix can only be effective if Li intercalation, and therefore Li ionic conductivity, is reversible.

Fig. 5 shows simulations for several Li-V-O and Fe-V-O compounds with tetrahedral and octahedral V coordination. Considering the high main edge intensity of the experimental spectrum, the octahedral VO_6 coordination, as found *e.g.* in LiVO_2 , is more probable than square-pyramidal VO_5 or tetrahedral VO_4 coordination. The spectra of LiV_2O_5

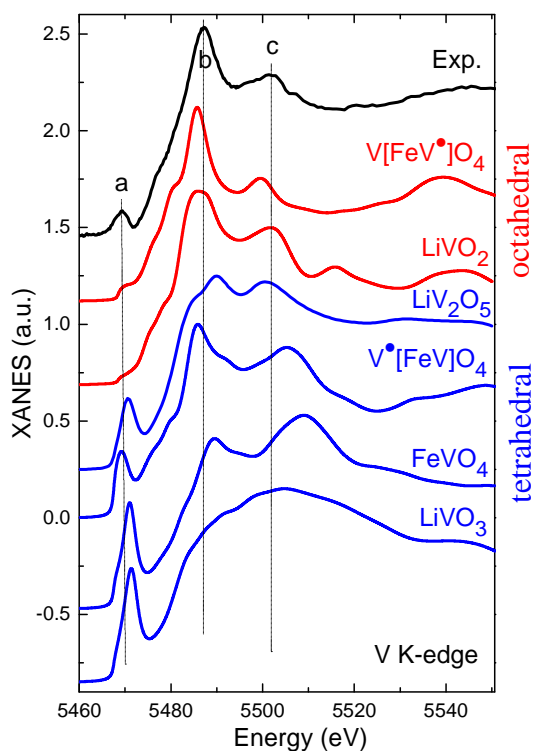


Fig. 5: FLAPW calculations for the series of lithium vanadates and iron vanadates with local octahedral (red) and tetrahedral (blue) vanadium environment. Upper black curve is the experimental V K-edge XANES spectrum for the ball-milled composite with (a) pre-edge, (b) main edge and (c) post-edge peaks. $V[FeV]O_4$ has vanadium on two different sites denoted by (•) and both sub-spectra are shown.

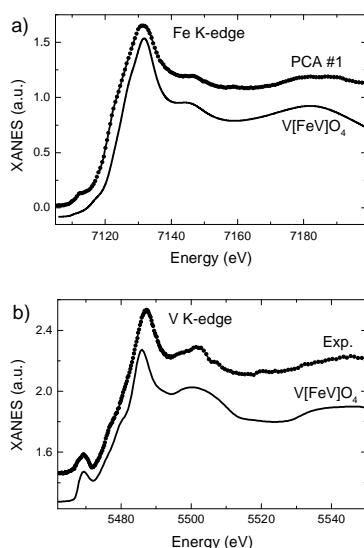


Fig. 6: Comparison of the FLAPW theoretical spectra of the mixed conducting matrix $V[FeV]O_4$ with a) the extracted Fe K-edge PCA spectrum of the new phase and b) the experimental V K-edge spectrum of $LiF/Fe(V_2O_5)$. The total V K-edge spectrum of $V[FeV]O_4$ was obtained by a superposition of spectra with octahedral and tetrahedral V positions (*c.f.* Fig. 5).

(square-planar), $FeVO_4$ and $LiVO_3$ (tetrahedral) show intense pre-edge features due to $p-d$ hybridisation effects. However, the oxygen octahedral around V in $LiVO_2$ are not distorted, and thus the pre-edge intensity is smaller than in the experiment.

The inverse spinel $V[FeV]O_4$, which was derived from $Fe^{3+}[Fe^{2+}V]O_4$ [8] by changing the Fe^{3+} atom on the tetrahedral site (8a) into a V^{3+} atom, is a special case as the crystal structure consists of V in octahedral as well as tetrahedral coordination. The interpolated V K-edge spectrum of $V[FeV]O_4$ shown in Fig. 3a has therefore a pre-edge due to $p-d$ hybridisation and a high main edge due to V in octahedral coordination, and resembles the experimental spectrum well. Additionally, the calculated Fe K-edge spectrum of $V[FeV]O_4$ shown in Fig. 3b also matches the PCA spectrum of the new Fe^{2+} component and shows a very high main edge due to Fe on octahedral sites. The fraction of the octahedrally coordinated V in $LiVO_2$ cannot be excluded because of the similarity of the V-K edge XANES spectra for the series of octahedrally coordinated compounds. The formation of $LiVO_2$ most likely occurs *via* intercalation of LiF into V_2O_5 with concomitant F/O^{2-} anion exchange.

Conclusion

We found that addition of V_2O_5 to a mixture of Fe and LiF improves the cycle life of the composite dramatically. During ball milling of $LiF/Fe(V_2O_5)$, a mixed conducting matrix (MCM) consisting of $Li_xVO_{2-x}F_x$ and $V[FeV]O_4$ phases is formed, which is responsible to for the improvement in capacity and cyclic performance.

Acknowledgements

The authors gratefully acknowledge the ANKA synchrotron light source of the Karlsruhe Institute of Technology for granting beam time on the INE beam line for the experiment.

References

- [1] M.S. Whittingham, *Chem. Rev.* **104** (2004) 4271–4302.
- [2] G.G. Amatucci, N. Pereira, *J. Fluorine Chem.* **128** (2007) 243–262.
- [3] G. Smolentsev, A.V. Soldatov, *Computat. Mat. Sci.* **39** (2007) 569–574.
- [4] S. Ramasamy, J. Jiang, H. Gleiter, R. Birringer, U. Gonser, *Solid State Commun.* **74** (1990) 851–855.
- [5] M.D. Dyar, D.G. Agresti, M.W. Schaefer, C. a. Grant, E.C. Sklute, *Annu. Rev. Earth Planet. Sci.* **34** (2006)
- [6] J. Wong, R.P. Messmer, D.H. Maylotte, *Phys. Rev.* **B30** (1984) 5596–5610.
- [7] M. Giorgetti, *J. Electrochem. Soc.* **146** (1999) 2387.
- [8] J.C. Bernier, P. Poix, *Ann. Chimie* **2** (1967) 81–89.

Near-surface density profiling of Fe ion irradiated Si (100) using extremely asymmetric diffraction by variation of the wavelength

B. Khanbabaee¹⁾, S. Facsko²⁾, U. Pietsch¹⁾

¹⁾ Solid State Physics, University of Siegen, D-57068 Siegen, Germany

²⁾ Helmholtz-Zentrum Dresden-Rossendorf, 01314 Dresden, Germany

The bombardment of the solid surfaces with energetic noble gas ions can be used for fabrication of the self-organized nanostructures on the surfaces[1]. Recently, a number of experimental studies have shown that the simultaneous incorporation of the foreign atoms, in particular metal atoms like Fe, during ion beam irradiation has tremendous influence on self-organized surface patterning[2]. At present, many aspects of influence of the co-deposited metal atoms are not fully understood. One of the key points of understanding is the investigation of the density variation at the regions just below the surface in which the incorporated Fe atoms may influence the patterning process. In this context, we study the surface modifications after direct off-normal Fe ion irradiation on Si(100), without assistance of noble gas ions. Considering the low energy of implanted Fe ions the ion beam-induced damage is limited only to a depth of few nanometers. Therefore surface sensitive methods are requested for the investigation of the near-surface region. This can be performed using extremely asymmetric x-ray diffraction (EAD) techniques. In EAD, due to refraction effect, Bragg peak is shifted from the position calculated by kinematic theory. The amount of this peak shift ($\Delta\theta$) depends on effective incidence angle and the mass density of the material allowing to extract the variation of surface density by monitoring different Bragg peak shifts.

The EAD scheme can be realized under fixed scattering geometry by varying the photon energy[3]. Small incidence angles α_i can be tailored by probing a lattice plane tilted by angle φ with respect to the surface normal where $\alpha_i = \theta_B(E) - \varphi$, and θ_B is Bragg angle (Fig. 1a).

In this work, we show the results of energy-dispersive EAD for determination of the surface density of Fe ion irradiated silicon samples. we examined Si(100) wafers irradiated with 5 keV Fe ions under 65° incidence angle with respect to the surface normal at two different total fluences of 1×10^{16} ions cm^{-2} (sample 1) and 5×10^{17} ions cm^{-2} (sample 2), respectively. Fig. 1b shows the rocking curves (RCs) for the sample 2 at $h\nu = 8715$ eV (black), $h\nu = 8810$ eV (magenta), $h\nu = 8840$ eV (olive), $h\nu = 8860$ eV (red) and $h\nu = 8875$ eV (blue). Due to grazing incidence angles, a part of x-rays is reflected from sample's edge. Each RC consists of an intense sharp peak with approximately zero peak shifts which corresponds to a Si (311) reflection from the sample's edge and a broader peak with larger peak shift which corresponds to Bragg reflection from the surface. With increasing photon energy and consequently decreasing α_i the surface Bragg peak starts to shift from the position of kinematical Bragg angle towards the maximum possible Bragg peak shift $\Delta\theta = \alpha_c$ (critical angle of total external reflection). The edge-peak is not affected by changing the energy and is used as a reference for the evaluation of the angular position of measured surface peaks.

Fig. 1c shows a comparison between the measured RCs for the samples 1 (red), 2 (blue) and non-irradiated Si (black) at $h\nu = 8840$ eV ($\alpha_i = 0.08^\circ$). It can be seen that the deviation from the kinematical Bragg peak position decreases from the non-irradiated Si(100) over sample 1 to sample 2 caused from reduction of the surface density[4]. Quantitatively, these density variations can be determined by fitting the measured Bragg peak shifts with calculated ones according to Eq. 1, from Ref. [4].

Fig. 1d shows the measured (open circle) and calculated (solid lines) Bragg peak shifts ($\Delta\theta$) versus photon energy/incidence angle for the samples 1 (red), 2 (blue) and non-irradiated Si (black). The fitting of the peak shifts after calibrated to Cu $K\alpha$ radiation reveals a surface density of $\rho_1 = 2.11$ g/cm^3 and $\rho_2 = 1.79$ g/cm^3 , for the samples 1 and 2, respectively, which are 13% and 26% smaller than the measured value for non-implanted silicon $\rho = 2.32$ g/cm^3 .

These values are in good agreement with obtained results for these samples using EAD at non-coplanar scattering geometry for Si (311) reflection[4]. In the presented case, the systematically reduction of density at the sample surface that increases with ion fluence can be relevant with developing a pattern on the irradiated surface.

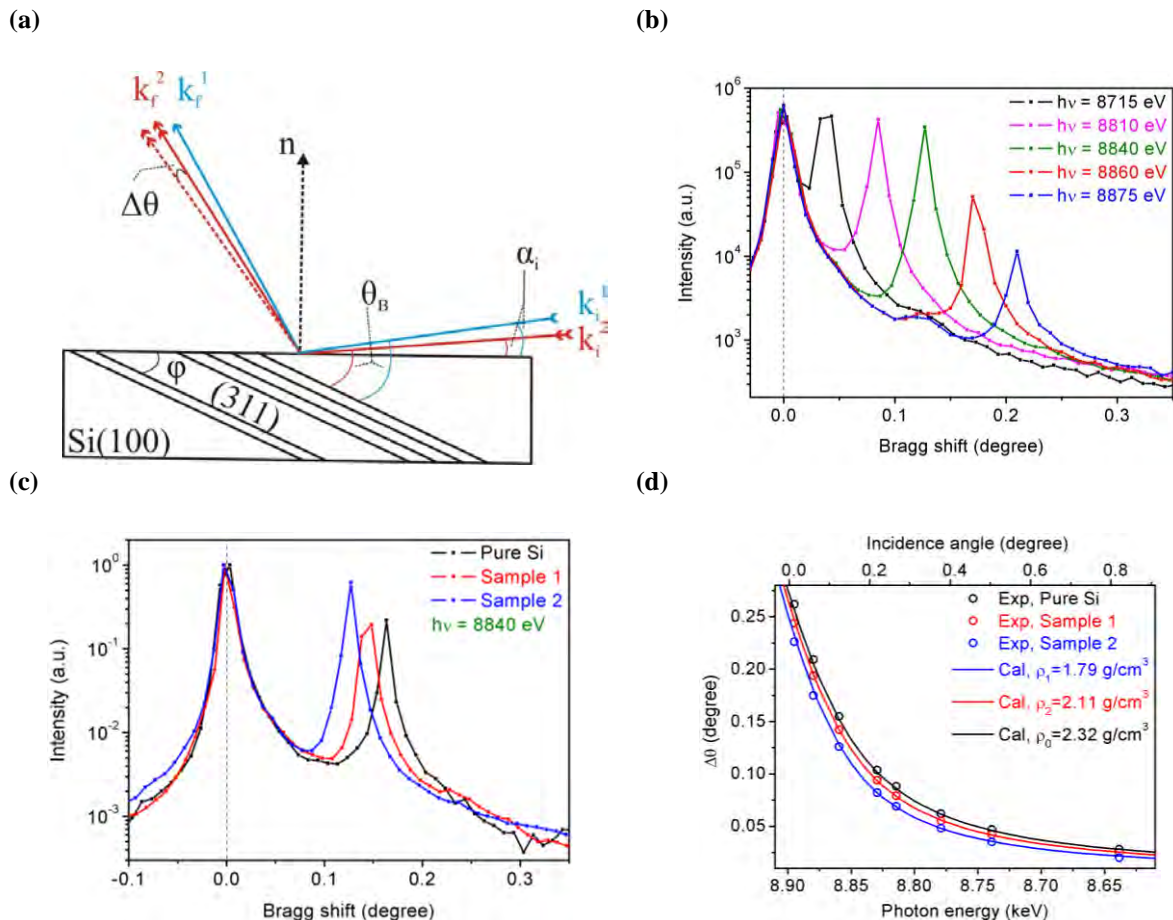


Fig.1: (a) The coplanar EAD geometry. The oblique lines tilted by angle φ with respect to the crystal surface showing the 311 lattice plane. The incidence angles (α_i) are changed by varying the incident wavevectors (k_i) via varying x-rays energy and consequently varying Bragg angles. While for incoming beam at large incidence angle (k_i^1), the reflected beam (k_f^1) is observed at kinematic Bragg peak position, for a beam at lower incidence angle (k_i^2), the reflected beam (k_f^2) shifts with value of $\Delta\theta$ with respect to kinematic Bragg peak position (dashed red arrow). n is the surface normal vector. (b) The measured rocking curves (RCs) of Si (311) reflection versus Bragg peak shift ($\Delta\theta$) for sample 1 at different photon energies of $h\nu = 8715$ eV (black), $h\nu = 8810$ eV (magenta), $h\nu = 8840$ eV (olive), $h\nu = 8860$ eV (red), and $h\nu = 8875$ eV (blue). (c) The comparison of rocking curves (RCs) of Si (311) reflection for the samples 1 (red), 2 (blue), and non-irradiated Si (black) at $h\nu = 8840$ eV ($\alpha_i = 0.08^\circ$). (d) The measured (open circles) and calculated (solid lines) dynamical Bragg peak shifts ($\Delta\theta_B$) versus wavelength/incidence angle for the samples 1 (red), 2 (blue) and non-irradiated Si (black).

Acknowledgements

This work is supported by Deutsche Forschungsgemeinschaft through FOR 845. We acknowledge the Synchrotron Light Source ANKA for provision of beamtime at the PDFIF beamline and we would like to thank Stephen Doyle for the excellent support during the synchrotron experiments.

[1] W.L. Chan, E. Chason, Journal of Applied Physics **101** (2007) 121301.

[2] B. Khanbabaee, B. Arezki, A. Biermanns, M. Cornejo, D. Hirsch, D. Lützenkirchen-Hecht, F. Frost, U. Pietsch, Thin Solid Films **527**, (2013) 349.

[3] H.-G. Bruhl, T. Baumbach, V. Gottschalch, U. Pietsch, B. Lengeler, Journal of applied crystallography **23/4** (1990) 228.

[4] B. Khanbabaee, A. Biermanns, S. Facsko, J. Grenzer, U. Pietsch, Journal of applied crystallography **46/2** (2013) 505.

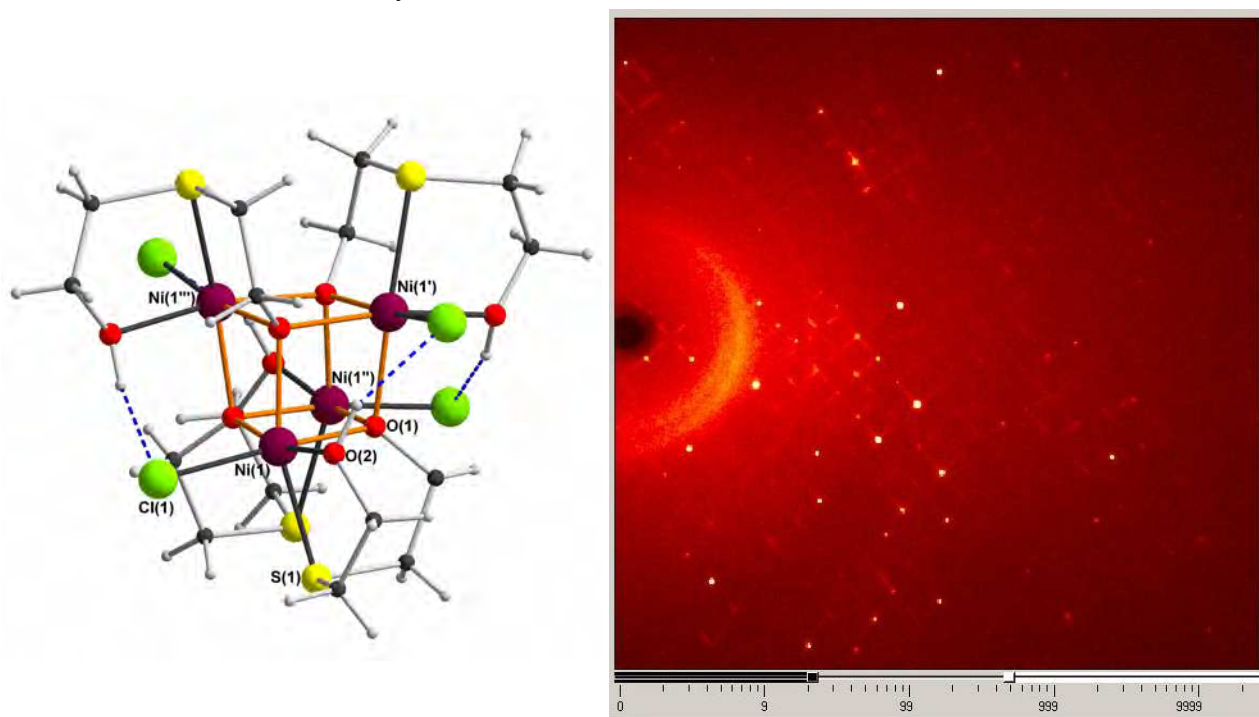
Crystallographic Characterisation of Large Paramagnetic Aggregates of Transition-Metal Cations

Christopher E. Anson¹⁾, Gernot Buth²⁾, Annie K. Powell¹⁾

¹⁾ Karlsruhe Institute of Technology, Institut für Anorganische Chemie, Engesserstr. 15, D-76131 Karlsruhe

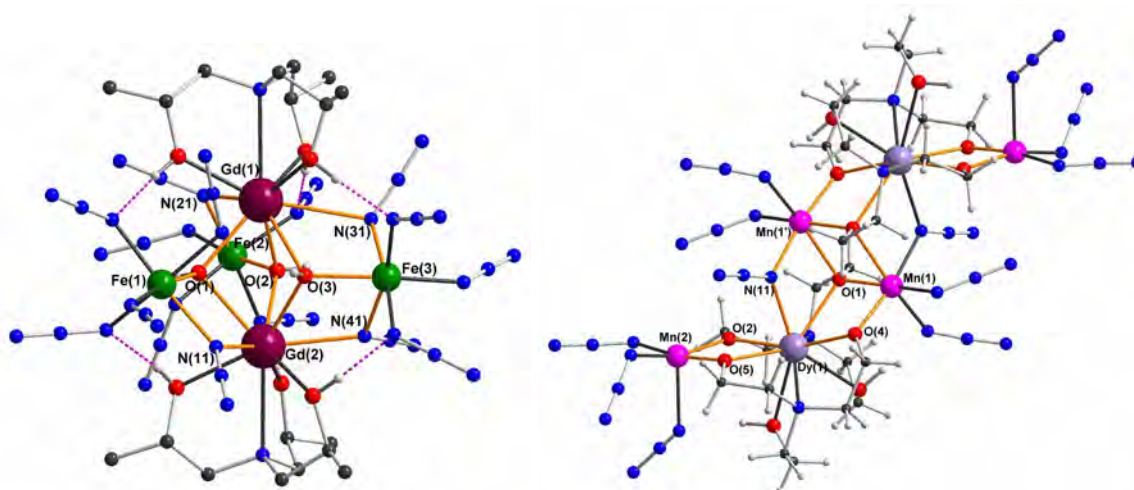
²⁾ Karlsruhe Institute of Technology, Institut für Synchrotronstrahlung, Hermann-von-Helmholtz-Platz 1, D-76344 Eggenstein-Leopoldshafen

The heterocubane complexes $[M^{\text{II}}_4(\text{HOC}_2\text{H}_4\text{SC}_2\text{H}_4\text{O})_4(\text{Cl})_4]$ ($M = \text{Co}, \text{Ni}$) might have been expected to crystallise in an unexceptional manner. Both compounds formed very small crystals, which were measured at ANKA, and were found to be isomorphous, crystallising in the tetragonal space group $I4_1/a$ with $Z = 12$. One of the independent molecules in the asymmetric unit could be refined straightforwardly, whereas the other showed a rather strange whole-molecule disorder. More unusually, the diffraction from both compounds showed the spot-like Bragg reflections to be joined by rather well-defined lines of diffuse reflection. Such behaviour does not appear to have been reported before, and would not have been visible without the high-brilliance synchrotron beam. The phenomenon is currently under investigation; it will be of interest to see if it is related to the molecular disorder in some way.



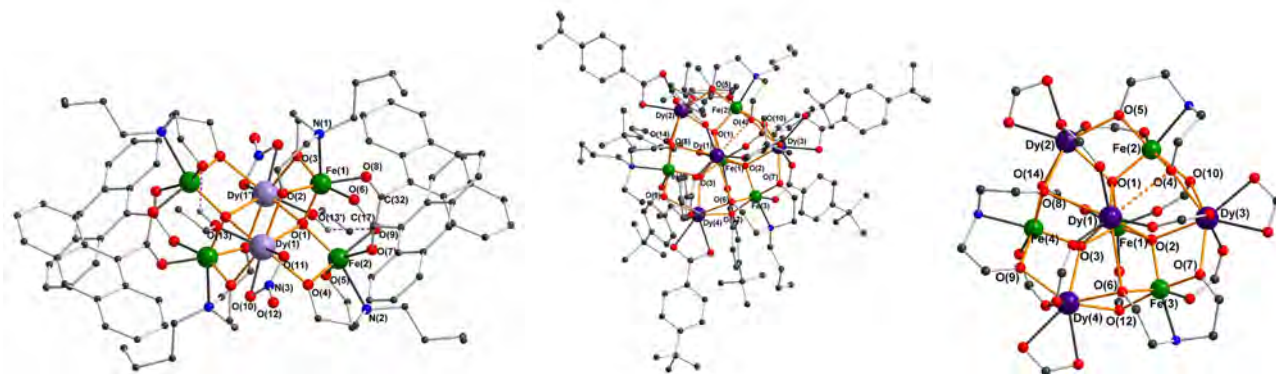
Molecular Structure of $[\text{Ni}^{\text{II}}_4(\text{HOC}_2\text{H}_4\text{SC}_2\text{H}_4\text{O})_4(\text{Cl})_4]$ (left) and a frame from the measurement showing the spot-like reflections joined by straight lines of diffuse reflection (right).

There is current interest in charged polynuclear metal complexes with large counterions that have melting points below 100 °C, and which thus can act as magnetically-active “ionic liquids”. We have recently found that such compounds can be catalytically active, in addition to their magnetic properties. The structures of two such compounds, $(\text{NBu}_4)_3[\text{Fe}_3\text{Gd}_2(\mu_3\text{-OH})_3(\text{Me-teaH}_3)_3(\mu\text{-N}_3)_4(\text{N}_3)_{11}]\cdot\text{CH}_2\text{Cl}_2\cdot\frac{1}{2}\text{EtOH}$ and $(\text{NBu}_4)_2[\text{Mn}_4\text{Dy}_2(\text{teaH})_4(\mu\text{-N}_3)_2(\text{N}_3)_{10}]$ have been determined. The counteranions with their *n*-butyl chains result in low diffraction intensity at higher angles, necessitating measurement on ANKA-SCD. The negative charges on the clusters resulted from the high number of azide ligands; these also promote favourable ferromagnetic interactions between metal centres, and in the Fe_3Gd_2 complex the N_5O coordination environment of the Fe^{III} cations may result in Spin-Crossover. Magnetic studies are being carried out.



Structures of the $[\text{Fe}_3\text{Gd}_2(\mu_3\text{-OH})_3(\text{Me-teaH}_3)_3(\mu\text{-N}_3)_4(\text{N}_3)_{11}]^{3-}$ and $[\text{Mn}_4\text{Dy}_2(\text{teaH})_4(\mu\text{-N}_3)_2(\text{N}_3)_{10}]^{2-}$ cluster anions.

Complexes of the type $[\text{Fe}^{\text{III}}_4\text{Ln}_2(\mu_4\text{-O})_2(\text{nbdea})_4(\text{anth-9-CO}_2)_4(\text{NO}_3)_2(\text{EtOH})_2] \cdot n\text{THF}$ are of interest not only for their magnetic properties (the Dy analogue is a Single-Molecule Magnetic with a high blocking temperature) but because they can be obtained in three different crystal forms, which differ in the number of lattice THF molecules ($n = 6, 2$ or 0), although the molecules are isostructural. This series thus allows a study of the effects of loss of lattice solvent molecules on the magnetic properties; such effects, which generally lead to an increase in intermolecular magnetic interactions, are relatively common in the literature but unfortunately often ignored. The complexes with $n = 2$ or 6 form large crystals, but the solvent-free version, which give rise to the most interesting magnetic behaviour, forms very small crystals. The solvent-free Fe_4Dy_2 and Fe_4Gd_2 structures have been measured at ANKA in order to determine the interactions between molecules.



Structures of “solvent-free” $[\text{Fe}_4\text{Dy}_2(\text{O})_2(\text{nbdea})_4(\text{anth-9-CO}_2)_4(\text{NO}_3)_2(\text{EtOH})_2]$ (left), $[\text{Fe}_4\text{Dy}_4(\text{O})_3(\text{nbdea})_3(\text{O}_2\text{C-C}_6\text{H}_4\text{-}^t\text{Bu})_{12}]$ (centre) and the core of the Fe_4Dy_4 cluster (right)

We have found that solvothermal synthetic methods can allow access to coordination clusters with structures very different from those obtained from syntheses at ambient conditions. For example, the clusters $[\text{Fe}_4\text{Dy}_4(\mu_4\text{-O})_3(\text{nbdea})_3(\text{O}_2\text{C-C}_6\text{H}_4\text{-}^t\text{Bu})_{12}] \cdot 4(\text{acetone}) \cdot \text{MeCN}$ and its Fe_4Y_4 analogue with a novel “double star” core were obtained under solvothermal conditions, whereas a similar recipe under ambient conditions gives the structurally very different $[\text{Fe}_4\text{Y}_2(\mu_3\text{-OH})_2(\text{nbdea})_4(\text{O}_2\text{C-C}_6\text{H}_4\text{-NO}_2)_8]$. All three compounds diffracted very weakly, but were measurable at ANKA giving excellent quality datasets.

Acknowledgements

We thank the DFG (Center for Functional Nanostructures) for financial support.

Sulphur speciation in basaltic melts

A. Fiege¹⁾, H. Behrens¹⁾

¹⁾ Leibniz Universität Hannover, Institut für Mineralogie, Callinstraße 3, D-30167 Hannover, Germany

Scientific Background

Sulphur is a ubiquitous element on Earth and because of its polyvalent properties it participates in various bio-/geo-/chemical processes. It is the third most abundant volatile in magmatic systems, besides H₂O and CO₂. In (silicate) melt-fluid systems, sulphur strongly partitions into the (aqueous) fluid phase and, thus, considering that the H₂O solubility in silicate melts decreases significantly with pressure (P; [e.g., 1]) large amounts of S can be released to the atmosphere during volcanic eruptions. The released sulphur species – especially SO₂ – have a high potential for climate impact [2, 3]. S and S-isotope fluid-melt distribution strongly depends on, e.g., sulphur speciation/oxygen fugacity (fO_2), pressure, temperature and melt composition [4 to 9]. Hence, understanding of S degassing is central to understand Earth's sulphur cycle. However, the available dataset for the partitioning of S between fluid and melt as well as the S isotope fractionation upon S degassing is still limited, especially for basaltic systems (melts with relatively low silica contents; ~50 wt% SiO₂). Thus, an ongoing research project focuses on the investigation of the distribution of sulphur and sulphur isotopes upon decompression under various conditions (e.g., temperature, oxygen fugacity (fO_2) and water content), with special attention on the influence sulphur speciation in the melt. Here, an accurate determination of the S speciation in the glasses experimental samples is a prerequisite to allow an interpretation of S and S-isotope distribution data obtained during this project. To date, XANES spectroscopy is the only reliable technique to analyse sulphur speciation in silicate melts with low sulphur contents (< 300 ppm).

Research projects

The goal of this session at ANKA's SUL-X beamline was to analyze the speciation of sulphur in basaltic glasses in the frame of a current research project at our institute funded by the Deutsche Forschungsgemeinschaft (DFG; BE1720/25-1). The melt compositions of the analysed glasses correspond to an alkali-rich basalt glass (~46.8 wt% SiO₂, ~10.5 wt% MgO) and a Mg-poor basaltic glass (~52.5 wt% SiO₂, ~0.9 wt% MgO). The experimental approach of the isothermal decompression experiments comprises a three step procedure: *i) Basaltic starting glass*: Synthetic anhydrous basaltic glass were prepared by melting a mixture of oxide (Si, Al, Ti, Fe, Mg, Mn) and carbonate (Na, Ca, K) powders in a PtRh crucible at T = 1600°C for 2 hours and quenching the melt in a water bath. *ii) S-bearing starting glass*: Hydrous sulphur-bearing glasses were synthesized in internally heated pressure vessels (IHPV) at ~1050°C, 400 and variable fO_2 ($\log(fO_2) = \text{QFM to QFM} +4.2$; QFM: quartz-fayalite-magnetite buffer), using a mixture of the anhydrous basalt (Mg-poor or alkali-rich), de-ionized H₂O (3 to 7 wt%) and CaSO₄·2H₂O as a S source (300 to 1200 ppm S). *iii) Isothermal decompression experiments*: The volatile-bearing glasses were crushed and re-melted in IHPVs at high pressure (~400 MPa) and 1050, 1150, 1200 or 1250°C for ~5 min. Subsequently, the pressure was released continuously at constant T and at a rate of 0.1 MPa/s (\approx fast explosive Plinian eruption style) to final pressure of 70 MPa. The samples were either directly isobarically quenched to preserve strongly non-equilibrium conditions or annealed for various times (0 to 6 h) at final P-T conditions before quenching to approach near-equilibrium between melt and fluid. The resulting experimental products consist of a chemically homogeneous glass matrix and S-rich quenched fluid inclusions (bubbles).

Analytical methods

The major element compositions (including S and Cl contents) of the quenched glasses were determined using an electron microprobe (EMP; Cameca SX-100 at the Leibniz Universität Hannover, LUH). The water content was measured by Karl Fischer Titration (LUH) and by FTIR spectroscopy (Bruker IFS 88, LUH). A Cameca IMS 1280 at the Woods Hole Oceanographic Institution was used to measure the S isotope composition of the glasses (³⁴S/³²S ratios). The S concentration in the starting glasses and partially degassed glasses ranges from 300 to 1200 ppm. XANES spectroscopy at sulphur K edge (2472 eV) was conducted at ANKA's SUL-X beamline to investigate the S speciation in the

glasses. A beam size of $200 \times 100 \mu\text{m}$ was applied to measure bulk sulphur speciation on bubble free areas in the experimental glasses. In contrast to previous session, analyses with a $60 \times 60 \mu\text{m}$ beam size to determine small scale variations in sulphur speciation throughout the glass and to evaluate possible contribution of sulphur species in quenched fluids to the spectra were not performed because the interpretation of these spectra was often difficult and only qualitative results could be obtained; e.g. the data indicate that H_2S is the dominating species in the fluid at $\sim\text{QFM}+1$ and SO_2 is the dominant species at $\sim\text{QFM}+3$.

Doubly polished thin sections were used for all XANES measurements to allow identifying adequate spots for each analysis at the microscope (e.g. areas without bubbles). The spectra were collected in the fluorescence mode and mainly quick XAFS scans (Bragg axis is continuously running; ~ 330 energy points; energy increments: 0.3 eV in the edge region (~ 2.46 to ~ 2.50 keV) and 1 eV in the pre- and post-edge region) were performed to avoid irradiation damages [10].

Results and Discussion

XANES analyses of oxidized samples ($\sim\text{QFM}+3$) reveal a sharp sulphate peak (S^{6+}) at an energy of ~ 2481.4 eV while spectra of experiments at $\log(f\text{O}_2) < \text{QFM}+1$ typically show a distinct sulphide signal at 2468.4 to 2472.8 eV and/or a broad sulphide peak at ~ 2476.8 eV. Spectra obtained for samples processed at intermediate redox conditions ($\sim\text{QFM}+1$ to $\text{QFM}+2$) show sulphate and sulphide features. The peak positions are in good agreement with our previous XANES data gained at ANKAs SUL-X beamline (MR98, MR113, 166) and recent studies; e.g. [11].

The $\text{S}^{6+}/\Sigma\text{S}$ ratios were determined for each glass using the approach of Jugo et al. [11]. A slight shift of the sulphide-sulphate transition in glasses towards more oxidizing conditions when compared to Jugo et al. [11] (see Fig. 1) may be related to differences in P, T and (bulk) H_2O content [12]

The XANES data obtained at ANKA from 2009 to 2011 contributed significantly to 2 recent publications [13, 14] and to various abstracts (8 in total). At least one more publications is planned based on the excellent results obtain during the latest XANES session at the SUL-X beamline.

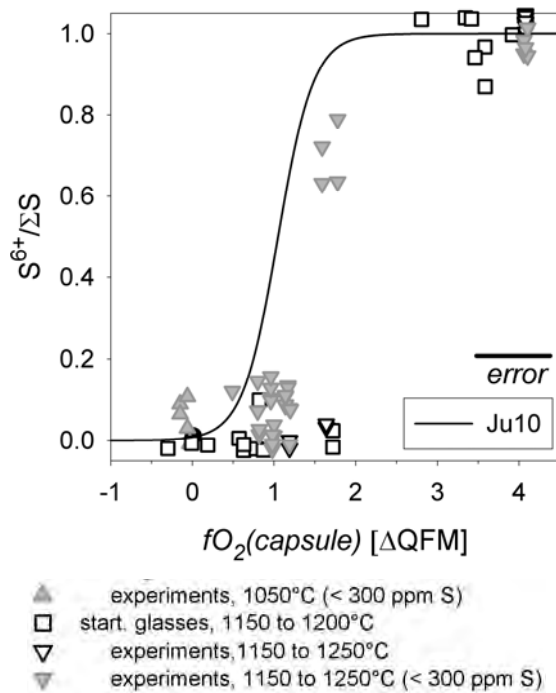


Figure 1: Results of S $\text{K}\alpha$ XANES analyses on S-bearing basaltic melts conducted during our last session. Ju10: Jugo et al. (2010); [11]

Acknowledgements

Dr. Jörg Göttlicher and Dr. Ralph Steininger are greatly acknowledged for their support and patience during the beamtime. This work is funded by the DFG.

References

- [1] Holtz F., Behrens H., Dingwell D.B., Johannes W. (1995), *Am. Mineral.* 80, 94-108; [2] Bluth G.J.S., Doiron S.D., Schnetzler C.C., Krueger A.J., Walter L.S., *Geophys. Res. Lett.* 19 (1992), 151-154; [3] Mandeville C.W., Webster J.D., Tappen C., Taylor B.E., Timbal A., Sasaki A., Hauri E., Bacon C.R. (2009), *Geochimica Et Cosmochimica Acta* 73, 2978-3012; [4] Nagashima, S., Katsura T., *Bul. Chem. Soc. Jpn* 46 (1973), 3099-103; [5] Ooura M., Hanada T. (1998), *Glass Techn.* 39-2, 68-73; [6] Botcharnikov, R., Behrens H., Holtz F., Koepke J., Sato, H., (2004), *Chem. Geol.* 213, 207-225; [7] Lesne, P., Kohn, S.C., Blundy, J., Witham, F., Botcharnikov, R.E., Behrens, H. (2011), *J. Petrology* 52, 1737-1762; [8] Webster J.D., Botcharnikov R.E. (2011), *Rev. Mineral. Geochem.* 73, 247-283; [9] Taylor B.E. (1986) *Rev. Mineral.* 16, 185-225; [10] Backnäs L., Stelling J., Behrens H., Göttlicher J., Mangold S., Verheijen O., Beerkens R.G.C., Deubener J. (2008), *J. Am. Ceram. Soc.* 91, 721-727; [11] Jugo P.J., Wilke M. & Botcharnikov E.B. (2010), *Geoch. Cosmoch. Acta* 74, 5926-5938; [12] Baker D.R., Moretti R. (2011) *Rev. Mineral. Geochem.* 73, 167-213; [13] Fiege A., Behrens H., Holtz F., Adams F. (2014), *Geoch. Cosmoch. Acta.* 125, 241-264; [14] Fiege A., Holtz F., Shimizu N., Mandeville C.W., Behrens H., Knipping J.L. (2014), *Geoch. Cosmoch. Acta.*, *in press.*

Mechanism of extraction of uranium(VI) in an ionic liquid with a neutral extractant: determination of the extracted complexes stoichiometry by EXAFS

C. Gaillard¹⁾, I. Billard²⁾, Y. Pipon¹⁾, D. Ternova²⁾,

¹⁾ Institut de Physique Nucléaire de Lyon, University of Lyon, 4 rue Enrico Fermi, 69622 Villeurbanne, France

²⁾ Institut Pluridisciplinaire Hubert Curien, University of Strasbourg, rue du Loess, 67037 Strasbourg, France

The aim of the experiment was to measure the EXAFS spectra at the uranium L₃-edge (17166 eV) of samples containing extracted uranyl ions in an ionic liquid (C₄mimTf₂N) with the extractant molecule tributylphosphate TBP. Modelling of the uranyl extraction data fits with a double extraction mechanism involving uranium anionic species at high acidic concentration and uranium cationic species at low acidic concentration.^{1, 2} Thus, U extraction may not be achieved through the formation of a neutral complex (commonly formed in the usual organic solvents), but by an ion exchange process between a charged complex and the ionic liquid ions. At low acid concentration, the formation of species [UO₂.xTBP]²⁺ is supposed. At high acid concentration, we could postulate the extraction of [UO₂(NO₃)₃.xTBP]⁻. In both cases, x has to be determined and the nitrate stoichiometry has to be confirmed.

At this stage, we wanted to verify the extraction of charged complexes in the ionic liquid phase by characterizing the stoichiometry and structure of uranium extracted species by EXAFS.

Measurements were led on the INE beamline in fluorescence mode. An average of 8 scans was made on each sample. We could analyse 6 samples during 3 days ([UO₂²⁺] = 0.01 M), their corresponding EXAFS/FT spectra are shown in figure 1.

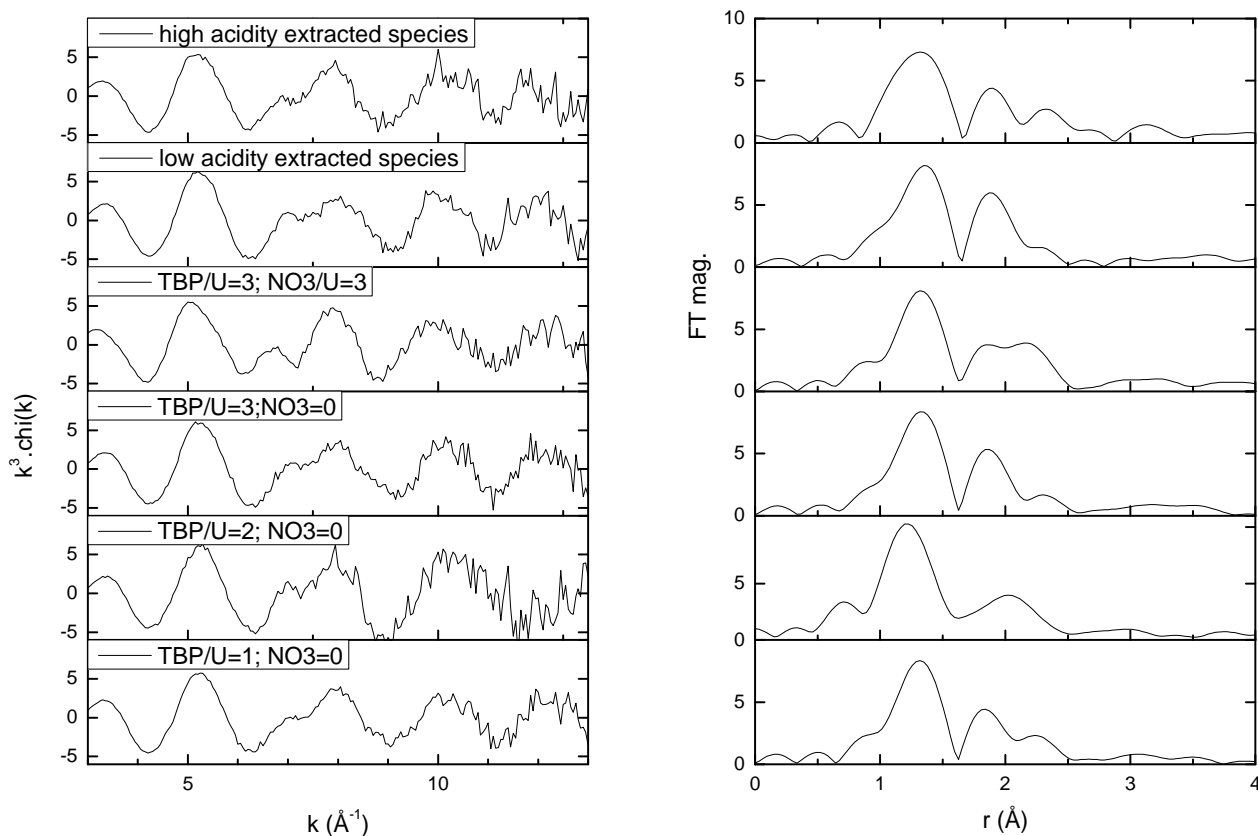


Figure 1: EXAFS and corresponding FT of analysed samples.

At low acidic concentration, the best fit result indicates that the extracted complex contains an average of 2 TBP molecules, and no nitrate ions. This confirms our uranyl extraction model at these experimental conditions, with a cation exchange mechanism. At high acidic concentration, it was not possible to get a stable fit of the data taking into account either (i) TBP molecule(s); (ii) nitrate ions bound in bidentate or monodentate fashion; (iii) TBP and nitrate group(s).

Acknowledgements

We acknowledge the team of INE beamline for their assistance during experiment.

References

1. M. Bonnaffé-Moity, A. Ouadi, V. Mazan, S. Miroshnichenko, D. Ternova, S. Georg, M. Sypula, C. Gaillard and I. Billard, *Dalton Trans.*, 2012, **41**, 7526.
2. I. Billard, A. Ouadi, E. Jobin, J. Champion, C. Gaillard and S. Georg, *Solv. Extr. Ion Exch.*, 2011, **29**, 577.

Structural investigation of self-irradiation damaged AmO₂

Damien Prieur ¹⁾, Jean-François Vigier ¹⁾, Thierry Wiss ¹⁾, Arne Janssen ¹⁾, Jörg Rothe ²⁾, Andrea Cambriani ²⁾, Joseph Somers ¹⁾

¹⁾ European Commission, Joint Research Centre, Institute for Transuranium Elements, P.O. Box 2340, 76125 Karlsruhe, Germany

²⁾ Institut für Nukleare Entsorgung, Hermann-von-Helmholtz-Platz, 76344 Eggenstein-Leopoldshafen, Germany

Introduction

Under non-operating conditions (reactor shut down or storage time), damages accumulate in nuclear fuel pellets due to the spontaneous radioactive decays of actinide elements. These self-irradiation induced-defects affect the fuel thermophysical properties, which can be detrimental for both reactor performance and safety. In the case of α emitters, the elastic collision leads to well-known phenomena at the structural scale such as amorphization, allotropic transitions, lattice parameter expansion, defect formation and pellet swelling at the macroscopic scale. These changes are particularly true for ²⁴¹Am which exhibits a very high α activity ($1.3 \times 10^{11} \text{ } \alpha \cdot \text{g}^{-1}$) associated to the emission of a $\sim 5.5 \text{ MeV}$ α particle and a $\sim 90 \text{ keV}$ ²³⁷Np recoil nucleus. In this context, this work aims to study the structure of a self-irradiation damaged AmO₂ by XRD, XAS and TEM. As this sample has been synthesized ~ 40 years ago, the cumulative α decay dose was estimated at $\sim 1.4 \times 10^{20} \text{ } \alpha \cdot \text{g}^{-1}$ corresponding to $\sim 36 \text{ dpa}$ (displacements per atom). Investigating more accurately the self-irradiation damages for high cumulative α decay dose in AmO₂ is of great interest to understand the mechanisms occurring and to extrapolate these to the irradiation damages produced in the conventional fuels, which crystallizes in the same fluorite structure as AmO₂.

Experimental

The XAS measurements have been performed on 4 mg of powdered sample that had been mixed with 55 mg of BN. The XAS data have been collected at the Angströmquelle Karlsruhe (ANKA) synchrotron, under dedicated operating conditions (2.5 GeV, 100-160 mA) on the Institut für Nukleare Entsorgung (INE) beamline [1]. A Ge [422] double-crystal monochromator coupled to collimating and focusing Rh-coated mirrors was used. XAS spectra were collected at room temperature in both transmission and fluorescence modes at Np L_{III} (17610 eV) and Am L_{III} (18510 eV) edges.

Results

According to various studies, the lattice parameter of fresh AmO₂ ranges from 5.372 to 5.377 Å. After ~ 100 days of self-irradiation ($\sim 1 \cdot 10^{18} \text{ } \alpha \cdot \text{g}^{-1}$), the unit cell reaches a saturation value between 5.385 and 5.392 Å, which corresponds to an increase of 0.2 - 0.3 % of the initial lattice parameter. An exponential law is usually employed to describe the unit cell evolution with the cumulative decay dose. This implies that the lattice parameter will not change in time, once the saturation value is reached. Based on the refinement of the XRD pattern, a lattice parameter of 5.394(1) Å was derived for the damaged AmO₂ sample [2]. Compared to fresh AmO₂, there is clearly an increase of the lattice parameter with the self-irradiation. Therefore, our value is in fair agreement with the previously reported unit cell parameter of damaged AmO₂. One can conclude that the lattice parameter increases up to 100 days of self-irradiation and after this period the unit cell does not evolve significantly during the following 40 years.

The structural parameters have been derived from the analysis of the EXAFS data [2]. In the case of the reference AmO₂, the first and second Am – O distances are equal to 2.326 (5) and 4.46 (1) Å. For the damaged AmO₂, those distances are equal to 2.335 (1) and 4.48 (1) Å, respectively. Compared to the reference AmO₂, this corresponds to an increase of 0.4 (1) % of the Am - O bond lengths, which is in fair agreement with the unit cell expansion as derived by XRD. The first Am – Am distances are equal to 3.80 (1) and 3.81 (1) Å for the reference and damaged AmO₂, respectively. Considering the experimental uncertainty, no significant variation can be concluded. The second Am - Am bond length is equal to 5.40 (1) Å, which is in good agreement with the lattice parameter measured by XRD, i.e. 5.394 (1) Å, supporting the increase of the lattice parameter by 0.3 %. Taking into account XRD and EXAFS results, one can conclude that both O

and Am sub-lattices are affected by the self-irradiation. An increase of ~ 0.4 (1) % of the O and Am interatomic lengths as well as of the lattice parameter is observed. This expansion of the cell distances can be understood from the ballistic effects and associated elastic collisions which conduct to atomic displacements. It is interesting to note that the process of damage creation is permanent and continuous, while the lattice expansion is only limited to the first 100 days of self-irradiation.

Figure 1 presents the modulus of k^3 -weighted experimental Fourier transforms of the reference and the damaged AmO_2 [2]. The main difference between the fresh and the aged samples is an overall amplitude decrease in the latter AmO_2 sample. It suggests that the damaged AmO_2 is more disordered compared to the reference AmO_2 . In addition to the overall amplitude of the whole FT range, one can observe that the shells are better resolved in the reference AmO_2 than in the damaged between 6 and 10 Å. This can be easily understood as the recoil nucleus from ^{241}Am α decay is expected to redistribute thousands of atoms.

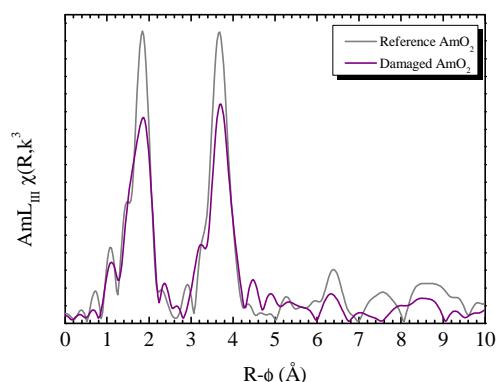


Figure 1 : FT modulus of reference and damaged AmO_2 .

Conclusion

The structure of damaged AmO_2 (36 dpa) has been studied by coupling XRD, XAS and TEM measurements. This unique combination has shown that a fluorite structure with a high level of crystallinity is maintained despite 40 years of self-irradiation. However, an increase of the lattice distances and the presence of nanometer size He bubbles have also been observed. These features are directly linked to the emission of an alpha-particle and a recoil nucleus.

Acknowledgements

The authors acknowledge Co Boshoven, Jean-Yves Colle, Sébastien Gardeur, Antony Guiot, Patrick Lajarge and Emmanuel Vermorel for their help in the sample preparation and Daniel Bouxière for the XRD acquisition. The authors are grateful to ANKA for provision of beamtime. Dr. Kathy Dardenne and Dr. Tonya Vitova are thanked for their help during the XAS data acquisition.

References

- [1] J. Rothe, S. Butorin, K. Dardenne, M.A. Denecke, B. Kienzler, M. Löble, et al., The INE-Beamline for actinide science at ANKA, Rev. Sci. Instrum. 83 (2012) 043105–043105–13.
- [2] D. Prieur, J-F. Vigier, T. Wiss, A. Janssen, J. Rothe, A. Cambriani, J. Somers, Structural investigation of self-irradiation damaged AmO_2 , JSSC 212 (2014) 7-12.

XAFS investigation of a genuine HAWC glass fragment sampled from the Karlsruhe Vitrification Plant (VEK)

K. Dardenne¹, E. González-Robles¹, J. Rothe¹, N. Müller¹, G. Christill², B. Kienzler¹, V. Metz¹, G. Roth¹ and H. Geckeis¹

Karlsruhe Institute of Technology, ¹Institute for Nuclear Waste Disposal (KIT-INE), ²Sicherheit und Umwelt (KIT-SUM), Hermann-von-Helmholtz-Platz 1, D-76344 Eggenstein-Leopoldshafen, Germany

Introduction

The Karlsruhe Reprocessing Plant (WAK) was operated from 1971 to 1991 as a pilot facility for reprocessing of spent nuclear fuels from German research reactors and commercial power plants. Reprocessing activities resulted in $\sim 60 \text{ m}^3$ of highly active waste concentrates (HAWC) stored on-site in liquid form. An important step in the current decommissioning and dismantling of the WAK was the HAWC vitrification in the Karlsruhe Vitrification Plant (VEK) constructed close to the HAWC storage facilities [1,2]. A total of 2.2 g from sections of genuine HAWC glass rods were retained during the vitrification process and transferred to the INE shielded box line for later glass product characterization.

Experimental

In 2013 a mm sized fragment with a contact dose rate of $\sim 590 \mu\text{Sv/h}$ (Fig. 1, left) was selected and mounted in a specially designed sample holder (Fig. 1, right) for pilot XAS/XRF investigations at the INE-Beamline at ANKA. The experiment aimed at elucidating the potential of direct actinide / radionuclide speciation (with an emphasis on the fission products Se and Tc, which are regarded as contributing to the initially mobile fraction of the radionuclide inventory in spent nuclear fuel and waste glasses following corrosive waste degradation in a geological repository) in highly active nuclear materials and assessing the possible influence of the γ -radiation field surrounding highly active samples on the XAS detection electronics.

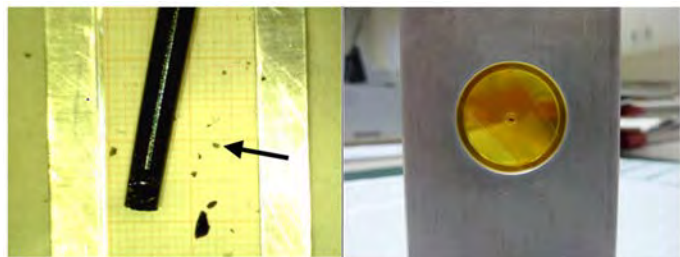


Fig. 1: HAWC glass fragment (arrow) selected for investigation at INE-Beamline (left, scale in mm); glass fragment inside a double containment mounted in the sample holder (right) prior to the transport to ANKA.

Results

While the influence of the γ -radiation field turned out to be negligible, initial radionuclide speciation studies by XAS were most promising. Exemplarily, Fig. 2 depicts normalized Se K-edge (left) and Tc K-edge XANES measurements (right) of the HAWC glass fragment and corresponding Se and Tc reference samples, respectively. Edge position and simple spectral fingerprint analysis point to the presence of Se in the glass as selenite oxoanion (SeO_3^{2-}) as in Na_2SeO_3 . Pronounced dampening of the near-edge fine structure indicates dispersion of the SeO_3^{2-} oxoanions in the glass matrix, where the crystalline ordering such as in the Na_2SeO_3 reference is lost. Tc is dispersed as pertechnetate oxoanion (TcO_4^-) in the glass matrix as in the aqueous Tc(VII)/ HClO_4 reference sample, which is unequivocally proven by the edge shift

relative to Tc(IV)O_2 and the pronounced pre-edge feature at ~ 21056 eV indicative of tetrahedral oxygen coordination.

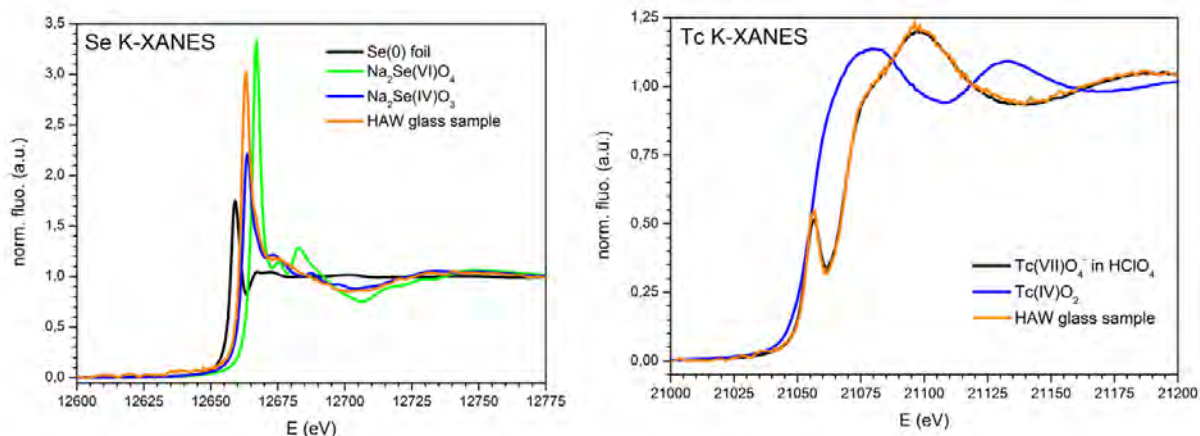


Fig. 2: Normalized Se K- (left) and Tc K-XANES spectra of the HAWC glass fragment and corresponding reference spectra.

In addition to Se and Tc discussed above and the plethora of elements contained in the glass fragment, the focus of these initial XAFS investigations was on the possibility for direct actinide speciation by recording corresponding L3-edge XAFS data. Th was not expected to be contained in the glass and, hence, was not detectable in XAFS scans across the Th L3-edge. Only a very tiny absorption signature was detected by scanning the energy across the Cm L3-edge. This signal was not sufficient to obtain any useful XANES data. This is in full agreement with the known composition of the HAWC oxide residue [1], where the Cm content is expected to reach about 1/10 of the Pu content, which, in turn, amounts to $\sim 1/30$ of the U content of the HAWC glass. The concentrations of Am and Np are expected to reach twice the value obtained for Pu. For all actinide elements besides Th and Cm (U, Np, Pu, Am) as well as for Zr registration of high quality XANES data was possible - for some of these elements even reasonable EXAFS spectra were recorded. The XANES analysis reveals that uranium is present as U(VI), neptunium as Np(V), plutonium as Pu(IV), americium as Am(III) and zirconium as Zr(IV) in the HAWC glass, as expected from the oxidizing conditions during the HAWC vitrification process [3].

Acknowledgements

A. Bauer, Ch. Marquardt (both KIT-INE) and Th. Hoffmann (KIT-SUM) are acknowledged for invaluable technical and logistic support during preparation of these experiments. ANKA is acknowledged for the provision of beamtime.

References

- [1] G. Roth, S. Weisenburger, *Vitrification of high-level liquid waste: glass chemistry, process chemistry and process technology*, Nucl. Engineering and Design **202**, 197-207 (2000)
- [2] F. J. Fleisch, M. Weishaupt, G. Roth, W. Grünewald, W. Tobie, S. Weisenburger, *Verglasungsanlage VEK - Erfolgreiche heiße Inbetriebsetzung und erste Betriebserfahrungen*, in: Jahrestagung Kerntechnik, Berlin, Germany (2010)
- [3] K. Dardenne, E. González-Robles, J. Rothe, N. Müller, G. Christill, B. Kienzler, V. Metz, G. Roth, and H. Geckeis, *XAS and XRF investigation of a genuine HAWC glass fragment obtained from the Karlsruhe vitrification plant (VEK)*, submitted to J. Nucl. Mater. (2014)

In-situ XAS measurements at high temperature on transuranium-bearing oxide fuels and precursors

F. Lebreton^{1),2)}, P.M. Martin³⁾ M. Caisso^{1),4)}, L. Ramond¹⁾, D. R. Neuville⁵⁾, M. Bataille¹⁾, T. Delahaye¹⁾

¹⁾ CEA, DEN, DTEC/SDTC/LEMA – 30207 Bagnols-sur-Cèze, France

²⁾ GEMH/ENSCI – 87065 Limoges, France

³⁾ CEA, DEN, DEC/SESC/LLC – 13018 Saint-Paul-lez-Durance, France

⁴⁾ Institut Européen des Membranes, UMR 5635 CNRS-ENSCM-UM2, CC047, Université Montpellier 2, 34095 Montpellier, France

⁴⁾ Géochimie & Cosmochimie, CNRS-IPGP, Paris Sorbonne Cité – 75005 Paris, France

As the measurements were performed this month, this report was sent as a preliminary report. A final experimental report giving a more precise description of the results will be issued in July.

During this stay, the first X-ray Absorption Spectroscopy measurements on transuranium-bearing samples at high temperature and under controlled atmospheres were performed. The data were collected using an experimental set-up especially developed for this experiment.

XANES (X-ray Absorption Near Edge Structure) measurements were performed on uranium-gadolinium and uranium-amerium samples from 300 to 1400 K at both U and Am L3 edges. The samples were WAR (Weak Acid Resin) microspheres loaded with U and Am or Gd. These compounds are used as potential new precursor for the fabrication of mixed oxide nuclear fuels and transmutation targets for fast neutrons reactors. Using this new in-situ XAS set-up, the calcination under air of these amorphous compounds to an oxide was monitored through the determination of the cation oxidation states and local symmetry at different temperatures.

The first results highlight the oxidation of uranium during the oxide formation while amerium remains mostly trivalent. Once calcination was completed, the reduction of the same sample under Ar-H₂(4%) was then performed in-situ and monitored. It was shown that a reduced U(+IV)/Am(+III) mixed oxide is obtained at high temperature. After cooling down to room temperature in 10 minutes, a slight oxidation of uranium was observed, leading to a mixed +IV/+V oxidation state in the final mixed oxide. A final sample close to what was previously observed with our past ex-situ XAS was thus obtained. This TALISMAN-JRP therefore allowed the achievement of the main objective of this project: performing high temperature XAS measurements on transuranium-bearing samples. Moreover, the developed experimental setup is now fully validated and would be available for the study of other actinide systems.

Structural investigation of uranium-neptunium mixed dioxides

Damien Prieur ¹⁾, Jean-François Vigier ¹⁾, Laura Martel ¹⁾, Kathy Dardenne ²⁾, Joseph Somers ¹⁾

¹⁾ European Commission, Joint Research Centre, Institute for Transuranium Elements, P.O. Box 2340, 76125 Karlsruhe, Germany

²⁾ Institut für Nukleare Entsorgung, Hermann-von-Helmholtz-Platz, 76344 Eggenstein-Leopoldshafen, Germany

Introduction

Understanding the incorporation mechanism of minor actinides (MA), i.e. Np, Am, Cm, in uranium dioxides and mixed U-Pu oxides (MOX) as solid-solutions is essential starting point for the detailed understanding of these materials, which will become particularly relevant, as they are considered as fuels and targets for the transmutation of the minor actinides in fast neutron reactors. This is an innovative approach to dramatically reduce the long term radiotoxic impact of these materials and is considered in two modes: the homogeneous MA recycling scenario which relies on the introduction of a few per cent of MA in all of the fuel pins of the reactor and, the heterogeneous MA recycling concept which considers deployment of the MA in a UO₂ matrix in dedicated fuel rods and assemblies. As such fuels contain no Pu in the fresh fuel, they are often referred as "targets". Despite being the most abundant minor actinide in spent fuel, targets bearing Np have not been, to our knowledge, the subject of any complete structural study using local structure techniques. We focus our attention here on a most basic solid solution system U_{1-x}Np_xO₂. In addition, the oxidation state of uranium in these compounds remains uncharacterised, despite its potential importance as U can adopt higher oxidation states than IV, i.e. V and VI.

Experimental

The XAS measurements have been performed on 4 mg of powdered sample that had been mixed with 55 mg of BN. The XAS data have been collected at the Angströmquelle Karlsruhe (ANKA) synchrotron, under dedicated operating conditions (2.5 GeV, 100-160 mA) on the Institut für Nukleare Entsorgung (INE) beamline [1]. A Ge [422] double-crystal monochromator coupled to collimating and focusing Rh-coated mirrors was used. XAS spectra were collected at room temperature in both transmission and fluorescence modes at U L_{III} (17166 eV) and Np L_{III} (17610 eV) edges.

Results

The oxidation states have been determined from XANES at U L_{III} and Np L_{III} edges [2]. The corresponding spectra are presented in Figure 0 with those of U(IV)O₂ and Np(IV)O₂ reference materials. Their inflection points and white lines were found at 17170.3 (5) eV and 17175.5 (5) eV and at 17616.5 (5) eV and 17621.8 (5) eV, respectively. Within the uncertainty of 0.5 eV, there is no variation of the inflection point and the white lines in the U_{1-x}Np_xO₂ samples compared to the pure dioxides. This shows that uranium and neptunium have an oxidation state of IV for all the compositions. The oxidation state IV of Np in the U_{1-x}Np_xO₂ is consistent with previous Mössbauer results.

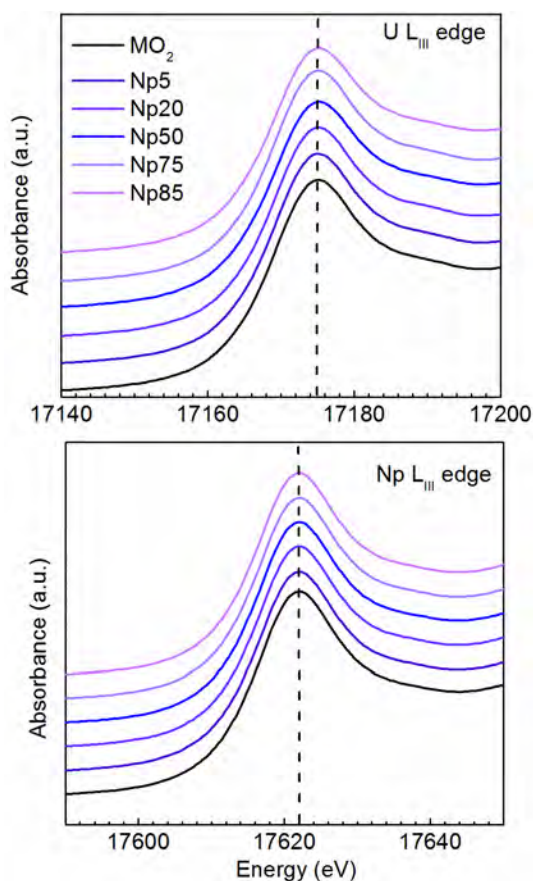


Figure 1: XANES spectra at the U LIII and Np LIII edges of MO_2 ($M=\text{U}$ or Np) and of the $\text{U}_{1-x}\text{Np}_x\text{O}_2$ samples.

Conclusion

Uranium-Neptunium mixed dioxides are considered as fuels and targets for the transmutation of the minor actinides in fast neutron reactors. A local and atomic scale structural analysis was performed on a series of $\text{U}_{1-x}\text{Np}_x\text{O}_2$ ($x = 0.01; 0.05; 0.20; 0.50; 0.75; 0.85$) synthesized by the sol-gel external gelation method, for which longer range structural analysis indicates that the process yields solid-solutions. The oxidation state of IV for uranium and neptunium cations was confirmed using U LIII and Np LIII edge XANES. The atomic scale structure was probed with ^{17}O magic angle spinning nuclear magnetic resonance (MAS-NMR) for the anion. Structural distortions due to the substitution of U by the smaller Np cation were detected by ^{17}O MAS-NMR. In addition, for $\text{U}_{1-x}\text{Np}_x\text{O}_2$ ($x = 0.20, 0.75, 0.85$), a slight preference for oxygen surrounded by four cations of the same type was observed.

Acknowledgements

The authors acknowledge Co Boshoven, Sébastien Gardeur, Antony Guiot, Patrick Lajarge and Emmanuel Vermorel for their help in the sample preparation and Daniel Bouxière for the XRD acquisition. The authors are grateful to ANKA for provision of beamtime.

References

- [1] J. Rothe, S. Butorin, K. Dardenne, M.A. Denecke, B. Kienzler, M. Löble, et al., The INE-Beamline for actinide science at ANKA, Rev. Sci. Instrum. 83 (2012) 043105–043105–13.
- [2] L. Martel, J-F. Vigier, D. Prieur, S. Noury, A. Guiot, K. Dardenne, J. Boshoven, J. Somers, Structural investigation of U-Np mixed dioxides using XRD, XANES and NMR, Inorg. Chem. (2014) submitted.

EXAFS study of Am(III) complexation with oxalate as a function of pH

D.R. Fröhlich¹⁾, A. Skerencak-Frech²⁾, K. Dardenne²⁾, J. Rothe²⁾, P.J. Panak¹⁾²⁾

¹⁾ Ruprecht-Karls-Universität Heidelberg, Physikalisch-Chemisches Institut, D-69120 Heidelberg

²⁾ Karlsruher Institut für Technologie, Institut für Nukleare Entsorgung, D-76344 Eggenstein-Leopoldshafen

Introduction

Due to their long half-lives and high radiotoxicities, the transuranium elements (Np, Pu, Am) are of particular interest with respect to the long-term safety assessment of a repository for high-level nuclear waste in a deep geological formation. In the case of natural clays as host rock, the related pore waters are known to contain organic compounds which can occur in high concentrations. Besides macromolecular organic molecules (e.g. humic substances), low molecular weight compounds are present in these natural waters at concentrations in the millimolar range. In this context, oxalate is of certain interest as it is a natural organic ligand with strong complexation properties and may also be formed as a result of radiolytic degradation of more complex organic compounds [1].

Oxalate can be bound to cations in different coordination modes (end-on, side-on) and it is possible that the coordination mode changes as a function of different system parameters. As the pH value is one of the key parameters in aquatic chemistry, the coordination of Am(III) by oxalate is studied at varying the pH. The structural data obtained for Am(III) in this work is also suitable to estimate the complexation behaviour of other trivalent actinides (e.g. Pu(III)).

Experimental procedure

Solutions of 1 mM Am(III) and 0.01 M oxalate at different pH values (1, 3, 5) were prepared in the radiochemical laboratories at the INE (KIT, Karlsruhe).

Am L_{III}-edge EXAFS spectra were collected in fluorescence mode at an angle of 90 ° using the 5 pixel Ge detector (Canberra Ultra-LEGe). All measurements were performed at room temperature. For data evaluation the software packages EXAFSPAK, Athena 0.8.061, and Artemis 0.8.012 were used. Theoretical scattering phases and amplitudes were calculated with FEFF8.40 using the crystal structures of Nd₂(C₂O₄)₃·10 H₂O [2] or Eu(CH₃COO)₂·0.5 H₂O [3]. In all cases, the models were fit to the k³-weighted raw EXAFS spectra.

Results

Figure 1 shows the measured k³-weighted Am L_{III}-edge EXAFS spectra and the related Fourier Transforms. While the spectra at pH 1 and pH 3 reveal similar structures, the EXAFS spectrum at pH 5 shows significant differences. This difference is also clearly visible in the related Fourier Transforms. At low pH, two peaks at higher distance are identified. Thereby, the carbon atoms of the coordinating oxalate are located at ≈ 3.30 Å. This value is in good agreement with the metal-carbon distances in different crystal structures of lanthanide-oxalate compounds, where oxalate is bound side-on (3.20-3.30 Å). [2,4] Furthermore, an additional peak, which originates from various multi-scattering paths, is visible at around 4.55 Å. This also points towards a side-on coordination.

In contrast to this, the structural data obtained at pH 5 differs considerably from the data at lower pH. The Am-C distance is significantly shifted towards higher distance (3.44 Å). Furthermore, another neighbour is located at 4.05 Å which may be a distal carbon or oxygen atom. Lastly, the strong signal of the multi-scattering contributions disappears completely under these experimental conditions. This is a strong indication that the coordination mode has changed. In case of a bi-dentate end-on coordination, a shorter carbon distance around 2.9 Å would be expected. The long distance of 3.44 Å is attributed to a mono-dentate coordination and is in good agreement with calculated values for U(VI) oxalate [5]. However, further studies are necessary to clarify the change in coordination mode of oxalate under these experimental conditions.

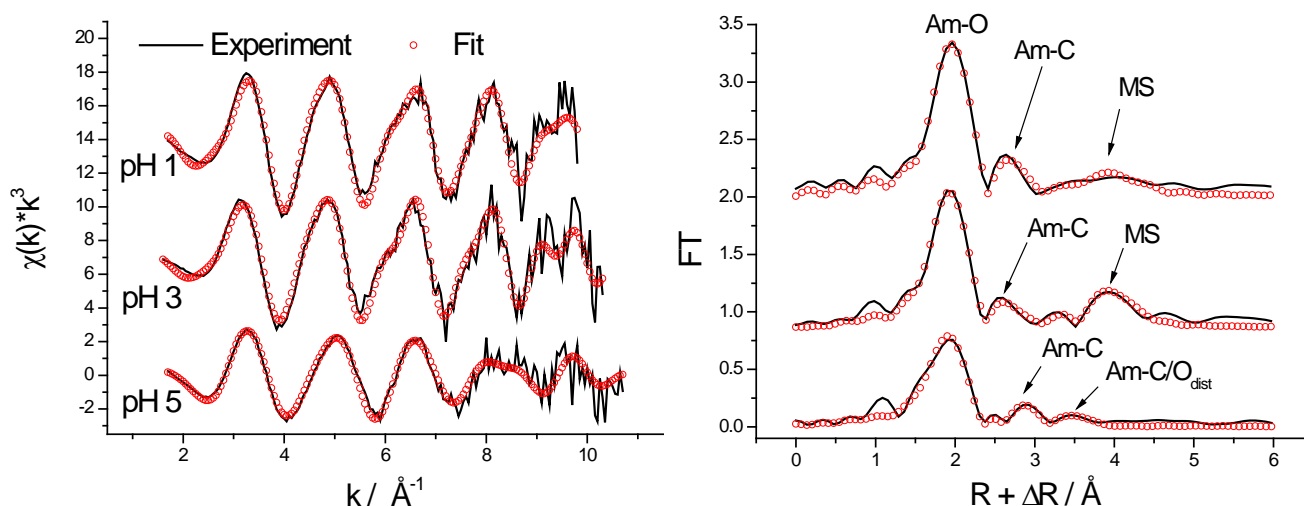


Figure 1: k^3 -weighted Am L_{III} -edge EXAFS spectra and related Fourier transforms as a function of pH.

Table 1: Structural parameters determined for 1 mM Am(III) in the presence of 0.01 M oxalate as a function pH (errors given in brackets).

	Am-O			Am-C			Am-C/O _{dist}		
	N	R / Å	$\sigma^2 / \text{Å}^2$	N	R / Å	$\sigma^2 / \text{Å}^2$	N	R / Å	$\sigma^2 / \text{Å}^2$
pH 1	9.1 (0.6)	2.47 (0)	0.007 (1)	3.2 (0.6)	3.31 (1)	0.001 (2)	-	-	-
pH 3	9.8 (0.6)	2.46 (1)	0.009 (1)	3.2 (1.3)	3.30 (1)	0.002 (3)	-	-	-
pH 5	7.4 (0.5)	2.42 (1)	0.011 (1)	3.5 (0.9)	3.44 (1)	0.004 (2)	3.5*	4.05 (2)	0.006 (3)

$S_0^2 = 0.9$, *coupled to N of the carbon shell

Acknowledgements

This work has been supported by the German Federal Ministry of Economics and Technology (BMWi) under contract number 02E11031.

References

- [1] W. Hummel, G. Anderegg, L. Rao, I. Puigdomenech, O. Tochiyama, Chemical thermodynamics of compounds and complexes of U, Np, Pu, Am, Tc, Se, Ni and Zr with selected organic ligands, NEA-OECD, Elsevier, Amsterdam, (2005).
- [2] W. Ollendorff, F. Weigel, The structure of some lanthanide oxalate decahydrates, $\text{Ln}_2(\text{C}_2\text{O}_4)_3 \cdot 10 \text{H}_2\text{O}$, with Ln = La, Ce, Pr, and Nd, Inorg. Nucl. Chem. Lett., 5, 263-269, (1969).
- [3] P. Starynowicz, Synthesis and crystal structure of europium (II) diacetate hemihydrate, $\text{Eu}(\text{CH}_3\text{COO})_2 \cdot 0.5 \text{H}_2\text{O}$, J. Alloy Compd., 268, 47-49, (1998).
- [4] T. Bataille, D. Louer, Yttrium sodium oxalate tetrahydrate, $[\text{Y}(\text{H}_2\text{O})]\text{Na}(\text{C}_2\text{O}_4)_2 \cdot 3 \text{H}_2\text{O}$, Acta Crystallogr. C, 55, 1760-1762, (1999).
- [5] V. Vallet, H. Moll, U. Wahlgren, Z. Szabó, I. Grenthe, Structure and bonding in solution of dioxouranium(VI) oxalate complexes: Isomers and intramolecular ligand exchange. Inorg. Chem., 42, 1982-1993, (2003).

Eu³⁺ and Gd³⁺ sorption at Aragonite and Calcite

F. Heberling¹⁾

¹⁾ Karlsruhe Institute of Technology, Institute for Nuclear Waste Disposal, Hermann-von-Helmholtz-Platz 1, D-76344 Eggenstein-Leopoldshafen, Germany

Introduction

The sorption of trivalent lanthanides at Aragonite and Calcite is investigated in the context of studies for the safe disposal of nuclear waste. Trivalent lanthanides are used here as non-toxic chemical homologues for the trivalent actinides Am³⁺ / Cm³⁺. Sorption reactions with the ubiquitous CaCO₃ modifications Aragonite and Calcite have the potential to significantly retard the radionuclide transport towards the biosphere in the scenario of water intrusion into a nuclear waste disposal. Furthermore, the investigation of lanthanides' adsorption at Aragonite and Calcite surfaces, incorporation into the crystal structures, and the influence of lanthanides on the recrystallization of the metastable Aragonite to the, at standard conditions, thermodynamically more stable modification Calcite, aims at an understanding of the surface reactivity of Aragonite and Calcite, the driving forces for mineral recrystallization, and how impurities act on them.

In the context of this studies we investigated four samples by means of bulk EXAFS Spectroscopy at the Eu and Gd L₃-edges at 6977 eV and 7243 eV, respectively: 1) Aragonite that was reacted in a batch type recrystallization experiment with Eu³⁺ containing solution for 580 days, 2+3) Aragonite that was reacted with Gd³⁺ containing solution for 24 hours, and 4) Calcite that was precipitated very slowly during 70 days in a mixed flow reactor in the presence of Eu³⁺.

Experimental details

After their preparation in aqueous solution, the mineral powders are separated from the solution by filtration through 0.45 µm Durapore Membrane (Millipore), dried in an oven at 105°C overnight, and measured as dry powders. For EXAFS measurements in fluorescence mode the powders are enclosed between two 25 µm Kapton® membranes. For each sample 4-8 spectra are recorded in an energy range from 200 eV below the absorption edge to 544 eV above the edge ($k = 12 \text{ \AA}^{-1}$). Behind the sample an Fe-foil is measured in parallel in absorption mode for the purpose of energy calibration (Fe-1s energy at 7112 eV). For measurements in fluorescence mode the fluorescence emission is recorded by a Vortex silicon drift detector in a range of ±300 eV above and below the Lα₁ fluorescence emission lines at 5850 eV and 6053 eV for Eu and Gd, respectively.

Results and Discussion

Due to the rather complex structure of aragonite, including coordination shells with neighbours at various distances from the central cation, a detailed analysis of the Aragonite data is still pending. Measured spectra (black line) and model calculations (red line) for the Eu³⁺ doped calcite (sample 4) are shown in Figure 1.

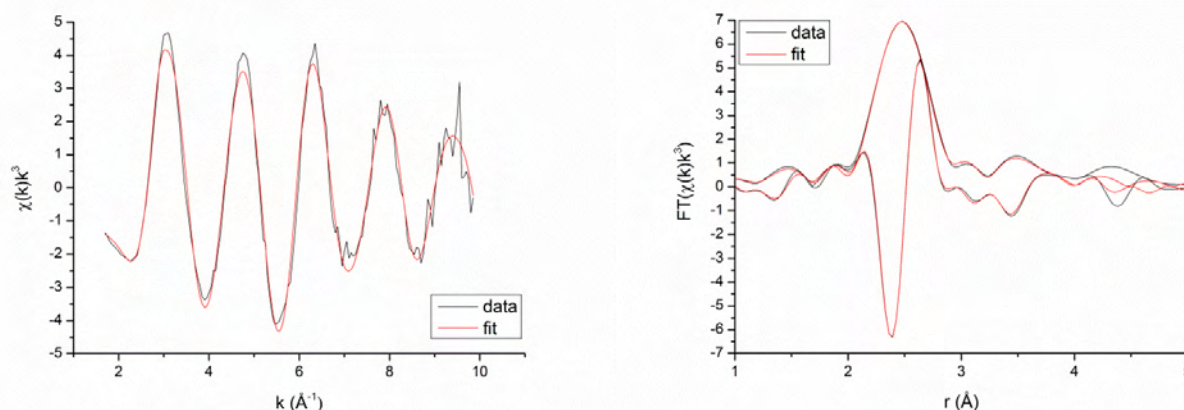


Figure 1: EXAFS spectra in k -space (left) and R -space (right) measured on Eu³⁺ doped calcite. Measured spectra (black lines) are shown along with model calculations (red lines).

Table 1: Modelling results for the Eu^{3+} doped calcite sample in comparison to coordination numbers (CN) and bond distances (r) in the ideal calcite structure. General parameters in the model: $S_0^2 = 1$ (fixed), $\Delta e_0 = 5.9 \pm 0.8$ eV, 24 independent points, 21 variables, k -range: $2\text{--}10 \text{ \AA}^{-1}$, R -range: $1.7\text{--}4.8 \text{ \AA}$, phase correction: path 1, R -factor 0.013

	EXAFS-model			ideal calcite structure	
	CN	r (\AA)	σ^2 (\AA^2)	CN	r (\AA)
O	6.9 ± 0.4	2.431 ± 0.005	0.009 ± 0.001	6	$2.35 (+0.08)$
C-bidentate	1.6 ± 0.9	3.01 ± 0.07	0.01 ± 0.01	0	-
C-monodentate	6 ± 2	3.31 ± 0.06	0.014 ± 0.008	6	$3.20 (+0.11)$
O-monodentate	$6 \pm 2^*$	3.50 ± 0.04	0.013 ± 0.005	6	$3.44 (+0.06)$

*: defined equal to previous path

The corresponding details of the EXAFS model are given in Table 1 along with coordination numbers and bond distances as they are found around Ca^{2+} cations in the ideal calcite structure. It is obvious that the structural environment of Eu^{3+} in calcite is not equivalent with the ideal calcite structure. It might be interpreted a distorted calcite structure, in which one of the coordinating carbonate ligands is not coordinated to the metal centre in a monodentate fashion as in the ideal calcite structure, but in a bidentate fashion. This explains both, the elevated coordination number of the first backscattering path (6.9 vs. 6) and the carbon neighbour at 3.01 \AA . However, this interpretation is not in line with previous laser spectroscopic studies (Marques Fernandes et al., 2008; Schmidt et al., 2008; Stumpf and Fanghanel, 2002). It might be that Eu^{3+} in calcite does not exhibit a single incorporation species, but a mixture of various incorporation and/or surface species, which would of course complicate an EXAFS analysis. A thorough comparison between the result presented here, other spectroscopic methods, and previous results will be necessary before a sound conclusion about the Eu^{3+} environment in the calcite structure can be drawn.

Acknowledgements

The work was financially supported by the European Union's European Atomic Energy Community's (Euratom) Seventh Framework Program FP7-Fission-2010 under grant agreement number 269688 (CP-SKIN). I gratefully acknowledge provision of beam-time by ANKA and the outstanding support by the INE-Beamline Team.

References

- Marques Fernandes, M., Schmidt, M., Stumpf, T., Walter, C., Bosbach, D., Klenze, R., Fanghanel, T., 2008. Site selective time resolved laser fluorescence spectroscopy of Eu^{3+} in calcite. *Journal of Colloid and Interface Science* 321, 323-331.
- Schmidt, M., Stumpf, T., Fernandes, M.M., Walther, C., Fanghanel, T., 2008. Charge compensation in solid \solutions. *Angew Chem Int Edit* 47, 5846-5850.
- Stumpf, T., Fanghanel, T., 2002. A time-resolved laser fluorescence spectroscopy (TRLFS) study of the interaction of trivalent actinides (Cm(III)) with calcite. *Journal of Colloid and Interface Science* 249, 119-122.

Fate of Lu(III) during 2-line ferrihydrite transformation

N. Finck, M. Bouby, K. Dardenne

Karlsruhe Institut of Technology, Institute for Nuclear Waste Disposal, Hermann-von-Helmholtz-Platz 1, D-76344 Eggenstein-Leopoldshafen, Germany.

Introduction

Iron oxides are widespread in nature [1]. They are found in soils, rocks, lakes, rivers ... where they are regulators of the concentration and distribution of pollutants such as heavy metals. Commonly found are ferrihydrite and its transformation products hematite and goethite. In nuclear waste disposal sites, iron (hydr)oxides may also form by the corrosion of drum steel where they can serve as sink for radionuclides through surface adsorption and/or structural incorporation. The way how radionuclides are immobilized directly impacts the retention strength. The most effective retention may occur by structural entrapment, as a result of direct precipitation or recrystallization / transformation in the presence of the radionuclides. 2-line ferrihydrite was prepared and aged in the presence of Lu(III) (as surrogate of trivalent actinides). After several years of ageing, the solid phases were characterized by XRD and the Lu(III) local chemical environment was probed by X-ray absorption spectroscopy at the INE-beamline.

Experimental

Suspensions (~3 g/L) of 2-line ferrihydrite were prepared according to [1] and left to age at pH ~6 at room temperature in the presence of Lu(III) ($[Lu(III)]_{tot} = 10^{-3}$ mol/L) for either 11 years (sample T2) or 7 years (sample T5). The suspensions were centrifuged for 35 minutes at 4000 rpm and the solids separated from the supernatants. Chemical analyses indicated that ~70 % of total Lu and ~8 % of total Fe are present in the supernatant of T2 (T2_super), and ~63 % of total Lu and ~0.1 % of total Fe are present in the supernatant of T5 (T5_super). XRD data indicated that the solid phase in T2 (T2_solid) consists of ~70 % hematite and ~30 % goethite, whereas it consists of 100 % hematite in T5 (T5_solid). These results are consistent with SEM micrographs showing only rhombohedra typical of hematite in T5 (both supernatant and solid phase). In the supernatant of T2, only needles are present indicating the presence of goethite and the solid phase contains both rhombohedra and needles indicating the presence of hematite and goethite. These results are consistent with the XRD data. The Lu L_3 -edge was probed to gain information on the local chemical environment in the supernatants and in the solid phases.

Results

XAS data were collected at the Lu L_3 -edge for the supernatants and the solid phases. Data were also recorded for the aqua ions (sample Lu(III)_{aq}) and used as reference. For T2 and T5 samples, the supernatant was separated from the solid just before the measurement and placed in a cell having Kapton windows to collect fluorescence data. The wet pastes (solids) were washed with very few millilitres of water and dried before measurements.

The experimental and modelled data are presented in Figure 1. For both supernatants, only a single oxygen shell (8 atoms at 2.31 Å) was used to model the data. The fit results are identical to those of Lu(III)_{aq}, indicating that Lu(III) free aqua ions are present in the supernatants.

The spectra collected for the solid phases differ from those of the supernatants, especially at $k > 6 \text{ \AA}^{-1}$. Furthermore, the spectral signatures indicate a binding environment in T2_solid different from that in T5_solid. This is indicated by the spectral differences in the $6 < k < 10 \text{ \AA}^{-1}$ range, and in the Fourier transforms in the 2.5 – 4.0 Å range from the detection of atomic shells beyond the first O shell. The data of T2_solid were modelled considering 6 oxygen atoms at 2.20 Å and next nearest Fe (2 atoms at 3.08 Å) O (~3 atoms at 3.32 Å) and Fe (~2 atoms at 3.47 Å) shells. The first ligand shell in T5_solid consists in 2 O subshells at 2.19 Å (~3 atoms) and at 2.33 Å (~4 atoms). Higher distances neighbours are Fe (~2 atoms at 3.38 Å) and several O shells. The first ligand shell of T2_solid is consistent with the presence of Lu in an octahedral environment. In contrast, the split first shell in T5_solid may indicate the presence of surface sorbed Lu, where the shell at 2.33 Å is consistent with water molecules from the hydration sphere and the

shell at 2.19 Å with binding to the surface oxygens. The differences in the binding environment is also evidenced from the distance to the first Fe shell, which is larger in T5_solid.

Taking into account the XRD data, some preliminary conclusions can be drawn for the solid phases. Lu is predominantly surface retained on hematite (T5_solid contains 100 % hematite) and very likely structurally retained in goethite (T2_solid contains ~30 % goethite and ~70 % hematite). However, there is no obvious reason why ~30 % of the solid phase in T2_solid should retain the majority of Lu. The synthesis of selectively hematite or goethite in the presence of Lu(III) in a more rapid way could help understanding the data from the ageing tests. For the supernatants, the data indicate the presence of only free aqueous ions. However under the present chemical conditions (pH ~ 6), Lu would be expected to be retained at the surface of the mineral and not prevail as free ions. Given the sensitivity of XAS, it appears very likely that at least part of Lu is surface sorbed but this contribution cannot be distinguished from that of the non-surface sorbed Lu. Similarly, if part of Lu is sorbed at the surface of hematite in T2_solid, its contribution may be overwhelmed by that of Lu incorporated in goethite.

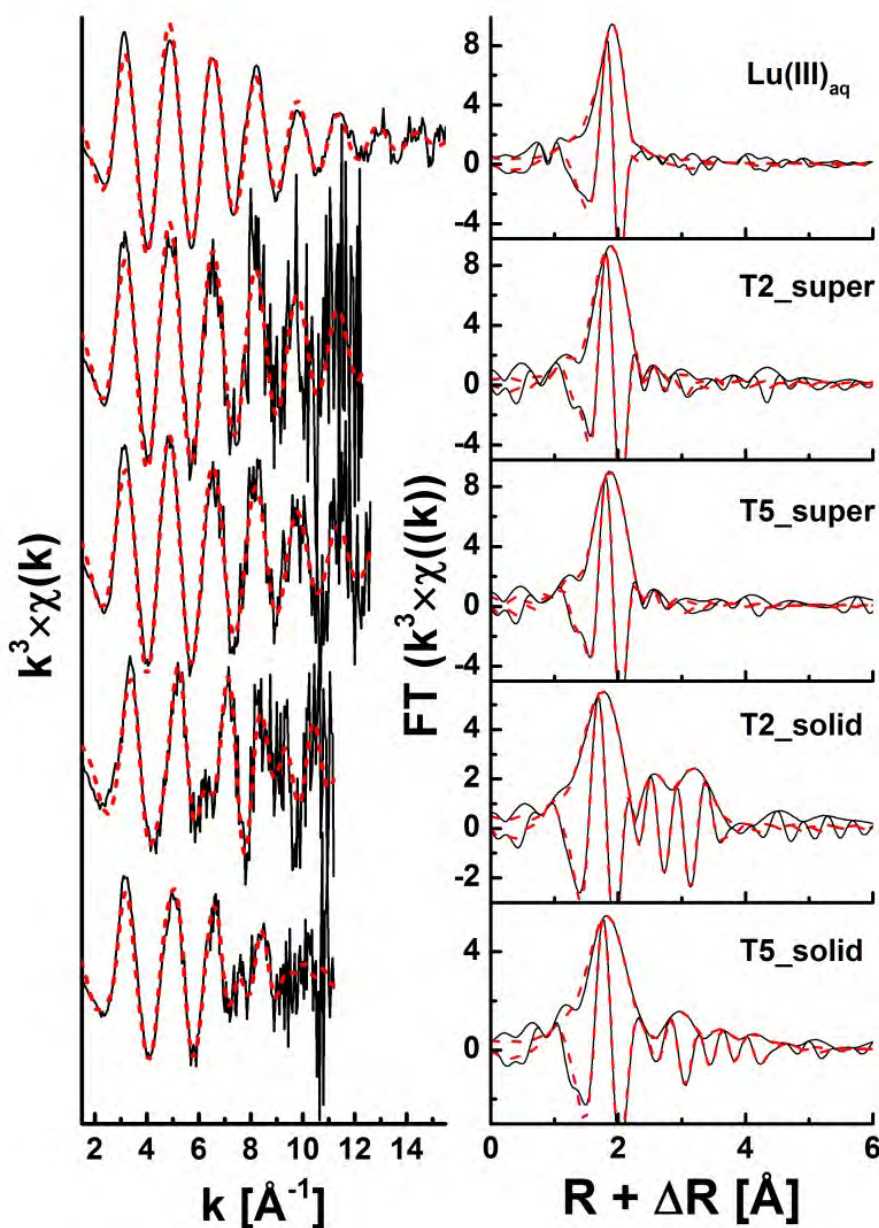


Figure 1. Experimental (solid black lines) and modeled (dashed red lines) EXAFS spectra (left) with the corresponding Fourier transforms (right)

Reference

[1] *Iron Oxides in the Laboratory. Preparation and Characterization* (1991) Schwertmann U. and Cornell R. M., VCH Publishers, Weinheim, Germany.

Acknowledgements

ANKA is acknowledged for provision of synchrotron radiation beam time.

Speciation of Nd(III) in $\text{MgCl}_2\text{-Mg}(\text{NO}_3)_2$ systems

M. Herm, X. Gaona, K. Dardenne, N. Finck, M. Altmaier

Karlsruhe Institute of Technology, Institute for Nuclear Waste Disposal (KIT-INE), Hermann-von-Helmholtz-Platz 1, D-76344 Eggenstein-Leopoldshafen, Germany

Introduction

In long-term safety analyses for deep geological nuclear waste repositories a reliable prediction of the chemical behavior of actinides in aqueous solutions is necessary. Although geological or geotechnical barriers may prevent formation water from contacting the waste, intrusion of aqueous solutions into a repository has to be taken into account. Porewater in certain sedimentary bedrocks as well as water potentially intruding salt rock repositories will be characterized by high ionic strength and high Na^+ , Mg^{2+} and Cl^- concentrations. An(III) and An(IV) are the most relevant actinide redox states under the reducing conditions which develop after the closure of deep underground repositories for nuclear waste. In repositories containing waste from nuclear fuel reprocessing, high concentrations of nitrate (≥ 1.0 M) and slow nitrate reduction kinetics may affect the aqueous speciation of radionuclides and thus impact their mobilization into the biosphere.

Experimental

Samples were prepared and stored in Ar glove boxes ($\text{O}_2 < 5$ ppm). Batch solubility experiments were performed from undersaturation with $\text{Nd}(\text{OH})_3(\text{am})$ in 0.1–6.02 m NaCl-NaNO_3 , 0.25–5.2 m $\text{MgCl}_2\text{-Mg}(\text{NO}_3)_2$ and 2.91/4.02 m $\text{CaCl}_2\text{-Ca}(\text{NO}_3)_2$ background electrolytes at $7.5 \leq \text{pH}_m \leq 13$. Nitrate concentrations ranged between 0 and 8.0 m per batch solubility experiment. The $m_{\text{Nd(III)}}$ was determined by ICP-MS after 10 kD (2–3 nm) ultrafiltration. Solid phases were characterized using XRD and SEM-EDX. TRLS measurements were performed with $\sim 10^{-7}$ M Cm(III) per sample, with 5.61/6.02 m NaCl-NaNO_3 , 0.25/4.1 m $\text{MgCl}_2\text{-Mg}(\text{NO}_3)_2$ and 4.02 m $\text{CaCl}_2\text{-Ca}(\text{NO}_3)_2$ as background electrolyte, containing 0 to 8.0 m NO_3^- and $1.0 \leq \text{pH}_m \leq 9.0$. For EXAFS measurements a sample out of the 4.06 m $\text{MgCl}_2\text{-Mg}(\text{NO}_3)_2$ batch solubility experiment, containing 5.81 m NO_3^- at pH_m 8.15 and $m_{\text{Nd(III)}} = 1.49 \times 10^{-3}$ m was used after 10 kD (2–3 nm) ultrafiltration. Nd L_{III} edge x-ray absorption fine structure (XAFS) spectra are recorded at the INE-Beamline at ANKA. Spectra are energy calibrated to the first inflection point in the XANES of a Mn metal foil (6.539 keV), measured simultaneously. The XAFS signal is

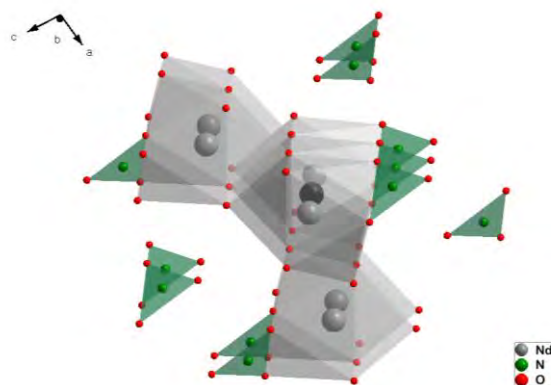


Fig. 1: Perspective view of structure cluster used for the data modelling, $\text{Nd}(\text{OH})_2\text{NO}_3$, ICSD 63550, [2]. The Nd on the centre of the cluster is drawn in black.

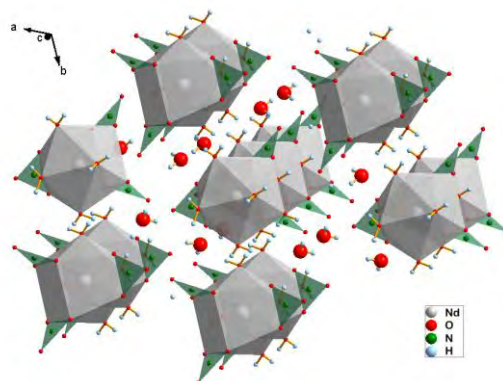


Fig. 2: Perspective view of neodymium trinate $\text{Nd}(\text{NO}_3)_3(\text{H}_2\text{O})_4(\text{H}_2\text{O})_2$, ICSD 37181 [4].

recorded at room temperature in fluorescence mode using a vortex Si-drift detector. Si<111> crystals are used in the double crystals monochromator, operating in fixed-exit mode. The parallel alignment of the crystal faces is detuned to ~70% of the maximum beam intensity at the beginning of each scan. The incident intensity is then held constant by means of a piezo-driven feedback system to the second crystal.

EXAFS fits are performed with D-Artemis, a program of the Demeter IFEFFIT package [2], using phase and amplitude data calculated for a 59 atom cluster (~5.8 Å diameter sized centred on the individual metal cations) shown in Fig. 1 [3]. Feff6L delivered as standard with the package was replaced by Feff8.4 for these calculations. For Mg atoms, single path scattering files for phase and amplitude are used. The k-range used in modelling is [2.45–9.6 Å⁻¹]. Fits are performed in the R-space [1.25–4.5 Å] simultaneously on the k¹-, k²- and k³-weighted data.

Table 1: Structural parameters for the reference structures taken into account.

Backscatterer	Nd(OH) ₂ NO ₃	Nd(NO ₃) ₃ (H ₂ O) ₄ (H ₂ O) ₂
	ICSD 63550 [2]	ICSD 37181 [3]
O	4 at 2.43–2.47 Å	4 at 2.44–2.46 Å 3 at 2.55–2.56 Å
O	5 at 2.61–2.67 Å	2 at 2.61 Å 1 at 2.71 Å
N	1 at 3.08 Å 1 at 3.57 Å 1 at 4.54 Å	3 at 2.98–3.08 Å
O	1 at 3.65 Å 2 at 3.96–4.02 Å 3 at 4.17–4.20 Å 3 at 4.32–4.38 Å	3 at 4.21–4.31 Å
Nd	1 at 3.84 Å 2 at 4.02 Å	
O	4 at 4.51–4.64 Å	4 at 4.53–4.59 Å
Nd	1 at 6.42 Å 2 at 6.75 Å	2 at 6.41–6.42 Å

Results

No significant enhancement in Nd(OH)₃(am) solubility occurs in NaCl–NaNO₃ and CaCl₂–Ca(NO₃)₂ mixtures compared to nitrate-free systems [1]. On the contrary, a clear increase in solubility occurs for MgCl₂–Mg(NO₃)₂ mixtures with $m_{\text{Mg}^{2+}} \geq 2.83$ m, $m_{\text{NO}_3^-} \geq 1.13$ m and pH_m 8–9. Provided the solubility control exerted by Nd(OH)₃(am) (confirmed by XRD and SEM-EDX in all systems with $m_{\text{Cl}^-} \leq 5.82$ m), the slope analysis of the experimental data in MgCl₂–Mg(NO₃)₂ mixtures indicates the formation of aqueous species Mg–Nd–OH–NO₃ with stoichiometries Nd:OH 1:1 (pH_m ≤ 8.3) and Nd:OH 1:2 (pH_m > 8.3).

Cm(III)–TRLFS data reveals the formation of aquatic “Cm(III)–OH–NO₃” species with pH_m ≥ 4.94 only in MgCl₂–Mg(NO₃)₂ systems. The absence of these species in CaCl₂–Ca(NO₃)₂ solutions under virtually the same experimental conditions (pH_m, I , $m_{\text{NO}_3^-}$) hints towards the participation of Mg²⁺ in the complex formation.

Based on the slope analysis, solid phase characterization and Cm(III)–TRLFS observations the species Mg[NdOHNO₃]³⁺ and Mg[Nd(OH)₂NO₃]²⁺ are expected to prevail in concentrated nitrate-bearing Mg–systems.

Under the EXAFS sample characteristics ($\text{pH}_m = 8.15$, $4.06 \text{ m MgCl}_2\text{-Mg(NO}_3)_2$ with 5.81 m NO_3^-), based on thermodynamics and TRFLS a mixture of neodymium nitrate (Fig. 2, Table 2) and a Nd di-hydroxo nitrate (Fig. 1, Table 2) likely including Mg is expected in this system. The k^2 -weighted Nd L_{III} edge EXAFS $\chi(k)$ of Nd species in the $\text{MgCl}_2\text{-Mg(NO}_3)_2$ mixture and respective Fourier transforms are shown in Fig. 3. EXAFS evaluation showed no visible Nd–Nd interaction. The data is well reproduced using five shells and the sample structure exhibits characteristics of a mixture of the $\text{Nd(OH)}_2\text{NO}_3$ [ICSD 63550] and $\text{Nd(NO}_3)_3(\text{H}_2\text{O})_4$ [ICSD 37181] compounds for the first neighboring shells, expected distances are given Table 1. The fit results are given Table 2.

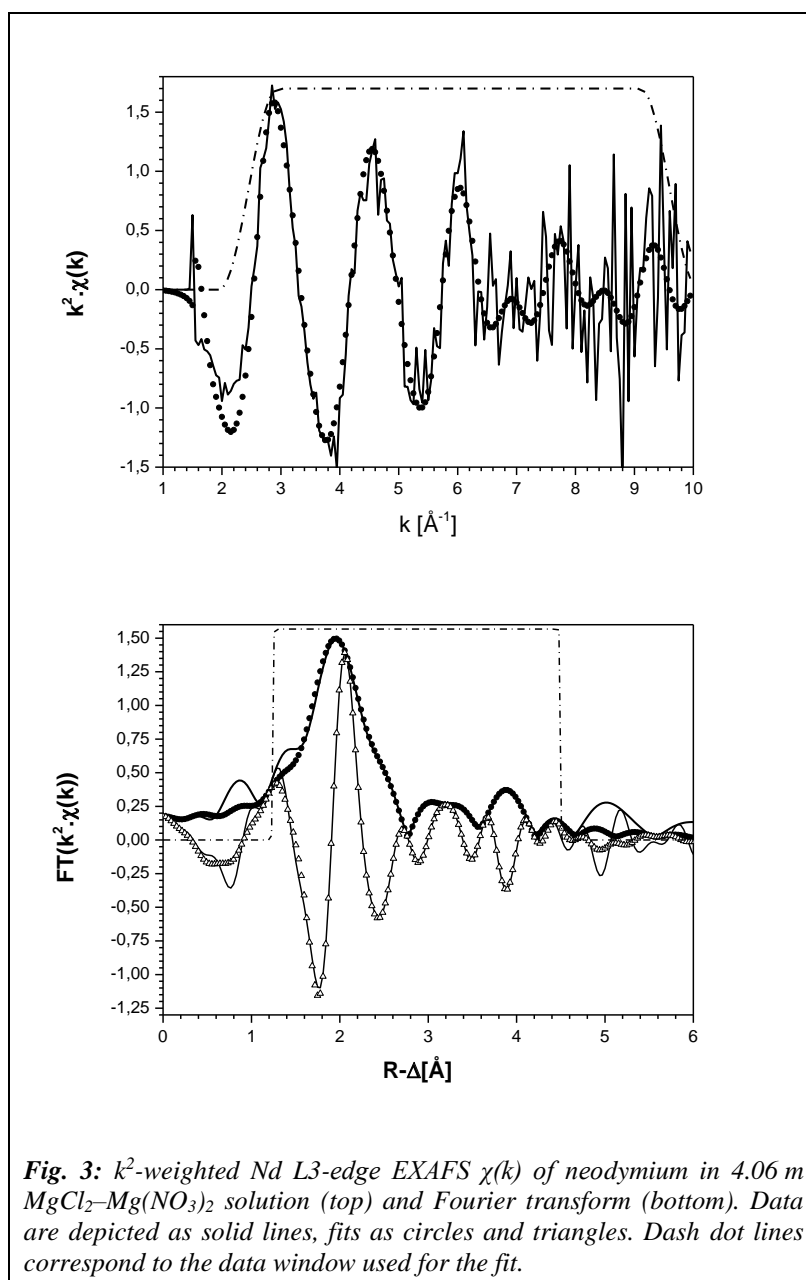


Table 2: Structural parameters obtained from EXAFS evaluation.

Sample	Backscatterer	R [Å], (± 0.01 Å)	N ($\pm 20\%$)	σ^2 [Å ²] $\times 10^{-3}$	ΔE_0 [eV]	goodness of fit (%)
Nd solution sample	O	2.46	6.1	3.1	8.9	1.0
	O	2.64	4.7	3.5		
	N	3.18	1.7	3.3		
	O/N	3.63	3.6	9.0		
	Mg	4.10	2.6	0.4		
	O	4.47	4.9	35		

R = distances, N = coordination numbers, σ^2 = EXAFS Debye-Waller factors, ΔE_0 = relative energy shifts held as global parameters for all atoms, S^0 set to 1

Acknowledgements

We thank the ANKA synchrotron source for providing the beamtime.

References

- [1] V. Neck, M. Altmaier, Th. Rabung, J. Lützenkirchen and Th. Fanghänel, *Thermodynamics of trivalent actinides and neodymium in NaCl, MgCl₂, and CaCl₂ solutions: Solubility, hydrolysis, and ternary Ca–M(III)–OH complexes*, Pure and Applied Chemistry **81**, 1555–1568 (2009)
- [2] B. Ravel and M. Newville, ATHENA and ARTEMIS: *data analysis for X-ray absorption spectroscopy using IFEFFIT*, Journal of Synchrotron Radiation **12**, 537–541 (2005)
- [3] D.F. Mullica, E.L. Sappenfield and D.A. Gossie, *Crystal structure of Neodymium and Gadolinium Dihydroxy-nitrate, Ln(OH)₂NO₃*, Journal of Solid State Chemistry **63**, 231-236 (1986)
- [4] D.J. Rogers, N.J. Taylor and G.E. Toogood, *Tetraaquatriniratoneodymium(III) Dihydrate, (Nd(NO₃)₃(H₂O)₄)(H₂O)₂*, Acta Crystallographica, Section C: Crystal Structure Communications **39**, 939-941 (1983)

Plutonium oxidation states speciation in perchloric acid by high-energy resolution XANES technique

I. Pidchenko¹⁾, D. Fellhauer¹⁾, T. Prüßmann¹⁾, K. Dardenne¹⁾, J. Rothe¹⁾, T. Vitova¹⁾

¹⁾Karlsruhe Institute of Technology, Institute for Nuclear Waste Disposal, Hermann-von-Helmholtz-Platz 1, D-76344 Eggenstein-Leopoldshafen, Germany

Introduction

Transuranium elements are the most hazardous long-lived wastes formed during nuclear fuel irradiation. Therefore, precise speciation analysis is of great importance for assessing and predicting their long-term radioecological behavior. It is especially relevant to plutonium (Pu), which may coexist in four (III, IV, V and VI) oxidation states under relevant environmental conditions [1]. In this work four different Pu oxidation states were synthesized and characterized by high-energy resolution X-ray absorption near-edge structure technique (HR-XANES) using the multi-analyzer crystal (MAC-Spectrometer) recently commissioned at the INE-Beamline. EXAFS investigation is performed to correlate oxidation states with average Pu-O bonding distances (not shown here).

Experimental details

Pu(III), Pu(IV) and Pu(V) aliquots were prepared starting from approximately 0.05 M Pu(IV) solution in 1 M HClO₄. Pu(IV) solution was first reduced to Pu(III) by applying a potential of ca. -0.4 V. Then 98% Pu(IV) containing solution was prepared by oxidation of Pu(III) to Pu(IV) ($E = +0.9$ V). After taking the aliquote, Pu(IV) was quantitatively oxidized to Pu(VI) ($E = +1.9$ V). For preparation of Pu(V), Pu(VI) in 1 M HClO₄ was first neutralized with NaOH before adding 1 M NaClO₄ as electrolyte (10^{-4} M HClO₄, pH ca. 4) for electrolysis. Finally, Pu(VI) was carefully reduced to Pu(V) by applying the potential of approximately +0.6 V. In addition to aqueous Pu(IV), solution containing Pu(IV) colloidal fraction (1 M HClO₄) was prepared. 350 μ l aliquote was taken from each Pu fraction before the following electrochemical step. UV-Vis spectra were measured to corroborate quantitative electrochemical transformations and specie stability prior and after HR-XANES measurements. Pu(IV) contained about 9% of Pu(VI) and in Pu(V) fraction 7% of Pu(VI) were found after the measurements.

In-house designed inert-gas cell [2] was used for Pu L₃ HR-XANES and EXAFS measurements. From 2 to 4 scans were collected for each sample. For energy calibration, the second inflection point of the Zr K-edge XANES spectrum of the simultaneously measured Zr foil was set to 18007 eV. The X-rays emitted from the sample were energy analysed by a Johann spectrometer in scanning geometry [3a,3b]. Pu L _{α 1} emitted fluorescence (14282 eV) was diffracted and focused on the Vortex SDD detector by five spherically bent Si(777) analyser crystals with 1 m bending radius at a Bragg angle of $\theta = 75.7^\circ$.

Results

The Pu L₃ conventionally measured XANES and the HR-XANES spectra are plotted in Fig. 1 a) and b), respectively. The most intense absorption resonances (white line, WL) have higher intensities for all HR-XANES spectra compared to the conventional XANES. Additionally, the Pu(V) and Pu(VI) HR-XANES spectra exhibit better energy resolved post-edge features. The energy distance between the WL and this resonance is sensitive to the bond distance between the Pu and axial O atoms in Pu(V) and Pu(VI) [1,4]. The Pu(VI) HR-XANES spectrum suggests presence of a pre-edge feature not present in the conventional spectrum. Its origin will be elucidated by future quantum chemical calculations. The differences in energy positions of the absorption edge of the HR-XANES spectra range from 18059.7 eV for Pu(III) to 18064.3 eV for Pu(VI) (Table 1).

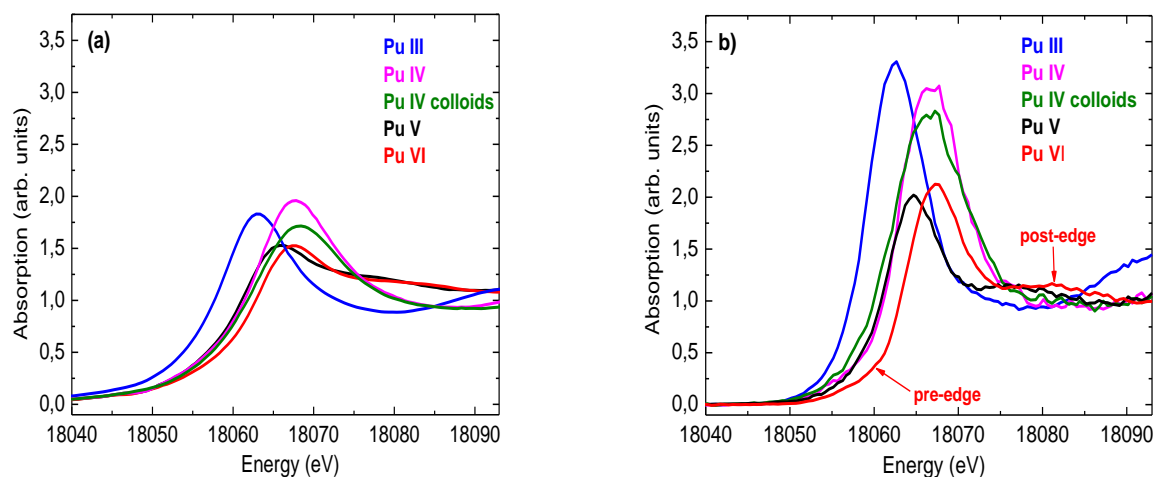


Fig 1: Pu L₃ edge conventional (a) and high-energy resolution (b) XANES spectra of Pu(III), Pu_{aq}(IV), Pu_{col}(IV), Pu(V) and Pu(VI).

Table 1: Energy positions of the absorption edge of the Pu(III)_{aq}, Pu(IV)_{aq}, Pu(IV)_{col}, Pu(V)_{aq} and Pu(VI)_{aq} L₃ HR-XANES.

Pu specie	E position: 2 nd derivative crossing, eV	E shift, eV
Pu (III), aq	18059.7	0
Pu (IV), col	18062.8	3.1
Pu (IV), aq	18062.8	3.1
Pu (V), aq	18061.6	1.9
Pu (VI), aq	18064.3	4.6

Conclusion

Pu L₃ HR-XANES spectra were measured for the first time using the MAC-Spectrometer at the INE-Beamline. The spectra have reduced spectral broadening resulting in better energy resolved features and appearance of a pre-edge resonance in the Pu(VI) spectrum. The HR-XANES experimental technique favours detection of minor contributions of Pu oxidation states in oxidation state mixtures.

Acknowledgements

We thank ANKA for the provided beamtime and the radiation protection team of INE for the support.

References

- [1] Conradson, S. D., et al., (1998) Polyhedron, **17**, 599-602.
- [2] Rothe, J., et al., (2012) Review of scientific instruments, **83**, 043105.
- [3a] Glatzel, P., et al., Catalysis Today, 2009, **145**(3–4): p. 294-299.
- [3b] Kleymenov, E., et al., (2011) Review of scientific instruments, **82**, 065107.
- [4] Den Auwer, C., et al., (2003) European Journal of Inorganic Chemistry, 3843-3859.

Characterisation of the environment of U and Th in the effluent of a uranium treatment plant

T. Fernandes¹⁾, K. Dardenne²⁾, J. Rothe²⁾, D. Schild²⁾, E. Soballa²⁾

¹⁾ Amphos 21, Passeig de Garcia I Faria 49-51, 1-1, 08019 Barcelona, Spain

²⁾ Karlsruhe Institute of Technology, Institute for Nuclear Waste Disposal, Hermann-von-Helmholtz-Platz 1, D-76344 Eggenstein-Leopoldshafen, Germany

Introduction

These are pilot experiments on U, Th contaminated sludge material collected from the decantation basins of a uranium treatment plant. These samples are unique, both in chemical and radiological terms. The porewaters have high ionic strength (ranging from 0.2 to 1.8 molal) and the alpha activity in the solid phase is mainly attributable to uranium and thorium-230. All natural isotopes of uranium are present, in natural abundances, in the waste.

Aim of the pilot experiment was to assess the μ -XAFS / μ -XRF capabilities at the INE-Beamline [1] for U speciation and elemental distribution investigations of these samples prepared as dried thin films. Spatially resolved μ -XRF and μ -XAFS were applied to identify and characterize U hot spots in the material. In addition, the first confocal 3D U distribution was recorded at the beamline.

Motivation

The motivation for this work is to understand the mechanism controlling the limited mobility of radionuclides in the waste, as identified in previous investigations, and thereby evaluate the migration potential of these radionuclides in the contaminated material and tailor future remediation strategies.

Experimental Method

Samples for μ -XAFS/XRF were prepared as dried thin films mounted on self-adhesive carbon pads fixed to standard ESCA sample holders (Fig. 1). Regions of interest (ROI) with high local U concentration were identified from SEM backscattering images. To avoid material crumbling off in vertical position during XAFS measurements, samples were fixed by transparent acrylic lacquer (nail polish) afterwards. Unavoidable morphology changes were monitored in visible light microscopy (VLM) images recorded to relocate the original ROIs (Fig. 3 right). These images were compared to VLM images later on recorded at the beamline μ -focus experimental station, enabling navigation of the sample relative to the X-ray beam spot.



Fig. 2: Polycapillary setup for μ -XAFS/XRF measurements at the INE-Beamline – the SDD is depicted with a secondary capillary mounted for confocal measurements (in-depth resolved).

A scanning 2D μ -XRF using a monochromatic X-ray beam focused to 25 μ m spot size was performed at the INE-beamline at an incident energy above the U and Th L3 edges to be able to locate U/Th hot spots in the thin films. A polycapillary optic mounted on a hexapod positioning unit was used at the INE-Beamline to focus monochromatic radiation delivered by the double crystal monochromator (DCM) equipped with a pair of Ge<422> crystals into a beam spot-size of \sim 25 μ m at the sample surface. The sample holder was mounted on a three-axis positioning stage with the thin film sample surface at a 45° angle to the incident beam (Fig. 2). The y and z stage axes (the x-axis determines the focus) were used to scan selected areas and precisely position the samples in the beam path. A silicon drift detector (SDD, SIINT Vortex-60EX) was used for collecting X-ray fluorescence radiation. U hot spots



Fig. 1: Dried and lacquer-fixed sludge material (sample A left, sample B right) was not investigated), mounted on ESCA sample holder for μ -XAFS/XRF investigations.

identified in element distribution maps reconstructed from the scanning μ -XRF measurements were selected for μ -XAFS scans. U L3 μ -XAFS spectra were recorded by registering the windowed U L α fluorescence intensity. The DCM energy was calibrated relative to the first inflection point in the K-XANES of a Y foil defined as 17.038 keV.

Preliminary Results

Preliminary results are summarized for the uranium distribution in “spot b”, sample A (cf. SEM images in Fig. 3). SEM images reveal that U in the sludge samples is not present as compact phases, but as finely dispersed particles of sub- μ m dimension.

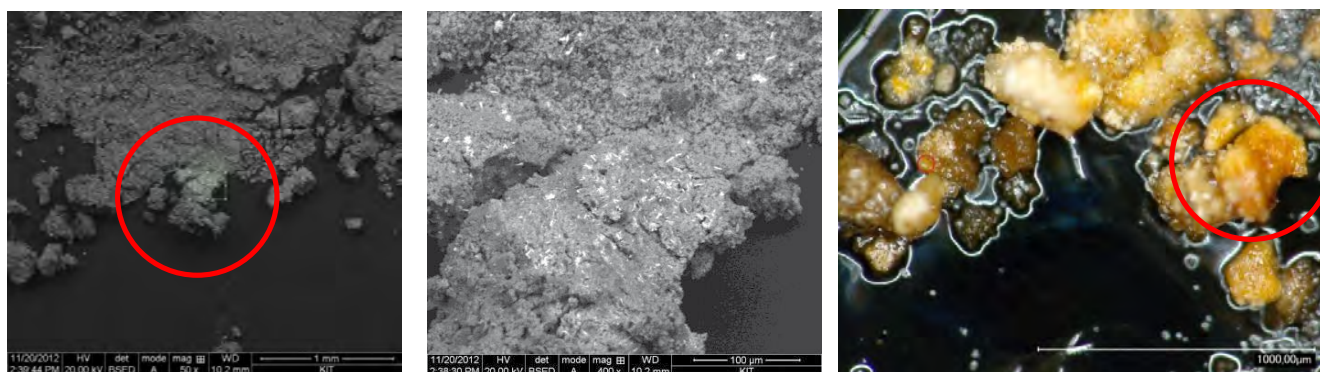


Fig. 3: *Left and middle:* Consecutive series (scale bar, 1mm and 0.1mm) of SEM images zooming into ROI at “spot b” (sample A) – bright spots indicate increased concentrations of uranium. *Right:* VLM image depicting ROI around “spot b” (sample A) recorded after lacquer fixation (note the bright fringes!). Although the morphology was changed significantly, the uranium hot spots were easily relocated in XRF mappings of corresponding sample areas (cf. Fig. 4).

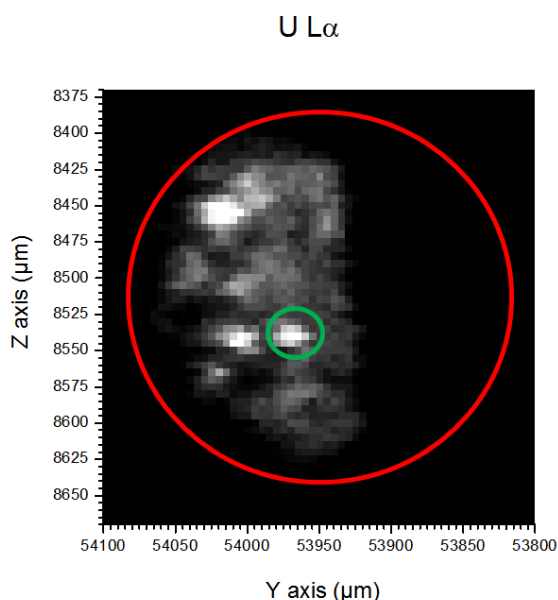


Fig. 4: X-ray gray scale image (windowed U L α fluorescence line) of uranium distribution in ROI “spot b” with a max. intensity of 1050 counts/pixel, map size 300x300 μ m², 61x61 points with 5 μ m step size, excitation energy 17.5 keV. The green circle corresponds to the position where the μ -XANES (focused beam spot size \sim 25 μ m) was recorded, cf. Fig. 5.

With the help of VLM images taken after sample fixation (Fig. 3 right) we were able to relocate the ROIs with the VLM images taken at the beamline. An XRF map (300x300 μ m², 5 μ m step size) was recorded for the red circled region in Fig. 3 using an excitation energy of 17.5 keV.

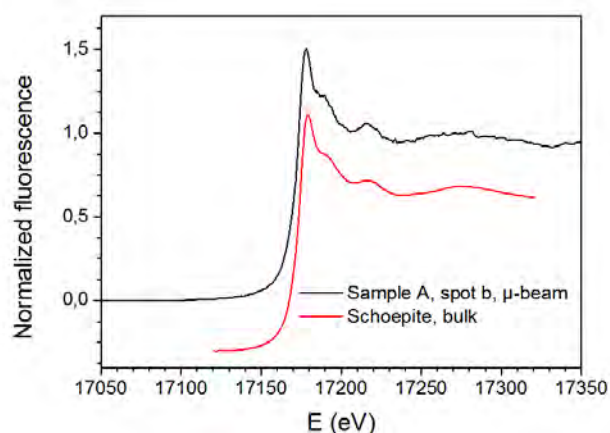


Fig. 5: Normalized U L3- μ -XANES spectrum obtained from U hot spot (“spot b” in sample A), green circle in Fig. 4. The transmission “bulk” spectrum of U(VI) in meta-schoepite is shown for comparison (spectra vertically shifted for clarity). The spectral fingerprint points to a similar U speciation in the sludge material.

A U L3 μ -XANES with \sim 25 μ m beam spot size (Fig. 5) was recorded for an uranium hot spot localized in the XRF map (green circle in Fig. 4). The comparison of the XANES fingerprint obtained for the uranium hot spot in the sludge material and a bulk XANES measurement on meta-schoepite points to a similar U(VI)

speciation in the sludge material and the mineral phase. μ -XANES measurements on different sample positions in addition to bulk measurements will be performed to derive a comprehensive U speciation in the sludge material.

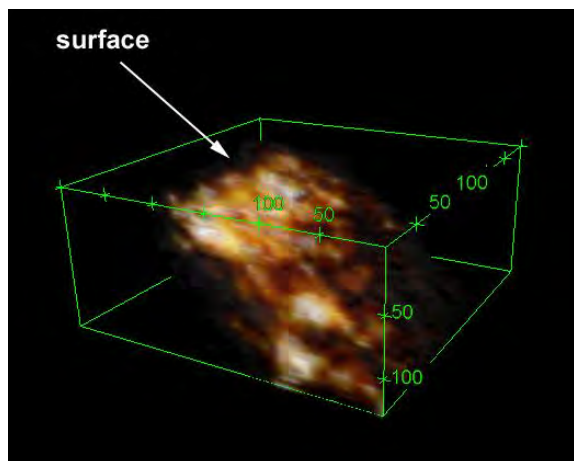


Fig. 6: 3D U distribution in contaminated sludge sample (sample A, "spot b"). Scales are in μm .

3D XRF maps applying a confocal detection scheme (Fig. 2) - offering in-depth special resolution - were recorded for the same "spot b" location on sample A. This detection mode allows the reconstruction of 3D elemental distributions. The reconstructed 3D U distribution is shown in Fig. 6.

As depicted in the MCA overview spectrum in Fig. 7, the sludge sample contains various other elements. Distribution maps for the elements marked in red are available and will be available for elements marked in black. Further data evaluation is in progress.

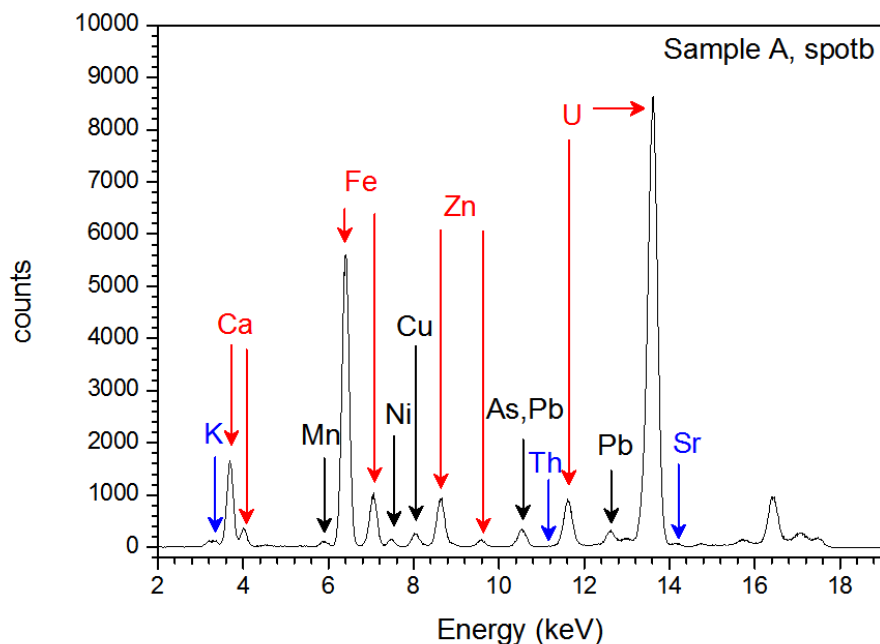


Fig. 7: MCA spectrum corresponding to the average elemental distribution in linear scale, obtained by integrating the fluorescence signal over the full area mapped in Fig. 4

Conclusion:

This pilot experiment was successful and proved the feasibility of such investigations on natural samples at the INE-Beamline. The first 3D reconstruction of an actinide element distribution was achieved at the beamline using confocal XRF detection geometry. This investigation is foreseen to be continued and completed in a future beamtime slot.

References:

[1] The INE-Beamline for actinide science at ANKA, J. Rothe, S. Butorin, K. Dardenne, M. A. Denecke, B. Kienzler, M. Löble, V. Metz, A. Seibert, M. Steppert, T. Vitova, C. Walther, and H. Geckeis, Rev. Sci. Instrum. 83, 043105 (2012)

Investigation of Ca, Ba and Cs molybdates in a Mo bearing borosilicate glass

S. Bahl*, A. Kutzer, G. Roth, H. Geckeis and T. Vitova

Karlsruhe Institute of Technology, Institute for Nuclear Waste Disposal, P.O. Box 3640, 76021 Karlsruhe, Germany
(*correspondence: sebastian.bahl@kit.edu)

One option to dispose solid Mo(VI)- and Cs(I)-rich residual material remaining in tanks after vitrification process of high level liquid waste (HLLW) is its immobilisation in borosilicate glass. Due to its low solubility in borosilicate glass melts, Mo(VI) tends to form molybdate-rich phases during the vitrification process [1]. These phases may crystallize during melt cooling and are able to incorporate radionuclides within their crystal structure. If water-soluble alkali molybdates are formed, the release of radioactivity into the environment will be facilitated in case of water intrusion into a deep geological repository. The chemical composition of the formed phases depends strongly on the used borosilicate glass composition. Understanding factors favouring the formation of water insoluble crystalline Mo(VI) phases in borosilicate glasses allows development of glass compositions capable of incorporating high Mo loadings.

In the here presented project, a multi-component borosilicate glass [2] with varying loadings of $\text{Cs}_3\text{PMo}_{12}\text{O}_{40}$ representing a simulated nuclear waste residues (NWR) was prepared and were characterized by several techniques. Powder X-ray diffraction (XRD) and Raman spectroscopy studies confirm formation of crystalline CaMoO_4 and BaMoO_4 phases for total MoO_3 -concentrations above 5.3 wt%. Results from scanning electron microscopy (SEM) and energy-dispersive X-ray spectroscopy (EDX) investigations agree with results obtained from XRD and Raman spectroscopy. We find for 5.3 wt% MoO_3 -loading formation of spheres with diameter of about 500 nm with increased Mo, Ba and Ca content compared to the glassy matrix.

Ba and Cs L_3 edge X-ray absorption near edge structure (XANES) spectra of glass samples are measured at the INE-Beamline, ANKA. The incident X-ray beam was monochromatized by double crystal monochromator using Si(111) crystals.

The Ba and Cs L_3 edge XANES spectra are shown in **Fig. 1**. Linear combination least squares fit analyses (LCLS) of the Ba L_3 edge XANES spectra of the glass samples using the reference spectra of crystalline BaMoO_4 and an amorphous reference sample (Ba-SiBMo) was performed. Ba-SiBMo contains Mo and Ba homogenously dispersed in the borosilicate glass. The results show that the positive charge of the MoO_4^{2-} units is compensated by Ba^{2+} acting as a counter anion in the samples. Emphasized in **Fig. 2**, the spectrum of the 12.28 wt% MoO_3 sample is similar to the crystalline, the 3.38 wt% MoO_3 to the amorphous reference. **Fig. 2** also shows a quantitative estimation of the degree of participation of crystalline BaMoO_4 in the glass as a function of the MoO_3 concentration derived from LCLS analyses. The contribution of crystalline BaMoO_4 increases from about 25 % to about 60% from the 1 wt% to the 12 wt% MoO_3 sample. For concentrations higher 9 wt% MoO_3 most of the Ba occurs in crystalline environment.

The Cs L_3 edge XANES spectra are more similar to the spectrum of the amorphous reference Cs-SiBMo sample than to the spectrum of $\text{Cs}_3\text{PMo}_{12}\text{O}_{40}$. Further analyses are in progress.

We found no evidence for formation of crystalline water soluble alkali molybdates, indicating that the chemical composition of the glass composite material used could be favourable for immobilization of Mo-rich nuclear waste with this specific chemical composition.

References

- [1] W. Lutze and R. Ewing (1988). Radioactive Waste Forms for the Future. Amsterdam: Elsevier Science Ltd.
- [2] W. Grünewald, G. Roth, S. Hilpp, W. Tobie, A. Salimi, S. Weisenburger and B. Brendebach,

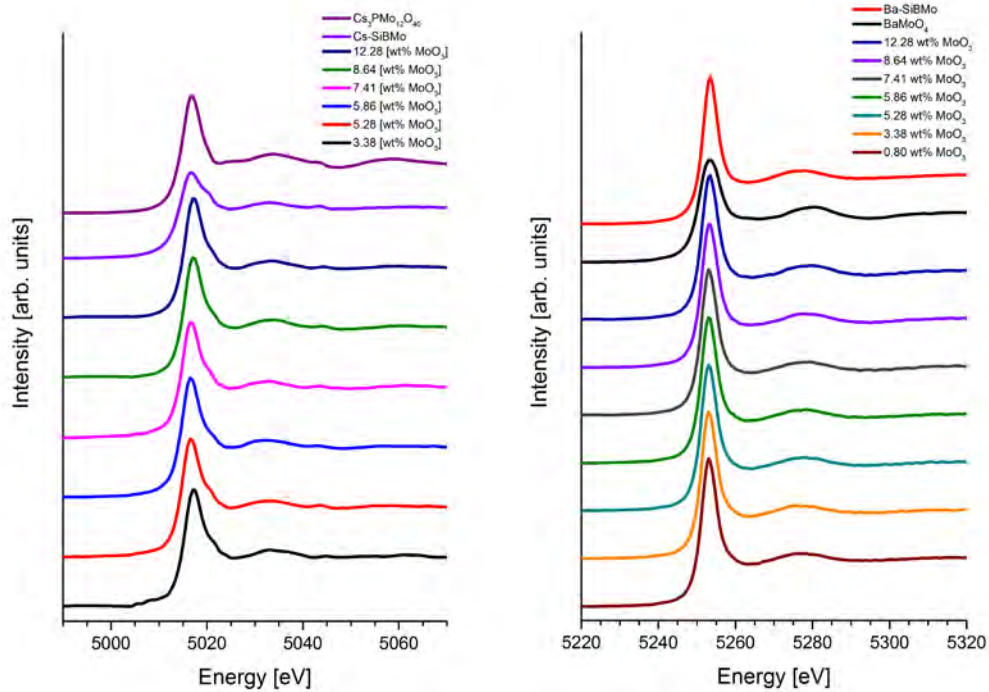


Fig. 1: Smoothed Cs (left) and Ba (right) L₃ edge XANES spectra of Mo bearing glass samples with increasing Mo concentration and crystalline and amorphous references.

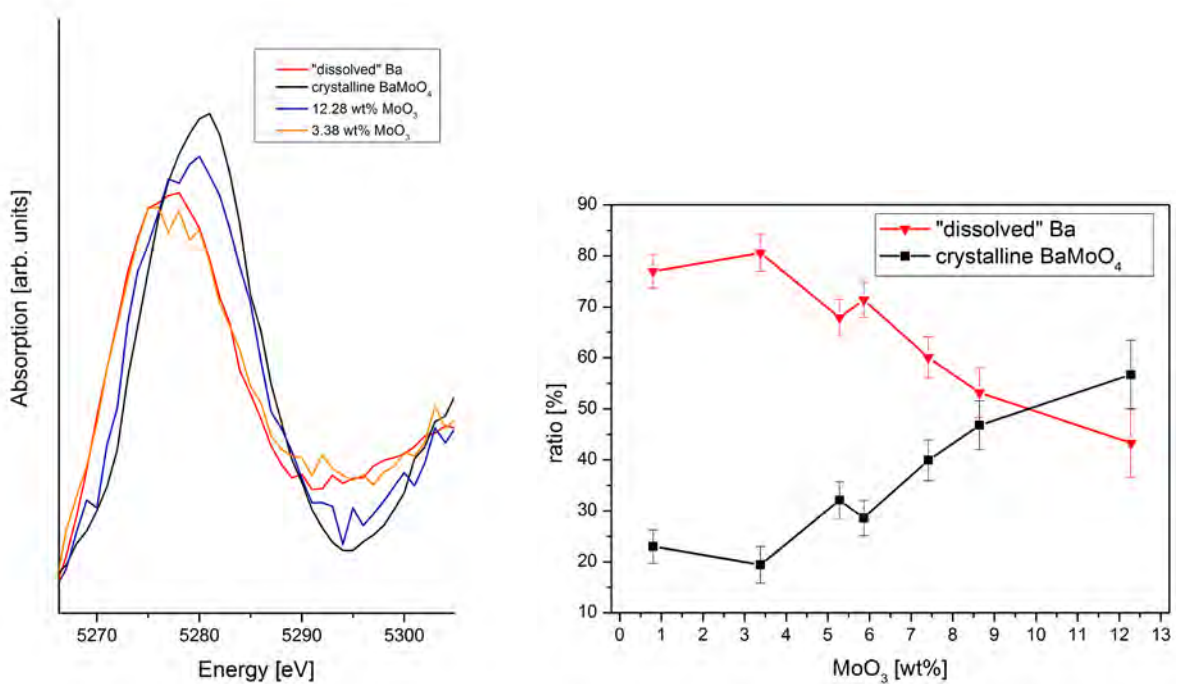


Fig. 2: Left: Smoothed Ba L₃ edge XANES spectra of selected glass samples and references. Right: Results of least square fit analysis of Ba L₃ edge XANES spectra.

EXAFS investigation on actinide and lanthanide transferrin complexes

N. Bauer^{1),2)}, D. R. Fröhlich^{1),2)}, K. Dardenne¹⁾, J. Rothe¹⁾, P. J. Panak^{1),2)}

¹⁾ Karlsruhe Institute of Technology (KIT), Campus Nord, Institute for Nuclear Waste Disposal (INE),
P.O. Box 3640, 76021 Karlsruhe (D)

²⁾ University of Heidelberg, Department of Physical Chemistry, Im Neuenheimer Feld 253, 69120 Heidelberg (D)

In case of accidental release of radionuclides into the environment, actinides represent a severe health risk to human beings after being incorporated by e.g. inhalation, ingestion or wounds. Contrary to other metals, actinides have no known essential function in biochemical reactions. For a better understanding of the actinide behavior and their toxic effects in man a fundamental knowledge on the mechanisms of relevant biochemical reactions in the body is needed which can be an important prerequisite for the design and success of potential decontamination therapies.^[1]



Figure 1: 3D structure of human serum transferrin with N-lobe (green) and C-lobe (red). Each lobe houses one Fe(III) metal binding site.^{[2] [3]}

Transferrin is an iron carrier protein in the blood. Since about 30 % of the protein is complexed to iron in normal blood serum, non-saturated transferrin is available for the complexation of other metal ions. Literature data on the structure of actinide transferrin complexes are rare. Most complexation studies have been performed with indirect speciation methods (filtration, centrifugation etc.). Our fluorescence spectroscopic results on Cm(III) transferrin show for the first time the formation of two different actinide transferrin species depending on experimental conditions (pH, protein concentration). In order to obtain detailed structural information on the complexes, EXAFS investigations were performed.

Experimental

Am(III), Eu(III) and Np(V) transferrin solutions (Eu(III)-Tf: $c(\text{Eu(III)}) = c(\text{Tf}) = 6 \cdot 10^{-4}$ M; Np(V)-Tf: $c(\text{Np(V)}) = c(\text{Tf}) = 5 \cdot 10^{-4}$ M; Am(III)-Tf: $c(\text{Am(III)}) = c(\text{Tf}) = 1 \cdot 10^{-3}$ M; Am(III)-Tf (70 K): $c(\text{Am(III)}) = 5 \cdot 10^{-4}$ M, $c(\text{Tf}) = 2.4 \cdot 10^{-3}$ M) at pH 7.2 and 8.5 were prepared in the radiochemical laboratories at the INE (KIT, Karlsruhe).

Am/Eu/Np L_{III}-edge EXAFS spectra were collected in fluorescence mode in standard detection geometry at the INE-Beamline. The measurements were either performed at room temperature or at ~77 K (Am(III) only) using a liquid N₂ cryostat (OI OptistatDN). The data evaluation was performed using the software packages Athena 0.8.061^[4] and EXAFSPAK.^[5] Theoretical scattering phases and amplitudes were calculated with FEFF8.40^[6] using the crystal structure of Fe-Transferrin (RCSB-PDB entry: 3QYT) and replacing Fe by Am, Np, or Eu. The best theoretical model was fit to the k³-weighted raw Am/Np/Eu L_{III}-edge EXAFS data.

Discussion

The k³-weighted Am L_{III}-edge EXAFS spectra and the related Fourier Transforms of the Am(III) transferrin samples at pH 7.2 and 8.5 recorded at low temperature are shown in fig. 2. Both show clearly visible differences in the whole k-range. While the spectrum at pH 7.2 can be described

with one coordination sphere ($N = 8.7$, $R = 2.47 \text{ \AA}$) in good agreement with data for the Am(III) aquo ion^[7], the sample at pH 8.5 shows a more complicated coordination structure. This spectrum has been fitted with one, two or three coordination spheres (table 1). Again about 9 neighbors are present in the first shell but the distance is significantly shorter ($R = 2.38 \text{ \AA}$) as expected in case of strong multidentate coordination of Am(III) at the transferrin binding cleft. Unspecific binding to functional groups at the protein would result in longer distances and can be excluded. The consideration of two additional coordination shells ($N \approx 3$ at $3.72\text{-}3.73 \text{ \AA}$, $N \approx 7$ at 5.19 \AA) is followed by a slight but visible improvement of the fit (see reduced errors in table 1). The presence of these coordination spheres points to the formation of a complex but well-defined bonding environment in the Am(III) transferrin complex. However, EXAFS does not allow to distinguish between coordinating N- or O-atoms.

In contrast to Am(III), Np(V) spectra did not show any complexation by transferrin, probably due to the less pronounced complexation properties of Np(V). In the case of Eu(III), the sample at pH 7.2 shows the presence of several coordination spheres at higher distances. The corresponding spectra were recorded at room temperature, hence the low signal/noise ratio resulted in a high reduced error (2.04).

In conclusion, the present study confirms the formation of an Am(III) transferrin species at pH 8.5 which is in good agreement with previous TRLS studies on the interaction of Cm(III) with transferrin. Furthermore, the related structural parameters were determined for the first time and confirm that Am(III) is incorporated into the transferrin structure at the Fe(III) binding site.

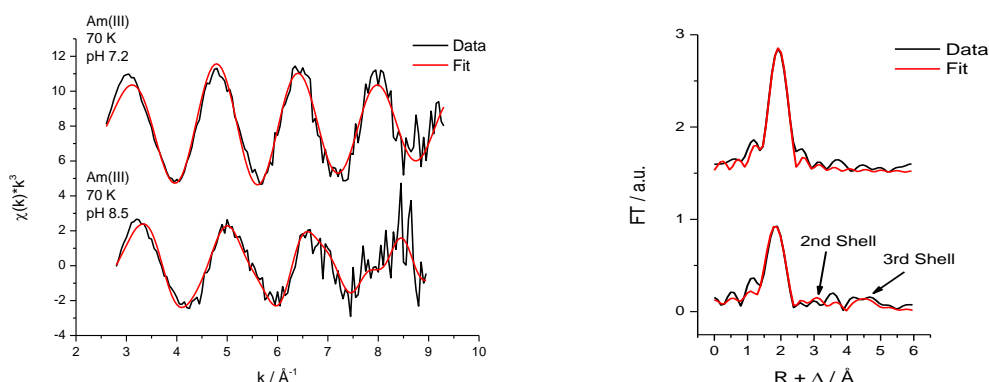


Figure 2: Left: Experimentally measured (black) and fitted (red) EXAFS spectra at the Am L_{III} -edge of the Am(III) transferrin complex at pH 7.2 and 8.5 (both recorded at 70 K); Right: Corresponding experimentally measured (black) and fitted (red) Fourier Transforms.

Table 1: Summary of the best-fit parameters of the EXAFS spectra of the Am(III) transferrin samples ($\sim 77 \text{ K}$).

M	T [K]	pH	1 st Shell			2 nd Shell*		3 rd Shell*		ΔE_0	Red. Er.
			N	R / \AA	$\sigma^2 / \text{\AA}^2$	N	R / \AA	N	R / \AA		
Am	70	7.2	8.7 (0.5)	2.47 (1)	0.007 (1)	-	-	-	-	-6.2 (0.6)	0.41
			8.8 (1.0)	2.38 (1)	0.013 (2)	-	-	-	-	-3.8 (1.0)	0.67
Am	70	8.5	8.6 (1.0)	2.38 (1)	0.012 (2)	3.0 (1.0)	3.73 (3)	-	-	-3.8 (0.9)	0.63
			8.8 (1.0)	2.38 (1)	0.013 (2)	2.8 (1.0)	3.72 (3)	6.8 (2.3)	5.19 (3)	-4.0 (0.9)	0.59

* $\sigma^2 / \text{\AA}^2$ was set to 0.003 and fixed during the fit

- [1] A. E. V. Gorden, J. D. Xu, K. N. Raymond, P. Durbin, *Chem. Rev.* **2003**, 103, 4207-4282.
- [2] J. Wally, P. J. Halbrooks, C. Vonnrhein, M. A. Rould, S. J. Everse, A. B. Mason, S. K. Buchanan, *J. Biol. Chem.* **2006**, 281, 24934-24944.
- [3] H. Z. Sun, H. Y. Li, P. J. Sadler, *Chem. Rev.* **1999**, 99, 2817-2842.
- [4] B. Ravel, M. Newville, *J. Synchrotron Radiat.* **2005**, 12, 537-541.
- [5] G. N. George, Pickering, I.J., Stanford/USA, **2000**.
- [6] A. L. Ankudinov, C. E. Bouldin, J. J. Rehr, J. Sims, H. Hung, *Physical Review B* **2002**, 65.
- [7] P. G. Allen, J. J. Bucher, D. K. Shuh, N. M. Edelstein, I. Craig, *Inorg. Chem.* **2000**, 39, 595-601.

Zr(IV) co-precipitation with clay minerals

N. Finck, K. Dardenne

Karlsruhe Institute of Technology, Institute for Nuclear Waste Disposal, Hermann-von-Helmholtz-Platz 1, D-76344 Eggenstein-Leopoldshafen, Germany.

Introduction

Several countries operating nuclear power plants decided to vitrify their high level nuclear wastes (HLW) and place them in deep repositories. However, ground water may move through the repository barriers over extended periods of time and come in contact with the waste glass. Various studies showed that under repository relevant conditions, clay minerals may form as secondary phases upon glass corrosion [1]. Unfortunately, radionuclides (RNs) will also be released upon waste matrix dissolution. However, the formation of secondary phases in the presence of RNs may have the potential to incorporate them in the bulk structure. This structural retention may lead to an effective immobilization, especially if a solid solution forms.

The long-term radiotoxicity of the HLW is mainly determined by the long-lived and radiotoxic actinides. In clay-based repositories, reducing conditions are expected to prevail so that the actinides U, Np and Pu may occur in trivalent and tetravalent oxidation states. The retention of trivalent lanthanides by co-precipitation with clay minerals has been investigated in the past [2,3], but data for tetravalent cations are still missing. The present study reports on the retention of tetravalent cations by co-precipitation with hectorite, a clay mineral detected in glass corrosion studies [1]. Specifically, tetravalent zirconium was used as homologue for Pu(IV) because of similar hydrolysis and colloid chemistry [4].

Experimental

The magnesian smectite hectorite was synthesized in the presence of Zr(IV) following a procedure described elsewhere [2]. A brucite precursor was first freshly precipitated in the presence of Zr(IV) (sample ZrCopBru) and washed several times. The resulting slurry was refluxed in the presence of LiF and a silica sol to crystallize hectorite (sample ZrCopHec). XRD data assessed the formation of brucite (ZrCopBru) or clay mineral (ZrCopHec) and no separate phase could be detected. The zirconium local chemical environment was probed by collecting Zr *K*-edge X-ray absorption spectroscopy (XAS) data at the INE-Beamline at Anka [5]. The energy calibration was done by setting the first inflection point of a Zr foil measured along all samples in transmission to 17998 eV. Powder XAS data were collected for the Zr(IV) stock solution (sample Zr(IV)_{aq}, [Zr(IV)]_{tot} ≈ 35 μmol/L) and ZrCopBru, and polarized XAS [6] data were collected for ZrCopHec prepared as oriented sample. Polarized XAS was shown to be a powerful tool in studies of cations retention by clay minerals [7].

Results

Data collected in the XANES region are presented in Fig. 1. All samples exhibit different white line (WL) features. From the free ions to ZrCopBru, the WL broadening indicates a change in the Zr chemical environment. The hectorite crystallization lead to an additional broadening and splitting of the WL, indicating that the environment further changed. These broadening and splitting can be attributed to degenerate levels in the valence band which increase with

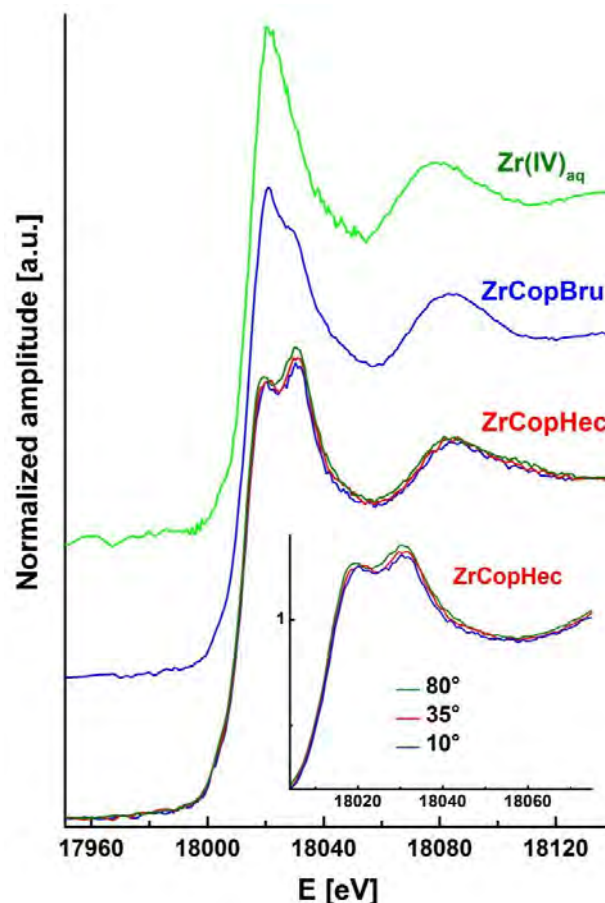


Fig. 1: XANES data of the samples.

decreasing Zr site symmetry [8]. Furthermore, the data of ZrCopHec show an angular dependence, pointing to the presence of Zr in an anisotropic environment. These results hint to a gradual change in the Zr environment from the free ions to the fully crystallized clay mineral.

Structural information on the Zr environment was obtained by fits to the EXAFS data (Fig. 2). The data of the Zr(IV) ions were modeled considering an O neighboring shell at 2.25 Å. In ZrCopBru, the distance to the first O shell decreased to 2.18 Å and next nearest Mg shells were detected at 2.85 and 3.42 Å. These cationic shells can be explained by face and edge-sharing, respectively, between the Zr and Mg polyhedra. The data of ZrCopHec were modeled considering oxygen, magnesium and silicon neighbors at 2.07, 3.04 and 3.22 Å, respectively. These distances are within uncertainties identical to values reported for octahedral cations in hectorite [9]. These results strongly point to Zr located at a clay octahedral site. Additional information can be obtained from the angular dependence of the data. The first contribution of the Fourier transformation increases with increasing angle, suggesting that Zr is located out-of-plane. The substitution of a divalent (e.g., Mg) for a tetravalent (e.g., Zr) cation also implies a charge compensating mechanisms. This can be achieved by substitution by monovalent cation (e.g., Li) for example. In any case, the octahedral site may be distorted with Zr located out-of-plane. Finally, no Zr neighbors were detected, ruling out the precipitation of polynuclear species.

This is the first study to report experimental evidence on tetravalent cation retention by incorporation in the bulk structure of clay minerals. The data show the possibility to entrap tetravalent cations, i.e., actinides, at clay octahedral sites by co-precipitation in aqueous environment. The neoformed secondary phases thus represent an additional barrier to the RN migration to the repository far field. However, the results do not allow to conclude about thermodynamic stability.

References

- [1] Jollivet et al. (2012) *J. Nucl. Mater.* **420**, 508-518.
- [2] Finck et al. (2009) *Environ. Sci. Technol.* **43**, 8807-8812.
- [3] Finck et al. (2012) *Miner. Mag.* **76**, 2723-2740.
- [4] Cho et al. (2005) *Anal. Bionanal. Chem.* **383**, 28-40.
- [5] Dardenne et al. (2009) *J. Phys.: Conf. Ser.* **190**, 012037.
- [6] Manceau et al. (1998) *Phys. Chem. Miner.* **25**, 347-365.
- [7] Schlegel and Manceau (2006) *Geochim. Cosmochim. Acta* **70**, 901-917.
- [8] Li et al. (1993) *Phys. Rev.* **B48**, 10063-10073.
- [9] Seidl and Breu (2005) *Z. Kristallogr.* **220**, 169-176.

Acknowledgements

The synchrotron light source ANKA is acknowledged for provision of synchrotron radiation beam time.

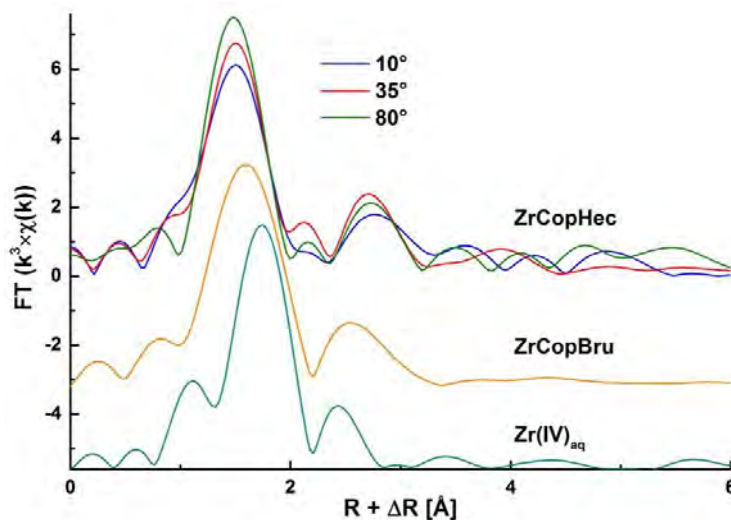


Fig. 2: Powder and polarized Fourier transforms of the samples.

Pu L₃ edge high energy-resolution X-ray absorption near edge structure investigations of actinide partitioning complexes

T. Prüßmann¹⁾, I. Pidchenko¹⁾, N. L. Banik¹⁾, K. Dardenne¹⁾, J. Rothe¹⁾, T. Vitova¹⁾

¹⁾Karlsruhe Institute of Technology, Institute for Nuclear Waste Disposal, Hermann-von-Helmholtz-Platz 1, D-76344 Eggenstein-Leopoldshafen, Germany

Introduction

One of the major steps in the partitioning and transmutation (P&T) strategy for reduction of the long-term radiotoxicity of spent nuclear fuel is the separation of 5f elements from their chemically similar 4f counterparts. This separation is necessary as the lanthanides (*Ln*(III)) fission products have large neutron cross sections and thereby compromise transmutation efficiency in the nuclear fission process. Selective liquid-liquid extraction of actinides (*An*(III)) from *Ln*(III) has been demonstrated using soft donor extracting agents such as heterocyclic N-donor ligands, e.g., bistriazinylpyridines (BTP) [1] and bistriazinylbipyridines (BTBP) [2] with separation factors (SF) for Am(III) over Eu(III) higher than 100 (SF=distribution ratio D_{Am}/D_{Eu} ; $D_M = [M]_{org}/[M]_{aq}$). Optimization of the partitioning ligands is a topic of global interest, as the present ligands do not yet fulfil all criteria for application in an industrial process. Such optimization implies basic understanding of the chemical and physical processes responsible for ligand selectivity for *An*(III) over *Ln*(III). It was shown that BTPs act as tridentate ligands, forming 1:3 complexes with *An*(III) and *Ln*(III) in the solid state and in organic solution [3, 4]. Spectroscopic data available demonstrate thermodynamically favoured *An*(III) extraction from nitric acid solution into the organic phase over *Ln*(III). However, we found with extended X-ray absorption spectroscopy (EXAFS) only subtle structural differences between the *An*(III)-BTP and *Ln*(III)-BTP complexes in organic solution, which may not fully explain *An*(III)/*Ln*(III) selectivity [4, 5]. High-energy resolution X-ray absorption near edge structure (HR-XANES) investigations will elucidate small electronic differences between complexes of *An*(III) and *Ln*(III) bound to N-donor ligands.

Experimental Description

Pu(III) and Pu(IV) samples (see Table 1) were synthesised in the Institute for Nuclear Waste Disposal (INE), KIT.

Table 1: Investigated Pu(III) and Pu(IV) samples

Sample name	Sample description
Pu(III)NO ₃	Pu(III) = $2 \cdot 10^{-3}$ M in 0.4 M HNO ₃ , 0.01M Rongalite
Pu(III)BTP	Pu(III) = $1.5 \cdot 10^{-3}$ M in 0.4M HNO ₃ , 0.01M Rongalite + 40mM BTP in kerosine:octanol (7:3)
Pu(IV)NO ₃	Pu(IV) = $1 \cdot 10^{-3}$ M in 1M HNO ₃
Pu(IV)BTP	Pu(IV) = $1 \cdot 10^{-3}$ M in 1M HNO ₃ + 40mM BTP in kerosin : octanol (7:3)

HR-XANES spectra at the Pu L₃ edge (18057 eV) have been collected at the INE-Beamline. The incident beam was monochromatized by a Ge(422) double crystal monochromator (DCM). The X-rays emitted from the sample were energy analysed by a Johann spectrometer in scanning geometry [6]. The L_{α1} emission line (14282 eV) was diffracted and focused on the Vortex SDD detector by five spherically bent Si(777) analyser crystals with 1 m bending radius at a Bragg angle of $\theta = 75.7^\circ$. The full width at half maximum (fwhm) of the measured Pu L_{α1} emission line is 12 eV. This value is similar to the value (10 eV) obtained for metallic Pu in experiment with 1.7 eV experimental energy resolution [7]. It was not possible to measure the absolute

experimental energy resolution due to the low number of elastically scattered photons that were effectively measured by the detector.

Results

In Figure 1a, features A and C are not resolved in the transmission spectrum of Pu(III)BTP. The Pu L₃ edge HR-XANES Pu(III)NO₃ and Pu(III)BTP spectra exhibit A, B and C features characteristic also for L₃ edge HR-XANES spectra of isostructural lanthanide complexes reported previously [8]. The A, B and C resonances in the Pu HR-XANES are less resolved due to the higher core-hole lifetime broadening contribution for actinides (3.7 - 4.2 eV) compared to lanthanides (1 - 2.1 eV). The most intense resonance (white line, WL, B) is broader in the Pu(III)BTP spectrum compared to the Pu(III)NO₃ spectrum. In addition, feature C is visible only in the Pu(III)BTP spectrum. Further investigations are needed to verify presence of a pre-edge feature (A). The Pu(IV)NO₃ spectrum is shifted ~5 eV to higher energies compared to the Pu(III)NO₃ spectrum due to the higher Pu oxidation state (Figure 1b). The Pu(IV)BTP spectrum is shifted only about ~2.5 eV, indicating a partial reduction of Pu(IV) to Pu(III) upon complexation with BTP.

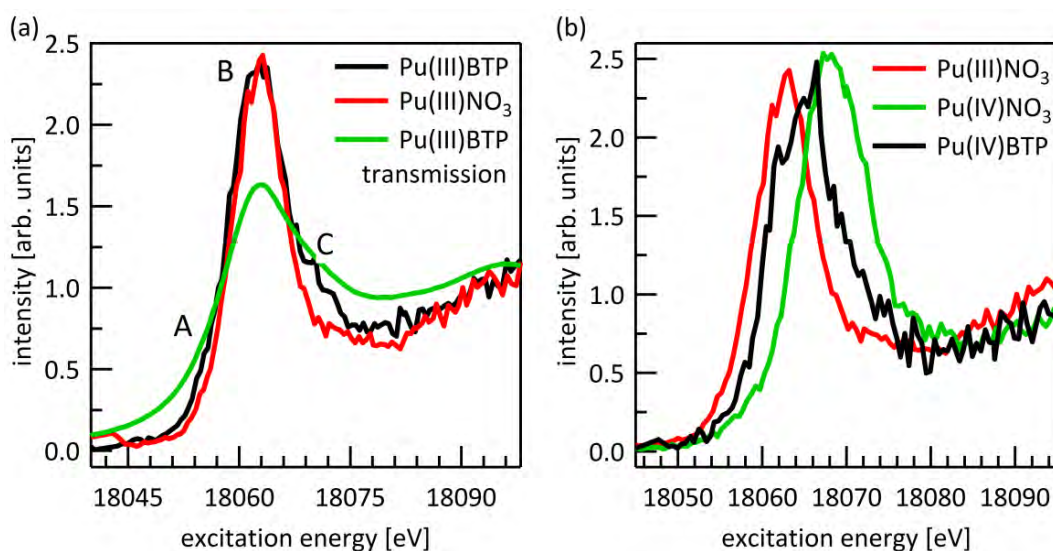


Figure 1: Pu L₃ edge XANES in transmission mode of Pu(III)BTP (a), Pu L₃ edge HR-XANES spectra of Pu(III)NO₃, Pu(III)BTP, (a) and Pu(III)NO₃, Pu(IV)NO₃, Pu(IV)BTP (b).

Conclusion and Outlook

Pu L₃ edge HR-XANES Pu(III)NO₃ and Pu(III)BTP spectra display similar absorption features to Ln compounds. While Pu(IV)NO₃ is stable, Pu in Pu(IV)BTP is partially reduced to Pu(III). The HR-XANES investigations will be extended to other An systems. Quantumchemical calculation with the FEFF9 code will help to interpret the observed spectral features and find differences compared to the LnBTP complexes.

Acknowledgments

We thank ANKA for the provided beamtime.

References

- [1] Kolarik, Z., U. Mullich, and F. Gassner, Solvent Extraction and Ion Exchange, 1999. **17**(5): p. 1155-1170.
- [2] Geist, A., et al., Solvent Extraction and Ion Exchange, 2006. **24**(4): p. 463-483.
- [3] Drew, M.G.B., et al., Inorganic Chemistry Communications, 2001. **4**(1): p. 12-15.
- [4] Denecke, M.A., et al., Inorganic Chemistry, 2005. **44**(23): p. 8418-8425.
- [5] Banik, N.L., et al., Dalton Transactions, 2010. **39**: p. 5117-5122.
- [6] Glatzel, P., et al., Catalysis Today, 2009. **145**(3-4): p. 294-299.
- [7] Booth, C.H., et al., Proceedings of the National Academy of Sciences of the United States of America, 2012. **109**(26): p. 10205-10209.
- [8] Prüßmann, T., et al., Journal of Physics: Conference Series, 2013. **430**(1): p. 012115.

A multi-analyser crystal spectrometer at the INE-Beamline

T. Prüßmann¹⁾, K. Dardenne¹⁾, M. Denecke¹⁾, P. Glatzel²⁾, I. Pidchenko¹⁾, J. Rothe¹⁾, T. Vitova¹⁾

¹⁾Karlsruhe Institute of Technology, Institute for Nuclear Waste Disposal, Hermann-von-Helmholtz-Platz 1, D-76344 Eggenstein-Leopoldshafen, Germany

²⁾European Synchrotron Radiation Facility, BP 220, F-38043 Grenoble Cedex, France

Introduction

In 2012, design and manufacturing of a Johann type [1] multi-analyzer crystal spectrometer (MAC-Spectrometer) for high energy resolution X-ray emission spectroscopy (HRXES) have been completed (Fig. 1). The MAC-Spectrometer assembly is based on a spectrometer installed at the ID26 beamline in the European synchrotron radiation facility (ESRF) [2] and comprises a mobile and a stationary positioning unit, both supplied by HUBER Diffractionstechnik GmbH (Rimsting, Germany). The five analyzer crystal positioning stages possess four degrees of freedom each. The crystal stages are mounted on a common granite block. This block is fixed on a mobile rack hosting power supplies and motion controllers for all 23 spectrometer motors. The stationary detector positioning unit has three degrees of freedom (a long and a short linear stage and a rotation stage), which allow the detector to be moved along the Rowland circle. Mechanical spectrometer performance tests and adaptation of the control software, as well as commissioning, have been performed and the spectrometer is now installed for use at the INE-Beamline for actinide research.

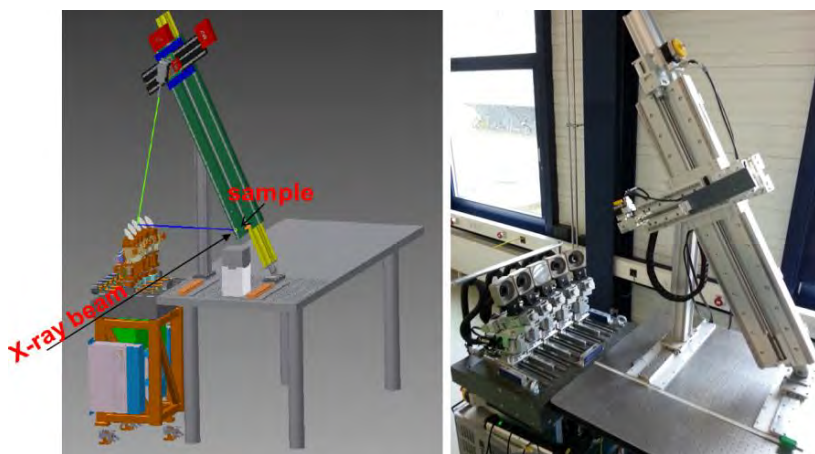


Fig. 1: 3D CAD model (left), photo of the MAC-Spectrometer during initial mechanical performance tests (right).

Experimental details

The primary X-ray beam was monochromatized by a Ge(422) double crystal monochromator. For detailed description of the INE-Beamline see [3]. The sample, crystals and detector were positioned on a Rowland circle in the vertical plane with diameter of 1 m equal to the bending radius of the spherically bent analyzer crystals.

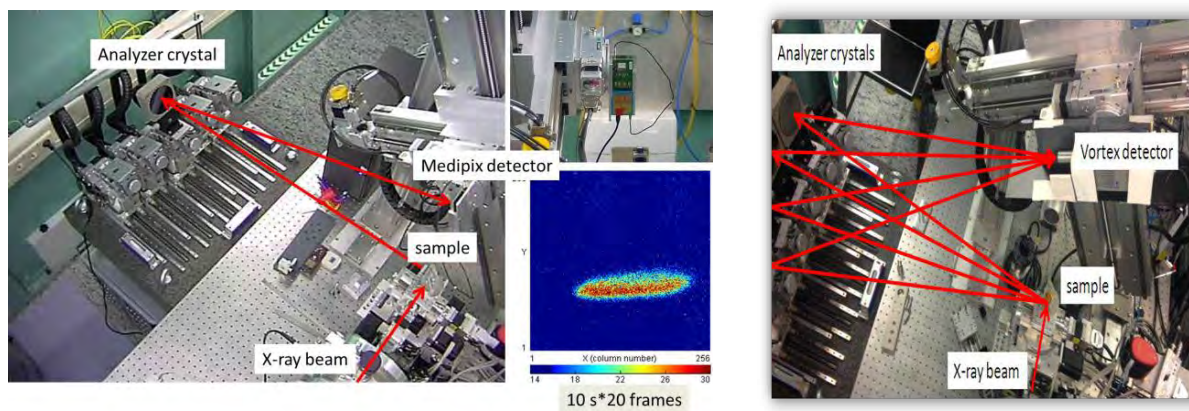


Fig. 2: Photo of the MAC-Spectrometer in dispersive (left) and scanning geometry (right) during commissioning at the INE-Beamline. The image measured with the Medipix detector shows focused Cu $K\alpha_1$ emission (left).

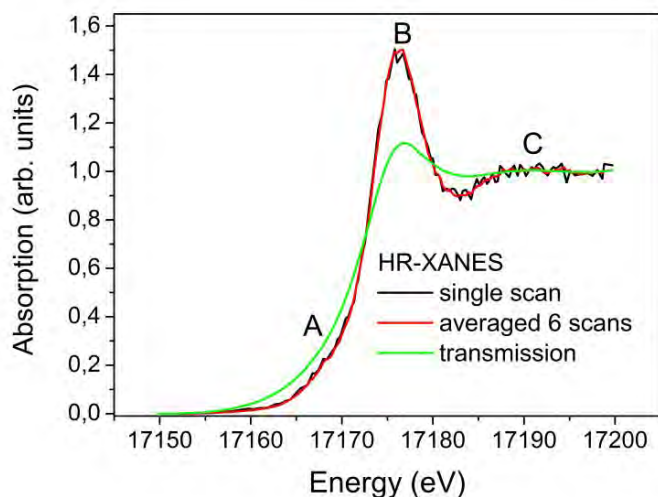
The initial alignment was performed by using the incident X-rays elastically scattered from a Teflon sample. The 9570.4 eV X-rays were energy dispersed by a Ge(555) analyzer crystal set at 82.55° Bragg angle and imaged on a Medipix position sensitive detector (see Fig. 2 left). The experimental energy resolution was

estimated by measuring the full-width at half maximum of the elastically scattered peak. The obtained value is 0.1 eV larger than the calculated value of 1.9 eV [4] and implies minor deviations of the positions of the sample, crystal and/or detector from the ideal Rowland circle geometry and/or source size effects [5].

The MAC-Spectrometer was used in scanning geometry during the U $L\alpha_1$ (13614) measurements (see Fig. 2 right). The emitted fluorescence from the uranium mineral metastudtite was diffracted by the 5 Ge(777) analyzer crystals and focused on a SDD VORTEX detector. The MAC-Spectrometer was set at the maximum of the U $L\alpha_1$ emission line (77.39° Bragg angle), while scanning the primary energy to obtain U L_3 edge (17166 eV) high-energy resolution X-ray absorption near edge structure (HR-XANES) spectra. It was not possible to measure the experimental energy resolution at this photon energy due to the low elastic scattering cross section.

The first U L_3 edge HR-XANES spectrum

The U L_3 edge HR-XANES spectra of the mineral metastudtite measured 30 and 180 minutes, respectively,



are shown in Fig. 3. All spectral features are better energy-resolved compared to the simultaneously measured transmission mode spectrum (see Fig. 3). The multiple scattering resonance C, sensitive to the bond distance between U and the axial O atoms, is well separated from the most intense resonance B (white line, WL). The asymmetry of the WL at about 17168 eV indicates presence of a pre-edge structure A, previously reported [5]. For further examples of applications of the MAC-Spectrometer see [6].

Fig. 3: U L_3 edge HR-XANES of metastudtite measured 30 minutes (black). 180 minutes (red) and XANES spectrum measured simultaneously in transmission mode.

Conclusion and Outlook

The MAC-Spectrometer in Johann geometry is now installed and available for use by the ANKA community. Three different sets of 5 analyzer crystals are currently available: Si(111), Si(220) and Ge(111). A He-environment around the spectrometer is currently being designed, which will allow HRXES investigations for M edges of actinides by minimizing the absorption of the low energy 3-4 keV photons in air. Its installation and tests will be performed in August 2013. The spectrometer can be currently used with a SDD VORTEX or KETEK detector in scanning geometry.

Acknowledgements

We acknowledge ANKA for the provided beamtime, thank Aurora Walshe for providing the metastudtite sample and Angelica Cecilia, Michael Fiederle and Elias Hamann for providing the Medipix detector.

References

- [1] Johann, H.H., *Zeitschrift für Physik*, 1931. **69**(3-4): p. 185-206.
- [2] Bergmann, U. and P. Glatzel, *Photosynthesis Research*, 2009. **102**(2-3): p. 255-266.
- [3] Rothe, J., et al., *Review of Scientific Instruments*, 2012. **83**(4).
- [4] de Groot, F.M.F., M.H. Krisch, and J. Vogel, *Physical Review B*, 2002. **66**(19).
- [5] Kleymenov, E., et al., *Review of Scientific Instruments*, 2011. **82**(6): p. 065107-7.
- [6] Vitova, T., et al., *Physical Review B*, 2010. **82**(23): p. 235118.

EXAFS investigations on incorporated Eu(III) in brucite at high ionic strength

M. Wiedemann, N. Finck, V. Metz, H. Geckeis

Karlsruhe Institute of Technology, Institute for Nuclear Waste Disposal (INE), Hermann-von-Helmholtz-Platz 1, D-76344 Eggenstein-Leopoldshafen, Germany

Motivation

A reliable description of the retention mechanisms of trivalent actinides in the near-field is necessary in long-term safety analyses for radioactive waste repositories in deep geological formations. For the Asse II salt mine (Germany) and the Waste Isolation Pilot Plant (USA), where low / intermediate level radioactive waste products are emplaced, brucite-bearing materials, $\text{Mg}(\text{OH})_2(\text{cr})$, and MgO are used as sealing materials and engineered buffer, respectively [1][2]. Recent studies on co-precipitation of Eu(III) [3] as well as Cm(III) [4] with $\text{Mg}(\text{OH})_2(\text{cr})$ in MgCl_2 systems at low ionic strength ($I = 0.2$ molal) show an incorporation of the lanthanides and actinides into the octahedral $\text{Mg}(\text{OH})_2$ structure. Yet, there is no published study available dealing with the retention mechanisms of lanthanides / actinides with $\text{Mg}(\text{OH})_2(\text{cr})$ at elevated ionic strength. The present study focuses on co-precipitation experiment at higher ionic strengths ($I = 1.2$ and 5.2 molal), where the structure of synthetic $\text{Mg}(\text{OH})_2:\text{Eu}$ are analysed by means of extended X-ray absorption fine structure (EXAFS).

Experimental

Synthetic $\text{Mg}(\text{OH})_2:\text{Eu}(\text{s})$ was prepared by co-precipitation of 0.4 molal MgCl_2 solution (*EuCopBrcA*) and 0.4 molal $\text{MgCl}_2 / 4$ molal NaCl solution (*EuCopBrcB*) with 2.1 molal NH_4OH solution and 700 ppm of a 0.1 molal Eu(III) stock solution, respectively. The 0.1 molal Eu(III) stock solution was prepared by dissolving Eu_2O_3 (REacton, 99.99 %, Alfa Aesar) in 2 % HClO_4 . Europium L_3 -edge EXAFS spectra were recorded at the INE-Beamline for Actinide Science. The energy was calibrated by setting the K-edge of a Fe foil at 7.112 keV. All spectra were collected in fluorescence-yield detection mode using a silicon drift detector (Vortex, SII Nano Technology). The data were analysed using *Athena* and *Artemis* interfaces to the *Iffefit* software [5]. The data fit was performed in R-space using *feff8.4*. The amplitude reduction factor S_0^2 was set to 1.0 to correctly reproduce the number of Eu(III) neighbouring O atoms in water.

Results and discussion

Experimental and modelled EXAFS results for *EuCopBrcA* and *EuCopBrcB* are shown in Fig. 1. Both EXAFS spectra do not show a single wave frequency of monotonically decreasing amplitude, indicating the presence of several cationic shells. The first FT contribution of both samples are related to O atoms bound to Eu and are fitted using two O shells at $d[\text{Eu-O1}] = 2.30 \pm 0.01 \text{ \AA} / 2.33 \pm 0.01 \text{ \AA}$ and $d[\text{Eu-O2}] = 2.46 \pm 0.02 \text{ \AA} / 2.52 \pm 0.01 \text{ \AA}$ (Table 1). These distances are typical of 6-fold and 9-fold coordination, respectively [6]. The fit results indicate low coordination numbers, but the total number of detected O atoms suggests a strained octahedral environment. Contributions at longer distances are modelled using Mg atoms. One Mg shell ($d[\text{Eu-Mg1}] = 3.37 \pm 0.01 \text{ \AA}$) was used to model the data of *EuCopBrcA*. For *EuCopBrcB* a split Mg shell at a mean distance of $\sim 3.47 \text{ \AA}$ is suggested from backscatterers detected at $d[\text{Eu-Mg1}] = 3.36 \pm 0.01 \text{ \AA}$ and $d[\text{Eu-Mg2}] = 3.58 \pm 0.03 \text{ \AA}$. At $d[\text{Eu-Mg3}] = 3.90 \pm 0.07 \text{ \AA}$ a possible additional Mg shell was detected. A C shell (< 1 atom at 2.75 \AA) was added for *EuCopBrcA*, corresponding to a potential bidentate binding of a carbonate [3]. No Eu backscatter was detected, excluding the presence of $\text{Eu}(\text{OH})_3(\text{s})$.

The mineral brucite consists of MgO_6 octahedra ($d[\text{Mg-O}] = 2.10 \text{ \AA}$) sharing O-O edges ($d[\text{O-O}] = 2.78 \text{ \AA}$; $d[\text{Mg-Mg}] = 3.14 \text{ \AA}$) [7]. Considering the O1 shell and assuming that Mg and Eu polyhedra share edges, the calculated Eu-Mg interatomic distance for *EuCopBrcA* is $d[\text{Eu-Mg}] = \sqrt{(2.30^2 - 1.39^2) + 1.58} = 3.41 \text{ \AA}$ and for *EuCopBrcB* $d[\text{Eu-Mg}] = \sqrt{(2.33^2 - 1.39^2) + 1.58} = 3.45 \text{ \AA}$, respectively. This calculated value is remarkably close to the sum of the distance between neighbouring octahedral cations in brucite and the difference in ionic radius between Mg and Eu ($3.14 + 0.23 = 3.38 \text{ \AA}$). This distance is very close to $d[\text{Eu-Mg1}]$ but is smaller than $d[\text{Eu-Mg2}]$. It is therefore very likely that Eu substitutes, at least partly, for Mg in brucite and the next nearest Mg shell splits into two subshells (Mg1 and Mg2) in order to accommodate this

large cation. Considering the O2 shell, the calculate $d[\text{Eu-Mg}]$ interatomic distance would be significant larger (3.61 – 3.68 Å) than $d[\text{Eu-Mg}_2]$. The structural strain produced by the substitution very likely leads to cancellation effects and thus low numbers of detected neighbours.

EXAFS investigations of co-precipitation experiments at different ionic strengths indicate the incorporation of Eu(III) into the octahedral structure of brucite. Due to the larger ionic radius of Eu(III) the substitution of Mg produces a structural distortion of the MgO_6 octahedra. No significant effect of the ionic strength on the incorporation mechanism was observed in the co-precipitation experiments ($I = 1.2$ and 5.2 molal).

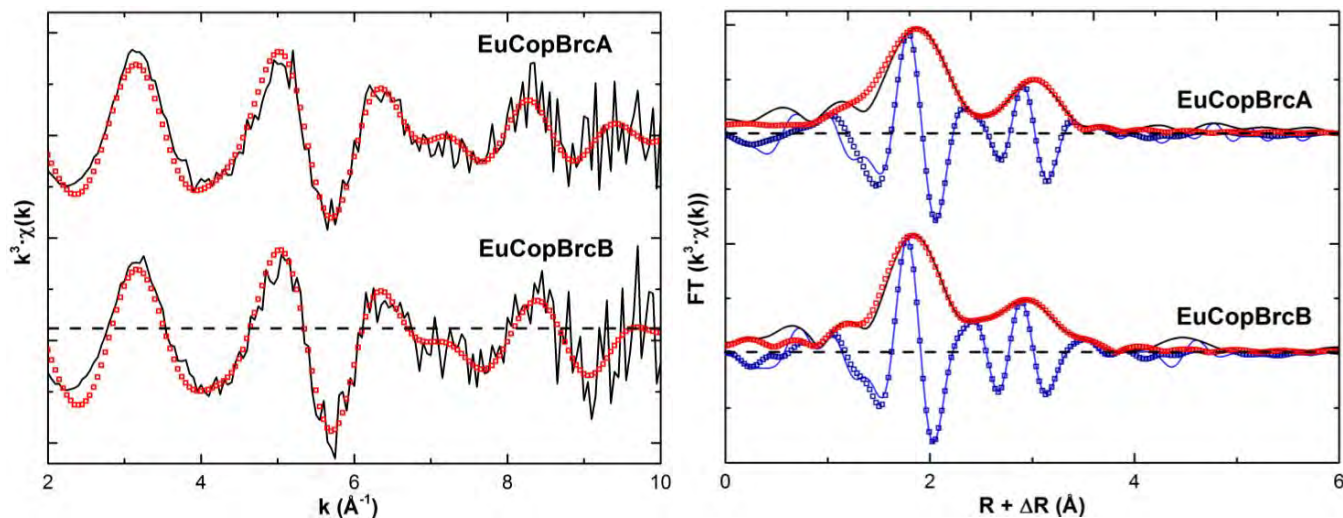


Fig. 1: Experimental and modelled (squares) XAS spectra (left) and the corresponding Fourier transforms (right) of both samples.

Table 1: Quantitative EXAFS analysis of the samples. R is the interatomic distance, N is the coordination number, σ^2 is the mean square displacement taking into account the thermal and structural disorder (Debye-Waller factor), ΔE is the energy shift and R_f is the figure of merit for the fit (* Parameter held fixed during the fitting procedure).

Sample		O1 shell	O2 shell	Mg1 shell	Mg2 shell	Mg3 shell	C1 shell	ΔE	R_f
<i>EuCopBrca</i>	R (Å)	2.30(1)	2.46(2)	3.37(1)	-	-	2.75*		
	N	3.3(5)	3.2*	3.6(4)	-	-	0.9*	5.6(8)	0.0017
	σ^2 (Å ²)	0.007*	0.007*	0.009*	-	-	0.009*		
<i>EuCopBrcaB</i>	R (Å)	2.33(1)	2.52(1)	3.36(1)	3.58(3)	3.90(7)	-		
	N	4.2(3)	2.3*	4.5*	1.7*	0.8*	-	6.5(1.0)	0.0006
	σ^2 (Å ²)	0.005*	0.005*	0.008*	0.007*	0.009*	-		

Acknowledgements

The authors would like to thank our colleague K. Dardenne for her technical support at the INE-Beamline for Actinide Science. The ANKA synchrotron light source is gratefully acknowledged for provision of beam time. The research leading to these results have been financially supported in part from the Federal Ministry of Education and Research (BMBF) project VESPA.

[1] BfS, Annual Report 2010. Federal Office for Radiation Protection, Salzgitter, 2011, 33-42.

[2] Brush, L.H., Snider, A.C., Xiong, Y., Leigh, C.D., Use of MgO as the engineered barrier in the WIPP, Denver Annual Meeting, Geological Society of America, Denver, 2004, 296.

[3] Finck, N., Bouby, M., Dardenne, K., Geckeis, H., Mineralogical Magazine 76, 2012, 2723-2740.

[4] Brandt, H., Bosbach, D., Panak, P.J., Fanghänel, T., Geochimica Et Cosmochimica Acta 71, 2007, 145-154.

[5] Ravel, B., Newville, M., Journal of Synchrotron Radiation 12, 2005, 537-541.

[6] Shannon, R.D., Acta Crystallographica Section A 32, 1976, 751-767.

[7] Odaniel, H., Zigan, F., Rothbaue, R., Bartl, H., Kuzel, H.J., Acta Crystallographica S 21, 1966, A66.

Formation behavior of ternary Me-UO₂-CO₃ species in weakly alkaline condition (Me = Ca²⁺ and Mg²⁺)

J.-Y. Lee¹, X. Gaona², M. Vespa², K. Dardenne², J. Rothe², T. Rabung², M. Altmaier², J.-I. Yun¹

¹Department of Nuclear and Quantum Engineering, KAIST, 291 Daehak-ro, Yuseong-gu, Daejeon 305-701, Republic of Korea

²Karlsruhe Institute of Technology, Institute for Nuclear Waste Disposal (KIT-INE), Hermann-von-Helmholtz-Platz 1, D-76344 Eggenstein-Leopoldshafen, Germany

Introduction

An adequate understanding of the chemical behaviour of radionuclides in natural groundwater systems is highly relevant for the assessment of the far-field of deep geological repositories for high-level nuclear waste. In natural groundwater systems, a predominant formation of ternary Me-UO₂-CO₃ species (Me = Ca²⁺ and Mg²⁺) has been reported in the omnipresence of earth-alkaline metal ions and high carbonate concentrations in the aquatic environment [1-3]

The objective of the present work was to investigate the stoichiometry and stability of the ternary Me-UO₂-CO₃ species in the well-defined chloride media. The collection of U-L_{III} EXAFS data at the INE-beamline at ANKA conveys fundamental structural and stoichiometric information on the Me-UO₂-CO₃ species. Finally, EXAFS data have been analysed and compared with those obtained by time-resolved laser fluorescence spectroscopy (TRLFS).

Experimental

All the samples were prepared at KIT-INE laboratories. A stock solution of U(VI) was diluted with deionized water to a concentration of U(VI) to 10⁻³ M. The acidity of the samples was set to 8.1 with TRIS buffer and well-defined chloride solutions. The concentration of carbonate ions in the aqueous U(VI) samples was fixed by the addition of 0.05 M Na₂CO₃. The total Ca²⁺ and Mg²⁺ concentrations were adjusted by addition of appropriate volumes of CaCl₂ and MgCl₂ stock solutions, respectively. The ionic strengths for the solutions containing Ca²⁺ and Mg²⁺ ions were set to 0.1 M Na/HCl. Aqueous ion concentrations were quantified using conventional analytical methods, e.g., ICP-MS for UO₂²⁺ and ICP-OES for Ca²⁺ and Mg²⁺.

The solution of each sample was transported to the INE-Beamline at ANKA synchrotron facility, and the U-L_{III} EXAFS spectra were collected accordingly. Obtained EXAFS spectra were analyzed by using Demeter IFEFFIT package [4]. For gaining complementary information on the structural properties and chemical speciation of ternary Me-UO₂-CO₃ complexes, TRLFS was additionally employed. The forth-harmonic (266 nm) of nano-second pulsed laser beam from Nd:YAG laser (Continuum Minilite-I) was utilized for the excitation of aqueous U(VI) samples. The fluorescence emission was collected with optical fiber and then delivered into a Czerny-Turner type spectrometer coupled with an ICCD camera (Andor Technology).

Results

As shown in Fig. 1(a) and 1(b), increase in fluorescence intensity from TRLFS data of uranium(VI) species was measured with raising both Ca²⁺ and Mg²⁺ ion concentrations, representing the complexation of Ca²⁺ and Mg²⁺ ions with uranium(VI) species. The blue-shifted fluorescence peak positions compared with those of UO₂²⁺ free ions [5] were observed and remained unchanged at all earth alkaline metal ion concentrations. According to the measured fluorescence peak wavelengths located at 466, 485, 505, 527, and 551 nm, uranium(VI) species formed in the present work could be ascribed to Ca/Mg-UO₂-CO₃ complexes [6].

Two different fluorescence lifetimes for each Ca- and Mg-bound uranyl species were evaluated from the bi-exponential decay curve of fluorescence intensity (Table 1). Relatively short fluorescence lifetimes of 16.3 ± 0.2 ns and 17.9 ± 0.3 ns at low Ca^{2+} and Mg^{2+} ion concentrations revealed predominant formation of $\text{CaUO}_2(\text{CO}_3)_3^{2-}$ and $\text{MgUO}_2(\text{CO}_3)_3^{2-}$ species in accordance with literature data, respectively [3,6]. On the other hand, at high Ca^{2+} ion concentration, the fluorescence lifetime was significantly increased from 16.3 ± 0.2 to 30.9 ± 0.3 ns, indicating major formation of $\text{Ca}_2\text{UO}_2(\text{CO}_3)_3(\text{aq})$ species. As well as Ca^{2+} , the fluorescence lifetime of Mg- $\text{UO}_2\text{-CO}_3$ species was also increased to be 50.8 ± 0.7 ns at high Mg^{2+} concentration. Longer fluorescence lifetime of U(VI) species can be attributed to the formation of $\text{Mg}_2\text{UO}_2(\text{CO}_3)_3(\text{aq})$ species in terms of Mg^{2+} ion concentration and fluorescence lifetime increment tendency. However, due to the lack of literature data on the formation and spectroscopic properties of $\text{Mg}_2\text{UO}_2(\text{CO}_3)_3(\text{aq})$ species, its fluorescence properties identified first in the present work could not be directly compared with literatures, as summarized in Table 1.

EXAFS technique has been employed to investigate the chemical stoichiometry of Ca/Mg- $\text{UO}_2\text{-CO}_3$ complexes. The k^3 -weighted U- L_{III} edge EXAFS spectra of Ca/Mg- $\text{UO}_2\text{-CO}_3$ species and respective Fourier transforms are represented in Fig. 2. Peak shift tendency to the longer distance at around 4 Å with increasing Ca^{2+} and Mg^{2+} ion concentration was identified in the $|\chi(R)|$ spectra, as shown in the inset of Fig. 2(c) and 2(d). Preliminary results of the simulated molecular structure of Ca/Mg- $\text{UO}_2\text{-CO}_3$ species from the crystal structure of mineral liebigite [ICSD 31270] indicate that the peak shift to longer distance could be ascribed by the increment in U-Ca/Mg contributions located at around 4 Å and hence represents further complexation behavior of Ca/Mg ions to uranium(VI) carbonato complex.

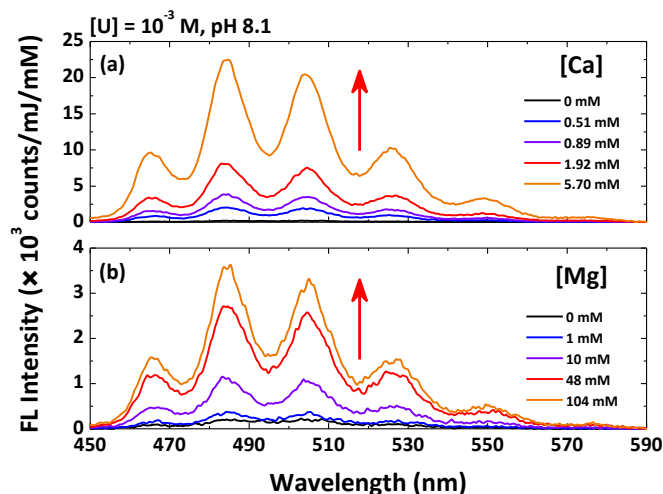


Fig. 1: Fluorescence spectra of Ca/Mg- $\text{UO}_2\text{-CO}_3$ complexes at pH 8.1

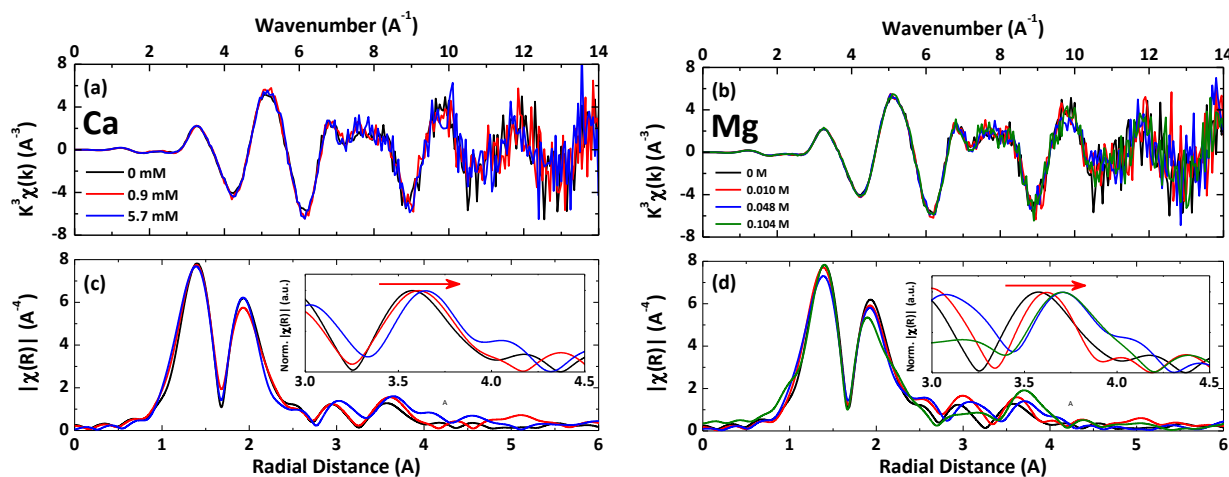


Fig. 2: (a, b) Uranium k^3 -weighted L_{III} edge EXAFS spectra and (c, d) Fourier transform without considering phase correction for both Ca- and Mg- $\text{UO}_2\text{-CO}_3$ species

Table 1: Spectroscopic properties of *Me-UO₂-CO₃* species (*Me* = Ca²⁺ and Mg²⁺)

U(VI) species	Fluorescence wavelength (nm)	Fluorescence lifetime (ns)	Ref.
CaUO ₂ (CO ₃) ₃ ²⁻	466-485-505-527-551	16.3 ± 0.2	p.w.
	466-485-505-527-550	12.7 ± 0.2	[3]
		9 ~ 13	[7]
Ca ₂ UO ₂ (CO ₃) ₃ (aq)	466-485-505-527-551	30.9 ± 0.3	p.w.
	466-485-505-527-551	29.2 ± 0.4	[3]
	465-484-504-526-551	43 ± 12	[1]
MgUO ₂ (CO ₃) ₃ ²⁻	466-485-505-527-551	17.9 ± 0.3	p.w.
	466-485-505-527-551	18.2 ± 2.7	[6]
Mg ₂ UO ₂ (CO ₃) ₃ (aq)	466-485-505-527-551	50.8 ± 0.7	p.w.

Acknowledgements

We thank the ANKA synchrotron source for providing the beamtime. We would also like to thank C. Walschburger and S. Moisei-Rabung for technical support with ICP-MS/OES measurements.

References

- [1] G. Bernhard, G. Geipel, V. Brendler, and H. Nitsche, *Speciation of Uranium in Seepage Waters of a Mine Tailing Pile Studied by Time-Resolved Laser-Induced Fluorescence Spectroscopy (TRLFS)*, *Radiochimica Acta* **74**, 87-91 (1996)
- [2] W. Dong and S. C. Brooks, *Determination of the Formation Constants of Ternary Complexes of Uranyl and Carbonate with Alkaline Earth Metals (Mg²⁺, Ca²⁺, Sr²⁺, and Ba²⁺) Using Anion Exchange Method*, *Environmental Science & Technology* **40**(15), 4689-4695 (2006)
- [3] J.-Y. Lee and J.-I. Yun, *Formation of ternary CaUO₂(CO₃)₃²⁻ and Ca₂UO₂(CO₃)₃(aq) complexes under neutral to weakly alkaline conditions*, *Dalton Transactions* **42**(27), 9862-9869 (2013)
- [4] B. Ravel and M. Newville, *ATHENA and ARTEMIS: data analysis for X-ray absorption spectroscopy using IFEFFIT*, *Journal of Synchrotron Radiation* **12**, 537-541 (2005)
- [5] C. Moulin, I. Laszak, V. Moulin, and C. Tondre, *Time-Resolved Laser-Induced Fluorescence as a Unique Tool for Low-Level Uranium Speciation*, *Applied Spectroscopy* **52**(4), 528-535 (1998)
- [6] G. Geipel, S. Amayri, and G. Bernhard, *Mixed Complexes of Alkaline Earth Uranyl Carbonates: A Laser-induced Time-resolved Fluorescence Spectroscopic Study*, *Spectrochimica Acta, Part A: Molecular and Biomolecular Spectroscopy* **71**(1), 53-58 (2008)
- [7] O. Prat, T. Vercouter, E. Ansoborlo, P. Fichet, P. Perret, P. Kurttio, and L. Salonen, *Uranium Speciation in Drinking Water from Drilled Wells in Southern Finland and Its Potential Links to Health Effects*, *Environmental Science & Technology* **43**(10), 3941-3946 (2009)

Charge transfer at the interface between cobalt phthalocyanine and epitaxially grown MnO

M. Glaser¹, H. Peisert¹, H. Adler¹, U. Aygül¹, M. Ivanovic¹, P. Nagel², Micheal Merz², S. Schuppler², T. Chassé¹

¹Institut für Physikalische und Theoret. Chemie, Universität Tübingen, 72076 Tübingen, Germany

²Karlsruher Institut für Technologie, Institut für Festkörperphysik, 76021 Karlsruhe, Germany

Introduction:

A main reason for the growing interest in transition metal phthalocyanines (TMPc) is their possible application in optoelectronic devices, most recently also applications in spintronic devices are discussed. The properties of possible devices are strongly influenced by interactions at interfaces between the TMPcs and the substrate. Interfaces between several Pcs and metals have been investigated by our group using photoexcited electron spectroscopies (XPS, Resonant photoemission (ResPES), Auger spectroscopy (XAES) and X-ray absorption spectroscopy (XAS)). In particular at interfaces between open shell TMPcs like CoPc and FePc and metals, charge transfer processes can be observed [1,2].

Beside metals, transition metal oxide (TMO) thin films are promising substrates for applications of TMPcs – also in the view of a magnetic coupling between the organic molecules and the substrate. The aim of this project is the extension of recent studies to TMPc/TMO interfaces. We focus on MnO epitaxially grown on Ag(100), a system which shows unique chemical and physical properties depending e.g. on the MnO thickness [3].

Experimental details:

The XAS and XPS measurements were carried out at the soft x-ray beamline WERA. Polarization dependent X-ray absorption spectra were acquired at different incident angles of light and normalized to equal step heights beyond ionization threshold. The photoemission spectra were measured at normal emission angle using excitation energies of 1100 eV (core levels) and 210 eV (Mn3s core levels, surface sensitive) and were energy calibrated to the Ag3d core level signal of the Ag(100) single crystal. The MnO substrate was prepared in-situ by deposition of Mn on single crystalline Ag(100) at a low partial pressure of oxygen (2.0×10^{-7} mbar). The CoPc films were deposited on the oxide substrate at ultra-high vacuum conditions from a temperature-controlled crucible at evaporation rates in the range of 1 to 4 Å per minute.

Results:

Polarization dependent N K-edge spectra provide information about the molecular orientation of the organic molecules. The typical angular dependency of these features reveals the presence of flat lying molecules, enabling the assignment of transitions in TM absorption spectra.

Co2p core level spectra of the 2.5 monolayer (ML) CoPc film (see Fig. 1a) show besides the main line at binding energy (BE) 780.6 eV an additional peak at BE 778.6 eV. The relative intensity increases drastically with decreasing film thickness and dominates the spectrum for film thicknesses of 1ML and lower, we assign therefore this peak to an interface species. The lower binding energy (close to the value expected for metallic Co) can be understood by a charge transfer from the MnO substrate to Co^{2+} of CoPc.

Polarization dependent Co L-edge spectra in Fig. 1b exhibit two groups of Co 2p_{3/2} excitations between 775 and 785 eV with different polarization dependence: at grazing incidence (20°) the intensity of feature A is maximal (i.e. the transition is z-polarized related to the molecular axis), whereas at normal incidence (90°) a group of excitations, denoted B1 and B2 in Fig. 1, dominate the spectrum (xy-polarized). The shape of the spectra is comparable to highly oriented CoPc films of the thickness of about 3 nm, reflecting bulk properties. The lower intensity of B2

compared to Ref. [1] and the presence of A0 indicate charge transfer processes at the interface. The interaction at the interface becomes more pronounced for coverages in the monolayer range: The features A1 and B2 are disappeared and at grazing incidence a new feature A0 dominates the spectrum with the same angular dependence as feature A1. The feature A0 can be interpreted as a new unoccupied level as a result of a hybridization between the Co of the CoPc and the MnO substrate (cf. also Refs. [2a] and [2c]).

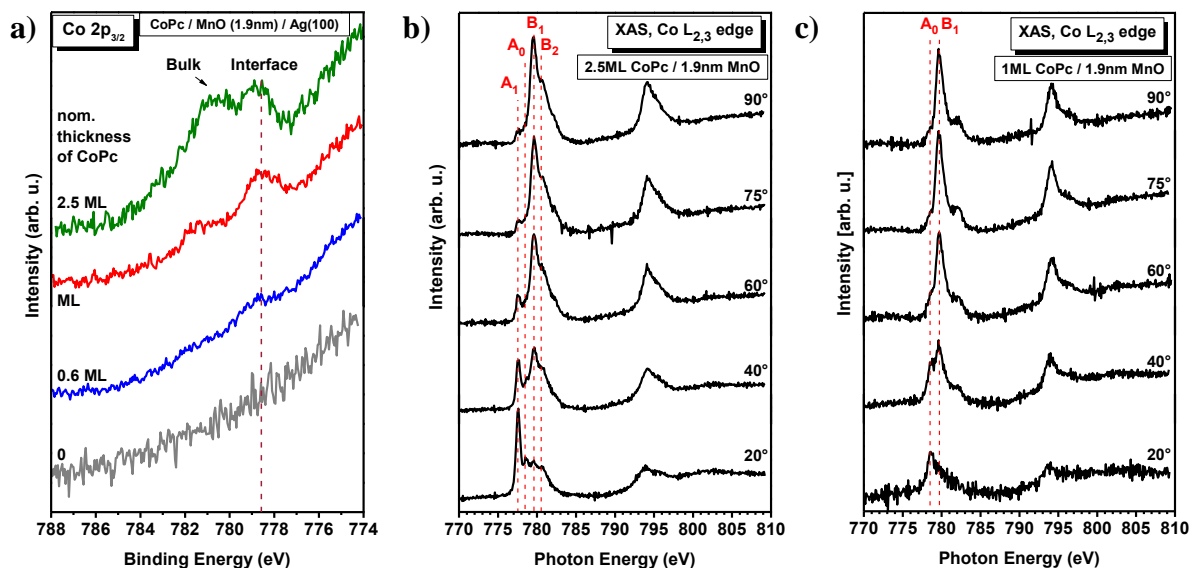


Fig. 1 a) Co2p core level photoemission spectra for CoPc on MnO. The interface feature is a result of a charge transfer to the Co atom. b) and c) show Co L-edge spectra of a 2.5 monolayer (ML) and 1 ML CoPc film, respectively, measured at different incident angles. With decreasing thickness a new feature A0 appears and the features A1 and B2 disappear confirming the charge transfer at the interface.

Mn L-edge absorption spectra (not shown) do not exhibit a significant change after the evaporation of CoPc. This may indicate that the charge transfer occurs not locally between Co and Mn. On the other hand, spectral changes might be hidden due to the low percentage of interacting Mn atoms. Surface sensitive XPS measurements of Mn3s core levels, which are affected significantly by the configuration of the 3d electrons [3], show a shift of 0.1 eV to lower binding energy after the evaporation of CoPc. A possible explanation is charge transfer back to substrate (via ligands) or a semiconductor surface band bending due to doping of MnO.

Acknowledgement

Technical support by W. Neu (Tübingen) and by the WERA team at ANKA is gratefully acknowledged. For financial support we thank the German Research Council (CH 132/22-2). ANKA Angströmquelle Karlsruhe is acknowledged for the provision of beamtime.

References:

- [1] H. Peisert, I. Biswas, U. Aygül, A. Vollmer, T. Chassé *Electronic structure of cobalt phthalocyanine studied by resonant photoemission: localization of Co related valence band states*, Chem. Phys. Lett. 493 (2010) 126–129.
- [2] a) F. Petraki, H. Peisert, I. Biswas, U. Aygül, F. Latteyer, A. Vollmer, T. Chassé *Interaction between Cobalt Phthalocyanine and Gold studied by X-ray Absorption and Resonant Photoemission Spectroscopy*, J. Phys. Chem. Lett. 1 (2010) 3380–3384; b) F. Petraki, H. Peisert, F. Latteyer, U. Aygül, A. Vollmer, T. Chassé *Impact of the 3d electronic states of cobalt and manganese phthalocyanines on the electronic structure at the interface to Ag(111)*, J. Phys. Chem. C 115 (2011) 21334–21340; c) J. Uihlein, H. Peisert, M. Glaser, M. Polek, H. Adler, F. Petraki, R. Ovsyannikov, M. Bauer, T. Chassé *Communication: Influence of graphene interlayers on the interaction between cobalt phthalocyanine and Ni(111)*, J. Chem. Phys. 138 (2013) 081101.
- [3] M. Nagel, I. Biswas, P. Nagel, E. Pellegrin, S. Schuppler, H. Peisert, T. Chassé, *Ultrathin transition metal oxide films: Thickness dependence of the electronic structure and local geometry in MnO*, Phys. Rev. B 75 (2007) 195426.

XMCD study of the intrinsic magnetic properties of $\text{Co}_2\text{Cr}_{1-x}\text{Fe}_x\text{Al}$

J. Geck¹, C.G.F. Blum¹, A. Omar¹, P. Nagel², S. Wurmehl¹

¹ IFW Dresden, Helmholtzstr. 20, 01069 Dresden, Germany

² Forschungszentrum Karlsruhe GmbH, Institute for Synchrotron Radiation, Hermann-von-Helmholtz-Platz 1, D-76344 Eggenstein-Leopoldshafen, Germany

Aims of experiment

The aim of this experiment was to clarify, why the magnetism of bulk $\text{Co}_2\text{Cr}_{1-x}\text{Fe}_x\text{Al}$ does not at all agree with the expected behaviour. Our previous work already identified an unexpected transformation via a so-called spinodal decomposition in Cr-rich $\text{Co}_2\text{Cr}_{1-x}\text{Fe}_x\text{Al}$. Based on this observation, we also developed a route to grow homogenous single crystals, which enabled us to compare the magnetic properties of spinodal decomposed and homogeneous samples. Our measurements of the macroscopic magnetization already revealed a clear difference between these two types of samples. However, such macroscopic measurements cannot provide insights regarding the microscopic origin of the differences in the magnetic properties. The aim of the present XMCD studies was therefore to perform an element-resolved study of the microscopic magnetism in order to address the exactly this point.

Experimental procedure

Prior to the XMCD measurements, we to great care to prepare clean sample surfaces using a so-called in-situ cleaving device. In this way, fresh sample surfaces could be prepared at a pressure of about 5×10^{-8} mbar. After the sample surface has been prepared the sample was immediately transferred into the measuring-chamber providing pressures better than 5×10^{-9} mbar. The XMCD measurements have been performed at the Cr, Fe and Co L_{23} -edges at fixed temperature and in a magnetic field of ± 1 Tesla. Monitoring the spectra as a function of time showed no degradation of probed sample during the time of the measurements.

Results

We measured successfully the XMCD at the Cr, Fe and Co L_{23} -edges of a homogeneous $\text{Co}_2\text{Cr}_{0.4}\text{Fe}_{0.4}\text{Al}_{1.2}$ and 2 spinodal decomposed samples namely, Co_2CrAl and $\text{Co}_2\text{Cr}_{0.6}\text{Fe}_{0.4}\text{Al}$. Our preliminary analysis of the data already provides important insights: while for both the homogeneous and the spinodal decomposed the Fe carries a similar spin moment of $1.9 \mu_B/\text{Fe}$, the Cr moment for the two samples is significantly different. For the homogenous and the spinodal decomposed sample for find a Cr spin moment of $0.45 \mu_B/\text{Cr}$ and $0.25 \mu_B/\text{Cr}$, respectively. The present XMCD measurements therefore show that the local magnetism of Cr is most strongly affected by the spinodal decomposition. This result is in perfect agreement with our analysis of the spatially-resolved chemical composition, where we found that Cr in the two type of samples occurs in two different chemical environments.

Acknowledgements

We would like to thank S. Schuppler and M. Merz for their most valuable support during the experiment at ANKA.

Semi-polar GaN grown on prepatterned sapphire substrate X-ray investigation

S. Lazarev¹⁾, S. Bauer¹⁾, M. Mantilla¹⁾

¹⁾ Karlsruhe Institute of Technology (KIT), Synchrotron Facility ANKA, Hermann-von-Helmholtz-Platz 1, 76344 Eggenstein-Leopoldshafen, Germany

In the experiment two semi-polar (11-22) GaN samples S1 and S2 without and with SiN mask were investigated. Sketches of the samples are shown in the Fig.1 (middle and right).

In order to investigate influence of defects such as basal plane stacking faults (BSFs) on diffuse X-ray scattering, three dimensional (3D) reciprocal space maps (RSMs) were recorded with linear detector Mithen 1K at X-ray energy of 10keV. The detector was placed horizontally (out of diffraction plane) and rocking curve scans were performed. The scheme of the experiment is presented in the Fig.1 (left).

First, we have recorded the 3D RSMs of symmetric 11-22 reflections, not affected by BSFs. In the Fig.2.a view of symmetric 11-22 reflection of the sample S1 is presented. For better understanding of diffuse X-ray intensity distribution, cuts of 3D RSMs were performed in different crystallographic directions. In the Fig.1.b cut of 11-22 reflection of plane containing [0001] direction of BSFs is demonstrated. As it was predicted, there was no additional BSFs diffuse intensity along [0001] direction.

In the Fig.1c-f., asymmetric 20-23 reflection of the sample S1 is presented. In the plane containing [0001] axis BSFs diffuse intensity (streak 1) along [0001] direction is observed, see Fig.1c and Fig.1d. Cut of the reflection with coplanar diffraction plane is presented in the Fig.1e and Fig.1f. The BSFs diffuse intensity is not observed in this plane and that is the reason why for BSFs diffuse investigation non-coplanar geometry and 3D reciprocal space mapping are required.

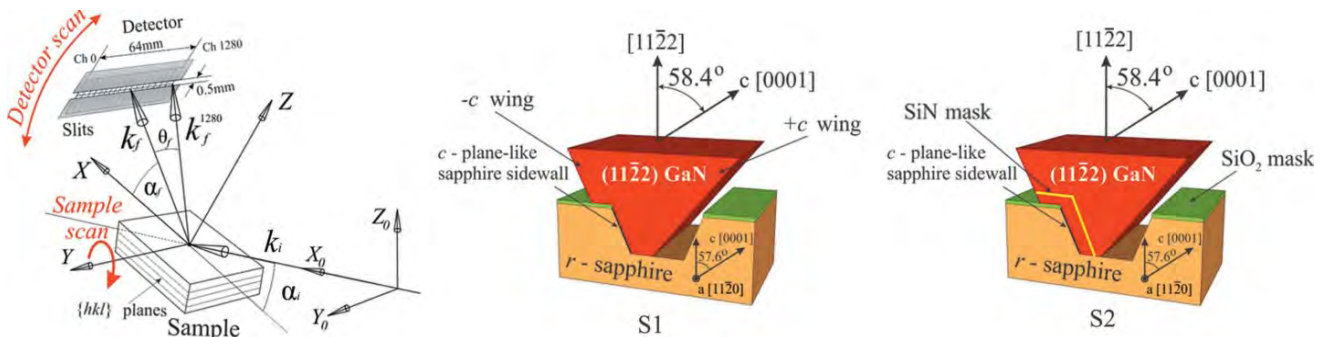


Fig. 1. Scheme of the experiment (left) and sketches of semi-polar GaN samples S1 and S2.

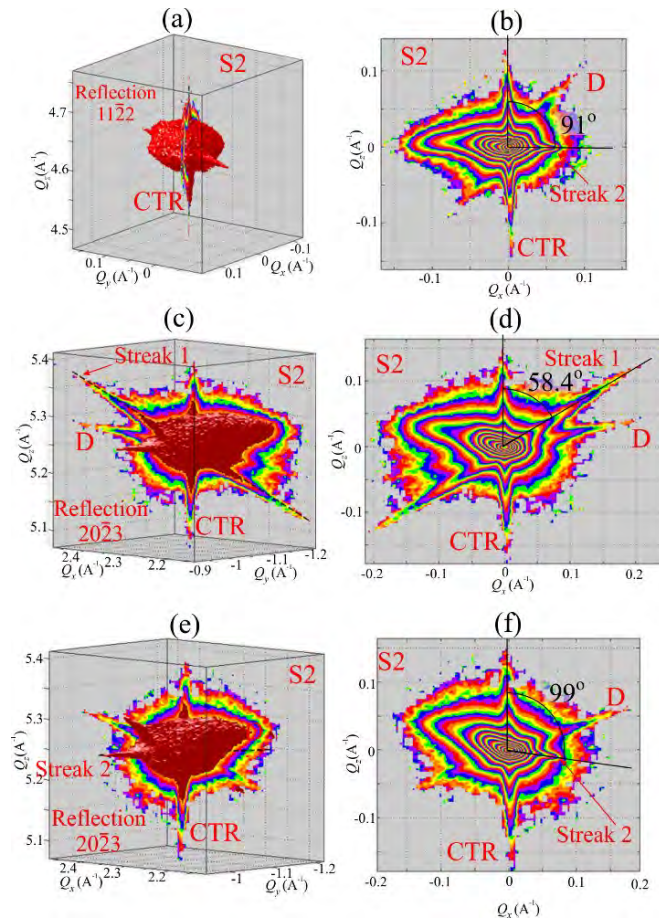


Fig. 2. 3D RSMs of GaN reflections 11-22 and 20-23 of the sample S1 (a, c, e) and their cuts (b, d, f).

Further the BSFs intensity distributions along [0001] direction of samples S1 and S2 were compared. In the Fig.3.a and Fig.3.b this comparison is presented in log-linear and log-log scales. The influence of SiN mask was demonstrated directly from the comparison of BSF streaks tails. The diffuse intensity of tails is proportional to BSF density. Therefore, the BSF density of the sample S1 without SiN mask is higher than of the sample S2 with SiN mask.

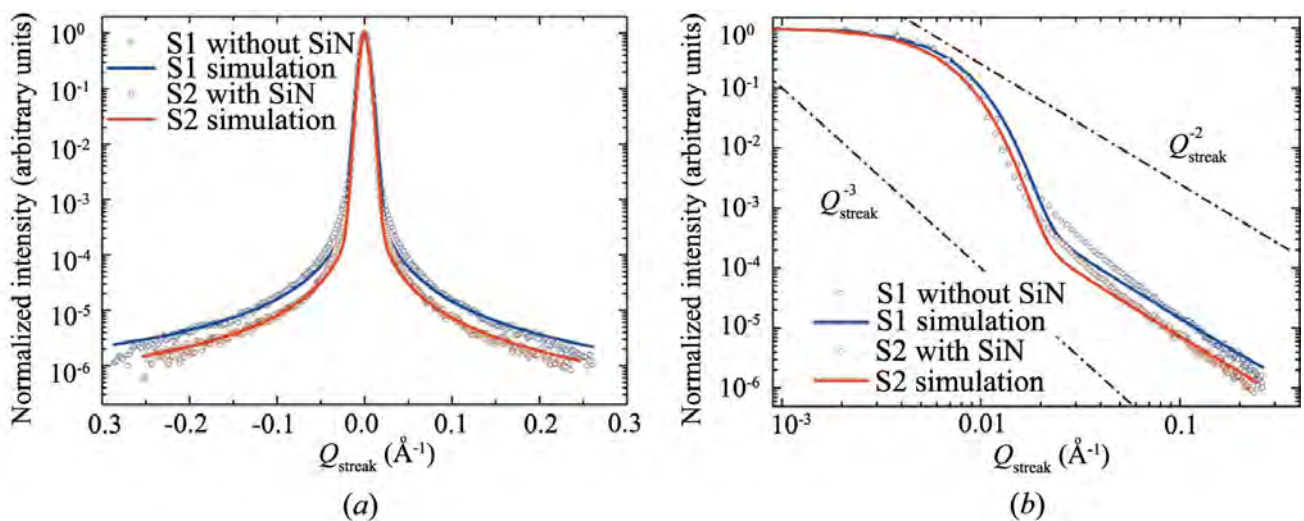


Fig. 3. Profiles in log scale along BSF streak (streak 1) for samples S1 and S2 together with the simulated curves calculated using the Monte Carlo method, showing a good agreement. (b) Comparison of profile tails for the measured and simulated data in log-log scale for S1 and S2.

Using model of Prof. Dr. Vaclav Holy from Charles University in Prague, the densities of BSFs were calculated using Monte Carlo simulation from BSF streak intensity distribution. As a result of calculations, the BSF density is found to be $7.9 \times 10^3 \text{ cm}^{-1}$ for the sample S1, while being $4.4 \times 10^3 \text{ cm}^{-1}$ for the sample S2.

The results of the investigation were published in Journal of Applied Crystallography (impact factor: 3.343): Lazarev S., Bauer S., Meisch T., Bauer M., Tischer I., Barchuk M., Thonke K., Holy V., Scholz F., and Baumbach T. «3D Reciprocal space mapping of diffuse scattering for the study of stacking faults in semipolar (11-22) GaN layers grown from sidewall of r- patterned sapphire substrate» *Journal of Applied Crystallography* (2013), **46**, 1425-1433.

Acknowledgements

We would like to thank Dr. Gernot Buth, the beamline scientist at the SCD beamline at ANKA (Karlsruhe Institute of Technology), for his support during the beamtime.

Interfacial electronic structure of iron phthalocyanine on epitaxial grown manganese oxide films

M. Glaser¹⁾, H. Peisert¹⁾, J. Uihlein¹⁾, H. Adler¹⁾, M. Polek¹⁾, P. Nagel²⁾, M. Merz²⁾,
S. Schuppler²⁾, T. Chassé¹⁾

¹⁾ Institut für Physikalische und Theoretische Chemie, Universität Tübingen, Auf der Morgenstelle 18, 72076 Tübingen, Germany

²⁾ Karlsruher Institut für Technologie, Institut für Festkörperphysik, 76021 Karlsruhe, Germany

Introduction:

Phthalocyanines are a fundamental class of organic semiconductors which can combine with almost all metal atoms in the periodic table forming significantly stable (thermal, chemical, photochemical) complexes, with numerous applications. Transition metal phthalocyanines (TMPcs) are promising candidates for optoelectronic devices and are most recently in the discussion on applications in spintronic devices. The properties of possible devices however can be strongly influenced by interactions at interfaces. In particular for open shell TMPcs like CoPc and FePc on metal substrates charge transfer processes across the interface were observed involving the central metal atom of the TMPc (see e.g. Ref. [1]). Most recently, we have shown that a charge transfer occurs also for CoPc on a transition metal oxide (TMO) (see report A2013-021-002660). As TMO we used a thin film of MnO epitaxially grown on Ag(100) - a system which shows unique chemical and physical properties depending e.g. on the film thickness [2]. Thus, such interfaces exhibit very interesting properties, also a magnetic coupling between the organic molecules and the substrate might occur. In order to gain a more systematic knowledge on interactions of TMPcs on MnO we extend our studies to iron phthalocyanine (FePc). In addition, the MnO film thickness was varied.

Experimental details:

Polarization dependent X-ray absorption spectroscopy (XAS) and X-ray photoemission spectroscopy (XPS) measurements were carried out at the soft x-ray beamline WERA. The spectra were normalized to equal step heights beyond ionization threshold. The energy scale of the spectra was calibrated using the Ni L-edge of NiO. The photoemission spectra were measured at normal emission angle using different excitation energies in order to vary the surface sensitivity. The MnO substrate was prepared in-situ at the WERA beamline by deposition of Mn on single crystalline Ag(100) at a low partial pressure of oxygen (2.0×10^{-7} mbar). Thin films of TMPcs in the range of a mono layer (ML) up to multilayer (~ 3 nm) were deposited at ultra-high vacuum conditions, evaporation rates were between 1 and 4 Å per minute.

Results:

A charge transfer between TMPcs and substrates can generally occur via different channels; both the central metal atom and the macrocycle might be involved. We focus on charge transfer processes between the central metal atom of the TMPc and the substrate, since the electronic structure of the central metal atom can be significantly changed affecting also magnetic properties. From the angular dependence of N K-edge absorption spectra (not shown) we conclude that the molecules grow highly ordered, oriented parallel to the substrate surface. This enables polarization dependent investigations of the (unoccupied) electronic structure of the central metal atom using XAS.

First, we discuss Fe2p core level spectra as a function of the FePc thickness on a 3.6 nm thick MnO film in Fig. 1a. The spectrum of the 3 nm FePc layer (see Fig. 1a) exhibit a multiplet structure typical for a bulk film, the maximum intensity is observed at a binding energy (BE) of

707.3 eV. With decreasing film thickness the shape changes and an additional species at the lower BE side appears. The relative intensity of this feature increases with decreasing film thickness points to an interface species. The energetic shift to about 1.5 eV lower binding energies can be caused by: i) final state charge transfer screening effects in photoemission or ii) by a charge transfer from the substrate to the Fe ion of FePc.

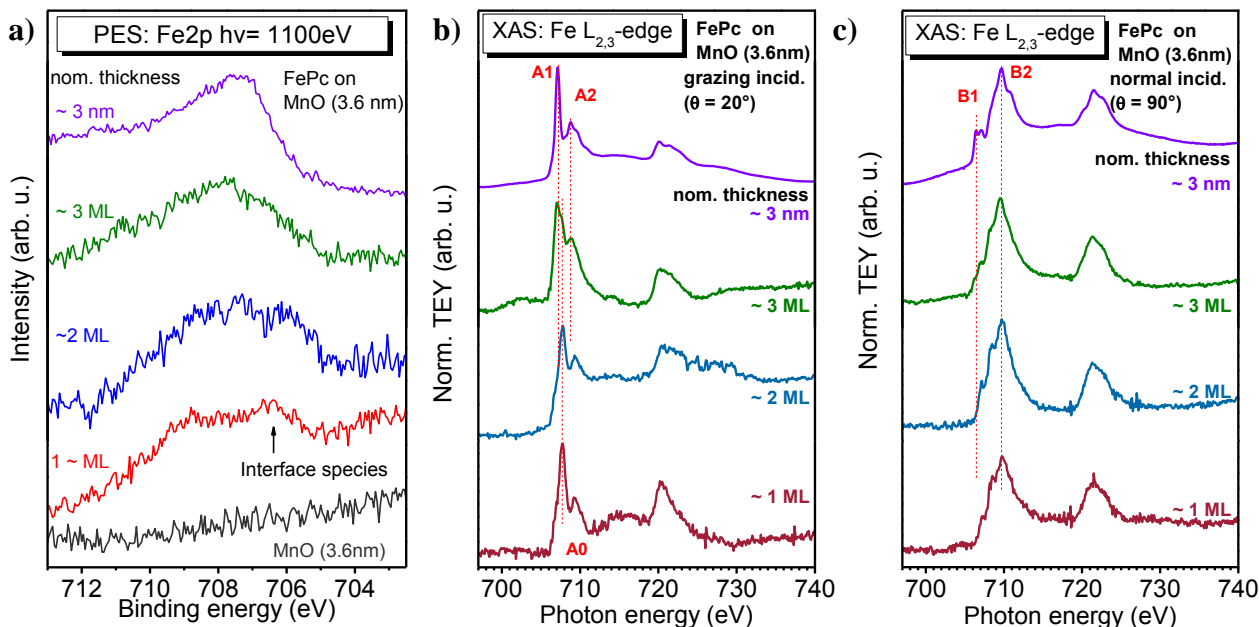


Fig. 1 FePc on a 3.6 nm thick MnO film: a) Fe2p core level photoemission spectra b) & c) XAS spectra for selected angles as a function of the FePc film thickness. The observed changes can be understood by a charge transfer from the substrate to the Fe ion of FePc.

In Fig. 1 b) & c) we show the corresponding XAS spectra for two selected angles as a function of the FePc film thickness. According to the adsorption geometry of FePc we probe at grazing incidence (Fig. 1b) transitions into orbitals oriented out of the molecular plane (denoted A1 and A2), whereas at normal incidence (Fig. 1c) transitions polarized within the molecular plane are observed (denoted B1 and B2). At the lowest coverage significant changes are visible in the XAS spectra: a new feature A0 appears with the same angular dependence as feature A1 at grazing incidence and B1 disappears at normal incidence. This behavior resembles that of FePc on Ag(111) or Ni(111) and confirms the charge transfer from the substrate to FePc accompanied by a redistribution of the d-electrons. Analogously, A0 may be understood by the formation of a new unoccupied level as a result of hybridization between Fe and substrate orbitals.

Acknowledgement

Technical support by W. Neu (Tübingen) and by the WERA team is gratefully acknowledged. For financial support we thank the German Research Council (PE 546/5-1). ANKA Angströmquelle Karlsruhe is acknowledged for the provision of beamtime.

- [1] a) F. Petraki, H. Peisert, I. Biswas, et al., *Interaction between Cobalt Phthalocyanine and Gold studied by X-ray Absorption and Resonant Photoemission Spectroscopy*, J. Phys. Chem. Lett. 1 (2010) 3380–3384; b) F. Petraki, H. Peisert, U. Aygül, et al. *Electronic Structure of FePc and Interface Properties on Ag(111) and Au(100)*, J. Phys. Chem. C. 116 (2012) 11110; c) J. Uihlein, H. Peisert, H. Adler, et al. *Interface between FePc and Ni(111): Influence of Graphene Buffer Layers*, The Journal of Physical Chemistry C, 118 (2014) 10106-10112.
- [2] M. Nagel, I. Biswas, P. Nagel, E. Pellegrin, S. Schuppler, H. Peisert, T. Chassé, *Ultrathin transition metal oxide films: Thickness dependence of the electronic structure and local geometry in MnO*, Phys. Rev. B 75 (2007) 195426.

Environmental conditions of formation of low-temperature pyrite in sediments near Jeníkov, Czech Republic

Final report for the proposal ENV-249

Users: Prof. Juraj Majzlan, University Jena (DE); Stefan Kiefer, University Jena (DE)

The most common arsenic-bearing mineral in the Earth's crust is pyrite, nominally FeS_2 . Because pyrite is abundant in the crust and can incorporate trace or minor amounts of As in its crystal structure, it is the largest reservoir of this toxic element. Normally, As^- substitutes for S^- within the structure. Therefore, very good negative correlation between As and S in pyrite crystals is expected and essentially always confirmed. Within our extensive work on pyrite crystals of variable origin, we have encountered an unusual set of pyrite crystals from Jeníkov in Czech Republic. In these crystals, As and S do not correlate at all, implying a different substitution mechanism. Furthermore, As does not correlate with Fe, either positively or negatively.

The micro-X-ray absorption spectroscopy (μ -XAS) at the As *K* edge indicates that at all spots, As is present in the reduced form (as As^-). EXAFS measurements at selected spots indicate that the local environments in the “normal” and “unusual” pyrite are identical (Fig. 1). We are in a process to refine the number of As and S neighbors of the As atoms in the studied pyrite. We assume that As is mostly covalently bonded to S, increasing the overall entropy of the solid solution.

The question of the substitution mechanism, however, remains unanswered. Our hypothesis that As in the unusual pyrite is present as As^{3+} was not confirmed. We will perform additional imaging with a field-emission gun scanning electron microscope to search for nanoscale inclusions in the unusual pyrite which could possibly explain our chemical analyses of this pyrite type.

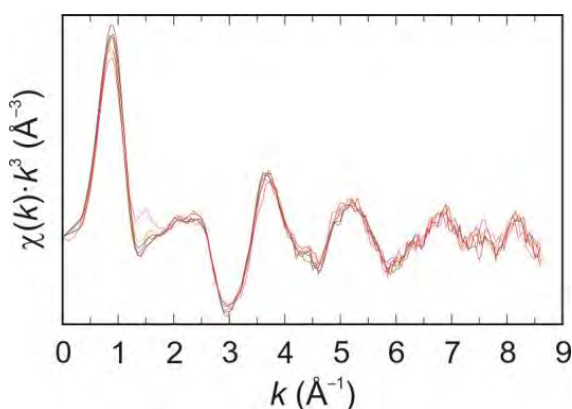


Fig. 1. EXAFS spectra (at the As *K* edge) of the “unusual” (magenta) and “normal” (all other colors) pyrite. Note that there is no statistical significant difference between the two sets of spectra.

Structure of (Ca-)Fe(III)-phosphate and mode of As(V) incorporation into Fe oxidation products

A. Voegelin¹⁾, A.-C. Senn¹⁾, R. Kaegi¹⁾, S. J. Hug¹⁾, S. Mangold²⁾

¹⁾ Eawag, Swiss Federal Institute of Aquatic Science and Technology, Überlandstrasse 133, CH-8600 Dübendorf, Switzerland

²⁾ Forschungszentrum Karlsruhe GmbH, Institute for Synchrotron Radiation, D-76344 Eggenstein-Leopoldshafen, Germany

Introduction

The oxidation of dissolved Fe(II) in aerated water leads to the formation of nanometre-sized Fe(III)-precipitates. These precipitates may act as immobilizing sorbents or colloidal carriers and profoundly impact the cycling of Fe and other major and trace elements in aquatic and terrestrial systems, including toxic As which is of major concern with respect to its impacts on human and environmental health. In previous work, we investigated the effects of phosphate, silicate and Ca on the structure of Fe oxidation products (Kaegi et al., 2010; Voegelin et al., 2010). These studies indicated that amorphous Fe(III)-phosphate forms first during Fe(II) oxidation in phosphate-containing groundwater. In the absence of phosphate, the presence of silicate at a molar Si/Fe ratios >0.2 induces the formation of a ferrihydrite-type precipitates, whereas poorly crystalline lepidocrocite forms dominantly at lower Si/Fe ratios. In a recent study, we further investigated the dynamics of Fe(III)-precipitate formation in the presence of phosphate, especially the initial formation of Fe(III)-phosphate and its transformation during further Fe(II) oxidation (Voegelin et al., 2013). The aim of the current project continuation was twofold: (i) Obtain new insight into the structure of Ca-Fe(III)-phosphate formed during oxidation of Fe(II) in Ca- and P-containing water. (ii) Investigate the mode of As(V) uptake by different Fe oxidation products. For this purpose, Fe(III) precipitates were synthesized by Fe(II) oxidation in aqueous solutions at pH 7.0 and analysed by Fe and As K-edge X-ray absorption spectroscopy (XAS).

Materials and Methods

Different Fe(III)-precipitates were synthesized in 8 mM NaHCO₃ or 4 mM CaCO₃ electrolyte adjusted to pH 7.0 using CO₂ gas. After addition of phosphate (NaH₂PO₄·H₂O) and arsenate (Na₂HAsO₄·7H₂O) as required, 0.5 mM Fe(II) (FeSO₄·7H₂O) were spiked to the aerated solutions to initiate Fe(II) oxidation (details for 4 selected samples in Table 1). Four h after Fe(II) addition, Fe(II) oxidation was complete. The precipitates were collected on 0.1-µm filter membranes, dried overnight under a stream of dry air, mixed with cellulose and pressed into 13-mm pellets for XAS analysis. In addition, samples were also prepared for complementary analyses by transmission electron microscopy (TEM) and X-ray diffraction (XRD).

Results and Discussion

The imaginary parts of the Fourier-transformed Fe K-edge EXAFS spectra of selected precipitates are shown in Figure 1A. Comparison of the spectra of amorphous Fe(III)-phosphate (Fe-P (Na)) and Fe(III)-arsenate (Fe-As (Na)) formed in Na background electrolyte revealed a marked difference in the region of second-shell atoms due to the presence of either P or As. Simultaneous analysis of these two spectra by structural model fitting showed that Fe(III) in these precipitates occurred in mono- to oligomeric form and provided clear evidence for edge-sharing Fe-Fe linkage. Interestingly, we further found that the spectra of Fe(III)-precipitates formed at high P/Fe ratios in the presence of Ca (Fe-P (Ca)) systematically differed from the spectra of analogous precipitates formed in the absence of Ca (Fe-P (Na)). Based on linear combination and structural model fitting, we attribute this difference to a higher degree of both edge- and corner-sharing Fe linkage in the presence of Ca. In combination with TEM and XRD data, these XAS-based results unequivocally confirm the formation of mixed amorphous Ca-Fe(III)-phosphate in the presence of Ca.

With respect to the mode of arsenate uptake by different Fe(III)-precipitates, the As K-edge XAS results shown in Fig. 1B indicate a marked difference in second-shell As(V) coordination between As(V) associated with lepidocrocite (Lp* (Ca)) and amorphous Ca-Fe(III)-phosphate (Fe-P (Ca)). On the other hand, differences in As(V) coordination seem less pronounced between As(V) co-precipitated with Fe(III)-phosphate (Fe-P (Na)) or Ca-Fe(III)-phosphate (Fe-P (Ca)), indicating a limited effect of Ca on the mode of As(V) co-precipitation. Further analysis of the As K-edge XAS results by structural model fitting will be performed on the basis of our results on bulk precipitate structure and Fe coordination.

Conclusions and Outlook

Our results provide evidence for the structural incorporation of Ca into mixed Ca-Fe(III)-phosphate during Fe(II) oxidation in aerated natural waters containing Ca and P. Ongoing work aims at elucidating the impacts of structural Ca incorporation on the reactivity of Ca-Fe(III)-phosphate, namely with respect to the susceptibility of the formed precipitates towards reductive dissolution, transformation during aging, and As uptake. Further insight into the mode of As(V) incorporation into mixed Ca-Fe(III)-phosphate/arsenate will be gained by analyzing the As K-edge EXAFS spectra by structural model fitting. This work will contribute to a better mechanistic understanding of Ca-Fe(III)-phosphate formation during Fe(II) oxidation in natural waters and its impact on the fate of co-transformed As.

Acknowledgements

We thank Thomas Rüttimann and Irene Brunner for their help in the laboratory. ANKA is acknowledged for the provision of synchrotron beamtime.

Table 1: Synthesis conditions of selected precipitates studied by Fe and As K-edge EXAFS spectroscopy. The precipitates were formed by oxidation of 0.5 mM Fe(II) in aerated 8 mM bicarbonate-buffered aqueous solution at pH 7.0. P/Fe(II) and As(V)/Fe(II) indicate the initial molar oxyanion/Fe(II) ratios in the synthesis solutions.

	P/Fe(II)	As(V)/Fe(II)	background electrolyte
Fe-P (Na)	1.5	0.013	8 mM Na-bicarbonate
Fe-P (Ca)	1.5	0.013	4 mM Ca-bicarbonate
Fe-As (Na)	0	1.5	8 mM Na-bicarbonate
Lp* (Ca)	0	0.013	4 mM Ca-bicarbonate

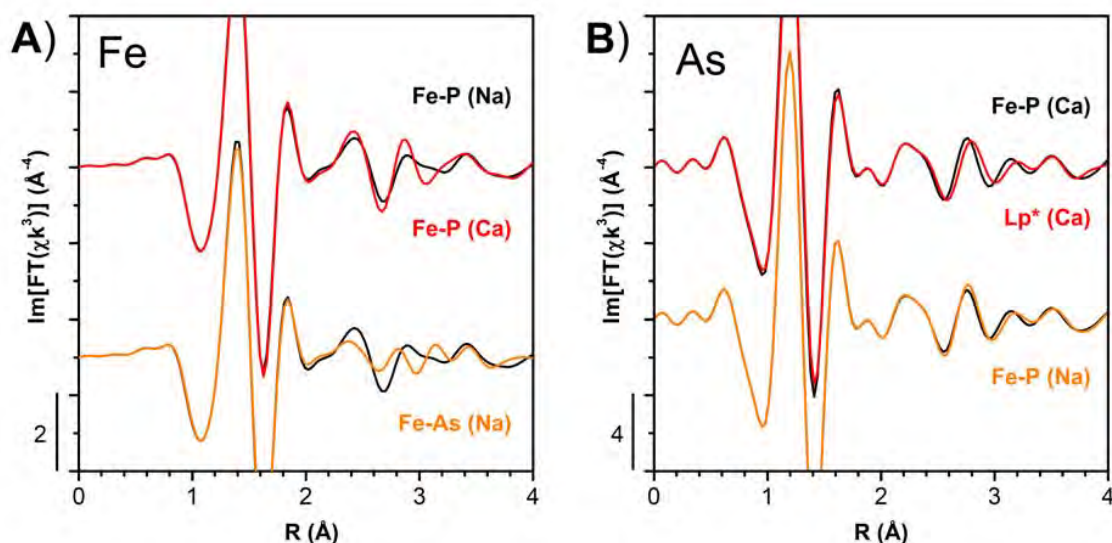


Fig. 1: (A) Imaginary part of the Fourier transformed Fe K-edge EXAFS spectra of the samples Fe-P (Na) (black), Fe-P (Ca) (red) and Fe-As (Na) (orange). (B) Imaginary part of the Fourier transformed As K-edge EXAFS spectra of the samples Fe-P (Ca) (black), Lp* (Ca) (red) and Fe-P (Na) (orange). Synthesis conditions are given in Table 1.

References

- Kaegi, R., Voegelin, A., Folini, D., Hug, S.J., **2010**. Effect of phosphate, silicate, and Ca on the morphology, structure and elemental composition of Fe(III)-precipitates formed in aerated Fe(II) and As(III) containing water. *Geochim. Cosmochim. Acta* 74, 5798-5816.
- Voegelin, A., Kaegi, R., Frommer, J., Vantelon, D., Hug, S.J., **2010**. Effect of phosphate, silicate, and Ca on Fe(III)-precipitates formed in aerated Fe(II)- and As(III)-containing water studied by X-ray absorption spectroscopy. *Geochim. Cosmochim. Acta* 74, 164-186.
- Voegelin, A., Senn, A.-C., Kaegi, R., Hug, S.J., Mangold, S., **2013**. Dynamic Fe-precipitate formation induced by Fe(II) oxidation in aerated phosphate-containing water. *Geochim. Cosmochim. Acta* 117, 216-231.

Speciation of Arsenic in aerosol samples with K-edge XANES in fluorescence mode-continuation

C. Vanhoof⁽¹⁾, K. Tirez⁽¹⁾, J. Peters⁽¹⁾, P. Berghmans⁽¹⁾, C. Cornelis⁽¹⁾, E. Adriaensens⁽²⁾, E. Roekens⁽²⁾, F. Meirer⁽³⁾, S. Smolek⁽⁴⁾, A. Maderitsch⁽⁴⁾, C. Strel⁽⁴⁾, R. Steiniger⁽⁵⁾ and J. Göttlicher⁽⁵⁾

(1) Flemish Institute for Technological Research (VITO), Boeretang 200, 2400 Mol, Belgium

(2) Flemish Environment Agency, Department Air, Communication and Environment, Section Air, Kronenburgstraat 45, B-2000 Antwerp, Belgium

(3) Utrecht University, Inorganic Chemistry and Catalysis, Universiteitsweg 99, 3584 CG Utrecht, Netherlands

(4) Vienna University of Technology, Atominstitut, Stadionallee2, 1020 Vienna, Austria

(5) ANKA, KIT, Eggenstein-Leopoldshafen, Germany

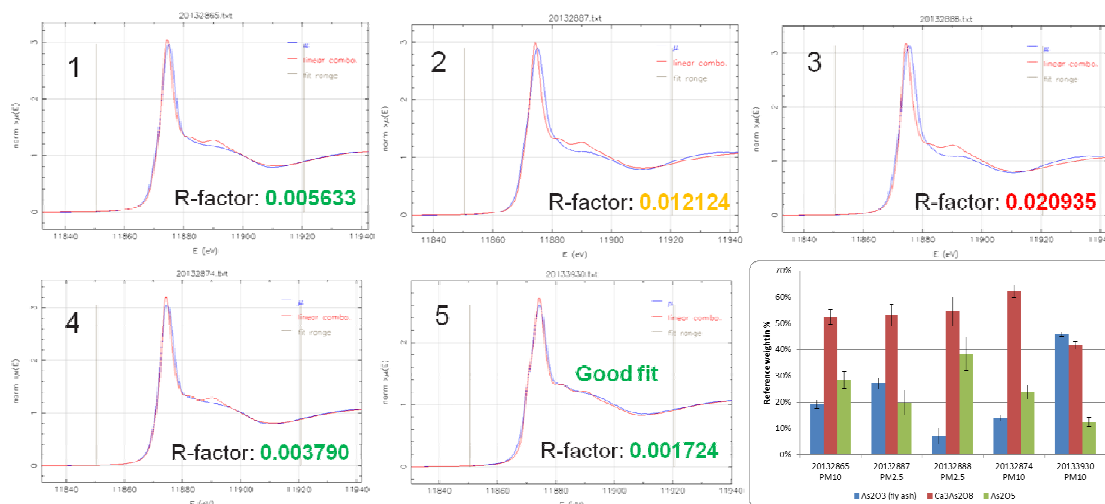
Beamtime: 5 – 8.11.2013 ANKA SUL-X A2013-022-005236

Notwithstanding the As concentrations in particulate matter are generally quite low, in some hotspot regions increased concentration levels occur due to local industrial activities. For these regions ingestion of soil and dust particulates could give a significant exposure to As. Because of the relatively high toxicity and carcinogenicity of arsenic via inhalation, special attention is required to assess the health risks of arsenic in air. There is a toxicological difference between As(III) and As(V), where trivalent arsenic is considered to be the most toxic.

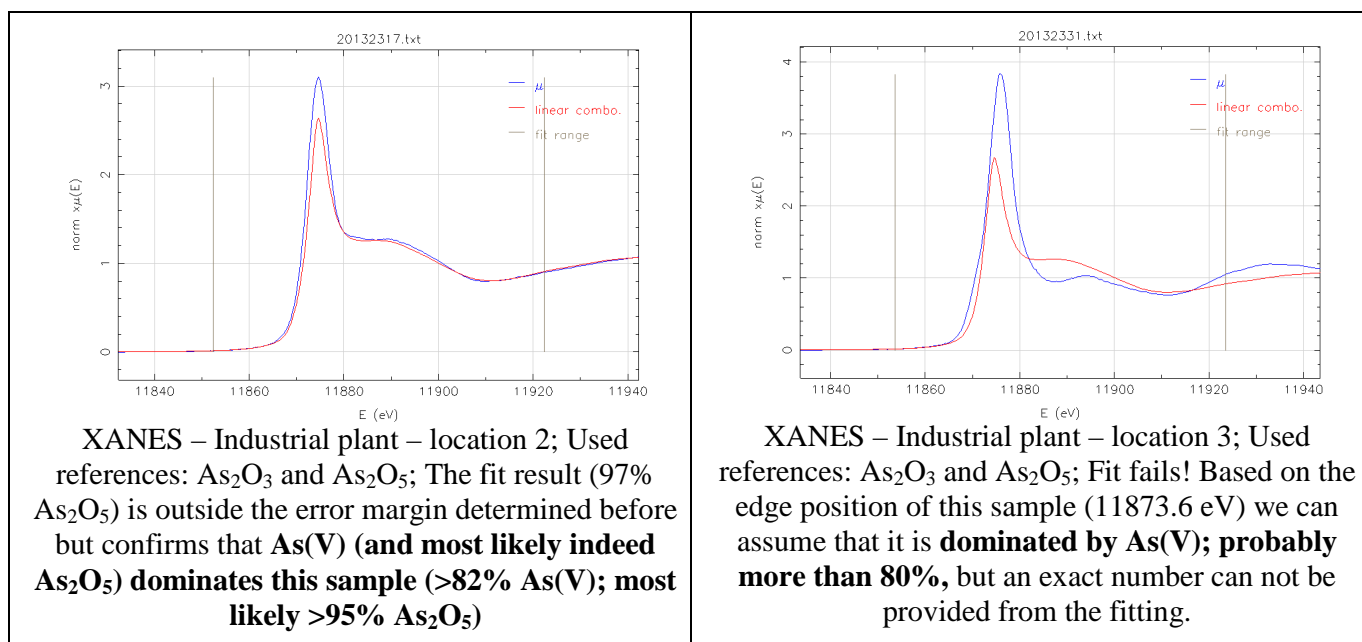
At a hot spot location near an industrial plant air samples were collected to determine the total element concentration of arsenic and its speciation form. Simultaneously ambient particulate matter (PM10) was collected on a daily basis during 1 month using 4 different filter samplers. Samplers 1 to 3 collected PM10 dust on 1) a Tissue Quartz filter, 2) a cellulosenitrate filter and 3) an PTFE filter for the determination of the total As content. Analyses were performed by three independent laboratories using EDXRF, WDXRF and EDXRF, respectively. In spite of a wide range of variables, the corresponding results of the three laboratories were in good agreement. Sampler 4 collected PM dust on an Ashless cellulose nitrate filter for As speciation analysis using HPLC-ICP-MS after microwave extraction in 25 ml water solution containing 100 mM ascorbic acid and 1000 mM H₃PO₄. Both As(III) and As(V) species were detected in the different samples, and the more toxic As(III) species was found between 30 and 70% of the total As fraction. Moreover, the sum of As(III) and As(V) contents agrees well with the total As content determined by XRF.

For XANES analyses, performed under vacuum at the SUL beamline at ANKA, filter samples were loaded with PM10 dust at locations near the industrial plant (plant 1), but also at 2 other industrial locations (plant 2 and 3). The XANES, showing both As(III) and As(V) species, were fitted using As₂O₅ (As(V)), Ca₃(AsO₄)₂ (As(V)) and fly ash (As(III) present as As₂O₃) as reference materials, of which the last two samples most likely represent the source of As pollution at the monitoring site. The samples of industrial plant 2 and 3 are dominated by As(V), present as As₂O₅. In all samples of industrial plant 1, both Ca₃(AsO₄)₂ (As(V)) and As₂O₃ (As(III)) were detected, while only for some samples As₂O₅ was also present as species. We might hypothesize that the As₂O₅ comes from As₂O₃ that has been oxidized during storage/time. The range of observed As₂O₃ oxidation (0 to 50%) falls in the range that was also observed on As₂O₃ spiked filters that were measured with HPLC-ICP-MS. Besides the good agreement between the two methods on As(III) and As(V) fractions, the XANES data complemented HPLC-ICP-MS results (providing only total As(V) fractions without speciation) by differentiating the As(V) forms (i.e., Ca₃(AsO₄)₂ and As₂O₅).

All sample evaluation was done using IFEFFIT Athena software package with linear combination fitting using several standards.



XANES – Industrial plant – location 1; Used references: As fly ash, $\text{Ca}_3\text{As}_2\text{O}_8$ and As_2O_5 ; 1: PM_{10} before improvement of plant, 2: $\text{PM}_{2.5}$ before improvement of plant, 3: $\text{PM}_{2.5}$ before improvement of plant, 4: PM_{10} before improvement of plant, 5: PM_{10} after improvement of plant; Fractions of different As species calculated from XANES results: Fraction As_2O_3 (As(III)): 7 – 46%, Fraction $\text{Ca}_3\text{As}_2\text{O}_8$ (As(V)): 42 – 62%, Fraction As_2O_5 (As(V)): 12 – 38%.



Discussion of results

Presence of As(III) and As(V): fraction is concentration dependent.

Source of contamination: As_2O_3 (As(III)) and $\text{Ca}_3\text{As}_2\text{O}_8$ (As(V)) was confirmed by XANES analysis: As_2O_3 (As(III)): 7 – 46%, $\text{Ca}_3\text{As}_2\text{O}_8$ (As(V)): 42 – 62%

Conversion of As(III) to As(V) during storage/sampling: As_2O_3 oxidised to As_2O_5 : confirmed by XANES analysis: As_2O_5 (As(V)): 12 – 38%

Conclusions

- **HPLC-ICP-MS after extraction: Speciation of As(III) and As(V) is possible and quantified, conversion of As(III) to As(V) observed during storage, sum of As(III) and As(V) is in correspondence with XRF results**
- **XANES measurements: Speciation of As(III) and As(V), As(III) present as As_2O_3 (Source 1 of industrial plant), Differentiating of the As(V) forms is possible and quantified, $\text{Ca}_3(\text{AsO}_4)_2$ (Source 2 of industrial plant) and As_2O_5 (Hypothesis: from oxidisation of As_2O_3)**

Synchrotron based X-ray diffraction study of the hydrothermal behavior of (Al, Na, K, Sr, Ba)-stabilized Ca_2SiO_4 polymorphic modifications

K. Pöhler¹⁾, H. Pöllmann¹⁾, K. Garbev²⁾, P. Stemmermann²⁾, P. Ullrich²⁾, B. Gasharova³⁾, R. Steininger⁴⁾

¹⁾ University of Halle, Faculty for Applied Geosciences and Geography, Mineralogy/Geochemistry, Von-Seckendorff Platz 3, 06120 Halle/Saale, Germany

²⁾ KIT, Institute of Technical Chemistry (ITC), Hermann-von-Helmholtz-Platz 1, D-76344 Eggenstein-Leopoldshafen, Germany

³⁾ KIT, Institute of Photon Science and Synchrotron Radiation (IPS), Hermann-von-Helmholtz-Platz 1, D-76344 Eggenstein-Leopoldshafen, Germany

⁴⁾ KIT, ANKA, Hermann-von-Helmholtz-Platz 1, D-76344 Eggenstein-Leopoldshafen, Germany

Introduction

According to the world council for sustainable development the cement industry has a global contribution to the CO_2 emission of about 8% [1]. Therefore the focus has increased on research for new binding materials as well as clinker substitutes for cement production. A recently developed binding material, based on hydraulic calcium hydrosilicates is Celitement [2]. This new kind of binder is produced in a two step process. In the first step a calcium silicate hydrate e.g. $\alpha\text{-C}_2\text{SH}$ ($\text{C}=\text{CaO}$, $\text{S}=\text{SiO}_2$, $\text{H}=\text{H}_2\text{O}$) is synthesized in an autoclave. In a second step, this precursor is activated by milling. The formation of $\alpha\text{-C}_2\text{SH}$ takes place under hydrothermal conditions at 200°C and saturated steam pressure (~ 16 bar) [2,3]. With respect to the used raw materials two fundamental approaches can be distinguished: 1) hydrothermal treatment of $\text{Ca}(\text{OH})_2$ and SiO_2 in the molar ratio of 2 or 2) hydrothermal treatment of modifications of C_2S . The investigation presented here shall in particular clarify the question how aluminium and potassium contents in C_2S affect its hydrothermal reaction to $\alpha\text{-C}_2\text{SH}$.

Experimental

The formation of $\alpha\text{-C}_2\text{SH}$ under hydrothermal conditions from different C_2S -containing starting materials has been investigated in situ by time resolved X-ray diffraction measurement (XRD) performed at the beamline SUL-X of the ANKA Synchrotron radiation facility in Karlsruhe (Germany). A specially designed reaction cell developed at the KIT was used, meeting both, the resistance against hydrothermal conditions and the requirements of the beamline [4]. The experiments took place in transmission mode with a monochromatic beam of 16keV (double crystal monochromator, Si (111)). The beam was focussed to a spot size of $150 \times 300 \mu\text{m}$ on the sample. A CCD collected diffraction patterns in an angular range of 4 to $30^\circ 2\theta$. The first qualitative evaluation of the results was done with HighScore Plus (Panalytical). For quantification of phase compositions Topas (Bruker) was used in Launch Mode.

As starting materials C_2S samples were synthesized using the Pechini method [5]. Pure C_2S runs resulted in a mixture of $\beta\text{-C}_2\text{S}$ with a small proportion of $\alpha'_\text{H}\text{-C}_2\text{S}$. In samples with coupled substitution of aluminium and potassium for silicon and calcium in C_2S the $\alpha'_\text{H}\text{-C}_2\text{S}$ modification is stabilized.

Results

In the course of the hydration process pure C_2S directly transforms to $\alpha\text{-C}_2\text{SH}$, without any formation of intermediate phases. Crystallization starts immediately after reaching 200°C (after 30 minutes reaction time). The amount of the phases that are initially present in the starting material $\alpha'_\text{H}\text{-C}_2\text{S}$ and $\beta\text{-C}_2\text{S}$ decreases continuously until both are completely consumed. If doped C_2S was used as starting material, hemi carbonate and hydrogrossular developed as

intermediate phases at the absolute beginning of the hydrothermal reaction. Additionally small amounts of calcite have been detected. The hemi carbonate disappeared quickly after starting the heat treatment whereas hydrogrossular remained till the end of the experiment and showed changes in its lattice parameter (from 12.540(3)Å to 12.291(2)Å; Fig. 1).

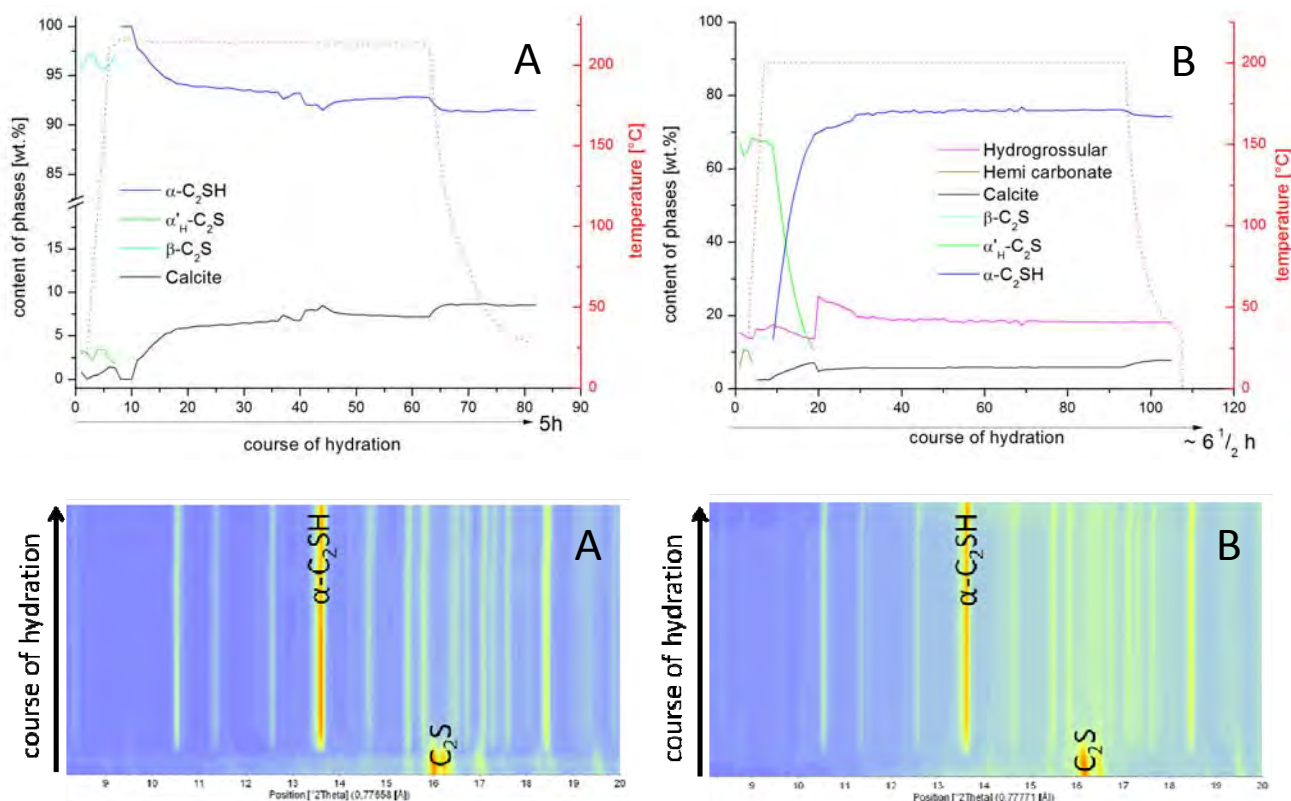


Fig. 1: Time resolved development of the phase composition during the hydrothermal treatment of C₂S (A) and C₂S with 5wt.% Al₂O₃ and 5wt.% K₂O (B)

Conclusion

The change in the lattice parameter of hydrogrossular indicate an enrichment in silicon by substitution of (OH)₄⁴⁻. The silicon, which is incorporated into the hydrogrossular, is not available for the formation of α-C₂SH. Thus, in addition the mixture enriches in Ca(OH)₂. Furthermore the presence of hydrogrossular implies that aluminium, which was previously incorporated in the C₂S phases, was not incorporated into α-C₂SH. It could be also established, that the starting materials show differences in the dissolution rates. The β-modification of C₂S is present up to 30 minutes, whereas α'_H-C₂S remains detectable up to 1h after the start of the thermal treatment. That implies that the α'_H modification of C₂S is more stable under hydrothermal conditions compared to β-C₂S.

References

- [1] J. G. J. Olivier, G. Janssens-Maenhout, J. A. H. W. Peters, PBL Neth. Environ. Assess. Agency (2012) The Hague/Bilthoven.
- [2] P. Stemmermann, U. Schweike, K. Garbev, G. Beuchle, Cem. Int. 5 (8) (2010) 52-66
- [3] P. Stemmermann, K. Garbev, U. Schweike, G. Beuchle, German patent, PCT/EP2006/007475
- [4] P. Ullrich, P. Stemmermann, K. Garbev, B. Gasharova, Build. Mat. anal. Halle/Saale, 2013
- [5] M. P. Pechini, US Patent # 3,330,697 (1967)

Conference contributions, where results from the ANKA measurements were presented:

1. K. Pöhler, P. Ullrich, H. Pöllmann, P. Stemmermann, K. Garbev: Incorporation of aluminium and potassium in C_2S – Synthesis, Characterization and Hydration, 22th Annual Meeting of the German Crystallographic Society (DGK) 2014, poster presentation, 17-20.03.2014 Berlin
2. K. Pöhler: Untersuchungen des Einbaus von Fremdionen in die Struktur der Hydratphase $\alpha-C_2SH$: Synthese, Charakterisierung und Anwendung, 10.te Hallesche Diskussions- und Arbeitstagung Mineralogische und Technische Kristallographie - AK15 Mineralogische und Technische Kristallographie, oral presentation, 21.-22.07.2014 Halle/Saale

Coming up:

3. K. Pöhler, H. Pöllmann, P. Stemmermann, K. Garbev: Synthesis and Characterization of the different modifications of doped Dicalcium Silicates (C_2S), 92nd Annual Meeting Deutsche Mineralogische Gesellschaft (DMG), oral presentation, 21-24.09.2014 Jena
4. K. Pöhler, H. Pöllmann, P. Stemmermann, K. Garbev: Studies on the influence of the incorporation of foreign ions into the structure of C_2S and related hydrate phases, Tagung Bauchemie (Gesellschaft Deutscher Chemiker (GDCh)), poster presentation, 6.-8.10.2014 Kassel

Publications in scientific journals in preparation

1. K. Pöhler, H. Pöllmann, P. Ullrich, R. Steininger, P. Stemmermann, K. Garbev: Investigation and Hydration Studies on Dicalcium Silicate synthesized in presence of Aluminium and Potassium. Part 2: An In situ XRD study. Cement and Concrete Research

Micro-XRF and micro-XRD study of radionuclide uptake by argillaceous rocks

J. Osán¹⁾, M. Fábíán¹⁾, S. Török¹⁾, F. Gergely¹⁾, A. Kéri¹⁾, R. Dähn²⁾, R. Simon³⁾

¹⁾ Centre for Energy Research, Hungarian Academy of Sciences, P.O. Box 49, H-1525 Budapest, Hungary

²⁾ Laboratory for Waste Management (LES), Paul Scherrer Institute, 5232 Villigen PSI, Switzerland

³⁾ Karlsruhe Institute of Technology, Institute for Synchrotron Radiation, Hermann-von-Helmholtz-Platz 1, D-76344 Eggenstein-Leopoldshafen, Germany

Introduction

Argillaceous rocks are considered in many radioactive waste management programmes as suitable host rock formations for the deep geological disposal of radioactive waste. Clay minerals, which are important components in such rock types, have generally strong radionuclide retention properties. Transport in natural barriers depends strongly on the retardation as chemical sorption or other physical processes. Consequently, understanding of sorption processes and the physico-chemical parameters, which influences them, is becoming increasingly important. The present study focused on the interaction of escaped radionuclides with the host-rock surrounding the planned high-level radioactive waste (HLW) repositories in Hungary (Boda Claystone Formation – BCF) and in Switzerland (Opalinus Clay – OPA). The aim was to identify on the microscale the mineral phases of the host rock responsible for the uptake of key radionuclides representing transuranium elements, fission and corrosion products. For this reason, combined synchrotron-radiation micro-XRF mapping and micro-XRD measurements were performed on thin sections subjected to sorption experiments using inactive Cs(I), Ni(II), Zn(II), Nd(III) and natural U(VI) ions.

Materials and Methods

The investigated rocks were prepared from geochemically characterized cores from drillings in BCF and OPA. Thin sections were prepared on 350 µm thick high-purity silicon wafers from BCF and OPA. The average thickness of the sections was 30–60 µm. Samples were subjected to 24–72 hour sorption experiments with one ion of interest added using synthetic porewater for all elements of interest and a 0.1 M NaCl solution for Nd and U as background electrolyte. The experiments were performed at the FLUO beamline of ANKA. The white beam of a bending magnet was monochromatized by a W/Si multilayer double monochromator. A silicon-drift detector was used to collect fluorescence spectra. The combined micro-XRF/micro-XRD measurements were performed at a primary beam energy of 17.5 keV using a compound refractive lens for focusing a beam down to a spot size of $2 \times 5 \mu\text{m}^2$. Elemental maps were recorded for the adsorbed element (Cs, Ni, Zn, Nd, U) as well as for the major and minor elements of the rock (e.g. K, Ca, Fe, Pb) using a 5 µm step size and 4–10 s counting time per pixel. The elemental maps served as a basis for selection of positions of interest for µ-XRD analyses, and for investigating correlation between the element of interest and elements representative for distinct minerals. Elemental maps collected during the previous beamtime (June 2013) using a 7.1 keV excitation energy were used for selection of positions for µ-XRD investigations of samples treated with Cs(I) or Nd(III). Diffraction images were collected from selected positions of the samples employing a 130 mm diameter CCD detector, using a 60–120 s counting time. Corrections for detector tilt and azimuthal integration were performed using the *XRDU*A software [1].

Results

Since Zn(II) treated samples were used for bulk and microscale EXAFS experiments in order to obtain information on the uptake mechanism, Zn(II) treated thin sections were also investigated using micro-XRF/XRD. As it was previously observed for Cs and Ni [2,3], micro-XRD results of selected positions revealed that Zn is also associated to illite and smectite phases (see Figure 1 and 2 for OPA). A good correlation was found between Zn X-ray intensity and illite as well as montmorillonite content ($r = 0.66$).

For Cs(I) and Ni(II), no significant difference in the uptake was observed for samples treated with synthetic porewater at pH 8 or with 0.1 M NaCl solution at pH 7. For Nd(III) and U(VI), the argillaceous matrix was found the most responsible for the uptake when synthetic porewater was applied for the uptake experiments. Significant enrichments of Nd and U around Ca-rich phases were found only when 0.1 M NaCl was used as background electrolyte.

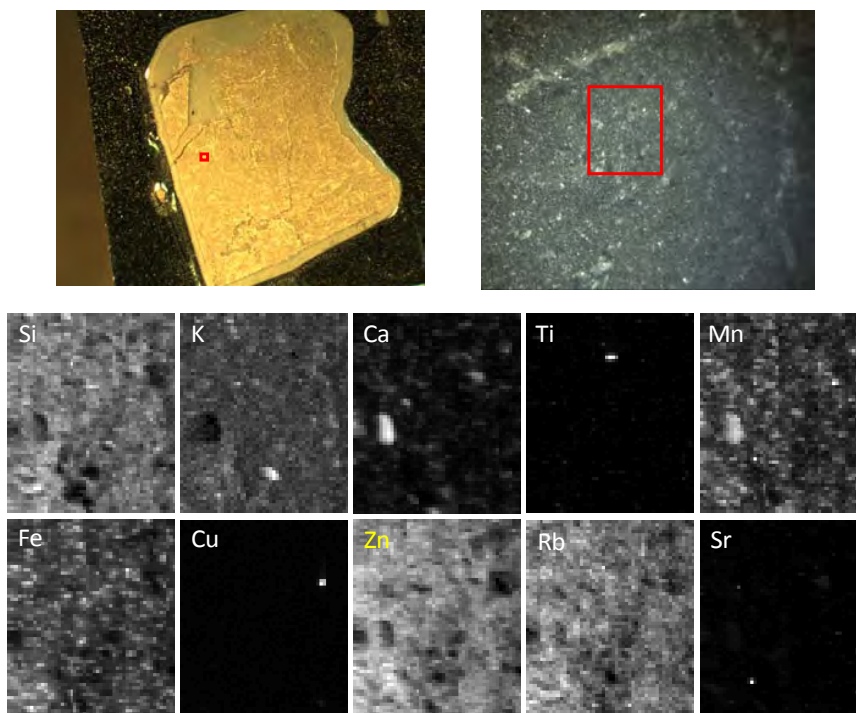


Figure 1. Optical images (above) and elemental maps(below) for a sample area of $0.3 \times 0.25 \text{ mm}^2$ on sample OPA-5 treated with Zn^{2+}

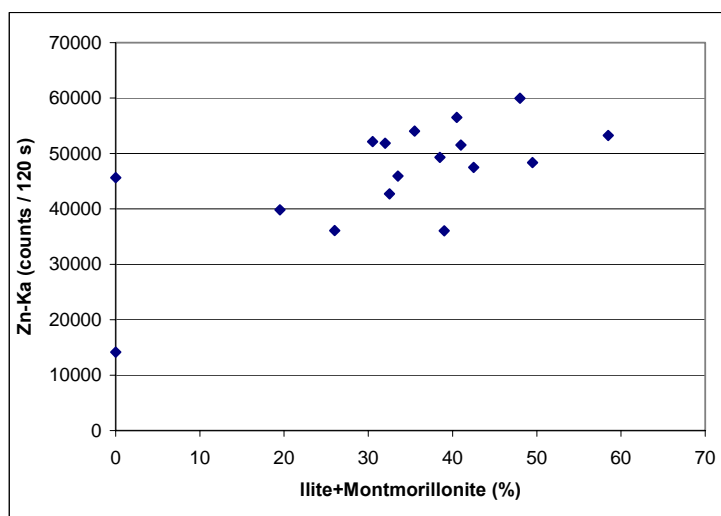


Figure 2. Combined micro-XRF/XRD result for sample OPA-5 treated with Zn^{2+}

Acknowledgements

The research leading to these results has received funding from the Swiss-Hungarian Cooperation Programme through Project n° SH/7/2/11. The courtesy of the Public Limited Company for Radioactive Waste Management (PURAM, Hungary) for providing the samples for analysis was also appreciated.

References

- [1] De Nolf W, Janssens K., Surface and Interface Analysis, 42, 411-418, 2010
- [2] Breitner D., Osán J., Török S., Sajó I., Dähn R., Máthé Z., Szabó C., X-ray microspectroscopic investigations of Ni(II) uptake by argillaceous rocks of the Boda Siltstone Formation in Hungary, NEA Clay Club Proceedings, 2011
- [3] Osán J., Kéri A., Breitner D., Fábíán M., Dähn R., Simon R., Török S., Spectrochimica Acta Part B, 91, 12-23, 2014

Micro-EXAFS study of radionuclide uptake by argillaceous rocks

J. Osán¹⁾, M. Marques Fernandes²⁾, R. Dähn²⁾, E. Eltayeb²⁾, Á. Szabó¹⁾, R. Steininger³⁾, J. Göttlicher³⁾

¹⁾ Centre for Energy Research, Hungarian Academy of Sciences, P.O. Box 49, H-1525 Budapest, Hungary

²⁾ Laboratory for Waste Management (LES), Paul Scherrer Institute, 5232 Villigen PSI, Switzerland

³⁾ Karlsruhe Institute of Technology, Institute for Synchrotron Radiation, Hermann-von-Helmholtz-Platz 1, D-76344 Eggenstein-Leopoldshafen, Germany

Introduction

Argillaceous rocks are being considered in many radioactive waste management programmes as suitable host rock formations for the deep geological disposal of radioactive waste. Clay minerals which are important components in such rock types have generally strong radionuclide retention properties. Transport in natural barriers depends strongly on retardation like chemical sorption or other physical processes. Consequently, an understanding of sorption processes, and of the physico-chemical parameters, which influences them, is becoming increasingly important. The present study focuses on the interaction of escaped radionuclides with the host-rock surrounding the planned high-level radioactive waste (HLW) repositories in Hungary (Boda Claystone Formation – BCF) and in Switzerland (Opalinus Clay – OPA). The aim of the experiment is to study the uptake mechanism of Zn(II) and U(VI) on microscopic scale using micro-EXAFS, both on the clayey matrix and the fracture infilling phases. The proposed micro-EXAFS analyses should give clues on the coordination environment of the radionuclides and thus on the strength of the chemical bonds involved. This information is essential to test basic assumptions made in safety analysis calculations.

Materials and Methods

The rocks investigated were prepared from geochemically characterized cores from drillings in BCF and OPA. Thin sections were prepared on 350- μm thick high-purity silicon wafers from two BCF cores (D11 – West Mecsek Anticline and IB4 – Gorica Block) and OPA. The average thicknesses of the sections are 30-60 μm . Samples were subjected to 24–72 hour sorption experiments with one ion of interest added, using synthetic porewater for Zn and U, as well as a 0.1 M NaClO₄ solution for U as background electrolyte. The micro-EXAFS experiments were performed at the SUL-X beamline of ANKA, using a monochromatic microbeam of 50 μm in diameter employing Kirkpatrick-Baez mirrors for focusing. A Si(111) monochromator and a seven-element Si(Li) energy dispersive X-ray detector were used for the measurements. Carefully pre-selected positions on the previously measured areas on thin rock sections were investigated. In order to re-locate the positions of interest, small elemental distribution maps were collected for the adsorbed element (U, Zn) as well as for the major and minor elements of the rock (e.g. K, Ca, Fe). The elemental distribution maps were also visualized using IDL based on the ROI data. Measurements were performed at the K absorption edge of Zn and the L₃ absorption edge of U. Micro-EXAFS measurements helped determining whether the elements of interest are present on the rock surfaces as sorption complexes or precipitates, as well as to gain local structural information. Six thin sections were investigated, representing both OPA and BCF treated with one of the three elements of interest. 2–4 positions of interest were measured on each thin section with different amount of the sorbed element detected. Micro-EXAFS spectra were collected on several spots, with sufficient number of scans to get a good statistics for data evaluation. The analysis was mainly based on standard data refinement using FEFF. The Athena software package was used for pre-treatment of EXAFS spectra.

Results

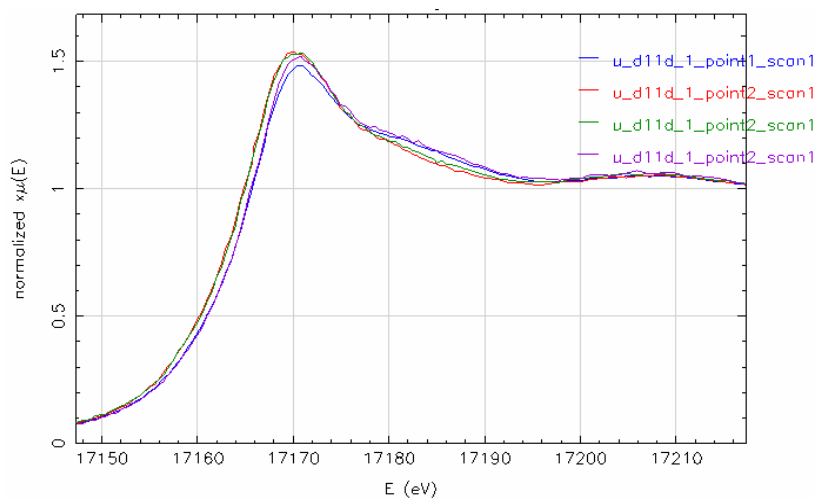


Figure 1. U-L₃ XANES spectra collected at two positions on the mapped area of sample D11-D.

Measurements at the U L₃-edge were not successful because of the photoreduction of uranium caused by the high-intensity microbeam at positions with high uranium concentration. The first scans at both positions (blue and purple lines on Fig. 1) show the features of U(VI), while the repeated scans (red and green lines on Fig. 1) resulted in XANES spectra more similar to U(IV), a clear shift of the absorption edge was observed towards lower energies. At positions with low uranium concentrations (for samples treated with modelled porewater solution) the overlapping with Rb-K α makes EXAFS – even XANES – measurements unfeasible.

Acknowledgements

The research leading to these results has received funding from the Swiss-Hungarian Cooperation Programme through Project n° SH/7/2/11. The courtesy of the Public Limited Company for Radioactive Waste Management (PURAM, Hungary) for providing the samples for analysis is also appreciated.

References

[1] Breitner D, Osán J, Török S, Sajó I, Dähn R, Máthé Z, Szabó C. X-ray microspectroscopic investigations of Ni(II) uptake by argillaceous rocks of the Boda Siltstone Formation in Hungary. NEA Clay Club Proceedings 2011

Micro-EXAFS study of radionuclide uptake by argillaceous rocks

J. Osán¹⁾, M. Marques Fernandes²⁾, R. Dähn²⁾, E. Eltayeb²⁾, R. Steininger³⁾, J. Göttlicher³⁾

¹⁾ Centre for Energy Research, Hungarian Academy of Sciences, P.O. Box 49, H-1525 Budapest, Hungary

²⁾ Laboratory for Waste Management (LES), Paul Scherrer Institute, 5232 Villigen PSI, Switzerland

³⁾ Karlsruhe Institute of Technology, Institute for Synchrotron Radiation, Hermann-von-Helmholtz-Platz 1, D-76344 Eggenstein-Leopoldshafen, Germany

Introduction

Argillaceous rocks are being considered in many radioactive waste management programmes as suitable host rock formations for the deep geological disposal of radioactive waste. Clay minerals which are important components in such rock types have generally strong radionuclide retention properties. Transport in natural barriers depends strongly on retardation like chemical sorption or other physical processes. Consequently, an understanding of sorption processes, and of the physico-chemical parameters, which influences them, is becoming increasingly important. The present study focuses on the interaction of escaped radionuclides with the host-rock surrounding the planned high-level radioactive waste (HLW) repositories in Hungary (Boda Claystone Formation – BCF) and in Switzerland (Opalinus Clay – OPA). The aim of the experiment is to study the uptake mechanism of Ni(II) and Zn(II) on a microscopic scale using micro-EXAFS, both on the clayey matrix and the fracture infilling phases. The proposed micro-EXAFS analyses should give clues on the coordination environment of the radionuclides and thus on the strength of the chemical bonds involved. This information is essential to test basic assumptions made in safety analysis calculations.

Materials and Methods

The rocks investigated were prepared from geochemically characterized cores from drillings in BCF and OPA. Thin sections of 30-60 µm were prepared on 350-µm thick high-purity silicon wafers from BCF and OPA. Samples were subjected to 24–72 hour sorption experiments with one ion of interest added, using synthetic porewater as background electrolyte. The micro-EXAFS experiments were performed at the SUL-X beamline of ANKA, using a monochromatic microbeam of 50 µm in diameter employing Kirkpatrick-Baez mirrors for focusing. A Si(111) monochromator and a seven-element Si(Li) energy dispersive X-ray detector were used for the measurements. In order to find the positions of interest, small elemental distribution maps were collected for the adsorbed element (Ni or Zn) as well as for the major and minor elements of the rock (e.g. K, Ca, Fe). Micro-EXAFS measurements were performed at the K absorption edges of Ni and Zn. Around six thin sections – 3 for Ni and 3 for Zn – were planned to be investigated, representing both OPA and BCF. At least four positions of interest on each thin section were prior to the synchrotron experiments selected with a standard XRF instrument reflecting different amount of the sorbed elements.

Results

Technical reasons of the synchrotron caused a two days beamtime loss, therefore only the measurements at the Ni K-edge could be performed. Because of the high iron content of the thin sections, positions with relatively high Ni load could be measured, whereas positions with low Ni content were below the detection limit of micro-EXAFS. Both for OPA and BCF thin sections, Ni was found to be present as a precipitate at positions with high Ni load, and inner sphere complexation was identified for lower Ni load on the same thin section. The present measurements confirmed the behaviour of Ni uptake assumed from preliminary measurements at HASYLAB Beamline L [1].

Acknowledgements

The research leading to these results has received funding from the Swiss-Hungarian Cooperation Programme through Project n° SH/7/2/11. The courtesy of the Public Limited Company for Radioactive Waste Management (PURAM, Hungary) for providing the samples for analysis is also appreciated.

References

[1] Breitner D, Osán J, Török S, Sajó I, Dähn R, Máthé Z, Szabó C. X-ray microspectroscopic investigations of Ni(II) uptake by argillaceous rocks of the Boda Siltstone Formation in Hungary. NEA Clay Club Proceedings 2011

About the relation between tetrahedral charge and Fe-content of dioctahedral smectites and the role of tetrahedral iron

S. Kaufhold¹⁾, J.W. Stucki²⁾, N. Finck³⁾, R. Steininger⁴⁾, A. Zimina⁴⁾, R. Dohrmann¹⁾, K. Ufer¹⁾, M. Pentrák²⁾,
L. Pentráková²⁾,

1) BGR, Bundesanstalt für Geowissenschaften und Rohstoffe, Stilleweg 2, D-30655 Hannover, Germany

2) Department of Natural Resources and Environmental Sciences, University of Illinois, W-321 Turner Hall, 1102 South Goodwin Ave, Urbana, IL 61801, USA

3) INE, Karlsruhe Institute of Technology, 76344 Eggenstein-Leopoldshafen

4) ANKA, Karlsruhe Institute of Technology, 76344 Eggenstein-Leopoldshafen

Abstract of paper (to be submitted to Clays and Clay Minerals)

Natural aluminosilicates can contain Fe in tetrahedral or octahedral coordination. Amongst smectites, tetrahedral iron is known to occur in Fe-rich nontronites but few indications exist for the presence of tetrahedral Fe in dioctahedral smectites (montmorillonite – beidellite). Within a set of 38 different bentonites a good correlation of tetrahedral charge and Fe-content was found. All materials with large tetrahedral charge were rich in Fe. No exceptions were observed. This could be explained by a general tendency of Fe to enter the tetrahedral layer. Based on a constant ratio of tetrahedral and octahedral iron the tetrahedral charge would increase with increasing iron content and hence explain the correlation. To investigate this correlation, nine materials were selected and investigated by Mössbauer-, UV-Vis spectroscopy, XANES, and XAFS with respect to tetrahedral Fe (Fe^{IV}). The results clearly proved the absence of any relation between Fe-content and tetrahedral Fe. Tetrahedral Fe can be present in Fe-poor bentonites and absent in the case of Fe-rich materials. This means that Fe-rich bentonites have larger tetrahedral charge which is caused by Al^{IV} and Fe-poor materials contain less Al^{IV} . The most probable explanation for this indirect relation is based on the facts that i) the coordination of ions in the weathering/smectite forming solutions determines the coordination in the precipitates and ii) that the $\text{Al}^{\text{IV}/\text{VI}}$ ratio increases with increasing pH. Hence, the correlation could be explained if the pH of weathering solutions generally was larger in Fe-rich rocks compared to more acidic rocks. The relation between tetrahedral charge and Fe-content can be probably explained by different geochemical milieus throughout formation of smectites which affects the coordination of dissolved Al.

Redox-speciation of organic sulphur in natural organic matter - stability of organic sulfur compounds and implications for anaerobic electron transfer

Z.-G. Yu¹⁾, J. Göttlicher²⁾, R. Steininger²⁾, K.-H. Knorr¹⁾

¹⁾Hydrology Group, Institute of Landscape Ecology, University of Münster, Heisenbergstr.2, 48149 Münster, Germany

²⁾ANKA Synchrotron Radiation Facility, Karlsruhe Institute of Technology, 76344 Eggenstein-Leopoldshafen, Germany

Aims of the experiment and scientific background

Sulfur cycling in anaerobic systems has been studied for many years, as it has been found that sulphate reduction contributes significantly to anaerobic respiration, i.e. breakdown of organic carbon into CO₂ [1-3]. However, measured sulphate reduction rates were mostly too high to be sustained by considering only inorganic sulphate pools within the wetlands or sediments [2]. A sulfur recycling process involving organic matter has thus been suggested to replenish the oxidized sulfur pool [4]. It is known that upon reaction of hydrogen sulphide (formed by sulphate reduction) with organic matter, sulfur can partly be re-oxidized and again fuel sulphate reduction [5]. However, sulfur cycling in presence of organic matter is a leaky process, as sulfur is to some extent and in different oxidation states bound to organic matter, leading to an enrichment of sulfur in organic matter [6]. Thus, the recycling of sulfur is limited and cannot explain continuous sulphate reduction. While bacteria can reduce intermediate oxidation states of inorganic sulfur, it is to date still unclear to which extent organic sulfur species is involved in microbial sulfur cycling. Only for smaller molecules it has been shown that e.g. sulfonates and sulphate esters may be used by certain bacteria for reduction [7], but it is not known, if sulfur in complex organic matter macromolecules is accessible for bacterial recycling and could fuel sulphate reduction in deeper peat deposits. The existence of highly oxidized sulfur species in natural organic matter has already been demonstrated [8, 9]. So far, no studies exist on organic sulfur speciation in wetland soils over depth, as related to peat age or degree of decomposition. Within an earlier project (ENV-236) at the ANKA SUL-X Beamline, we aimed at determining sulfur redox states in samples from depth profiles of two peatlands in southern Patagonia [10] by linear combination fittings (LCF) of S-K-edge XANES spectra with reference spectra of known compounds. Moreover, we investigated humic acid before and after reaction with H₂S. Within this project we have analyzed additional natural samples from Patagonia and the Thuringian forest to cover a broader range of peat properties and degree of decomposition. Moreover, samples before and after biotic incubation under sulfate reducing conditions were investigated and we subjected such peat material also to atmospheric oxygen to allow for re-oxidation. The aim of this project was i) to further refine the repertoire of reference substances for an improved analysis of organic sulfur speciation at ANKA as e.g. proposed by Manceau & Nagy [8], ii) to systematically study the forms of organically bound sulfur in natural peat samples to understand its long-term fate, and iii) to study changes in organic sulfur speciation in in-vitro incubations under sulphate-reducing or sulphide-oxidizing conditions to understand short term cycling processes of organic sulfur.

Results of the analysis of reference compounds and LCF

Measured sulphur species with an oxidation state of around 0 showed considerable overlap and could not clearly be distinguished (Table 1, Fig. 1). Some references, especially references involving a R-S-S-R structure, also produced double peaks, spanning from 2471 eV to 2475 eV, and thus involving the entire range observed for thiols, R-S-R structures and S heterocycles. It seemed thus impossible to identify the individual compounds in mixtures of such compounds. The use of such reference spectra in LCF may, however, be useful to reproduce broadened peaks around 2472 eV, which were often observed for natural samples compared to more defined peaks of simple reference compounds. Most suitable for fitting of spectra of natural samples were sulphate ester, 4,4'-Sulfonyldibenzoic acid, L-Methionine sulfoxide, cysteine, and 2,5-Bis(5-tert-butyl-benzoxazol-2-yl)thiophene, and 5,5'-Dithiobis(2-nitrobenzoic acid) (compare Fig. 1). In spite of this non-uniqueness in fitting results, using these selected (Fig. 1 top left) organic and additional inorganic model compounds one may nevertheless sufficiently determine an average sulphur redox state, for which the exact compound does not necessarily be known. To allow for relative comparison we calculated a sulphur oxidation index, dividing the sum of oxidized organic S by the sum of reduced species (see Table 2,3).

Table 1: Measured sample list of sulphur references

Name of Chemicals	Peak max. (eV)	Original S %
Sodium sulfate	2482.1	22.5
Sulfuric acid mono(2-aminoethyl) ester (98%)	2482.1	22.21
Sodium methanesulfonate (98%)	2480.2	26.56
4,4'-Sulfonyldibenzoic acid (97%)	2479.1	10.13
L-Methionine sulfoxide (99%)	2475.2	19.17
L-Cysteine (97%)	2472.1	25.61
L-Cystine (98%)	2472.2	26.1
4,4'-Dithiodibutyric acid -(95%)	2471.6	25.51
5,5'-Dithiobis(2-nitrobenzoic acid) (99%)	2471.3	15.98
L-Methionine (98 %)	2471.9	21.02
Poly(p-phenylene sulfide)	2471.3	29.35
Elemental sulfur	2471.5	100
Zinc sulfide	2471.1	32.83
Sodium sulfide	2471.1	41.02
2,5-Bis(5-tert-butyl-benzoxazol-2-yl)thiophene	2472.9	7.43

Results of analysis of natural peat samples to understand the long-term fate of organic S

The results supported that oxidized organic sulfur species such as sulphate esters decrease with peat depth and thus with peat age (Fig 1, bottom, Table 2). Contrarily, reduced organic sulfur compounds such as those containing sulfhydryl groups, increased with depth. Interestingly, sulfoxides could only be detected in oxidized, surface-near samples or in plant material; sulfoxides thus seem to undergo complete reduction after burial under anaerobic conditions [14]. Organic sulfur speciation seemed to be related to the degree of decomposition of the peat, which is in turn to a large extent determined by the conditions *before* burial of peat in the anaerobic part of the sediment. However, there was still a notable decrease of oxidized and increase of reduced organic sulfur deeper in the profile, supporting that organic sulfur seems to be continuously reduced, albeit at slower rates. At the site in the Thuringian Forest that had undergone exceptionally high sulfate deposition in the past, we could identify a clear enrichment of reduced organic sulfur in the layers affected by the high sulfur pollution.

Table 2: Measured samples (selected) of natural peat samples. The S-oxidation index of organic sulfur was calculated by dividing the sum of oxidized organic sulfur species (sulfate esters, sulfones, sulfoxides) by the sum of reduced organic S species (R-S-R, R-SS-R bridging structures, thiols and sulfur heterocycles), as obtained from Linear Combination Fitting. Organic sulfur contents were derived by subtraction of Chromium Reducible Sulfur (CRS) from total sulfur contents (elemental analysis).

Sample	Depth	% org. S	Org. S-oxidation index	Sample	Depth	% org S	Org. S-oxidation index
PBr2	-5	95.97	1.27	Beerberg	-6	98.13	1.59
Patagonia	-15	94.96	1.04	Germany	-16	98.50	0.81
	-25	93.74	0.75		-28	94.22	0.27
	-35	93.04	0.57		-38	87.29	0.30
	-45	96.03	1.23		-48	78.94	0.27
	-55	96.41	0.81		-58	83.00	0.51
	-65	96.63	0.67		-68	86.17	0.66
	-75	95.39	0.52		-78	87.90	0.65
	-85	95.53	0.57		-83	85.91	0.69
	-95	94.62	0.45		-110	87.76	0.62
	-105	95.54	0.49		-120	85.36	0.62
	-115	95.40	0.36		-140	86.61	0.55
	-125	95.41	0.46		-160	89.95	0.57
	-135	95.37	0.46		-180	93.14	0.57
	-145	94.76	0.43		-200	92.56	0.58

Results of analysis of incubated peat samples to study short term turnover

To address the question which organic sulphur species may typically form in natural anoxic, sulfidic systems, we incubated peat samples of commercial bog peat, inoculated with a small amount of peat from a harvesting site to introduce an active microbial community. Samples were amended with sulphate, acetate or sulfide and incubated under anoxic conditions for 6 weeks (Table 3). Again, S K-edge XANES spectroscopy was used to determine the major organic sulphur species. The original peat prior to incubation contained 71% reduced organic S (R-S-H, R-S-R, R-S-S-R), and 26% oxidized S (R-SO₃, R-SO₂-R, R-SO₄-R), whereas the treatment with sulfide or sulphate addition comprised 76~ 81% reduced organic S, and only 21~19 % oxidized S. In a

parallel treatment amended with sulphate or sulfide and subjected to subsequent re-oxidation with O₂, notable oxidization of organic sulphur was observed: oxidized organic S increased from 19 to 21%, while reduced organic S decreased from 81 to 79%. Our results imply that organic sulphur species actively take part in sulphur cycling in anaerobic systems. Moreover, investigating the stability of organic sulphur compounds in peat soil towards abiotic and biotic reduction and oxidation is essential for the understanding of environmental sulphur cycling in anaerobic systems.

Table 3: Overview of incubated peat and freeze-dried DOM samples. Values of $\delta^{34}\text{S}$ of added sulfate was 3.6 ‰ and $\delta^{34}\text{S}$ of added sulfide was 17.3 ‰. Note that under no additional sulfur addition, the organic sulfur oxidation index decreases during anoxic incubation, while there is little change in $\delta^{34}\text{S}$. When sulfur is added (as sulfate or sulfide), the oxidation index decreases only in the sulfide treatment or in the sulfate treatment with additional amendment of an electron donor to accelerate sulfate reduction.

Incubated peat sample	Incubation condition	Incubation Period	Treatment	% S	$\delta^{34}\text{S}$	Org. S-oxidation index
Oxic peat	oxic	6 weeks	None	0.17	6.98	0.46
Anoxic Peat	anoxic	6 weeks	None	0.19	6.30	0.42
Acetate Peat	anoxic	6 weeks	CH ₃ COONa	0.18	6.55	0.39
SO ₄ ²⁻ Peat	anoxic	6 weeks	Na ₂ SO ₄	0.33	2.39	0.61
SO ₄ ²⁻ -Acetate Peat	anoxic	6 weeks	Na ₂ SO ₄ ; CH ₃ COONa;	0.35	3.57	0.23
S ²⁻ Peat	anoxic	6 weeks	Na ₂ S	0.21	8.11	0.35

Freeze-dried DOM sample	Incubation Period	Sulfide dosing times	Intended concentration of Sulfide (μM)	% S	$\delta^{34}\text{S}$	Org. S-oxidation index
Non-reduced HA	2 m	0	0	n.d.	n.d.	0.84
Non-reduced HA	2 m	1	250	n.d.	n.d.	0.87
Non-reduced HA	2 m	2	500	n.d.	n.d.	0.46
Reduced HA	2 m	0	0	n.d.	n.d.	0.95
Reduced HA	2 m	2	500	n.d.	n.d.	0.76
Reduced HA	2 m	3	750	n.d.	n.d.	0.55

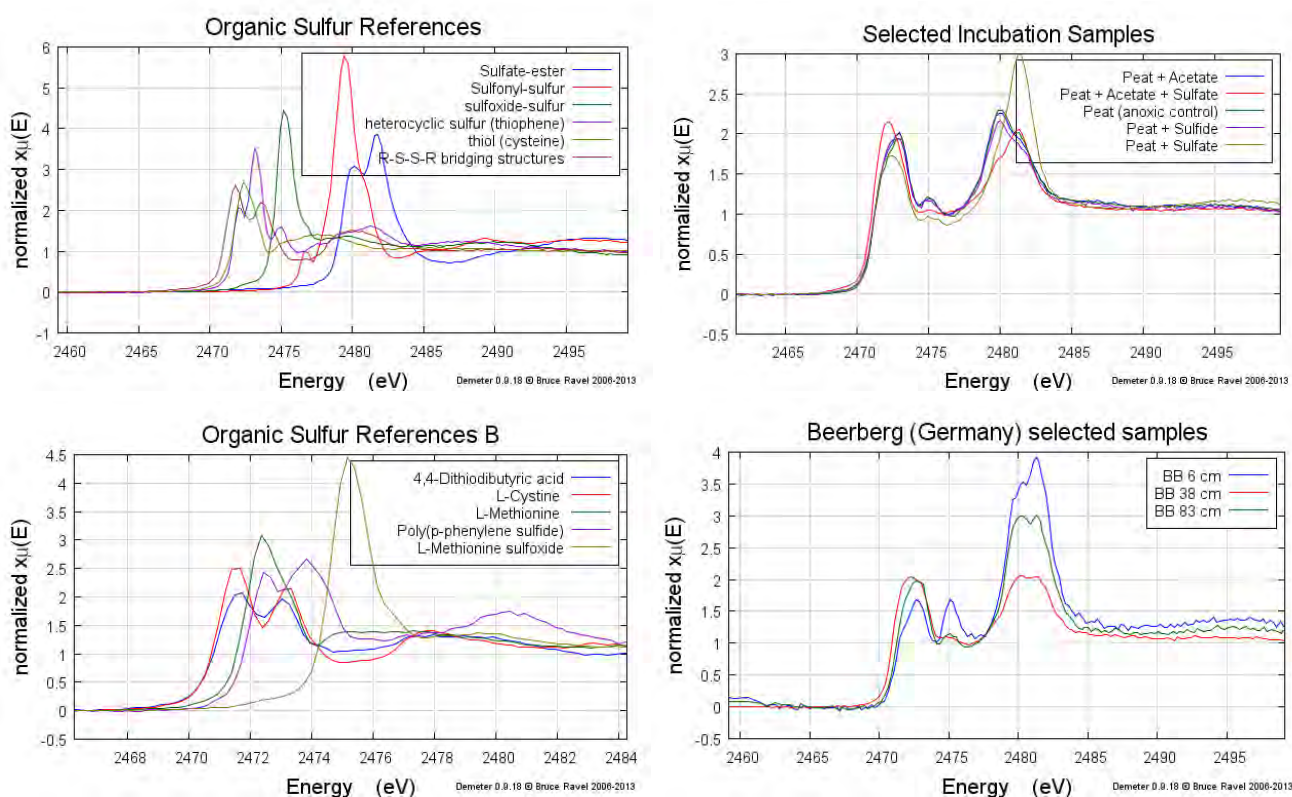


Figure 1. Organic S references spectra used for linear combination fitting (LCF) (top left), spectra of incubated peat samples to investigate short term turnover (top right), references not used for LCF due to ambiguous results (bottom left), and selected peat samples from a peatland subjected to high sulphur deposition (mainly affected depth of ~38 cm, compared to unaffected peat layers at 83 cm depth) (bottom right). For calculation of the organic sulphur oxidation index, sulfate esters, sulfonyl sulphur and sulfoxide sulphur were considered as oxidized organic S, and thiophene, thiols and R-S-S-R bridging structures were considered as reduced organic sulphur.

Related conference contributions

Z.-G. YU., J. Göttlicher, S. Peiffer, K.-H. Knorr. Dissolved Organic Matter Drives Sulfur Cycling under Anaerobic Conditions – Ecological Implication for Anoxic Sulfur Cycling and Electron Transfer in Peatlands. Biogeomon 2014, 8th International Symposium on Ecosystem Behavior. July 13 th -17th, 2014. University of Bayreuth, Germany

K.-H. Knorr, T. Broder, S. Wagner, R. Steininger, and J. Göttlicher: Accumulation of Sulfur from Atmospheric Deposition in Obrotrophic Bogs – Comparing Organic Sulfur Speciation in a High Deposition Site in the Thuringian Forest, Germany, and in a Pristine Site in South Patagonia, Chile. Biogeomon 2014, 8th International Symposium on Ecosystem Behavior. July 13 th -17th, 2014. University of Bayreuth, Germany

Acknowledgements

We acknowledge the comprehensive support from Dr. Ralph Steininger during measurement, and the ANKA for provision of Beamtime at the SUL-X beamline. Additional analyses were carried out at the laboratory of the Institute of Landscape Ecology, University of Münster.

References

1. Jorgensen, B. B., Mineralization of organic matter in the sea bed - the role of sulphate reduction. *Nature* **1982**, 296, (5858), 643-645.
2. Pester, M.; Knorr, K.-H.; Friedrich, M. W.; Wagner, M.; Loy, A., Sulfate-reducing microorganisms in wetlands - fameless actors in carbon cycling and climate change. *Frontiers in Microbiology* **2012**, 3.
3. Urban, N. R.; Brezonik, P. L.; Baker, L. A.; Sherman, L. A., Sulfate Reduction and Diffusion in Sediments of Little-Rock Lake, Wisconsin. *Limnol. Oceanogr.* **1994**, 39, (4), 797-815.
4. Blodau, C.; Mayer, B.; Peiffer, S.; Moore, T. R., Support for an anaerobic sulfur cycle in two Canadian peatland soils. *J. Geophys. Res.* **2007**, 112, G02004.
5. Heitmann, T.; Blodau, C., Oxidation and incorporation of hydrogen sulfide by dissolved organic matter. *Chem. Geol.* **2006**, 235, (1-2), 12-20.
6. Ferdelman, T. G.; Church, T. M.; Luther, G. W., Sulfur enrichment of humic substances in a Delaware salt marsh sediment core. *Geochim. Cosmochim. Acta* **1991**, 55, (4), 979-988.
7. Kertesz, M. A., Riding the sulfur cycle - metabolism of sulfonates and sulfate esters in Gram-negative bacteria. *FEMS Microbiol. Rev.* **2000**, 24, (2), 135-175.
8. Manceau, A.; Nagy, K. L., Quantitative analysis of sulfur functional groups in natural organic matter by XANES spectroscopy. *Geochim. Cosmochim. Acta* **2012**, 99, (0), 206-223.
9. Jokic, A.; Cutler, J. N.; Ponomarenko, E.; van der Kamp, G.; Anderson, D. W., Organic carbon and sulfur compounds in wetland soils: insights on structure and transformation processes using K-edge XANES and NMR spectroscopy. *Geochim. Cosmochim. Acta* **2003**, 67, (14), 2585-2597.
10. Knorr, K. H.; Göttlicher, J., ENV-236: Speciation of organic sulfur in humic acids and natural organic matter after reaction with hydrogen sulfide. In *Experimental reports*, Karlsruhe Institute of Technology, ANKA Synchrotron Radiation Facility: 2013.
11. Limpens, J.; Berendse, F.; Blodau, C.; Canadell, J. G.; Freeman, C.; Holden, J.; Roulet, N.; Rydin, H.; Schaepman-Strub, G., Peatlands and the carbon cycle: from local processes to global implications - a synthesis. *Biogeosciences* **2008**, 5, (5), 1475-1491.
12. Broder, T.; Blodau, C.; Biester, H.; Knorr, K. H., Peat decomposition records in three pristine ombrotrophic bogs in southern Patagonia. *Biogeosciences* **2012**, 9, (4), 1479-1491.
13. Kuhry, P.; Vitt, D. H., Fossil carbon/nitrogen ratios as a measure of peat decomposition. *Ecology* **1996**, 77, (1), 271-275.
14. Ratasuk, N., & Nanny, M. a. (2007). Characterization and quantification of reversible redox sites in humic substances. *Environmental Science & Technology*, 41(22), 7844–50. Retrieved from <http://www.ncbi.nlm.nih.gov/pubmed/18075097>

Synchrotron radiation CD of single strand and covalent bridged collagens to define structure changes at wavelength below 200 nm

U. Meyberg, M. Körling, A. Geyer

Philipps-University Marburg, institut of organic chemistry, Hans-Meerwein-Straße, 35043 Marburg

Samples of single strands and covalent bridged synthetic collagens were measured at ANKA CD12 beamline. The collagens contained 5-7 POG (Proline-Hydroxyproline-Glycine) repeating units per chain. Of special interest was the wavelength region from 170-200 nm. With conventional CD spectroscopy this region is deficiently available because of their limited light flux.

Within our measurement time we took CD spectra of several collagens and especially measured temperature series to investigate the folding and refolding behavior at wavelengths below 200 nm.

Samples:

UM113.S ((POG)₆Ahx), FW229 ((POG)₇Gly), FW183_SP ((POG)₇]₃LysLysAhx) and FW201_13 ((POG)₅]₃LysLysAhx)

The measured CD spectra show reliable data of the samples down to 172-175 nm.

The temperature series which take most of the measurement time show us a sigmoidal process of the CD signal at 199 nm. The melting temperature we read out of the minimum at 199 nm fits well with the literature known melting points for these collagens. We also observed a second maximum at 182 nm which shows an unlinear process in temperature series. Unfortunately the measurement software was not designed to measure short wavelength regions. So we had to spend a lot of time for each temperature series. The try of measure short wavelength areas failed on a noise in the data by turn off and switch on the high voltage of the detector.

This problem is solved by a software update, so we are interested in measure our samples in more detail.

Special thanks to Joachim Bürck for supporting us during our time at ANKA.

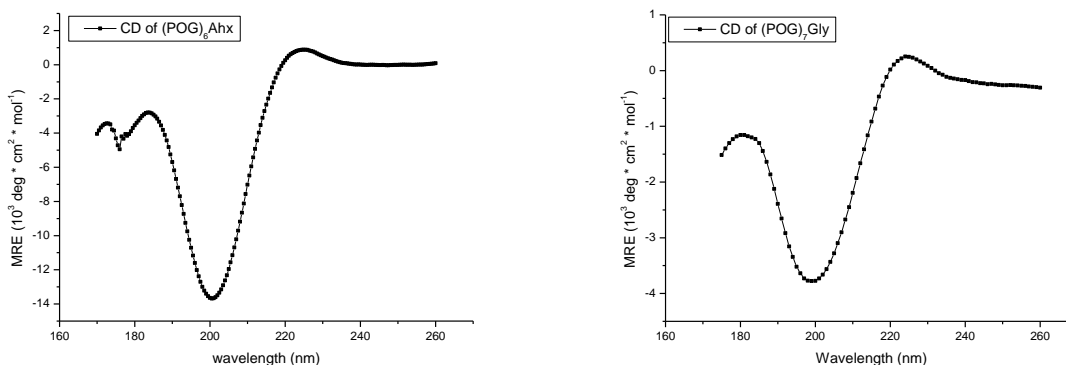


Fig. 1: CD spectra of the single strands collagenes with 6 (POG) repeating units on Ahx (left) and 7 (POG) repeating units on Gly (right). In both cases we could measure a second maximum at 182 nm witch is not possible with conventional CD.

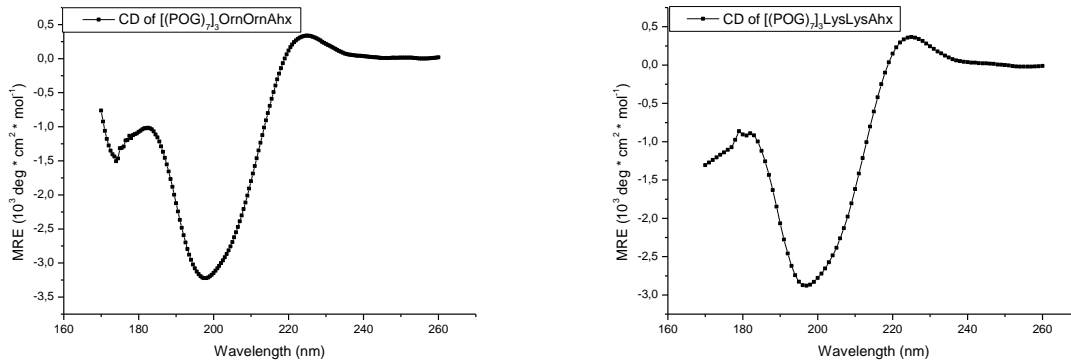


Fig. 2: CD spectra of the covalent bridged collagenes with 5 (POG) repeating units on LysLysAhx (left) and 7 (POG) repeating units on LysLysAhx (right). Also for the both covalent bridged collagenes we measured the second maximum at 182 nm.

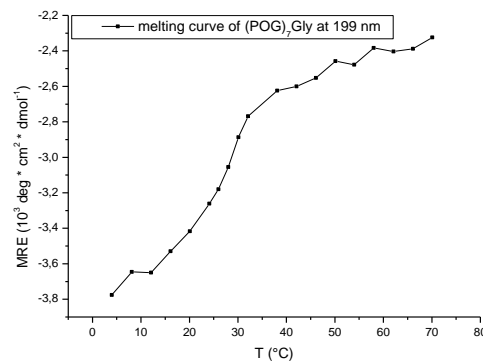
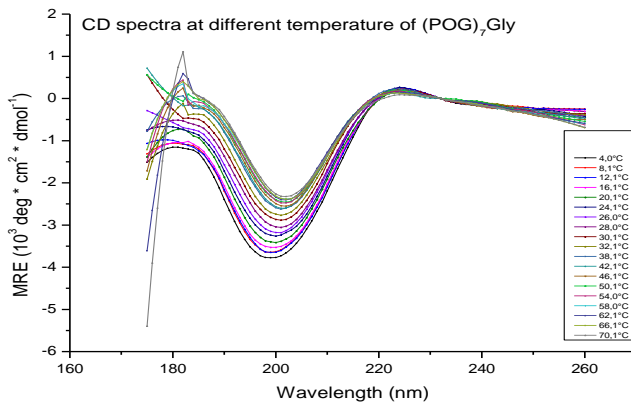


Fig. 3: (left) CD spectra from the temperature serie of the single strand Colagene with 7 (POG) repeating units on Gly. The nonlinear process at 199 nm and 185 nm is visible. The MRE of the second maximum seems to change similar to the minimum. (right) Definition of the melting temperature at 199 nm.

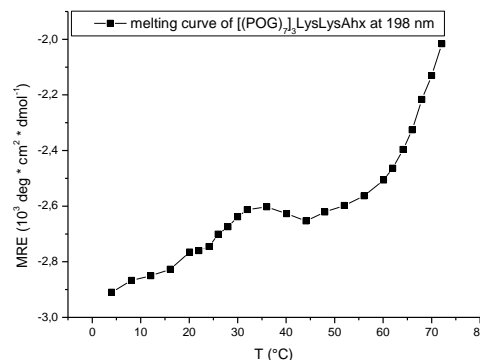
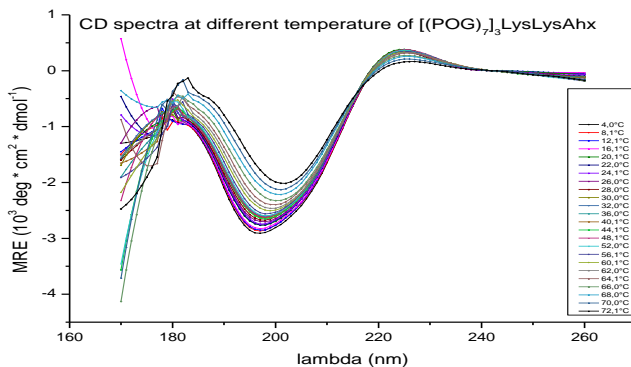


Fig. 4: CD spectra of the covalent bridged collagenes with 7 (POG) repeating units on LysLysAhx at rising temperature. Also here the nonlinear process at 199 nm and 185 nm is visible. The MRE of the second maximum seems to change similar to the minimum. (right) Definition of the melting temperature at 199 nm.

repeating units on LysLysAhx at rising temperature. Also here the nonlinear process at 199 nm and 185 nm is visible. The MRE of the second maximum seems to change similar to the minimum. (right) Definition of the melting temperature at 199 nm.

Influence of antimicrobial peptides on the morphology of phospholipid bilayers

Stephan L. Grage¹⁾, Sergii Afonin¹⁾, Sezgin Kara¹⁾, Anne S. Ulrich^{1),2)}
beamline scientist: Gernot Buth³⁾

¹⁾ Karlsruhe Institute of Technology, Institute of Biological Interfaces IBG-2, Karlsruhe, Germany

²⁾ Karlsruhe Institute of Technology, Institute of Organic Chemistry, Karlsruhe, Germany

³⁾ Karlsruhe Institute of Technology, ANKA, Karlsruhe, Germany

Summary

Membrane-active antimicrobial peptides are a potent class of antibiotics which act by perturbing the cell membrane of pathogenic bacteria. Goal of the experiments at the SCD beamline at ANKA was to get insight into how these peptides interact with lipid membranes. To this aim, a series of x-ray small angle scattering and reflectometry techniques was explored and a sample setup evaluated which allows experiments on well hydrated oriented lipid bilayers. Using GISAXS (grazing incidence small angle x-ray scattering) we characterized the morphology and membrane thickness of oriented bilayers of several representative lipids and changes induced by added antimicrobial peptides. A detailed analysis has not yet been possible for this report, but expected structures such as hexagonal phases, as well as changes in lipid thickness upon addition of the peptides were observed. This way, our experiments laid the basis for future studies of membrane-active peptides and biological membranes using x-ray scattering techniques at ANKA.

Samples

Four different model membranes were studied, which each reflect a particular physical property of natural membranes:

1. Dilauroyl-phosphatidylcholine (DLPC), forming comparatively thin bilayers
2. Dipalmitoleoyl-phosphatidylethanolamine (DPOPE), causing a high negative spontaneous curvature
3. Diphytanoyl-phosphocholine (DPhPC), forming membranes with high mechanical stability
4. Palmitoyl-oleoyl-phosphatidylcholine (POPC), representing a planar membrane without particular spontaneous curvature nor particular mechanical stability, and possessing a similar thickness as DPhPC and DPOPE

The influence of antimicrobial peptides on the above lipid membranes was examined using three representative membrane active peptides:

peptide	origin	secondary structure	membrane activity
PGLa	skin of frog <i>Xenopus laevis</i>	alpha-helix	toroidal wormholes
BP100	designed antibiotic	alpha-helix	membrane thinning
Gramicidin S	<i>A. migulanus</i>	cyclic beta-sheet	peptidic pore

The peptides were reconstituted into the lipid membranes at two peptide:lipid ratios of 1:200 and 1:50 by co-dissolving the peptide and the lipid in methanol. Samples with oriented multilayers of membranes were produced by spreading each of the solutions on a thin glass slide (7.5mm x 24mm x 0.06mm), drying under vacuum to remove the solvent, and successive incubation at near 100% humidity to hydrate the bilayers. The last step leads to a self assembly of stacks of several 1000 hydrated bilayers, oriented parallel to the glass surface. The amount of 0.5mg of sample material on each glass slide was optimized to achieve a smooth coverage of the slide.

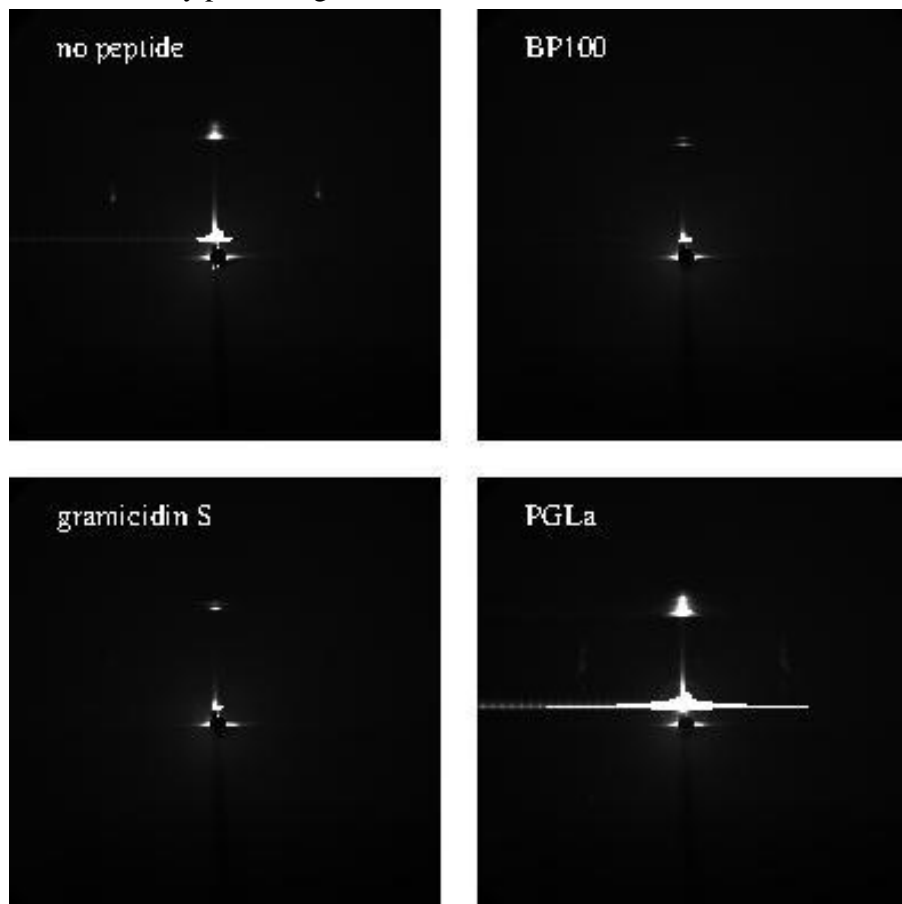
Experimental setup

The samples were mounted in the centre of a six-circle with the beam either passing through the sample (for SAXS experiments) or glancing over the sample (for GISAXS experiments). A sample chamber equipped with x-ray transparent kapton windows, and connected to a continuous flow of nitrogen gas with 100% relative humidity kept the membrane samples hydrated. The experiments were performed at room temperature. A wavelength of 1.393Å was used.

A Princeton CCD detector with 2084x2084 pixels (136x136mm) was placed at a 90cm sample-detector distance. Each exposure was performed three times with different exposure times of 1.25s, 10s and 80s. For the GISAXS experiments, the angle between incident beam and sample surface was varied between 0.01° and 0.15° in steps of 0.01°. Transmission SAXS experiments were discontinued after initial trials without signal.

Results

After evaluation of two of the proposed techniques, we focussed on GISAXS experiments. The samples turned out to be scattering too weakly for transmission SAXS experiments, and may require a preparation optimized for transmission experiments in future experiments. The GISAXS experiments, on the other hand, resulted in very promising data.



A representative set of scattering images of GISAXS experiment on DPOPE membranes is shown in the adjacent figure. The example images were obtained from oriented membranes without additional peptide, with BP100, gramicidin S or PGLa at a peptide:lipid ratio of 1:50. Above the direct beam in the centre of the images, a bright scattering signal is clearly visible. The position of this signal corresponds to a repetitive structure of $\sim 35\text{\AA}$ repeat distance, which agrees well with typical bilayer thicknesses and indicates that this signal originates from the stack of oriented bilayers. The position of this multilayer reflex changes in samples containing peptide compared with the pure DPOPE lipid sample. The GISAXS experiments were hence able to pick up an influence of the peptides on the membrane

thickness. We found the largest influence on the membrane repeat spacing in DPOPE membranes and POPC membranes. Less influence was found in the DLPC and DPhPC membranes, possibly as a consequence of the small thickness of DLPC and the large stability of DPhPC membranes.

Interestingly, additional weak reflexes off the vertical central line of the image were observed in the DPOPE without peptide (see figure). These signals likely indicate the presence of hexagonal structures, which would agree well with hexagonal lipid phases characteristic for phosphatidylethanolamine (PE) lipids under adequate sample conditions. In the presence of BP100 or gramicidin S, the hexagonal signatures vanished, while they stayed in the PGLa containing sample, indicating a different influence of the peptides on the membranes. The DPhPC lipid samples observed a different reflex pattern, possibly indicating the formation of cubic lipid phases.

Though a detailed analysis has not yet been done at the time of writing this report, it can be concluded that it was possible to identify characteristic lipid morphologies and address structural changes due to the interaction of antimicrobial peptides with the lipid bilayers in the conducted GISAXS experiments. On the basis of the experience gained in this first study we hope to continue these potent experiments on biological membranes at the SCD beamline.

Acknowledgements

We gratefully acknowledge Dr. Gernot Buth for his support at the instrument, the IT support at ANKA for their help during the experiment as well as Daniel Gauder and IBG-2 workshop for the construction of the sample chamber. We thank Dr. Parvesh Wadhvani and Dr. Marina Berditsch for the peptides.

SRCD Measurements of Mystic in Membrane-Mimetic Environments

M. Textor¹⁾, S. Keller¹⁾

¹⁾ University of Kaiserslautern, Institute of Molecular Biophysics, Erwin-Schrödinger-Straße 13, 67663 Kaiserslautern, Germany

Materials and Methods

For a comparison of Mystic structure in different membrane-mimetic systems, SRCD spectra of the protein solubilised in lauryldimethylamine oxide (LDAO) micelles as well as reconstituted in large unilamellar vesicles (LUVs) composed of 1-palmitoyl-2-oleoyl-*sn*-glycero-3-phosphocholine (POPC) were recorded at the UV-CD12 beamline. Additionally, oriented circular dichroism (OCD) spectra were obtained on samples of reconstituted Mystic.

Reconstitution of Mystic was achieved with an assay based on detergent removal by cyclodextrin complexation. Briefly, 2-hydroxypropyl- β -cyclodextrin (HP β CD, molar substitution degree 1.0) was titrated to a mixture of LDAO, Mystic and POPC. Progression from the micellar phase to the vesicular phase was monitored by isothermal titration calorimetry (ITC) and formation of LUVs was verified by dynamic light scattering (DLS). The reconstitution was carried out at 25 °C in buffer consisting of 50 mM Tris, 50 mM NaCl, pH 7.4. The chosen protein-to-lipid ratio (P:L) was 1:200 and the sample was supplemented with additional HP β CD after reconstitution to ensure that the residual detergent concentration was below the CMC of 1.9 mM. Afterwards, concentrators (10 kDa, Amicons, Millipore) were used for concentration and buffer exchange to 50 mM Tris, 50 mM NaF, pH 7.4. For blank spectra, samples were prepared similarly but in the absence of protein.

To acquire SRCD data, a CaF₂ demountable cell with a pathlength of 12.2 μ m or a Suprasil quartz glass cuvette with a pathlength of 0.1 mm was used. Typically, three repeats were recorded at 25 °C over a wavelength range of 175–330 nm at 0.5-nm steps with a dwell time of 1500 ms. The repeats were averaged, the blank spectrum was subtracted, and the resulting spectrum was offset based on the 310–330 nm range.

In preparation for OCD measurements, 80 μ L of a sample after reconstitution was deposited on a quartz glass window with a diameter of 2 cm; after evaporation of the solvent in air for at least 2 h, the sample was hydrated for 14–16 h at room temperature in a saturated K₂SO₄ environment. For an OCD spectrum, eight single spectra were averaged, each being measured at a different azimuthal angle of the OCD cell at 45° steps.

Results

At the UVCD-12 beamline, an SRCD spectrum of LDAO-solubilized Mystic was recorded down to 171 nm, which is comparable to data on the same sample acquired with our conventional CD spectrometer (Chirascan-plus, Applied Photophysics) in terms of data quality (Fig. 1A). An increased ellipticity of the 190-nm band in the SRCD spectrum can be ascribed to the constant slit width of the beamline setup, which results in a decreasing bandwidth with shorter wavelengths and thus in a higher apparent ellipticity compared with the bench-top spectrometer.

The SRCD spectrum of Mystic reconstituted in POPC-LUVs resembles the one for the solubilized protein, showing the typical signature of an α -helical protein with negative bands at 208 and 222 nm. By contrast, the spectrum of Mystic after reconstitution in DLPC shows a slightly decreased $\theta_{208}/\theta_{222}$ ratio. For reconstitutions in the presence of DMPC viable spectral data could not be obtained.

Furthermore, thermal and chemical stability of Mystic after reconstitution was investigated. Unfolding of reconstituted Mystic from POPC-LUVs as well as from mixed POPC/POPG-LUVs (7.5 % POPG) was possible in presence of 9.8 M urea, as illustrated by the corresponding random-coil-like spectra (Fig. 1A). Also, a temperature series on reconstituted Mystic shows almost complete unfolding at 90 °C and turns out to be reversible to some extent, as evidenced by the partial recovery of secondary structure after re-equilibration to 25 °C. Similar results were obtained for a temperature series on Mystic reconstituted in DLPC (data not shown). Moreover, Mystic membrane topology was examined by OCD measurements (Fig. 1C). Whereas absorption flattening was highly pronounced at a P:L ratio of 1:50 as indicated by the low $\theta_{190}/\theta_{222}$ ratio, a decent spectrum was obtained for a P:L ratio of 1:100 and a dilution of 1:3 of the original lipid vesicle

solution. Since the band at 208 nm is still present at a $\theta_{208}/\theta_{222}$ ratio of ~ 1 , a parallel orientation of Mystic helices with respect to the POPC acyl chains can be excluded.

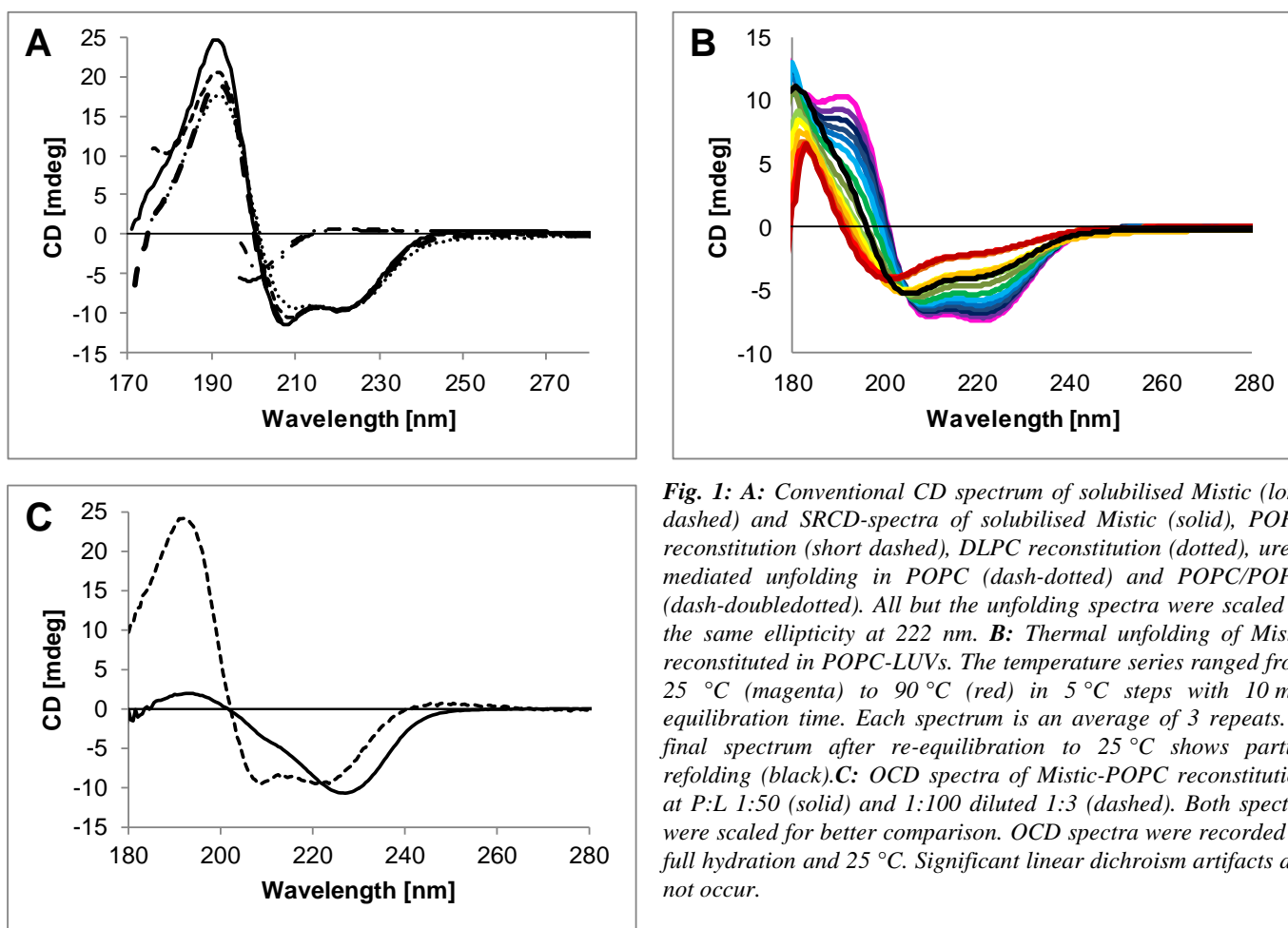


Fig. 1: **A:** Conventional CD spectrum of solubilised Mystic (long dashed) and SRCD-spectra of solubilised Mystic (solid), POPC reconstitution (short dashed), DLPC reconstitution (dotted), urea-mediated unfolding in POPC (dash-dotted) and POPC/POPG (dash-doubledotted). All but the unfolding spectra were scaled to the same ellipticity at 222 nm. **B:** Thermal unfolding of Mystic reconstituted in POPC-LUVs. The temperature series ranged from 25 °C (magenta) to 90 °C (red) in 5 °C steps with 10 min equilibration time. Each spectrum is an average of 3 repeats. A final spectrum after re-equilibration to 25 °C shows partial refolding (black). **C:** OCD spectra of Mystic-POPC reconstitution at P:L 1:50 (solid) and 1:100 diluted 1:3 (dashed). Both spectra were scaled for better comparison. OCD spectra were recorded at full hydration and 25 °C. Significant linear dichroism artifacts did not occur.

Discussion and Conclusions

A comparison of the CD-spectra for solubilised and reconstituted Mystic does not reveal any significant differences in secondary structure. In conclusion, physicochemical differences between LDAO micelles and POPC-LUVs such as permittivity or lateral pressure are too subtle to cause a structural rearrangement.

A decreased $\theta_{208}/\theta_{222}$ ratio, as seen for Mystic reconstituted in DLPC, has been related to oligomerisation previously, which would imply increased absorption flattening; however, these data have to be taken cautiously, since corresponding DLS data were inconsistent, and a small amount of precipitate indicated suboptimal reconstitution. Additionally, we could show in the meanwhile that DLPC is prone to complexation by 2-HP β CD, rendering this lipid rather unsuitable for the applied reconstitution protocol. Likewise, data on DMPC reconstitution were even more questionable.

With regard to the temperature series, the incomplete and partially reversible unfolding of Mystic reconstituted in POPC suggests a high stability comparable to other α -helical membrane proteins, which in general appear resistant to complete unfolding due to the high energetic penalty associated with the exposure of hydrogen bond donors or acceptors. However, it seems that Mystic can be unfolded from the bilayer in the presence of urea, which is not the case for typical membrane proteins. A more probable explanation for the data concerning urea unfolding may be that Mystic is not accommodated within the membrane as proposed previously. In line with this premise, OCD data clearly negate a transmembrane orientation in POPC-LUVs. This suggests Mystic being monotopic, peripheral or even having an in-plane orientation; however, its exact orientation remains to be elucidated.

Acknowledgements

We thank Dr. Jochen Bürck, Siegmur Roth and Bianca Posselt for helpful discussions and assistance.

Determining Levels and Distributions of Various Trace Metals in Human Skin: An investigation involving paraffin embedded and freeze-dried samples

E. Dao¹⁾, A. Al-Ebraheem¹⁾, C. Li¹⁾, E. Desousa¹⁾, M. Farquharson¹⁾

¹⁾ Medical Physics & Applied Radiation Sciences, McMaster University, 1280 Main St. W., L8S 4L8, Hamilton, Canada

Introduction

Skin has two main functions; to act as a barrier against microorganisms and to prevent the loss of water. Human skin contains two main layers; the superficial epidermis and the deeper dermis. The epidermis is composed of five sub-layers. From most superficial, the sub-layers are the stratum corneum (SC), stratum lucidum (SL), stratum granulosum (SG), stratum spinosum (SS) and stratum basale (SB).

Formalin, the 4% formaldehyde solution in water, is commonly used as a fixative for the preservation of samples. It is often combined with embedding the sample in paraffin wax. An alternative method of sample preservation is freeze-drying. Freeze-drying is a method that dehydrates samples by the process of sublimation, which is the direct phase transformation of solid water (ice) to gaseous water (water vapor).

Method

All skin samples were extracted from cadavers donated for scientific research to the McMaster University Anatomy Department. Samples were extracted using a Miltex circular biopsy punch resulting in a roughly cylindrical shape. Samples were acquired from 10 locations on the body of members of the general population – feet (2), thighs (2), arms (2), palms (2), chest and back. Each core was immediately frozen upon extraction. Before being prepared for mounting, the excess fat was removed using a scalpel and the core was halved lengthwise to produce two semi-cylindrical blocks. The two halves will be prepared using two different methods, paraffin embedding and freeze-drying.

For paraffin embedding, one semi-cylindrical block was placed in a 10% neutral buffer formalin. After 16-20 hours, the block was transferred to 70% ethanol and taken to the McMaster University Histology lab for further preparation and mounting. For freeze-drying, the other semi-cylindrical block was immediately returned to the -80°C freezer for microtoming at a later time. For both types of sample preparation, the sample was microtomed into sections of 15µm thickness. Each slice was mounted onto 4µm thick ultralene film on a plastic holder.

Prepared samples were then transported for analysis on the FLUO beamline at the ANKA (Angströmquelle Karlsruhe) synchrotron facility in Karlsruhe, Germany. FLUO is an X-ray microprobe beamline covering the energy range of 1.5-33 keV. The beam used had a spot size of 10µm × 5µm (H × V). For the current work, a beam energy of ~10 keV was used. An online beamline microscope, in combination with a laser positioning system, was used for aligning the beam on the surface of the sample. The fluorescence was recorded with a single-element Vortex Silicon Drift Detector with a Si wafer and a Be entrance window that was placed in a standard 45-degree geometry.

Raster scans were performed for 10 seconds per pixel, for 650-3200 pixels per map, in step sizes of 10µm × 5µm (H × V). The maps covered a large enough area of the sample to encompass both the epidermis and a portion of the dermis of skin. For the current work, a total of 31 samples were measured, with 26 of those corresponding to matched pairs – one sample was paraffin embedded and the other was freeze dried.

Data analysis consisted of peak fitting raster scan spectra using AXIL peak-fitting software, which is designed to perform analysis of XRF spectra by separation of peak overlap and background removal. The

fitted $K\alpha$ peak areas were normalized to scatter peaks (combined Compton and coherent scatter contributions) in order to correct for beamline intensity (storage ring current) drops over the duration of a single raster scan. Finally, normalized data were then mapped in Exelis Interactive Data Language (IDL) ver. 6.2. In these maps, the third dimension (z data) is represented by the scatter-normalized peak areas. These 2D surface maps provide a view of the elemental distribution within each sample, extending down from the skin surface, showing the mapped elemental distributions in various layers of skin.

Results

The coherent scattering peak is seen at ~ 10.7 keV and the Compton scatter feature appears at a slightly lower energy. Characteristic x-ray peaks are observed at lower energies. The Compton scatter low-energy tail feature narrowly avoids the Zn $K\alpha$ peak. The morphology of both sample types is seen in the light microscopy images, on the left of Figure 1, for two representative samples.

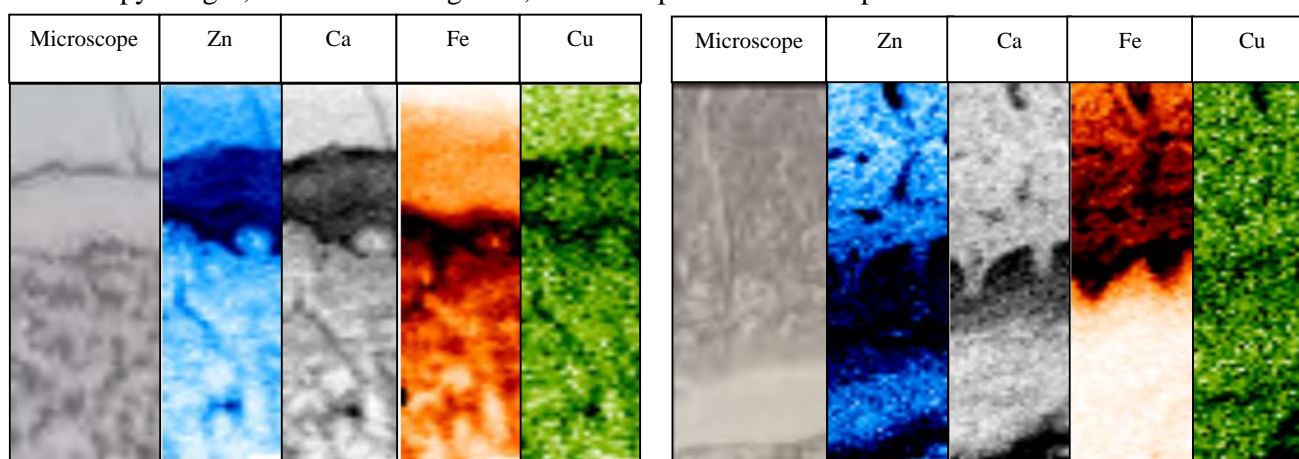


Fig. 1: Light microscopy images, followed by 2D surface maps produced in IDL, corresponding to two samples. The image on the left is for 6rffd and the right is for 6rffe.

Out of the 29 independent samples, statistical analysis was performed on 11 match pair samples. A match pair sample contains one freeze-dried sample and its matching paraffin embedded sample. The statistics allowed certain questions to be investigated. First, is there a significant difference between the skin layers for each sample preparation type (freeze-dried and paraffin embedded)? Second, is the percent difference (PD) between the epidermis and dermis the same for both sample preparation types? Lastly, is the percent difference in the same skin layer for both sample preparation types the same for both layers of skin?

It can be found that there is a statistically significant difference between the epidermis and dermis in both the freeze-dried and paraffin-embedded samples for calcium, copper and zinc. It is interesting to see that unlike calcium, copper and zinc, the levels of iron do not change significantly between the epidermis and dermis, in agreement with the literature. This was true for both types of sample preparation. Further analysis was performed since the epidermis is not a gross structure but is comprised of sub-layers. Further analysis of iron reveals that the difference between the two epidermis intermediate layers in the freeze-dried samples is statistically significant. The difference between the first epidermis intermediate layer, the layer closer to the dermis, and the dermis is also statistically significant in the paraffin embedded samples. At this moment in time it is unknown as to why the levels of iron differ in this pattern. A possible suggestion is that the sample preparation techniques compromise an epidermal layer, causing the iron to “leak” into other layers and similarly into the dermis.

Conclusion

In conclusion, it was determined that the levels of calcium, copper and zinc differ significantly in the epidermis and dermis of the skin for both freeze-dried samples as well as formalin-fixed, paraffin embedded samples. However, this trend is not seen with iron. Iron has significantly different levels in the two epidermis intermediate layers for the freeze-dried samples and significantly different levels in the first, deeper epidermis intermediate layer and the dermis.

The Effect of Processing Conditions on the Secondary Structures of Synthetic Collagen Nanofibers

Murat Kazanci

Bahcesehir University, School of Medicine, Basic Sciences, Biophysics, 34734, Göztepe, Istanbul, Turkey

Introduction

Collagen is the most abundant protein in human body, making up about 25% to 30% of the whole body protein content [1]. It is the main component of fascia, cartilage, tendons, bone and skin. The most striking feature of the fibrillar collagen molecule is its unique secondary structure, called as PP II helix. The central domain of the collagen α -chains folds into a tight, left handed helix, with an axial residue-to-residue spacing of about 0.286 nm and an angular separation of 108° [2-4]. Since collagen is a natural substance for the human body and its bioactivity is well known, it has been widely used as a scaffold material. Collagen based biomaterials are the most frequently used and clinically available bio-macromolecules. The rich chemistry of collagen allows engineers to alter the physicochemical properties such as porosity, crystallinity, cross-link density and mix with different copolymers. These in vitro characteristics allow controlled interaction with the host resulting in predictable tissue ingrowth and biodegradation rates. In order to produce collagen biomaterials in different forms, first it should be solubilized in appropriate solvents. Then, there is a need to find suitable production methods to regenerate collagen. Electrospinning is a popular scaffold fabrication strategy in tissue engineering. During the spinning processes, there are many different physical forces acting on the material [5]. The strength, resorption rate, and biocompatibility of collagenous biomaterials are profoundly altered by the production method and processing conditions.

The main concern is how all these regeneration processes will affect or alter the original secondary structure of the collagenous biomaterials. In a recent publication together with our collaborator Dr. Jochen Bürck from the Institute of Biological Interfaces IBG-2 at KIT, we showed that even in the best conditions electrospun collagen nanofibers could preserve only 42% of the native structure [5]. We successfully demonstrated the unfolding effect of fluorinated solvents that are widely used in electrospinning process to obtain collagen nanofibers. Therefore, it was decided to use another alternative solvent system, namely ethanol/acidic acid mixture. Besides, we employed an alternative collagen nanofiber production method, namely self-assembly of collagen fibers. All these regeneration processes and solvents in the process have tremendous impact on the final materials' end use properties.

We used SRCD to investigate the amount of natural triple helix structural conformation that was preserved in the electrospun collagen nanofibers. The possible effects of different preparation methods on the secondary structure of collagen materials were assessed. Furthermore, we performed temperatures series of experiments, starting from 15°C to 90°C , in order to demonstrate the temperature effect on unfolding behaviour of collagen. Special attention was given to the PP-II band that gives the information about triple helix structural conformation of collagen biomaterials. There was an apparent need to use the UV-CD12 beamline SRCD setup with its orders of magnitude higher photon flux to obtain the full spectral information down to possibly $\sim 175\text{ nm}$ - 180 nm on potential collagen biomaterials. This allowed us for a more accurate secondary structure analysis using SRCD reference spectra of thermally denatured native collagen in combination with the CCA+ algorithm for spectral deconvolution of the sample spectra.

Experimental details

First, electrospun collagen nanofibers were prepared by two different methods; a) 10% w/v collagen solution was prepared by dissolving collagen in TFE and b) 2% collagen and 2% PEO blend was dissolved in 0.5 M HAC and ethanol mixture at 1:1 ratio [6]. The second method was self-assembly, where the collagen nanofibers were obtained by ionic interactions. Basically, collagen acidic solution co-extruded with fiber buffer solution through a tube into the distilled water to form collagen fibrils. The third method was the film casting. The collagen solutions were dried at ambient conditions on flat silicon molds. All products were dissolved in diluted Acetic Acid (0.05M) for SRCD experiments. The reason of choosing the acidic solvent is to preserve the triple helix secondary structure of collagen. All material preparation processes were performed in Istanbul, Bahcesehir University.

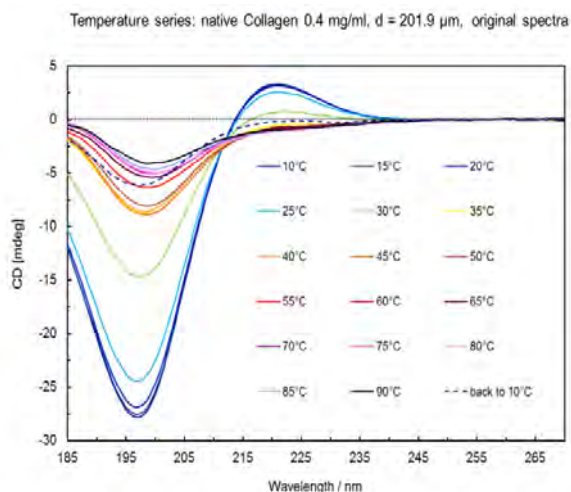
Results:

Fig.1. SRCD spectra of unfolding behaviour of native collagen in 0.05M Hac solution based on thermal denaturation.

casted collagen film, obtained from acidic acid in red, self-assembled collagen fibers in blue, collagen-PEO mixed electrospun nanofibers obtained from EtOH/HAc in pink (dashed line) and electrospun collagen nanofibers obtained from TFE in green (dashed line). The spectra showed that PP-II fraction ratio scores the lowest value for the electrospun collagen nanofibers. The self-assembled collagen fibers give an increased triple helix fraction. A 1.5 fold higher fraction ratio was obtained for the electrospun collagen nanofibers, comparing with the results in our previous publication. The differences mainly seem to be due to the preparation temperature of the collagen nanofiber samples for SRCD experiments. In previous studies collagen was dissolved in 0.05M acidic acid at ambient temperatures (approx. 25° C), while the current study, the dissolution temperature was kept always at 15° C. Variation in dissolution temperatures of collagen could cause discrepancies in the CD results, because they may lead to irreversible collagen unfolding. Nevertheless, the results showed that the electrospinning proces resulted in a certain loss of the native folded fraction. Among all the production process, the casted collagen film products preserved the native structure the best.

References:

- 1-) Di Lullo, G. A.; Sweeney, S. M.; Korkko, J.; Ala-Kokko, L.; San Antonio, J. D. Mapping the ligand-binding sites and disease-associated mutations on the most abundant protein in the human, type I collagen. *J. Biol. Chem.* 2002, 277, 4223–4231.
- 2-) Hsu, S.; Jamieson, A., M.; Blackwell, J. Viscoelastic studies of extracellular-matrix interactions in a model native collagen gel system. *Biorheology* 1994, 31, 21–36.
- 3-) Holmes., D., F.; Graham, H. K.; Trotter, J., A.; Kadler, K., E. STEM\TEM studies of collagen fibril assembly. *Micron.* 2001, 32,273–285.
- 4-) Silver, F., H.; Birk, D., E. Molecular-structure of collagen solution-comparison type-I, type-II, type-III and type-V. *Inter. J. Biol.Macromol.* 1984, 6, 125–132.
- 5-) Bürck, J., Heissler, S., Geckle, U., Ardakani, M. F., Schneider; R., Ulrich, A. S., Kazanci, M. (2013) Resemblance of Electrospun Collagen Nanofibers to Their Native Structure. *Langmuir* 2013, 29 : 1562-1572.
- 6-) Dong, B.; Arnoult, O.; Smith, M., E.; Wnek, G., E. Electrospinning of collagen nanofiber scaffolds from benign solvents. *Macromol. Rapid Commun.* 2009, 30, 539–542.

SRCD measurements of native collagen were performed at a temperature series, ranging from 10° C to 90° C (Fig.1). It was an overnight experiment, using the UV-CD 12 in-house developed thermal scan software program. The temperature was increased by 5° C in every step. The highest folded fraction ratio was obtained at the start temperature, 10° C (dark blue color). The increase in temperature caused the decrease of the triple helix fraction. There was a melting temperature around 30° C (light green), that confirmed our previous results [5]. When the temperature was increased above 40° C, the structure became gradually more and more unfolded and turned into random coil. We have chosen the 15° C and 90° C spectra, respectively as the reference values for a completely folded/unfolded triple helix fraction to assess the fraction ratios at different conditions. Fig.2. shows the SRCD spectra of native collagen at 15° C in black,

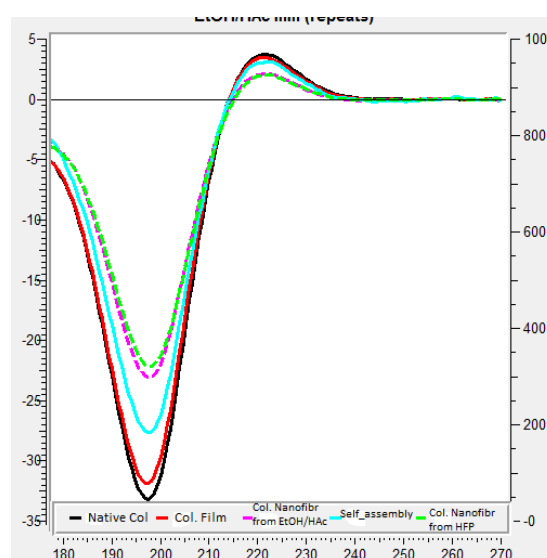


Fig.2. SR-CD spectra of native collagen, collagen film, self-assembled collagen fibers, and electrospun collagen nanofibers from TFE and EtOH/HAc mixture.

Comparison of Manganese Concentration and Distribution in Human Osteoporotic and Non-Osteoporotic Bone using Synchrotron Micro X-Ray Fluorescence Imaging

M. Rauwolf¹⁾, B. Pemmer¹⁾, J. Prost¹⁾, A. Roschger²⁾, S. Smolek¹⁾, A. Maderitsch¹⁾, C. Strel¹⁾, P. Roschger²⁾, P. Wobraschek¹⁾, R. Windhager³⁾, S. Lang⁴⁾, R. Simon⁵⁾, K. Klaushofer²⁾, J.G. Hofstaetter^{2), 3)}

¹⁾ Atominstitut, Technische Universität Wien, Stationaltee 2, 1020 Vienna, Austria

²⁾ Ludwig Boltzmann Institute of Osteology at the Hanusch Hospital of WGKK and AUVA Trauma Centre Meidling, 1st Med. Dept., Hanusch Hospital, 1140 Vienna, Austria

³⁾ Department of Orthopaedic Surgery, Vienna General Hospital, Medical Univ. of Vienna, Austria

⁴⁾ Department of Pathology, Vienna General Hospital, Medical Univ. of Vienna, Austria

⁵⁾ Forschungszentrum Karlsruhe GmbH, Institute for Synchrotron Radiation, Hermann-von-Helmholtz-Platz 1, D-76344 Eggenstein-Leopoldshafen, Germany

Introduction

Osteoporosis is characterized by a low bone mass and a micro-architectural deterioration of bone tissue with a consequent increase in bone fragility and susceptibility to fracture. As the population continues to age, the effects of osteoporosis will become increasingly prevalent [1]. Osteoporosis already affects more than 75 million people in Europe, Japan and the United States. The general prevalence of osteoporosis rises from 5% among women aged 50 years to 50% at 85 years of age; among men, the comparable figures are 2.4% and 20% [2].

A recent study [3] hypothesizes that manganese is an essential mineral for calcium fixation (or incorporation) into bones. This theory is based on the finding that a decrease in manganese content in antlers causes a 27% reduction in the required impact energy to break antler bone material.

The aim of our current and ongoing work is to test this hypothesis by determining manganese concentration and distribution in osteoporotic and non-osteoporotic human bone. The purpose of these first measurements was to show that it is possible to measure manganese in bone, optimize our measuring system and to prove that the measured peak at 5.9keV is indeed manganese and not a sum of a Ca-K_α escape peak and a Ca-K_β peak. Therefore we measure four human iliac crest biopsy bone samples - two osteoporotic (sample 1 and 2) and two non-osteoporotic samples (3 and 5) - of male patients in the age of 49 to 57. During the measurements the experimenters were not aware which samples were the osteoporotic and which the non-osteoporotic samples.

All samples were fixed in 70% EtOH, dehydrated in alcohol and embedded in polymethylmethacrylate (PMMA). After trimming, surfaces of the PMMA-blocks were polished and carbon-coated for qBEI measurements. The carbon coating does not affect the μ -XRF measurements [4].

Experimental

Confocal μ -XRF at the FLUO beamline is the method of choice for the analysis. This set-up allows us to obtain the lateral distribution of the elements of interest at given depth by moving the sample normal to the sample surface or directly measure depth profiles in the sample. In case of analysis of thick heterogeneous samples the confocal setup can help to eliminate the unwanted contribution of deeper sample layers to the X-ray fluorescence spectra, and therefore to improve the overall spatial resolution of the system.

Our measurements require an aluminum filter in the path of rays between the sample and detector to suppress a fraction of the calcium fluorescence and to prevent the appearance of a sum peak (of a Ca-K_α escape and Ca-K_β peak or a Ca-K_β escape and a Ca-K_α peak) at the position of the Mn-K_α line (at 5.9keV). As the filter also suppresses a (smaller) fraction of the manganese fluorescence, we tested two Al filters with different thickness (10 μ m and 20 μ m) to find an optimal Mn-to-Ca ratio for this analysis.

All samples were measured at 9.2keV set by a W/Si multilayer monochromator, with a beam size of 24 x 18 μ m² and a depth resolution of 33 μ m at 4.51keV (Ti-K_α). Two scan areas on each sample were selected from the qBEI in reference to bone histomorphology. The optimal surface plane for each scan region was determined by performing depth scans on several points in the chosen scan areas. Maps of the distribution of

single elements were obtained using the micro-XRF software package (spectrum fitting performed by AXIL) at the beamline. The step size was $20 \times 15\mu\text{m}^2$ for each scan.

Results

The $20\mu\text{m}$ Al turned out to be the ideal filter to reduce the Ca fluorescence enough to make sure that the peak at 5.9keV could not be a Ca sum peak but still allowed us to measure Mn. As one can see from figure 1 it was possible to measure manganese in bone samples with the set-up at the FLUO beamline. As the sample preparation requires the use of steel tools, contaminations in the holes and cracks of the PMMA with Fe, Ni, Cr and Mn are inevitable. These contaminations can be found quite easily by identifying the coincidence of high Fe, Ni, Cr and Mn intensities. Nonetheless all Mn values outside the Ca-ROI were interpreted as contamination and zeroized to avoid any misinterpretation.

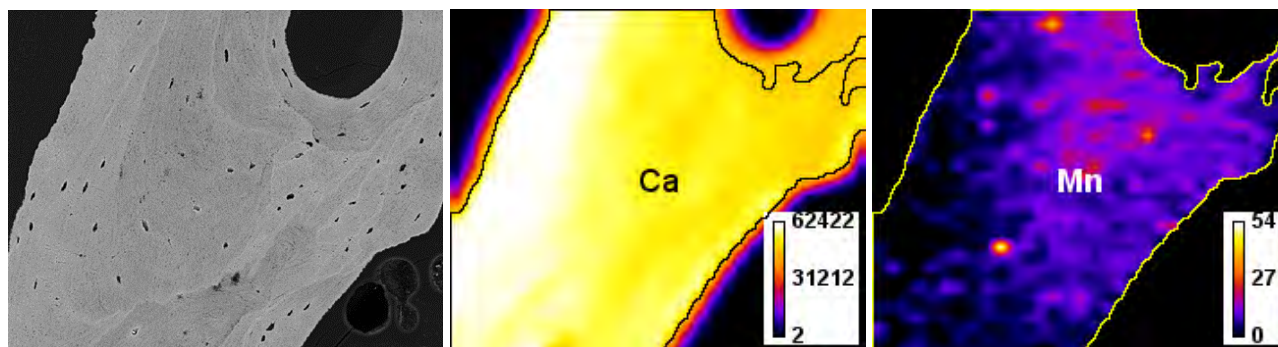


Fig. 1: Sample 2 Area A - qBEI image ($570\mu\text{m} \times 450\mu\text{m}$) and element maps of calcium (Ca) and manganese (Mn). Mn values outside of the Ca ROI (yellow line in the Mn map) were set to zero. Resolution: $20\mu\text{m} \times 15\mu\text{m}$ per pixel; Scan area: $600\mu\text{m} \times 495\mu\text{m}$; Acquisition time: 23 sec. per pixel; Normalized to cps and 100mA ring current.

The results for all measured areas are shown in table 1. To calculate the ratios the medians of Ca and Mn in the Ca ROI were used.

Sample	Area	Mn/Ca-ratio*10000
2	A	1.3
2	B	1.1
5	A	2.3
5	C	2.8
1	A	0
1	C	0
3	A	0.12
3	B	0.18

Table 1: Results for the iliac crest biopsy bone samples of 49 to 57 year old male patients

While the results of these measurements look promising as Mn was found in three of the four samples, a larger sample size is needed to draw a conclusion about the influence of Mn in osteoporosis. Due to beam losses at ANKA during this beam time it was only possible to measure four of our prepared samples. We hope to be able to measure our remaining samples during a future beam time.

Acknowledgements

The ANKA Ångströmquelle Karlsruhe is acknowledged for the provision of beam time, and we would like to thank Dr. Rolf Simon for the support at the FLUO beamline.

References

- Frederickson, C. J., Koh, J.-Y., and Bush, A. I. "The neurobiology of zinc in health and disease." *Nature Reviews Neuroscience* 6.6 (2005): 449–462.
- Mills, C. F. Trace elements in human nutrition and health. Geneva: WHO, 1996.
- Landete-Castillejos, T., et al. "Alternative hypothesis for the origin of osteoporosis: The role of Mn." *Frontiers in Bioscience E 4* (2012): 1385–1390.
- Roschger, P., Plenk, H. Jr., Klaushofer, K. and Eschberger, J. "A new scanning electron microscopy approach to the quantification of bone mineral distribution: backscattered electron image grey-levels correlated to calcium K alpha-line intensities." *Scanning microscopy* 9.1 (1995): 75–86; discussion 86–78.

The chemical forms of sulfur in prostate cancer tissue analysed by means of XAS

J. Czapla-Masztafiak¹, K. Okoń², M. Gałka³, R. Steininger⁴, J. Göttlicher⁴ and W. M. Kwiatek¹

¹Institute of Nuclear Physics PAN, ul. Radzikowskiego 152, 31-342 Kraków, Poland

²Chair of Pathomorphology, Jagiellonian University Medical College, ul. Grzegorzewska 16, 31-531 Kraków, Poland

³Gabriel Narutowicz City Specialist Hospital, ul. Prądnicka 35-37, 31-202 Kraków, Poland

⁴Karlsruhe Institute of Technology, ANKA Synchrotron Radiation Facility, Hermann-von-Helmholtz-Platz 1, D-76344 Eggenstein-Leopoldshafen, Germany

Overview

XANES technique was used to determine the chemical forms of sulfur in different morphological parts of prostate tissue. The prostate tissue samples were obtained during surgery on patients suffering from prostate cancer and benign prostatic hyperplasia (BPH) that was used as reference, non-cancerous samples. Tissues were formalin-fixed, paraffin embedded by the routine histological protocol, cut into 15 μm thick sections in a standard cryostat and placed on 1,5 μm thick Mylar foil. Another adjacent section was used for histological examination.

S K-edge μ -XANES measurements were performed at the wiggler beamline SUL-X using a 7-element Si(Li) fluorescence detector (Gresham, now SGX SensorTech). Full XANES spectra were collected from 5 cancerous tissue samples on the tumor and margin areas and from 2 BPH tissue samples.

Results

Preliminary analysis of the obtained spectra showed that there are three different forms of sulfur in examined samples: reduced sulfur, oxidized sulfur and small amounts of sulfur at an intermediate oxidation state. Although the spectra obtained from different points showed no difference in shape their main differences resulted from the intensity of the peaks corresponding to the content of various forms of sulfur (Fig. 1).

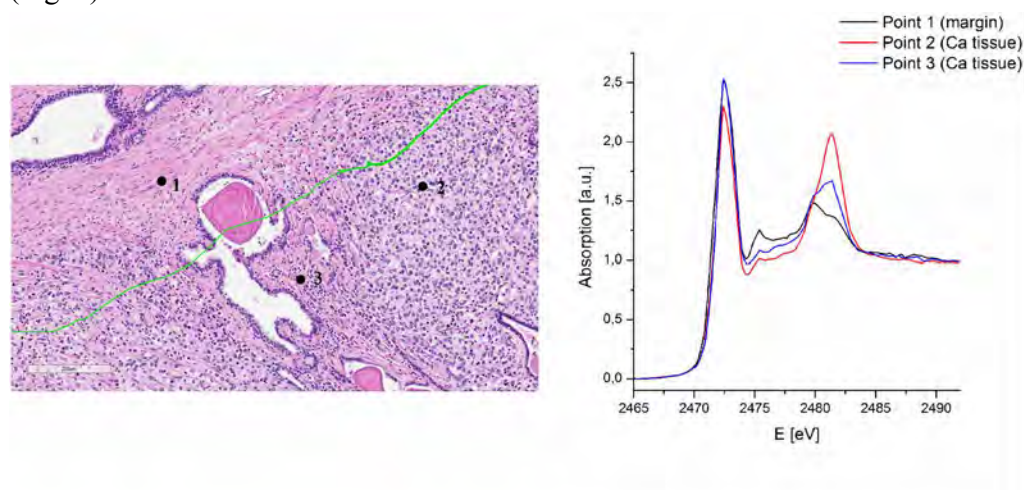


Fig. 1 Left - microscopic image of prostate cancer tissue with marked border between the area of the tumour (Ca tissue) and the tumour margin (green line). Right - sample sulfur K-edge XANES spectra obtained from selected points (1, 2, 3) of the tissue.

In order to analyse these differences in details Principal Component Analysis (PCA) in the Unscrambler X software were performed. In total 138 XANES spectra were analysed. The operations of PCA express the original data matrix (in this case, a set of XAS spectra) as the product of two new matrices: the first matrix contains loadings, which are mathematical constructs describing independent sources of variation within the dataset and the second one contains scores, which express the relative variance in the experimental data matrix explained by each component. Based on scores values variance plots were generated in which the

proximity between any two points (samples) on the plot is directly proportional to their similarity. Additionally, loadings plots for each component were obtained (Fig. 2).

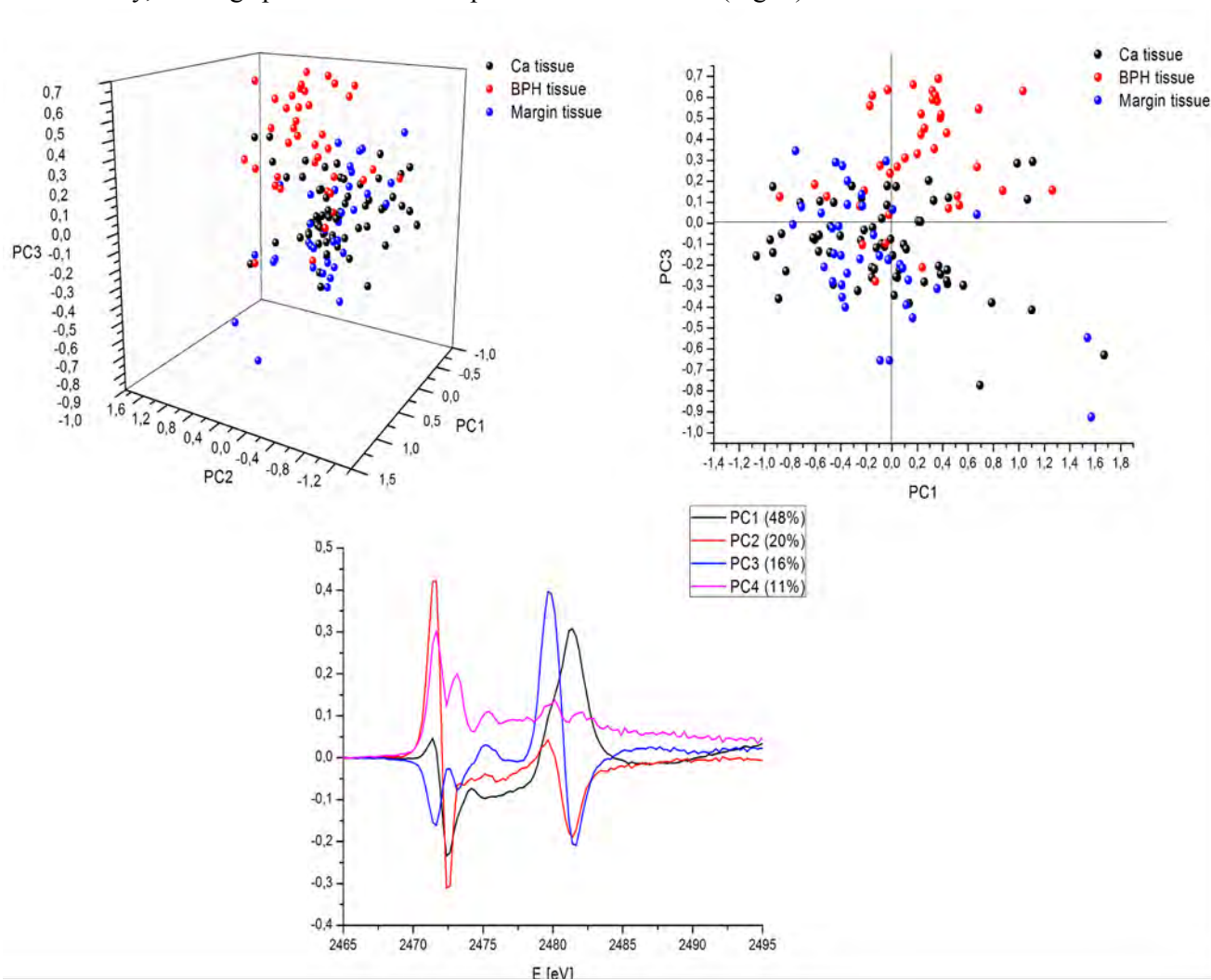


Fig. 2. Top – PCA 3D and 2D score plots for different types of prostate tissue. Bottom – corresponding loadings plots for each component. Numbers in parentheses indicate the percentage of variance explained by each component.

The obtained results showed that the spectra measured for non-cancerous tissue clearly separate from the spectra of prostate cancer tissue. There was no separation between spectra collected in the areas of tumour and margin. It was found that the separation of spectra between cancerous and non-cancerous tissue occurs along PC3 (Principal Component 3). Detailed analysis of the loading plot of PC3 showed that the differences are mainly due to the different ratio of sulfur +5 oxidation state (which corresponds to the energy peak at approx. 2479 eV) to the sulfur +6 oxidation state (which corresponds to the peak at energy approx. 2482 eV) and the shift to higher energy which occurs in spectra taken from cancerous tissues. This result may suggest a redox imbalance in case of prostate cancer tissue.

The results of detailed analyses will be used to prepare the manuscript and will be presented during international conference XRM2014, Melbourne, Australia, October 2014.

Interaction of putative amyloidogenic peptides from human Septin 2 with membrane models

Julio Cesar Pissuti Damalio; Jose Luiz Lopes; Patricia Kumagai
University of Sao Paulo, Sao Carlos Institute of Physics, Sao Carlos, Sao Paulo, Brazil

Introduction

Septins are members of a conserved group of GTP-binding and filament-forming proteins involved in cytokinesis and a variety of other important cellular processes [1], such as including their role in cytokinesis, cell division, exocytosis and membrane trafficking. Although hetero-oligomeric complexes of septins have been extensively investigated, homo-oligomeric structures have also been observed, and characterized as amyloid filaments, which are involved in neurodegenerative diseases [2-4]. A wide range of human pathologies are associated with uncontrolled protein misfolding, which promotes the conversion of polypeptide chains from the soluble globular state into well-organized fibrillar aggregates rich in β -sheet structure [5, 6]. Recently, our group reported the self assembly of human septin 2 (SEPT2) into amyloid-like fibrils and identified the putative regions in its primary structure predicted to be responsible for this process [4]. Furthermore, we showed the occurrence of conformational changes in SEPT2 induced due to the interaction with DPPC (dipalmitoyl phosphatidyl choline) vesicles, could lead the protein assembly into β -sheet structures. However, it is still unclear the factors that can affect the protein-membrane interactions and trigger the protein assembly in fibrillar structures.

Methodology

In this present study, the synthetic peptide ${}_{147}\text{HCCFYFISP}_{155}$ corresponding to the predicted putative amyloidogenic region of human SEPT2, was obtained by Solid Phase Peptide Synthesis (SPPS) and its interaction with different membrane models was investigated. Membrane models were composed of SDS (sodium dodecyl sulfate) and HPS (N-hexadecyl-N,N-dimethyl-3-ammonio-1-propanesulfonate) micelles (at different concentrations) and POPA, 1-palmitoyl-2-oleoyl-sn-glycero-3-phosphate and POPE, 1-palmitoyl,2-oleoyl-sn-glycero-3-phosphoethanolamine lipid vesicles (at a 1:30 peptide to lipid molar ratio). The influence of TFE (trifluoroethanol) and temperature (thermal melting over the range from 20°C to 80°C; using 10°C steps) on the peptide secondary structure were also investigated. All the SRCD spectra were obtained at the CD12 beamline located at the ANKA Synchrotron, Germany. For all measurements the peptide was in acetonitrile 5% and three scans were collected over the wavelength range from 280 to 175 nm, with 0.5 nm step size, a 1.5s of dwell time (1s for baselines), at 20°C in a 0.0109 cm pathlength suprasil quartz cell. The final spectra were obtained after subtracting the buffer for each sample and they were converted to delta epsilon units, using a mean residue weight of 139.5 on CDTTool software [7].

Results and Discussion

In aqueous solution, the SRCD spectrum of the peptide ${}_{147}\text{HCCFYFISP}_{155}$ exhibits a negative peak at 193 nm and a small positive peak around 182 nm, which are characteristic of low content of ordered secondary structure content (Figure 1A). The presence of HPS micelles did not induce significant conformational changes on the peptide (albeit for a small decrease of the negative band around 193 nm and increase of the negative band around 225 nm), resulting the peptide into a unordered conformation. On the other hand, in the presence of the SDS micelles, a β -sheet conformation was triggered on the peptide structure, with a negative band around 215 nm and a positive band around 195 nm (Figure 1A).

A similar behavior was observed in the presence of the vesicles in solution. In the presence of POPE vesicles, no changes in secondary structure of the peptide were observed, whilst the POPA vesicles led to higher ordering, indicated by a negative band at 222 nm and a positive band at 200 nm (Figure 1.B).

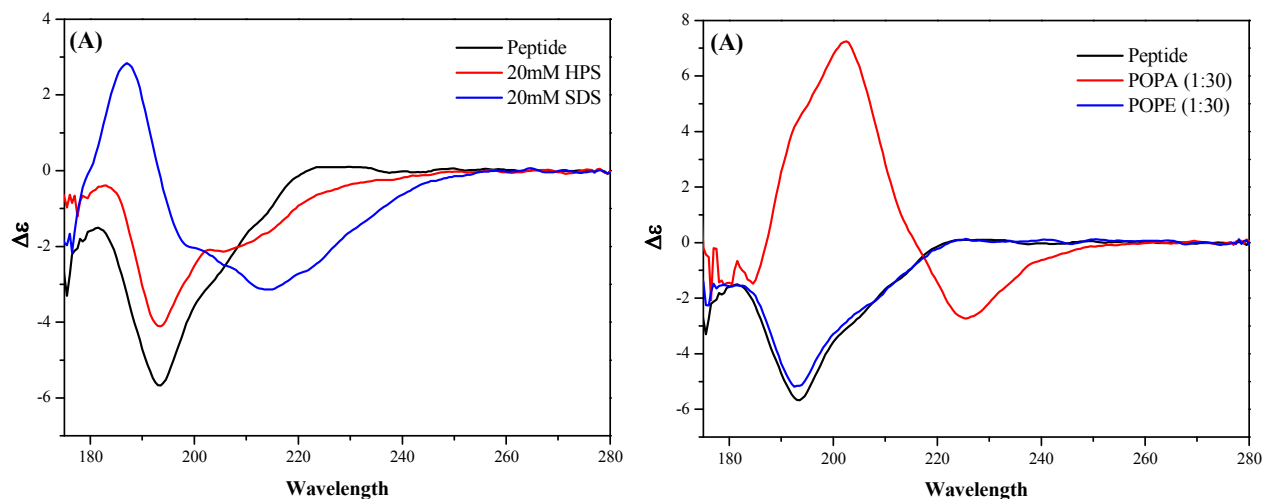


Figure 1: Influence of micelles (A) and vesicles (B) in the secondary structure of the peptide.

Our results indicated that the presence of negatively charged partners (both micelles or vesicles) can induce significant conformational changes in the peptide. In the case of SDS micelles, a β -sheet characteristic spectrum was observed, what is compatible with amyloid structures assemble.

Thermal melting of the peptide, the peptide in the presence of SDS or POPA have showed a decrease of the negative and positive bands. The photomultiplier voltage has changed as well, indicating that the samples precipitated along the melting (data not shown). Furthermore, the peptide samples containing 10, 20, 30, 50 or 75% of TFE only showed a higher ordering in secondary structure (data not shown).

Acknowledgements

We wish to thank Dr. Edson Crusca for the peptide synthesis. This research was supported by FAPESP (grants number 2013/20414-4 to JLSL and 2012/04527-0 to JCPD).

References

- [1] L.H. Hartwell. *Exp Cell Res*, 69 (1971) 265-276.
- [2] W. Garcia, A.P.U. de Araujo, F. Lara, D. Foguel, M. Tanaka, T. Tanaka, R.C. Garratt. *Biochemistry-Us*, 46 (2007) 11101-11109.
- [3] A. Kinoshita, M. Kinoshita, H. Akiyama, H. Tomimoto, I. Akiguchi, S. Kumar, M. Noda, J. Kimura. *Am J Pathol*, 153 (1998) 1551-1560.
- [4] J.C. Pissuti Damalio, W. Garcia, J.N. Alves Macedo, I. de Almeida Marques, J.M. Andreu, R. Giraldo, R.C. Garratt, A.P. Ulian Araujo. *Biochimie* (2011).
- [5] D.J. Selkoe. *Nature*, 426 (2003) 900-904.
- [6] P. Westermark, M.D. Benson, J.N. Buxbaum, A.S. Cohen, B. Frangione, S.I. Ikeda, C.L. Masters, G. Merlini, M.J. Saraiva, J.D. Sipe. *Amyloid-Journal of Protein Folding Disorders*, 12 (2005) 1-4.
- [7] Lees, J. G., B. R. Smith, B. A. Wallace. 2004. *Anal. Biochem.* 332:285–289.

Rechargeable Li-Batteries: Mechanistic Insights by In Operando X-ray Diffraction

C. Weidmann¹⁾, H. Sommer^{1),2)}, T. Brezesinski¹⁾

¹⁾ Karlsruhe Institute of Technology, Institute of Nanotechnology, Battery and Electrochemistry Laboratory (BELLA), Hermann-von-Helmholtz-Platz 1, D-76344 Eggenstein-Leopoldshafen, Germany

²⁾ BASF SE, D-67056 Ludwigshafen, Germany

The development of high performance electrochemical energy storage systems for stationary and mobile applications (i.e., grid storage, vehicles etc.) that meet future demands is of particular importance. The current lithium-ion battery market predominantly makes use of lithium metal oxide cathodes (LCO, NMC, NCA, LMO etc.) as lithium source and graphite as the negative electrode material. With these materials – they are limited in terms of capacity – safe and reliable batteries can be achieved.

Composite materials with the general formula $x\text{Li}_2\text{MnO}_3 \cdot (1-x)\text{LiMO}_2$ ($M = \text{Mn, Ni, Co}$), referred to as HE-NMC, have been shown to deliver much higher specific capacities, and therefore, higher energy densities on cell level, but suffer from capacity fading and voltage decay during electrochemical cycling. The underlying degradation mechanisms have not been fully understood yet. Nonetheless, they are often associated with structural transitions – layered-to-spinel – and lattice distortions.

Both to gain mechanistic insights into the operation of batteries using HE-NMCs and to be able to correlate structural data with electrochemical processes, *in operando* X-ray diffraction (XRD) measurements were conducted in transmission mode on $5 \times 5 \text{ cm}^2$ pouch cells at the PDIFF beamline using a Pilatus 300k detector. Multiple cells of different composition were investigated. However, the XRD data did not reveal any structural changes of the HE-NMC materials after the formation cycle, which might be simply due to the fact that transitions only occur after prolonged cycling, i.e., several hundreds of cycles.

Apart from the HE-NMC-containing electrodes, the same setup was also used to analyze lithium-sulfur (Li-S) batteries with the objectives to better understand (1) the cell chemistry and (2) the contribution of crystalline compounds. Sulfur is currently one of the most promising cathode-active materials for next generation Li-batteries. Part of the reason for is the high theoretical energy density of the Li-S system ($\sim 2500 \text{ Wh kg}^{-1}$) and the fact that sulfur is abundant and of low cost. However, there are several performance and safety concerns preventing it up to now from being used on a commercial scale.

A series of *in operando* XRD measurements was conducted on Li-S pouch cells using sulfur cathodes with a non-optimized composite microstructure. To our knowledge, there are only a few such *in operando* studies available in the literature. **Fig. 1** shows both XRD patterns of a Li-S battery that was discharged to 1.7 V with respect to Li/Li^+ and the corresponding voltage-capacity curve. What we found is that nanocrystalline Li_2S (grain size $< 10 \text{ nm}$) is formed on discharge and sulfur recrystallizes in the monoclinic crystal system (beta-allotrope) during cycling [1]. The latter finding is somewhat surprising, given that beta- S_8 is not supposed to be stable at ambient conditions (alpha- S_8 is thermodynamically favored). Overall, the data show that all of the crystalline sulfur reacts with lithium to form lithium polysulfides (the sulfur peaks are completely gone by the end of the first discharge plateau) and cubic Li_2S is probably already present with the beginning of the second discharge plateau (see broad peak at $2\theta \approx 15.5^\circ$ in **Fig. 1**). In addition, variations of d -spacing indicate lattice strain in the beta- S_8 .

Taken together, synchrotron-based *in operando* XRD provides valuable insights into the operation of rechargeable Li-batteries and the results may help to develop future electrode materials with improved cycling performance.

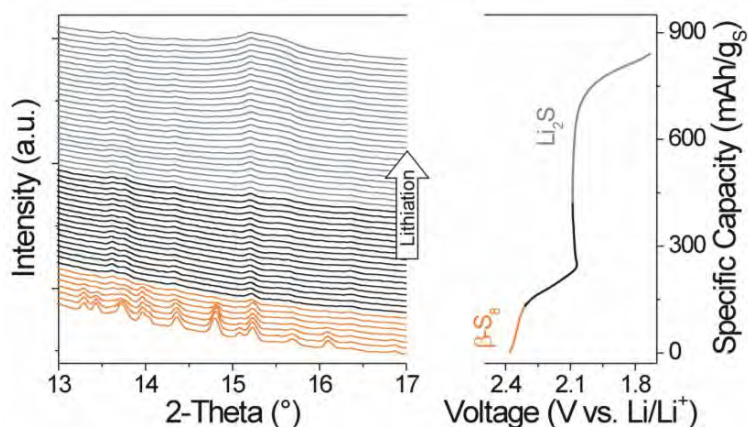


Fig. 1: Left: In operando XRD patterns ($\lambda = 0.08856$ nm) of a Li-S pouch cell discharged to 1.7 V with respect to Li/Li⁺ at a rate of C/5. Right: Voltage-capacity curve.

[1] Kulisch, J.; Sommer, H.; Brezesinski, T.; Janek J. "Simple Cathode Design for Li-S Batteries: Cell Performance and Mechanistic Insights by In Operando X-ray Diffraction" *Phys. Chem. Chem. Phys.*, **2014**, 16(35), 18765-18771.

Acknowledgements

We thank Jörn Kulisch, Artur Schneider, Jürgen Janek, Sven Glatthaar, Lea de Biasi, Holger Gesswein and Stephen Doyle for assistance with materials characterization and data analysis. This study is part of projects being funded within the BASF International Network for Batteries and Electrochemistry.

Investigation of plastic deformations in duplex steel with a 384x384 EROSITA pnCCD and a white X-ray synchrotron source.

A. Abboud¹⁾, N. Pashniak¹⁾, S.Send¹⁾, A. Algashi¹⁾, U.Pietsch¹⁾

¹⁾ University of Siegen, Department of Solid State Physics, Walter-Flex-Str. 3, D-57068 Siegen, Germany

Aim of the experiment:

Testing the new technique of residual stress analysis using an energy-dispersive detector – pnCCD. Investigation of duplex steel samples with very high loaded cycle fatigue (VHCF).

Experiment and results:

The pn-CCD module (384x384 pixels²) [1],[2],[3] with a read out frequency of 96Hz was used for developing a new approach of stress-strain analysis based on Energy-Dispersive Laue Diffraction using a white beam [4]. The aim was to test the new technique using an energy-dispersive detector and to find the limits of residual stress measurements in stressed Cu, Si and duplex steel.

The measurements were performed at TOPO-TOMO beam line which provides a white beam regime. The photons energy range was 5-40 keV.

Duplex steel:

Due to the simultaneous 2D-position and energy resolution of the pnCCD, distortions in lattice spacing as well as the energy shifts of the corresponding Bragg peak were determined just in a single shot experiment without any additional rocking of the sample.

The duplex steel 1.4462 (X2CrNiMoN-22-5-3) sample was previously stressed by applying 1.27×10^8 cycles and $G=375\text{MPa}$ at Ultrasound VHCF machine. The sample was investigated along the direction of stress distribution on the marked crack area whilst keeping the sample in transmission geometry using a white beam with the size $25 \times 25 \mu\text{m}^2$. The sample was measured in 6 position with a step $25 \mu\text{m}$. The data acquisition was performed collecting 50 000 frames per single measurement. For the data visualization we have used offline analysis to plot the intensity images of every scanned position. (Fig.1)

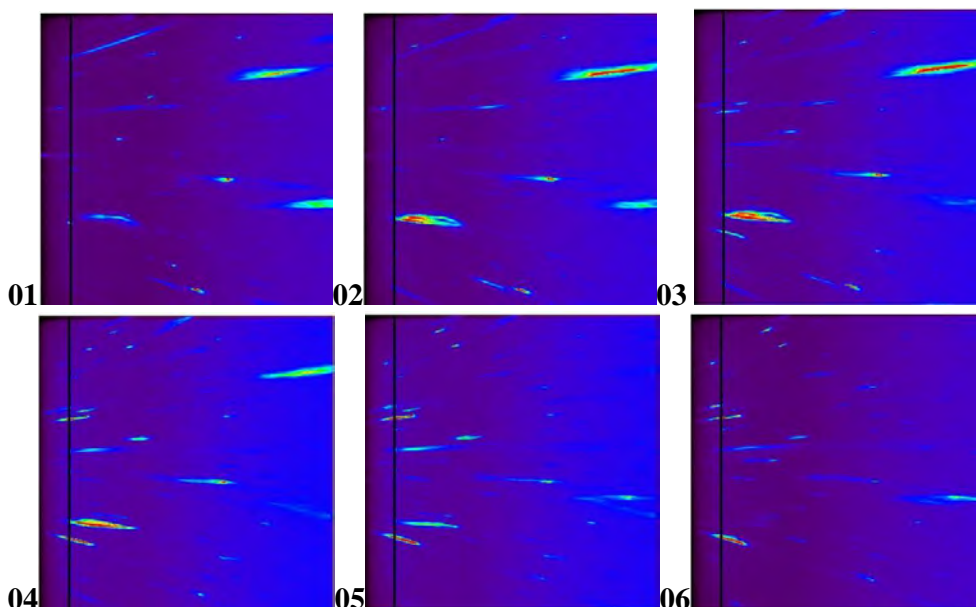


Fig. 1: The 2-D intensity images of every position 01, 02, 03, 04, 05, 06. The energy information for every point of acquisition could be extracted depends on the requirements for data analysis.

For selected positions the indexing of the peaks was done as well as the evaluation of the positional variation of selected Bragg peaks in space and energy. Every reflection was indexed rather as austenite or as ferrite.

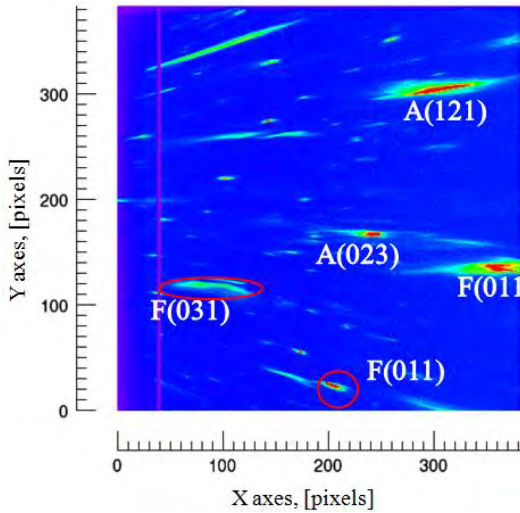
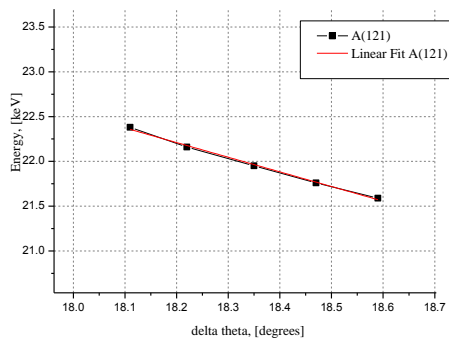


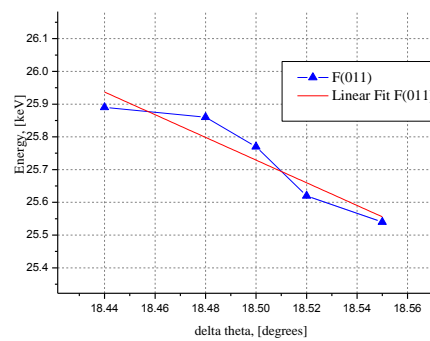
Fig. 2: 2-D intensity image of position 01 was indexed from extracted position and energy information of each reflection.

In general, the structural changes and stress-strain characteristics can be obtained by analysis of the shifts of the corresponding Bragg peaks with respect to the non-stressed sample by scanning the sample with monochromatic beam.

In the case of white beam using energy dispersive detector the additional rotation of the sample or scanning is not necessary. We could investigate the deviation from the Bragg's law (if present) of every reflection.



a)



b)

Fig. 3: Scanned position 01. The area of the peak was divided into 5 sectors and for each of sector the energy profile as the function of position was plotted.

a) a linear fit of the $\Delta E/\Delta\theta$ distribution of the selected reflection A(121), yields a slope -1.64 ± 0.06

a) a deviation from the Bragg's law of the selected reflection F(011).

The linear fit of the $\Delta E/\Delta\theta$ distribution of the Laue spot [5] yields a certain slope, from the numbers one can distinguish between:

- a) rotation caused by GNDs
- b) shear
- c) bending
- d) mixed shear and bending

Performing additional simulations one can calculate from the experimental data which processes are occurred in the stressed sample. Using the energy dispersive pnCCD provides a gain time and fast realization of the experiment. Deviation from the Bragg's law analyzing further could work as a marker of a crack position occurring after certain number of loaded cycles.

References

- [1] W. Leitenberger, R. Hartmann, L. Strüder, J.of Applied Crystallography 42, 6, 1139-1146 (2009)
- [2] L.Strüder et al. The MPI/AIT X-Ray imager – high speed pn CCDs for X-Ray detection. Nucl. Instr. And Meth. A, 288:227-235, 1900.
- [3] S. Send, A. Abboud, R. Hartmann, M. Huth, W. Leitenberger, N. Pashniak, J.Schmidt, L. Struder, and U. Pietsch, " Characterization of a pnCCD for applications with synchrotron radiation, Nuclear Instruments and Methods in Physics Research A 711(2013), 132-142
- [4] S. Send, M. von Kozirowski, T. Panzner, S. Gorfman, K. Nurdan, A. H. Walenta, U. Pietsch, W. Leitenberger, R. Hartmann, and L. Struder, " Energy-dispersive Laue diffraction by means of a frame-store pnCCD, Journal of Applied Crystallography 42 (2009), 1139-1146
- [5] A. Abboud , C. Kirchlechnerb, J.-S. Micha, O. Ulrich, S. Send, N. Pashniak,, R. Hartmann, L. Strüder, J Keckes and U. Pietsch, - Energetic Structure of μ Laue Peaks from Plastically-Deformed Cu Micro-Beam Revealed by a Three-Dimensional X-ray Detector-, (submitted)

Acknowledgements

Acknowledgment to the beam line scientist T.Müller for helping to organize the experiment.
Additional acknowledgment to financial BMBF support – project 05K10PSB

Influence of annealing on the molecular orientation of polymer/fullerene blends

U. Aygül¹⁾, U. Dettinger¹⁾, D. Batchelor²⁾, S. Mangold²⁾, H. Peisert¹⁾, T. Chassé¹⁾

¹⁾ Institut für Physikalische und Theoretische Chemie, Universität Tübingen, 72076 Tübingen, Germany

²⁾ Karlsruher Institut für Technologie, Institut für Synchrotronstrahlung (ISS), 76021 Karlsruhe, Germany

Introduction

The active layer of efficient bulk heterojunction type organic solar cells consist of a donor material, mostly low band gap (LBG) polymers, and an acceptor material, which is a fullerene molecule in most cases. The electronic structure and the molecular orientation of the low band gap polymer is of fundamental importance for device properties. The molecular ordering and orientation affects for example the mobility of the charge carriers significantly and determines hence device operation. Near Edge X-Ray Absorption Fine Structure spectroscopy (NEXAFS) is an ideal technique to study the orientation in ultrathin films [1] and next to this geometric information NEXAFS also probes the electronic structure of the unoccupied orbital density of states, essential for determining the transport/mobility in such devices.

We have used the angular dichroism of the sulfur K-edge NEXAFS spectra of the respective polymers to probe the orientation of the extended π -conjugated system. In our previous work we applied this method to the investigation of LBG polymers [1] and we showed that the acceptor molecule PCBM affects the molecular orientation of the investigated polymers (see report A2012-020-002726). The aim of the present project is the study of the influence of annealing on the molecular orientation of such polymer/fullerene blend films (Si-PCPDTBT/PCBM and C-PCPDTBBT/PCBM). The results are submitted for publication [2].

Experimental details

Polymer films were prepared ex-situ by doctor blade casting in a glovebox with N₂-atmosphere and stored under well-defined ambient conditions. The film thickness was about 50nm, determined by atomic force microscopy (AFM) and also UV/VIS spectroscopy. Annealing was carried out in dark and under N₂-atmosphere. NEXAFS experiments were carried out at the XAS beamline. The beamline energy resolution at the sulfur edge is circa 300 meV and displays a polarization degree of > 0.95. X-ray absorption spectra were measured in fluorescence yield mode in order to avoid an increased surface sensitivity.

Results

Thermal annealing is a widely used method to optimize the morphology and improve the efficiency of the photovoltaic cell. It leads to phase separation of the blend film and to increased crystallinity [3,4]. First experiments on a P3HT/PCBM blend have revealed that thermal annealing at 120 °C leads to improved degree of orientation in these films and is thus an essential step in the sample preparation. However, the same experiments carried out for the blends of the low band gap polymers C-PCPDTBT and Si-PCPDTBT showed almost no influence of annealing on the molecular orientation of these polymers.[Report A2012-020-002726]

For an improvement of the ordering, phase separation and diffusion of the molecules in the blend are necessary. The annealing temperature however may depend on the considered polymer and might be significantly higher than 120°C; an important parameter in this context is e.g. the respective glass transition temperature, which is not known for all materials. We therefore carried out experiments after annealing to higher temperatures for Si-PCPDTBT/PCBM and PCPDTBT/PCBM with a mixing ratio of 1:1. The corresponding absorption spectra for C-PCPDTBT/PCBM and Si-PCPDTBT/PCBM after annealing to 150°C and 175 °C are displayed in Figures 1 and 2, respectively, as a function of the angle of incidence.

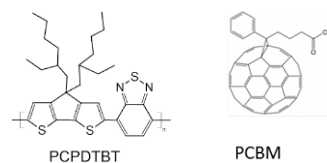
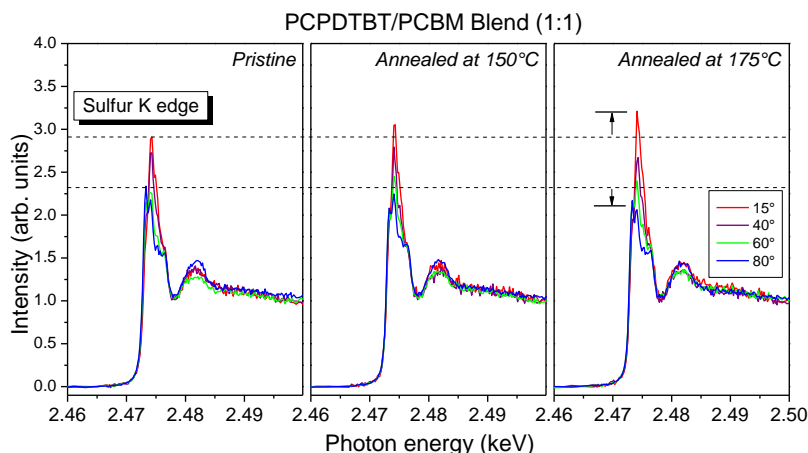


Fig. 1: Angle dependent S-K edge NEXAFS spectra of C-PCPDTBT blends after preparation and annealing to 150° and 175°C. The more pronounced dichroism after annealing to 175 °C points to a higher degree of orientation.

For PCPDTBT/PCBM distinct changes after the both annealing steps at 150°C and 175°C appear. The dichroism of the sulfur absorption edge increases which implies that more domains with a preferred molecular orientation of the PCPDTBT are formed after annealing to 150°C and 175°C. A preferred molecular orientation implies however also that the degree of ordering is high. Similar to P3HT/PCBM after annealing to 120°C the dichroism of the NEXAFS spectra of PCPDTBT/PCBM after annealing to 175°C is now comparable to the pure polymer. Presumably, the phase separation of PCPDTBT and PCBM associated with a higher degree of ordering requires higher temperatures than for P3HT/PCBM.

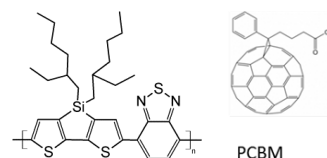
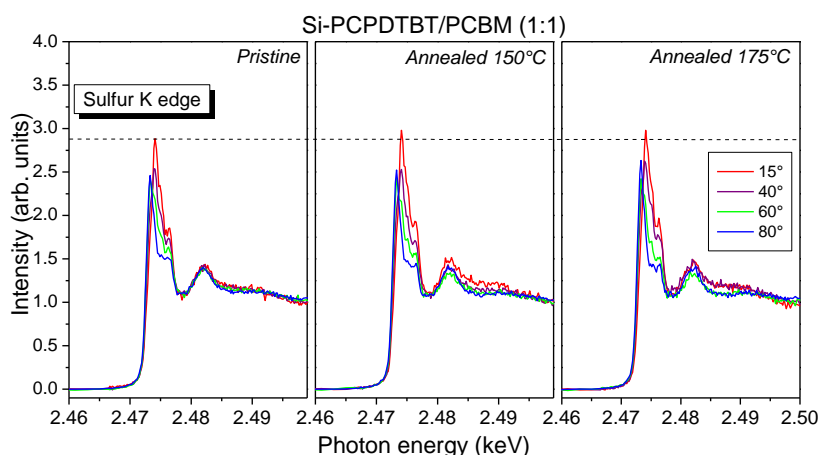


Fig. 2: Angle dependent S-K edge NEXAFS spectra of Si-PCPDTBT blends after preparation and annealing to 150° and 175°C. Only minor changes after the annealing procedure are visible.

For Si-PCPDTBT/PCBM, only minor changes can be observed after the annealing steps; the annealing up to 175°C has only weak influence on the preferred molecular orientation of the π -conjugated system of Si-PCPDTBT in the blend film. Perhaps even higher temperatures are needed for the phase separation but were not carried out due to the risk of damaging the polymer.

Acknowledgements

For financial support we thank the DFG (CH 132/24-1). ANKA Angströmquelle Karlsruhe is acknowledged for the provision of beamtime. We thank H.-J. Egelhaaf (Belectric OPV) for helpful discussions.

References

- [1] U. Aygül et al. *Molecular orientation in polymer films for organic solar cells studied by NEXAFS*, J. Phys. Chem. C 116 (2012) 4870-4874.
- [2] U. Aygül, H. Peisert, D. Batchelor, U. Dettinger, M. Ivanovic, S. Mangold, M. Förster, I. Dumsch, S. Kowalski, S. Allard, U. Scherf, T. Chassé, *Molecular Orientation in Polymer/Fullerene Blend Films and the Influence of Annealing* (submitted).
- [3] W. Ma, C. Yang, X. Gong, K. Lee, A.J. Heeger, *Adv. Funct. Mater.* 15 (2005) 1617-1622.
- [4] D.E. Motaung et al. *J. Mater. Sci.* 44 (2009) 3192-3197.

X-ray absorption spectroscopy on $(1 - x)\text{Bi}_{1/2}\text{Na}_{1/2}\text{TiO}_3$ - $x\text{BaTiO}_3$ of different composition

F. Pforr, M. Major, W. Donner

Technische Universität Darmstadt, Institute of Materials Science, Alarich-Weiss-Straße 2, D-64287 Darmstadt, Germany

Introduction

Lead-containing ferroelectrics like $\text{Pb}_x\text{Zr}_{1-x}\text{TiO}_3$ should be replaced by lead-free systems in the medium term. The future perspectives of lead-free ferroelectrics have been described by Rödel et al. [1]. One promising candidate is the solid solution of $\text{Bi}_{1/2}\text{Na}_{1/2}\text{TiO}_3$ (BNT) and BaTiO_3 (BT), designated as $(1 - x)\text{Bi}_{1/2}\text{Na}_{1/2}\text{TiO}_3$ - $x\text{BaTiO}_3$ (BNT-100 x BT, BNT-BT), which was first reported by Takenaka et al. [2]. The ferroelectric parameters of solid solutions near the morphotropic phase boundary (MPB) around BNT-6BT were cited as $d_{33} = 125$ pC/N and $\epsilon_{33}^T/\epsilon_0 = 580$ [1]. Considering the strong composition dependence of the ferroelectric properties of BNT-BT, it seems likely that the Ba^{2+} content crucially influences the local Bi^{3+} environment. Previous studies show that the Bi^{3+} ion plays a crucial role for the ferroelectric properties of BNT-based materials. In addition, the local structure around these ions differs from the average crystal structure. Our recent XAS measurements at SUL-X will give us the opportunity to track the evolution of the element-specific local structure across the MPB.

Experimental Description

X-ray absorption spectra of different BNT-BT powders and a comprehensive library of standards were recorded at the SUL-X beamline. The BNT-100 x BT powders used were seven ball-milled single crystals with compositions ranging from BNT-0BT to BNT-10BT, but also three calcined powder samples of BNT-0BT to BNT-16BT. The library of standards included the closely related ferroelectric perovskites BaTiO_3 and PbTiO_3 . All powder samples were measured in the form of polyethylene-based pressed pellets using the sample holders for six pellets. Each spectrum was measured between two and seven times with the aim of ensuring good measurement statistics in the most promising datasets. The position of the beam on the sample was changed every two to three scans. Although burn marks were visible on the pellets, the XAS signal did not change appreciably between single scans.

Twelve EXAFS measurements (ten samples and two standards) were carried out at the Bi-L₃ edge (13269 - 14399 eV) using transmission geometry. After that, seven samples and one standard were measured at the Ti-K edge from 4816 to 5350 eV, three standards to 5518 eV, and two samples to 5946 eV. In addition to the transmission signal, the fluorescence signal was recorded at the same time, using the single photodiode detector. Finally, the Ba-L₂ edges (5474 - 6008 eV) of seven samples and seven standards were investigated in fluorescence and transmission geometries. A test measurement at the Ba-L₃ edge (5097 - 5631 eV) had shown that the chances of obtaining data in reasonable quality would be best at the Ba-L₂ edge due to the less pronounced underlying EXAFS wiggles from the Ti-K edge. The quality of the fluorescence data was good at both edges.

Results

Since the Ti-K and Ba-L₃ edges were recorded in one single scan, these measurements could be used to verify the expected sample compositions with regard to the Ba/Ti ratio. The edge step ratio in BaTiO_3 was used as a standard to which the edge step ratios of the BNT-BT samples were normalised. The results showed conclusively that most of the assumed compositions required a slight correction. The corrected values are used throughout this report.

As can be seen in figure 1, the data show a significant composition dependence of the Bi-L₃ edge spectra and a less pronounced composition dependence of the Ti-K edge. There is no significant composition dependence of the Ba-L₂ edge EXAFS, however. This implies that whereas the addition of Ba^{2+} to

the BNT lattice strongly influences the local environment of the ferroelectrically active Bi^{3+} cations and to a lesser extent also that of the less active Ti^{4+} cations, the local environment of the present Ba^{2+} cations is not changed significantly by the addition of further Ba^{2+} in the given composition range. A homogeneous distribution of Ba^{2+} on a local scale can thus be assumed. Furthermore, it seems likely that the BT doping induces further changes in the local structure of BNT – particularly in the local Bi^{3+} environment – beyond the plain presence of Ba^{2+} in the lattice.

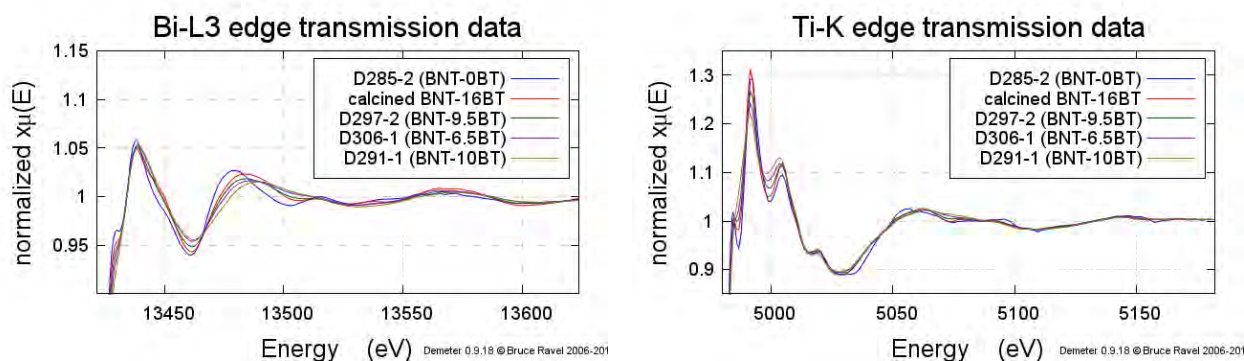


Figure 1: Bi-L₃ edge (left) and Ti-K edge (right) XAS of ball-milled single crystals D285-2 (BNT-0BT), D297-2 (BNT-9.5BT), D306-1 (BNT-6.5BT), D291-1 (BNT-10BT), and calcined BNT-16BT powder.

Conclusion and Outlook

The XAS results qualitatively confirm our expectation that, due to the significant changes of the average structure in the range of low BT concentrations, the changes of the local structure would also be very noticeable. Furthermore, the changes of the local structure seem to be rather localised around the Bi^{3+} cations. We have high hopes of obtaining a proper atomistic model of these structural changes by performing a full EXAFS analysis in the further course of the data evaluation.

In order to achieve this, a model will be constructed for the local cation environments in BNT-0BT based on the known average structure and the information contained in the Ti-K pre-edge structure, as demonstrated by Shuvaeva et al. [3]. The measured standards and the models by Gröting et al. [4] will provide further guidance. Once we have successfully completed an EXAFS fit, ideally by co-refining the Bi^{3+} and Ti^{4+} environments, we will trace the evolution of these environments with increasing BaTiO_3 doping level across the MPB. This will allow us to specify the influence of the BT doping on the local structure of BNT much more precisely than it has been possible previously.

References

- [1] J. Rödel, W. Jo, K. T. P. Seifert, E.-M. Anton, T. Granzow, and D. Damjanovic, *Journal of the American Ceramic Society*, **92** (2009), 1153, DOI:10.1111/j.1551-2916.2009.03061.x
- [2] T. Takenaka, K. Maruyama, and K. Sakata, *Japanese Journal of Applied Physics*, **30** (1991), 2236, DOI:10.1143/JJAP.30.2236
- [3] V. A. Shuvaeva, D. Zekria, A. M. Glazer, Q. Jiang, S. M. Weber, P. Bhattacharya, and P. A. Thomas, *Physical Review B*, **71** (2005), 174114, DOI:10.1103/PhysRevB.71.174114
- [4] M. Gröting, S. Hayn, and K. Albe, *Journal of Solid State Chemistry*, **184** (2011), 2041, DOI:10.1016/j.jssc.2011.05.044

Threading dislocations in GaN studied by synchrotron radiation x-ray topography

S. Sintonen¹⁾, S. Suihkonen¹⁾, H. Jussila¹⁾, A. Danilewsky²⁾, T.O. Tuomi¹⁾

¹⁾Aalto University School of Electrical Engineering, Department of Micro- and Nanosciences, Espoo, Finland

²⁾Albert-Ludwigs-Universität Freiburg, Crystallographic Department, 79104 Freiburg, Germany

Introduction

GaN based optoelectronic and power devices have raised the demand of low defect density native GaN substrates. However, due to the low defect density (as low as $5 \times 10^3 \text{ cm}^{-2}$) in state of the art crystals, defect characterization with conventional methods suitable for higher dislocation density materials is becoming increasingly difficult.

White beam synchrotron radiation x-ray topography (SR-XRT) is a convenient and non-destructive characterization method suited for materials with dislocation density $\sim 10^4 \text{ cm}^{-2}$ and below. This study discusses the back reflection SR-XRT image contrast of threading screw dislocations and threading mixed dislocations in c-plane GaN. Two distinct SR-XRT contrast types were determined corresponding to screw and mixed type dislocations.

Experimental Description

The studied sample was a 350 μm thick free-standing c-plane GaN wafer grown by the ammonothermal method, provided by Ammono S.A. Back reflection topographs were recorded at the white beam TopoTomo beamline synchrotron source ANKA at Karlsruhe Institute of Technology. Images were recorded with the sample tilted 7.5° about the horizontal axis perpendicular to the incident beam and sample to film distance 80 mm.

Results

Figure 1 (a) shows a small part of a symmetric 0006 topograph and simulated threading screw dislocations are shown in figure 1 (b). The excellent resolution and imaging conditions of the ANKA TopoTomo beamline has enabled detailed study of threading dislocation contrast in GaN for the first time. The large white features are caused by threading screw dislocations or groups of threading dislocations with overlapping strain fields. The white feature size depends on the size of the strain field and is the smallest for a single dislocation, labelled 1c in figure 1 (b), and corresponds to a Burgers vector $\mathbf{b} = \mathbf{c}$, where \mathbf{c} is the out of plane lattice vector. The larger features are a result of net Burgers vectors $\mathbf{b} = n\mathbf{c}$, i.e. a superposition of threading screw dislocations spaced within $\approx 5 \mu\text{m}$ from each other.

The smaller circular features with a half moon-like black and white appearance are threading mixed dislocations. Six distinct black to white contrast directions were observed, corresponding to six different edge dislocation components of the mixed dislocation Burgers vector. Examples of all six contrast directions are shown in figure 2. The contrast of mixed dislocation types 1 and 4 are changes with the diffraction vector from $\mathbf{g} = [0006]$ in figure 2 (a) to $\mathbf{g} = [02\bar{2}11]$ in figure 2 (b). The opposite slant of two threading screw dislocations labelled L and R in figure 2 (b) indicates left (L) and right (R) handedness.

Conclusion and Outlook

The synchrotron radiation x-ray topography contrasts of threading screw and mixed dislocations were accurately imaged for the first time. Simulations of threading screw dislocations and threading screw dislocation clusters agree well with experimental images. A detailed study of threading dislocation contrast, including results presented above, has been submitted to the Journal of Applied Physics [1]. The newly gained knowledge of threading dislocation contrast has been utilized in a large area synchrotron radiation x-ray topography study of threading dislocations in GaN, submitted to Applied

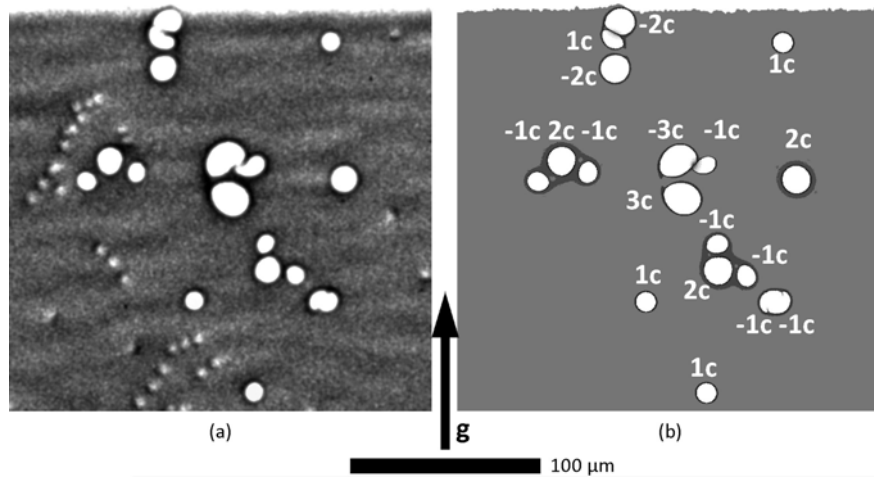


Figure 1: 0006 back reflection (a) and simulated (b) images of individual screw dislocations and screw dislocation clusters. The sign and magnitudes of the Burgers vectors are marked on the simulated image.

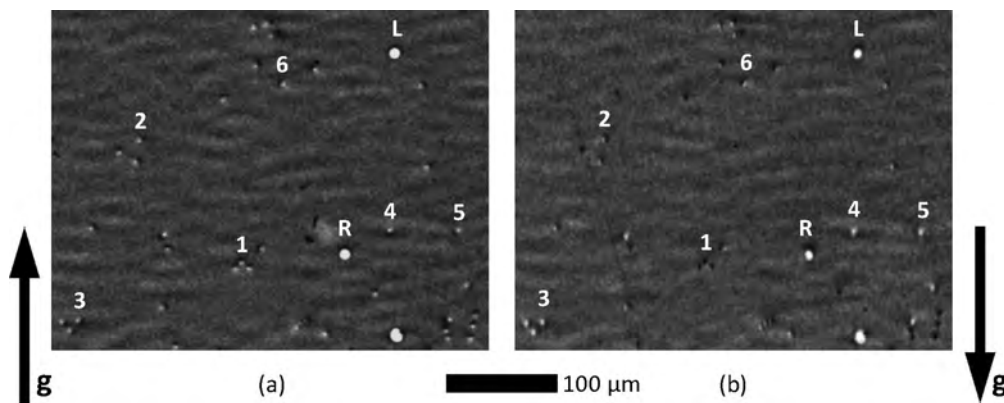


Figure 2: Symmetric 0006 (a) and asymmetric $02\bar{2}11$ (b) topographs of mixed dislocations. Examples of six distinct black to white contrast directions are labelled with numbers 1 to 6. Two elemental screw dislocations marked L and R have opposite slant in the $02\bar{2}11$ topograph due to opposite handedness.

Physics Express [2]. The dislocation types, quantities and distribution were determined by large area topography measurements recorded at the TopoTomo beamline.

Acknowledgements

We acknowledge the Synchrotron Light Source ANKA for provision of instruments at the TopoTomo beamline and we would like to thank T. Müller and H. Schade for excellent assistance. This work was also supported by the Aalto MIDE projects DEGRADE, Aalto AEF project MOPPI, ANKA EU project A2013-021-002621 and the Academy of Finland projects 13138115 and 13251864.

References

- [1] Sakari Sintonen, Mariusz Rudziński, Sami Suihkonen, Henri Jussila, Michael Knetzger, Elke Meißner, Andreas Danilewsky, Marcin Zajac, Turkka O. Tuomi, and Harri Lipsanen. Synchrotron radiation x-ray topography analysis of threading dislocations in GaN. *Submitted to J. Appl. Phys.*, 2014.
- [2] Sakari Sintonen, Sami Suihkonen, Henri Jussila, Andreas Danilewsky, Marcin Zajac, Turkka O. Tuomi, and Harri Lipsanen. Large area analysis of dislocations in ammonothermal GaN by synchrotron radiation x-ray topography. *Submitted to Appl. Phys. Express*, 2014.

Stability domain of alumina thermally grown on Fe-Cr-Al- based alloys exposed to molten Pb

A. Jianu¹, A. Weisenburger¹, R. Fetzer¹, A. Heinzl¹, G. Müller¹, S. Doyle²

¹Karlsruhe Institute of Technology, Institute for Pulsed Power and Microwave Technology, Hermann-von-Helmholtz-Platz 1, D-76344 Eggenstein-Leopoldshafen, Germany

²Karlsruhe Institute of Technology, Institute for Synchrotron Radiation, Hermann-von-Helmholtz-Platz 1, D-76344 Eggenstein-Leopoldshafen, Germany

Heavy liquid metals (HLM), namely lead and lead-based alloys, are under consideration for energy-related applications (e.g. hydrogen production, concentrated solar power and nuclear reactors) due to their low chemical reactivity with oxygen and water in comparison to other liquid metals (such as sodium) and to their beneficial thermal and neutronic properties.

However, HLM compatibility with structural steels, in terms of corrosion and mechanical resistance, causes considerable concern [1]. While at temperatures below 500 °C the corrosion issue can be addressed effectively for both austenitic and ferritic/martensitic steels with the aid of a protective Fe-based oxide scale grown by adding small quantities of oxygen into HLMs [1], at higher temperatures the corrosion control becomes significantly more difficult due to the enhanced solubility of steel alloying elements and the faster kinetic. Therefore passivation films, which are better than those usually found in Fe-Cr systems, need to be developed.

Steels alloyed with strong oxide-forming elements (e.g. Al, Si) were tested in lead and lead-based alloys containing small amounts of oxygen (10^{-8} - 10^{-6} wt.%) in a first attempt to push the temperatures above 500°C. The protection of such steels was provided by a thin, continuous oxide scale, grown during the exposure to oxygen-containing HLM. The key factor consists in the appropriate Al or Si concentration, leading to their selective oxidation.

Unfortunately, in case of Al addition, the required minimum content might negatively affect the mechanical properties of the steel. This is why, for steel protection against corrosion attack above 500 °C, it was proposed to replace the alloying of the steel with Al with the so-called GESA procedure, which was developed at Karlsruhe Institute of Technology and which consists in plasma spraying deposition of Al-containing layers (e.g. Fe-Cr-Al-Y) followed by intense pulsed electron beam processing (GESA - abbreviation of the German facility name **G**epulste **E**lektron**S**trahl **A**nlage).

The objectives of the current study consists in (i) defining the stability domain of alumina, grown as protective scale on Fe-Cr-Al-based alloys, exposed to oxygen-containing liquid lead in the 400-600°C temperature range and (ii) finding an experimental criterion concerning Al/Cr ratio optimization for a selective oxidation of aluminium at the surface of Fe-Cr-Al-based alloys exposed to liquid lead.

The experiments in oxygen-containing stagnant liquid lead at exposure temperatures of 400, 450, 500, 550 and 600°C were performed on samples made of Fe-Cr-Al-based bulk model alloys [2].

The structure of the oxide, grown on the Fe-Cr-Al-based alloy samples showing smooth morphology at the surface, was investigated by GI-XRD at ANKA synchrotron, using two wavelengths: $\lambda=0.11794$ nm and $\lambda=0.12397$ nm. The oxide is either κ -Al₂O₃ transient alumina (PDF card No. 26-31), as can be concluded from the example shown in Fig. 1a (Fe-12Cr-7Al exposed at 550 °C), or a mixture of two alumina polymorphs: κ -Al₂O₃ and θ -Al₂O₃, - Fig. 1b (Fe-16Cr-8Al exposed at 600°C). For identification of the phase constituents in the oxide scale grown on the samples with rough-granular surface, XRD analysis were performed using CuK α radiation ($\lambda=0.15405$ nm).

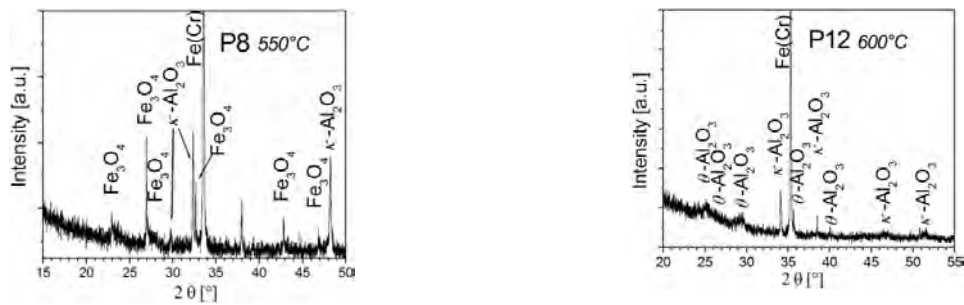


Fig. 1: XRD patterns of (a) P8 (Fe-12Cr-7Al) and (b) P12 (Fe-16Cr-8Al) taken after exposure in oxygen-containing liquid lead at 550 °C and 600 °C, respectively.

The results obtained on Fe-Cr-Al bulk model alloys were combined with the results concerning Fe-Cr-Al-based modified surface layers [3] in order to draw a comprehensive picture of the alumina stability domain in Fe-Cr-Al ternary diagram (Fig. 2).

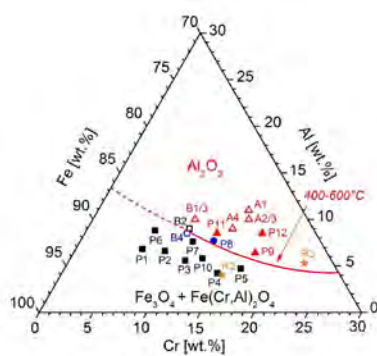


Fig.2 : Oxide "map" for the oxidation of Fe-Cr-Al-based model bulk alloys and modified surface layers exposed to oxygen-containing molten lead, in the temperature range 400-600 °C (■ : alloy sample forming Fe-based oxide scale; ▲ : alloy sample forming alumina scale; △ : modified surface layer sample forming alumina scale; □ : modified surface layer sample forming Fe-based oxide scale; ● : alloy sample forming both Fe-based oxide and alumina scale; ○ : modified surface layer sample forming both Fe-based oxide and alumina scale; ★ : alumina-forming alloys [4,5].

Based on these results an experimental criterion concerning the minimum Al concentration required to form a slowly growing and protective alumina scale on Fe-Cr-Al-based alloys and on modified surface layers was defined:

$$C_{Al} = 15.3 - 0.81 (C_{Cr}) + 0.0156 (C_{Cr})^2 \text{ [wt. \%]}, \quad (1)$$

for chromium content in the range 10-25 wt.% and 400-600°C temperature range.

Acknowledgments

Financial support by GETMAT (FP7-212175), LEADER (FP7-249668) and MatISSE (FP7-604862) projects within the EU-7th Framework program is gratefully acknowledged. The grazing incidence We acknowledge the Synchrotron Light Source ANKA for provision of beamtime at the PDIFF beamline and we would like to thank Stephen Doyle for assistance.

References

- [1] Handbook on Lead-Bismuth Eutectic Alloy and Lead Properties, AEN/NEA Nuclear Energy Agency, OECD, Nuclear Science, 2007, ISBN 978-92-64-99002-9.
- [2] A. Weisenburger, A. Jianu, S. Doyle, M. Bruns, R. Fetzer, A. Heinzl, M. DelGiacco, W. An, G. Müller, J. of Nucl. Mater. 437 (2013) 282-292.
- [3] R. Fetzer, A. Weisenburger, A. Jianu, G. Müller, Corros. Sci. 55 (2012) 213-218.
- [4] S. Takaya, T. Furukawa, G. Müller, A. Heinzl, A. Jianu, A. Weisenburger, K. Aoto, M. Inoue, T. Okuda, F. Abe, S. Ohnuki, T. Fujisawa, A. Kimura, J. Nucl. Mater. 428 (2012) 125-130.
- [5] M. Del Giacco, A. Weisenburger, A. Jianu, F. Lang, G. Mueller, J. Nucl. Mater. 421 (2012) 39-46.

NEXAFS, EXAFS and XRD study of KI one-dimensional crystals within CNTs

A. Zimina¹⁾

¹⁾Karlsruhe Institute of Technology, ANKA, Herrmann-von-Helmholtz-Platz 1, D-76344 Eggenstein-Leopoldshafen, Germany

Introduction

The synthesis and characterization of isolated one-dimensional crystals is a formidable challenge for material chemistry and analysis. The 1D crystals within the carbon nanotubes (CNTs) [1] are protected from the environment and their size is controlled by the diameter of the tubes. The arisen questions are how the electronic properties of the 1D crystals changes compared to the bulk material and if the 1D-crystal interacts with the CNT.

The mixture of singlewall, doublewalls and multiwalls CNTs produced by the CCVD synthesis was filled with KI using the method of the capillary technique [1]. The KI filling yield is moderately good with 20-30% of all observed tubes. The energy dispersive X-ray spectroscopy confirms the filling material as rocksalt-like KI with the number of atomic layers controlled by the internal diameter of the nanotubes. The observed distortions in the K-I distances are assumed to be due to the interaction between the KI crystals with the tube or/and due to the difference in K:I coordination from the bulk crystal.

Experimental Description

The short-order arrangement in the KI 1D crystals inside the CNTs was probed by the X-ray Absorption Spectroscopy at the I L₃ (4557eV) and K K (3608eV) edges with the energy resolution of 0.3 eV in partial fluorescence mode recording the I L_{α_{1,2}} and K K_{α_{1,2}} emission lines using the energy dispersive fluorescence detector. The measurements were carried out under vacuum to reduce the air absorption of photons and to improve the signal quality.

The crystalline structure of the KI crystals was probed by the X-ray Powder Diffraction method using CCD detector in transmission mode.

Results

The near edge absorption fine structure of the I L₃ and K K spectra (XANES) (Fig.1) reflects the iodine 5d/6p and potassium 3d/4p unoccupied states in the conduction band, respectively. These states are sensitive to the changes in the interatomic distances and bond strength between potassium and iodine atoms. The extended X-ray absorption fine structure (EXAFS) (Fig.2) of the spectra is related to the local distribution of atoms around the absorbing ion and reflect the changes in the atom arrangement. The analysis of the I L₃ EXAFS spectrum is difficult due to the rising of the I L₂ absorption structure 295 eV above the L₃ edge.

Changes in the shape of the absorption spectra were observed at both K and I edges and confirmed the redistribution of the unoccupied states which, in turn, hint to the changes in the K-I distances or/and to the formation of the new bond to carbon atoms. The more pronounced changes are observed at the distribution of the K 3d/4p unoccupied states (Fig.1, left): the energy position of the spectral features does not change, the narrow peaks at the low energy part of the band became broader and the its relative intensity are modified compared to the bulk material.

The EXAFS signal of the KI@MWCNTs measured at the K K-edge up to $k=10\text{\AA}^{-1}$ is significantly different from the scattering signal of the KI bulk material: the new feature at the $R=2.2\text{\AA}$ appears additional to the K-I ($R=3.15\text{\AA}$) and K-K($R=4.2\text{\AA}$) related peaks. For the identification of the spectral features further simulation are needed.

The analysis of the diffraction pattern of the KI@MWCNTs confirmed the rocksalt-type of the crystal structure of the KI with the lattice parameters very close to the the KI bulk structure within the available accuracy.

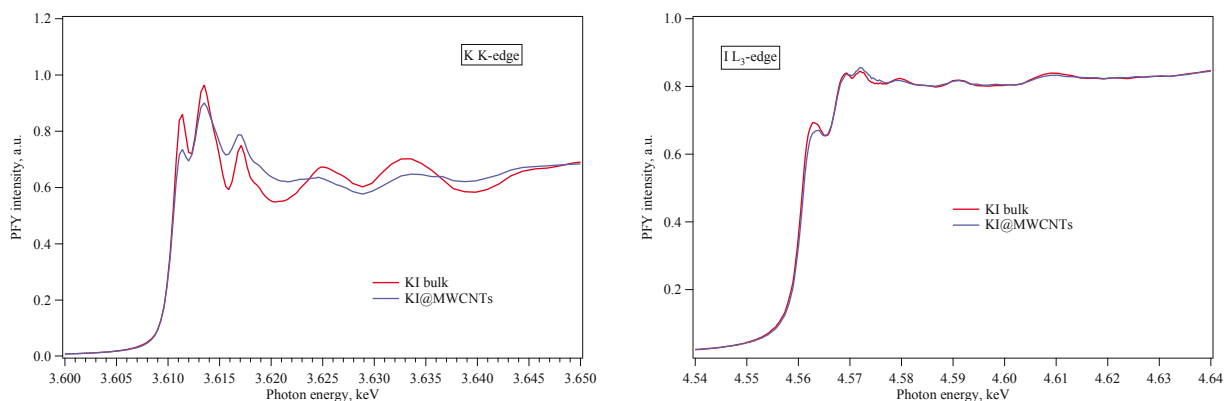


Figure 1: NEXAFS spectra of KI bulk and KI@MWCNTs taken at the K K edge (right) and I L₃ edge (left).

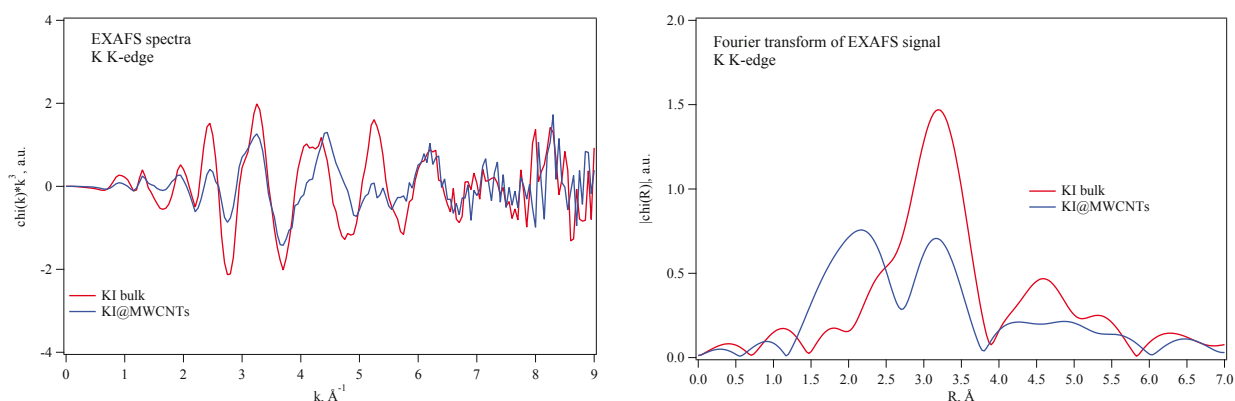


Figure 2: EXAFS spectrum (right) and Fourier transform of the EXAFS signal (left) of KI bulk and KI@MWCNTs taken at the K K edge.

Conclusion and Outlook

The high quality of the NEXAFS and EXAFS spectra allowed to further understand the short-range order arrangement of the K and I atoms in the one-dimensional structures intercalated into carbon nanotubes. From the behavior of the spectra the conclusion about the changes in the electronic states at the K site can be made. Based on XRD measurements, the crystalline structure of KI inside the carbon nanotubes is confirmed to be rocksalt with the lattice parameters close to the bulk material. The present results are in agreement with the results obtained by other methods and will be further compared with the DFT calculations [2].

Acknowledgments

The ANKA Ångströmquelle Karlsruhe is acknowledged for the provision of beamtime and we would like to thank R. Steininger and J. Göttlicher for assistance using SUL beamline.

References

1. J. Sloan et al., Chemical Physics Letters **329**, 61 (2000)
2. Yam et al. Appl. Phys. Lett. **85**, 4484 (2004)

Small Angle Grain Boundaries in Multi-Crystalline Silicon for Photovoltaics

A. N. Danilewsky¹⁾, C. Carl¹⁾

University of Freiburg, Kristallographie, Hermann-Herder-Str. 5, D-79104 Freiburg, Germany

A study of twin-, large-angle- and small-angle grain boundaries in multi-crystalline silicon (mc-Si) is performed on the basis of Electron Backscatter Diffraction (EBSD) and Synchrotron X-ray Topography (SXRT) at TopoTomo beamline, ANKA, KIT [1]. Two nearest neighbour wafers from one directional solidified Si-column are analyzed in order to get information about the evolution of grain boundaries during crystal growth. Thereby, the emphasis was placed on the evolution of one particular and its neighboring grains. In case of straight line $\Sigma 3$ -grain boundaries, no change is observed if the twin plane corresponds to a $\{211\}$ plane. Significant changes are found for non-straight line boundaries during the growth process. Whereas curved $\Sigma 3$ -grain boundaries are formed and eliminated very frequently, the $\Sigma 9$ - and $\Sigma 27a$ -grain boundaries undergo only minor changes.

By means of SXRT, the microstructure of the analyzed grain shows numerous small-angle grain boundaries with angles in the range between 0.003 and 0.02 degrees, corresponding to a theoretical dislocation density in the order of magnitude of $10^7 - 10^8 \text{ cm}^{-2}$. The experiments give evidence that the small-angle grain boundaries with larger angles extend, while the smaller ones vanish during growth.

The topograph in Fig. 1 reveals one small-angle grain boundary extending from the large-angle grain boundary. With respect to its width w , the tilt was calculated to be 0.003° , which corresponds to a dislocation density of about 10^7 cm^{-2} .

The corresponding etch pit pattern can be seen in Fig. 1b. It shows that the small-angle grain boundary found in the topography can be correlated to a line of etch pits of such a high dislocation density that the pits become uncountable. Therefore, it can be concluded that the dislocation clusters – a linear accumulation of dislocations perpendicular to large-angle grain boundaries – proposed from etch pit patterns [2] correspond to small-angle grain boundaries as seen in the $3\ 1\ 11$ topograph in Fig. 1a and reported in more detail elsewhere [3]. Furthermore, the dislocation densities, which are calculated from the tilt values of these small-angle grain boundaries, correlate well with the published values between 10^7 cm^{-2} and 10^8 cm^{-2} for these so-called dislocation clusters [2].

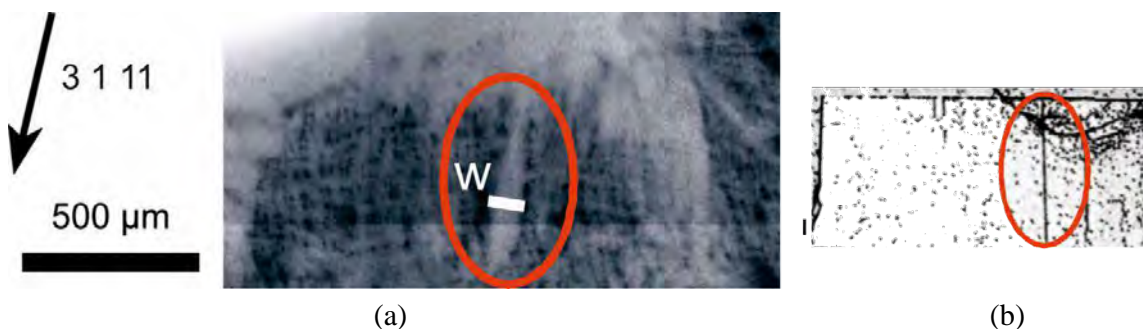


Fig. 1: a) the $3\ 1\ 11$ topograph shows a small angle grain boundary. From the distance “ w ”, a tilt angle of 0.003° and a dislocation density of 10^7 cm^{-2} is estimated. b) The etch pit pattern from the same area shows the correlation between the small-angle grain boundary and the straight aligned etch pits, often referred to as dislocation clusters.

By comparison of the evolution of the grain from wafer 1 to wafer 2 in Fig. 2, significant changes during growth are observed:

The tiny small-angle grain boundaries at pos. 1 joined the largest accumulation of dislocations in wafer 2. In addition, the largest accumulation of dislocations at pos. 2 in wafer 1 has disappeared given the formation of the $\Sigma 3$ -grain boundary. Finally, the other large accumulation of dislocations at pos. 3 in the lower half of the

grain increased drastically and a shift of the lower border of the grain resulted. All in all, the comparison of the pos. 1 to pos. 3 gives evidence that an already large accumulation of dislocations or, more generally, areas of an already high dislocation density become larger during crystal growth.

On the other hand, at pos. 4 the single small-angle grain boundaries at the left side of the grain cannot be identified in wafer 2. It seems that they have moved into the direction of the larger accumulations located to their right during crystallisation, which forms the highest accumulation of dislocations in the centre of the grain in pos.1. This indicates the enlargement of already large accumulations of dislocations is related to the attraction of dislocations in areas of lower dislocation density to areas of higher dislocation density. The tilts of the small angle grain boundaries range from $0.003 - 0.02^\circ$ corresponding to dislocation densities between 10^7 and 10^8 cm^{-2} .

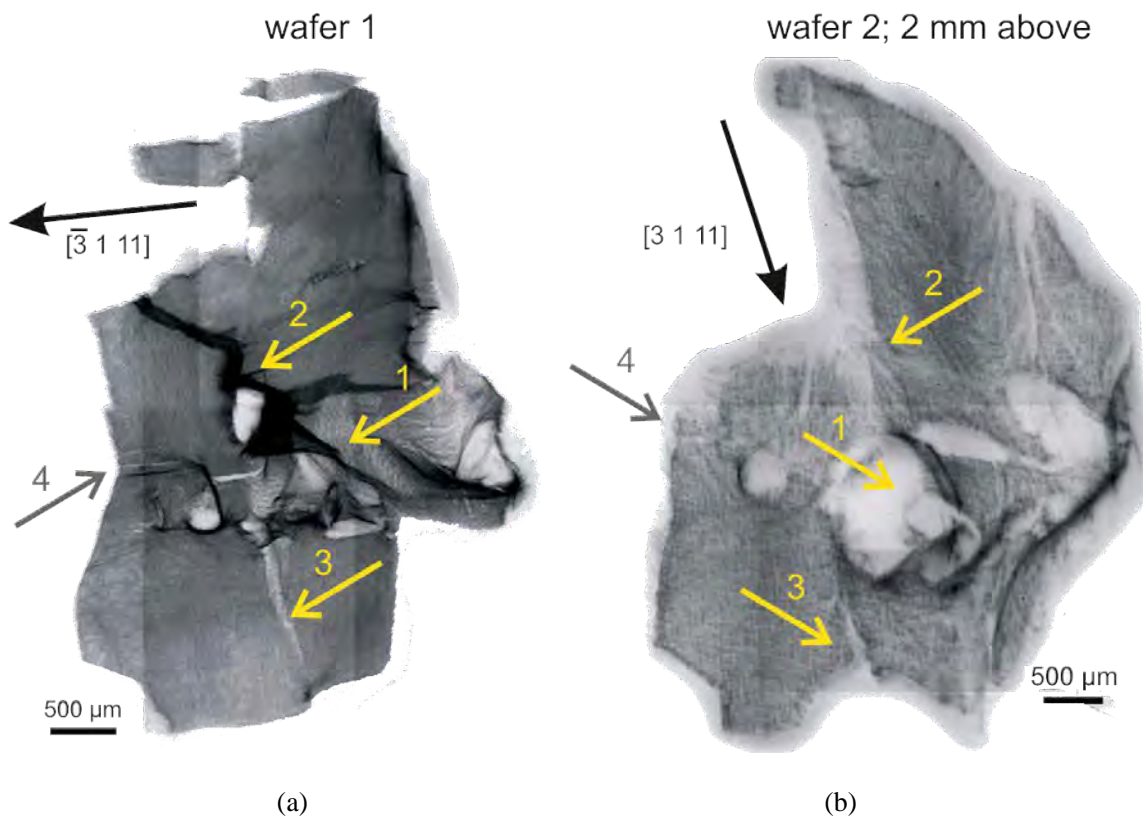


Fig. 2: $3\ 1\ 11$ topographs showing the evolution of small-angle grain boundaries and accumulations of dislocations of one grain during 2 mm of growth from wafer 1 (a) to wafer 2 (b): Larger accumulations of dislocations in positions 1 – 3 extend, while small-angle grain boundaries in pos. 4 vanish.

The study will be continued with *in-situ* experiments using also GaAs because of the intrinsic network of dislocations. In this case it will be much easier to analyse the interaction of the intrinsic dislocation pattern with the new formed thermal slip bands compared to mc-silicon with an highly irregular distribution of intrinsic dislocations. A manuscript with the actual results is submitted to *J. Appl. Cryst.* 2014.

References

- [1] Carl, E.-R., Danilewsky, A. N., Meißner, E., Geiger, T., *J. Appl. Cryst.* (2014), submitted.
- [2] Möller, H.J., Funke, C., Rinio, M. & Scholz, S. (2005). *Thin Solid Films* 487, 179.
- [3] Oriwol, D., Carl, E.-R., Danilewsky, A.N., Sylla, L., Seifert, W., Kittler, M., Leipner, H.S. (2013). *Acta Mat.* **61**, 6903.

Identification of Fe-bearing phases in cements

E. Wieland¹, M. Vespa², R. Dähn¹, B. Lothenbach³

¹ Paul Scherrer Institut, Laboratory for Waste Management, CH-5232 Villigen PSI, Switzerland

² Karlsruhe Institute of Technology, Institute for Nuclear Waste Disposal, Hermann-von-Helmholtz-Platz 1, D-76344 Eggenstein-Leopoldshafen, Germany

³ Empa, Laboratory for Concrete and Construction Chemistry, CH-8600 Dübendorf, Switzerland

Background and objectives

Ordinary Portland cement (OPC) is among the most important cementitious binders currently used worldwide and its production releases large quantities of CO₂ into the atmosphere. This is of great concern in connection with climate change and has led to increasing search for alternative binders to reduce the CO₂ release.

Unhydrated cement mainly consist of the clinker phases, i.e. alite (Ca₃SiO₅), belite (Ca₂SiO₄), aluminate (Ca₃Al₂O₆) and alumino-ferrite (Ca₄(Fe_{1-x}Al_x)₄O₁₀), and minor amounts of added gypsum (CaSO₄·2H₂O) and limestone (CaCO₃). In contact with water the hydration process starts as clinker phases are unstable in water and dissolve slowly while secondary precipitates such as calcium silicate hydrates (C-S-H), ettringite and other hydrate phases form. This process can be modelled thermodynamically to predict the composition of hydrated cement as a function of time and varying cement compositions [e.g. 1]. The predictive capability of the modelling rests strongly on the detailed knowledge of the speciation of the matrix-forming elements such as Fe. In this context, an extensive study is currently being undertaken to identify the Fe-bearing phases in hydrating OPC and alternative binders, i.e. cements containing supplementary materials such as fly ash, slags and silica fume, and synthetic cements using X-ray absorption fine structure (XAFS) spectroscopy [2, this work]. Here, we report on XAFS investigations on aged OPC samples, cementitious mixes containing OPC and silica fume, as well as Al-free synthetic cements that are studied as surrogate for alternative binders.

Sample preparation and XAS measurements

A series of relevant Fe(0, II, III) reference compounds were analysed. The compounds were either commercial products, e.g. Fe(0) powders, or Fe(III)-bearing cement phases that had been synthesized in the framework of earlier studies [2,3], e.g. ferrite (C₂F, C₄AF) [3] and Fe-siliceous hydrogarnets synthesized at room temperature and equilibrated for 1 and 3 years (Fe-Hg-20-1y, Fe-Hg-20-3y) and under hydrothermal conditions and ageing times of 1 year and 5 days (Fe-Hg-80-1y, Fe-Hg-110-5d [3]), and hydrothermally synthesized Al/Fe solid solutions of siliceous hydrogarnet aged for 5 days (Fe-Al-Hg-110-5d [4]). The cement samples comprised strongly hydrated and aged OPC samples, i.e. a sulphate-resisting cement aged at a high water/cement (w/c) ratio (w/c = 1.3) for 30 days (HTS S1) [1] and an OPC sample (w/c = 0.45) prepared in 1958-59 (OPC LTS 15) [2], low-alkali cements containing OPC and silica (LAC and ESDRED cements) aged for 1 year, and synthetic cements with varying compositions of gypsum (0%, 6%, 26%) and calcite (0%, 5%) and two different Fe contents (added as ferrite) aged for 30 days [4]. The cementitious materials were crushed, packed in Plexiglas holders and sealed with Kapton tape. Fe K-edge (7.112 keV) XAFS measurements were conducted at room temperature in transmission (references) or fluorescence mode (cements).

Results

We were able to identify Al/Fe-siliceous hydrogarnet as the only Fe-bearing cement phase in the strongly hydrated and the aged OPC samples (Fig. 1). Comparison of the structural data obtained from data fitting [5] and a Wavelet analysis of the experimental data indicate that in strongly reacted and aged OPCs, that is in cement systems where the hydration process is complete, Al/Fe-siliceous hydrogarnet is the thermodynamically most stable phase. In the latter cement phase, Al(III) is partially replaced by Fe(III) in the hydrogarnet structure.

For the synthetic cements we observed the presence of mainly ferrite (C₂F) as Fe-bearing phase, suggesting that only very small amounts of secondary Fe-bearing cement phases had formed during the hydration process in the given time period (Fig. 2). In the cement systems containing silica fume as supplementary material (ESDRED, LAC) ettringite was found to be the main Fe(III)-bearing cement phase as thermodynamic modelling suggests absence of Al/Fe-siliceous hydrogarnet.

Fig. 1: Fe K-edge experimental spectra of the cement paste samples OPC LTS 15 and HTS S1 along with the hydrogarnet reference samples for a) k^3 -weighted, normalized, background-subtracted EXAFS spectra; b) Radial Structure Functions (modulus and imaginary parts) obtained from the Fourier transform of the EXAFS spectra; c) experimental (solid line) and theoretical (dashed line) k^3 -weighted EXAFS function of the Fourier-backtransform spectra (range: $R+\Delta R=1-4.4$ Å). Structural parameters are reported elsewhere [5].

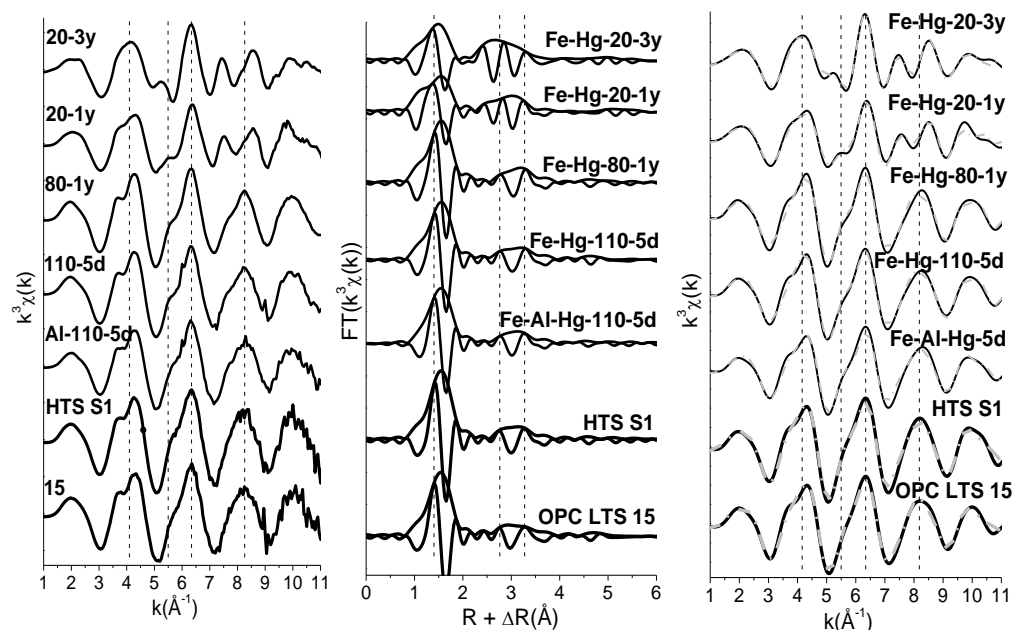
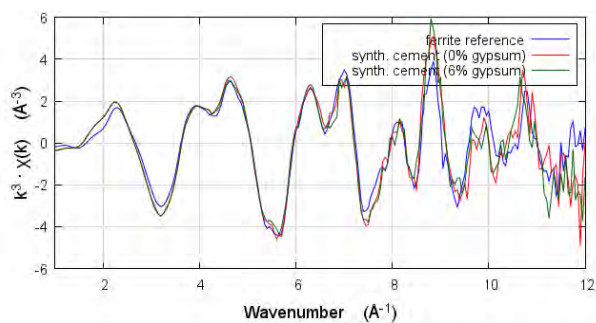


Fig. 3: Comparison of the Fe K-edge EXAFS spectra of the synthetic cements with the reference spectra (ferrite)



Conclusion

Al/Fe-bearing siliceous hydrogarnet was identified as the thermodynamically stable Fe-bearing phase in fully hydrated and aged OPC. This phase, however, was not observed in blended cement systems containing silica fume as supplementary materials and in synthetic cements. There, the Fe speciation is dominated by Fe(III) bound in ettringite in the OPC/silica mixtures and Fe(III) bound to ferrite in the synthetic Al-free cements.

References

- [1] Lothenbach, B., Wieland, E., 2006. A thermodynamic approach to the hydration of sulphate-resisting Portland cement. *Waste Manage.* 26, 706-719.
- [2] Dilnesa, B.Z., Wieland, E., Lothenbach, B., Dähn, R., Scrivener, K.L., 2014a. Fe-containing phases in hydrated cements. *Cem. Concr. Res.* 58, 45-55.
- [3] Dilnesa, B.Z., Lothenbach, B., Renaudin, G., Wichser, A., Kulik, D., 2014b. Synthesis and characterization of hydrogarnet $\text{Ca}_3(\text{Al}_x\text{Fe}_{1-x})_2(\text{SiO}_4)_y(\text{OH})_{4(3-y)}$. *Cem. Concr. Res.* 59, 96-111.
- [4] Dilnesa, B.Z., 2012. Fe-containing hydrates and their fate during cement hydration: Thermodynamic data and experimental study, Thesis No. 5262, Swiss Federal Institute of Technology, Lausanne.
- [5] Vespa, M., Wieland, E., Dähn, R., Lothenbach, B., 2014. Identification of the thermodynamically stable Fe-containing phase in aged cement pastes. *Chem. Mater.* (submitted).

Acknowledgements

Dr. S. Mangold from the XAS beamline is gratefully acknowledged for his help with the measurements. Thanks are extended to Prof. K. Scrivener and Dr. B. Dilnesa for providing the aged pastes and reference materials, respectively, and to D. Kunz for preparing the EXAFS samples. Partial financial support was provided by the National Cooperative for the Disposal of Radioactive Waste (Nagra), Switzerland.

Relationship between the chemical structure of low band gap polymers and self-organization properties

M. Ivanovic¹⁾, U. Aygöl¹⁾, U. Dettinger¹⁾, A. Tournebize¹⁾, D. Batchelor²⁾, S. Mangold²⁾, H. Peisert¹⁾, T. Chassé¹⁾

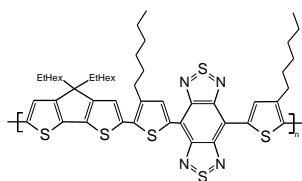
¹⁾ Institut für Physikalische und Theoretische Chemie, Universität Tübingen, 72076 Tübingen, Germany

²⁾ Karlsruher Institut für Technologie, Institut für Synchrotronstrahlung (ISS), 76021 Karlsruhe, Germany

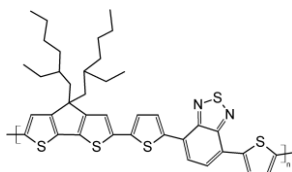
Introduction

Recent research efforts related to organic photovoltaics are mainly focussed either on the increase of the efficiency or the improvement of the stability of devices. An approach to improve the efficiency of donor-acceptor based bulk heterojunction (BHJ) organic photovoltaic cells is the use of low band gap (LBG) polymers as donor materials. The lower optical band gap results in an improved efficiency essentially caused by an increased absorption in the visible and near infrared regions of the solar spectrum. As a consequence several research groups are focused on the synthesis of new LBG polymers; however, a reliable prediction of the arrangement of these materials in thin films is often difficult. On the other hand, the morphology and ability for self-organization affects several basic processes such as the energy (exciton) transfer, charge separation and charge transport. These parameters are significantly influenced by the processing conditions including pre- and post-processing treatments of the film. In particular the thermal post-annealing leads to changes of optical properties and to phase separation of the blend film; an optimal domain size of BHJ solar cells in the order of a few 10 nm can be achieved.[1] We have shown that NEXAFS (Near Edge X-Ray Absorption Fine Structure) is an excellent technique to investigate the bulk orientation of polymers in thin films and in particular for blend systems with small domain sizes.[2-3]

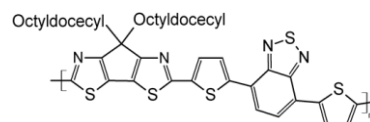
The aim of the present work is the investigation of such relations between the chemical structure of the LBG polymer and the ordering in the blend material. We study the LBG polymers PCPDTTBTT (1), PCPDTTBTT (2) and PCPDTzTBTT (3) and their blends (1:1) with the fullerene derivative PCBM using NEXAFS (see Fig. 1). Compared to the more common LBG polymer PCPDTBT and related polymers recently studied [3], the LBG polymers (1) and (2) contain additional (hexyl-)thiophene groups. It could be expected that these modifications improve the tendency for self-organization, since poly-3-hexyl-thiophene shows very good film forming properties.



PCPDTTBTT (1)



PCPDTTBTT (2)



PCPDTzTBTT (3)

Experimental details

Polymer films were prepared ex-situ by doctor blade casting in a glovebox with N₂-atmosphere and stored under well-defined ambient conditions. The film thickness was about 50nm, determined by atomic force microscopy (AFM) and also UV/VIS spectroscopy. Annealing was carried out in dark and under N₂-atmosphere. NEXAFS experiments were carried out at the XAS beamline. The beamline energy resolution at the sulfur edge is circa 300 meV and displays a polarization degree of > 0.95. X-ray absorption spectra were measured in fluorescence yield mode in order to avoid an increased surface sensitivity.

Results

First, we discuss briefly the influence of the introduction of additional thiophene groups in the polymer structure on self-organization properties at the example of as prepared PCPDTTBTT and PCPDTBBT in Fig. 1. The feature at the lowest photon energy, denoted B1, is related to the benzothiadiazole subunit, whereas T1 can be assigned to thiophene.[3] Clearly visible from Fig. 1 is the more distinct angular dependency of both features in the case of PCPDTTBTT indicating a preferred edge-on orientation and possibly a higher degree of ordering. After a post-deposition annealing of the sample, the angular dependence of the intensities is even stronger, in particular in the case of blends (not shown).

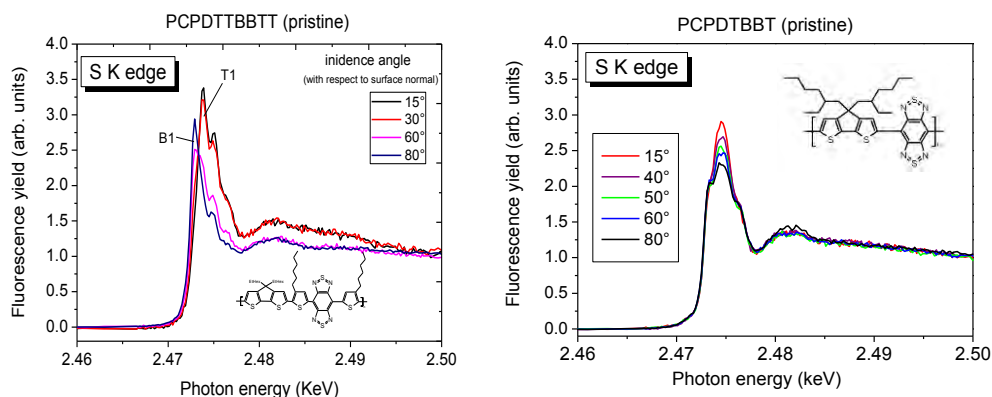


Fig.1: Series of S1s excitation spectra of a) PCPDTTBTT and b) PCPDTBBT [3] films on ITO as a function of the angle θ between the sample normal and the electric field vector of the p-polarized synchrotron light.

Also S-K absorption spectra of PCPDTzTBTT show a distinct angular dependence and thus a high degree of orientation as illustrated in Fig 2 for the prominent angle of 15° . The effect of post-annealing however results in a complete change of the orientation visible in Fig. 2 as a clear change of the B1/T1 intensity ratio. In the case of a blend this behaviour is less pronounced.

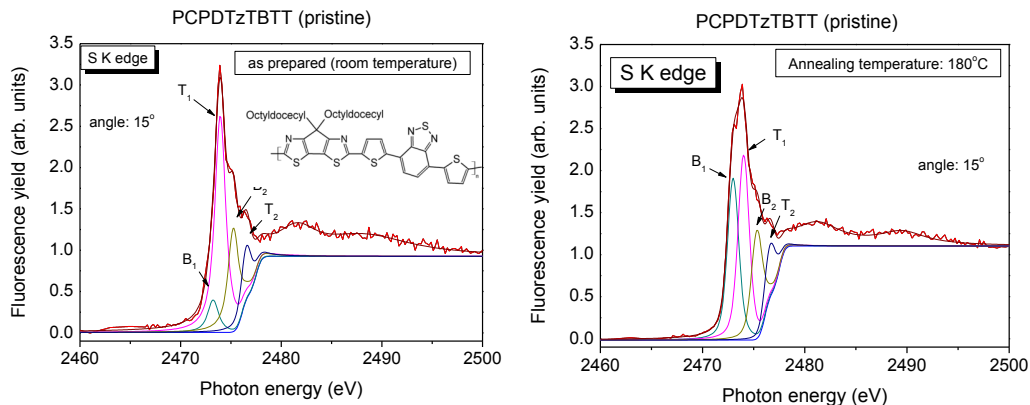


Fig.1: S1s excitation spectra of PCPDTzTBTT as a function of the annealing temperature at $\theta=15^\circ$.

Acknowledgements

For financial support we thank DFG (CH 132/24-1). ANKA Angströmquelle Karlsruhe is acknowledged for the provision of beamtime. We thank the group of Prof. Scherf (Wuppertal) for the synthesis of the polymers.

References

- Kohn, P.; Rong, Z.; Scherer, K. H.; Sepe, A.; Sommer, M.; Müller-Buschbaum, P.; Friend, R. H.; Steiner, U.; Hüttner, S., *Macromolecules* **2013**, *46* (10), 4002-4013.
- Aygül, U.; Batchelor, D.; Dettinger, U.; Yilmaz, S.; Allard, S.; Scherf, U.; Peisert, H.; Chasse, T., *J Phys Chem C* **2012**, *116* (7), 4870-4874.
- Aygül, U.; Peisert, H.; Batchelor, D.; Dettinger, U.; Ivanovic, M.; Tournebize, A.; Mangold, S.; Förster, M.; Dumsch, I.; Kowalski, S.; Allard, S.; Scherf, U.; Chassé, T., *Solar Energy Materials and Solar Cells* **2014**, *128* (0), 119-125.

Real time investigation of thin films growth in sputter deposition processes

P. Walter^{1),2)}, A-C Dippel¹⁾, U. Klemradt²⁾

¹⁾Deutsches Elektronen-Synchrotron DESY, Notkestr. 85, 22607 Hamburg, Germany

²⁾2nd. Institute of Physics B, RWTH Aachen University, 52074 Aachen, Germany

Introduction

Sputter deposition is a versatile and industrially important deposition technique for thin films. There is an increasing demand for tailoring the characteristics of thin film ferroelectric materials for the needs of the semiconductor industry. The actual film properties are largely determined by the sputtering parameters such as gas, pressure conditions and power settings [1-3]. Depending on the particular application of the layers, for example tuneable capacitors, non-volatile random access memories, electro-optical devices or thermistors [4-8], the electrical properties of the thin films have to be tuned accordingly to achieve optimum performance. Inherently, these macroscopic parameters are influenced by the microstructure and crystallographic state of the films. Therefore, in the context of miniaturisation of microelectronic circuits and devices and the necessary adaption of film thickness and grain size, the deposition process has to be studied *in situ*. These *in situ* investigations of ferroelectric thin films during sputter deposition is the goal of this experiment. We have therefore developed an online sputtering chamber to determine the influence of the processing parameters on nucleation, crystallisation and microstructure evolution during film growth of Barium Titanate (BaTiO_3) layers. This requires a deep understanding of the processes involved in sputtering of thin films which can be accomplished best via *in situ* time resolved X-ray powder diffraction (XRPD).

Experimental Description

We received four days of beam time at the PDIFF beam line. The energy was adjusted to 17keV and the focus was set to $400\mu\text{m}$ times $500\mu\text{m}$. It took half a day to mount and align the chamber on the heavy-duty 3-circle powder diffractometer. As detector the Princeton CCD-camera was chosen and chamber is designed to do the measurements in grazing incidence geometry. However, taken into account the pumping procedure to get an appropriate vacuum, the deposition process of one hour to reach a film thickness of 150nm, the heating and cool down period of the sample of 1 hour also breaking the vacuum for sample changing, it took at least 4 hours for measuring one sample. During the whole process, from the start of the deposition to the final annealed thin film, we took diffraction patterns with 2sec to 10sec exposure time per frame. An important part of this research is the investigation of the kinetics and dynamics during the crystallisation process and also the sputter parameter dependence of the crystallisation behaviour. During this beam time the focus was set on different wafer materials and the deposition behavior at different substrate temperatures during deposition. We measure SiO_2 at four different temperatures (100°C, 200°C, 300°C and 400°C) with a final annealing up to 750°C and Si at 200°C, 300°C and 400°C and also Quartz and MgO at 400°C also with a final annealing up to 750°C.

Results

The XRPD- pattern taken during the deposition at different temperatures shows quite different structural properties of the layers. No microcrystallisation peak can be detected if the annealing temperature is lower than 300°C. It also shows a different behavior in the crystallisation with the different wafer materials. For the first time one was able to see the whole thin film production from the first atomic layer to the entire crystallised final film. Figure 1a shows the growth of the amorphous film deposited at 400°C and the microcrystallisation of the peaks 110 and 111. Figure 1b shows the crystallisation while annealing the wafer up to 750°C.

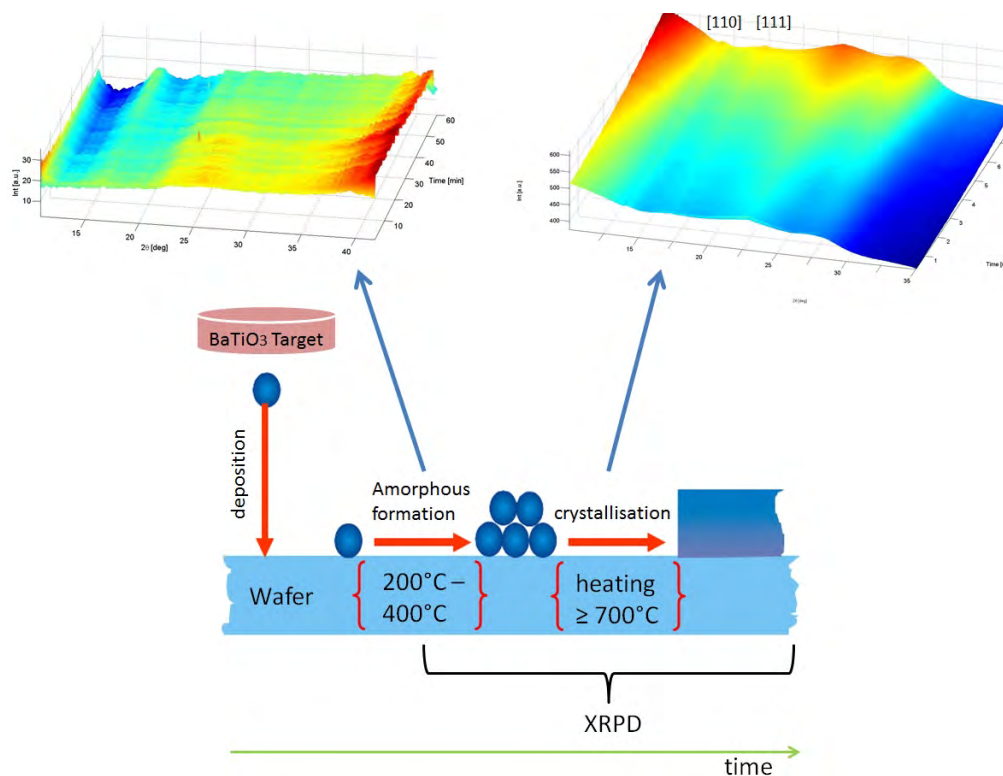


Figure 1: Principle measurement method and some selected results. Patterns were taken at the PDIFF beam line with 17keV and 10sec per pattern. BaTiO₃ were deposited on SiO₂ with the final thickness of 150nm. Figure 1a. shows the growth of the amorphous BaTiO₃ peak deposited at 400C. Figure 1b. shows the crystallisation of BaTiO₃ at 700C. The broad peaks are due to thermal effects of the SiO₂ wafer. Figure 1c. shows the basic schema of the deposition and crystallisation process.

Conclusion and Outlook

The data analysis is still in progress. For additional characterisation of the films prepared during the beam time, we will perform surface, microscopic and electrical investigations. Anyhow, a publication of the new chamber and all its opportunities and its flexibility will be submitted soon, also with some selected results from the measurement from the PDIFF beam line.

Acknowledgements

The ANKA Ångströmquelle Karlsruhe is acknowledged for the provision of beamtime, and we would like to thank Stephen Doyle for assistance using the PDIFF beam line.

References

- [1] Shih, W.-C., Chiang, M.-H. (2009). Journal of Materials Science: Materials in Electronics, 21(8), 844848. [2] J. H. Kim, S. Hishita, Journal of Materials Science 30, 4645-4650 (1995). [3] K. Uchino, N. Lee, T. Toba, N. Usuki, H. Aburatani, Y. Ito, J. Ceram. Soc. Jpn. 100 1091 (1992). [4] A. C. Dippel, T. Schneller, J. Dornseiffer, R. Waser, J. Sol-Gel Sci. Technol. 57 (2011) 36. [5] Hennings, M. Klee, R. Waser, Adv. Mater. 3 (1991) 334. [6] J. Scott, C. DeAraujo, L. McMillan, H. Yoshimori, H. Watanabe, T. Mihara, M. Azuma, T. Ueda, T. [7] Ueda, D. Ueda, G. Kano, Ferroelectrics 133 (1992) 47. [8] D. Hennings, M. Klee, R. Waser, Adv. Mater. 3 (1991) 334.

Mechanical behavior and microstructural analyses of ultra-high strength pearlitic steel wires: new insights on the strengthening mechanism and the cementite dissolution during cold drawing of the pearlitic steel wires.

S. Djaziri¹⁾, C. Kirchlechner¹⁾, G. Dehm¹⁾

¹⁾ Max-Planck-Institut für Eisenforschung GmbH, Max-Planck-Straße 1, D-40237 Düsseldorf, Germany

Objective and expected results

The experiment was dedicated to the investigation of the mechanical properties and microstructural changes of high strength pearlitic steel wires. The pearlitic steel wires are described by a fine lamellar microstructure of two phases; a soft ferrite matrix containing hard cementite lamellae. Pearlitic steel is of interest for many engineering applications such as tire cords, conveyors, springs, hoses and bridge cables. Indeed, they exhibit a strong tensile strength through the cold drawing process, where recently a strength of more than 6 GPa has been realized [1]. Special attention is paid to the strengthening mechanism where the measurements at ANKA will clarify whether the high tensile strength is due to a refinement of the microstructure or from a carbon supersaturation of the matrix.

Results and the conclusions of the study

Our aimed experiment based on the PDIFF beamline of the ANKA synchrotron source is ideally suited for such a study since it allows characterizing the internal structure of cold-drawn pearlite with the aimed resolution in time and strain. The samples studied in this work were pearlitic steel wires of eutectoid composition (0.81 wt.% C) provided by Nippon Steel Corporation. The samples were cold-drawn at different strains, covering a true strain range from $\varepsilon=0$ to $\varepsilon=5.5$. The details of these samples are listed in Tables 1.

The experiments consisted in *ex-situ* measurements for microstructural characterization of the cold-drawn steel wires. Diffraction patterns for both profile analysis and residual stress analysis were collected using an area detector (Princeton CCD-camera) mounted on the 4-circle kappa goniometer of the PDIFF beamline. The energy was set to 16 keV and the incident beam size was 0.4 mm (H) \times 1 mm (V), (FWHM). The residual stress analysis was carried out using the $\sin^2\psi$ method. This set-up allows for a precise determination of the lattice strain where we could reach a strain resolution of 10^{-4} .

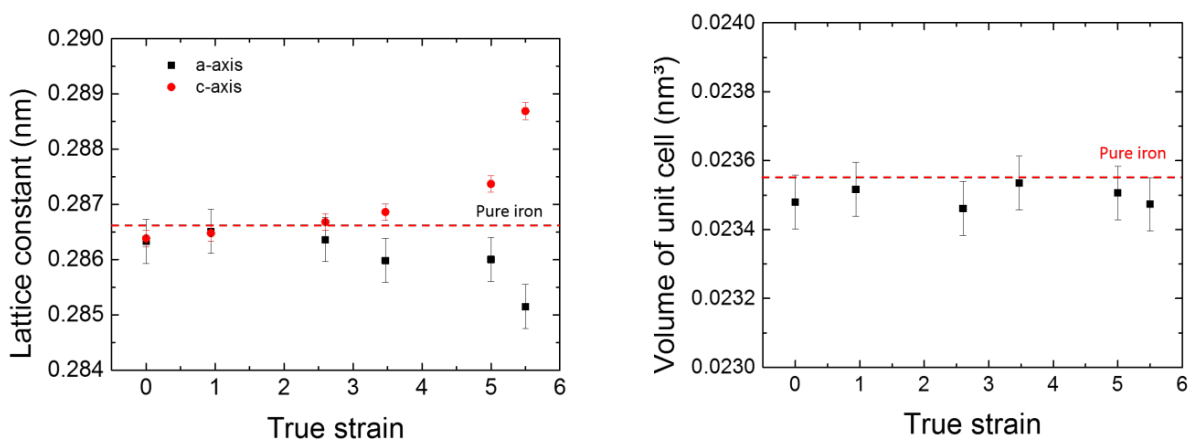
It was found that the apparent plastic deformation of the steel wires up to high strain levels is controlled by the residual stresses present in the wire which is almost 30% of the obtained tensile strength. The analysis of the ferrite diffraction peaks revealed that the unit cell of ferrite transformed from the BCC structure to the BCT structure with an unchanged volume of the lattice cell (Fig.1). The obtained data shows a very good agreement with the study of Taniyama et al. [2]. The microstructural changes can be related to the enrichment of carbon atoms in the ferrite matrix during progressive severe deformation.

Moreover, *in-situ* tensile tests were performed in order to determine the feasibility of using our in-house tensile machine. The aim of these tests was to characterize the load partition between the ferrite matrix and the cementite phase. Therefore, diffraction patterns were recorded *in-situ* during a step by stepwise tensile tests in transmission geometry allowing the use of the $\sin^2\phi$ method [3]. The straining set-up was successfully mounted in the PDIFF beamline. However, the studied wires were difficult to handle. Thus, the set-up was changed to accommodate different wires especially the thinnest ones ($\sim 20 \mu\text{m}$) that exhibit very high tensile strength ($\sim 7 \text{ GPa}$).

In summary, the experiment was very successful. Nevertheless, additional experiments are needed to determine the stress distribution between the ferrite matrix and the cementite phase during in-situ experiments using the new set-up. We are actually preparing a paper for publication of these latter results.

Table 1: Summary of strain and tensile strength of the steel wires of eutectoid composition.

Diameter (mm)	True strain	Tensile strength (MPa)
1.70	0	1448
1.07	0.94	2000
1.50	2.6	-
0.30	3.47	3275
0.05	5	4323
0.058	5.5	-

Fig. 1: Estimated lattice parameters along a axis and c axis (left) and cell volume of α -ferrite lattice as a function of the drawing strain (right), the dashed line corresponds to pure iron. (Results for the eutectoid composition).

Acknowledgements

We would like to thank Suzuki Metal Industry Co., Ltd. and Nippon Steel Corporation, for providing the cold drawn specimens. We also thank ANKA for provision of synchrotron radiation facilities and specially Dr. Stephen Doyle from PDIFF/ANKA for his excellent support during the beamtime.

References

- [1] Y.J. Li, P. Choi, S. Goto, C. Borchers, D. Raabe, R. Kirchheim, Evolution of strength and microstructure during annealing of heavily cold-drawn 6.3 GPa hypereutectoid pearlitic steel wire, *Acta Materialia*, 60, 4005-4016 (2012).
- [2] A. Taniyama, T. Takayama, M. Arai, T. Hamada, Structure analysis of ferrite in deformed pearlitic steel by means of X-ray diffraction method with synchrotron radiation, *Scripta Materialia*, 51, 53-58 (2004).
- [3] J. Böhm, P. Gruber, R. Spolenak, A. Stierle, A. Wanner and E. Arzt, Tensile testing of ultrathin polycrystalline films: A synchrotron-based technique, *Rev. Sci. Instrum.*, 75, 1110-1119 (2004).

In-situ Radiography of an Emulsification Process

T. Farago¹⁾, T. Dos Santos Rolo¹⁾, A. Hensel²⁾, M. Kraut²⁾

¹⁾ Karlsruhe Institute of Technology, Institute for Photon Science and Synchrotron Radiation, Hermann-von-Helmholtz-Platz 1, D-76344 Eggenstein-Leopoldshafen, Germany

²⁾ Karlsruhe Institute of Technology, Institute for Micro Process Engineering, Hermann-von-Helmholtz-Platz 1, D-76344 Eggenstein-Leopoldshafen, Germany

Experimental results

The experiment was a continuation of the one from previous year with modifications made to the setup. We used the emulsification device optimized for X-ray radiation. Thanks to the modification we were able to observe the process with 10 500 frames per second. Moreover, we used remote flow rate adjustment, so we were able to use the beam time more efficiently. We observed the inlet and outlets of the device only because the tremendous speed achieved in the middle part of the device due to its small diameter made it unfeasible to temporally resolve any process inside. However, we were able to observe the jet formation and deceleration in the outlet giving rise to droplet formation. Moreover, the formation at the very end of the outlet was temporally well resolved.

Due to the flow rate instability, which is a hardware-related problem, we were not able to make a solution with a concentration of oil and emulsifier in such a way that the droplets we observed wouldn't be too large. The flow was either too slow to let the solution inside the device or too fast, sometimes we experienced bursts of the oil which were too fast for our temporal resolution.

Given the fact that we observed the droplet formation we conclude that the process we expected happens at specific combinations of water/oil/emulsifier concentrations and flow speeds. However, we were not yet able to analyze the resulting videos due to flow instabilities.

Future plan

We will use different, more precise pumps in order to provide a steady flow in experimental setup. Moreover, we will implement flow rate sensors in order to measure the current flow rate with high precision which will help to match the measurement and image data and verify the experimental outcome.

Moreover, we would like to optimize the imaging setup in such a way that we would be able to record videos at more than 50 000 FPS in order to observe the process closer to the middle small-diameter channel.

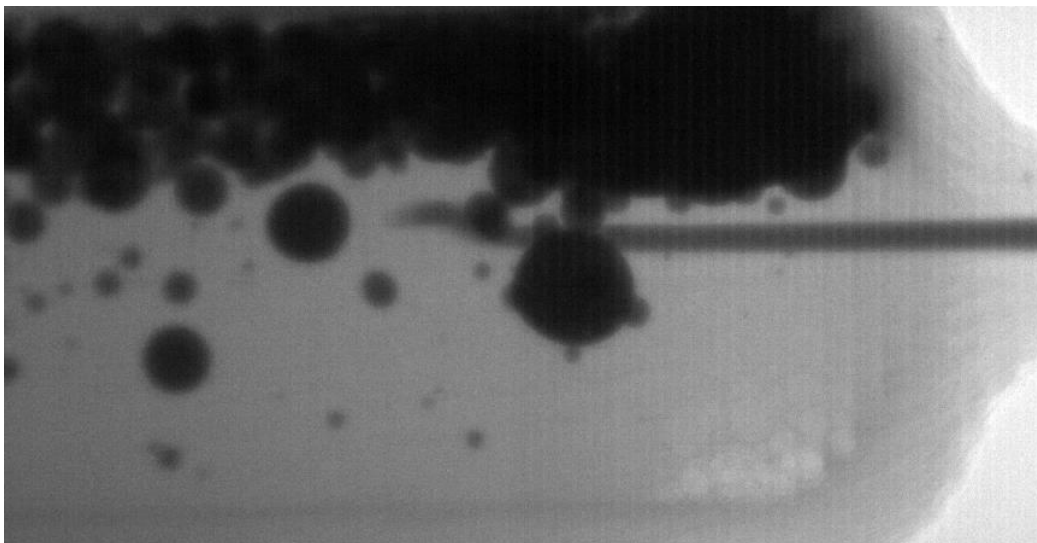


Figure 1: Outlet of the emulsifier with a jet coming from the middle small diameter part of the device

Crystallographic Characterisation of Large Paramagnetic Aggregates of Transition-Metal Cations

Christopher E. Anson¹⁾, Gernot Buth²⁾, Annie K. Powell¹⁾

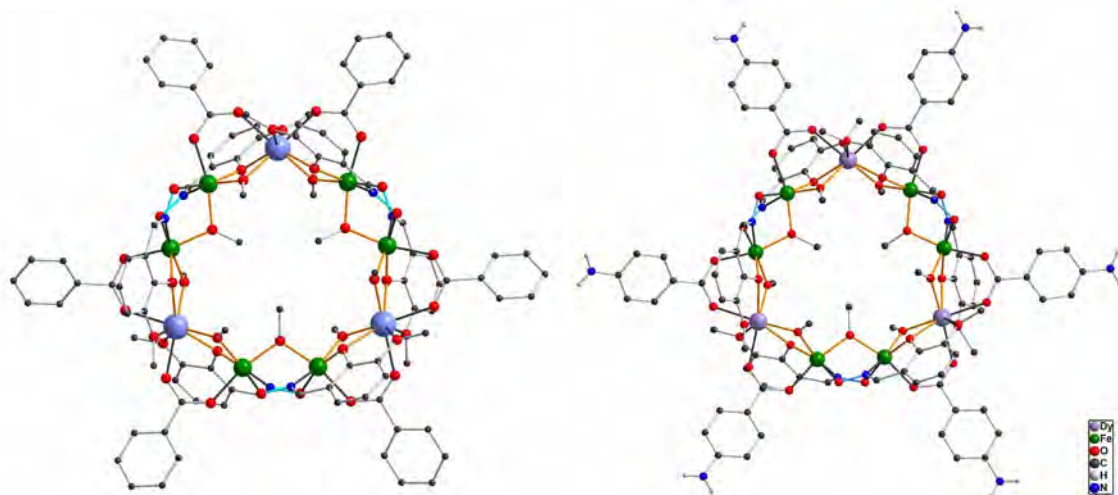
¹⁾ Karlsruhe Institute of Technology, Institut für Anorganische Chemie, Engesserstr. 15, D-76131 Karlsruhe

²⁾ Karlsruhe Institute of Technology, Institut für Synchrotronstrahlung, Hermann-von-Helmholtz-Platz 1, D-76344 Eggenstein-Leopoldshafen

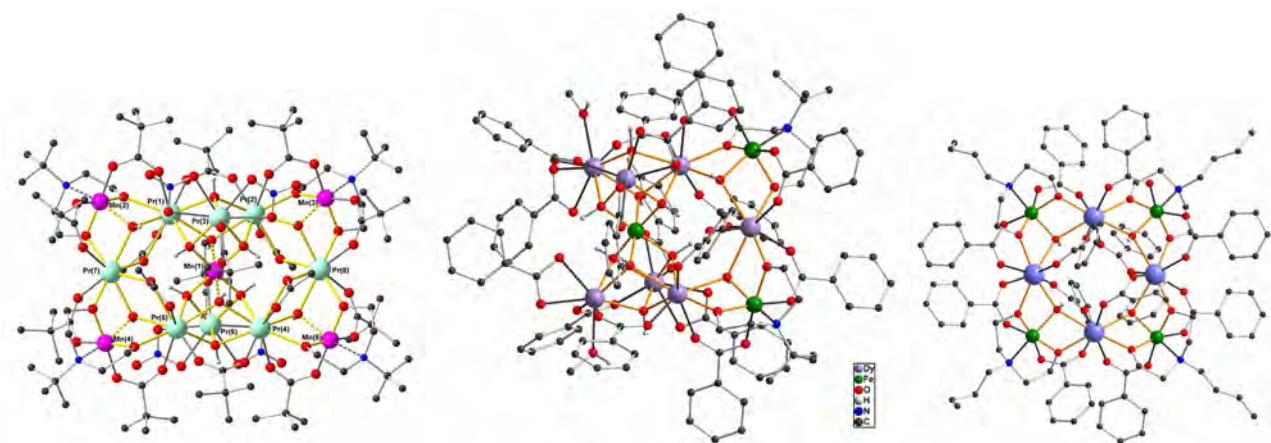
We have synthesised a series of isostructural nonanuclear ring-like complexes with formulae $[\text{Fe}^{\text{III}}_6\text{Ln}^{\text{III}}_3(\mu\text{-OMe})(\text{vanox})_6(\text{O}_2\text{CAR})_6]$ for all the heavier lanthanides ($\text{Ln} = \text{Tb} - \text{Lu}$). Such symmetrical single-stranded rings with an odd number of metal centres are particularly unusual. We have been investigating the changes in magnetic properties on varying the lanthanide ion; the Fe_6Dy_3 compound in particular shows good Single-Molecule Magnet (SMM) behaviour. It was therefore unfortunate that the dysprosium analogue typically gives twinned crystals that diffract rather poorly – it could be shown that the compound was isostructural to the others, but a structure of high precision was needed for theoretical calculations of the magnetic behaviour. Very small single crystals were eventually obtained, and these needed the high brilliance X-rays of the SCD beamline to be measured.

We are also investigating the effects on the magnetism of using differently *para*-substituted benzoate ligands. We have previously shown for a series of tetranuclear Fe_2Dy_2 complexes that the SMM behaviour changes significantly when electron-withdrawing or accepting substituents (i.e. with different Hammett coefficients) are present on the ring, and wish to extend this investigation to the larger Fe_6Dy_3 rings, since these have three-fold symmetry and a simple topology. The two carboxylate oxygens coordinating to each Dy^{3+} ion are oriented *cis* to each other, so changes in electron density on these oxygens will alter the symmetry of the ligand field and change the nature of the Dy^{3+} single ion anisotropies. In addition to the parent benzoate complex, we have measured the crystal structures of Fe_6Dy_3 analogues with amino, nitro (two different crystal modifications) and *t*-butyl substituents on their benzoate ligands on SCD. These and others are currently being studied by a combination of ac-magnetic susceptibility and ^{57}Fe Mößbauer spectroscopy.

It would also be of interest to obtain an analogous structure with Gd^{3+} , as an odd-nuclearity ring of magnetically-isotropic metal ions would be expected to show interesting spin-frustration effects. With benzoate as ligand, however, Tb^{3+} was the lightest lanthanide for which such rings could be obtained, but with the electron-poor *p*-nitrobenzoate it has finally proved possible to crystallise a Fe_6Gd_3 ring, but the crystals were again very small and could only be measured at ANKA. This ring is under magnetic investigation.



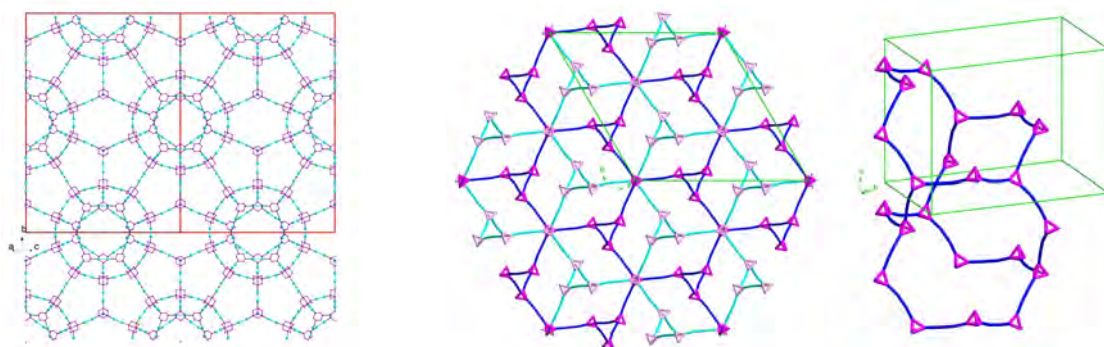
Structures of $[\text{Fe}_6\text{Dy}_3(\mu\text{-OMe})_9(\text{vanox})_6(\text{benzoate})_6]$ (left) and $[\text{Fe}_6\text{Dy}_3(\mu\text{-OMe})_9(\text{vanox})_6(\text{benzoate})_6]$ (right); organic H-atoms omitted for clarity).



Structure of $[\text{Fe}_3\text{Dy}_7(\mu_3\text{-OH})_{10}(\text{tbdea})_2(\text{benz})_{16}]$ (centre) combining structural motifs with $[\text{Mn}^{\text{III}}_5\text{Ln}^{\text{III}}_8(\text{OH})_{12}(\text{tbdea})_4(\text{piv})_{12}(\text{NO}_3)_4(\text{OAc})_4]^-$ (left) and $[\text{Fe}_4\text{Dy}_4(\text{OH})_4(\text{nbdea})_4(\text{benz})_{12}]$ (right)

We have found that solvothermal synthetic methods can allow access to coordination clusters with structures differing from those obtained under more ambient conditions. For example, we have now determined the structure of $[\text{Fe}_3\text{Dy}_7(\mu_3\text{-OH})_{10}(\text{tbdea})_2(\text{benz})_{16}]$, which combined structural motifs from our previously-published (Ako et al., *Inorg. Chem.*, **2009**, 48, 6713) clusters $[\text{Mn}_5\text{Ln}_8(\text{OH})_{12}(\text{tbdea})_4(\text{piv})_{12}(\text{NO}_3)_4(\text{OAc})_4]^-$, which had also been measured at ANKA, and the “square-in-square” topology exemplified by $[\text{Fe}_4\text{Dy}_4(\text{OH})_4(\text{nbdea})_4(\text{benz})_{12}]$.

Some syntheses of polynuclear complexes go as planned, some do not. Attempts to obtain a heterometallic cluster from $[\text{Cu}_2(\text{O}_2\text{CBut})_4(\text{OH}_2)_2]$ and $\text{Dy}(\text{NO}_3)_3$ in a MeOH/MeCN solvent mixture gave instead two different MOFs, in which $\{\text{Cu}_2(\text{O}_2\text{CBut})_4\}$ moieties are linked between nitrogen atoms from two urotropin (hexamethylenetetramine) ligands. Depending on the reaction conditions, two very different networks could be obtained. The urotropin appears to have resulted from condensation of methanal (from oxidation of MeOH) and NH_3 (from hydrolysis of MeCN, probably catalysed by Dy^{3+}). The structure of both networks could be determined from measurements of the very weakly-diffracting crystals on SCD. One network, in which all four nitrogen atoms of each urotropin coordinate to a copper centre within a $\{\text{Cu}_2(\text{O}_2\text{CBut})_4\}$ dimer, crystallises in cubic *Fd-3m* (with a very large unit cell, $a = 61.899 \text{ \AA}$) and shows the MTN topology typical of the zeolite ZSM-39 (sodalite) structure displaying two types of 5^{12} (i.e. dodecahedral) and $6^4 5^{12}$ cages. The structure of the second MOF involves two mutually-interpenetrating networks, in which each urotropin only coordinates to three copper dimers. The topology is now even more unusual, with threefold helices of copper dimers being cross-linked into a 3-D network, such that the smallest rings in each network involve ten urotropins and ten dimers.



$\{\text{Cu}_2(\text{pivalate})_4\}$ /urotropin MOF showing MTN (ZSM-39 sodalite) topology (left, pivalate ligands omitted for clarity); MOF with interpenetrating network topology involving 10-membered rings (centre and right, distinct networks shown as dark blue and light blue lines)

Acknowledgements

We thank the DFG (Center for Functional Nanostructures) for financial support.

Electronic structure investigations of ultrathin EuxSi1-x films, nano-islands, and nano-wires by XANES and EXAFS on the Eu L3 edge

S. Stankov, A. Seiler, O. Bauder, S. Ibrahimkutty

KIT, Laboratory for applications of synchrotron radiation LAS, Karlsruhe, Germany

Beamtime 27.5.-30.5.2013 at SUL-beamline / T130527, local contacts: Jörg Göttlicher, Ralf Steininger

In total 8 Eu samples, 1 Sm sample and 2 Nd samples were measured during the beamtime. All samples were prepared under UHV conditions and covered with a layer of Nb or Y to protect them from oxidation during the transport to the beamline.

Measuring parameters: Source: Wiggler, DCM: Si(111), KBM: focused, sl4hg/vg 0.5mm/0.5mm, Measurements: High vacuum, Detector: 7 Element Si(Li) solid state from SGX Sensortech, (former e2v, former Gresham). Transition mode not possible due to a mm thick samples, here using fluorescence mode.

Europium:

For all samples EXAFS scans at the L3 edge were measured. Additionally EXAFS scans of the L1 edge were measured to get more information for the Eu samples.

The XANES spectra of the Eu L3 edge show for all samples a clear peak around 6976 eV. A pure Eu bulk samples was measured for comparison. All samples also show a (small) peak around 6983 eV, that is indicating Eu oxide, see fig 1.

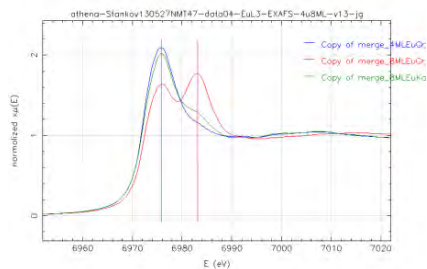


Fig 1: EuL3 XANES spectra, comparison of the samples 4MLEuGr, 8MLEuGr and 8MLEuKa. Eu peak at 6976 eV and oxide peak at 6983 eV.

The EXAFS region was investigated giving indication about the NN distance. In the pure Eu samples beside the Eu-Eu bond also a Eu-O bond was found, see fig 2. The EuSi samples mainly show a Eu-Si bond around $r = 2.65$ Å (not phase corrected, 0.4 Å has to be added to correct it), that could be the bonding in EuSi2 ($r = 3.12$ Å).

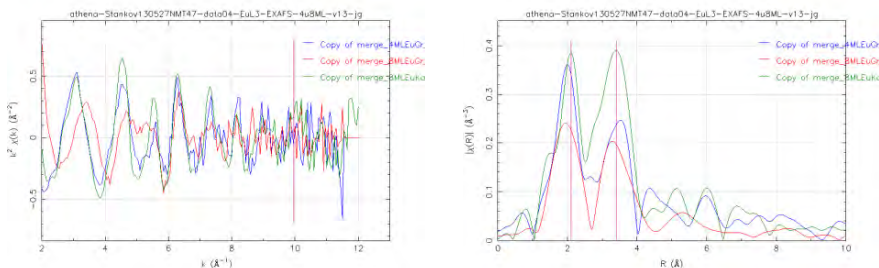


Fig 2: Eu L3 EXAFS k- and R-functions, comparison of the samples 4MLEuGr, 8MLEuGr and 8MLEuKa (k weight 1). The peak around 2 Å (not phase corrected) indicate Eu₂O₃, while the peak around 3.3 and 3.5, respectively (not phase corrected) indicate Eu-Eu bond which should be around 3.96 Å.

Eu L1 edge spectra were only useable for 1 sample (20 nm EuSi) due to huge noise in the edge region and very weak and noisy signal in the EXAFS region.

Samarium:

In Figures 3 the spectra of the Sm sample are compared to spectra of Sm₂O₃. The maximum of the white line in the XANES spectra is located at 6721.83 eV for the Sm sample and at 6722.65 eV for Sm₂O₃. The radial distribution function shows one intensive peak at about 3.36 Å, adding an approximate value for the phase shift of 0.4 the interatomic distance between Sm and nearest neighbour atoms is about 3.76 Å. The radial distribution function (k weight 2) of the Sm₂O₃ sample shows a distance at about 1.92 Å (not phase corrected) which most probably describes the Sm-O distance in Sm₂O₃ (ICSD database value of 2.35 Å, collection code 33650). Important is, that the radial distribution function of the Sm sample does not show significant contribution of Sm – O distances in the RDF. This should stand for no or a small fraction of oxidation in the Sm sample, see fig 4.

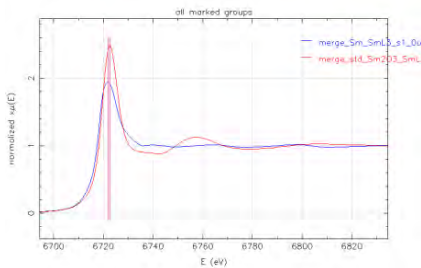


Fig 3: Sm L3 XANES spectrum of the Sm sample compared to the spectrum of Sm₂O₃.

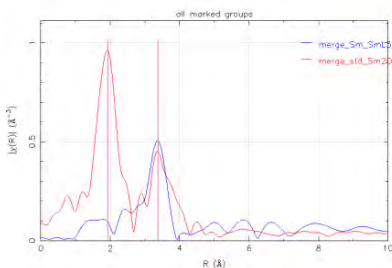


Fig 4: Radial distribution function of the Sm sample compared to the radial distribution function of Sm₂O₃ (k weight 2). The radial distribution function of the Sm₂O₃ sample shows a distance at about 1.92 Å (not phase corrected) which most probably describes the Sm-O distance in Sm₂O₃. There is another distance for both, the Sm sample and the Sm₂O₃ at about 3.37 Å (not phase corrected).

Neodymium:

In fig 5 the two spectra of the Nd samples are compared, showing a peak at 62156 eV and at 6226 eV for one sample, that is, as expected, an indication for oxide. Also the RDF shows for both samples a Nd-Nd bonding peak at 2.1 Å and for the oxidized sample additionally a peak at 3.9 Å (not phase corrected), see fig 6.

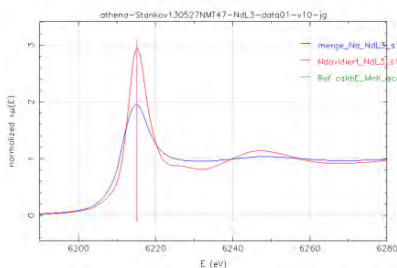


Fig 5: Nd L3 XANES spectra of sample Nd_{NdL3} and Ndoxidiert_{NdL3}, maximum whitelines at about 6215.2 eV.

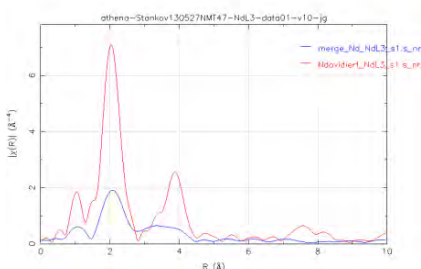


Fig 6: Radial distribution function, not phase corrected (Fourier Transform from Nd L3 EXAFS functions, k weight 3) of sample Nd_{NdL3} (blue) and Ndoxidiert_{NdL3} (red).

Crystallographic Characterisation of Large Paramagnetic Aggregates of Transition-Metal Cations

Christopher E. Anson¹⁾, Gernot Buth²⁾, Annie K. Powell¹⁾

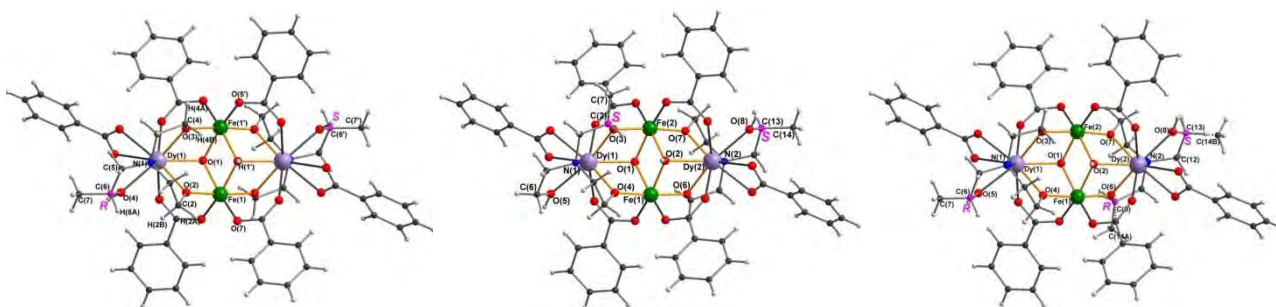
¹⁾ Karlsruhe Institute of Technology, Institut für Anorganische Chemie (AOC), Engesserstr. 15, D-76131 Karlsruhe

²⁾ Karlsruhe Institute of Technology, Institut für Photonenforschung und Synchrotronstrahlung (IPS), Hermann-von-Helmholtz-Platz 1, D-76344 Eggenstein-Leopoldshafen

We have previously shown that complexes of the type $[\text{Fe}^{\text{III}}_2\text{Dy}^{\text{III}}_2(\mu\text{-OH})_2(\text{teaH})_2(\text{O}_2\text{CAR})_6]$ (teaH_3 = triethanolamine) are a useful “testbed” for more fundamental studies of Single-Molecule Magnet (SMM) behaviour. For example changing the substituent on the benzoate ligands alters the orientation of the Dy^{III} easy axes and thus the barrier to relaxation of the magnetisation (Powell *et al.*, *Dalton Trans.*, **2013**, 42, 8926; Mereacre *et al.*, *J. Am. Chem. Soc.*, **2011**, 133, 15335). Replacing simple triethanolamine in the synthesis with the (racemic) proligand Me-teaH₃ in which one of the ethanol arms now bears a methyl substituent (thus creating a chiral centre) gave the analogue $[\text{Fe}^{\text{III}}_2\text{Dy}^{\text{III}}_2(\mu\text{-OH})_2(\text{Me-teaH})_2(\text{O}_2\text{CAR})_6]$ (*R,S*-**1**), which formed large crystals in which, as expected, the cluster molecules were centrosymmetric ($P\bar{1}$, $Z = 1$), with one $(\text{Me-teaH})^{2-}$ ligand as the *R*-, the other as the *S*-enantiomer.

With enantiomerically pure *S*-Me-teaH₃, however, the product crystallised more slowly, forming very small crystals that could only be measured on ANKA-SCD. The unit cell was similar to that for (*R,S*-**1**), but the space group was now clearly acentric $P1$, and the structure could be refined showing that we had indeed obtained (*S,S*-**1**), with both $(\text{Me-teaH})^{2-}$ ligands as the *S*-enantiomer (Flack χ parameter = 0.001(18)). With the *R*-ligand, crystallisation took much longer, and also gave very small crystals. In this case the data from SCD were of sufficient quality to show not just that (*R,R*-**1**) had co-crystallised with a small amount of the *meso*-diastereomer (*R,S*-**1**), but to quantify the extent of the ligand racemisation; the (*R,R*-**1**):(*R,S*-**1**) ratio in the crystal was 62:38.

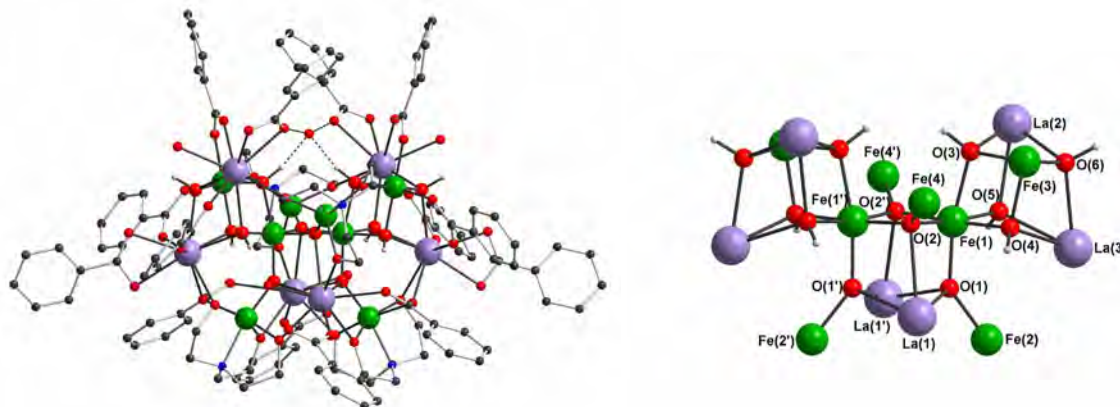
Comparison of the magnetic properties of the diastereomers (*R,S*-**1**) and (*S,S*-**1**) show that the latter is a significantly better Single-Molecule Magnet than its centrosymmetric counterpart. It appears that the symmetry-breaking forced by the use of the enantiomerically-pure ligand has suppressed Quantum Tunnelling of Magnetisation in (*S,S*-**1**), and *ab initio* calculations are underway to confirm this. This immediately suggests a synthetic strategy toward better SMMs, which is now being developed by us.



Structures of $[\text{Fe}_2\text{Dy}_2(\mu_3\text{-OH})_2(\text{Me-teaH})_2(\text{O}_2\text{CPh})_6]$: *R,S*-**1** (left); *S,S*-**1** (centre); {62% *R,R*-**1**+ 38% *R,S*-**1**} (right)

During the investigation of the original $[\text{Fe}^{\text{III}}_2\text{Ln}^{\text{III}}_2(\mu\text{-OH})_2(\text{teaH})_2(\text{O}_2\text{CAR})_6]$ series (*vide supra*), it was found that analogues could be easily obtained with almost all the lanthanides. However, with lanthanum itself very small deep orange crystals (needles or blocks, depending on the La^{3+} salt used) were obtained instead. Both crystal structures could be determined on ANKA-SCD, and in each case the same isostructural tetradecanuclear cluster $[\text{Fe}^{\text{III}}_8\text{La}_6(\text{O})_4(\text{OH})_8(\text{tea})_4(\text{O}_2\text{CPh})_{14}(\text{OH}_2)_4]$ had formed; the two crystal forms differ only in the unit cell (monoclinic $C2/c$ for the needles, triclinic $P\bar{1}$ for the blocks) and lattice solvent content. It is not uncommon for La^{3+} , with its larger ionic radius, to give complexes with different structures to those from the other lanthanides. The cluster

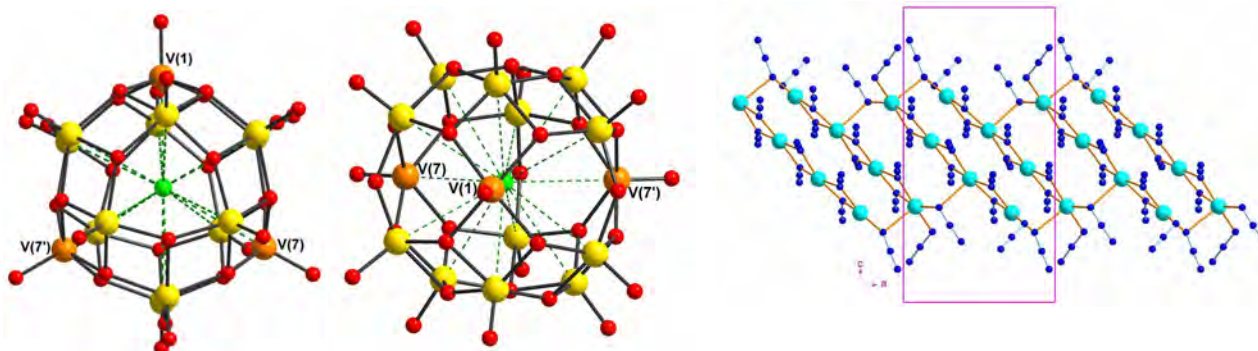
core is made up of three corner-sharing $\text{Fe}_2\text{La}_2(\text{O})_4$ or $\text{Fe}_2\text{La}_2(\text{OH})_4$ heterocubane motifs, in which the oxo ligands of the central cubane coordinate to four additional Fe centres. The spin structure within this novel cluster topology will be probed by a combination of magnetic susceptibility and ^{57}Fe Mössbauer spectroscopy.



Structure of $[\text{Fe}_8\text{La}_6(\text{O})_4(\text{OH})_8(\text{tea})_6(\text{benzoate})_{14}(\text{OH}_2)_4]$ (C2/c form) and the tricubane cluster core (Fe green, La violet, O red, N blue, C black; organic H-atoms omitted).

Aerobic oxidation of VCl_3 in the presence of triethylamine gives small black crystals. The crystal structure identified these as $(\text{Et}_3\text{NH})_6[(\text{V}=\text{O})_{15}(\text{O})_{21}]\text{Cl}$, crystallising in space group P6_522 . The core topology is not unusual; neither is the mixed-valence formulation ($\text{V}^{\text{IV}}_8\text{V}^{\text{V}}_7$ in this case). What is unusual (apart from the interstitial chloride within a closed metal cage) is that three vanadiums (which describe the corners of an equilateral triangle and are shown orange in the figure) are fully-localised V^{IV} from Bond Valence Sum calculations, whereas the others show delocalised valences. The magnetic properties are also unusual for this class of compound. One proposed model, which is now under investigation, involves very strong antiferromagnetic coupling (possibly *via* double exchange) within the two sets of six mixed-valence vanadiums (yellow in the figure), and that these two units then act as metalloligands, mediating weaker coupling between the three “pure V^{IV} ” centres.

In a recent ANKA report, we described the structures of two azide-rich Fe_3Gd_2 and Mn_4Dy_2 coordination clusters with very low melting points. Attempts to extend this chemistry to copper as the transition metal gave very thin black needle-like crystals. Structural determination at SCD showed that instead of a heterometallic cluster, an unprecedented 1-D coordination polymer $(\text{Me-im-Bu}^t)_2[\text{Cu}^{\text{II}}_4(\mu\text{-N}_3)_6(\text{N}_3)_4]$ had been obtained. Linear ferromagnetically-coupled $\{\text{Cu}_4(\mu\text{-N}_3)_6\}$ units have been linked by further azides to form a “sheared ladder” polymeric topology. The individual ladders are insulated from each other by the organic imidazolium counteranions. Conductivity measurements are being carried out to determine whether this compound is a new class of inorganic semiconductor.



Two views of the V_{15} anion in $(\text{Et}_3\text{NH})_6[(\text{V}=\text{O})_{15}(\text{O})_{21}]\text{Cl}$ (V^{IV} orange, $\text{V}^{\text{IV/V}}$ yellow, O red, Cl green) (left); the Cu-azide “ladder” in $(\text{Me-im-Bu}^t)_2[\text{Cu}^{\text{II}}_4(\mu\text{-N}_3)_6(\text{N}_3)_4]$ (Cu cyan, N dark blue) (right)

Acknowledgements

We thank the DFG (Center for Functional Nanostructures and 3MET) for financial support.

Characterization of X-ray rolled prism lenses within MiQA project

H. Vogt¹⁾, M. Marschall¹⁾, V. Altapova²⁾

¹⁾ Karlsruhe Institute of Technology (KIT), Institute of Microstructure Technology (IMT), Hermann-von-Helmholtz-Platz 1, 76344 Eggenstein-Leopoldshafen, Germany

²⁾ Karlsruhe Institute of Technology (KIT), Laboratory for applications of synchrotron radiation (LAS), Hermann-von-Helmholtz-Platz 1, 76344 Eggenstein-Leopoldshafen, Germany

X-ray microscopy requires two types of optics: one for the imaging and one for the illumination. The illumination optic is required to fulfil the demand for multiple directions of illumination over the entire field of view to increase the resolution of the microscope. Usually in the field of synchrotron applications, these kind of optics are manufactured using high-aspect ratio processes like LIGA [1, 2]. While these processes yield high structure quality and comparable high aspect ratios, those aspect ratios are nevertheless limited due to the mechanical stability of the single structures and the process is time consuming as well as error prone. The tested optics do not require those processes: The base material is a some micrometre thick foil with triangular shaped ribs on one side, which is cut and rolled around a glass fibre, forming an refractive optics for X-rays (see Figure 1 left) and a SEM picture of a part of the structured foil showing some of the triangular shaped structures on the foil (right).

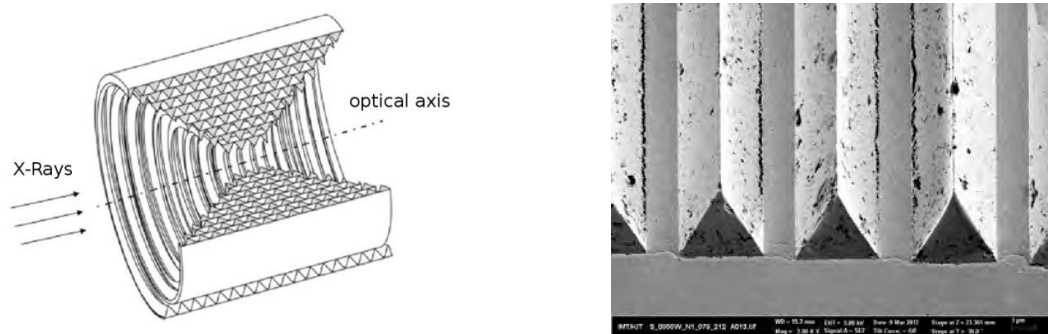


Figure 1: Principle of a rolled X-ray prism lens (RXPL)

The layout shown in Figure 1 with a continuous growth in the number of prisms with growing distance to the optical axis is meant to illuminate a small focal spot in the intended working distance. There are also other layouts which are meant to illuminate greater portions of a sample, or for applications like microscopy from defined angles in a defined distance. For this the layout of the RXPL is changed, in a way that every portion of the lens illuminates a desired region. This is done by altering the cut-layout of the foil. Figure 2 left shows such a layout and on the right a head-on radiographic picture of a lens acquired at the ANKA/TopoTomo Beamline, which was rolled with such a layout. The number of prisms jumps with growing distance from the optical axis and this is also visible in the right picture: the absorption increases stepwise with growing radius.

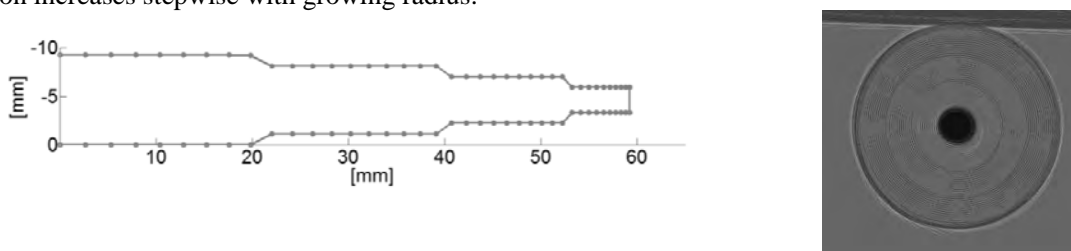


Figure 2: Condenser layout of an RXPL meant to illuminate a defined region on the optical axis (left) and head-on radiographic picture acquired at 30 mm detector distance at 30 keV at ANKA/TopoTomo (right)

To produce such optics the cutting and rolling process is crucial. Therefore the continuous monitoring and improvement of the changes done in the rolling and cutting processing of the foil is of upper-most importance. The only possibility doing this is using the radiographic possibilities at a synchrotron beamline in combination with a high resolution detector, like the one available at the ANKA/TopoTomo Beamline. Figure 3 shows a radiographic picture of a part of a condenser RXPL. In the middle the winding core (a glass fiber of 125 μm in diameter) is visible. There are two passages visible, where the number of prisms changes rapidly from the lower one to the higher one.

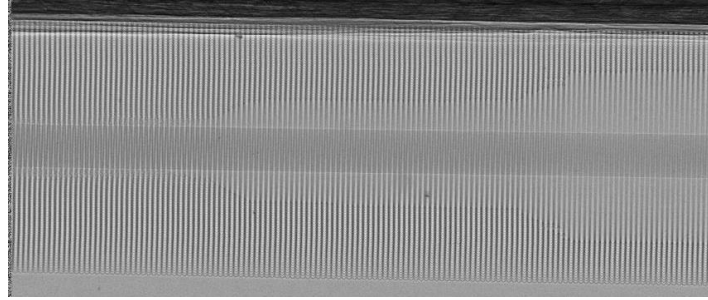


Figure 3: Radiographic side-view picture of a condenser RXPL at high energies

This lens was meant to illuminate a FWHM of 100 μm in a 2,5 m distance behind the lens at 30 keV. The measurements done with this lens proved to only slightly miss the desired distance (see Figure 4 left), while not fulfilling the demand for the 100 μm illuminated region: approx. only 40 μm where achieved (see Figure 4 right).

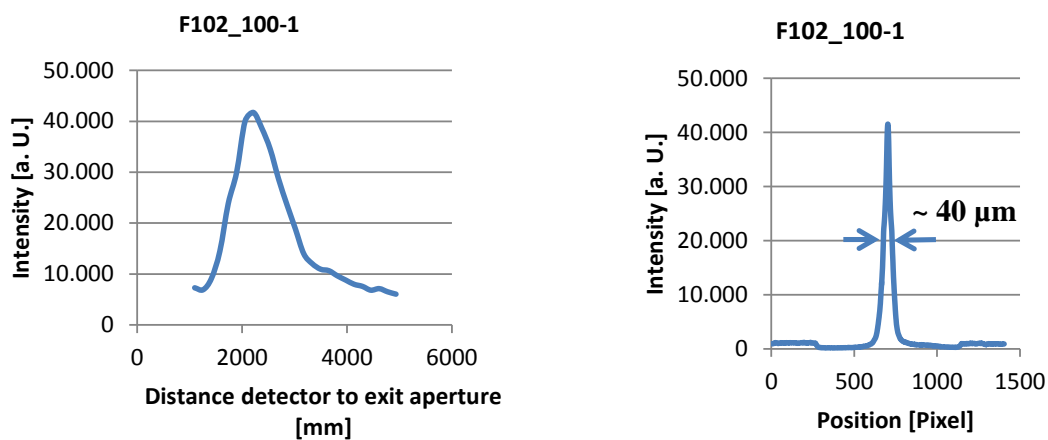


Figure 4: Intensity on the detector vs. distance of detector to lens exit aperture (left) and horizontal slice perpendicular to the optical axis through the focus and the position of maximum intensity along the optical axis (right)

This mismatch is due to inaccuracies in the lens and show that the fabrication process, still needs to be optimized.

References

1. Saile, V., *Introduction: LIGA and Its Applications*, in *LIGA and Its Applications* 2009, Wiley-VCH Verlag GmbH & Co. KGaA. p. 1-10.
2. Jefimovs, K., et al., *Beamshaping Condenser Lenses for Full-Field Transmission X-ray Microscopy*. *Journal of Synchrotron Radiation*, 2008. **15**: p. 106-108.

Acknowledgements

We acknowledge the Synchrotron Light Source ANKA for provision of instruments at their beamlines and we would like to thank Mrs. Venera Altapova for assistance.

The authors appreciate the support of the virtual institute „New X-ray analytic methods in material science“ of the Helmholtz association.

MFe₂O₄ (M = Co, Mg, Mn, Ni, Zn) nanoparticles as anode materials in Li-ion batteries: An in-situ study of the reaction pathway

S. Permien¹⁾, S. Indris²⁾, W. Bensch¹⁾

¹⁾ University of Kiel, Institute of Inorganic Chemistry, Max-Eyth-Str. 2, D-24118 Kiel, Germany

²⁾ Karlsruhe Institute of Technology, Hermann-von-Helmholtz-Platz 1, D-76344 Eggenstein-Leopoldshafen, Germany

Introduction

While hundreds of papers are published every year where new and better electrode materials for Li-based batteries are claimed, investigations of the reaction mechanisms during charge and discharge of such materials are scarce. A challenge for future applications of Li-batteries is the identification of materials which are composed of earth abundant, environmentally friendly and sustainable elements. Classically the batteries on the market work on the basis of Li intercalation and deintercalation reactions. During the last few years so-called “conversion” reactions are in focus of research.^[1] Spinels with general formula MFe₂O₄ (M = Co, Ni, Mn, and Zn) are promising candidates showing high capacity because of the complete reduction of M and Fe to the metallic state.^[2] A promising anode material is CoFe₂O₄ with high capacities of more than 1000 mAh/g.^[3] Addition of carbon helps to stabilize capacity over many cycles.^[4] But up to now the structural changes during Li insertion/deinsertion were not investigated in detail. The results of in-situ XRD studies (PDIFF beamline at ANKA) during Li insertion into nanosized CoFe₂O₄ are presented as a representative for spinels of the type MFe₂O₄.

CoFe₂O₄ nanoparticles were synthesized by mixing Co(NO₃)₂*6H₂O, Fe(NO₃)₃*9H₂O and citric acid in a ball mill for 2 h at 500 rpm. The viscous mixture was decomposed at 400 °C for 3 h.

Experimental

A custom built cell (40x40x15 mm) consisting of two aluminium plates with rectangular apertures (14x3 mm) in the centre and two sheets of Kapton foil windows glued on both sides was used. The active anode material was mixed with carbon (C65) and polyvinylidene fluoride as binder. The mixture was suspended in NMP (N-methylpyrrolidone), deposited on a thin Cu foil and dried. Li metal as counter electrode is attached on a Cu foil. A microporous polyethylene/polypropylene membrane was used as separator and 1 M LiPF₆ in an ethylene carbonate/dimethyl carbonate mixture is used as electrolyte. PDIFF Beamline was operated at 16 keV with a Princeton CCD detector. Powder patterns were collected within 5 min. Copper diffraction peaks were masked and 2D spectra were transformed with Area Diffraction machine.^[5]

Results and Discussion

During insertion of the first 0.5 Li per formula unit all reflections shift to smaller 2θ angles (Fig. 1, left) and the *a*-axis of CoFe₂O₄ increases linearly from 8.376 Å to 8.427 Å (Fig. 2, top right). The potential of the cell is dropping and a not well developed plateau at 1.5 V can be seen (Fig. 2, bottom right). Afterwards two phases can be identified and the spinel structure is successively transformed to a rock salt-like structure, which is accompanied by a significant intensity drop of the (311) peak of the spinel phase (17.4 °2θ). Simultaneously, the intensity of the (111) reflection of the new phase Co_{0.33}Fe_{0.66}O rises. After insertion of 2 Li per formula unit the reflections of the spinel phase cannot be detected anymore. Most likely Co on tetrahedral sites in the spinel moves to neighbouring empty octahedral sites, thus forming the NaCl-type structure. The *a*-axis lattice constant of the newly formed Co_{0.33}Fe_{0.66}O is 4.245 Å.

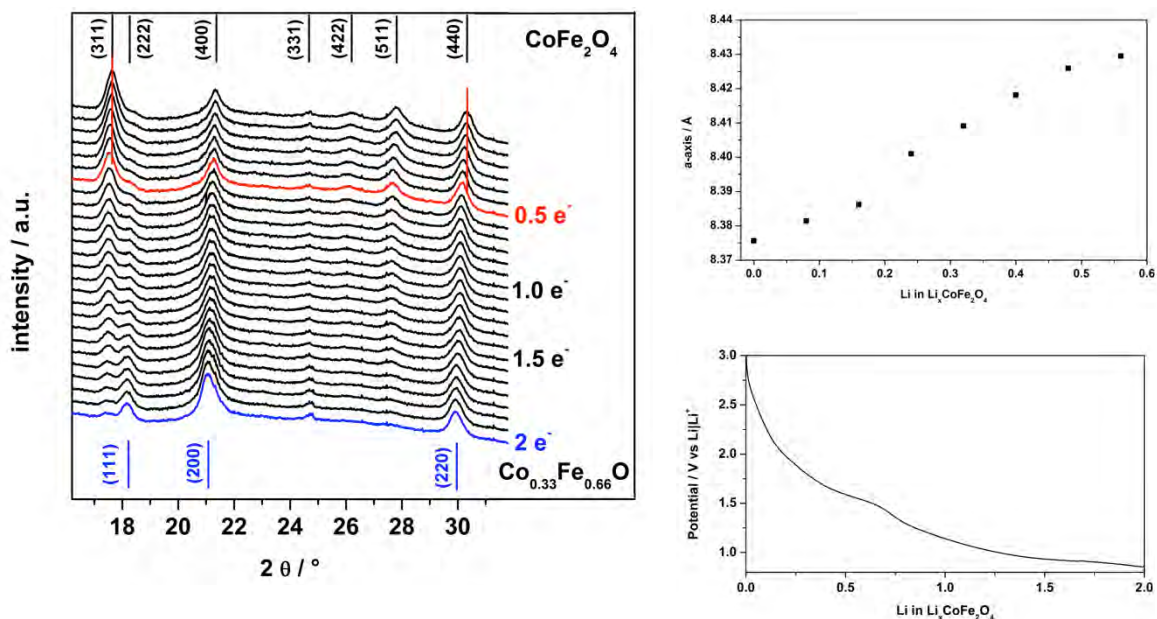


Fig. 1: *In-situ* XRD of CoFe_2O_4 during Li uptake of 2 Li per formula unit (left), increase of the a-axis during insertion of the first 0.6 Li (top right) and change of the cell potential during Li uptake (bottom, right).

After insertion of 2 Li a long plateau at 0.8 V has been observed (Fig. 2, right). During insertion of the next 6 Li per formula unit, the intensity of the reflections decreases. Probably $\text{Co}_{0.33}\text{Fe}_{0.66}\text{O}$ is transformed to metallic Fe, Co and Li_2O with particles being too small to be detected by XRD which was also reported for MnFe_2O_4 .^[2]

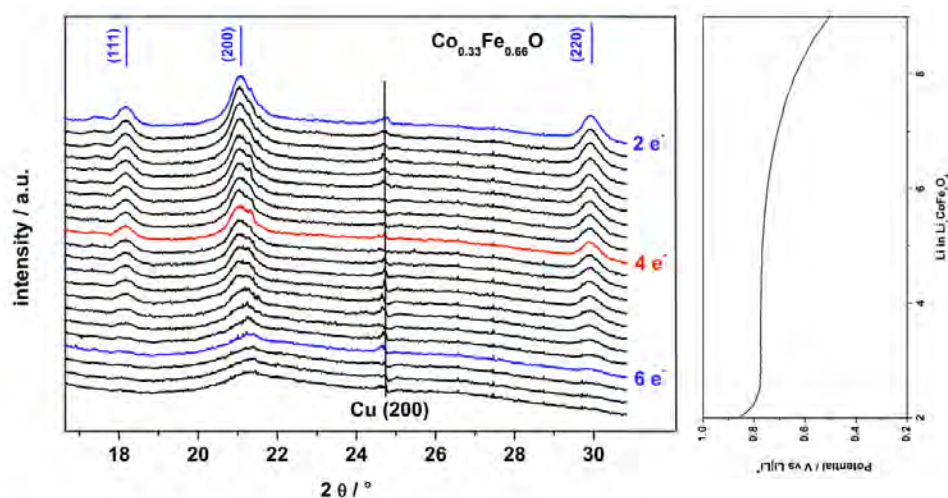


Fig. 2: *In-situ* XRD of CoFe_2O_4 during Li uptake between 2 and 6.5 Li per formula unit (left) and change of the cell potential (right)

Conclusion

It seems that Li insertion into CoFe_2O_4 nanoparticles is first accompanied by an intercalation and at a distinct Li content a structural transformation to a mono-oxide with NaCl-type structure occurs ($\text{Co}_{0.33}\text{Fe}_{0.66}\text{O}$) followed by full conversion to iron, cobalt and lithium oxide.

Reference

- [1] J. Cabana, L. Monconduit, D. Larcher, M. Rosa Palacin, *Adv. Energy Mater.*, **2010**, 22, 170–192.
- [2] S. Permien, H. Hain, M. Scheuermann, S. Mangold, V. Mereacre, A. K. Powell, S. Indris, U. Schürmann, L. Kienle, V. Duppel, S. Harm and W. Bensch, *RSC Adv.*, **2013**, 3, 23001-23014.
- [3] P. Lavela, J.L. Tirado, *J. Power Sources.*, **2007**, 172, 379-387.
- [4] H. Xia, D. Zhu, Y. Fu, X. Wang, *Electrochim. Acta*, **2012**, 83, 166-174.
- [5] Area Diffraction Machine Version 2 Beta248, **2007**.

INVESTIGATING POLARISATION AND SHAPE OF BEAM MICROWAVE SIGNALS AT THE ANKA STORAGE RING

J. Schwarzkopf, M. Brosi, C. Chang, E. Hertle, V. Judin, B. Kehrer, A.-S. Müller,
P. Schönfeldt, M. Schuh, P. Schütze, M. Schwarz, J. L. Steinmann, KIT, Karlsruhe, Germany
F. Caspers, CERN, Geneva, Switzerland

Abstract

At the ANKA synchrotron radiation facility measurements in the microwave range (10 to 12 GHz) employing a LNB (Low Noise Block), which is the receiving part of a Satellite-TV system, have been carried out. Experiments showed that the observed signal depends on the length of the electron bunches. Furthermore the temporal shape of the microwave signal depends on the detector's position along the accelerator. Due the LNB antenna's sensitivity to polarisation it was also possible to measure the polarisation along the several ns long signal, revealing polarised and non-polarised regions. This paper describes the experimental setup and summarises the observations of the systematic studies performed with the LNB system.

MICROWAVE RADIATION AT ANKA

Earlier experiments at ANKA, the synchrotron radiation facility of Karlsruhe Institute of Technology (Karlsruhe, Germany) showed that there is an electron beam correlated microwave signal visible at the infrared beamline IR1 [1], [2]. Further studies performed at the IR2 beamline and at the synchrotron light monitor port (SLM) confirmed these first observations. The detection of microwave radiation is an interesting fact since the coherent synchrotron radiation (CSR) suppression threshold frequency at ANKA can be calculated using [3]:

$$f_{\text{CSR,thr.}} = 2c \sqrt{\frac{h^3}{\rho}} \approx 60 \text{ GHz}$$

where c is the speed of light, $h = 32 \text{ mm}$ is the height of the ANKA vacuum chamber, $\rho = 5.559 \text{ m}$ is the ANKA bending radius. Although the waveguide cut-off at ANKA lies around 2.3 GHz.

DETECTION OF MICROWAVES

The LNB is a low-cost standalone microwave detector with a noise figure of $\approx 0.5 \text{ dB}$. Fig. 1 shows a schematic drawing of the LNB. It consists of a feed horn that focuses the incoming radiation to the antenna within the horn. Afterwards a bandpass filter selects the receiving frequency band of television, which is then amplified by a low noise amplifier (LNA). To have a better handling of the rf signal it is mixed down. The desired result of the mixing is the difference frequency which is separated from other mixing outcomes through another bandpass filter. A second LNA provides a clean signal above the noise level. This signal is an exact but just frequency shifted replica of the input signal.

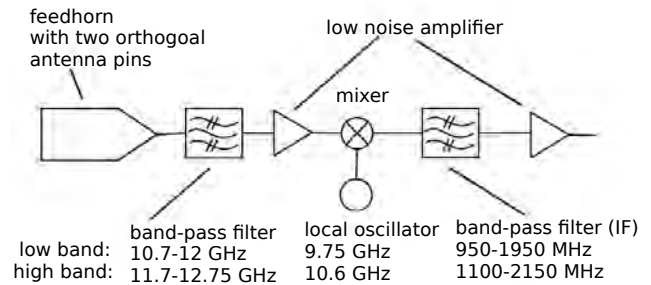


Figure 1: Schematics of the LNB principle. The central component is the rf-mixer to convert the signal to an easily handleable intermediate frequency of 2 GHz.

OBSERVATIONS

The results of microwave studies based on measurements at different positions (IR1, IR2, SLM) of the ANKA storage ring are presented here. The main point of attention was the characteristics of the detected microwave signal.

Polarisation Studies

The polarisation dependence of the signal at the IR1 beamline was measured to investigate the microwave signal's origin at the synchrotron radiation facility. The infrared beamline provides large aperture optics. Thus the transmission in the microwave range in form of free electro-magnetic waves or waveguide modes of the beamline pipe is expected. In Fig. 2, on the left plot the typical LNB signal with a rise synchronously to a single electron bunch pass is shown. After the first rise the signal increases for around 50 ns and then decreases during the next 200 ns to the noise level. Hypothetically only the first rise of the signal is caused by CSR. And the long signal tail is taken to be scattered fields, which are caused by discontinuities of the vacuum chamber and propagate to the experiment. This was investigated by rotating the linearly polarised LNB detector around the beamline axis. Thus measuring the average signal intensity of the first 4 ns of the LNB Signal (marked blue) for different detector orientations. We observe that the signal is significantly polarised, as shown in Fig. 2 (middle). For zero rad we observe maximum intensity. The vertical plane is adjusted to 0 rad. The observed linear polarisation corresponds to the expected characteristics of the synchrotron radiation for long wavelengths. The same analysis was also done for the trailing signal beyond the first 4 ns marked red in Fig. 2. As it is shown on the right plot in Fig. 2, the signal does not have a clear polarisation preference. The signal rise at about 2 rad can be explained through the decaying beam

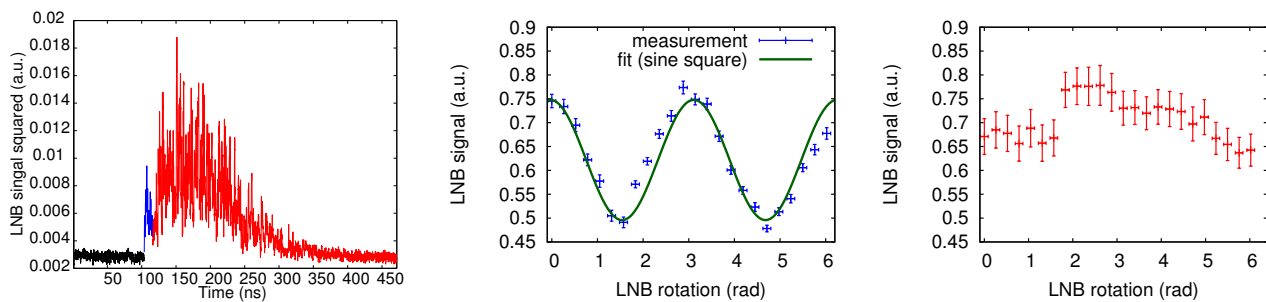


Figure 2: Left: Trace of the LNB detector signal. The blue part of the signal is used for the analysis shown in the middle plot and is clearly polarised. The red coloured long tail is not polarised. In the middle and right figure the change in signal strength due to a rotation of the detector and therefore changed detected polarisation is shown. For the first peak (blue part) the middle figure shows a sine squared behaviour. That is expected for the detection of polarised radiation with a polarisation sensitive detector. On the right figure the same analysis has been done for the red coloured signal tail, but the signal is significantly less polarised.

current. The change of the CSR intensity due to the change of charge was taken into account, but the small bunch length change corresponding to the current dependent bunch lengthening [5] was not. The observed polarisation property at the IR1 beamline is an indication for the combined nature of the signal source.

Geometrical Characteristics

In addition to polarisation also the geometrical properties of the microwave source at ANKA were investigated. The dependence of the signal intensity on the longitudinal distance between source and detector can give a useful hint to the nature of the signal origin. Fig. 3 shows this measurement with a decay of the signal. Purely geometrical considerations lead to a hyperbolic signal dependence. The reason is that the constant surface detector covers only a set amount of the irradiated solid angle which decreases with the distance to the source. Lateral movement of the microwave detector is shown in Fig. 4. The result cannot be explained by a single Gaussian distributed source, but well using a sum of 2 Gaussians. This fact supports the hypothesis of two signal sources, made in the polarisation chapter.

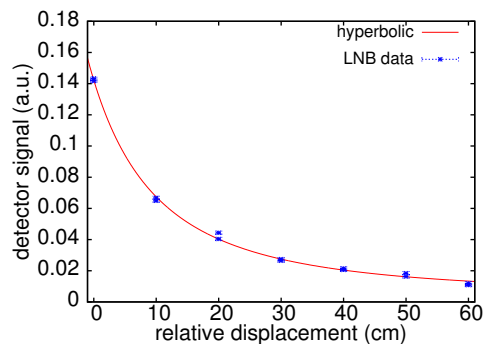


Figure 3: Increasing the longitudinal between source and detector the measured signal decreases. A reasons could be the divergence of the radiation (hyperbolic).

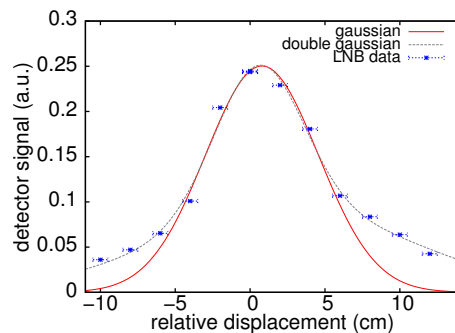


Figure 4: Variation of the signal strength for horizontal displacement of the detector in front of the source. There is still signal beside the window (< 7.5 cm), suggesting a wide angle of aperture and no parallel radiation. Furthermore a stepwise fit of two Gaussians suggests that there are two radiation source points.

Bunch Length Dependence

The CSR spectrum depends on the electron distribution being the source of the radiation. The distribution can be estimated by a Gaussian and described by the number of electrons and the bunch length. The bunch length influences the coherent emission of the bunch [4]. Fig. 5 shows the calculated spectrum for different bunch lengths. For a decreasing bunch length the spectrum becomes wider and the emitted power increases. The expected answer of an LNB can be deduced from the change of the spectrum within its narrow input band (black lines in Fig. 5). Fig. 6 the signal expected for an increasing bunch length.

Because the beam current decays during a measurement, it is important to know how this influences the measured signal. Therefore, we did a measurement with constant bunch length to neglect the effect of bunch lengthening. Furthermore the choice to measure at long bunch lengths reduces the effect on the expected power, see the marked area in Fig. 6. The analysis uses the the average signal of one revolution (≈ 368 ns). For comparison the integrated, calculated CSR

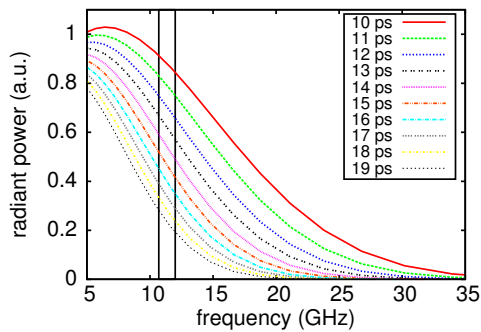


Figure 5: Calculated coherent synchrotron radiation spectra for different bunch lengths σ (in ps) and a constant number of electrons. The black lines indicate the receiving frequency band of an LNB.

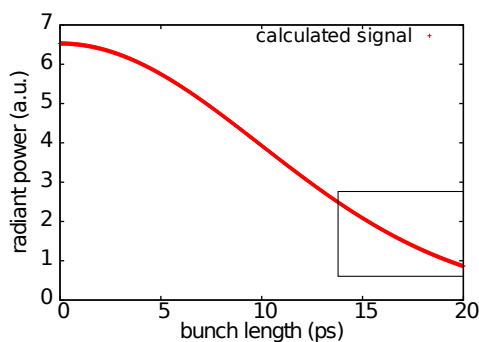


Figure 6: The expected response of an LNB to a variation in bunch length. The expectation is deduced from the behaviour of the spectrum. The signal increase with the decrease in bunch length gives a possibility to determine the bunch length from the signal strength.

power in the input band of the LNB, based on the measured bunch length and current is shown. The result is the confirmation of a quadratic current dependence as expected for CSR, shown in Fig. 7. With this knowledge the detector signal can be normalised to the bunch current. Fig. 8 shows the resulting residual dependence on the bunch length. At larger bunch lengths the measured signal behaves like the expectation for synchrotron radiation, which is drawn in green. The expectation is again based on measured bunch length and current as well as the analytical formula to calculate the synchrotron radiation spectrum [4]. The drop of the signal for the lowest measured bunch lengths can possibly be caused by the twofold nature of the measured signal, i.e. reflect the fact that in this region the signal is not dominated by CSR.

SUMMARY

As a result of the studies presented above, the universality and usefulness of the small, low-cost microwave detector LNB can be emphasised. The observations show evidences for the two different microwave signal sources at the ANKA storage ring, which are supposed to be CSR-microwaves and wake fields. Using a correct calibration a bunch length measurement with LNB signal can be approached.

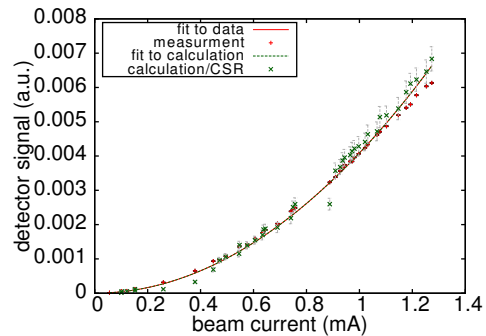


Figure 7: Quadratic dependence of the measured signal on the beam current. The green crosses are the expectation based on measured accelerator parameters and calculated from changes in the synchrotron radiation spectrum.

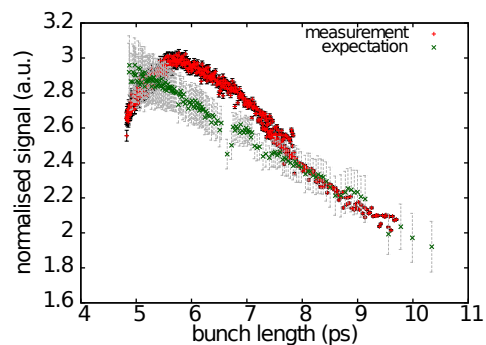


Figure 8: The normalised signal increases as expected to smaller bunch lengths. But shows an unexpected change in behaviour towards the lowest measured bunch lengths.

ACKNOWLEDGEMENT

The authors would like to express many thanks to the infrared group at the ANKA storage ring for their support in beam times. We would like to acknowledge the ANKA machine group for fruitful discussions and technical support. Work supported by the Initiative and Networking Fund of the Helmholtz Association (Grand No. VH-NG-320), the German Federal Ministry of Education and Research (Grant No. 05K10VKC and 05K13VKA).

REFERENCES

- [1] V. Judin et al., "Observation of microwave radiation using low-cost detectors at the ANKA storage ring", IPAC'11, San Sebastián, 2011, TUPC085
- [2] V. Judin et al., "Observation of Synchrotron Radiation Using Low Noise Block (LNB) at ANKA", DIPAC'11, Hamburg, 2011, TUPD39
- [3] R. Warnock, "Shielded Coherent Synchrotron Radiation and its Possible Effect in the Next Linear Collider", SLAC-PUB-5523, May 1991
- [4] L. I. Schiff, "Production of Particle Energies beyond 200 Mev" Review of Scientific Instruments, 1946 Vol. 17-1, pages 6-14
- [5] N. Hiller et al., "Status of Bunch Deformation and Lengthening Studies at the ANKA Storage Ring", IPAC'11, San Sebastián, 2011, THPC021

FLUCTUATION OF BUNCH LENGTH IN BURSTING CSR: MEASUREMENT AND SIMULATION

P. Schönfeldt*, A. Borysenko, E. Hertle, N. Hiller, V. Judin, A.-S. Müller,
S. Naknaimueang, M. Schuh, M. Schwarz, J.L. Steinmann
Karlsruhe Institute of Technology, Karlsruhe, Germany

Abstract

The ANKA electron storage ring of the Karlsruhe Institute of Technology (KIT, Germany) is regularly operated in low- α mode to produce short bunches for the generation of coherent synchrotron radiation (CSR). This paper evaluates systematic bunch length measurements taken in low- α operation of the ANKA storage ring. Above the bursting threshold not only the emission of CSR occurs in bursts, but also a continuous fluctuation of the bunch's length is observed. The measurements were carried out using concurrent multi-turn (using a streak camera, SC) as well as single-shot (using electro-optical spectral decoding, EOSD) methods. Furthermore, we compare information obtained on the fluctuation to simulations.

INTRODUCTION

For bunch charges above a threshold that depends on beam optics and RF voltage, bursts of CSR are observable. These define the so-called bursting instability. Bunch lengthening is a well known feature of this instability, but measurements have also shown oscillations of the bunch length that had the same periodicity as bursts measured at the same time [1].

There are two challenges one faces when trying to resolve fluctuations of the bunch length in low- α_c operation. First of all, the bunch length goes down to a few picoseconds, so one needs methods that are sensitive enough to resolve the length to sub-ps-accuracy, to be able to see fluctuations. EOSD as well as a SC can fulfill this. Secondly, the bunch length and longitudinal oscillation might have about the same magnitude. So one needs measurements that are not disturbed by the synchrotron oscillation. To meet these requirements, we had to operate the SC to resolve the synchrotron frequency. Doing this, the turn-by-turn fluctuation cannot be resolved directly, so we also did a cross check simulating SC images. Furthermore we compare our results to a simulation of the physics in longitudinal phase space based on the Vlasov-Fokker-Planck equation.

Table 1: ANKA Machine Settings

Circumference	110.4 m
f_s	7.7 kHz
V_{RF}	4×450 kV
Energy	1.3 GeV
Filling pattern	single bunch
Current range	$0.065 \text{ mA} < I < 2.0 \text{ mA}$
Bursting Threshold	$I_{th} \approx 0.07 \text{ mA}$

* patrik.schoenfeldt@kit.edu

Since all measurements mentioned in this paper were carried out with one single bunch inside the ANKA storage ring, interaction between different bunches does not have to be taken into account. The most important parameters used are shown in Table 1.

FLUCTUATION OF BUNCH LENGTH

Simulation

For the simulation of SC images (MSCI, *Mock Streak Camera Images*) we use bunch length and synchrotron frequency as input, and add realistic noise. The parameterized average bunch length is

$$\bar{l}(I_b) = \sqrt[q]{(l_0)^q + (k \times I_b^{3/7})^q} \quad (1)$$

with the bunch current I_b , the natural bunch length l_0 and the empirical fit parameters q and k . Since incoherent light is used for the SC, the number of photons hitting the screen is scaled proportional to I_b . This already allows investigation of statistical influences. As an additional input parameter, here we used the main bursting frequency, as measured using fast THz detectors [2] (see Fig. 1). For the length fluctuation an amplitude of 10 % has been assumed. The simulated images are subjected to the same analyzes chain as the actual measurements.

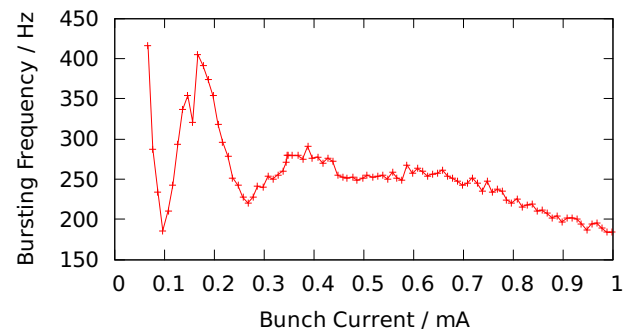


Figure 1: Main frequency at which radiation bursts occur plotted over bunch current. Actual measurement points have been connected to guide the eye. Note that the frequencies are a lot lower than the synchrotron frequency (7.7 kHz), which has to be resolved using the SC. This data is used as input parameter to create MSCl.

This simulation gives an impression of the fluctuation of bunch length that would be measured using the SC. For the bunch length the simulation on the one hand verifies that both sources of noise do not have a big impact on the measurements in the current range we present in this paper. On

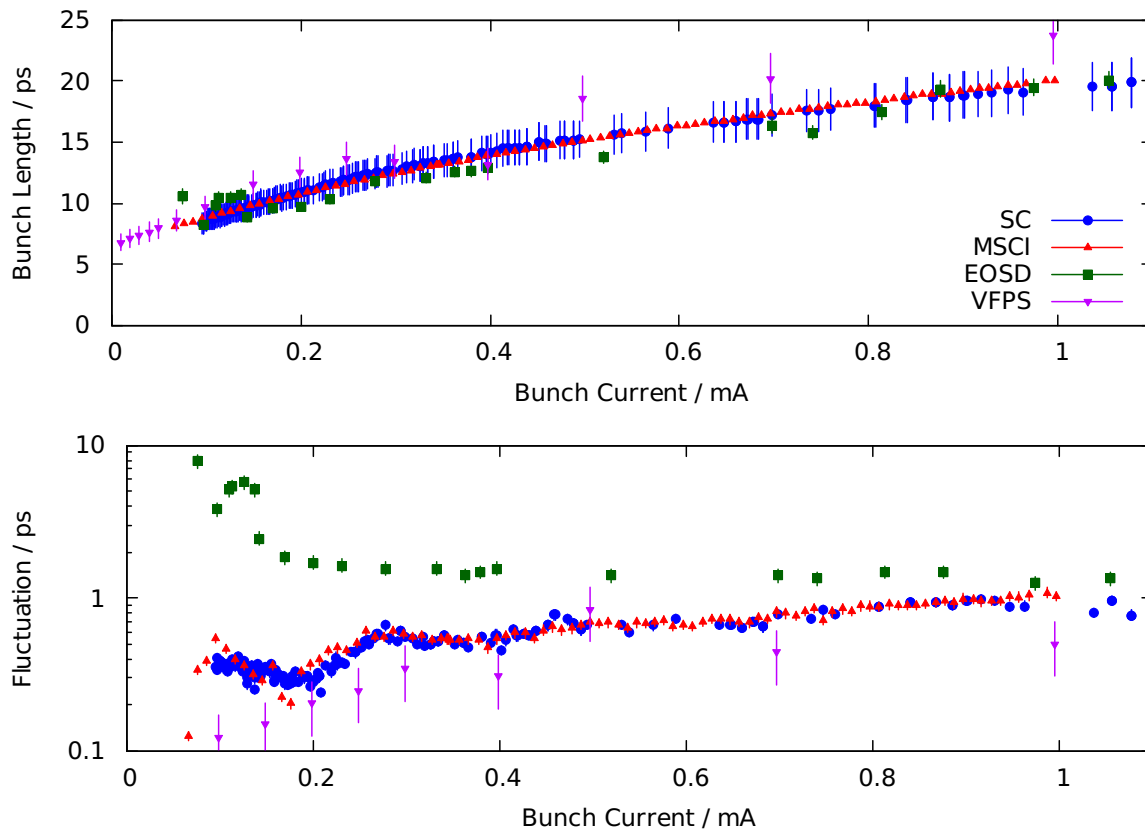


Figure 2: The upper plot shows bunch length (FWHM), the lower plot the fluctuation of bunch length obtained by all used methods. All results agree well. For the fluctuation (lower plot) on the other hand, there are some differences between the methods. The increase in measured fluctuation for low currents obtained using EOSD can be explained by the decreased shot-to-shot accuracy with decreasing electrical field. The MSCI approach which folds bunch length, the SC's time range, and the frequencies of the bursts reproduces the fluctuation directly obtained using the SC very well.

the other hand it gives evidence that the bursting frequency indeed has an impact on the measured fluctuation of bunch lengths. The results are shown in Fig. 2 and will be discussed in the results section.

The Vlasov-Fokker-Planck Solver (VFPS) used for the second simulation was originally implemented by M. Klein [3]. A brief explanation can be found in [4]. As for the MSCI some input parameters are derived from measurement data. The momentum compaction factor α_c and the slip factor η are calculated

$$\alpha_c \approx -\eta \approx \frac{f_s^2 \times 2\pi \times E/e}{f_{rev} \times \dot{V}_{RF}} \quad (2)$$

with the revolution frequency f_{rev} , the time derivative of the RF voltage $\dot{V}_{RF} \approx f_{RF} \times V_{RF,1} = 500 \text{ MHz} \times 450 \text{ kV}$, and the beam energy E . The energy spread σ_E has been derived from the natural bunch length $\sigma_{z,0}$ using

$$\sigma_E = \frac{\sigma_{z,0} \times 2\pi f_s}{\eta c}. \quad (3)$$

The accuracy of the VFPS data is limited by computation time as well as by the accuracy of the input parameters, particularly by $l_0 \approx \sigma_{z,0} \times 2.35 = (6.50 \pm .06 \pm .24) \text{ ps}$.

Especially for long bunch lengths, a large mesh has to be used. So only a limited number of synchrotron periods can be simulated in reasonable computation time, which means that statistics for the fluctuation is not optimal. Currently the number of simulated bursts is $N = 50$.

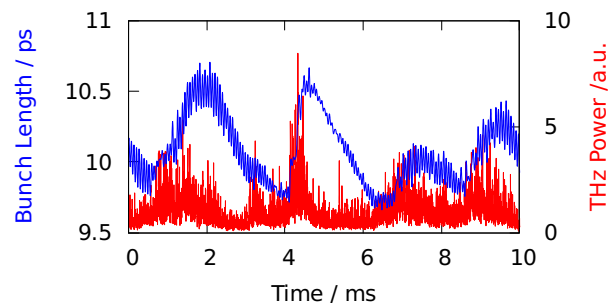


Figure 3: Example for a solution of the Vlasov-Fokker-Planck equation. At the time the bunch length (RMS $\times 2.35$, blue, left axis) starts to increase, the CSR (red, right axis) is bursting. When the CSR intensity drops, the bunches shorten again.

The qualitative result that correlates bursting CSR with fluctuations in the bunch length – as seen in Fig. 3 – agrees

well with the expectations: The bunch length is correlated to the emitted CSR power, both quantities fluctuate at the same frequency. While the frequency itself deviates from the measurements by a factor of about 2.5 (see also [4]), the pattern of the THz power looks similar to measured intensity fluctuations.

As for the MSCI, the results for the average bunch length as well as for the length fluctuation are shown in Fig. 2 and will be discussed in the results section.

Measurements

To measure bunch length and longitudinal profile we mainly use two methods. The used SC, a Hamamatsu C5680, has dual sweep which allows to record a bunch's profile continuously over time. Since we are interested in accurate measurements for short bunches, the amplitude of the synchrotron oscillation has to be taken into account. Hence the (slow) time axis has to be chosen in a way that the synchrotron oscillation is clearly visible. We then are able to deduct it and get an (averaged) bunch profile from the projection onto SC the position (fast time) axis. According to benchmarks using MSCI for constant bunch lengths this method gives an accuracy which is better than $\Delta l_{SC} < 0.3$ ps.

Additionally we do near field measurements using electro optical spectral decoding [5] to obtain the electron bunches' profile in a single pass-by. The statistical uncertainty of this method is limited by the field strength, thus can vary shot by shot depending on the distance between beam and electro-optical crystal. Furthermore there is a timing-dependent bias which in the worst case adds a deviation of up to one third (peak to peak) for bunch length. Thus the uncertainty for a single shot is $\Delta l_{EO} = 10$ %.

Discussion and Results

All measurement results (as well as simulation results) are shown and compared in Fig. 2. Note that the (average) bunch length \bar{l} obtained with both measurement methods agrees well (upper plot), but the standard deviation of the distributions

$$\sigma_l = \sqrt{\frac{1}{N-1} \sum_i^N (\bar{l} - l_i)^2} \quad (4)$$

(lower plot) show significant differences. For the values obtained by EOSD, there is an increase for currents below 0.3 mA, which can be explained by a very low signal to noise ratio. For any other case (real) fluctuation of the actual length give an important contribution to σ_l . The fact that streak camera measurements show lower values for the fluctuation can be explained by the averaging that even plays a role for slow burst: The slow time axis was set to 1 ms, the fastest fluctuation always happens with $f_s = 7.7$ kHz (cf. Fig. 3).

All results obtained for the bunch length (see upper plot in Fig. 2) match very well. There is a slight tendency that the

EOSD's average length is smaller than the one obtained by the SC. A possible explanation is that the single SC lengths are deducted from bunch profiles averaged over 1 ms.

For the fluctuation of bunch length (see lower plot in Fig. 2) the MSCI using bursting frequencies as input parameters match the real SC measurements almost perfectly. The VFPS data also agrees within the uncertainty estimation. As one would expect, the fluctuation decreases when the current is near the bursting threshold. The EOSD measurements for the lower currents ($I_b < 0.3$ mA) are influenced by a bad shot-to-shot accuracy. For the higher currents the EOSD results are larger but in the same range as the ones obtained using the SC. This feature is expected because of the averaging in every SC image. Also note that the change in the fluctuation obtained by SC is mainly caused by the changing bursting frequency: While over a wide current range the bunch length changes proportional to $I^{3/7}$, the measured fluctuation changes exponentially.

CONCLUSION AND OUTLOOK

This paper has presented both simulations and systematic measurements of the length of bunches above the bursting threshold. It has been shown that the bunch length fluctuates with the main frequencies of the THz bursts. Since at the SC the bursting frequency plays a big role when measuring length fluctuations, even a simple model for the amplitude gives sufficient results. Optimizations at the EOSD setup and continued work on the VFPS will help to also find a more accurate model for the fluctuation amplitude.

ACKNOWLEDGMENTS

We would like to acknowledge the ANKA infrared group for allowing access to the IR1 and IR2 beam lines.

Work supported by the Initiative and Networking Fund of the Helmholtz Association (Grand No. VH-NG-320), the German Federal Ministry of Education and Research (Grant No. 05K10VKC and 05K13VKA) and by the Helmholtz International Research School for Teratronics (HIRST).

REFERENCES

- [1] Y.-R. E. Tan et al. "Low Alpha Configuration For Generating Short Bunches", PAC 2009, TH6PFP009.
- [2] Advanced Compound Semiconductor Technologies GmbH, Merckstr. 25, D-64283 Darmstadt, Germany; www.acst.de
- [3] M. Klein "Optics Calculations and Simulations of Longitudinal Beam Dynamics for the Low-alpha Mode at ANKA", Verlag Dr. Hut, München.
- [4] V. Judin et al. "Bursting Patterns of Coherent Synchrotron Radiation in the ANKA Storage Ring", IPAC 2013, WEPEA011.
- [5] N. Hiller et al. "Status of Single-Shot EOSD Measurement at ANKA", IPAC 2014, WEOBB02.



ANKA is the Synchrotron Radiation Facility of the Karlsruhe Institute of Technology (KIT). The facility is operated by the Institute for Photon Science and Synchrotron Radiation (IPS) and started user operation in 2003.

As large-scale facility of the Hermann-von-Helmholtz Association of German Research Centers, ANKA is part of the national and European infrastructure offered to scientific and commercial users for performing excellent science and relevant technological development.



The Karlsruhe Institute of Technology (KIT) represents the merger of Universität Karlsruhe (TH) with the Forschungszentrum Karlsruhe. Both partners are joining their forces in KIT in order to achieve an unprecedented quality of cooperation. With approx. 9.300 employees and an annual budget of three-quarter billion €, KIT strives to become a leading institution in selected science disciplines world-wide.



With its 18 research centres and an annual budget of approx 3,8 billion €, the Hermann-von-Helmholtz Association of German Research Centers is Germany's largest research institution. The 36.000 employees produce top-rate scientific results in six research fields. The Helmholtz Association identifies and takes on the grand challenges of society, science and the economy, in particular through the investigation of highly complex systems.

Karlsruhe Institute of Technology (KIT)
ANKA - Synchrotron Radiation Facility
Campus North
Hermann-von-Helmholtz-Platz 1
76344 Eggenstein-Leopoldshafen
URN-Nr.: 90-441013

Directors:

Prof. Dr. Tilo Baumbach,
Prof. Dr. Clemens Heske,
Prof. Dr. Anke-Susanne Müller

www.anka.kit.edu